Analysis of the nonlinear behavior of inserts in sandwich structures : application to an innovative sizing method

Juan de Dios Rodriguez

▶ **To cite this version:**

Juan de Dios Rodriguez. Analysis of the nonlinear behavior of inserts in sandwich structures : application to an innovative sizing method. Mechanics of materials [physics.class-ph]. INSA de Toulouse, 2018. English. NNT : 2018ISAT0019 . tel-01960951

HAL Id: tel-01960951

https://theses.hal.science/tel-01960951

Submitted on 19 Dec 2018

HAL is a multi-disciplinary open access archive for the deposit and dissemination of scientific research documents, whether they are published or not. The documents may come from teaching and research institutions in France or abroad, or from public or private research centers.

L'archive ouverte pluridisciplinaire **HAL**, est destinée au dépôt et à la diffusion de documents scientifiques de niveau recherche, publiés ou non, émanant des établissements d'enseignement et de recherche français ou étrangers, des laboratoires publics ou privés.

Université Fédérale
Toulouse Midi-Pyrénées

THÈSE

En vue de l'obtention du

DOCTORAT DE L'UNIVERSITÉ DE TOULOUSE

Délivré par l'Institut National des Sciences Appliquées de Toulouse

Présentée et soutenue par

Juan de Dios RODRÍGUEZ RAMÍREZ

Le 18 octobre 2018

Analyse du comportement non-linéaire d'inserts de structures sandwichs : application à une méthode de dimensionnement innovante.

Ecole doctorale : **MEGEP - Mécanique, Energétique, Génie civil, Procédés**

Spécialité : **Génie mécanique, mécanique des matériaux**

Unité de recherche :
ICA - Institut Clément Ader

Thèse dirigée par
Bruno CASTANIE et Christophe BOUVET

Jury

M. Peter DAVIES, Rapporteur
M. Philippe VIDAL, Rapporteur
Mme Chiara BISAGNI, Examinateur
M. Pascal THEVENET, Examinateur
M. Bruno CASTANIÉ, Directeur de thèse
M. Christophe BOUVET, Co-directeur de thèse

Acknowledgements

I must thank all the people who surrounded me during these three years and a half. This work would not have been the same without them.

Special mention goes to my thesis advisors, Bruno CASTANIÉ and Christophe BOUVET, who were my examples to follow and who did not hesitate to put me in the right path, many, many times.

Also, to Xavier FOULQUIER Alain BUINOT, Marc CHARTROU, Olivier CHERRIER, Alexander CHARDONEAU et Mickaël DE SAN JOSE without them, this work would have lacked experimental evidence.

To the members of the jury, Peter DAVIES, Philippe VIDAL and Pascal THEVENET, for having kindly accepted to review my work and for their corrections.

To Chiara BISAGNI for accepting being president of the jury despite of his.

Also, to Mathieu DELOUBES, Jean-Paul GIAVARINI, Fatah KHERIS and the SOGECLAIR Aerospace for supporting my work.

To the CONACYT from Mexico for financing my studies, but also to the ICA members and the INSA Toulouse for giving me the opportunity to study in France.

To my friends, wherever you are, without them, this would have been a very short trip.

Many thanks to my family for their very special and unconditional support.

And finally, to Julie, for your kind love during all these years.

Résumé

Mots-clés : Structures Sandwich, Inserts, Nid d'abeille Nomex, E.F. non-linéaire

Introduction

Le dimensionnement des inserts pour les structures sandwich se fait à la lumière de quelques références bibliographiques, telles que le « Insert design handbook » de l'ESA [1], ou le « Military handbook 23A » des États Unis d'Amérique [2], qui recommandent l'usage de méthodes analytiques basées sur le travail de recherche développé par Ericksen en 1953 [3]. Cependant, cette méthode peut mener à des erreurs de la charge admissible d'arrachement d'environ ±20 % [4].

Objectif de la thèse

Le but de cette recherche est d'étudier la rupture des inserts de panneaux sandwich lors des charges d'arrachement.

Puis, il s´agissait de développer une méthode de dimensionnement d'inserts qui soit basée sur la méthode E.F.

Cette méthode devrait fournir des prédictions plus précises que les approches analytiques et au même titre, elle doit être facile et rapide à implanter.

Structure de la thèse.

Cette recherche est divisée en 5 chapitres qui couvrent des aspects différents impliqués dans la conception d'inserts :

- Le premier chapitre contient une introduction générale qui montre le contexte technologique et de recherche autour des inserts pour les panneaux sandwich.
- Le deuxième chapitre concerne l'état de l'art pour l'étude et l'analyse des structures du nid d'abeille Nomex.
- Le troisième chapitre est focalisé sur l'analyse de la rupture en cisaillement du nid d'abeille.
- Le quatrième chapitre, présente une étude des propriétés mécaniques de mousses polymériques syntactiques pour inserts.
- Enfin, dans le cinquième chapitre, tous les développements des chapitres précédents sont intégrés dans le développement d'un modèle E.F, réduit d'insert qui est utilisé extensivement pour tracer des cartes de type de rupture d'inserts.

State of the art of inserts for sandwich structures

Les structures de sandwich ne sont utilisées que pour le cadre principal des hélicoptères, quelques avions d'affaires, et pour les structures secondaires d'avions commerciaux [5]. En effet, ces structures sont très sensibles aux charges concentrées, telles que les impacts ou les sollicitations dues à l'assemblage [6], mais aussi parce que leur fabrication n´est pas encore bien maitrisée.

En ce qui concerne l'assemblage de panneaux sandwich au moyen d'inserts, les principaux problèmes sont les microfissures formées par la fatigue et le vieillissement du

potting, mais aussi le manque de compréhension du scénario de rupture après l'arrachement [7].

Selon plusieurs chercheurs, lorsqu'un insert est soumis à l'arrachement, l'évidence expérimentale suggère que la rupture des inserts est principalement occasionnée par l'endommagement de l'âme en cisaillement. En conséquence, la charge admissible de l'insert doit être proportionnelle à la résistance en cisaillement du nid d'abeille [8].

Pour cette raison, les modélisations mathématiques qui servent à calculer la charge admissible des inserts sont basées sur la résistance en cisaillement de l'âme. Et la plupart d'entre eux sont basées sur l'approche proposé par Ericksen en 1953. Cependant, même si ce modèle donne une approximation acceptable de la charge maximale (environ ±20 % d'erreur), le modèle est complexe et n'est pas simple pour l´implantation.

Aussi, étant donné que la rupture du nid d'abeille en cisaillement est directement liée à la rupture des inserts, une très bonne compréhension du comportement non linéaire en cisaillement du nid d'abeille est nécessaire afin de mieux comprendre la rupture des inserts.

Jusqu'à présent, la plupart de recherches sur le nid d'abeille se sont focalisées sur le comportement en compression ; seulement quelques-unes avaient été recensées sur le comportement en cisaillement.

Les modèles analytiques pour estimer la résistance en cisaillement du nid d'abeille se base sur l'hypothèse selon laquelle sa résistance est donnée au moment même où les cellules commencent à flamber [9], [10]. Cependant, ces modèles ne considèrent pas le post flambement élastique des cellules, et en conséquence, leurs estimations restent très éloignées de la réalité. Pour cette raison d'autres approches ont été utilisées par les chercheurs, comme la simulation numérique [11], [12].

Étude sur le comportement du nid d'abeille en cisaillement.

La première partie de cette recherche est focalisée sur l'étude expérimentale et numérique du nid d'abeille Nomex en cisaillement.

Quatre types d'éprouvettes ont été testées au moment où un système de corrélation d'image 3D enregistrait et mesurait simultanément le flambement des cellules.

De ces expériences, il a été possible de constater que le flambement des cellules est très complexe et que les conditions limites des cellules ont une grande influence sur les modes de flambement. De ce fait, l'évidence expérimentale suggère que les cellules collapsent de façon graduelle et non toutes en même temps.

Aussi, il a été observé que le flambement des cellules se produit même quand les contraintes de cisaillement sont très faibles. Cela indique qu'il n'est pas correct de définir un critère de faille du nid d'abeille en cisaillement basée sur le début du flambement des cellules.

De plus, il a été constaté que le flambement des cellules est élastique et réversible jusqu'à un certain point et que les conditions limites de ces dernières sont très importantes pour sa stabilité.

Puis, le même problème s´est présenté sur le plan numérique. Plusieurs modèles ont été développés sur Abaqus pour mieux comprendre le flambement des cellules à l'intérieur du nid d'abeille. Les modèles ont montré une bonne corrélation avec les résultats expérimentaux et il a été possible de décrire les différentes étapes du comportement non linéaire en cisaillement du nid d'abeille. Les conclusions et résultats obtenus ont mené à faire une publication sur ce sujet[13].

Finalement, une approche simplifiée pour considérer le flambement des cellules a été proposée. Cela permet de réduire le temps d'analyse de façon significative, de quelques heures à quelques minutes. Une autre publication sur ce sujet a été faite aussi [14].

Étude de la mousse syntactique pour inserts de panneaux sandwich

Les propriétés mécaniques de la mousse syntactique utilisée pour les inserts ont été étudiées. Une campagne d´essais expérimentaux a été menée pour étudier les propriétés en traction et compression. Aussi une autre campagne d'essais technologiques a été réalisée pour observer une rupture similaire à celle du potting lors qu'un essai d'arrachement d'insert est fait.

Le comportement classique des mousses syntactiques a été observé lorsque les essais de traction et compression ont été réalisés. La mousse devenait souple lorsque la concentration de microsphères augmente, et plus rigide quand il y avait moins de microsphères. Aussi, il a été constaté qu'en traction la rupture de la mousse se produit comme pour les matériaux fragiles. Alors que qu'en compression le matériau a un comportement très similaire à la plasticité parfaite.

Les essais technologiques ont permis d'observer des modes de rupture très similaires à ce qui arrive quand les inserts sont arrachés. La première rupture est la fracture du matériau due à la traction. Et la deuxième, la compression de la mousse quand le fastener n'est pas bien collé avec le potting.

En même temps, il a été possible de tester différentes configurations de spécimens et différentes concentrations des composants de la mousse en simultané au dégraissement des pièces métalliques. Puis, les résultats ont été comparés et plusieurs aspects intéressants ont été remarqués.

Quand la concentration de durcisseur était plus grande que celle recommandée par le fournisseur, la mousse devenait très souple et non fonctionnelle. D'autre part, quand la concentration de micro sphères était proche de 15 % du poids pondéral de la résine, la propriété de collage du potting devenait défectueuse, la même chose se produisait lorsque les pièces métalliques n'étaient pas dégraissées.

D'autre part, on pouvait constater lorsque la quantité de microsphères était inférieure à 11% du poids pondéral, quand les pièces métalliques étaient bien dégraissées et quand les spécimens ont été polymérisés à température ambiante.

Puis, une modélisation numérique du comportement en compression et traction de la mousse est proposée en utilisant un modèle de plasticité parfaite pour la compression, et une approche d'endommagement progressif pour la traction.

Cartes de rupture des inserts basées sur des essais virtuels

Les méthodes analytiques pour estimer la charge admissible à l'arrachement des inserts comportent en général une erreur d'environ ±20 %. Cette différence peut être attribuée à différentes causes.

La première est le grand nombre de paramètres qui doivent être utilisés pour les équations analytiques, qui s'ils ne sont pas correctement sélectionnés, peuvent conduire à des erreurs importantes.

Deuxièmement, le fait que les inserts soient la plupart du temps installés à la main, peut conduire à avoir des défauts très importants, notamment pour la taille de l'insert et le remplissage des cellules du nid d'abeille.

Pour cette raison, une étude de l'influence des défauts dans les inserts a été menée.

Les résultats de cette étude pour classifier les défauts des inserts peuvent se diviser en sept catégories :

- La forme du potting de l'insert
- Un faible collage entre le potting et le fastener
- La présence des boules d'air dans le potting.
- Les bords irréguliers du potting
- Un remplissage incomplet des cellules
- Des variations dans la concentration de microsphères
- Quand la taille du potting est insuffisante pour contenir le fastener.

De ces sept défauts, seulement deux doivent être considérés pour la conception d'inserts car son influence et sa fréquence d'apparition sont importantes. Il s'agit des bords irréguliers du potting et la variation de la taille de l'inserts.

Par la suite, un modèle d'insert virtuel est développé en utilisant les modélisations numériques des différents composants précédents, notamment pour le nid d'abeille et le potting. Aussi, les résultats de l'analyse des défauts d'inserts sont utilisés pour le développement de ce modèle.

Pour valider le modèle numérique d'insert, il est comparé à des essais d'arrachement des inserts testes expérimentalement par Bunyawanichakul lors de sa thèse [15]. Puisque l'influence des défauts est prise en compte, deux modélisations sont faites, la première considérant les pires cas, quand la taille de l'insert est petite, que les bords sont irréguliers et que le potting n'est pas collé au fastener. Et le deuxième, quand il n'y a pas de défauts, le cas d'un insert idéal.

Les résultats montrent que les courbes expérimentales se trouvent dans l'enveloppe crées à partir des simulations numériques du meilleur et pire des cas. Ce qui suggère que le modèle virtuel donne des résultats cohérents et assez précis.

Finalement, ce modèle numérique est utilisé intensivement pour créer des cartes de mode de rupture d'inserts. Plus d´une centaine de simulations et analyses ont été réalisées pour développer ces cartes de rupture qui montrent les charges admissibles avant le premier endommagement de l'insert et le type d'endommagement qui doit se produire selon la taille de l'insert, la résistance du matériau de potting, l'épaisseur des peaux du sandwich et la résistance du nid d'abeille.

Ces types de cartes peuvent être fournis aux ingénieurs pour accélérer le processus de essai/calcul pour le dimensionnement d'inserts.

Index

CHAPTER ONE: GENERAL INTRODUCTION 1

1.1 FROM AIRCRAFT TO INSERTS 3
1.1.1 The sandwich structure 3
1.1.2 Sandwich panels joints; a problem still to be investigated 5
1.1.3 Remarks on the insert design methods 7
1.1.4 Objectives of the thesis 8
1.1.5 Summary of the thesis 9

CHAPTER TWO: STATE OF THE ART OF INSERTS FOR SANDWICH STRUCTURES 11

2.1 INSERTS FOR SANDWICH STRUCTURES 13
2.1.1 Types 13
2.1.2 Testing standards 17
2.1.3 Pull-out experimental testing of inserts 18
2.1.4 Strength prediction of inserts by analytical approaches 31
2.1.5 Strength prediction of inserts by numerical approaches 45
2.1.6 Conclusions of the state of the art of insert analysis 52
2.2 SHEAR BUCKLING OF NOMEX® HONEYCOMB CORES 55
2.2.1 The honeycomb structure 55
2.2.2 Properties of the Nomex® paper 57
2.2.3 Shear testing of honeycomb cores 59
2.2.4 On the shear behavior of honeycomb cores. 61
2.2.5 Conclusions on the honeycomb's shear buckling 65

CHAPTER THREE: EXPERIMENTAL AND NUMERICAL ANALYSIS OF HONEYCOMB CORES 67

3.1 INTRODUCTION 69
3.1.1 Objectives and proposed methods 69
3.2 BENCHMARK OF SPECIMENS FOR SHEAR TESTING OF HONEYCOMB CORES 73
3.2.1 Specimens description 73
3.2.2 Verdict and test results 75
3.2.3 Conclusions 79
3.3 SHEAR TESTING OF HONEYCOMB CORES 81
3.3.1 Specimen fabrication 81
3.3.2 Test setup 83
3.3.3 Test results 84
3.3.4 Analysis of the buckling and postbuckling behavior of the cells 86
3.3.5 Conclusions 94
3.4 NUMERICAL STUDY OF SHEAR BUCKLING OF HONEYCOMB CELLS 99
3.4.1 Properties of the T-722 Nomex® paper 99
3.4.2 Study of the shear buckling of the Nomex® honeycomb core 100
3.4.3 Conclusions of the numerical analysis of the shear buckling 107
3.5 EXPERIMENTAL AND NUMERICAL STUDY OF THE CORE BOUNDARY CONDITIONS FOR INSERTS. 111
3.5.1 Numerical study 111
3.5.2 Experimental study 116
3.5.3 Conclusions on the boundary conditions 118
3.6 REDUCED CDM MODELING STRATEGY OF THE NONLINEAR SHEAR BEHAVIOR OF HONEYCOMB CORES 121
3.6.1 Analysis of the nonlinear shear stages of the honeycomb 121
3.6.2 Decoupled CDM approach for the shear behavior of honeycomb cores 124
3.6.3 Validation of the proposed approach 128
3.6.4 Conclusions 134
3.7 CONCLUSIONS 135

CHAPTER FOUR: STUDY OF SYNTHETIC POLYMER FOAMS FOR INSERTS 137

4.1 INTRODUCTION 139
4.1.1 Potting failure of inserts 139
4.1.2 Syntactic polymer foams as insert's potting material 140
4.1.3 Objectives and proposed methods 143
4.2 MECHANICAL CHARACTERIZATION OF SPF FOR THE INSERT'S POTTING 145
4.2.1 Study of the potting under uniaxial tension and compression 145
4.2.2 Study of the potting failure in inserts 151
4.2.3 Conclusions of the experimental study 159
4.3 NUMERICAL STUDY 161
4.3.1 Modeling of the potting behavior 161
4.3.2 Modeling of the potting pull-out tests 165
4.3.3 Results and discussion 166
4.4 CONCLUSIONS 169

CHAPTER FIVE: VIRTUAL TESTING OF INSERTS AND FAILURE MODE MAPS 171

5.1 INTRODUCTION 173
5.1.1 Insert sizing through the analytical methods 173
5.1.2 Insert sizing through F.E. modeling 175
5.1.3 Proposed methods 176
5.2 STUDY OF DEFECTS IN INSERTS 179
5.2.1 Analysis of the different defects of inserts 180
5.2.2 Evaluation of the criticality of defects in inserts 184
5.2.3 Analysis of variations of the potting radius 187
5.2.4 Conclusions about the defects in inserts 193
5.3 DEVELOPMENT OF THE INSERT F.E. MODEL 195
5.3.1 Description of the insert's experimental reference 195
5.3.2 Insert F.E. model features 206
5.3.3 Implementation of the behavior laws 208
5.3.4 Parametrization of the F.E. with Abaqus scripting 221
5.3.5 Conclusion about the F.E. modeling of inserts 223
5.4 DEVELOPMENT OF THE FAILURE MODE MAPS 225
5.4.1 Exploration of the influence of the principal design variables 225
5.4.2 Sweep of the real potting radius: from 9.5 to 23.5 mm 228
5.4.3 Swept of the potting properties 228
5.4.4 Sweep of the skin thickness 229
5.4.5 Failure mode maps 230
5.4.6 Insert mass optimization 235
5.4.7 Loss of linearity criteria (LLC) vs first failure criterion (FFC) 237
5.5 CONCLUSIONS 239

GENERAL CONCLUSIONS AND PERSPECTIVES 241

REFERENCES 247

ANNEX A: TABLES OF THE REAL POTTING RADIUS FOR INSERTS 253

List of figures

FIG. 1: STRUCTURAL USAGE OF COMPOSITES IN THE BOEING 787.[4], [5]. 3
FIG. 2: GENERAL DESCRIPTION OF A SANDWICH STRUCTURE. 4
FIG. 3: THE STARSHIP AND THE RAYTHEON PREMIERE I. 4
FIG. 4: RADAR ABSORBING SANDWICH PANELS WERE USED TO BUILD ZUMWALT-CLASS DESTROYER [13]. 5
FIG. 5: USE OF SANDWICH PANELS ON THE BOEING 767 [14] 6
FIG. 6: DIFFERENT TECHNIQUES TO JOIN PANELS: DIRECTLY BONDING THEM, ADDING REINFORCEMENTS OR DENSIFYING CORNERS OF THE CORE TO INCREASE ITS MECHANICAL PROPERTIES. [11] 6
FIG. 7: HIGH LOAD INSERT ON THE LANDING GEAR DOOR OF THE AIRBUS A330 7
FIG. 8: THESIS WORK PRESENTATION 9
FIG. 9: SEVERAL TYPES OF SANDWICH JOINTS [27]. 13
FIG. 10: COMPARISON OF THE SHUR-LOK FASTENER APPLICATIONS [35]. 14
FIG. 11: A) FORCE DISTRIBUTION OF A SCREW B) MECHANICAL FASTENER BEFORE INSTALLATION C) INSTALLED MECHANICAL FASTENER [6], [19], [36]. 15
FIG. 12: PARTIAL INSERT INSTALLATION PROCEDURE [32]. 15
FIG. 13: CUT OF A) A FULL POTTING INSERT, THE POTTING IS BONDED TO BOTH SKINS B) PARTIAL INSERT, BONDED TO ONLY ONE SKIN [20]. 16
FIG. 14: THROUGH THE THICKNESS INSERTS; A) HIGH LOAD CARRYING CAPABILITY INSERT TYPE AIRBUS [19] B) WITH FASTENER [20]. 16
FIG. 15: TEST STANDARDS OF A) SHEAR TESTING, B) PULL-OUT TEST, C) TORQUE TEST, [27], [39]. 18
FIG. 16: DAMAGE IDENTIFICATION [19]. 19
FIG. 17: EUROCOPTER INSERTS TYPE 1, 2 AND 3, [19]. 20
FIG. 18: PULL-OUT TEST OF A FULL POTTING INSERT [42]. 21
FIG. 19: PULL-OUT TEST SPECIMENS CUT IN HALF, SEVERAL FAILURE MODES WERE DETECTED [42]. 21
FIG. 20: INSERT DESCRIPTION AND FAILURE LOADS OF THE TESTS MADE BY SONG [33]. 22
FIG. 21: LOAD VS DISPLACEMENT CURVE AND SPECIMEN DESCRIPTION [26]. 22
FIG. 22: PULL-OUT FORCE VARIATION OF SEVERAL TESTS [20]. 22
FIG. 23: DAMAGE OF A PARTIAL INSERT IN A SHEAR TEST [32]. 23
FIG. 24: DETACHING OF THE FASTENER OF A SANDWICH PANEL INSERT, THIS MAY SUGGEST THAT THE POTTING WAS THE FIRST ELEMENT TO FAIL [32]. 23
FIG. 25: DAMAGE OF A PARTIAL INSERT IN A PULL-OUT TEST [27]. 24
FIG. 26: TESTING OF INSERTS OF DIFFERENT CHARACTERISTICS [21]. 24
FIG. 27: PULL-OUT TESTS OF INSERTS IN SANDWICH PANELS WITH ALUMINUM HONEYCOMB CORE [37]. 25
FIG. 28: PULL-OUT TEST PRESENTED BY BIANCHI [34]. 26
FIG. 29: POST IMPACT BEHAVIOR OF INSERTS PRESENTED BY MEZEIX [43]. 26
FIG. 30: PARAMETERS OF THE SANDWICH PANEL FOR THE MODEL OF ERICKSEN 31
FIG. 31: SHEAR STRESS DISTRIBUTION OF THE CORE ACCORDING TO [3] AND T VALUES TO CALCULATE THE MAXIMAL SHEAR STRESS USING EQ. 4. 33
FIG. 32: K_3 COEFFICIENT REPRESENTING THE SHEAR STRESS DISTRIBUTION IN THE CORE [44]. 34
FIG. 33: STRESS AND STRAIN OF THE SKINS GIVEN BY THE THOMSEN MODEL [46]. 35
FIG. 34: SIMPLIFICATION OF THE INSERT BY USING THE DIRECT APPROACH BY SIMPLE SHEAR [19]. 36
FIG. 35: APPROACH DESCRIPTION AND SHEAR STRESS DISTRIBUTION IN FUNCTION OF THE RADIUS AND SANDWICH PARAMETERS [2], [19]. 38
FIG. 36: ABACUS PROVIDED FOR THE SIZING OF INSERTS, THIS USES THE INSERT GEOMETRICAL AND MECHANICAL PARAMETERS TO CALCULATE THE K_3 COEFFICIENT [2]. 40
FIG. 37: MINIMAL AND AVERAGE Pss IN FUNCTION OF THE CORE HEIGTH AND THE THICKNESS OF THE SKINS [29]. 41
FIG. 38: FAILURE MODE VS CORE HEIGHT [1]. 42
FIG. 39: DISTRIBUTION OF THE SHEAR STRESS NEAR THE INSERT [29]. 42
FIG. 40: A) F.E. MODELING OF THE INSERT, AND B) : NONLINEAR BEHAVIOR AND DAMAGE SCENARIO [28]. 46

FIG. 41: REDUCED MODEL OF A PARTIAL INSERT [27]. 47
FIG. 42: A) TRANSVERSE SHEAR STRESS FOR THREE DIFFERENT POTTING HEIGHTS (MPA) IN A PULL-OUT TEST, B) SHEAR STRESS DISTRIBUTION THROUGH THE THICKNESS OF THE CORE AT A RADIUS OF 10.5 MM [20]. 47
FIG. 43: VIRTUAL TESTING OF INSERTS [21]. 48
FIG. 44: BUCKLING SIMULATION OF THE CORE OF AN INSERT BY ROY [26]. 49
FIG. 45: VARIATION OF THE POTTING GEOMETRIES FOR THE SAME PERFORATION RADIUS [25]. 50
FIG. 46: COMPARISON OF THE ANALYTICAL MODEL VS THE F.E. CALCULATION OF THE SHEAR STRESS IN THE CORE [25]. 50
FIG. 47: MODEL PARAMETERS AND DESCRIPTION [24]. 51
FIG. 48: SENSITIVITY OF THE DIFFERENT PARAMETERS ACCORDINGLY TO [24]. 51
FIG. 49: SENSITIVITY OF THE DIFFERENT PARAMETERS ACCORDINGLY TO THE ESA INSERT DESIGN HANDBOOK [1]. 52
FIG. 50: MANUFACTURING PROCESS OF NOMEX® HONEYCOMBS [53]. 55
FIG. 51: REGULAR GEOMETRIC FIGURES THAT ALLOWS FOR TESSELLATION. 56
FIG. 52: COMMON DEFECTS OF THE NOMEX® HONEYCOMB CELLS [57]. 57
FIG. 53: LOAD VS STRAIN CURVES IN THE FIBER AND TRANSVERSE DIRECTION OF THE NOMEX® PAPER [59]. 58
FIG. 54: TENSILE TESTS ON A) THE NOMEX® PAPER T-410 ALONE, B) THE NOMEX® PAPER WITH A THICK PHENOLIC COATING (BECOMES BRITTLE) [52]. 58
FIG. 55: TENSILE TESTS ON A COATED NOMEX® PAPER BY FISCHER [60]. 59
FIG. 56: THE NOMEX® HONEYCOMB STRUCTURE UNDER THE MICROSCOPE, THE PHENOLIC RESIN LAYER IS VISIBLE [62]. 59
FIG. 57: DIFFERENT SHEAR TESTING SPECIMENS FOR HONEYCOMB CORES: A) DOUBLE BLOCK, B) THREE-POINT BENDING, C) SINGLE BLOCK, D) FOUR-POINT BENDING TESTS, E) DOUBLE-DOUBLE BLOCK [63], [64], [66]. 60
FIG. 58: SHEAR TESTING OF HONEYCOMB CORES; EXPERIMENTAL VS NUMERICAL SCENARIOS [62]. 62
FIG. 59: MODELING OF A THREE POINT BENDING [74]. 62
FIG. 60: VIRTUAL SHEAR TESTING OF HONEYCOMB CORES [53]. 63
FIG. 61:IMPACT MODELING OF A NOMEX® HONEYCOMB SANDWICH PANEL; NUMERICAL VS EXPERIMENTAL RESULTS [75]. 64
FIG. 62: MODELING OF THE IMPACT ON AN ALUMINUM SANDWICH PANEL, EXPERIMENTAL VS NUMERICAL RESULTS [77]. 64
FIG. 63: IDENTIFICATION OF THE EFFECTIVE DAMAGE OF THE HONEYCOMB CORE. 70
FIG. 64: COMPARISON OF THE BUCKLING PATTERN OF TWO NOMEX® HONEYCOMB CORES SUBJECTED TO SHEAR LOADS: (A) AN INSERT SPECIMEN AFTER A PULL-OUT TEST WHERE THE CELLS HAVE PLASTICIZED (EXTRACT FROM [19]), VERSUS (B) A SINGLE RAIL SHEAR TEST (REPRODUCED FROM SEEMANN [53]). 71
FIG. 65: SPECIMENS FABRICATED FOR THE BENCHMARK STUDY AND TESTING OF A SINGLE RAIL SPECIMEN. 73
FIG. 66: CHARACTERISTICS OF THE MODIFIED DOUBLE LAP SPECIMEN. 75
FIG. 67: REPRESENTATIVE CURVES OF THE AVERAGE SHEAR STRESS VS GAMMA FOR THE DIFFERENT TYPE OF SPECIMENS. 76
FIG. 68: DISPLACEMENT FIELD MEASURED IN THE OUT-OF-PLANE DIRECTION OF THE SANDWICH BEAM. 76
FIG. 69: DISPLACEMENT FIELD MEASURED IN THE OUT-OF-PLANE DIRECTION THE DOUBLE LAP SPECIMEN. 77
FIG. 70: DISPLACEMENT FIELD MEASURED IN THE OUT-OF-PLANE DIRECTION OF THE DOUBLE SINGLE LAP SPECIMEN. 78
FIG. 71: COMPARISON OF THE SHEAR CURVES OF THE NORMAL AND MODIFIED DOUBLE LAP SPECIMENS. 79
FIG. 72: SPECIMEN DESCRIPTION FOR THE SHEAR TESTING OF HONEYCOMBS. 81
FIG. 73: ASSEMBLY OF THE TEST SPECIMENS, B) SPECIMENS IN THE MOLDS C) SPECIMENS READY FOR THE SECOND CURING PROCESS, D) MOLDS IN THE OVEN. 82
FIG. 74: THE 10 KN INSTRON MACHINE AND THE 2 VIC 3D CAMERAS. 83
FIG. 75: TEST RESULTS OF THE HRH-10 HONEYCOMB CORE. 84
FIG. 76: TEST RESULTS OF THE ALU 5052 HONEYCOMB CORE. 84
FIG. 77: AVERAGE SHEAR STRESS VS GAMMA CURVES OF THE HRH-78 IN W AND L DIRECTION. 85
FIG. 78: INCREMENTAL CYCLIC TESTING OF THE SPECIMEN 9. 85
FIG. 79: INCREMENTAL CYCLIC TESTING OF THE HRH-78 CORE: AVERAGE SHEAR STRESS VS GAMMA. 86
FIG. 80: EVOLUTION OF OUT-OF-PLANE DISPLACEMENTS MEASURED FROM A) 0 MM TO 0.04 MM AND B) 0 MM TO -0.04 MM. 87
FIG. 81: BUCKLING OF THE CELLS AT 0.24 MPA AND 0.4 MPA. 88
FIG. 82: BUCKLING EVOLUTION OF A CELL: FROM INITIAL BUCKLING TO COLLAPSE. 89
FIG. 83: NUMBER OF BUCKLES VS AVERAGE SHEAR STRESS AND GAMMA. 90
FIG. 84: BUCKLED CELLS AND AVERAGE SHEAR STRESS COMPARISON, ANALYSIS MADE BY OURSELVES. 91
FIG. 85: DESCRIPTION OF AN ARTIFICIAL NEURON. 92

FIG. 86: DESCRIPTION OF THE PRETREATMENT OF THE TEST VIDEOS. 92
FIG. 87: IMAGE OF CELLS BEFORE AND AFTER COLOR SEGMENTATION. 93
FIG. 88: EXAMPLES OF COLLAPSING AND NON-COLLAPSING CELLS TO TRAIN THE ANN. 94
FIG. 89: COLLAPSE OF THE CELLS ACCORDING TO THE RESULTS GIVEN BY THE ANN VS THE AVERAGE SHEAR STRESS. 94
FIG. 90: FAILURE SCENARIO OF THE SPECIMENS. 95
FIG. 91: COMPARISON OF A SPECIMEN BEFORE AND AFTER THE TEST. 97
FIG. 92: CELL WALL BOUNDARY CONDITIONS AND BUCKLING MODES. 100
FIG. 93: BUCKLING OF A CELL WALL (OUT-OF-THE-PLANE DISPLACEMENT) AND FORCE VS DISPLACEMENT CURVE. 101
FIG. 94: SINGLE CELL BOUNDARY CONDITIONS AND BUCKLING MODES. 102
FIG. 95: BUCKLING OF A SINGLE CELL (SCALE: 0 TO -0.1054 MM) AND FORCE VS DISPLACEMENT CURVE. 103
FIG. 96: THE BUCKLING SHAPE SUGGESTS THE IMPORTANCE OF THE SURROUNDING CELLS. 103
FIG. 97: BOUNDARY CONDITIONS OF THE DOUBLE LAP TEST MODEL. 104
FIG. 98: REAL TESTS VS SIMULATION OF HRH-78. 105
FIG. 99: CELL BUCKLING EXPERIENCED BY THE EXTERIOR AND THE INTERIOR OF THE SPECIMEN OF THE DOUBLE LAP TEST. 105
FIG. 100: AVERAGE SHEAR STRESS VS NODAL ROTATION OF THE DOUBLE LAP F.E. MODEL. 106
FIG. 101: AVERAGE SHEAR STRESS VS GAMMA OF THE DOUBLE LAP F.E. MODEL: WHEN THE NOMEX® PAPER WAS CONSIDERED TO BE TOTALLY ELASTIC THE CELLS DOESN'T COLLAPSE. 107
FIG. 102: DESCRIPTION OF THE NONLINEAR BEHAVIOR OF THE NOMEX® HONEYCOMB CORE HRH-78. 108
FIG. 103: CELL BUCKLING EXPERIENCED BY THE EXTERIOR AND THE INTERIOR OF THE SPECIMEN OF THE DOUBLE LAP TEST. 111
FIG. 104: CHARACTERISTICS OF THE SANDWICH BEAM MODEL WITH POTTING RESIN AT THE BORDERS. 112
FIG. 105: BUCKLING OF THE EXTERIOR AND INTERIOR CELLS OF THE SANDWICH BEAM WITH POTTING RESIN AT THE BORDERS. 113
FIG. 106: AVERAGE SHEAR STRESS VS GAMMA: DOUBLE LAP TESTS AND SANDWICH BEAM WITH POTTING AT THE BORDERS. 114
FIG. 107: AVERAGE SHEAR STRESS VS TOTAL NODAL ROTATION OF THE ELEMENTS: DOUBLE LAP TESTS VS SANDWICH BEAM WITH RESIN AT THE BORDERS. 114
FIG. 108: CHARACTERISTICS OF THE MODEL OF THE HONEYCOMB CORE WITHOUT SKINS. 115
FIG. 109: BUCKLING OF THE CELLS AND THE AVERAGE SHEAR STRESS VS GAMMA: THREE CASES. 115
FIG. 110: CHARACTERISTICS OF SANDWICH BEAM SPECIMENS WITH POTTING AT THE BORDERS. 116
FIG. 111: TESTING OF THE SANDWICH BEAM SPECIMENS WITH RESIN AT THE BORDERS, BEFORE AND AFTER THE TESTS. 117
FIG. 112: CURVES OF THE DOUBLE LAP TESTS VS THE SANDWICH BEAM TEST WITH POTTING AT THE BORDERS (W-DIRECTION). 118
FIG. 113: CURVES OF THE DOUBLE LAP TESTS VS THE SANDWICH BEAM TEST WITH POTTING AT THE BORDERS (L-DIRECTION). 118
FIG. 114: INCREMENTAL CYCLIC TESTING OF THE HTH-78 CORE: DAMAGED SHEAR BEHAVIOR OF THE HONEYCOMB STRUCTURE. 122
FIG. 115: CHANGE ON THE SHEAR STIFFNESS OF THE STRUCTURE: "ELASTIC BUCKLING" OF THE CELLS VS "BUCKLING & COLLAPSE" OF THE CELLS IN THE W DIRECTION. 122
FIG. 116: DETECTION OF THE COLLAPSE OF THE CELLS IN THE W DIRECTION THROUGH AN ANN (REMINDER). 123
FIG. 117: FITTING OF THE CURVE OF PERCENTAGE OF CELLS ABOUT TO BUCKLE WITH A PROBABILITY DISTRIBUTION FUNCTION; THE PROBABILITY DENSITY IS SHOWN IN BLUE. 124
FIG. 118: AVERAGE CURVES OF THE "DOUBLE RAIL TESTS" VS THE "SANDWICH BEAM WITH POTTING AT THE BORDERS". 125
FIG. 119: COMPARISON OF THE CELLS RIPPING IN A 3-POINT BENDING TEST WITH POTTING RESIN AT THE BORDERS AND A DOUBLE RAIL TEST. 125
FIG. 120: FITTING OF THE EXPERIMENTAL RAIL SHEAR TESTING CURVES OF THE HRH-78 IN THE W AND L DIRECTIONS USING THE CDM PROPOSED APPROACH. 127
FIG. 121: DENSITY DISTRIBUTION CURVES REPRESENTING THE BUCKLING AND COLLAPSE STAGES OF THE CELLS. 128
FIG. 122: MESH OF THE DOUBLE RAIL TEST MODEL. 129
FIG. 123: FORCE VS DISPLACEMENT CURVES OF THE DOUBLE RAIL TESTS: EXPERIMENTAL VS NUMERICAL RESULTS FOR THE W DIRECTION. 129
FIG. 124: MESH OF THE SANDWICH BEAM WITH POTTING AT THE BORDERS. 130
FIG. 125: FITTING OF THE EXPERIMENTAL SANDWICH BEAM WITH POTTING AT THE BORDER IN THE L DIRECTION USING THE CDM PROPOSED APPROACH THAT CREATES CONVERGENCE ISSUES. 131

FIG. 126: FITTING OF THE EXPERIMENTAL SANDWICH BEAM WITH POTTING AT THE BORDER IN THE L DIRECTION; LAW 2 AVOIDS CONVERGENCE ISSUES (SEE TABLE 10). 131
FIG. 127: FORCE VS DISPLACEMENT CURVES OF THE SANDWICH BEAM TESTS: EXPERIMENTAL VS NUMERICAL RESULTS. 132
FIG. 128: COMPARISON OF THE FAILURE SCENARIO OF THE NUMERICAL MODEL VS REAL TESTS, THE RESULTS ARE CONSISTENT. 132
FIG. 129: FORCE VS DISPLACEMENT CURVES OF THE SANDWICH BEAM TESTS: EXPERIMENTAL VS NUMERICAL RESULTS. 133
FIG. 130: TWO DIFFERENT LAWS ARE USED TO MODEL THE SHEAR BEHAVIOR OF THE HRH-78 CELLS, WITH AND WITHOUT THE EFFECT OF THE LATERAL STABILIZATION OF THE CELLS. 133
FIG. 131: FAILURE SCENARIO AFTER A PULL-OUT TEST PERFORMED BY YONG AND HEIMBS [32], [27]. 139
FIG. 132: FAILURE SCENARIO AFTER A PULL-OUT TEST PERFORMED TO DIFFERENT TYPE OF INSERTS. [19] 139
FIG. 133: DIFFERENCE BETWEEN THE FAILURE IN TRACTION AND COMPRESSION OF SYNTACTIC FOAMS. [90]141
FIG. 134: COMPARISON OF THE ANALYTICAL ESTIMATION VS THE EXPERIMENTAL RESULTS BY [90]..... 142
FIG. 135: CLASSICAL BEHAVIOR OF SYNTACTIC FOAMS IN COMPRESSION AND TRACTION BY [90] 142
FIG. 136: POTTING UNDER THE MICROSCOPE 143
FIG. 137: COMPRESSION TESTS MADE BY BUNYAWANICHAKUL ON THE ADHESIVE AV121-B ALONE WITH AND WITHOUT POROSITIES. 145
FIG. 138: SIZE OF THE COMPRESSION SPECIMENS AND VIEW OF THE SURFACES UNDER THE MICROSCOPE. .. 147
FIG. 139: SHAPE AND SET UP OF THE TRACTION TESTS SPECIMENS. 147
FIG. 140: EXPERIMENTAL CURVES OF THE TENSILE TESTS OF THE POTTING. 148
FIG. 141: TEST RESULTS OF THE COMPRESSION TESTS OF THE POTTING 149
FIG. 142: DENSITY OF THE SPF AS FUNCTION OF THE MICRO-SPHERES CONCENTRATION. 149
FIG. 143: EXPERIMENTAL EFFECTIVE YOUNG MODULI IN TRACTION AND COMPRESSION AS FUNCTION OF THE MICRO-SPHERES CONCENTRATION. 150
FIG. 144: RESISTANCE TO FAILURE UNDER TRACTION AND COMPRESSION AS FUNCTION OF THE MICRO-SPHERES CONCENTRATION. 150
FIG. 145: TEST SPECIMENS SUBJECTED TO PULL-OUT. 151
FIG. 146: GEOMETRY OF THE RODS AND POTTING CONTAINERS. 152
FIG. 147: TEST SET UP AND MEASURING OF THE PULL-OUT DISPLACEMENT OF THE ROD 154
FIG. 148: EXPERIMENTAL RESULTS OF THE TEST SPECIMENS TYPE 1. 154
FIG. 149: EXPERIMENTAL RESULTS OF THE TEST SPECIMENS TYPE 2. 155
FIG. 150: EXPERIMENTAL RESULTS OF THE TEST SPECIMENS TYPE 3. 155
FIG. 151: EXPERIMENTAL RESULTS OF THE TEST SPECIMENS TYPE 4. 156
FIG. 152: SUPPOSED POTTING FAILURE DUE TO TRACTION OF SPECIMENS EP1 AND EP5. 157
FIG. 153: CAUSES OF THE DETACHING OF THE METALLIC ROD. 158
FIG. 154: FAILURE OF THE POTTING IN SHEAR 159
FIG. 155: COMPARISON OF THE FAILURES OF INSERTS AND THE POTTING TEST; THE FASTENER WAS FIRMLY BONDED. 160
FIG. 156: COMPARISON OF THE FAILURES OF INSERTS AND THE POTTING TEST; THE FASTENER WAS NOT BONDED. 160
FIG. 157: ALGORITHM IMPLEMENTED IN TO AN UMAT TO REPRESENT THE POTTING MATERIAL BEHAVIOR. . 162
FIG. 158: COMPARISON OF THE EXPERIMENTAL AND NUMERICAL LAWS FOR THE POTTING WITH 7% OF MICRO-SPHERES 163
FIG. 159: COMPARISON OF THE EXPERIMENTAL AND NUMERICAL LAWS FOR THE POTTING WITH 10% OF MICRO-SPHERES 163
FIG. 160: COMPARISON OF THE EXPERIMENTAL AND NUMERICAL LAWS FOR THE POTTING WITH 13% OF MICRO-SPHERES 164
FIG. 161: MODELING OF THE TRACTION AND COMPRESSION TESTS. 164
FIG. 162: EXPERIMENTAL VS NUMERICAL RESULTS; TRACTION AND COMPRESSION TESTS. 165
FIG. 163: MODELING OF THE POTTING PULL-OUT TESTS. 165
FIG. 164: COMPARISON OF THE VERTICAL DISPLACEMENT FIELD BETWEEN THE EXPERIMENTAL AND NUMERICAL RESULTS FOR EP1 AND EP9 SPECIMENS. 166
FIG. 165: EXPERIMENTAL VS NUMERICAL RESULTS: LOADING CURVES OF THE SPECIMENS' TYPE 1 AND 2. 167
FIG. 166: EXPERIMENTAL VS NUMERICAL RESULTS: LOADING CURVES OF THE SPECIMENS' TYPE 3 AND 4. 167
FIG. 167: EFFECTIVE YOUNG MODULI: OBTAINED VALUES VS THE PREDICTION OF THE RULE OF MIXTURES... 168
FIG. 168: EXAMPLE OF THE APPLICATION OF THE ESA METHOD TO THE INSERT TYPE 1 (SEE NEXT SECTION) USING DIFFERENT HYPOTHESIS FOR THE MATERIALS AND GEOMETRIES. 174
FIG. 169: EXAMPLES OF VARIATIONS OF THE POTTING SHAPE FOR INSERTS [20], [30]. 180
FIG. 170: EXAMPLE OF DETACHING OF THE FASTENER [19], [32]. 181
FIG. 171: EXAMPLES OF THE FORMATION OF AIR BUBBLES IN INSERTS [19], [42]. 181

FIG. 172: EXAMPLES OF THE IRREGULAR BORDERS FORMED IN INSERTS DUE TO PARTIAL REMOVAL OF THE HONEYCOMB CELL WALLS [19], [20], [28]. 182
FIG. 173: EXAMPLES OF INCOMPLETE FILLING UNDERNEATH THE FASTENER BOREHOLES [19], [42]. 183
FIG. 174: EXAMPLES OF A) VARIATION OF THE MICRO-SPHERES CONCENTRATION OR POROSITIES, B) EXAMPLE OF AN INSERT ON WHICH THE INSERT IS SMALLER THAN THE INSERT RADIUS [33], [34]. 183
FIG. 175: DEFINITION OF THE EFFECTIVE POTTING RADIUS (EPR) AND THE REAL POTTING RADIUS (RPR) ACCORDING TO THE ESA [1]. 187
FIG. 176: EVIDENCE SHOWS THAT THE FAILURE APPEARS FROM THE POTTING REAL SHAPE INSTEAD OF FROM THE DOUBLE CELL WALLS. 189
FIG. 177: RESULTS OF THE SCRIPT DEVELOPED IN MATLAB: THE CELLS THAT ARE FILLED CHANGES WITH THE POSITION OF THE PERFORATION..... 190
FIG. 178: THE PERFORATION WAS TESTED FROM DIFFERENT CENTERS SHOWN IN BLUE. 191
FIG. 179: AVERAGE, MINIMAL, AND MAXIMAL NUMBER OF FILLED CELLS FOR DIFFERENT CELL SIZES (SC=1/8”, 3/16”, 1/4” AND 3/8”). 191
FIG. 180: AVERAGE, MINIMAL, AND MAXIMAL REAL POTTING RADIUS (RPR) FOR DIFFERENT CELL SIZES (SC=1/8”, 3/16”, 1/4” AND 3/8”). 192
FIG. 181: REAL POTTING RADIUS (RPR) FOR DIFFERENT CELL SIZES: ESTIMATION OF THE ESA VS THE OBTAINED RESULTS. 192
FIG. 182: GENERAL DESCRIPTION OF THE INSERTS TYPE 1, 2 AND 3. 195
FIG. 183: EXPERIMENTAL CURVES OF A) THE SHEAR TESTING OF THE HONEYCOMB CORE, B) THE ADHESIVE USED TO FABRICATE THE POTTING. 196
FIG. 184: A) SIZE OF THE FASTENER, B) SET-UP FOR THE PERFORMED PULL-OUT TESTS [19]. 197
FIG. 185: EXPERIMENTAL CURVES OF THE PULL-OUT TEST OF THE INSERTS TYPE 1 [19]. 197
FIG. 186: DAMAGE SCENARIO OF THE INSERTS TYPE 1 [19]. 198
FIG. 187: EXPERIMENTAL CURVES OF THE PULL-OUT TEST OF THE INSERTS TYPE 2 [19]. 199
FIG. 188: DAMAGE SCENARIO OF THE INSERTS TYPE 2 [19]. 199
FIG. 189: EXPERIMENTAL CURVES OF THE PULL-OUT TEST OF THE INSERTS TYPE 3 [19]. 200
FIG. 190: DAMAGE SCENARIO OF THE INSERTS TYPE 3 [19]. 200
FIG. 191: 1. TRAPPED AIR IN THE CELLS, 2. INSERT WAS NOT BONDED 3. THE INSERT IS IRREGULAR..... 201
FIG. 192: THE DIAL BORE GAUGE COULD HAVE BEEN POORLY POSITIONED, ALSO THE TOOL USED TO PULL-OUT THE INSERTS AUTHORIZED SMALL ROTATIONS..... 202
FIG. 193: THE INSERT STIFFNESS SHOULD BE GIVEN MOSTLY BY THE CORE SHEAR DEFORMATION. 202
FIG. 194: RANGE OF MINIMAL AND MAXIMAL STIFFNESS ACCORDING TO THE ESA REAL POTTING RADIUS FORMULATIONS. 203
FIG. 195: EXPERIMENTAL CURVES OF BUNYAWANICHAKUL WITH THE FIXED DISPLACEMENT, NOW THE VALUES ARE SET TO BE IN AN ACCURATE STIFFNESS RANGE. 204
FIG. 196: COMPARISON OF THE EXPERIMENTAL, ANALYTICAL AND NUMERICAL STIFFNESS OF THE INSERTS TYPE 2. 205
FIG. 197: COMPARISON OF THE EXPERIMENTAL, ANALYTICAL AND NUMERICAL STIFFNESS OF THE INSERTS TYPE 2. 205
FIG. 198: COMPARISON OF THE EXPERIMENTAL AND ANALYTICAL STIFFNESS OF INSERTS TYPE 3..... 206
FIG. 199: LOADING CURVES OF INSERTS TYPE 3 WITH THE MODIFIED DISPLACEMENT..... 206
FIG. 200: A) THE CORE NEAR TO THE INSERT IS DIVIDED INTO A DIFFERENT SECTION BECAUSE ITS BEHAVIOR IS DIFFERENT, B) THE FASTENER GEOMETRY IS SIMPLIFIED. 207
FIG. 201: REDUCED F.E. MODELS OF INSERTS TYPE 1,2 AND 3. 207
FIG. 202: COMPARISON OF THE EXPERIMENTAL, ANALYTICAL AND NUMERICAL STIFFNESS OF THE INSERTS TYPE 1. 208
FIG. 203: THE SHEAR BEHAVIOR MEASURED BY BUNYAWANICHAKUL IS VALID UNTIL THE CELLS STARTS TO FOLD, THEREFORE SEMI-EXPERIMENTAL CURVES WERE PROPOSED TO MIMIC THE ACTUAL BEHAVIOR. 209
FIG. 204: BEHAVIOR LAW IMPLEMENTED TO CONSIDER ONLY THE INITIAL BUCKLING OF THE CELLS. 210
FIG. 205: BEHAVIOR LAW IMPLEMENTED TO CONSIDER THE INITIAL BUCKLING OF THE CELLS AND THE COLLAPSE. 210
FIG. 206: SHEAR BEHAVIOR OF THE HONEYCOMB WHEN THE POTTING BORDERS ARE IRREGULAR, CAUSING A PREMATURE COLLAPSE OF THE CELLS WITH NO INCREASE IN THE SHEAR STRENGTH..... 211
FIG. 207: SHEAR BEHAVIOR OF THE HONEYCOMB WHEN THE POTTING BORDERS ARE IRREGULAR, CAUSING A PREMATURE COLLAPSE OF THE CELLS WITH INCREASE IN THE SHEAR STRENGTH..... 211
FIG. 208: COMPARISON OF THE EXPERIMENTAL AND NUMERICAL RESULTS, THE BUCKLING OF THE CELLS IS COINCIDENT WITH THE ALLOWABLE LOAD ACCORDING TO BUNYAWANICHAKUL IN REF. [19]. 211
FIG. 209: COMPARISON OF THE EXPERIMENTAL AND NUMERICAL RESULTS; THE POINT WHERE THE CELLS START TO COLLAPSE SHOULD BE THE ELASTIC LIMIT THE INSERT. [19]. 212

FIG. 210: CONSIDERING THE EFFECT OF THE IRREGULAR BORDERS IN THE HONEYCOMB CORE. 213
FIG. 211: COMPARISON OF THE EXPERIMENTAL AND NUMERICAL RESULTS CONSIDERING THE LATERAL STABILIZATION EFFECT ON THE CELLS SURROUNDING THE INSERT. 214
FIG. 212: SKIN'S SHEAR BEHAVIOR LAWS. 215
FIG. 213: THE INCLUSION OF THE SKIN DAMAGE ALLOWS A BETTER AGREEMENT WITH THE EXPERIMENTAL RESULTS. 215
FIG. 214: BEHAVIOR LAWS THAT DESCRIBES THE POTTING BEHAVIOR UNDER TENSION AND COMPRESSION. 216
FIG. 215: COMPARISON OF THE EXPERIMENTAL AND NUMERICAL RESULTS CONSIDERING THE POTTING FAILURE WHEN IS FIRMLY BONDED: TRACTION DAMAGE OF THE POTTING. 217
FIG. 216: COMPARISON OF THE NUMERICAL LOADING CURVES WHEN THE FASTENER IS NOT BONDED. 217
FIG. 217: COMPARISON OF NUMERICAL BEST AND WORST CASES AND THE EXPERIMENTAL RESULTS (TYPE 1), SEE ALSO FIG. 219. 218
FIG. 218: THE COMPARISON OF THE EXPERIMENTAL AND NUMERICAL FAILURE SCENARIO SHOWS A GOOD AGREEMENT. 219
FIG. 219: DIFFERENT FAILURES IN THE SIMULATION OF THE BEST CASE OF THE INSERT TYPE 1. 219
FIG. 220: COMPARISON OF NUMERICAL BEST AND WORST CASES AND THE EXPERIMENTAL RESULTS (TYPE 2). 220
FIG. 221: COMPARISON OF NUMERICAL AVERAGE CASE AND THE EXPERIMENTAL RESULTS (TYPE 3). 221
FIG. 222: DESCRIPTION OF THE SECTIONS CONTAINED IN THE PYTHON SCRIPT OF THE INSERT. 221
FIG. 223: DESCRIPTION OF THE MODEL GEOMETRY AND PARAMETERS. 222
FIG. 224: DESCRIPTION OF THE SUPPORT, DESCRIPTION OF THE MESHING PARAMETERS USED FOR THE MODEL. 222
FIG. 225: EXAMPLE OF A FAILURE MODE MAP FOR SANDWICH STRUCTURES [104]. 225
FIG. 226: FAILURE OF THE SKINS, POTTING AND HONEYCOMB CORE; INSERT FAILURE LOAD VS THE REAL POTTING RADIUS. 228
FIG. 227: FAILURE OF THE SKINS, POTTING AND HONEYCOMB CORE; INSERT FAILURE LOAD VS POTTING TRACTION'S RESISTANCE. 229
FIG. 228: DIFFERENT INSERT FAILURE MODES VS THE THICKNESS OF THE SKINS. 230
FIG. 229: FAILURE SURFACES OF THE CORE, THE POTTING AND THE SKINS: RPR VS POTTING TRACTION STRENGTH 231
FIG. 230: BOTTOM VIEW OF THE SURFACES: FAILURE MODE MAP OF INSERTS 232
FIG. 231: FAILURE MODE MAP OF INSERTS AND FAILURE LOAD. 232
FIG. 232: FAILURE SURFACES OF THE CORE, THE POTTING AND THE SKINS: SKIN THICKNESS VS RPR. 233
FIG. 233: FAILURE MODE MAP, SKIN THICKNESS VS RPR. 234
FIG. 234: FAILURE MODE MAP, SKIN THICKNESS VS RPR AND STRENGTH IN COLOR SCALE. 234
FIG. 235: POTTING MAS AND STRENGTH TO MASS RATIO VS REAL POTTING RADIUS 235
FIG. 236: POTTING MASS AND INSERT STRENGTH TO MASS RATIO VS POTTING TRACTION STRENGTH. 236
FIG. 237: OPTIMIZATION CHART FOR THE INSERT MASS. 237
FIG. 238: CALCULATION OF THE LINEAR LIMIT OF THE VIRTUAL TESTING LOADING CURVES: ALGORITHM AND EXAMPLE 238
FIG. 239: LINEAR LIMIT VS FIRST FAILURE CRITERIA. 238

Chapter one: General introduction

The purpose of this chapter is to present an introduction to the context and problems on which this thesis is developed. This starts from a review of the most common applications of sandwich panels to some issues of the inserts sizing methods.

1.1 FROM AIRCRAFT TO INSERTS 3
1.1.1 The sandwich structure 3
1.1.2 Sandwich panels joints; a problem still to be investigated 5
1.1.3 Remarks on the insert design methods 7
1.1.4 Objectives of the thesis 8
1.1.5 Summary of this thesis 9

1.1 From aircraft to inserts

Since the 1960's composites are being used for aeronautic applications. Mostly because they allow to reduce the weight of mechanical parts, the maintenance costs, the energy consumption, and in consequence, increasing the overall performance of aircraft.

The first commercial airplane of Airbus, the A300B4-200 for 266 passengers was fabricated in 1974 and had about 5% of its overall weight made of composites, weighed about 90 tons empty and its maximal landing load capability was of 126 tons for an effective load capacity of around 36 tons. In comparison, the new Boeing 787-8 (Fig. 1) or Airbus A350-800, can carry up to 300 passengers, has 50% of its respective overall weight in composites, weighs about 100 tons and has a maximal landing load capability of 190 tons for a maximal effective load capability of about 86 tons (up to 280 % more than the A300).

To keep improving the economic efficiency, composites are more and more used. However, there are some parts that can't be made of composites because of the local temperature or safety considerations, like the supports for the engines made of Marval steel or Inconel (nickel alloy) for some edges of the wings. The parts that were possible to replace with composites have already been replaced, like the fuselage or the wing box. Nowadays, the efforts are concentrated into optimizing costs because of the increasing demand for airplanes.

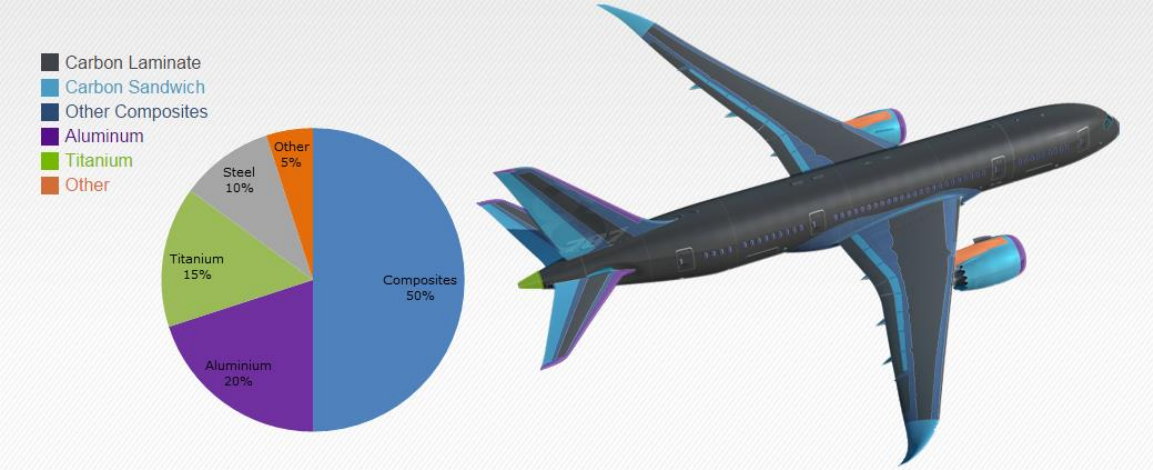

Fig. 1: Structural usage of composites in the Boeing 787.[16], [17].

The most common type of composite used for civil aircraft is Carbon Fiber Reinforced Polymer (CFRP) laminates with a majority of UD plies. For instance, the fuselage is almost entirely made of them (see Fig. 1). For this reason, most of the efforts of the composites community have been focused on these materials.

Other composites used for aircraft construction are sandwich panels with CFRP skins. Thanks to their high bending stiffness/weight ratio, these panels are ideal to design very lightweight structures, for aircraft control surfaces and helicopter primary structures for instance.

1.1.1 The sandwich structure

The sandwich structure consists of three main elements: two thin, stiff, and strong faces or skins and a thick, light, and weak core. The faces are adhesively bonded to the core to transfer the loads. Their working principle is simple: a thick core separates and maintains a certain distance between the skins, increasing the inertia and consequently the bending stiffness (see Fig. 2). Thus, they offer significantly higher bending and buckling stiffness compared to heavier laminates sheets.

Secondary functions of skins are to protect the core from the environment (avoid degradation, corrosion and moisture ingression), against low energy impacts and stabilize the core. Depending on the core material, it can be used for multifunctional purposes like increasing thermal or acoustic isolation, dynamic damping, furtive applications, active control, etc. Concerning the core, there are many types. The three main families are foam, cellular materials like honeycomb and balsa wood.

Because of their properties, these panels are used in many different fields, for example to build roofs or bridges in civil construction, for helicopters, aircraft or satellites in the aeronautic and aerospace domain, for thermal and acoustic isolation in the automotive sector, among many, many other applications.

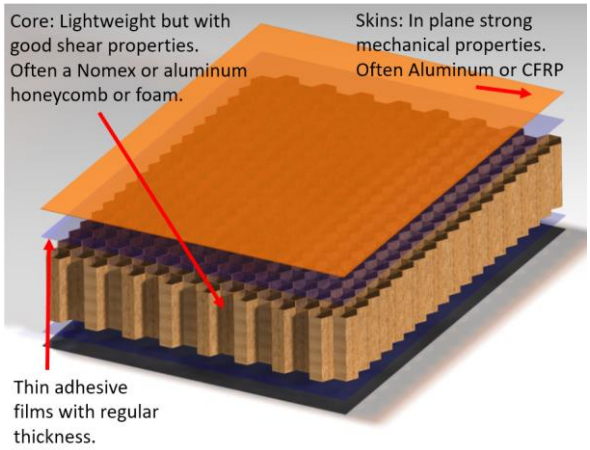

Fig. 2: General description of a sandwich structure.

The idea to introduce these superlight panels for aeronautical applications comes from the middle 10', however it was not until the 1930's that their use was widespread accepted [5].

For aeronautical panels, the most used type of sandwich is made with CFRP skins with Nomex® honeycomb core. The advantages that these sandwich structures offer are enormous compared to similar structures. Face to skin stiffener panels sandwiches are sometimes preferred in helicopters, general aviation up to business aircraft. Also, compared to the traditional metallic skin-stringer construction they offer big advantages allowing to reduce the number of parts by 85%, the cost by 90% and 50% on the fabrication time [18], [19].

In the late 80's Beechcraft developed the Starship, which was a business aircraft with 72% of its structural weight of composites, mostly CRFP sandwiches with Nomex® honeycomb core. Unfortunately, only 53 were fabricated and even less were sold. For this reason, Beechcraft determined that it was more profitable to re-buy the sold aircraft to destroy them rather than to keep providing the maintenance for the model. But all the acquired knowledge from the Starship design was used to design its successor, the Raytheon Premier I which is still in production today.

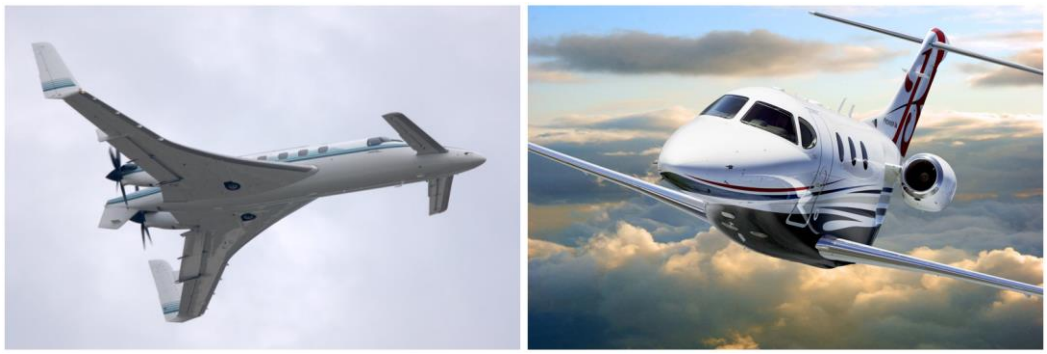

Fig. 3: The Starship and the Raytheon Premiere I.

These sandwich panels are so efficient that they are used to build almost all the main body of helicopter structures. This is the case for the Airbus NH90, the Sikorsky Black Hawk (front panels and doors), or the Eurocopter Tiger, on which the structure represents about 10% of the total weight (the remaining 90% is for the engine, pales, electronics, etc.).

The use of these panels has been extended even for spatial applications like satellites, spatial shuttles and launching systems. These panels are ideal for such structures because they are very stiff and light at the same time, which is very important since it is very expensive to send something to space. The cost to deploy a satellite ranges between 2000 and 31000 US$ per kg depending on size and weight, which can be around several hundreds of kilograms. Even the smallest reduction of weight could lead to a big reduction of the launching cost [20]–[22].

In naval construction, they are used from competition to defense boats. In some cases their applications reduce the water drafts and increase the resistance against intense fatigue loadings [23].

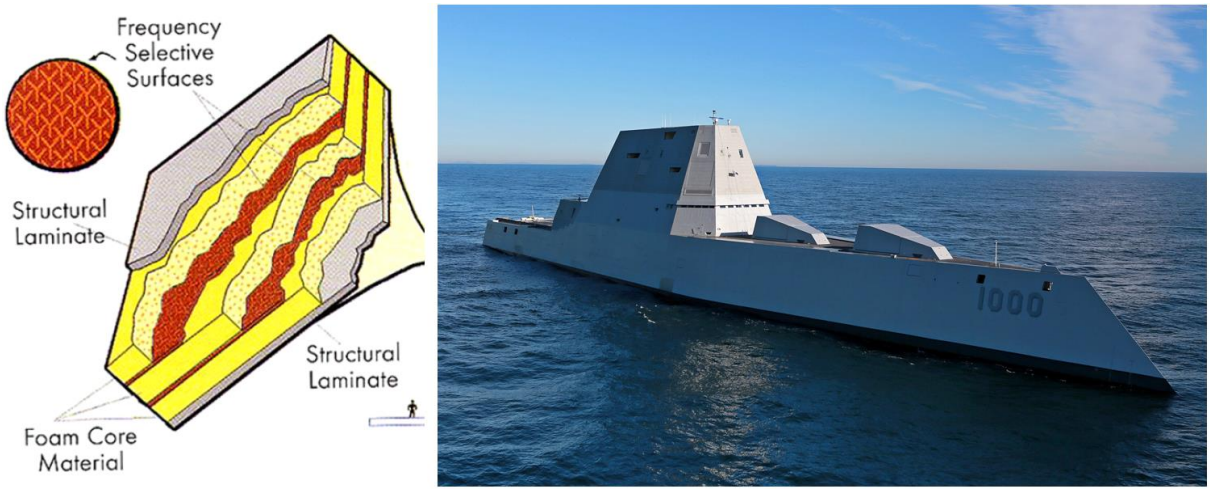

Fig. 4: Radar absorbing sandwich panels were used to build Zumwalt-class destroyer [24].

Some other interesting characteristics can be integrated into the sandwich design. In 1997 sandwich panels were used to construct an enclosure for the communication systems (the Advanced Enclosed Mast/Sensor) of the USS Arthur W. Radford, a Spruance-class destroyer of the United States Navy. They were used as a multi-functional design that helped to reduce maintenance cost of the sensors, reduce the height of the communication structure and to create stealth properties. This was accomplished by embedding radar absorbing materials in the core of the panels, a similar technology is also used for the Zumwalt-class destroyer (see Fig. 4) [24].

1.1.2 Sandwich panels joints; a problem still to be investigated

Despite the great advantages of sandwich structures, they are restricted to secondary structures of commercial aircraft such as doors in general, cabin interiors and control surfaces like ailerons, spoilers, etc. (see Fig. 5) [5], [7].

The reason is simply because the design is more complex and it is difficult to ensure the quality requirements. Therefore, these panels may not be properly designed for all the in-service conditions of these aircraft.

Even if there have been big efforts to study them [6], they are not well mastered in terms of the materials used for their fabrication, manufacturing process, fatigue, damage growth, debonding of the parts, their several failure modes, assembly, impacts, etc.

As proof of this, there are investigations indicating that the Boeing 767 flies with up to 40.4 Kg of water stocked in their sandwich panels [7]. This was apparently caused by the loss

of the sealing capabilities of the panel due to the sandwich fabrication defects and the fatigue on the joints. This is a common problem of helicopters too since they are structurally made of sandwich panels [25].

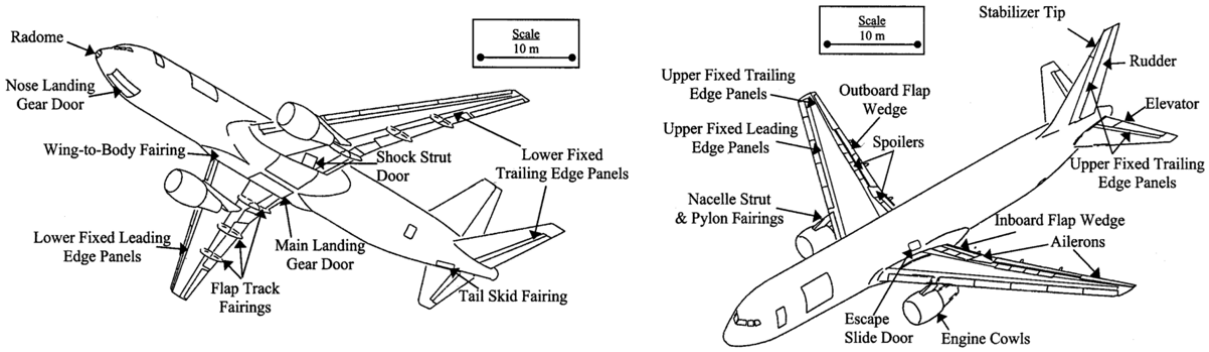

Fig. 5: Use of sandwich panels on the Boeing 767 [7]

More specifically, the assembly of a sandwich structure must accomplish some service functions; ensure the forces transmission, do not reduce the mechanical resistance of the panel, allows a precise alignment of the parts, be inexpensive and ensure the sealing of the inside of the panel.

In most cases, to avoid exposing the core to concentrated loads, the joining is made through the skins. This is very simple and easy to do, although the load capabilities are directly limited by the mechanical properties of the adhesive (see Fig. 6). This technique is very widespread for cabins of commercial aircraft although it is not the most common.

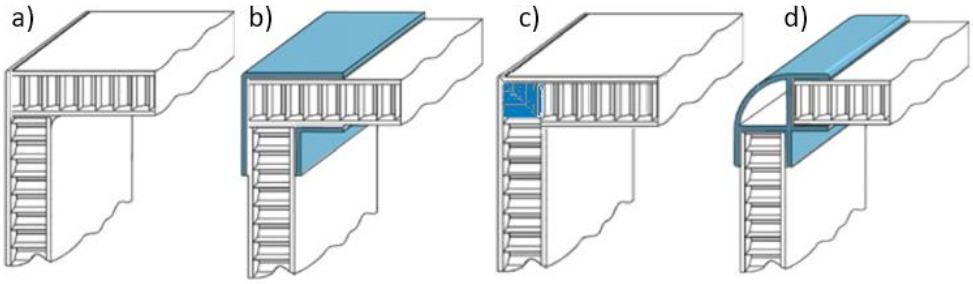

Fig. 6: Different techniques to join panels: directly bonding them, adding reinforcements or densifying corners of the core to increase its mechanical properties. [22]

Another technique consists of reinforcing the core so it can resist concentrated loads caused by the assembly. These reinforcements are called inserts. These joints can be divided in two types: high-load and low load carrying inserts.

An insert is often a densification of the core that arises the local mechanical properties, providing the panel with an area where a junction can be installed. Inserts distribute the concentrated forces in a way that the core and the skins can support them. This type of assembly is by far the most used in sandwich structures. Indeed, its principle and installation are simple most of the time handmade, which guarantees low costs (see Fig. 7).

Nevertheless, there are some fabrication defects that can't be avoided in the insert installation, like their irregular shape due to honeycomb geometry or the presence of air bubbles. This is relevant because inserts must be designed to support a desired load. Nevertheless, due to the complexity of the problem, the calculation process involves the simplification of several aspects like the geometry or the materials, that in consequence reduces the accuracy of the design methods.

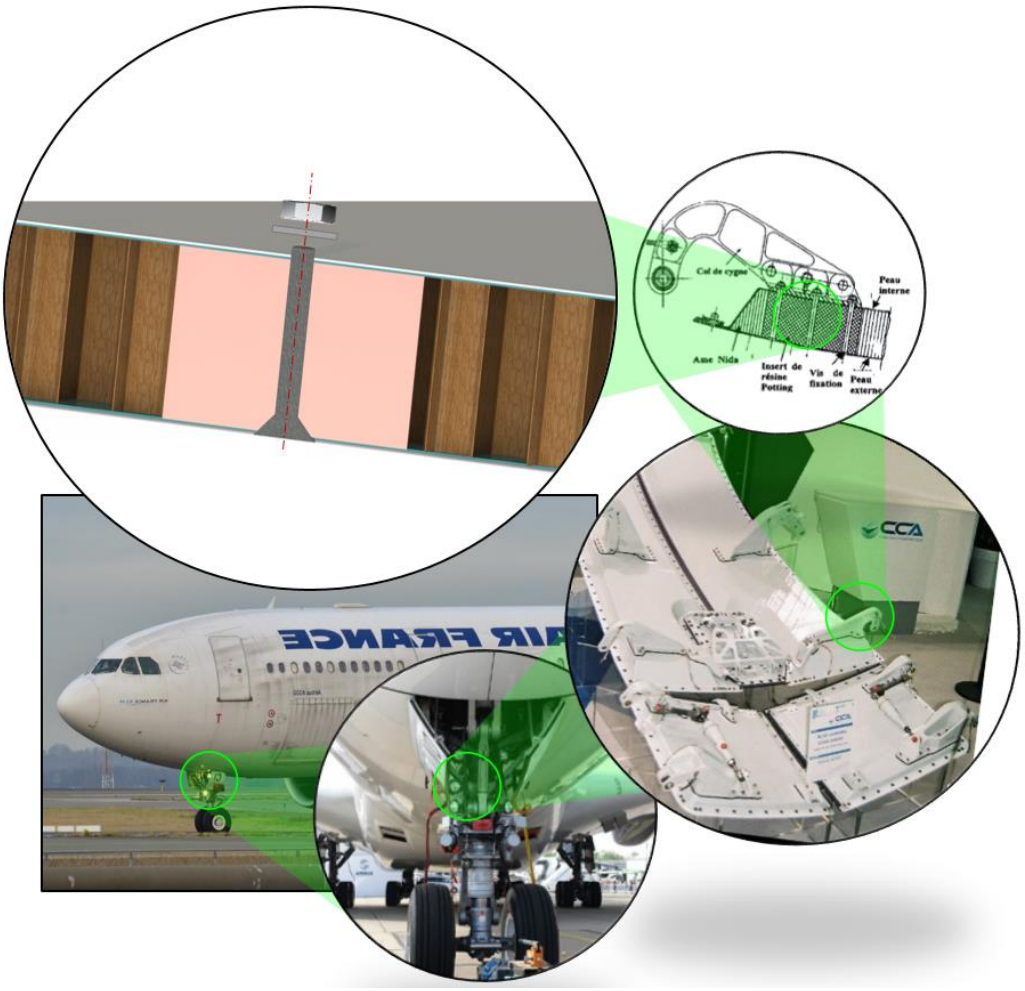

Fig. 7: High load insert on the landing gear door of the Airbus A330

1.1.3 Remarks on the insert design methods

In general, inserts are designed according to the design requirements of the sandwich panel. This means that there are several types of inserts for different situations, but in general they are selected depending on the load capability. For panels that require the use of bolts to be assembled, most of the time a metallic fastener is installed into the insert so it can provide a metallic surface and the thread for the bolt.

However, the size and materials used for the insert must be chosen according to the assembly requirements and thus a design process is necessary. To make the good choice of parameters, there are a few bibliographical references that give the main guidelines for the insert design; like the Insert Design handbook of the ESA [1], or the Military handbook 23A [2] of the Department of Defense of the United States. According to these documents, the insert size must be proportional to loading requirement and is calculated by means of an analytical approach based on the formulations developed by a researcher named Ericksen [3], of the Forest Products Laboratory in 1953.

Even so, at the end, inserts are tested to determine experimentally their actual strength, although the existing experimental failure criteria for inserts may be too simplistic, i.e. when a reduction of more than 5 % on the slope is reached, or a sudden drop in the force vs displacement curve is found, an irreversible damage has occurred and the insert fails causing what is called a structural rupture.

If the sizing method doesn’t provide calibrated strength values, the design and testing process requires more iterations and hence everything is slowed down, costing resources, time and money.

But also, the simplistic experimental failure criteria for inserts is not based on the understanding of the failure causes of the inserts, therefore, even if there is a reduction of 5% on the slope of the loading curve, the insert may remain undamaged after all.

However, there is an alternative method, based on the recent development of computing technology that allows a more precise analysis; the finite element analysis (F.E.A.). This approach is strongly suggested by Zenkert [5] for the insert design. This is proposed because of the unique and complex conditions that surround the insert for every application. Yet, this may not be very easy to do because it requires time and expertise, making it not very affordable for every situation.

If both approaches are compared, the analytical approach is easier to implement compared to the F.E.A. Also, companies prefer to neglect or absorb the overweight of inserts in the panel, instead of spending valuable resources just to save a few grams of weight. They use the analytical method for insert design because it is cheaper to ignore this overweight problem than to solve it. And thus, the analytical approach for insert design remains today as the most used method for the industry.

Even though it's true that the extra weight of a few grams per insert doesn't represent a significant problem for helicopters or planes where they are used to assembly just a few electronics panel racks or hydraulic systems, it does represent a major problem for spatial applications. This is because satellites may have up to 25,000 inserts [26].This means that an overweight of only 1 gram per insert can lead to an extra cost of about 75,000 dollars. So if this overweight is avoided the savings can be huge [27].

1.1.4 Objectives of the thesis

Following the methods recommended by the ESA or the Military Handbook 23-A may be slow, expensive and in the end, it may result in oversized inserts.

The aim of this research is to create another alternative for the insert design. This new approach should provide more accurate predictions than the analytical approaches but also should be easier and quicker to implement in comparison with the detailed modeling using the F.E. method.

All in all, our approach consists of the creation of failure mode maps of inserts based on simplified but accurate virtual tests by means of F.E. simulations.

This is very practical because charts are known to be very useful to represent complex phenomena in a very compact and simple form, and this is the case for the insert strength prediction. This type of tool may be very valuable for engineers as it will allow reducing costs on the embodiment design and validation stages.

Also, the F.E.A. is a powerful tool that allows obtaining very accurate predictions of the mechanical behavior of complex structures, still, the main disadvantage is the development time. But if the insert F.E. model is simplified and parametrized in a proper way, it may be suitable to perform virtual tests on any type of insert in a short time.

In practice the most common type of loading is the pull-out, which induces principally a shear buckling of the core that results in a nonlinear response of the insert as was demonstrated in a previous PhD in the laboratory (see ref. [15]). This aspect is interesting because initially we thought that the shear postbuckling behavior of the core can be elastic, and thus the insert strength might be underestimated. For this reason, our principal objective is to improve the understanding of the non-linear behavior of the insert, this includes:

- Study individually the nonlinear behavior of the skins, the honeycomb core and the potting.
- Improve the description of the failure modes.

Secondly, we want to understand what causes the oversizing of inserts but also propose a way to avoid it. This includes:

- Study of the accuracy of the analytical methods
- Study the influence of the interaction between the parts of the insert.
- Study the influence of defects on the insert behavior.

And finally, we want to develop a more efficient and accurate tool for the insert sizing that can replace the analytical approaches. This includes:

- Development of a reduced F.E. model.
- Development of charts of force vs geometry for the insert design.

1.1.5 Summary of the thesis

This research is divided in 5 chapters that cover different aspects involved in the inserts design:

- This first chapter is a global introduction that explain the context and motivations of this research.
- The second chapter is about the state of the art of knowledge of inserts in sandwich structures and Nomex® honeycomb cores.
- The third chapter is focused on the buckling analysis of honeycomb cores subjected to shear loads.
- In the fourth chapter a study about the mechanical properties of syntactic polymer foams for inserts is presented.
- In the fifth chapter, all the developments of the previous chapters are integrated in the development of a virtual insert model, which is presented and validated experimentally. Also, in this last chapter, the failure mode maps for inserts are developed using the developed insert model.

This thesis can be presented as a pyramid (see Fig. 8), on which the base is the experimental and numerical analysis of the materials that compose the sandwich and inserts. The second part is the analysis of the interactions between the materials. Finally, the tip of the pyramid consists of applying all the acquired knowledge to present an innovative approach for the insert sizing.

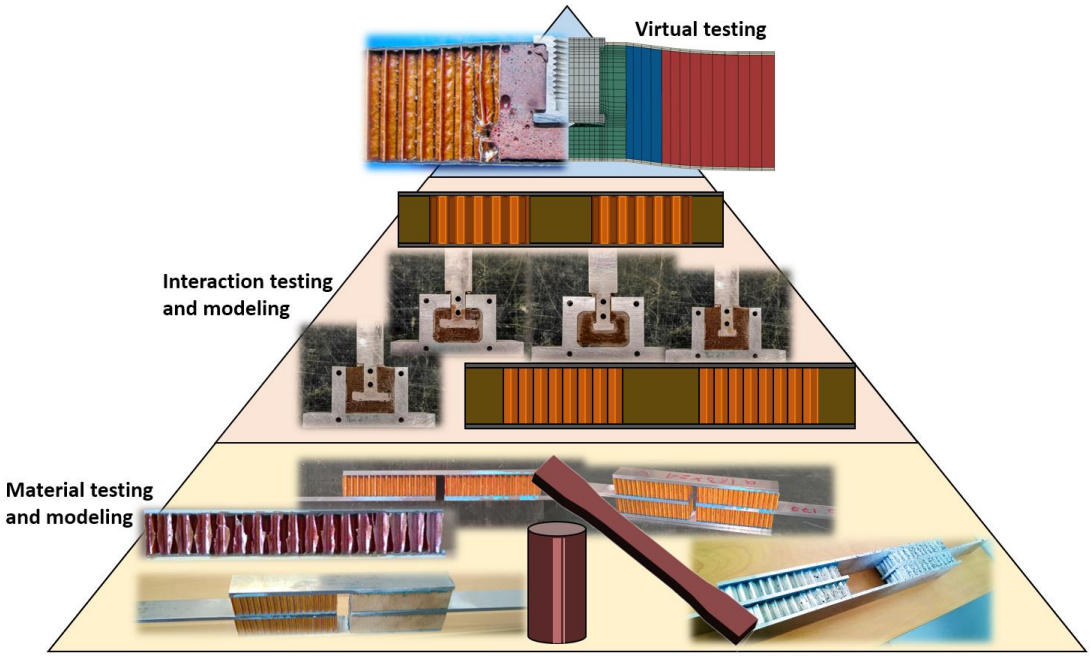

Fig. 8: Thesis work presentation

Chapter two: State of the art of inserts for sandwich structures

This chapter is a literature review of inserts for sandwich structures. First, the technical aspects of inserts are introduced including types and test standards. Then, a literature review of the experimental tests and the most common sizing methods for inserts is presented. The presented evidence indicates that investigating the honeycomb core shear buckling is necessary, and a section is dedicated to this subject. Finally, the conclusions are presented.

2.1 INSERTS FOR SANDWICH STRUCTURES 13
2.1.1 Types 13
2.1.2 Testing standards 17
2.1.3 Pull-out experimental testing of inserts 18
2.1.4 Strength prediction of inserts by analytical approaches 31
2.1.5 Strength prediction of inserts by numerical approaches 45
2.1.6 Conclusions of the state of the art of insert analysis 52
2.2 SHEAR BUCKLING OF NOMEX® HONEYCOMB CORES 55
2.2.1 The honeycomb structure 55
2.2.2 Properties of the Nomex® paper 57
2.2.3 Shear testing of honeycomb cores 59
2.2.4 On the shear behavior of honeycomb cores. 61
2.2.5 Conclusions on the honeycomb's shear buckling 65

2.1 Inserts for sandwich structures

The pull-out inserts strength in sandwich structures has been investigated by several researchers (see for example ref. [4], [28]–[41]). The experimental evidence shows that there are different failure scenarios depending on the insert geometry and components, also, the order of appearance of the failure modes is very important.

Moreover, the experimental tests show that the insert strength is principally related to the shear strength of the core. For this reason, some calculation methods have been developed to estimate the insert strength as function of the core shear resistance [3], [37].

All these aspects are presented in this section, starting by general aspects of inserts such as type and testing standards, followed by insert pull-out experimental tests and sizing methods, and finally a review on the honeycomb cores.

2.1.1 Types

Inserts have been studied since sandwich panels became popular for weight reduction applications. As there are many different uses for panels, the inserts have been designed accordingly. As result, they are made in several geometries, materials, for different load conditions, etc. Some of the most characteristic are shown in Fig. 9.

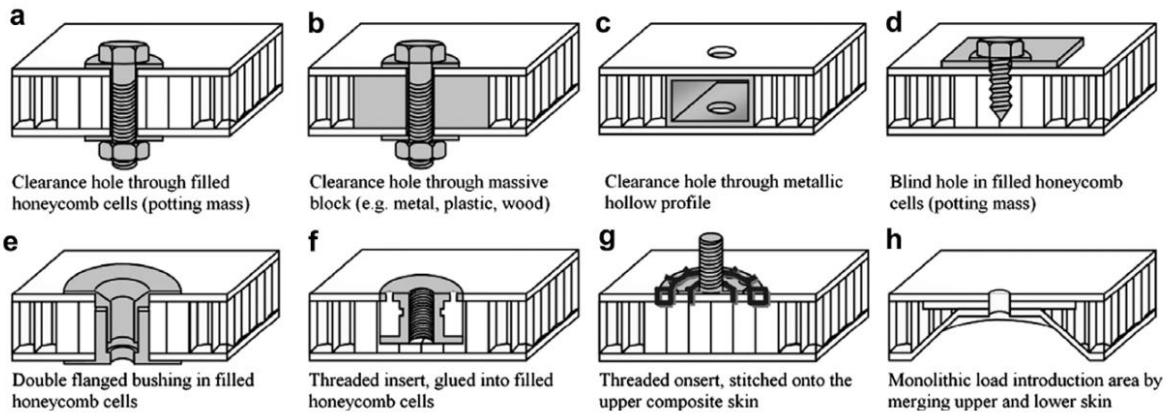

Fig. 9: Several types of sandwich joints [35].

The inserts a), b), c), e) and h) allows to put a bolt all along through the sandwich panel, to avoid the crushing of the sandwich the core is reinforced by different type of densifications. When a hole through the sandwich panel is undesirable, concepts like d), f), and g), can be used, the core is reinforced too, most of the cases with potting. Also, a fastener is used to provide the thread for the bolt. When the panel must remain intact a concept like g) can be used.

Concerning the fasteners, there are several, the more characteristics are shown in Fig. 10. They are commonly made of aluminum 2024 alloy. They can be divided by their installation procedure: the molded-in type and the mechanical type.

The molded in fastener is installed, fixed and retained by encapsulating it within the potting. The mechanical fastener is generally used for metallic panels, its principal characteristic is to be installed by compressing and capturing the face skins.

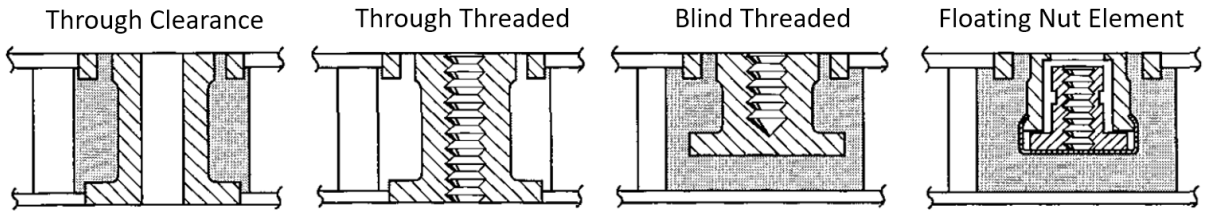

Fig. 10: Comparison of the Shur-lok fastener applications [42].

Meanwhile, inserts can be classified in different ways. One way to do this is by its shape, as proposed by Zenkert [5]. They are: Self-taping screws and rivets, flared cylinder (top hat), partial inserts and finally, through the thickness inserts. A qualitative comparison of the loads bearing for each insert is given in Table 1.

2.1.1.1 Self-taping screws and rivets

The screw and rivet can be classified as low-load carrying inserts. Their installation is very simple, a hole is made in one of the panel faces and then the rivet is placed, an adhesive can be used to increase the strength. They're used to attach light equipment to panel, like cabin safety equipment or shelves, although not used for aeronautical applications [15]. They're made to be used with thick face panels. Even if their mechanical resistance is not very high, they're inexpensive and the installation is very simple. The pullout, torsional and momentum forces are supported by the thread of the rivet and the skins or potting, thus the transverse and in plane strengths are relatively low, but the moment strength can be high.

	Self-taping screws and rivets	Flared cylinder or top hat	Partial or blind inserts	Through the thickness inserts
Pull out force	Low	Low	Low	Low
In-plane force (shear)	Low	Regular	Low	High
Moment	High	Low	Regular	Regular

Table 1: Comparison chart of performances given by Zenkert [5].

2.1.1.2 Flared inserts (top hat)

This insert type is recommended for metallic panels. Is stronger than the previously mentioned screws and rivets. Also, its installation is simple: A hole through the panel is made, then, an adhesive is placed under the neck of the fastener and pressed to the panel as shown in Fig. 11. In this way, the insert is (if desired) not bonded to the core, avoiding damaging it, although the insert strength decreases.

Due to its installation process, there are some disadvantages too. Its strength relies on the adhesive for transferring forces and moments, its installation deforms and may damage the skins in the closing procedure (skins may be damaged too) and a big stress-concentration is created at the base of the flared top.

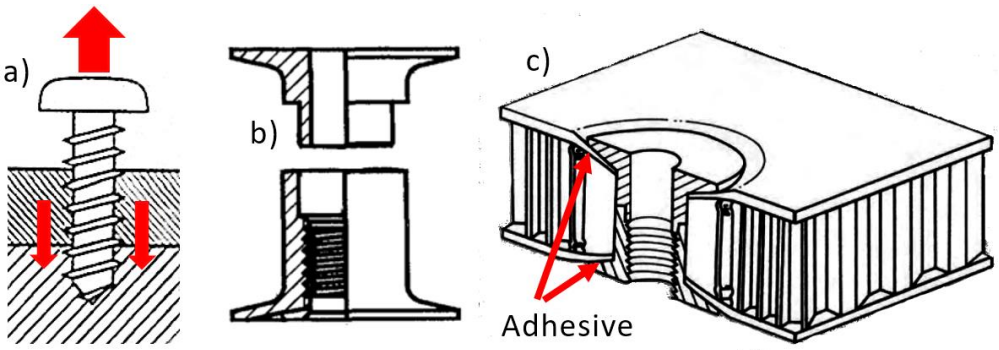

Fig. 11: a) Force distribution of a screw b) mechanical fastener before installation c) installed mechanical fastener [5], [15], [43].

2.1.1.3 Full potting, partial or blind inserts

This type is stronger than the one mentioned before. When the potting is bonded to both skins, it's called full potting insert, when is bonded only to one skin is called partial insert (although this is not recommended by the ESA)[37].

It is used when the requirements don't allow to drill both skins, for electronic racks attachment, cabin safety equipment, structural attachment to walls, shelves and fluid pipes in primary sandwich structures for helicopters. But there are more interesting cases like naval applications and for some special technologies in aircraft like stealth, that do not allow to perforate both sides of the panel. The installation process is all handmade and thus delicate and expensive. There are several ways of installing a partial insert, one is: drilling a hole through the panel (carefully), remove the core around where the insert will be placed (without damaging the skins), fill partially the hole with potting, place the fastener in to the resin and alginate it with the skins (using an installation tab), finally, fill the rest of the hole with potting (air bubbles must be avoided) and then curing or polymerizing the potting at room temperature (Fig. 12).

The performance of this insert can be increased by installing it under vacuum to avoid air bubbles [44] or by using different types of potting [35], different adhesives, or micro-spheres among other agents.

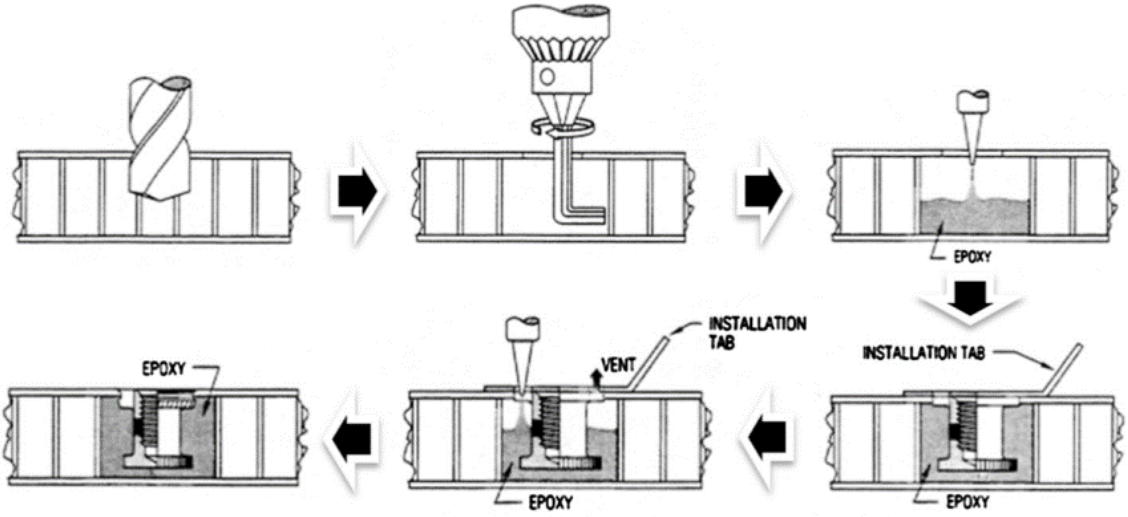

Fig. 12: Partial insert installation procedure [39].

This insert type is the most commonly studied. The force transfer is made through a bolt and the fastener installed in the insert. The interface between the fastener and the panel is made by the potting to bond the fastener and assure optimal contact (see Fig. 13).

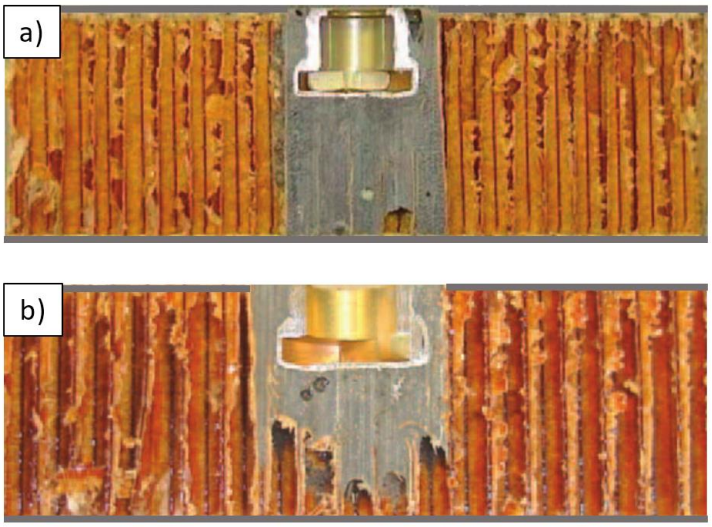

Fig. 13: Cut of a) a full potting insert, the potting is bonded to both skins b) partial insert, bonded to only one skin [28].

2.1.1.4 Through the thickness inserts

This type of insert is the strongest because it passes through all the thickness of the core and is bonded to both skins. It's used in flap and landing gear door junctions for commercial aircraft [15]. Its installation may be complex and varies according to the specifications. In some cases, the potting is pre-installed in the manufacturing phase of the panel, then, when the sandwich is fabricated, a hole is drilled to be able to pass a bolt, although it is difficult to assure a good position of the hole/potting during the drilling. These inserts may or not, have a fastener.

The main advantage of this insert is that both skins work simultaneously, allowing to transfer the tension and torsion forces to both skins increasing the insert pull-out and shear strengths.

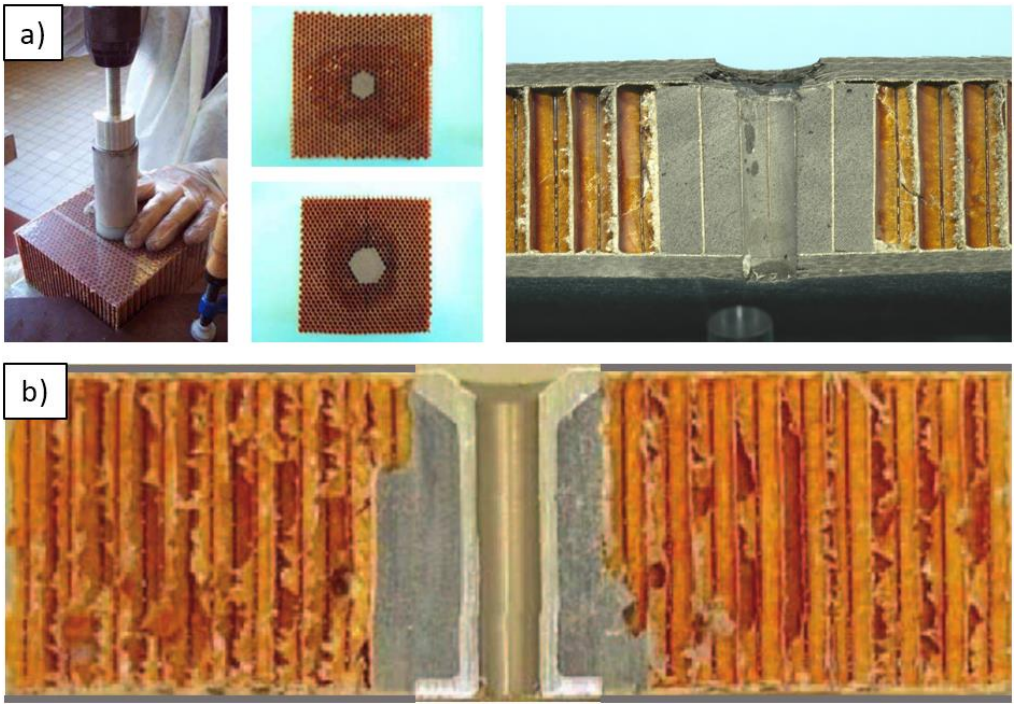

Fig. 14: Through the thickness inserts; a) High load carrying capability insert type Airbus [15] b) with fastener [28].

2.1.2 Testing standards

There are several references for insert testing. For this section the Insert Design Handbook of the ESA and the information provided by Shur-lok are considered [1], [45]. These standards should be followed to obtain reliable results. Some first general remarks are:

- A minimum of three specimens shall be tested.
- For molded-in fasteners a full cure of the compound shall be obtained prior to testing.
- The bolt shall be torqued to the value specified for the real installation.
- A dial indicator or automatic recorder shall be utilized to measure deflection.

In practice, the most common type of load is the pull-out load (perpendicular to the sandwich). Others that appear with less frequency are compression (typically avoided due to the large contact surface) or torque (only appears during the assembly process and not in service). However, according to [46], any load applied to an insert can be described as a linear combination of tension, shear or torque loads. Therefore, an insert must be validated by testing it under three different tests conditions: The pullout test, the shear test and the torque test.

Before proceeding to the tests the first step should be always to make a complete and detailed description of the sandwich panel, the insert, the fastener, the installation procedure and the potting material [46]. It is recommended that the test setup and procedure are completely described using illustrations or photos. Regarding the test conditions, they should also specify the test temperature and humidity, if apply. The load vs deflection curve shall be included for shear and pullout tests.

The rate of loading for the shear and flatwise tension tests shall be between 700 lbs. (3113 N) to 1200 lbs. (5337 N) per minute and for the torque test, approximately one revolution every five seconds at a steady rate [46].

2.1.2.1 Shear testing

- The shear test specimen shall be a rectangular section of 4.0 x 8.0 inches".
- Two fasteners shall be installed on the centerline, each one at 2.0 inches" from the specimen end (see Fig. 15-a).
- The shear test shall be conducted using two steel straps of 6.0 x 1.0 x 0.125 inches" (See Fig. 15 a)
- The specimen with straps attached shall be mounted in self-aligning jaws on the tensile machine.
- The loading direction should pass directly through the centerline of each fastener.
- The testing bolt should have the same strength than the bolt used for the real application.
- If a dial indicator is used, it shall be installed as close as possible to the pull straps to minimize error.

2.1.2.2 Pull-out and torque testing

- The specimen dimensions shall be a square of 4.0 inch, although other square sizes have been used on the literature like 80 mm according to the ESA [37], 140 mm by Bunyawanichakul [8], 50 mm by Kim [44], 127 mm by Heimbs [35] and 120 mm by Park [39].
- The insert shall be installed in the center of the specimen.
- The flatwise tension test shall be conducted with the specimen supported in a metal box frame fixture by a 2.5 inch diameter (70 mm according to the ESA [37]) steel ring with a 0.250 inch thick wall. The ESA gives the recommendations to fabricate this tool [37]
- The fastener shall be centered in the middle of the ring.

- The bolt or mandrel strength must be enough to support the maximal failure load of the insert.
- The loading direction should be perpendicular to the surface of the specimen.

2.1.2.3 Torque testing

- The bolt shall be of sufficient strength to achieve the required torque-out load, otherwise specified, the minimal strength shall be 200,000 psi. (See Fig. 15-c)
- The torque-out test shall be conducted with the specimen rigidly held or restraining fixture.

Once the tests have been finished, a "post mortem" analysis of the tested specimens should be made. This report must contain a complete and detailed description of the failure of the specimens, in this sense photographs are useful for clarification of the failure modes.

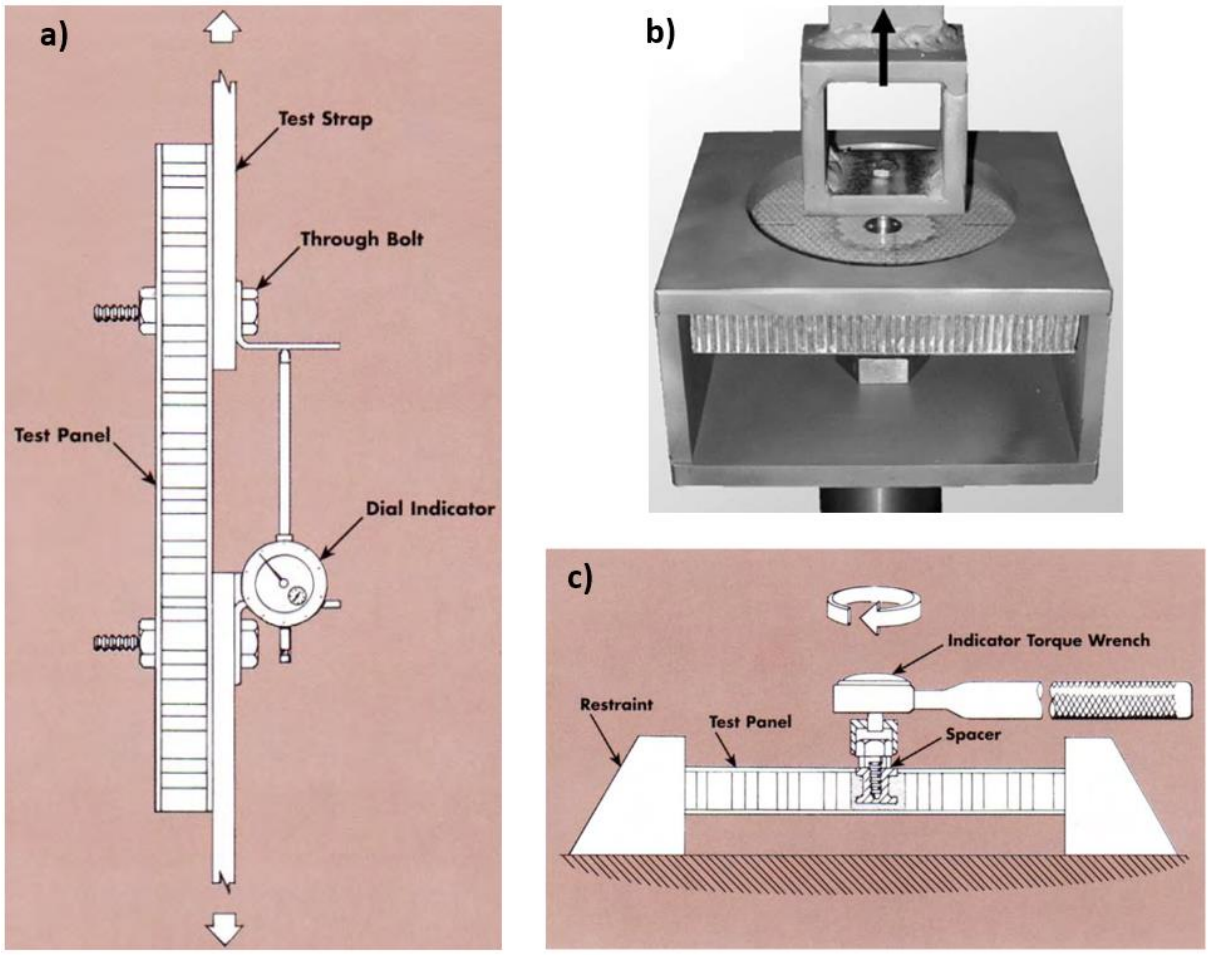

Fig. 15: Test standards of a) Shear testing, b) Pull-out test, c) Torque test, [35], [46].

2.1.3 Pull-out experimental testing of inserts

In the literature, there are several tests of inserts that have been conducted. The purpose of this section is to present those tests, including the insert characteristics, the test procedure, the load curves and the "post-mortem" analysis of the specimens. First the inserts in panels with CFRP skins and Nomex® honeycomb core are presented and later for aluminum panels.

2.1.3.1 Tests of inserts with thin CFRP skins and Nomex® honeycomb core

Panels with CFRP thin skins (the skin is considered to be thin if it is less than 21% of the core height [39]) and Nomex® honeycomb core are used for many applications like interior panels of commercial jets (737, 747, 777, 757, 767, A310, A320, etc.) and helicopters [47]. The Nomex® honeycomb is preferred in these cases because it is more resistant to fire, heat or corrosion, allows for electrical insulation and its fatigue properties are excellent, in comparison with aluminum honeycombs. A summary of these tests is presented in Table 2 and Table 3.

Bunyawanichakul did several tests during its PhD thesis [15]. Its work was focused on the identification of the phenomenology of insert damage. First, she studied a high load capability "through the thickness" insert that is used for the landing gear doors in Airbus aircraft; this insert had no fastener drowned in to the potting. In the study, they found that the nonlinearity of the loading displacement curve was related to the buckling of the Nomex® honeycomb core.

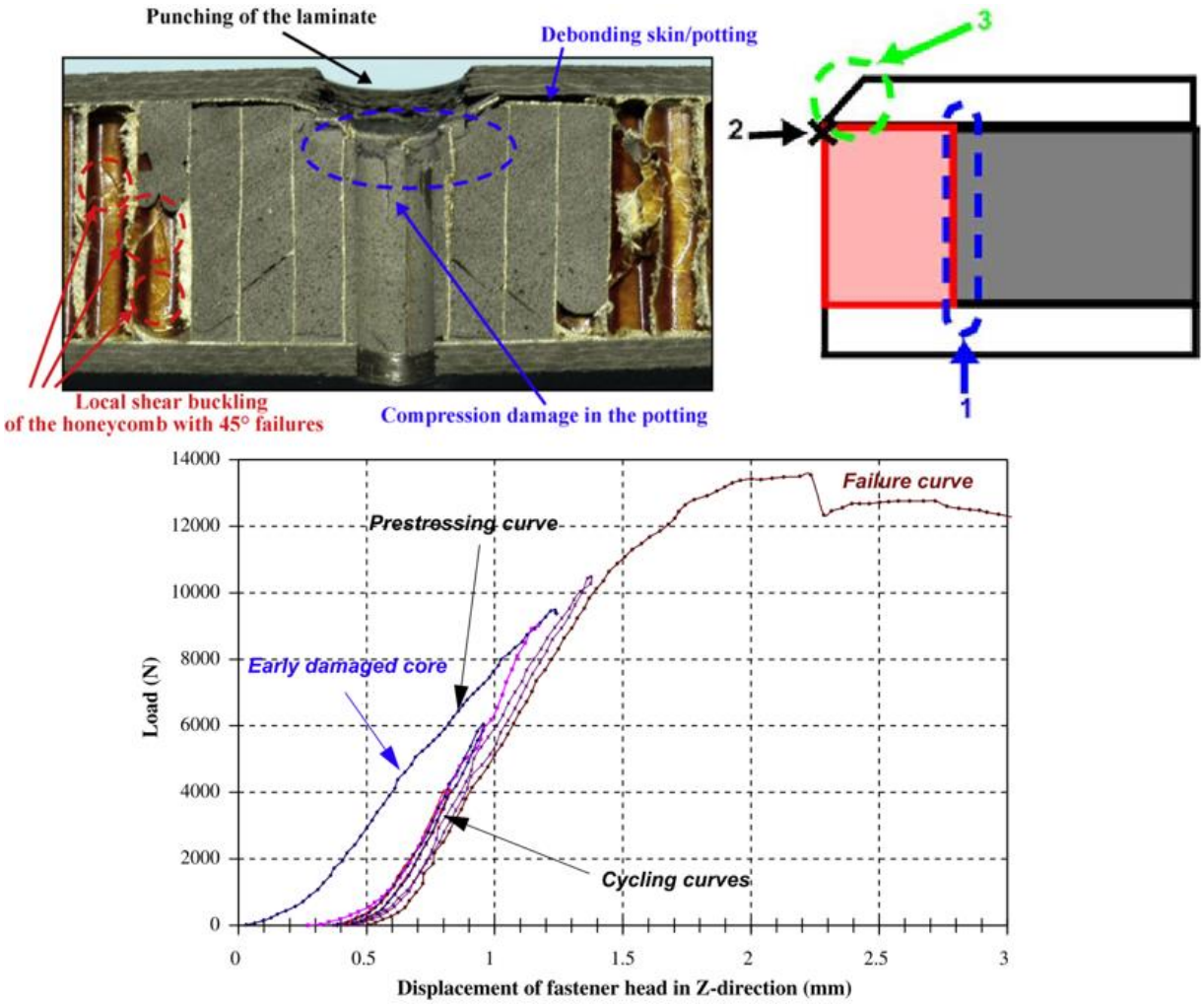

Fig. 16: Damage identification [15].

Different failure modes were detected (see ref. [15], [36]), by order of appearance they are:

- Buckling of the core
- Crushing failure of the potting material
- Delamination and matrix cracking of the skins
- Punch of the laminate
- Debonding of the skins and potting
- Failure of the potting material by crushing

Another part of the study was focused on the study of three types of inserts, two “full potting” inserts and another type of insert described as type 3. Four specimens of each type were tested to pull-out until complete failure. The study revealed that even for the same type of insert, the fabrication defects can generate a significant dispersion on the tests results. The “post mortem” specimens were cut in half and the resulting failure scenarios are shown in Fig. 17.

They found that, in the case of high loading inserts, the first significant damage was found in the core. This detected this by testing the insert until the first change in the slope, then stopped the tests and cut the specimens to analyse the failure scenario. Their conclusion was that the first nonlinearity of the loading curves was caused by the buckling of the Nomex® honeycomb core.

These conclusions are arguable for metallic inserts because for some specimens there was evidence that the fastener detached from the potting before the core started to be permanently damaged, which might suggest that the potting rupture can also be the first failure mode.

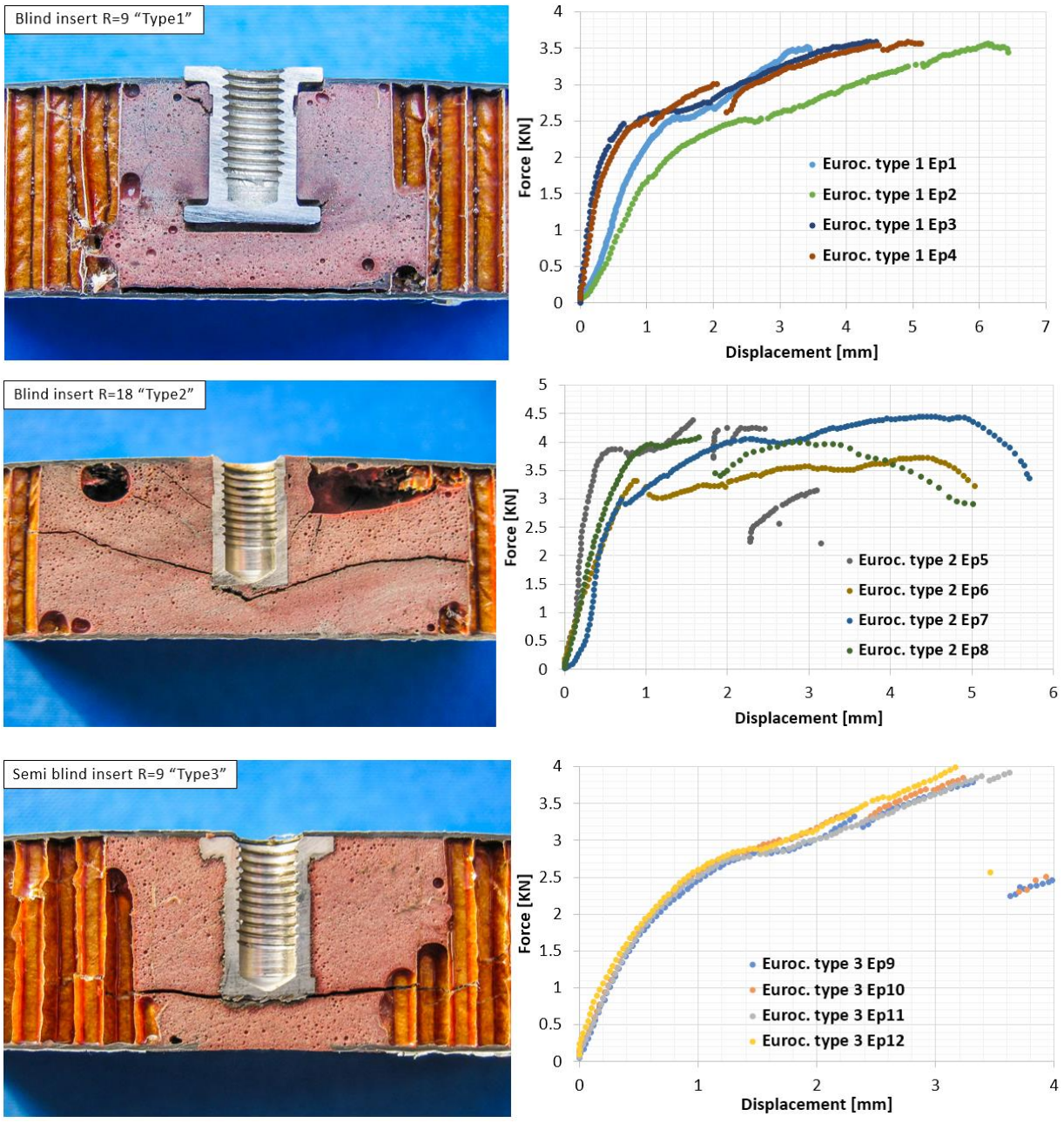

Fig. 17: Eurocopter inserts type 1, 2 and 3, [15].

In 2010, Kumsantia et al [48] investigated the failure scenario of "blind full potting" inserts by performing four pull-out tests. They didn't specify a failure criteria for the insert, however the investigation concluded that for this type of insert the first failure is strongly related to the shear failure of the core (see Fig. 18 and Fig. 19).

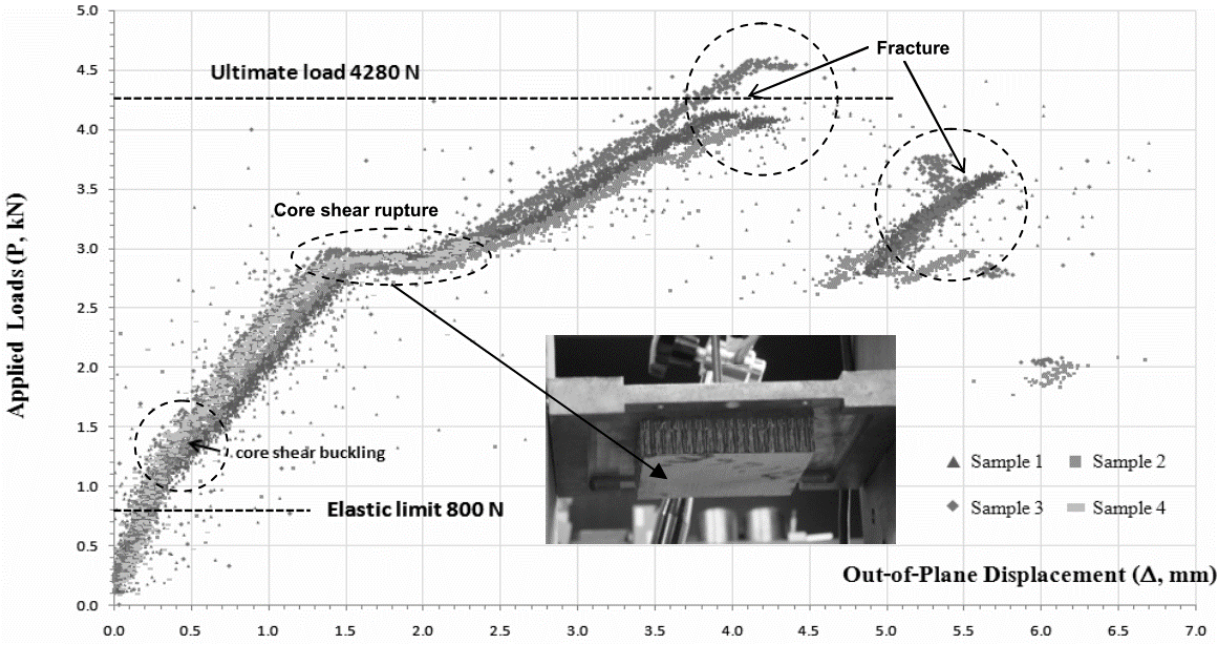

Fig. 18: Pull-out test of a full potting insert [48].

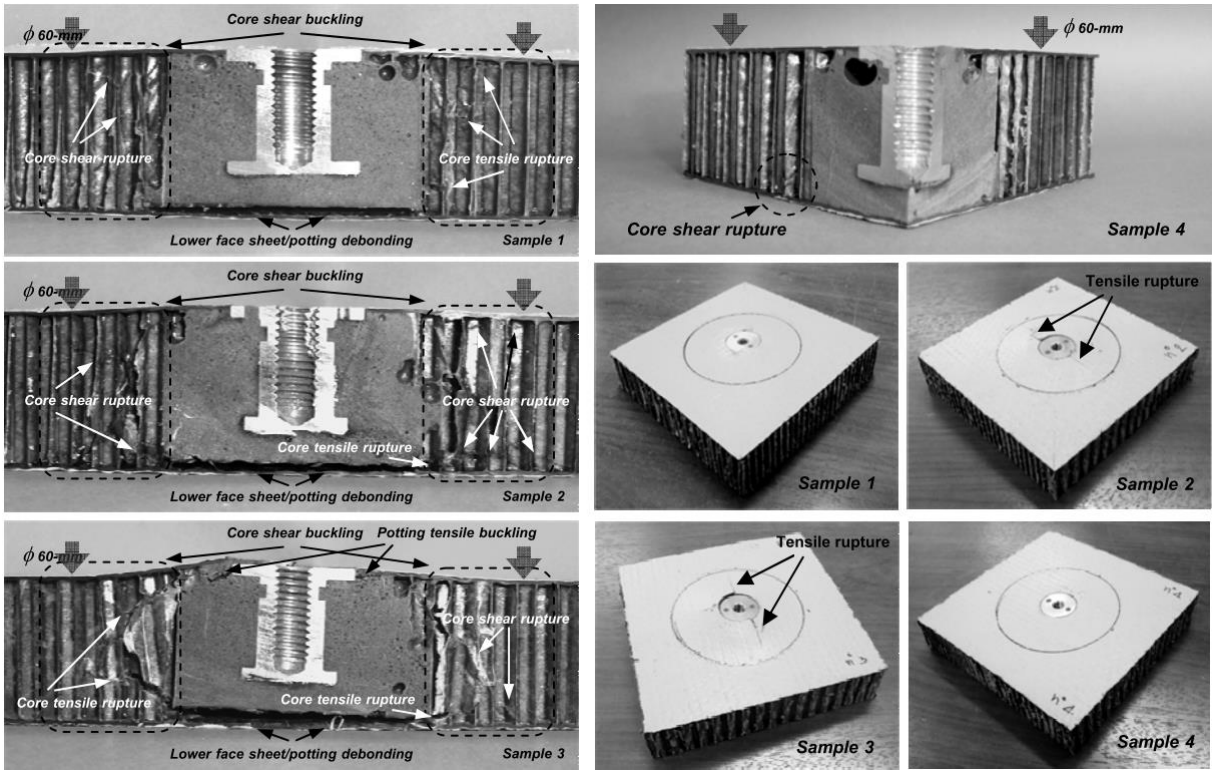

Fig. 19: Pull-out test specimens cut in half, several failure modes were detected [48].

In 2008 Song [40] tested 40 "through the thickness" inserts for a total of 8 different combinations subjected to pull-out (see Fig. 20). The goal was to study the effects of variations of parameters like the core height and density, and the thickness of the skins. The failure load was defined as the load which causes the first peak in the load-displacement curve.

The results showed that for this type of insert, the parameter which has the most important influence on the strength is the core density.

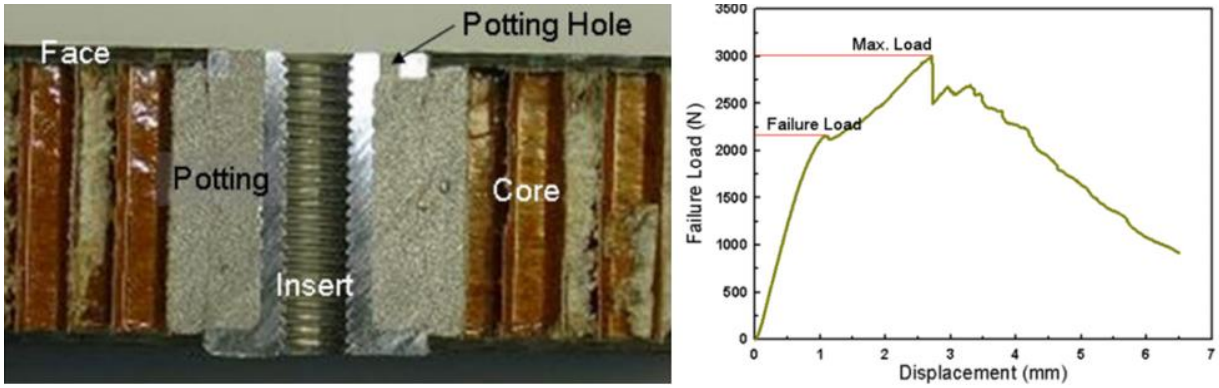

Fig. 20: Insert description and failure loads of the tests made by Song [40].

In 2013, Roy et al [33] tested 10 “through the thickness” inserts subjected to pull-out. The objective was to be able to predict the honeycomb local buckling load and identify the honeycomb properties for F.E. modeling.

To detect the failure, they used a criterion that consisted of detecting changes superior to 2% of the loading slope, compared to the initial linear regression (see Fig. 21). They concluded that the detection of the initial buckling of the honeycomb cells could be also a good criterion to detect in a precise manner the failure of the insert. This can be arguable because for some cases, the core is not the first component to fail, as suggested by the ESA in the Insert design handbook (see Fig. 38).

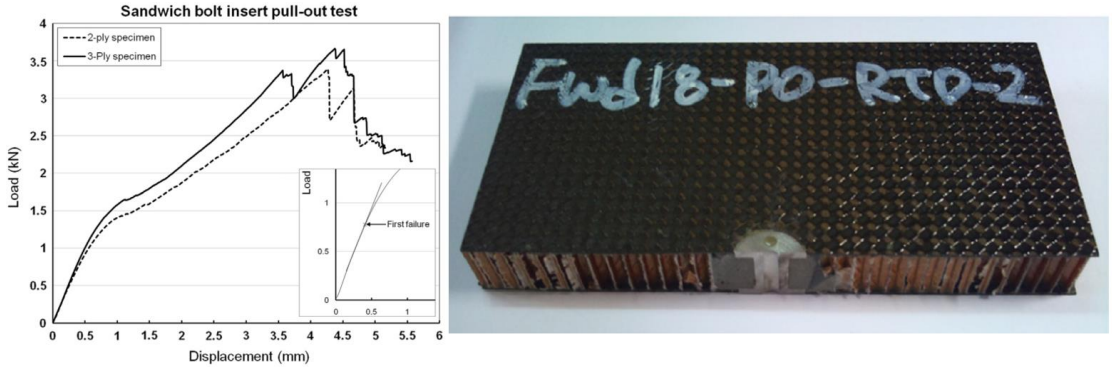

Fig. 21: Load vs displacement curve and specimen description [33].

Raghu et al. [28] performed several pull-out tests on three different type of inserts. The authors focused on investigating the effect of imperfections on the inserts, although, unfortunately, the complete experimental data of the insert tests were not provided.

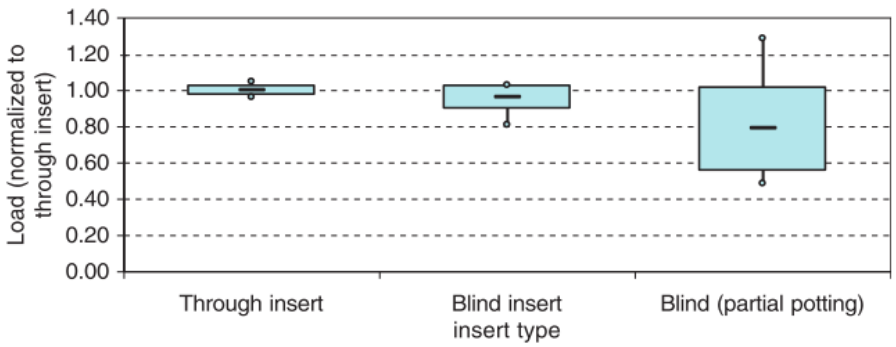

Fig. 22: Pull-out force variation of several tests [28].

This research is relevant because it investigates the fact that the imperfections may have an important influence on the tests results. First, they show the strength variation of several inserts (subjected to a pull-out test), trying to relate it to the variation of the sandwich and insert's parameters. More specifically, they studied the effect of the potting shape and honeycomb core defect for partial and through the thickness inserts (Fig. 22). They found that the potting radius may vary by 2.7% which was important for the test results. Concerning the core, they found a variation of 2.8% for the wall length and 11.8 % for the wall thickness.

In 2013, Bin Park et al [39] studied the strength of inserts under different environmental conditions. The motivation was to investigate the behavior of inserts subjected to different humidity, temperature and other factors. Regarding the case of room temperature conditions, by inspecting the "post mortem" specimens, they found that the first failure of inserts is related to the shear failure of the core (as previous work indicates) (see Fig. 23). They described the insert nonlinear behavior by dividing it into stages. The main failure modes were identified as the separation of the insert from the potting mass, potting mass fracture, and bearing failure of the upper face by the insert flange.

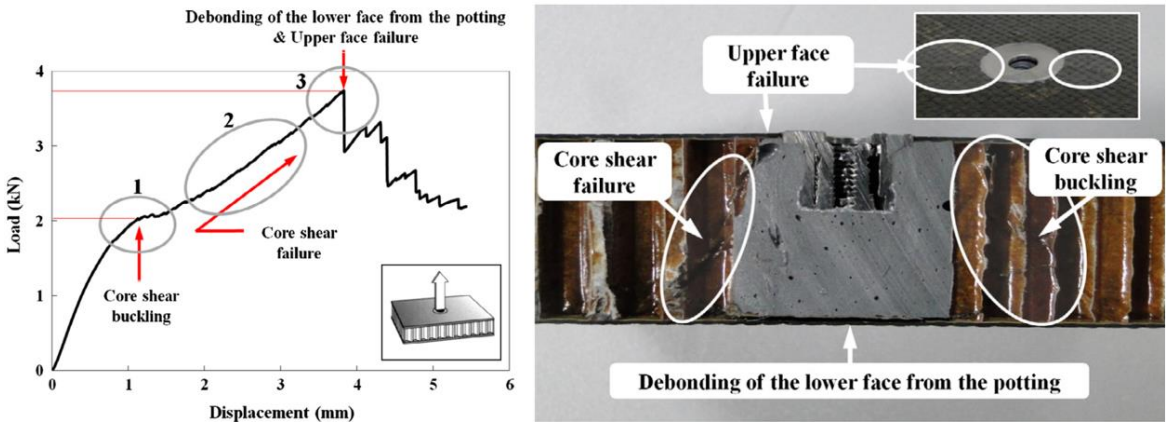

Fig. 23: Damage of a partial insert in a shear test [39].

On one of their tests it can be observed that the fastener is completely detached from the sandwich panel, before the core starts to be damaged. Also in comparison with their other tests the insert strength was nearly reduced nearly to the half. This might suggest that the potting failure may occur before the core is permanently damaged. (see Fig. 24)

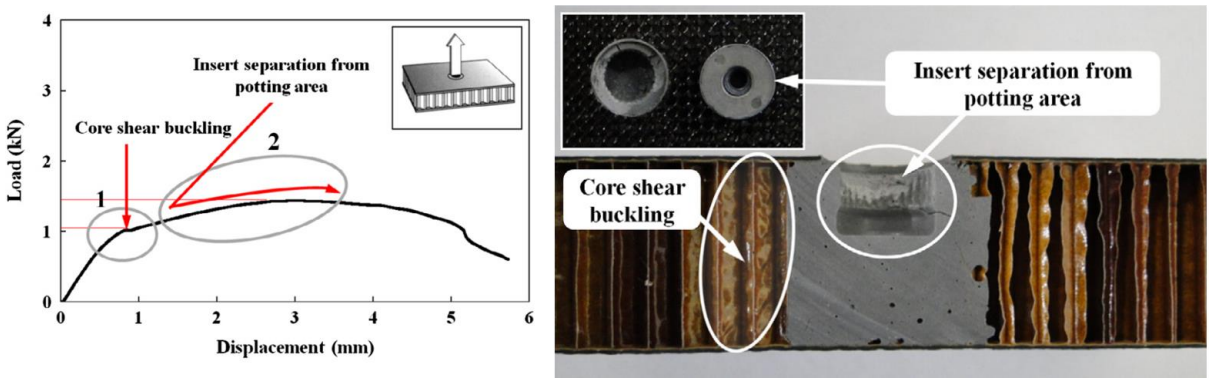

Fig. 24: Detaching of the fastener of a sandwich panel insert, this may suggest that the potting was the first element to fail [39].

In 2008, Heimbs and Pein [35] performed 12 pull-out tests on two different "full potting" inserts. Although both inserts had the same radius, the fastener used for both cases were different (Fig. 25). The study revealed that the shape of the fastener may affect the nonlinear behavior of the insert. The first damage at point A, (drop of the slope), is attributed to the shear failure of the honeycomb core adjacent to the potting mass. According to them, this

is evident due to the deformation of the inferior skin of sandwich panel. Then the load increases again up to point B, where it drops because of a tensile rupture of the potted honeycomb cells combined with a shear failure at the cell wall interfaces.

By inspecting their images, it can also be noticed that the potting seems to fail before the core starts to tear, although this is not very clear in the images.

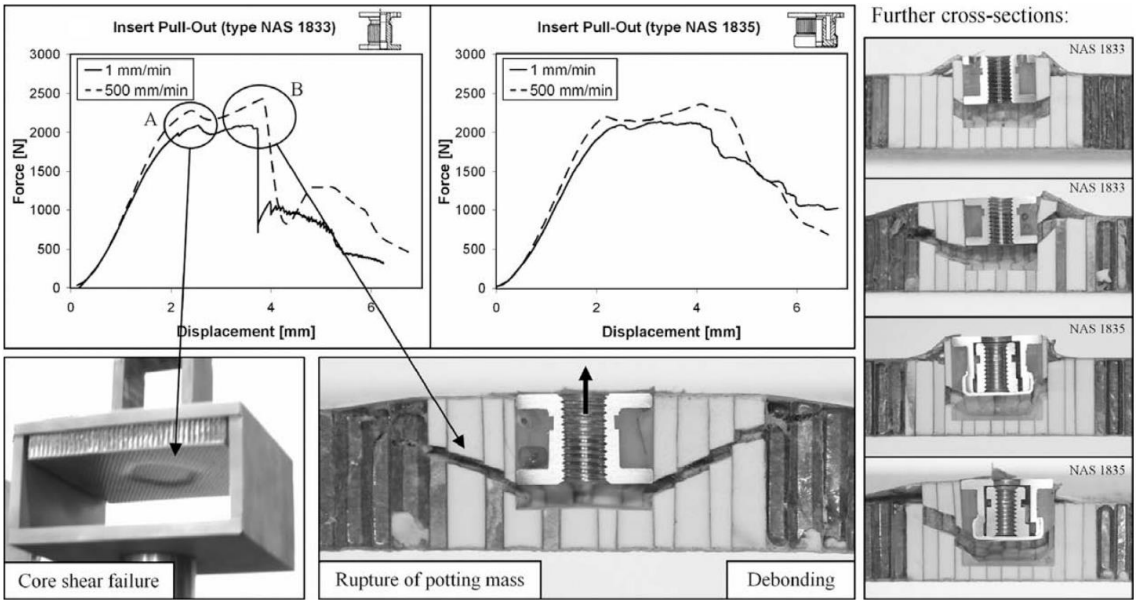

Fig. 25: Damage of a partial insert in a pull-out test [35].

Seeman et al. [34] studied the case of three "Blind full potting" inserts. The objective of the research was to investigate the technical aspects of virtual testing of inserts. First, the inserts were tested experimentally following the ESA recommendations. Concerning the F.E. modeling aspects about this research, they will be discussed later in this chapter.

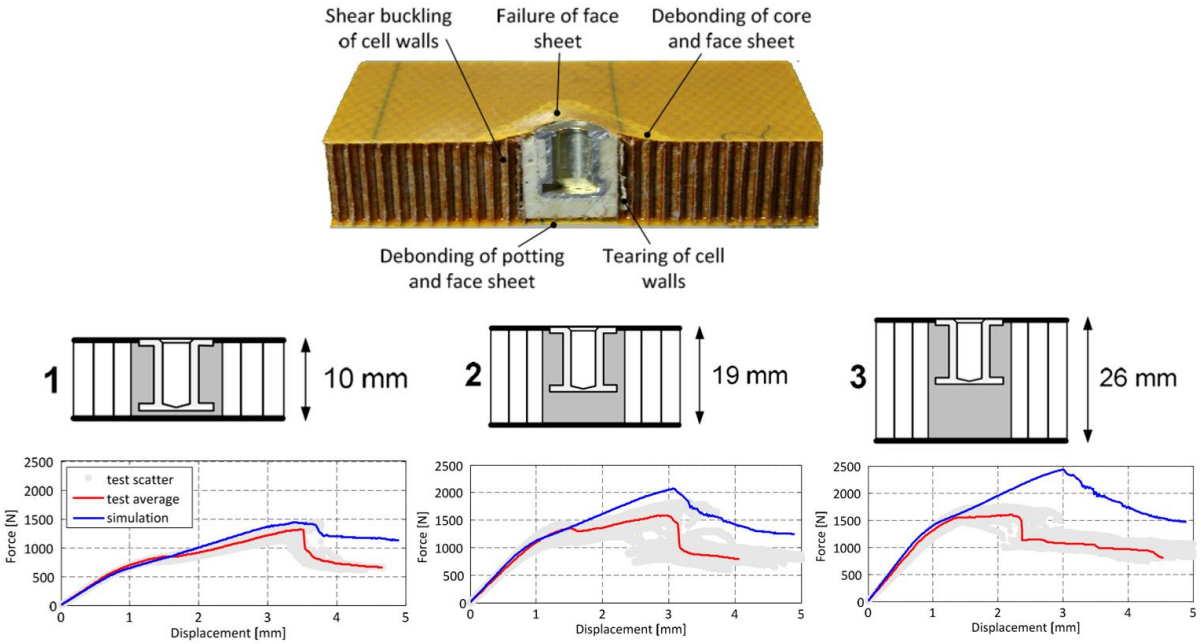

Fig. 26: Testing of inserts of different characteristics [34].

On the other hand, the experimental tests results are displayed in Fig. 26. It's interesting to mention that even for the same geometry of the inserts, their stiffness varies significantly, this is congruent to the fact that fabrication defects cause great dispersion. The identified failure mechanisms, by order of appearance were:

- Shear buckling of the walls
- Debonding of the face and core
- Failure of the face sheets
- Debonding of the potting material from the bottom skins.

2.1.3.2 Test of inserts with aluminum honeycomb core

Sandwich panels with CFRP skins and aluminum honeycomb cores are widely used for aerospace applications like satellites and space launchers, but also for some aircraft. The aluminum honeycomb core is preferred for these applications because its mechanical properties to weight ratio is the highest within the honeycomb cores, but also, because it is less expensive [19], [22].

In the literature, there are some tests of inserts on this kind of panels. As in the previous section, the insert description is given in Table 4 (see page 30).

One study was made by Kim and Lee in [44]. They studied the pull-out behavior of an insert that was formed by a metal bar and fixed with resin, also they studied the fatigue behavior of this type of inserts. They tested three types of bar shapes (see Fig. 27).

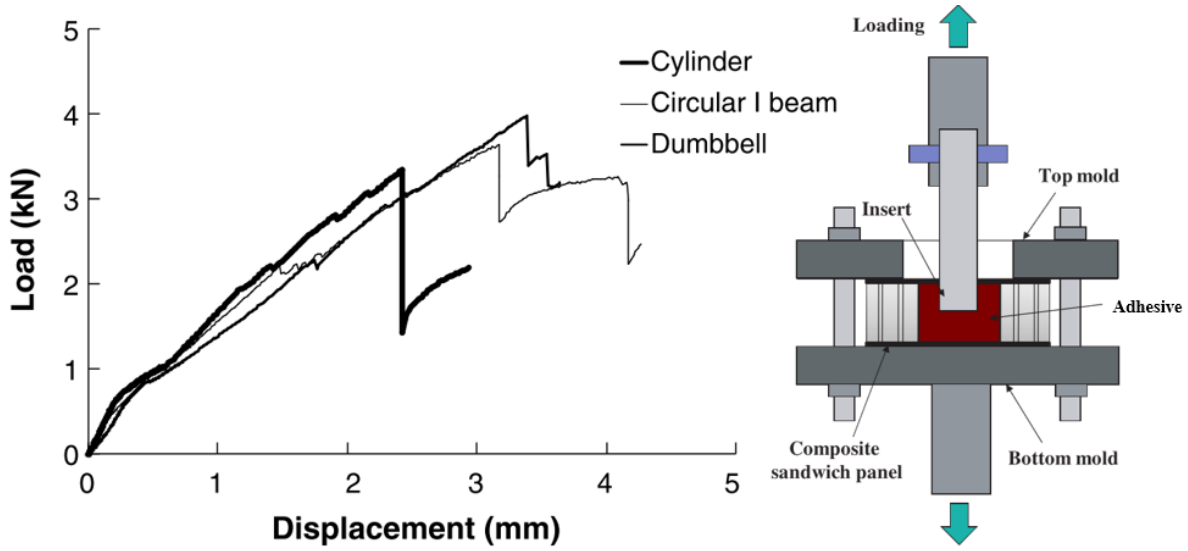

Fig. 27: Pull-out tests of inserts in sandwich panels with aluminum honeycomb core [44].

In 2008 Bianchi [41] performed 31 pull-out tests, 23 of them for a “through the thickness” insert (also called hot bonded as it’s installed in the manufacturing phase of the panel) and the other 8 “full potting” inserts (also called cold bonded insert). The aim was to compare both performances of each type of insert. The result was that the cold bonded inserts were more performant in terms of load carrying capability. Also, it’s interesting that the authors pointed out that the cells acted in a postbuckling regime by studying analytically the shear buckling load of a cell wall and comparing it to the actual stress, which are the same conclusions as those of Bunyawanichakul et al. in [8]. Also, they found that the potting material had a big influence on the strength of these inserts (see Fig. 28).

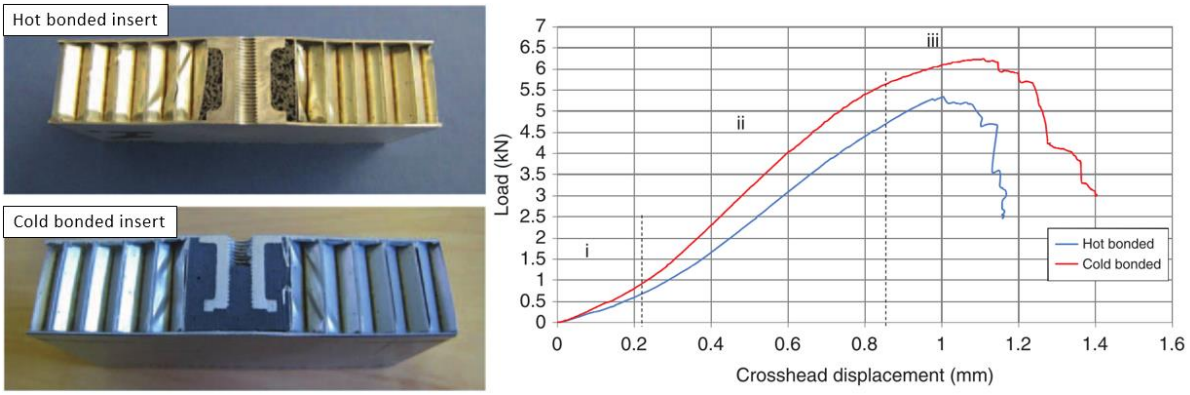

Fig. 28: Pull-out test presented by Bianchi [41].

2.1.3.3 Post-impact insert strength

In 2017 Mezeix studied the post impact behavior of inserts [49]. Their method was, first, to expose the insert to a low energy impact (50 J) and then submit it to a pull-out test. He found that the insert strength was reduced only by 10% compared to non-impacted coupons (see Fig. 29).

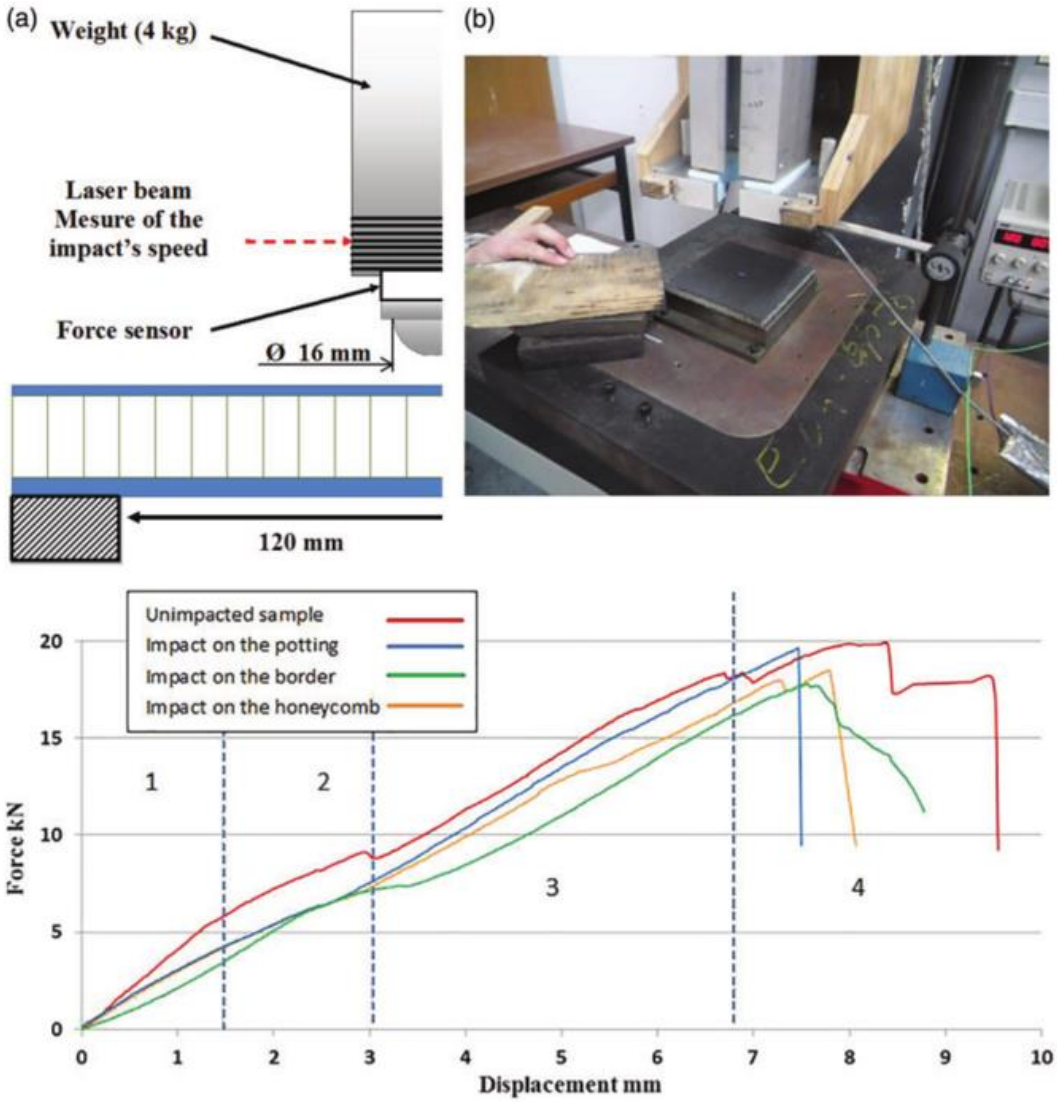

Fig. 29: Post impact behavior of inserts presented by Mezeix [49].

2.1.3.4 Summary of the insert pull-out testing review

The different tests show that the first failure mode is commonly the shear buckling of the core. Also, the influence of the core properties on the insert strength was proven, it was shown that when the core is higher or denser, the insert strength increases significantly. This explains why the insert calculation methods estimate the insert strength based on the shear resistance of the core.

However, there is also evidence that for some cases, the potting may fail before the core as can be seen in Fig. 17, Fig. 24 or Fig. 25.

Also, for all the experimental tests, there was a stiffness dispersion that might be related to the fabrication defects of the potting and core as Raghu explained in [28]. However, due to the complexity of the problem their respective influence is difficult to consider using the currently existing sizing methods.

All these results should be considered for the insert sizing methods, which are presented in the next section.

It's interesting to point that there is not a consensus to define a failure criteria for inserts, although some researchers suggested that the core shear buckling may be a good candidate.

Finally, as recommended by Shur-lok [46], all the properties of the presented insert specimens are identified and summarized in tables. For the sake of brevity, they are presented in Table 2 and Table 3 for CFRP sandwich and Table 4 for aluminum sandwich. The table's nomenclature is as follows:

For the skins, the reference and the layer orientations are identified for every specimen, also the thickness (e), the elastic moduli in the plane (E) and the Poisson ratio (v).

For the core, the reference, the thickness (C), the shear moduli in both directions (G_W & G_L), the maximal admissible shear stress in both directions (t_{admW} & t_{admL}) and finally the cell size.

For the insert, the potting reference is identified, the elastic moduli of the potting (E), the Poisson ratio(v), the radius of the support (a), and finally, the radius of the hole made to install the insert (b).

Concerning the test results, the experimental failure load is given (real test) and the failure criterion used to detect this load, although for most of the cases both parameters are not given by the authors.

	Skin				Core							Insert					Test	
	Reference	e [mm]	E [MPa]	v	Reference	C [mm]	G_W [MPa]	G_L [MPa]	t_adm W [MPa]	t_adm L [MPa]	Cell size [mm]	Potting reference	E [MPa]	v	a [mm]	b [mm]	Failure load [N]	Failure criteria
Blind full potting insert (Kumsantia 2010)	G0939/145.8 [0/90]	0.55	52000	0.09	Nomex® honeycomb 3.0 pcf	20	17	26	0.32	0.48	3.18	EA9396 STRUCTIL - 10%mb phenol	940	0.4	30	16.5	1200	Aprox.
Through the thickness insert (Song 2008) P01	wsn3k SK chemical [45,0]s	0.84	49108	0.34	PN2-3.0-1/8	17.8	24	46	0.72	1.41	3.18	Hysol EA9394	4237		30	7.5	1890	First peak
Through the thickness insert (Song 2008) P02	wsn3k SK chemical [45,0]s	0.84	49108	0.34	PN2-3.0-1/8	22.9	24	46	0.72	1.41	3.18	Hysol EA9394	4237		30	7.5	2320	First peak
Through the thickness insert (Song 2008) P03	wsn3k SK chemical [45,0]s	0.84	49108	0.34	PN2-3.0-1/8	27.9	24	46	0.72	1.41	3.18	Hysol EA9394	4237		30	7.5	2640	First peak
Through the thickness insert (Song 2008) P04	wsn3k SK chemical [45,0]s	0.84	49108	0.34	PN2-5.0-1/8	17.8	42	74	1.48	2.24	3.18	Hysol EA9394	4237		30	7.5	2740	First peak
Through the thickness insert (Song 2008) P05	wsn3k SK chemical [45,0]s	0.84	49108	0.34	PN2-8.0-1/8	17.8	73	115	2.03	2.9	3.18	Hysol EA9394	4237		30	7.5	4480	First peak
Through the thickness insert (Song 2008) P06	wsn3k SK chemical [45,0,45]s	1.26	39437	0.47	PN2-3.0-1/8	17.8	24	46	0.72	1.41	3.18	Hysol EA9394	4237		30	7.5	2620	First peak
Through the thickness insert (Song 2008) P07	wsn3k SK chemical [45,0]2s	1.68	49108	0.34	PN2-3.0-1/8	17.8	24	46	0.72	1.41	3.18	Hysol EA9394	4237		30	7.5	3170	First peak
Through the thickness insert (Song 2008) P08	wsn3k SK chemical [45,0]s	0.84	49108	0.34	PN2-3.0-1/8	17.8	24	46	0.72	1.41	3.18	Hysol EA9394	4237		30	7.5	1840	First peak
Through the thickness insert (Roy 2013)	Cytec G30-500-3k-PW/5276-1 [0,45]	0.2	49044	0.36	HRH-10-1/8-3.0	13	24.13	44.81	0.69	1.2	3.18	Magnobond 6398	2068	0.4	40	10.5	859	2% dev
Through the thickness insert (Roy 2013)	Cytec G30-500-3k-PW/5276-1 [0,45,0]	0.3	56669	0.26	HRH-10-1/8-3.0	13	24.13	44.81	0.69	1.2	3.18	Magnobond 6398	2068	0.4	40	10.5	893	2% dev
Through the thickness insert (Raghu 2009)	2 plies 7781 E-glass/phenolic [-,-]	0.51	2176	0.3	HRH-10-1/8-3.0	25.4	24.13	44.81	0.69	1.2	3.18	3M EC-2216 B/A Epoxy			40	10	-	-
Blind full potting insert (Raghu 2009)	2 plies 7781 E-glass/phenolic [-,-]	0.51	2176	0.3	HRH-10-1/8-3.0	25.4	24.13	44.81	0.69	1.2	3.18	3M EC-2216 B/A Epoxy			40	10	-	-
Blind partial potting (Raghu 2009)	2 plies 7781 E-glass/phenolic [-,-]	0.51	2176	0.3	HRH-10-1/8-3.0	25.4	24.13	44.81	0.69	1.2	3.18	3M EC-2216 B/A Epoxy			40	10	-	-

Table 2: Summary of insert pull-out tests performed by different researchers, the values in red are not specified by the respective researchers, also, information in empty fields is not available [28], [33], [40], [48].

	Skin				Core							Insert					Test	
	Reference	e [mm]	E [MPa]	v	Reference	C [mm]	G_W [MPa]	G_L [MPa]	t_adm W [MPa]	t_adm L [MPa]	Cell size [mm]	Potting reference	E [MPa]	v	a [mm]	b [mm]	Failure load [N]	Failure criteria
Blind full potting (Bin Park 2014)	Cytec 5250-4/T650-35 3K70PW [45,0,45]	0.65	47094	0.4	Gilcore HD322 2.0 pcf	25.4	11.7	20	0.31	0.552	4.76	Magnobond 6398	2068	0.4	40	10	1980	Core buckling
Blind full potting insert type 1 (Bunyawanichakul 2005)	G0939/145.8 [0/90]	0.55	52000	0.09	Nomex® phenolic 3.0 pcf	20	17	26	0.32	0.55	3.18	AV-121B-10%mb phenol	1312	0.3	30	9	1400	Aprox.
Blind full potting insert type 2 (Bunyawanichakul 2005)	G0939/145.8 [0/90]	0.55	52000	0.09	Nomex® phenolic 3.0 pcf	20	17	26	0.32	0.55	3.18	AV-121B-10%mb phenol	1312	0.3	30	18	1500	Aprox.
Full potting insert type 3 (Bunyawanichakul 2005)	G0939/145.8 [0/90]	0.55	52000	0.09	Nomex® phenolic 3.0 pcf	20	17	26	0.32	0.55	3.18	AV-121B-10%mb phenol	1312	0.3	30	9	2260	Aprox.
Through the thickness insert (Trap door Airplane) (Bunyawanichakul 2005)	G803/914 [0,45,]8s	2.6	41810	0.29	Nomex® honeycomb 3.0 pcf	20	24.13	31.71	0.55	0.8549	4.76	3M 3500-2B/A	1474	0.3	30	7.5	5500	Aprox.
Metallic Insert full potting (Heimbs and Pein 2009)	E-glass/phenolic Stesalit PHG 600-68-50	0.24	20000	0.06	Schütz Cormaster C1-3.2-48	14.6	25.5	41.9	1.21	0.8	3.18	Cytec BR 632 B4/Huntsman Araldite 2011	3200	0.3	50	19	1978	Aprox.
Blind full potting insert (Seeman et. al. 2016) case 1	PHG 600-44-50 / PHG600-68-50 glass				Nomex® honeycomb 3.0 pcf	10					3.18	Ureol 1356 a/b	800		40	16.5	650	Aprox.
Blind full potting insert (Seeman et. al. 2016) case 2	PHG 600-44-50 / PHG600-68-50 glass				Nomex® honeycomb 3.0 pcf	19					3.18	Ureol 1356 a/b	800		40	16.5	1050	Aprox.
Blind full potting insert (Seeman et. al. 2016) case 3	PHG 600-44-50 / PHG600-68-50 glass				Nomex® honeycomb 3.0 pcf	26					3.18	Ureol 1356 a/b	800		40	16.5	1200	Aprox.

Table 3: Summary of insert pull-out tests performed by different researchers, the values in red are not specified by the respective researchers, also, information in empty fields is not available [15], [34]–[36], [39].

	Skin				Core							Insert					Test	
	Reference	e [mm]	E [MPa]	v	Reference	C [mm]	G_W [MPa]	G_L [MPa]	t_adm W [MPa]	t_adm L [MPa]	Cell size [mm]	Potting reference	E [MPa]	v	a [mm]	b [mm]	Failure load [N]	Failure criteria
Blind partial potting insert (Jung Kim 2008)	USN150, SK Chemical [0,90]2s	0.5	51700	0.3	Alcore 5052 Alu 2.3 pcf perf.	20	76	145	0.61	1	6.35	Stycast epoxy 1090 + cylindrical fastener.	2100	0.3	40	7	3340	Max load
Blind partial potting insert (Jung Kim 2008)	USN150, SK Chemical [0,90]2s	0.5	51700	0.3	Alcore 5052 Alu 2.3 pcf perf.	20	76	145	0.61	1	6.35	Stycast epoxy 1090+ I shape fastener.	2100	0.3	40	7	3980	Max load
Blind partial potting insert (Jung Kim 2008)	USN150, SK Chemical [0,90]2s	0.5	51700	0.3	Alcore 5052 Alu 2.3 pcf perf.	20	76	145	0.61	1	6.35	Stycast epoxy 1090 + dumbbell shape fastener.	2100	0.3	40	7	4270	Max load
Through the thickness insert (Bianchi 2010)	Alu 2014	0.5	75000	0.3	5056 Alu 2.3 5.18pcf	19	220.6	579	2.06	3.44	6.35	Redux 219/2-NA	1034	0.3	40	7	5600	Max load
Blind full potting insert (Bianchi 2010)	Alu 2014	0.5	75000	0.3	5056 Alu 2.3 5.18pcf	19	220.6	579	2.06	3.44	6.35	Stycast epoxy 1090	2500	0.3	40	7	6180	Max load
SW-1 (J. Block 2004)	Carbon fiber [0,90]6	1.5	54000	0.3	CRIII 1/4-5052-0015P	50	164.75	334.7	0.757614	1.246907	6.35							
SW-2 (J. Block 2004)	Carbon fiber [0,90]6	1.5	54000	0.3	CRIII 1/8-5052-0007P	50	151	310	0.707107	1.136422	3.175							
SW-3 (J. Block 2004)	Carbon fiber [0,90]2	0.5	54000	0.3	CRIII 1/4-5052-0015P	50	164.75	334.7	0.757614	1.246907	6.35							
SW-4 (J. Block 2004)	Carbon fiber [0,90]2	0.5	54000	0.3	CRIII 1/4-5052-0007P	50	75.84	144.7	0.268322	0.457725	6.35							
SW-5 (J. Block 2004)	Carbon fiber [0,90]2	0.5	54000	0.3	CRIII 1/4-5052-0015P	20	164.75	334.7	0.944279	1.554125	6.35							
SW-6 (J. Block 2004)	Carbon fiber [0,90]2	0.5	54000	0.3	CRIII 1/4-5052-0007P	20	75.84	144.7	0.334432	0.570502	6.35							

Table 4: Summary of insert pull-out tests on aluminum honeymoon sandwiches performed by different researchers, the values in red are not specified by the respective researchers, also, information in empty fields is not available [41], [44].

2.1.4 Strength prediction of inserts by analytical approaches

The strength of an insert must rely on the strength of its components and the way they interact with each other. Since sandwich panels started to become popular, the need to calculate the strength of an insert becomes primordial. For these reasons, there are several works that are focused into developing a method to predict the insert strength.

This section is dedicated to present the most common analytical methods of strength prediction for inserts in sandwich structures. They are presented in order of complexity. Special emphasis is focused on the analysis of the shear stress in the core, as it's the core that causes most often the first failure of inserts as shown in the previous section.

2.1.4.1 The Forest Product Laboratory model (Ericksen)

In 1953, the U.S. Forest Product Laboratory published a work about the calculation of the bending stress on inserts in sandwich structures entitled "The bending of a circular sandwich panel under normal load", this work was carried on by Ericksen [3]. To the knowledge of the author this is the first analytical formulation that describes the shear stress distribution of the core of the panel, i.e. the prediction of insert strength based on the failure of the core. This approach calculates also the deflection of the panel due to bending and shear forces. The aim was to provide estimations that could be useful for design purposes. Several hypotheses were made:

- The core and facing materials are taken as isotropic and the facings are assumed to be of equal thickness.
- The effect of the bending of the core is neglected.
- The transverse shear stress in the core is constant over the thickness of the core.
- The transverse shear strains in the facings are neglected.
- The two facings have the same curvature.
- The thickness of the core remains the same under buckling.

The proposed equations are based on the theory of bending of homogenous circular plates. The insert effect is introduced into the equations by setting specific boundary conditions at the center of the panel. The model supposes that a load *P* is applied at the center of the panel and that the insert has a radius *b* and passes through all the thickness of the core, which is sufficiently representative of a pull-out test. The support tool of radius *a*, is considered as a ring that may provide two different boundary conditions: clamped and simply supported (see Fig. 30).

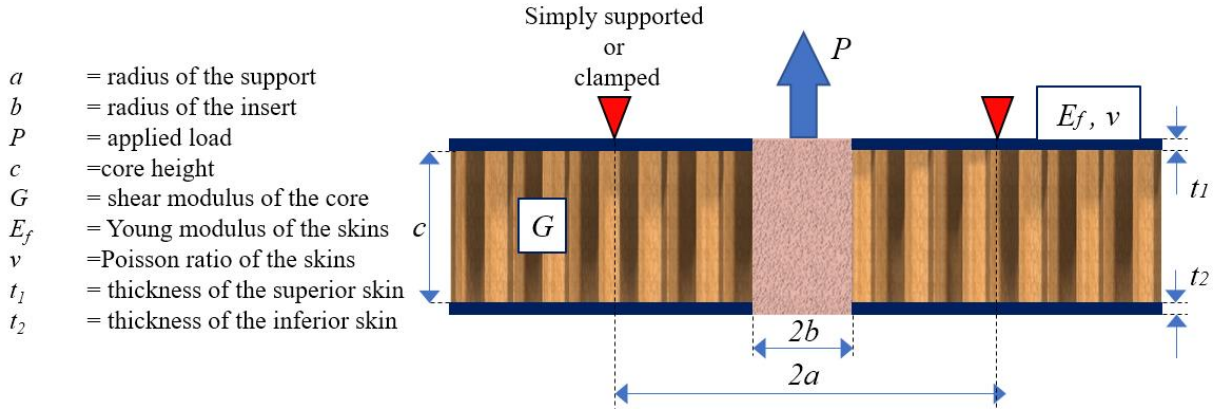

Fig. 30: Parameters of the sandwich panel for the model of Ericksen.

Also, the formulation requires the calculation of the inertias of the panel and other parameters:

$$I_m = \frac{t_1 t_2 (c + \frac{t_1+t_2}{2})^2}{t_1 + t_2}$$

$$I_f = \frac{t_1^3 + t_2^3}{12}$$

$$I = I_f + I_m$$

$$E = \frac{E_f}{1 - v^2}$$

$$\alpha = \sqrt{\frac{G(t_1 + t_2)I}{Ect_1 t_2}}$$

Finally, for the case when the support is clamped, the stress on the core is given by:

$$\tau(r) = \frac{PI_m}{2\pi I\left(c + \frac{f_1+f_2}{2}\right)} \left\{ \frac{1}{r} - \frac{I_1(\alpha r)}{ab} \left[\frac{bK_1(\alpha b) - aK_1(\alpha a)}{I_1(\alpha a)K_1(\alpha b) - I_1(\alpha b)K_1(\alpha a)} \right] - \frac{K_1(\alpha r)}{ab} \left[\frac{aI_1(\alpha a) - bI_1(\alpha b)}{I_1(\alpha a)K_1(\alpha b) - I_1(\alpha b)K_1(\alpha a)} \right] \right\} \quad (1)$$

And for the case when the support is simply supported, the stress in the core is given by:

$$\tau(r) = \frac{PI_m}{2\pi I\left(c + \frac{f_1+f_2}{2}\right)} \left(\frac{1}{r} - A + B \right)$$

where A and B are:

$$A = \frac{I_1(\alpha r)}{\alpha a b^2} \left[\frac{\alpha b^2 \left[K_0(\alpha b) - (1 - v)\frac{K_1(\alpha b)}{\alpha b} \right] + a(1 - v)K_1(\alpha a)}{I_1(\alpha a)\left[K_0(\alpha b) - (1 - v)\frac{K_1(\alpha b)}{\alpha b} \right] - K_1(\alpha a)\left[I_0(\alpha b) - (1 - v)\frac{I_1(\alpha b)}{\alpha b} \right]} \right]$$

$$B = \frac{K_1(\alpha r)}{\alpha a b^2} \left(\frac{a(1 - v)I_1(\alpha a) + \alpha b^2 \left[I_0(\alpha b) - (1 - v)\frac{I_1(\alpha b)}{ab} \right]}{I_1(\alpha a)\left[K_0(\alpha b) - (1 - v)\frac{K_1(\alpha b)}{\alpha b} \right] - K_1(\alpha a)\left[I_0(\alpha b) - (1 - v)\frac{I_1(\alpha b)}{\alpha b} \right)} \right)$$

where I and K represents the modified Bessel function of the first and second order respectively (which are defined by eq. 2 and 3 where x is a dummy variable that should be replaced by $\alpha b, \alpha a$ or αr) and the subscript 0 or 1 represent the series development order n, where, $\gamma = 0.5772$ is the Euler constant

$$I_n(x) = \begin{cases} \left(\frac{x}{2}\right)^n + \frac{1}{(n+1)!}\left(\frac{x}{2}\right)^{n+2} & n = 0, 1 \quad \text{if } x < 1 \\ \frac{e^x}{\sqrt{2\pi x}} & n = 0, 1 \quad \text{if } x > 1 \end{cases} \quad (2)$$

$$K_n(x) = \begin{cases} -\log\frac{x}{2} - \gamma - \frac{x^2}{4}\left(\log\frac{x}{2} + \gamma - 1\right) & n = 0 \quad \text{if } x < 1 \\ -\frac{1}{x} - \frac{x}{2}\left(\log\frac{x}{2} + \gamma - \frac{1}{2}\right) & n = 1 \quad \text{if } x < 1 \\ e^{-x}\cos(n\pi)\sqrt{\frac{\pi}{2x}} & n = 0, 1 \quad \text{if } x > 1 \end{cases} \quad (3)$$

An example of both shear stress distributions are plot in Fig. 31. They describe the stress in the core, for b < r < a.

The most important aspect of this model is that it allows to estimate the maximal shear stress induced to the core due to the pull-out of the insert. Then, this shear stress is compared to the maximal allowable shear stress of the core, allowing to calculate the maximal pull-out strength.

It's important to notice that for the clamped model the maximal shear stress is not located at the core/insert interface, but a little further (7.55 mm in the example).

Also, the shear stress at the insert/core interface for both models is different; for the simply supported case is not zero. This should be important but in practice it's not, because the insert sizing methods only consider the shear stress at the radius of the maximal shear stress (7.55 mm) which is very similar for both cases (around 0.8 MPa in this example).

The complexity of these equations is obvious. For this reason, the calculation of the maximal shear stress is simplified by substituting most of the difficult terms by a coefficient named *T* that can be calculated in function of the shape parameters of the insert. This is given by eq. 4 and the chart of Fig. 31-b, although only for the clamped case.

$$\tau_{max} = \frac{P I_m \alpha}{2\pi I (c + \frac{t_1+t_2}{2})} T \qquad 4$$

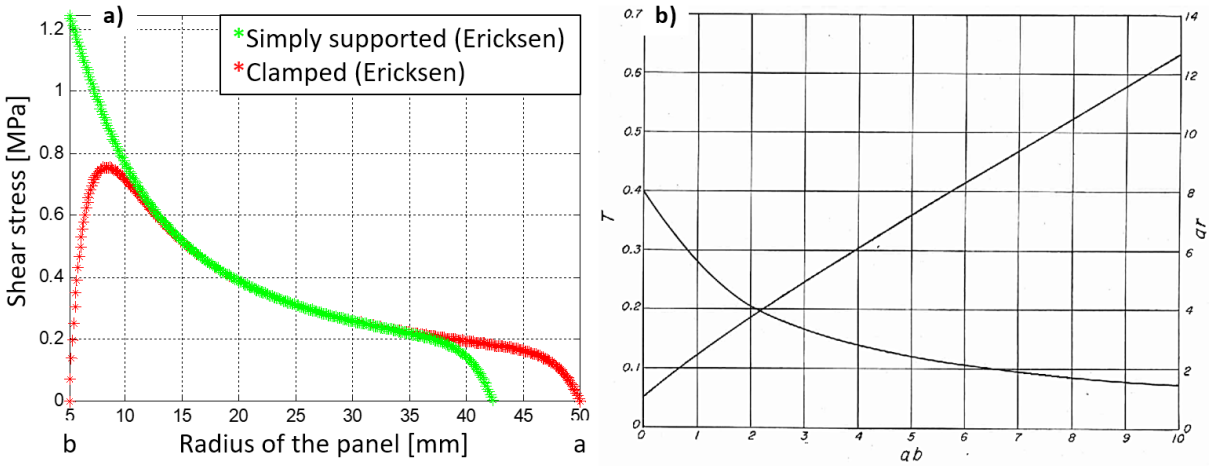

Fig. 31: Shear stress distribution of the core according to [3] and T values to calculate the maximal shear stress using eq. 4.

In 1973, the same model was retaken by Montrey, engineer of the same laboratory. The same equations were rewritten in a simpler way, also, the notation is different [50]:

$$\gamma = \frac{b}{a}$$

$$\lambda = 1 - \mu^2$$

$$D_m = \frac{E_1 t_1 E_2 t_2 h^2}{(E t_1 + E_2 t_2)\lambda}$$

$$D_f = \frac{E_1 t_1^3 + E_2 t_2^3}{12\lambda}$$

$$D = D_f + D_m$$

$$A = \alpha a$$

$$\alpha = \sqrt{\frac{hGD}{D_f D_m}}$$

$$\beta = \alpha r$$

The shear stress distribution was separated in two parts, first, a part that is proportional to the characteristics of the sandwich panel. And finally, an equation that gives the shape of the stress distribution given by the k_3 variable:

$$\tau_{max} = \frac{PD_m}{2\pi bhD} k_3$$

The shape of the shear stress distribution is given by the two boundary conditions, clamped and simply supported, $k_3^{(CLMP)}$ and $k_3^{(S.S.)}$ respectively:

$$k_3^{(CLMP)} = \frac{\gamma A}{\beta} - \frac{I_1(\beta)[\gamma K_1(\gamma A) - K_1(A)] - K_1(\beta)[\gamma I_1(\gamma A) - I_1(A)]}{I_1(A)K_1(\gamma A) - I_1(\gamma A)K_1(A)}$$

$$k_3^{(S.S)} = \frac{\gamma A}{\beta} - \frac{\Psi}{\Delta}$$

with

$$\Psi = A[I_0(A)K_1(\beta)+I_1(\beta)K_0(A)]-(1-\mu)\langle I_1(\beta)[\gamma K_1(\gamma A)-K_1(A)]-AK_1(\beta)[\gamma I_1(\gamma A)-I_1(A)]\rangle$$

$$\Delta = A[I_0(A)K_1(\gamma A)+I_1(\gamma A)K_0(A)]-(1-\mu)[I_1(A)K_1(\gamma A)-I_1(\gamma A)K_1(A)]$$

This shear distribution reveals that the maximal shear stress of the core is not localized at the potting/core interface, but slightly far from it (see Fig. 31 and Fig. 32). Also, due to the hypotheses that were made, there is no way to differentiate between a “through the thickness insert” and a “full potting partial insert”.

The same model and formulations have been used first for the Mil-HDBK-23A of the USA [2], and then for the insert design handbook of the ESA of 1987 [37] and posterior versions, as reference to analytically calculate the insert strength to pull-out, although this is only recommended for full potting inserts.

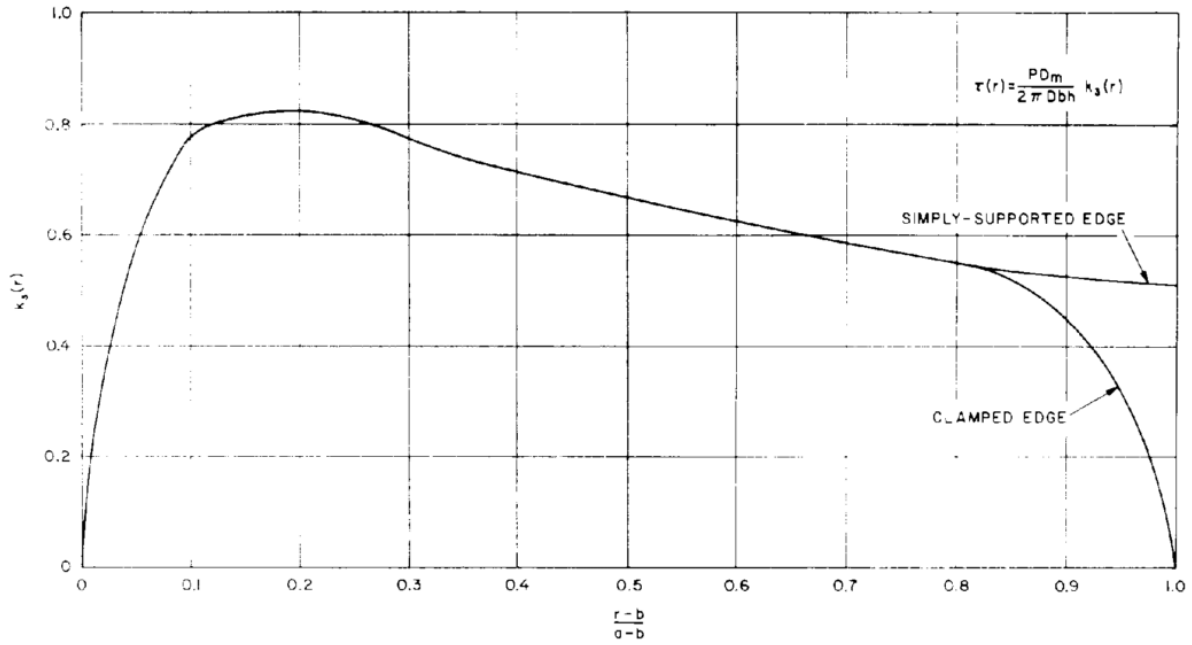

Fig. 32: k_3 coefficient representing the shear stress distribution in the core [50].

The presented model assumes that the value of the shear stress in the core at the potting/core interface is zero, which was proved to be wrong by more detailed models as will be presented in the following paragraphs.

2.1.4.2 The Thomsen model

In 1994, Thomsen proposed a high order approach that allowed to model some nonlinear aspects that are not considered by the classical theory of bending of homogeneous circular sandwich plates used by Ericksen. This includes the differences of the deflection of inferior and superior faces, the shear interaction between the skins and the core, the nonlinearities related to the geometry of the core, the transversal compression of the core, among others. Also, this approach was validated by comparison to experiments [51].

Then, in 1998, Thomsen and Rits used this same approach to model in a more precise manner than Ericksen, the internal stress of the core and skins and the potting interface [29], [30]. The hypothesis made for this model and are listed as follows:

- The face sheets are modelled as elastic plates, the effects of transverse shearing deformations may be accounted for. The materials of the skins are homogeneous, isotropic and elastically linear.
- The core material in both the potting and honeycomb regions is assumed to behave as a special type of transversely isotropic material only possessing stiffness in the through the thickness direction (this means that stress doesn't varies in through the thickness direction)
- The sandwich plate can be antisymmetric
- The top and bottom face sheets may deflect differently

As for the "through the thickness" inserts the boundary conditions are:

- When $r=b_i$: the insert has an infinite rigidity and there is a continuity of the displacements at the interface. This assumes that the insert is perfectly bonded to the core and the skins (see Fig. 33).
- When $r=b_p$: continuity of the fundamental variables across the potting/honeycomb interface (see Fig. 33).
- When $r=a$ it is assumed that the face sheet and honeycomb core mid-surfaces are simply supported (see Fig. 33).

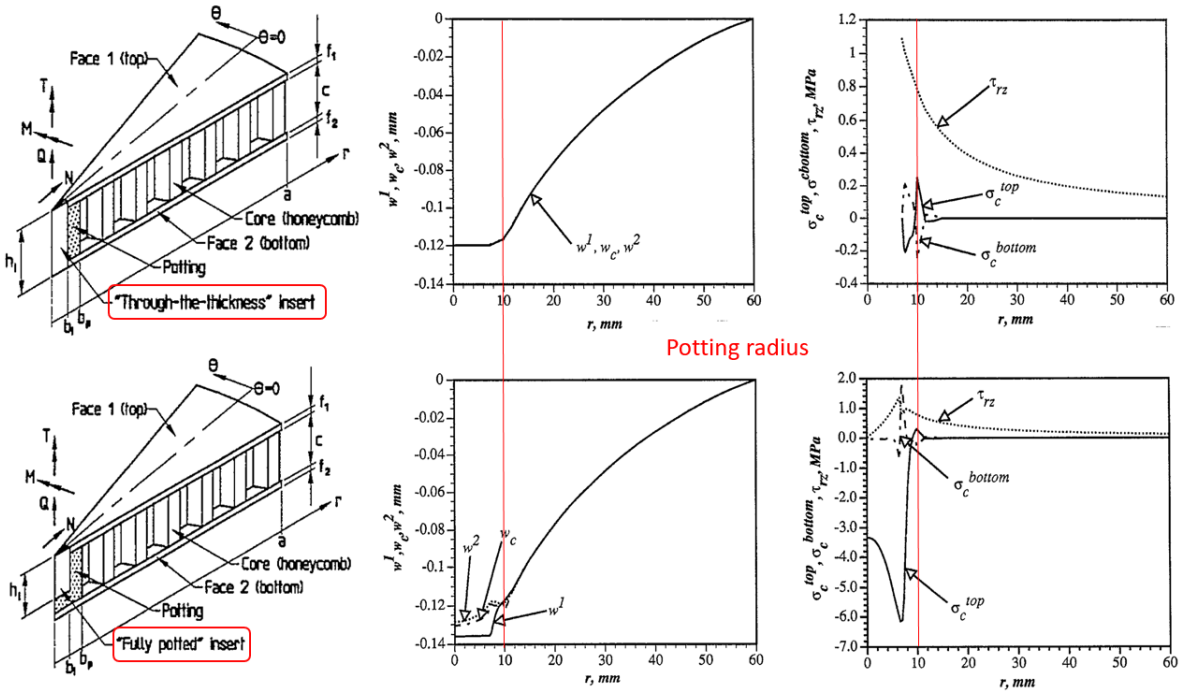

Fig. 33: Stress and strain of the skins given by the Thomsen model [29].

The stress equilibrium and kinematics are calculated for the core and skins. To do this, a system of 24 differential equations is used to obtain the stresses and deflections in the core and skins as function of the radius. They used this approach to model the stress distribution for a "through the thickness insert" and then for a "full potting insert", this comparison can be seen in Fig. 33. The results show the deflection and stress core vs the insert radius. The most notorious aspect in the curves can be seen at the radius of the potting $r_b=10\ mm$, where the core/potting transition is located.

In general terms, these results are similar to the Ericksen ones, although, more accurate. This is particularly relevant for full potting inserts, on which the maximal shear stress of the core is localized at the core/potting interface.

Also, it's worth mentioning that this approach was implemented by the European Space Agency into the ESAComp software that provides an easy-to-use environment for preliminary evaluation and analysis of these types of structures. Today this software belongs to Altair and can be used with the Altair's HyperWorks Suite.

2.1.4.3 Direct approach by simple shear

The direct approach by simple shear is the simplest one, although not the more accurate due to the hypotheses that are made, which are:

- The insert is considered as a rigid cylinder that goes all through the thickness of the panel.
- The thickness and rigidity of the skins are neglected.
- The applied pull-out force is distributed directly and totally into the insert/core interface.
- The maximal stress is located at the insert/core interface.
- Failure appears when the maximal allowed shear stress is reached at the interface.

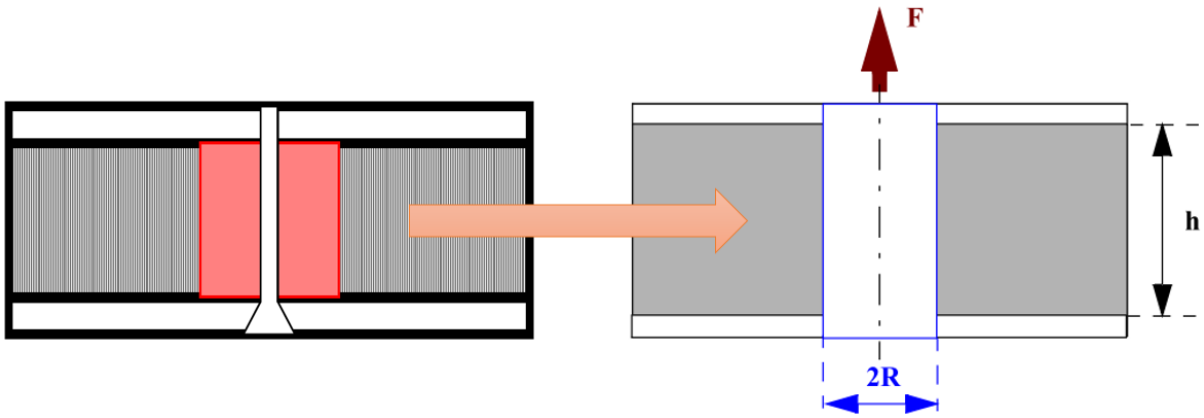

Fig. 34: Simplification of the insert by using the direct approach by simple shear [15].

If the maximal shear stress for the core is known, and considering that the insert has a cylindrical surface, the critical load can be easily calculated:

$$\tau_{max} = \frac{P_{crit}}{S}, \quad \text{and} \quad S = 2\pi Rh, \quad \text{then} \quad P_{crit} = 2\pi Rh\tau_{max}$$

This approach is very well known, Zenkert states that this is only a very rough estimation [5].

According to André [52], when the insert panel is not subjected to important bending deformation, the direct approach by simple shear estimates correctly the maximal pull-out force by 80% , compared to the maximal pull-out force in a test. In the other hand, if there is important bending deformation, using the direct approach by simple shear can lead to underestimate the

maximal pull-out force by nearly 100 %, therefore the direct approach is only recommended when the plate is not subjected to important bending. Nevertheless, the modified direct approach results a better option since it can estimate by 80% the maximal pull-out force in presence of considerable bending. This criterion is given by the relation between the maximal bending caused by the shear and the deflection:

$$\frac{\delta_{shear}}{\delta_{flex}} < 915$$

When the relation between these strains is less than 915 the direct approach by simple shear could be used. For other cases, the modified direct approach is recommended with the use of the Mil-Hbk 23 A (see next subsection)

In 2015, Wolff et al [38] did a study about the accuracy of this method. They found that there was an important discrepancy between the experimental and calculated failure loads. This approach underestimated the insert pull-out strength by 2% to 52% for best and worst cases respectively, with an average of 19%. The study was based on the experimental tests of Song [40], and Block [53], where the insert failure criterion was the first peak in the loading curve, attributed to the shear failure of the core (see Fig. 20).

2.1.4.4 Modified direct approach from the military handbook 23A

Another approach that is interesting to be take into account is the one presented by the US Military handbook 23A [2]. This approach is a combination of the simple shear approach and the approach developed by Ericksen, both presented previously in this work [3], [50]. It considers the following:

- The insert is installed in a sandwich plate, therefore cylindrical coordinates are used.
- The insert is considered as a cylinder that goes all through the thickness of the panel.
- The shear stress varies depending on considered distance measured from the interface.
- The maximal shear stress appears at a region near the insert.
- Failure appears when the maximal allowed shear stress is reached.

The core shear stress distribution varies depending on the clamping conditions and on the geometry parameters of the sandwich (see Fig. 35). This approach uses the formula of the simple shear approach but introducing a k_3 factor that corresponds to the maximal shear stress of the entire shear stress distribution chart (Fig. 36). In other words, this approach uses the average shear stress at the potting/core interface scaled by a coefficient k_3 to calculate the maximal shear stress on the core:

$$\tau_{max} = \frac{P}{2\pi hb} k_3$$

This coefficient k_3 is (presumably) calculated through the approach developed by Ericksen [3], and so this method can be seen as an intent to simplify the use of the equations by using a 2D chart, but keeping the accuracy of the analytical model.

The values of the coefficient k_3 can be found in the abacus provided by the book (see Fig. 35 and Fig. 36). To use this tool several parameters must be calculated before:

$$\frac{a}{b} \qquad \phi_a = \left(\frac{hG_c}{D_F}\right)^2 a \qquad c = \frac{2\pi haF}{p} \qquad D_f = \frac{1}{12}\left(\frac{E_1 t_1^3}{\lambda_1} + \frac{E_2 t_2^3}{\lambda_2}\right) \qquad \lambda_{1,2} = 1 - \nu_{1,2}^2$$

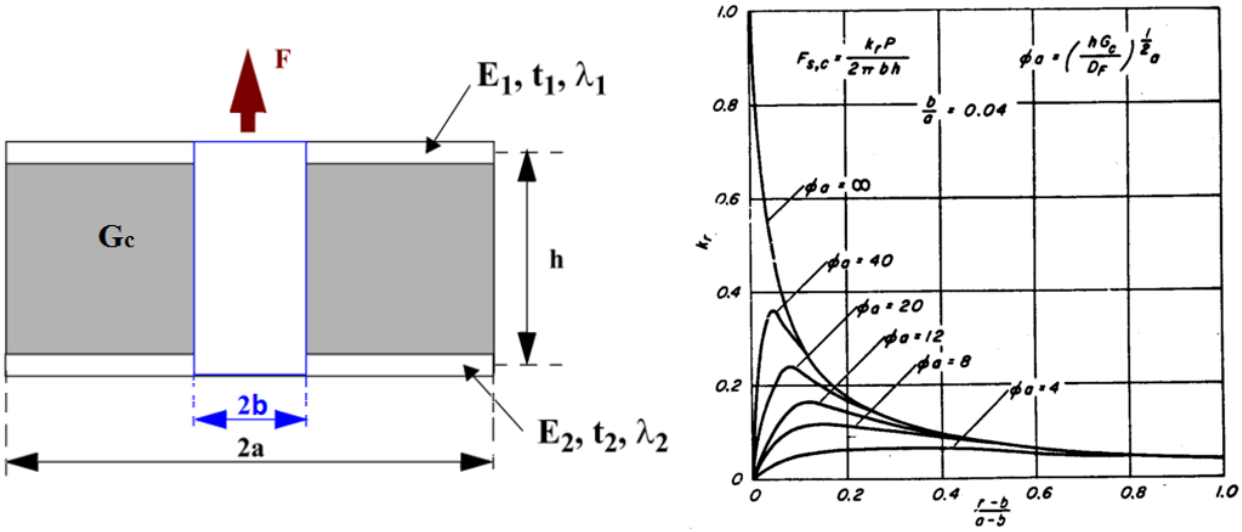

Fig. 35: Approach description and shear stress distribution in function of the radius and sandwich parameters [2], [15].

Two of the first three parameters must be calculated, then the value of k_3 is given by the intersection of the curves in Fig. 36, this is *b/a* vs ϕ_a , *b/a* vs c , or ϕ_a vs c .

2.1.4.5 Sizing by the ESA Design handbook

The ESA insert design handbook (ref [1], [37]) is one of the reference manuals for inserts sizing. In this manual, several themes about inserts and the sandwich standards are explained, such as norms, fabrication, installation process, test, controls, quality assurance, insert sizing under static loads, thermic and fatigue sizing, effects of the sandwich borders, effect of load distributions of groups of inserts, among many others. In this bibliography, only the approach to determine the insert strength to pull-out loads will be presented.

The first recommendation to calculate the size of an insert, is that the static strength capability P_{ss} of the insert must be larger than the required for the application P_{real}. This is done using a safety factor S:

$$P_{ss} \geq S\,P_{real}$$

Where, P_{ss} is the maximum load that the insert can really support, P_{real} is the load that will be applied to the insert and S is the factor of safety. If there isn't any specified factor of safety for the application, it is recommended to use the $S = 1.5$ standard for the aeronautical industry.

The book provides several 2D charts that give the average and minimal values of P_{ss} for a 9-mm fastener. The skins are made of 2024 aluminum, and the core is made principally of aluminum honeycomb, although for some cases a non-metallic honeycomb core is used. These charts are based on experimental tests and their calculations methods. The following hypotheses are made:

- The average P_{ss} values are calculated using the average values for the strength properties of the skins, the core and the potting material, also using the average potting dimensions.
- The minimal values of P_{ss} are calculated using the minimal values for the strength properties of the skins, the core and the potting material, also using the minimal potting dimensions.

- The principal variables that modify the insert P_{ss} are the core height C and the face thickness f.
- The potting height is determined by the size of the fastener and the height of the core. The minimal height of the potting is calculated from the fastener size, and the minimal and typical values are determined by:

$$h_p = \begin{cases} c & \text{if} \quad c \geq h_i \geq c - 7mm \\ h_{p_{min}} = h_i + 7mm & \text{if} \quad c > h_i + 7mm \\ h_{p_{av}} = h_{p_{min}} + A \tanh \frac{c - h_{p_{min}}}{h_{p_{min}}} & \text{if} \quad c > h_i + 7mm \end{cases}$$

With $A = 2.5$ for $S_c = 3.2$ and $A = 5$ for $S_c = 4.8$

- The potting size diameter b_p is a standard, depending on the diameter of the fastener. The average and minimal values of the potting diameter are given by equations 5, 6, 7, and 8 for a perforated metallic core and non-performed core respectively.

$$b_{p_{min}} = 0.93192 b_i + 0.874 S_c - 0.66151 \quad (5)$$

$$b_{p_{av}} = 1.002064 b_i + 0.940375 S_c - 0.7113 \quad (6)$$

$$b_{p_{min}} = 0.9 b_i + 0.7 S_c \quad (7)$$

$$b_{p_{av}} = b_i + 0.8 S_c \quad (8)$$

- The minimal values of P_{ss} are considered as A values (describing 99% of the population with a 95% of confidence) because the probability of having all the minimal values for every parameter in the insert is very low.

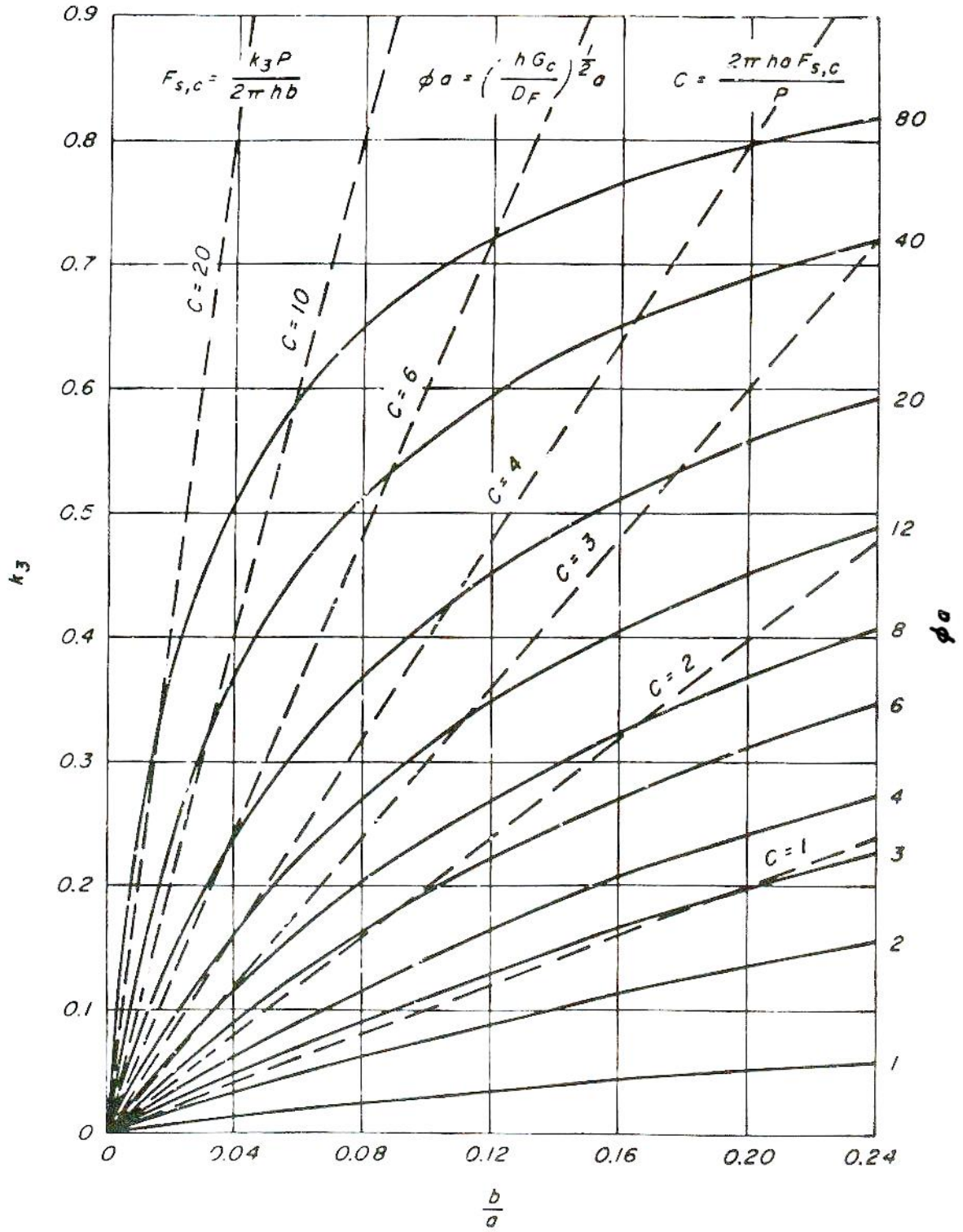

Fig. 36: Abacus provided for the sizing of inserts, this uses the insert geometrical and mechanical parameters to calculate the k_3 coefficient [2].

In the handbook, the P_{ss} value is obtained analytically and then validated by testing; the number of test is not given in the book, but the correlation between the test and the analytical calculations is given. An example of the proposed abacus can be seen in Fig. 37.

It is mentioned that the P_{ss} values given by the book for metallic honeycomb cores are reliable because many tests were carried out to back up the graphics, but for the non-metallic

honeycomb cores, the results are considered as preliminaries because the number of test was considered insufficient.

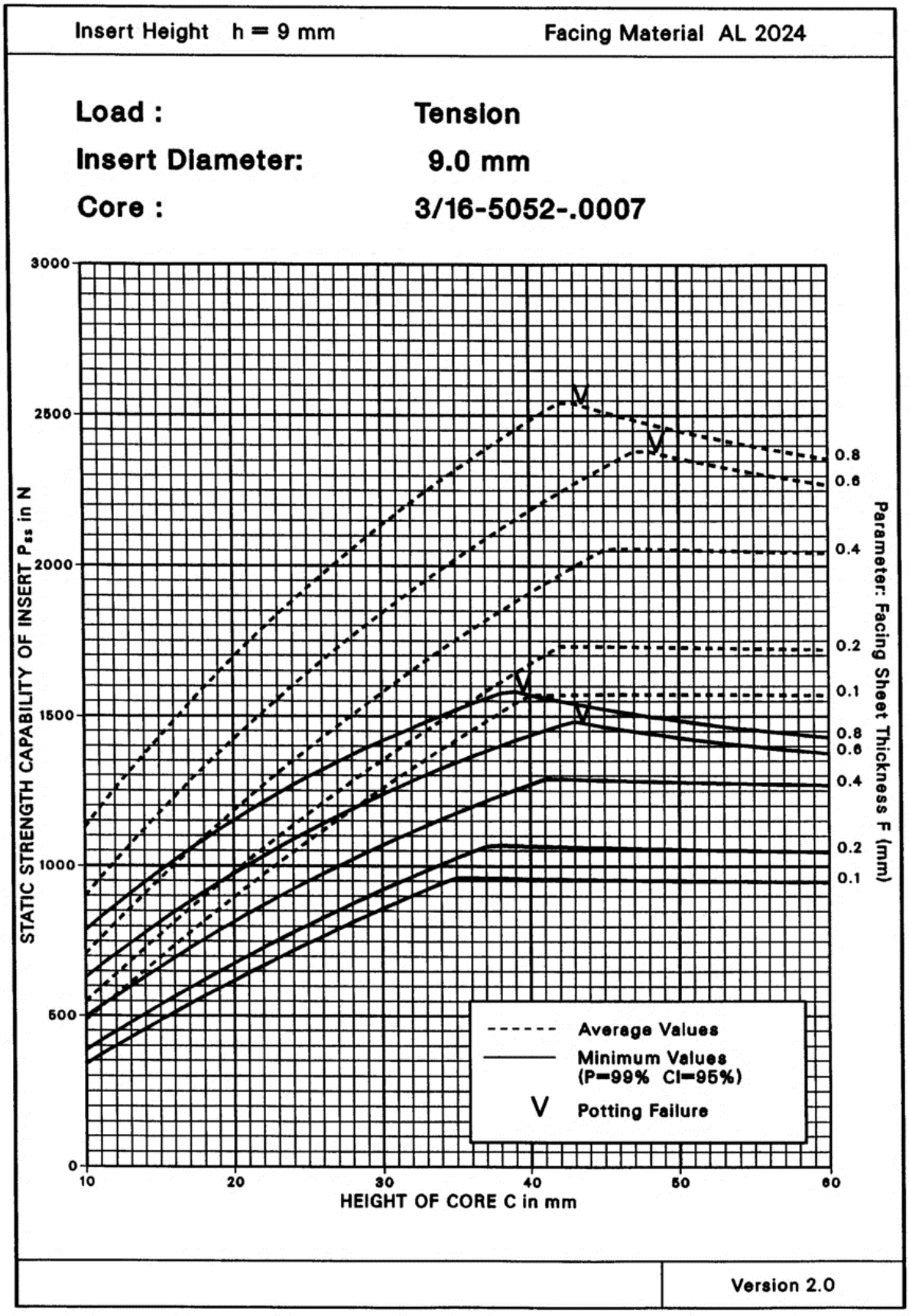

Fig. 37: Minimal and average P_{ss} in function of the core heigth and the thickness of the skins [37].

2.1.4.6 Failure modes after pull-out according to the ESA design book

The ESA insert design handbook describes 4 different types of failure modes when an insert is subjected to a pull-out force. They are separated in four cases: *A, B, C,* and *D*. The failure mode that is activated depends, most of all, on the core's height as shown in Fig. 38.

Each failure mode is governed by a different set of equations to calculate P_{ss}, the insert pull-out strength. Here, these approaches are presented.

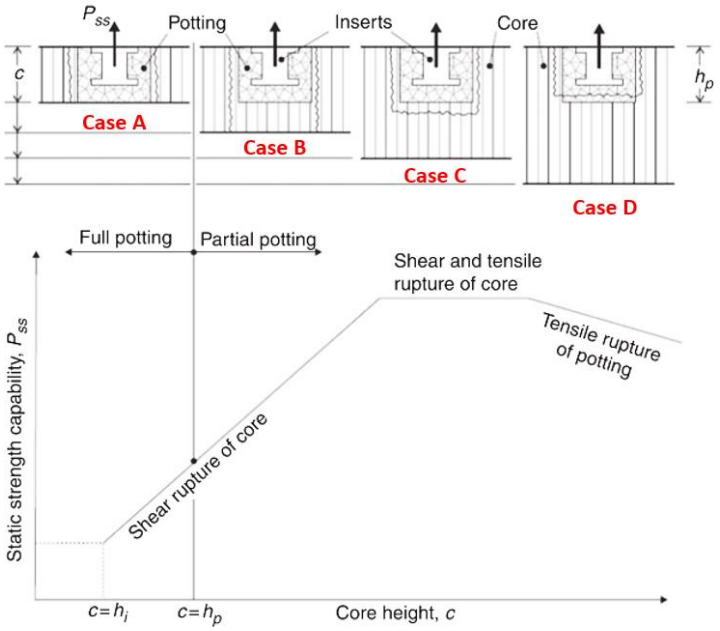

Fig. 38: Failure mode vs core height [1].

Case A: The core height is similar to the insert height: failure is caused by shear stress in the core.

This case applies for "full potting" and "through the thickness" inserts. Failure is due to the shear stress of the core near the core/potting interface, thus, the insert strength relies only on the core shear strength. This means that if the core height is increased, the area of the core that is subjected to shear stress increases too, and therefore, the insert strength P_{ss} increases proportionally to the core height C.

The maximal shear stress τ_{max} in the core that causes the failure is calculated using the approach developed by Ericksen [3] that allows to calculate the shear stress distribution $\tau(r)$ (equation 1) in the core for an insert installed in a sandwich plate (Fig. 39).

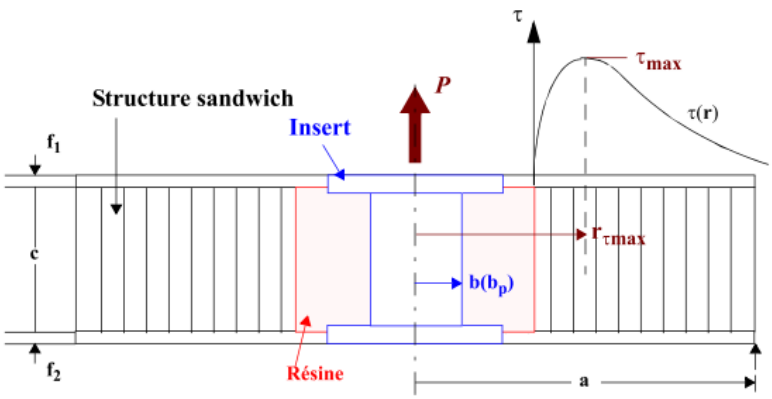

Fig. 39: Distribution of the shear stress near the insert [37].

For symmetric panels for aeronautical application ($\beta = \frac{c}{f} \geq 10$ & $f' = f$) and for $r < a$, the shear stress of the core is given by:

$$\tau(r) = \tau_{nom} \bar{C} K$$

Where, $\tau_{nom} = \frac{P}{2\pi bc}$ $\bar{C} = \frac{\beta}{\beta + 1}$ $K = \frac{b}{r}\left(1 - \sqrt{\frac{r}{b} e^{\alpha(b-r)}}\right)$

$$\alpha = \frac{1}{f}\sqrt{\frac{G_c}{E_f} 12(1 - v_f^2)\left(1 + \frac{\beta}{2}\right)}$$

This formula gives the curve of shear stress shown in the Fig. 39. At the interface of the core/insert the value is zero. The maximal shear value is reached at a $r_{\tau\, max}$ and then decreases rapidly, this model shows that the failure happens in the core near the insert.

$$r_{\tau_{max}} = \frac{b}{1 - e^{C_2(\alpha b)^n}}$$

With $C_2 = -0.931714$ and $n = 0.262866$

The maximal shear stress is given by evaluating r_{max} in $\tau(r)$, this is:

$$\tau_{\max} = \tau_{nom} \bar{C} K_{\max}$$

And finally, the critical load is given by:

$$P_{Acrit} = \frac{2\pi bc\tau_{crit}}{\bar{C} K_{max}}$$

where, τ_{crit} is the maximal allowable shear stress of the core.

Case B: The core height is slightly bigger than the potting height: failure is caused by shear stress in the core.

This case is for "partial" inserts, which have always a part of the core that is not filled with potting (see Fig. 13). When a pull-out load is applied, this part of the core under the potting is subjected to tensile stress. Then, although partially potted, the insert exhibits the same behavior as that of fully potted insert.

The core is slightly bigger than the potting, therefore, the tensile stress of the core under the potting is weak, and thus, failure will be caused by the shear failure of the core as for case A.

This happens until certain height of the core; when this certain height is reached, the tensile stress of the core under the potting is big enough to cause a tensile failure of the core (as will be presented in case C).

Thus, it can be said that case B starts when the core is thicker than the potting, and ends when the core under the insert starts to break due to tensile stress. This case is a transition between the failure mode of case A and case C.

The failure of case B relies totally in the core, this means that if the core thickness is increased, the area of the core that is subjected to shear stress increases too, and as for case A, P_{ss} increases as the height core C does; this applies for example for metallic cores.

However, for non-metallic cores, the fact that the core surrounding the potting is subjected to tensile and shear stress creates like a stress concentration phenomena that is

combined to the characteristic local buckling of non-metallic cores, reducing the strength of the insert. This is represented by a stress concentration factor given by equation 10, and so, the pull-out strength is given by eq. 9.

The procedure to calculate the insert pull-out strength of a partial insert should be: first, calculate the P_{ss} as if it were the case A, then re-calculate P_{ss} using the equations 9 and 10. It's important to remark that in this case the failure of the insert is imitated by two rupture modes; the shear failure of the core (case A) and secondly by tensile and shear stress as in case C. Therefore, also the approach C must be calculated for P_{ss} and finally the lower strength value will determine if the insert failure will be like case B or C.

$$P_{Bcrit} = P_{Acrit}\frac{1}{k_{t_{pp}}} \quad (9)$$

$$\frac{1}{k_{tpp}} = \left(\frac{h_p}{c}\right)^{0.62} \quad (10)$$

Case C: The core height is much bigger than the potting height; failure is caused by tensile stress and then shear stress in the core.

This is the case of a partial insert which height is much smaller than the core. Therefore, the core under the potting is subjected to a considerable tensile stress and breaks, then the tearing of the core propagates to all the core surrounding the insert. Then, it can be said that the failure is caused first by tensile stress of the core under the potting and then by shear stress surrounding the potting. The fact that failure appears under the potting, if the core height is increased the failure mode will still be the same. This means that the insert strength P_{ss} is independent of the core height C.

The ESA insert design handbook explains that, when a pull-out load P_{Ccrit} is applied to an insert, the reaction forces inside the panel are distributed as follows:

- The load component carried by the upper face sheet (P_F),
- The load component carried as shear stress in the core around the potting (P_S),
- The traction force carried by the core under the potting (P_N)

$$P_{Ccrit} = P_F + P_S + P_N$$

To estimate the load component carried by the skins P_F is as follows: The calculation of the pull-out strength for a "full potting" considers that the deflection of the panel is caused by the bending forces and the shear forces, including the force contribution of the two skins. This is useful because if the shear force that affects the core is calculated, and then subtracted to the calculated force of the full potting insert, as result we obtain the force contribution of the skins. So, the procedure will be, first calculate the pull-out strength as if it were a full potting insert $(P_{\tau max})$, and then subtract the shear force of the core, then, all should be divided by two to consider the force of only one skin. All of this is resumed as:

$$P_F = \frac{P_{\tau_{\max}} - 2\pi r_{\tau_{\max}} c\tau_{\max}}{2}$$

The contribution of the shear force of the core is given by the following equation, this considers only the core that is surrounding the potting, and the radius where the maximal shear stress is located.

$$P_S = 2\pi r_{\tau_{max}} h_p \tau_{max}$$

The contribution of the traction force in the core is given by:

$$P_N = \pi r_{\tau_{\max}}^2 \sigma_{max}$$

Where, σ_C is the normal stress under the resin in traction or compression. Then, the critical load that corresponds to the failure of the insert is given by:

$$P_{Ccrit} = \frac{P_{\tau_{\max}}}{2} + \pi r_{\tau_{\max}}(2h_p - c)\tau_{max} + \pi r_{\tau_{max}}^2 \sigma_{max}$$

This expression assumes that the break in traction or compression and shear happens at the same time. The book explains that this occurs because of the nonlinear effects of the buckling of the cells in the core/potting interface.

Case D: The core height is much bigger than the potting height but the core has high density: failure is caused by tensile stress of the potting and then shear stress in the core.

This is the case of a partial insert which height of the core is much bigger than the potting height, also the core flatwise strength is considerable high. When a pull-out load is applied, the tensile stress of the core under the potting, and the tensile stress of the potting itself are important. Since the core has high flatwise strength, failure occurs by tensile fracture of the potting, also the cells surrounding the insert are teared too. This failure is directly related to the potting strength and is given by:

$$P_{Dcrit} = 2P_{NRcrit}\frac{\dfrac{1-\psi}{1-2\psi}}{\dfrac{1-\psi}{1-2\psi} - \dfrac{\bar{C}K_{\max}r_{\tau\max}h_i}{bc}}$$

With:

$$P_{NRcrit} = \pi b_R^2 \sigma_{max}$$

$$\psi = \frac{c - h_i}{c}$$

Where, $\bar{C}, K_{max}, r_{tmax}, h_i$, etc. are the same parameters used for the case A.

2.1.5 Strength prediction of inserts by numerical approaches

The accuracy of the analytical methods to predict the insert strength is acceptable, although for some cases not so much.

Heimbs et al. [35] did several pull-out tests on “full potting” inserts. They used the approach recommended by the ESA to estimate the pull-out strength which they found was of 1630 N vs an experimental strength of 2220 N. This can be seen in two ways, the first one is that the analytical approach can lead to obtain a good estimation of the maximal pull-out force. The second way is that the estimated force was only 23% lower than the force in the test and therefore the analytical estimation underestimates the strength of the insert.

To obtain a more accurate approximation of the pull-out strength, Zenkert suggests the use of F.E. tools to model the insert behavior. In this section, several F.E. models of inserts are presented. The works are separated in homogenized models and detailed models.

2.1.5.1 Homogenized models

These models are geometrically simple, thus complex geometries of parts such as the irregular shape of the potting or the geometry of the honeycomb core are not considered. Instead, they are replaced with much simpler equivalent volumes. For the material's mechanical properties this is similar, the homogenized properties of the materials are considered instead of the exact properties; reducing the development and calculation time.

At the same time, the model must be able to reproduce the failure of the specimen, which is in most of the cases, in the range of the nonlinear behavior of the insert.

In 2008, Bunyawanichakul et al. [36] developed a F.E. model of an insert able to reproduce the initial part of the non-linear behavior when the insert is subjected to a pull-out load. The incorporated failure modes were: core shear buckling, plasticity of the potting and finally, damage of the composite skins.

The nonlinear behavior of the components, the core, potting and skins, were investigated separately, and then included into the material behavior of the insert model. Then, the model was developed under SAMCEF and the obtained results were very satisfactory, as shown in Fig. 40.

It was composed only of volume elements. The sandwich panel was simply supported and in the center the insert is pulled out through a bolt on which was imposed a displacement.

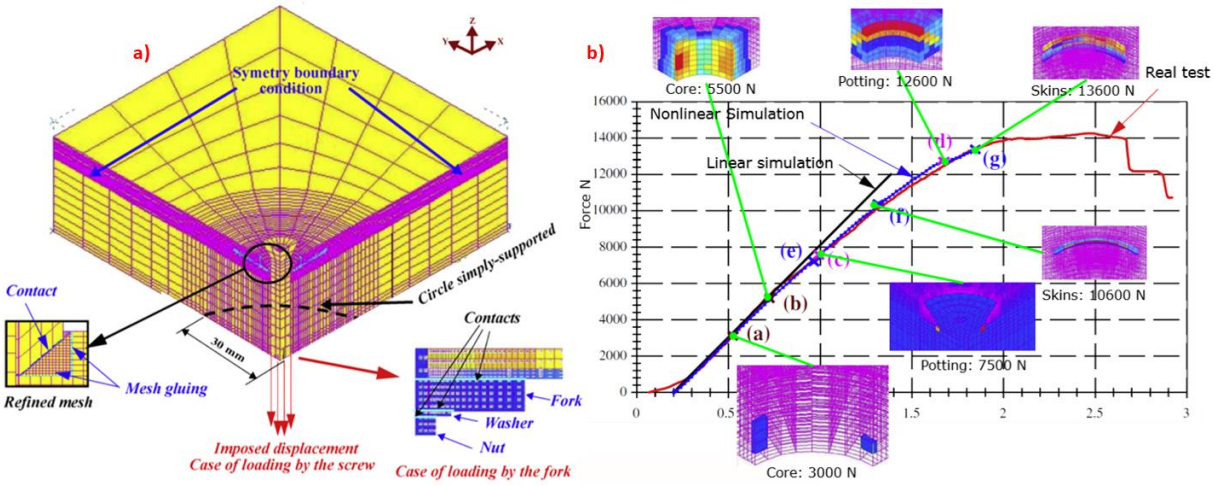

Fig. 40: A) F.E. modeling of the insert, and b) : Nonlinear behavior and damage scenario [36].

The simulation showed a good correlation with a real test, and therefore this model allows to predict the nonlinear behavior of the represented insert, except, as usually, for the initial nonlinear contact phase. With this FE model, all damage scenarios damages were described at the respectively pull-out forces as is showed in Fig. 40.

According to the authors of this research, the first failure mode is the core buckling near the potting. This is well represented in the FE model and can be seen in point (a) at a force of 3000 N: at this point the insert behavior is linear and it's the beginning of the shear buckling. Then at a force of 5500 N in point b) the model describes well the complete shear buckling failure of the core; the behavior of the insert changes and starts to be nonlinear. In point (c) the contact points between the potting and the bolt start to plasticize, but the softening of the full circle under the bolt is reached until point (d) at 12600 N. For the skins damage, it starts from 7100 N and has a good correlation until point (g) at 13600 N.

Another example of homogenized model is the one developed by Heimbs et al. in [35]. They developed a very simple model of insert that was suitable for use in large simulations, (as it consisted of only 100 elements). The simplified insert behavior correlated well the

experimental results as showed in Fig. 41. Unfortunately, the exact nonlinear characteristics that were used are not well explained. They just reported using two kinds of materials and that the insert is fixed using a spot-welding element.

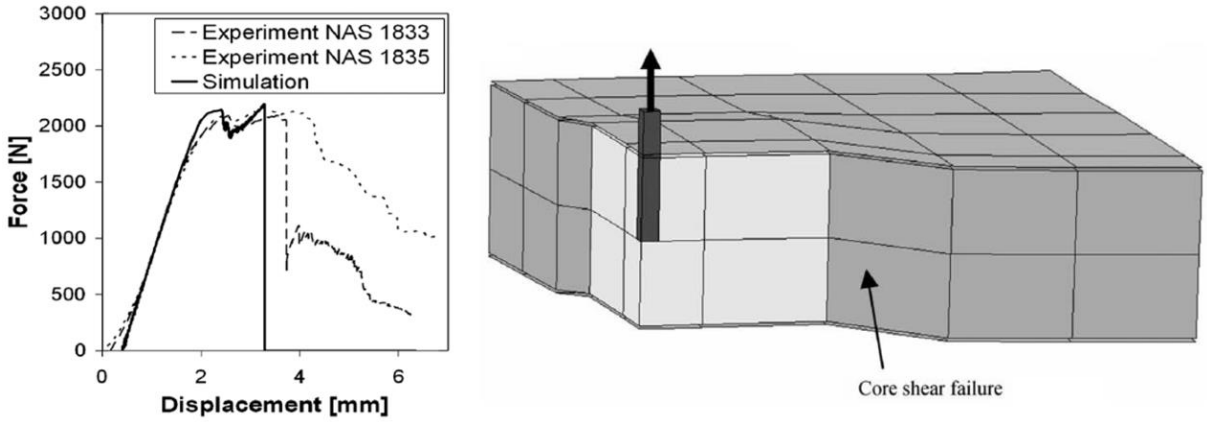

Fig. 41: Reduced model of a partial insert [35].

Another homogenized model was developed by Raghu in [28]. The objective was to understand the stress field of a "partial potting" insert. A homogenized model was preferred because it is easier and quicker to change the geometry and material parameters than for a detailed modeling. Also, the homogenized model allowed showing a continuous field which is very practical to plot a map of the stress distribution (see Fig. 42).

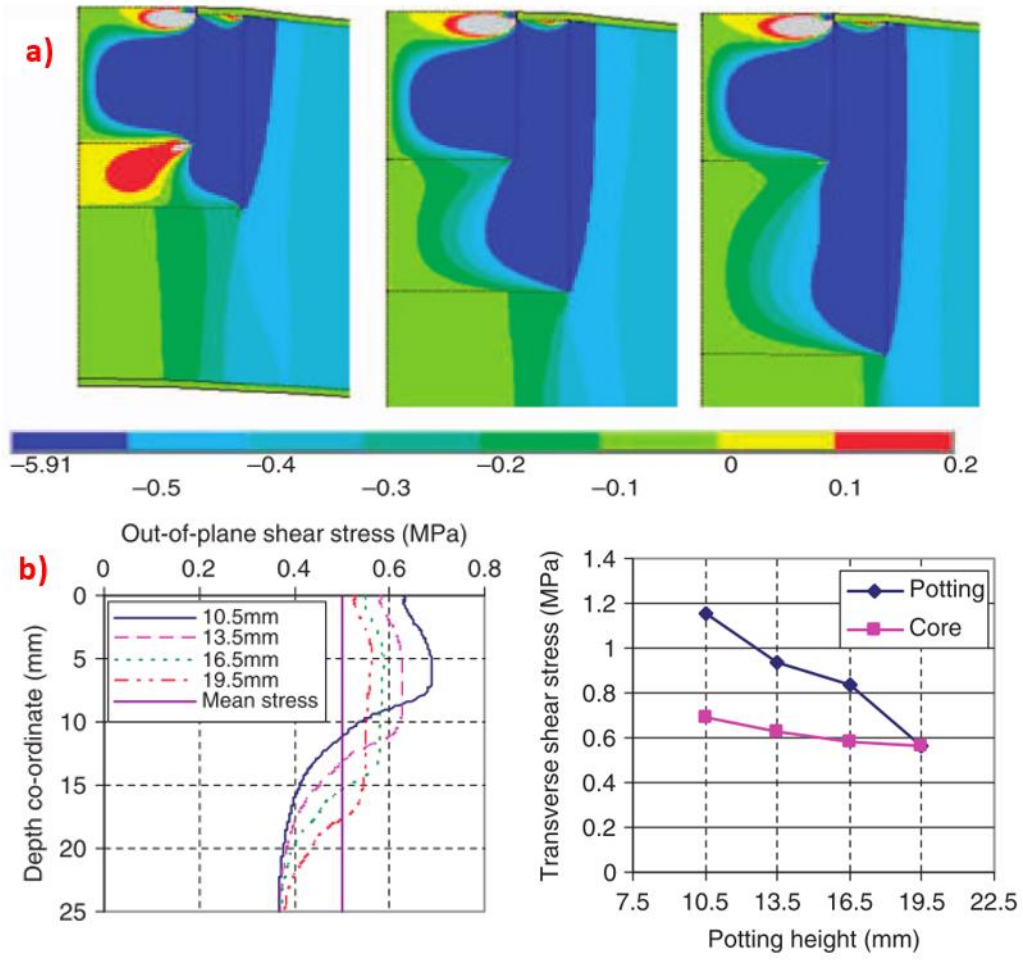

Fig. 42: a) Transverse shear stress for three different potting heights (MPa) in a pull-out test, b) shear stress distribution through the thickness of the core at a radius of 10.5 mm [28].

2.1.5.2 Detailed models

On the other hand, detailed models require considerable expertise, development time and high computational power, although the results should be more accurate than homogenized models. This is particularly important to include into the model the several failures of complex structures like the honeycomb core, which that can fail due to shear buckling, compression or even in tension.

In 2015 Seemann et al. [34] developed a detailed F.E. model of a “full potting” insert. The objective was to prove that a virtual testing of insert was suitable and therefore, every aspect was considered carefully.

For the modeling of the honeycomb core a study of the influence of the defects on the honeycomb wall was made, but also a study about the correct size of the elements and the properties of the Nomex® paper. For the potting, the different behavior, in compression and tension, was considered, as well as the irregular geometry of the potting. For the skins, a damage criteria and evolution were considered to model the failure.

The investment of time into the development of this model is huge. However, when the numerical and experimental results are compared, it can be said that it is worth it. The insert behavior correlates well (see Fig. 43) even for the nonlinear behavior (except for the 26-mm core).

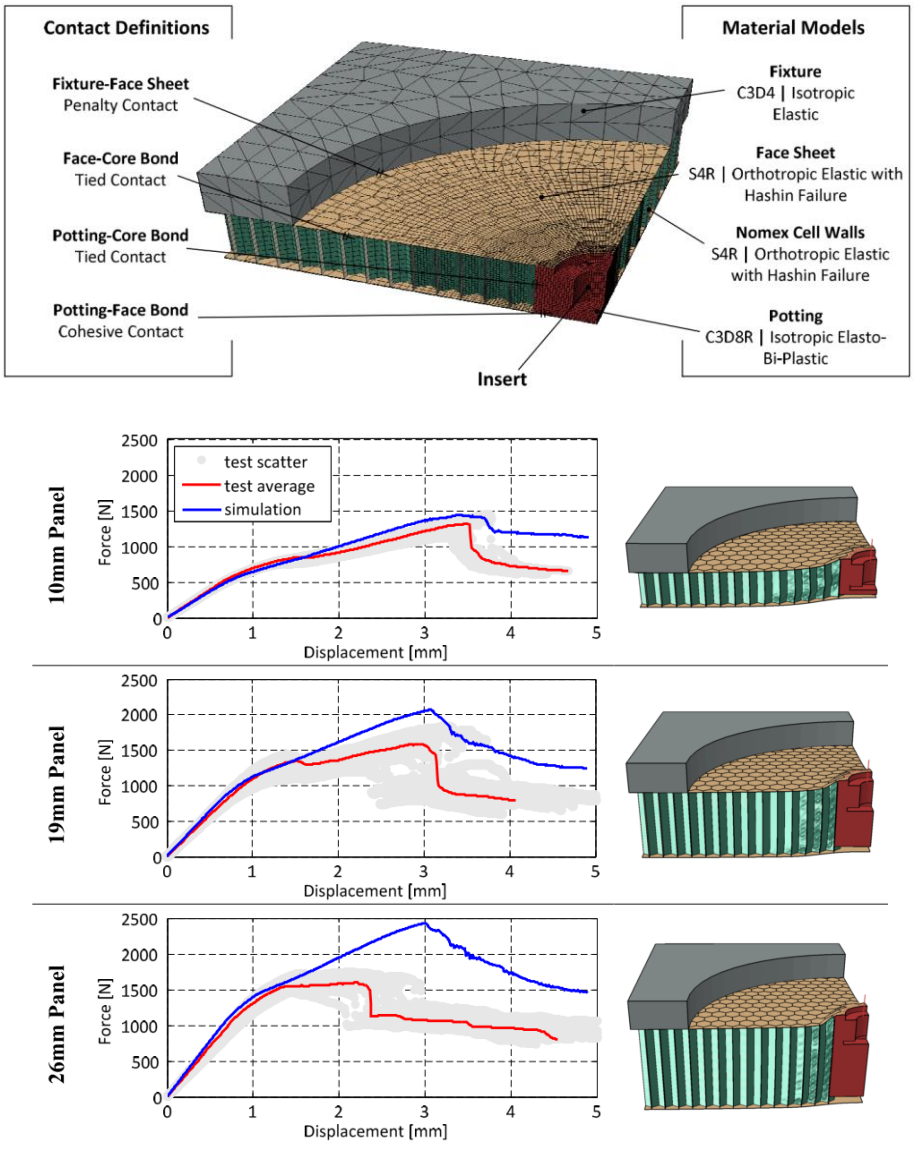

Fig. 43: Virtual testing of inserts [34].

Another detailed insert model was developed by Roy et al. in [33]. They modeled a single panel and a through the thickness aluminum insert installed into a Nomex® honeycomb panel. They focused in to show that the identification of the buckling of the core can be used as failure criteria.

To do this, they needed to "capture" the local buckling of the cells near the insert, and a refined model was necessary.

The simulation results showed that the buckling load of the core is only 5 to 13% higher than failure load of the experimental tests, therefore this criterion provides a better approximation than analytical results. Nevertheless, many solution sub-steps were required to obtain better precision, therefore the computation time was considerable.

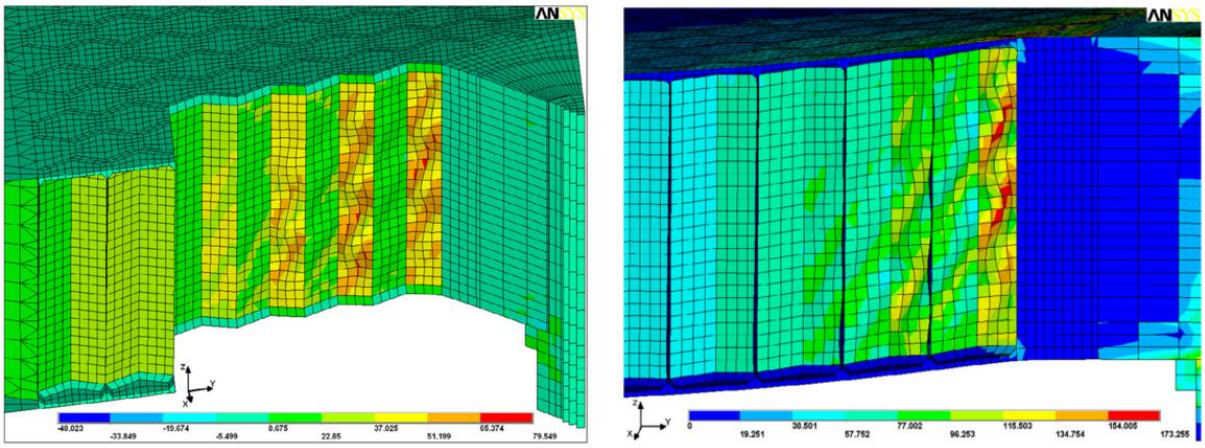

Fig. 44: Buckling simulation of the core of an insert by Roy [33].

The design of inserts for sandwich panels requires that the parameters of the inserts are completely known, also it could be useful to study the sensitivity of the insert pull-out strength against parameter variations. Results from a few researchers that studied this topic are presented here.

Song et al. [40] did a study on the sensitivity of parameters that included the tests of 80 insert samples. The changing parameters were the core height and density and the thickness of the skins. In total, 8 different types of specimens were tested (P01-P08). The information can be seen in Table 5.

	Core height (mm)	Core density (kg/m^3)	Skin thickness (mm)	Space between the hole and the skin (mm)	Failure Pull-out load (kN)
P-01	17.78	48	0.84	0	1.89
P-02	22.86	48	0.84	0	2.32
P-03	27.94	48	0.84	0	2.64
P-04	17.78	80	0.84	0	2.74
P-05	17.78	128.1	0.84	0	4.48
P-06	17.78	48	1.26	0	2.62
P-07	17.78	48	1.68	0	3.17
P-08	17.78	48	0.84	0.11	1.84

Table 5: Tabulation of the test parameters and the pull-out force values [40].

The results show that the most relevant parameter was the core density (in red), followed by the skin thickness and finally the core height.

In 2017, Slimane et al. [32] did a very detailed study on position of the inserts through a detailed modeling.

The aim was to study the stress variations caused by the position of the insert and its different possible shapes for the same nominal radius (see Fig. 45).

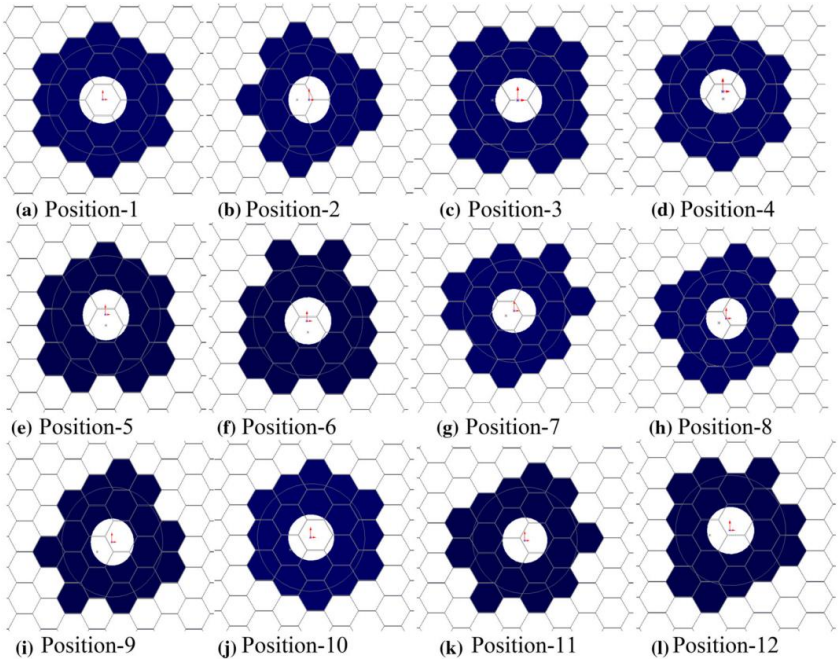

Fig. 45: Variation of the potting geometries for the same perforation radius [32].

The results were that the most significant parameter that determines the stress on the cell walls is the number of filled cells, which can cause a variation of 11% of the maximal stress on the cell walls. Also, there were small variations of the radius where the maximal shear stress of the core is located, thus it has an important influence on the failure of the honeycomb core.

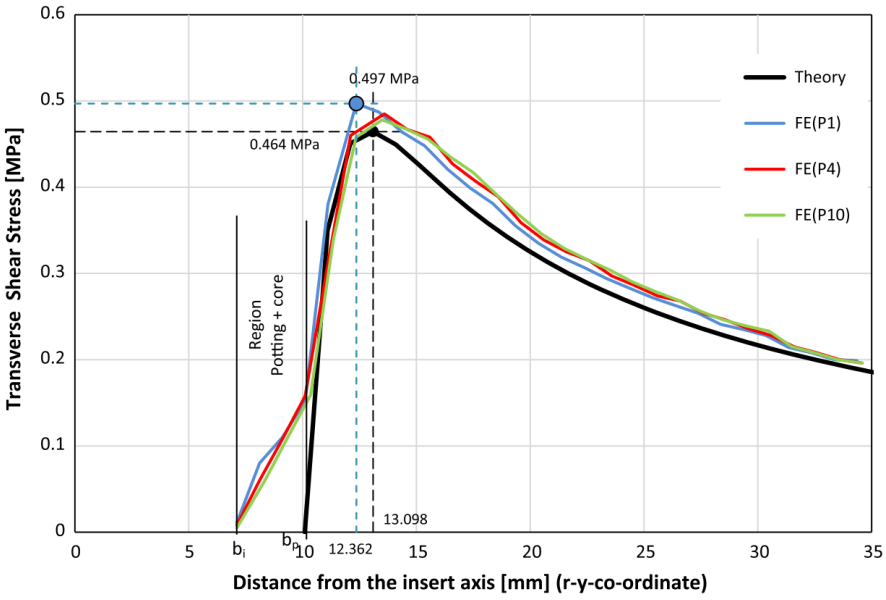

Fig. 46: Comparison of the analytical model vs the F.E. calculation of the shear stress in the core [32].

Also, they did a comparison of the core shear stress given by the analytical Ericksen model (the ESA version) and their F.E. model. While the Ericksen model considers the effective potting radius for the calculation, the F.E. modeling allows considering the exact geometry of the potting. Even so, they found that there was a good correlation between the numerical estimation and the analytical method of Ericksen. The only slight difference was that the shear stress at the insert was different due to the different potting radius used for the calculation.

Smith and Banerjee [31] explored the use of several analysis techniques to characterize the relationship between the applied pull-out load and the probability of failure in presence of parameters variation. The geometric parameters that were changing are shown in Fig. 47. Also, the mechanical properties of the components vary using a Gauss distribution. They focused in to explore small variations, the aim was to predict the reliability of an insert with the variation of defects during fabrication. The used methods were;

- Monte Carlo method: Sampling in the model to estimate the function of probability of failure.
- FORM (First order reliability method).
- Line sampling.
- Subset simulation.

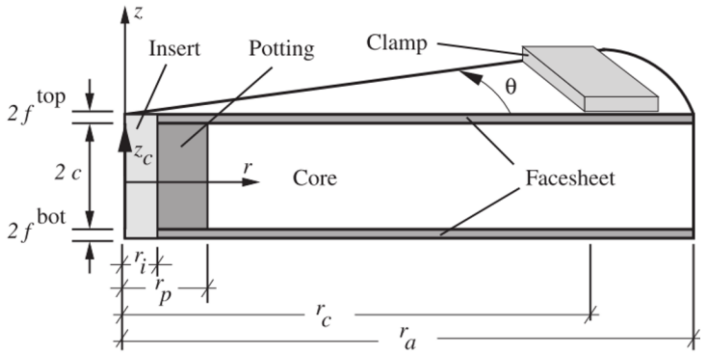

Fig. 47: Model parameters and description [31].

They consider two situations as insert failure criterion:

- The failure of two components.
- The failure of three components.

For the skins and the resin, the failure criterion was the Von Mises criterion (Tsai-Wu with isotropic properties). For the core, the shear failure and buckling were calculated using the formulations of Gibson and Ashby in ref. [9] (see equations 11, 12, 13 and 14).

As result, they give several graphics that shows the sensitivity of inserts failure in presence of parameter variation (see Fig. 48). The most significant parameters are the elasticity limits of the skins.

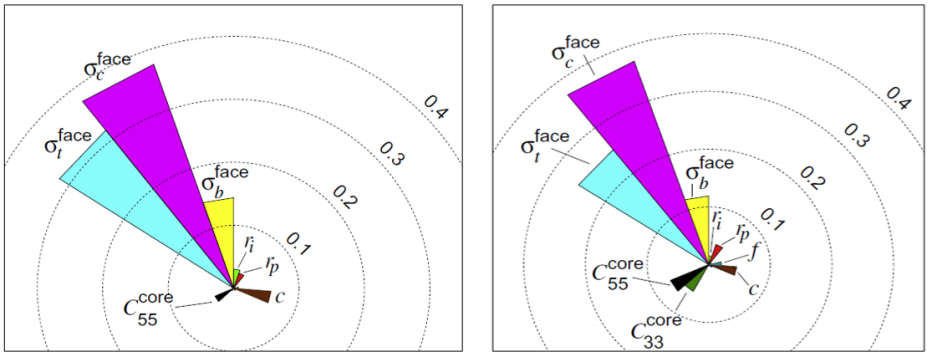

Fig. 48: Sensitivity of the different parameters accordingly to [31].

The ESA insert design handbook [1] presents another study on the parameters variation. They considered that once a component has failed, this causes the failure of the insert. This study is based on the model developed by Ericksen. A variation of 5% was used for each component. This was made for the case when the insert fails due to shear failure of the core and when the insert fails due to core tension under the potting (see Fig. 49). They concluded that the face sheet thickness had a very limited influence when the failure mode is the core shear or the tensile rupture of the core.

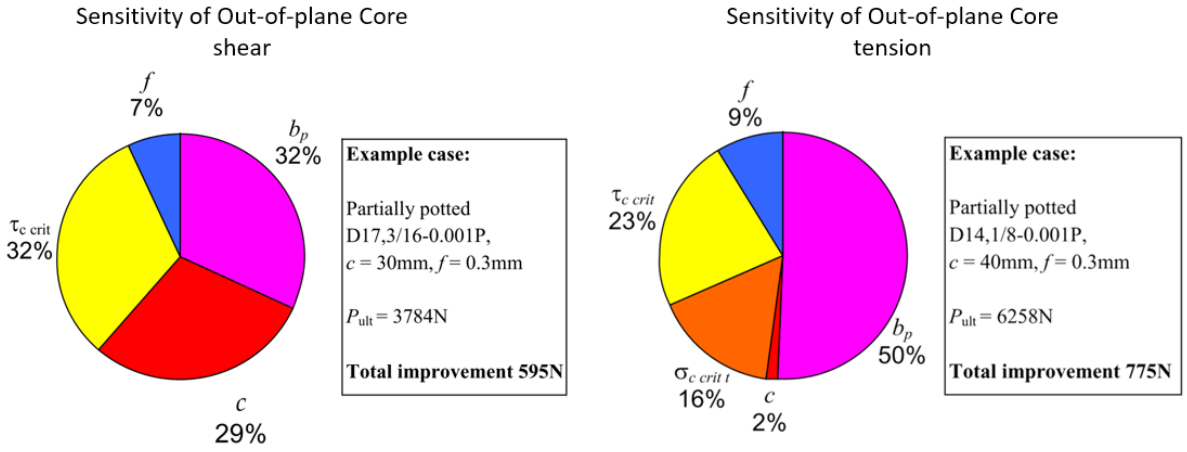

Fig. 49: Sensitivity of the different parameters accordingly to the ESA insert design handbook [1].

2.1.6 Conclusions of the state of the art of insert analysis

Sandwich structures are widely used for the main frame of helicopters, and for secondary structures of aircraft, the reason is because sandwich panels are not yet well mastered in terms of post impact, jointing and fabrication issues related to moisture.

Concerning the jointing through inserts, the principal problems are the microcracks formed by fatigue and aging of potting, but also the lack of understanding of the insert pull-out damage scenario.

Several pull-out tests have been performed on inserts, and the influence of defects has been reported to be important by several authors. The efforts to include these variations on the insert design have been increased through time, studying the influence of small variations, defects on the honeycomb cells, irregular shape and position on the potting, although there are no conclusive results in terms of providing a better approach to include these on the insert design.

There is evidence indicating that the insert failure is directly related to the core shear strength, although there are also indications that suggest that the potting might fail before the core.

Concerning the insert sizing methods, the most common are based on analytical approaches that introduce big errors to the design. The approach proposed by Ericksen in 1953, although it provides a good approximation, is very long and complex, thus not easy to implement.

In recent years, a virtual testing method has been proposed as an alternative showing accurate results, although the required expertise, development time, and computation resources are the principal disadvantage.

Since the core shear buckling is commonly the first failure mode when an insert is subjected to pull-out, the insert strength is calculated based on the shear resistance of the core. For this reason, a very good understanding of the shear failure of honeycomb cores is necessary.

However, most of research on honeycomb cores is focused on the buckling under compression and there is an important lack of general knowledge concerning its shear behavior.

For this reason, a detailed investigation of the shear buckling of honeycomb cores is necessary and a literature review of this subject is presented in the next section.

2.2 Shear buckling of Nomex® honeycomb cores

Nomex® honeycomb cores are used for the sandwich construction of aeronautical panels because they have excellent mechanical specific strength, stiffness and resistance to fatigue, they are good for electric and sound insulation applications and because the Nomex® honeycomb allows to support low energy impacts without the breaking of the core/skin interface as happens for aluminum honeycomb cores [22], [54].

The Nomex® honeycomb core is created by the expansion of glued layers of Nomex® paper, then the honeycomb is dipped in phenolic resin and finally cured, increasing its fire resistance, stiffness and density, as explained in [55], [56].

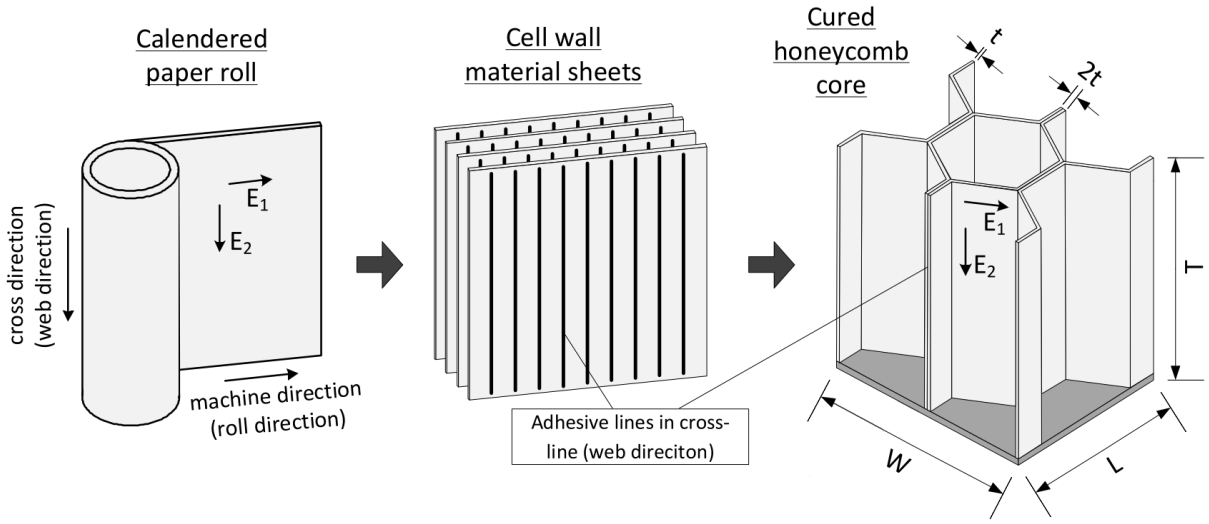

Fig. 50: Manufacturing process of Nomex® honeycombs [12].

The honeycomb's core has an orthotropic behavior. Its low density and structure result in a very low Young modulus in the L and W directions. However, its out-of-the plane shear moduli in both directions are relatively high when stabilized, which makes this core ideal for sandwich panels.

Also, the energy absorption capabilities of this structure are remarkable and several studies have been performed since the early 60's [57] [58]. Many other studies deal with the crush behavior of the core after a low-velocity/low-energy impact on a sandwich.

In the related literature, the main topic is clearly the compressive response, however, there are far fewer studies concerning the nonlinear shear behavior of honeycomb. This is not advantageous because when an insert is pulled-out, the core is subjected to shear stress.

In this section a literature review about Nomex® honeycomb core and the relevant aspects related to inserts is presented.

2.2.1 The honeycomb structure

The hexagonal geometry of the cells is inspired in some insect nests. The reasons why the nature has converged to the use of this particular structure are interesting. According to the most accepted theories today, these cavities are initially built as cylindrical cells that later transform into hexagonal cells due to the insect activities [12], [59]. If nature works like an optimization mechanism, then, the honeycomb might be the lightest, strongest and easiest to build shape there is.

Back to the engineering field, this honeycomb shape is used for sandwich panel cores because it has proven to be very light, strong and compact, although there are other shapes that can be used.

It is well known that there are only 3 regular shapes that can be perfectly assembled in 2D between themselves without gaps (allows for tessellation); the triangle, the square and the hexagon.

A comparison from a mechanical point of these three shapes properties can be made. They are assumed to be used as cells, and therefore they are hollow. In this sense, the perimeter represents also the mass that is used to build the shape. Consequently, the perimeter divided by the area represents the density of the shape. To evaluate their mechanical resistance, the second moment of inertia of the shape (as if it were a hollow cylinder with thickness "t") is calculated and assumed to represent the mechanical strength. Then, this inertia is divided by the shape surface. This last quantity represents the strength/area ratio of the three shapes.

Considering a similar size and thickness for all the shapes, they can be compared. Of the three shapes, the one with the highest inertia-surface ratio is the hexagon, this means the hexagon is the strongest shape (at least under compression). However, comparison of the perimeter-surface ratio shows that the hexagon is the second lightest.

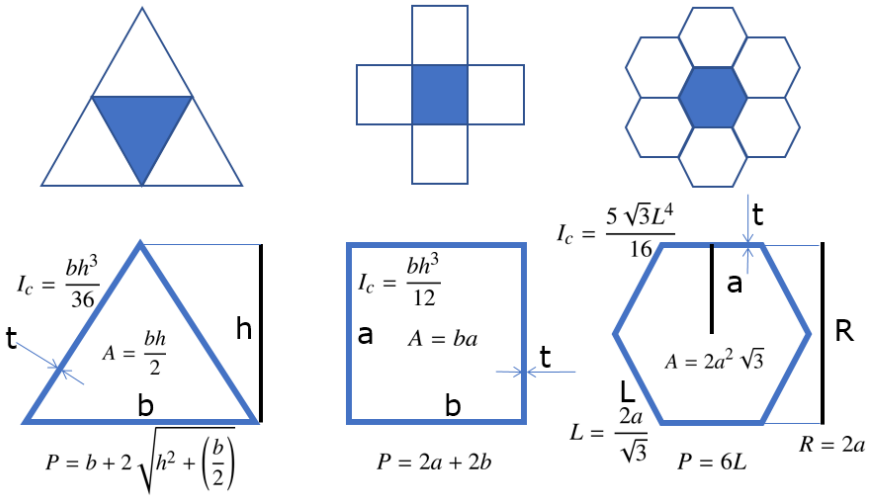

Fig. 51: Regular geometric figures that allows for tessellation.

2.2.1.1 Imperfections of the Nomex® honeycomb

Due to its fabrication process the Nomex® honeycomb core has many different defects. According to several researchers [35], its imperfections can be divided in different scales. Global imperfections might be irregular cell geometry (Fig. 52 a) or uneven or pre-buckled cell walls (Fig. 52 e). Local imperfections are surface roughness (Fig. 52 b), wall thickness variation (Fig. 52 c), deviation of fiber angle and finally resin accumulation in cell wall corners (Fig. 52 c). Micro imperfections are cracks, pores and variation of fiber volume fraction.

Fischer et al. [60] and Seeman et. al. [12] did a detailed study of how imperfections of the hexagonal geometry of Nomex® honeycomb affect their strength. They concluded that the variation of vertical waviness in the core affected significantly the strength of the core. Also, the resin concentration in the corners increase the core strength in compression.

Most of the work in the literature doesn't take into consideration the mentioned imperfections; they are limited to consider the average experimental mechanical properties of the materials that include these imperfections.

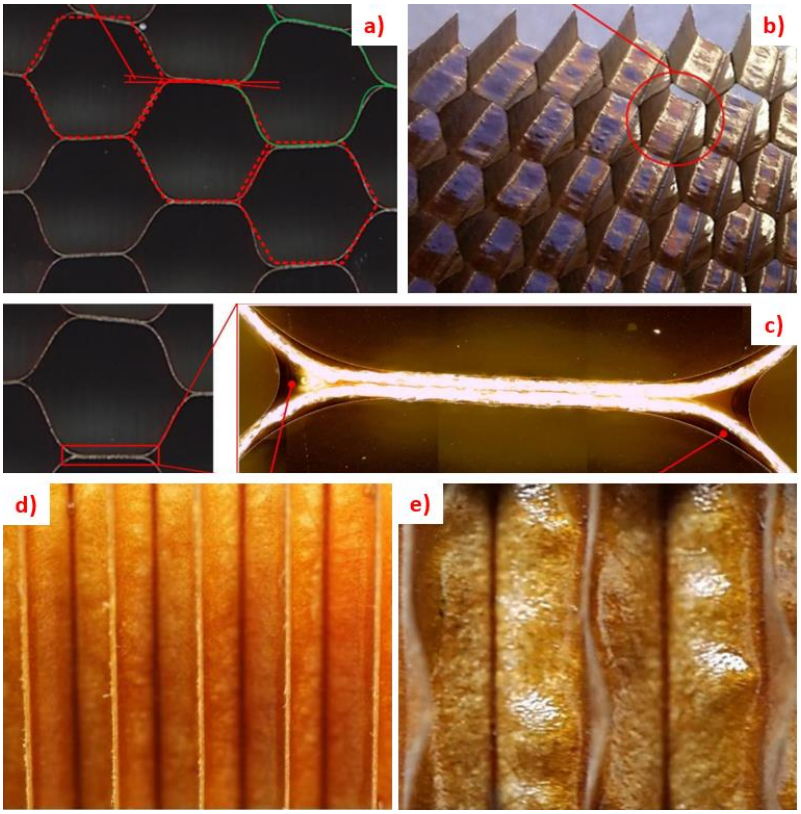

Fig. 52: Common defects of the Nomex® honeycomb cells [60].

2.2.2 Properties of the Nomex® paper

The Nomex® is a material that was developed by DuPont in the 60's. It's made of aramid fibers and its principally advantage is its resistance to heat and flames and its light weight. For this reason, its applications are many, equipment for firefighters, protection devices for electric generators, wind turbine generators, aircraft, trains, among many others [54].

There are several types of Nomex® papers used to fabricate honeycomb cores depending on the application, some examples are the paper T-410, which is used for electrical insulation applications [55], the T-722, restricted for ground transportation and naval applications because it doesn't satisfy the FAR 25.853 flammability afterglow requirement [19], and the T412, used for aeronautical applications [12], [61].

The properties of the T412 paper are not available on the web. However, Seemann et al. [12] somehow figured out the correct manner to ask for the mechanical properties to the manufacturer DuPont, and now, these properties can be seen in Table 6, where E_1 and E_2 are the elastic moduli, S_1 and S_2 are the tensile strengths and d_1 and d_2 are the elongations at rupture in the principal directions. The properties of the T412 paper vary according to the thickness; 2T412, 3T412 and 4T412. Nevertheless, the provided information concerns only the elastic domain of the material according to the ASTM D828.

Nomex® Type	Thickness [µm]	Density [g/cc]	E_1 [MPa]	E_2 [MPa]	S_1 [N/mm]	S_2 [N/mm]	d_1 [%]	d_2 [%]
2T412	47 - 65	0.54-0.94	3000	1700	3.63	1.23	6.1	3.5
3T412	71 - 91	0.67-0.91	3000	2000	6.01	2.33	6.7	5.1
4T412	94 - 117	0.72-0.94	3100	2200	6.13	1.7	8	5.3

Table 6: Mechanical properties of the Nomex® paper T412 according to Seemann [12].

In 2006, Chiang Foo et al. studied the properties of a Nomex® paper that is used to fabricate Nomex® honeycomb cores, although they didn't specify the exactly type of paper. The aim of the research was to test the mechanical properties of the paper alone (without the phenolic coating). They did tensile tests on the paper and then they give the load vs strain curve in [62] (Fig. 53).

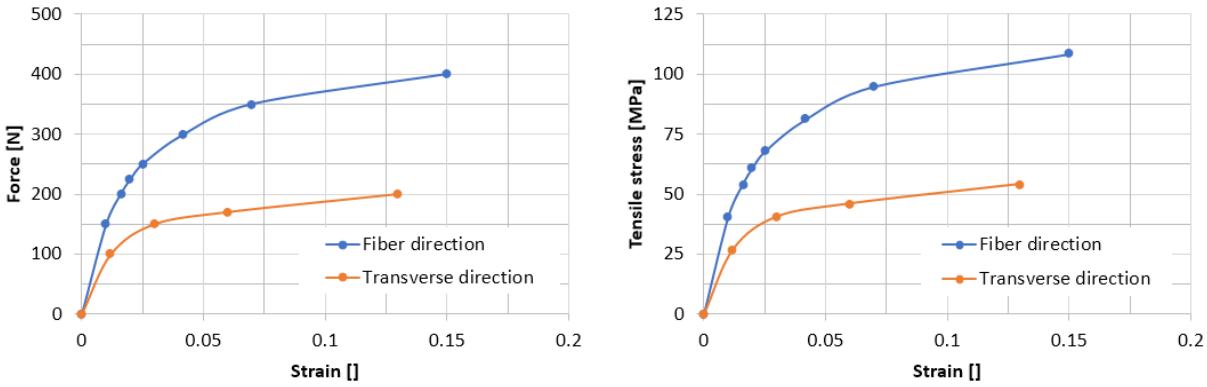

Fig. 53: Load vs strain curves in the fiber and transverse direction of the Nomex® paper [62].

As indicated by the charts, the Nomex® paper presents plasticity or damage (this aspect is not clear in the publication). They indicated that the wrinkling phenomena started to appear when the load reached about 300 N and 170 N in fiber and transverse directions respectively. The thickness of the specimens was of 0.125 mm by 180 mm length and 29.5 mm width. This results in an elastic modulus of E1=4067.8 MPa and E2=2259.88 MPa for the fiber and transverse directions respectively.

Concerning the resin used for the coating of honeycomb cores, it's a phenolic one although the exact type is unknown. Some studies provide a few experimental references. According to Seeman, Roy, Redjel, and other researchers, the Young moduli of this resin is in the range of E=5000 MPa, with a Poisson ratio of ν=0.36 and presents a predominant brittle behavior [12], [56].

What is more important though, is that the properties of the coated Nomex® paper differ considerably from the properties of the resin and paper alone. Roy et al. [56] performed tensile tests on coated and non-coated samples of Nomex® paper (see Fig. 54). They found that the thickness of the resin layer determined the nonlinear behavior of the coated paper. When the coating layer was thick (The paper and resin thickness were 0.05 mm and 0.123 mm respectively), the paper became stiffer and brittle, while for the non-coated sample the plastic behavior was predominant.

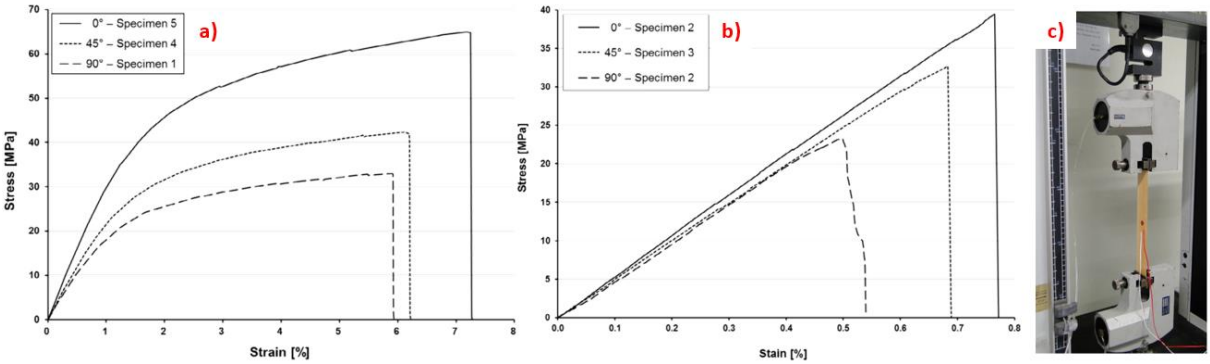

Fig. 54: Tensile tests on a) the Nomex® paper T-410 alone, b) the Nomex® paper with a thick phenolic coating (becomes brittle) [56].

Fischer et. al. [63] performed some tests on a pre-coated aramid paper (see Fig. 55), which is very similar to the Nomex® paper. The paper and resin thickness were of 0.2 mm and about 0.1 mm respectively. They found that the coated paper presented a relatively important plastic behavior.

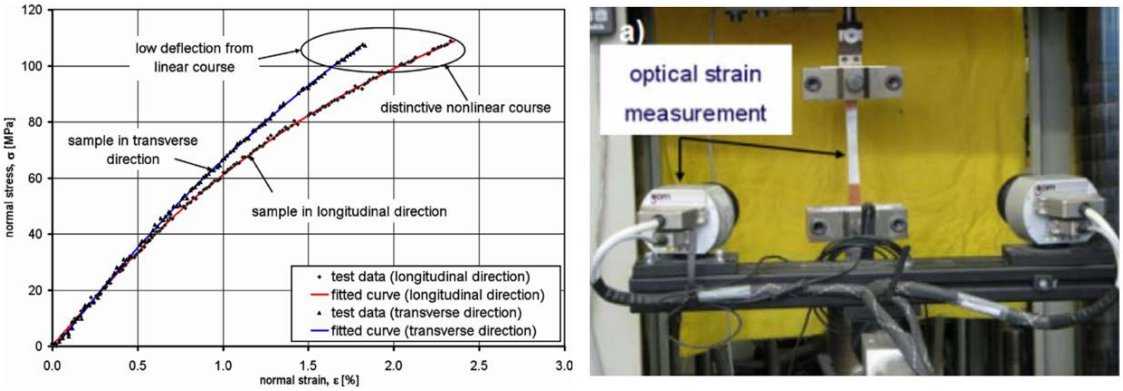

Fig. 55: Tensile tests on a coated Nomex® paper [63].

This phenomenon is named pseudo-ductility and has been studied by Wisnom [64]. When a brittle material is combined with a material that has a bigger strength, the nonlinear behavior of the resulting material presents something similar to a ductile behavior, depending on the percentage of each material.

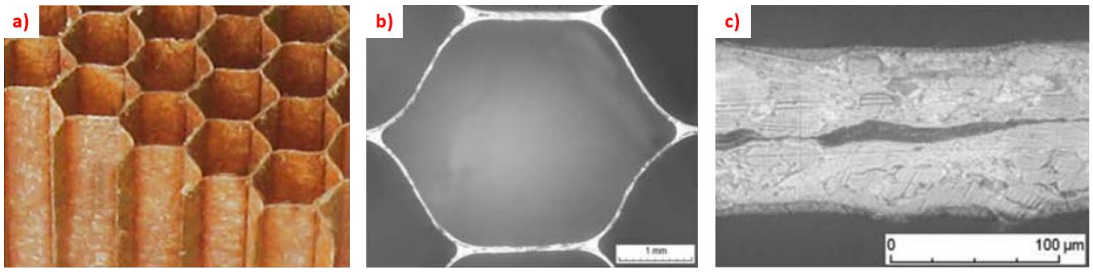

Fig. 56: The Nomex® honeycomb structure under the microscope, the phenolic resin layer is visible [65].

2.2.3 Shear testing of honeycomb cores

It is well known that, when a sandwich is subjected to a bending load, the core absorbs almost all the shear components of the force. Consequently, the shear properties of the core are very important for the sandwich design. Nevertheless, these properties are not as simple to determine as it may seem because the honeycomb core is a cellular structure and not a solid material.

There are various tests available for obtaining the shear properties of a honeycomb core although a pure shear test is not feasible. A very complete review about these testing methods was made by Kelsey in 1958 [66]. Some tests are standardized and some other tests have been done by other researchers. Here a brief description of them is presented.

2.2.3.1 Double block test

Kelsey is the only one who reported having done tests using the double block test. He stated that this is not the best testing option due to secondary effects that causes a non-uniform distribution of flexural stress due to the skins deformation, which can lead to big errors (see Fig. 57-a).

2.2.3.2 Three-point bending test

This test is standardized by the ASTM C393 [67] (see Fig. 57-b). It consists of submitting the core to shear stress by submitting a sandwich beam to an imposed displacement in the center of the beam that is simply supported. This type of test was used by Bunyawanichakul, Giglio among other researchers [36], [68]. This test provides accurate values as the rail test and is easier to fabricate. Although, according to Kelsey, there are very pronounced local effects at the support and imposed displacement points.

2.2.3.3 Single block test (Rail test)

This test is standardized by the ASTM C273 [69] and is strongly recommended by Hexcel [70] (see Fig. 57-c). It consists of subjecting only one block of honeycomb to shear stress by pulling the skins, which should be articulated to avoid undesired flexural forces. The recommended dimensions are at least 2 inches of width by 12 times the thickness of the core as length. This type of test has been used by Seemann, Bianchi, among others, [12], [71] [72]. According to Hexcel, the size of a sample of honeycomb should be of at least 7.5”x2”x0.625” for metallic, and 6”x2”x0.5” for non-metallic honeycombs.

The only disadvantage of this specimen is that its manufacture is not easy because of the articulated skins [73].

2.2.3.4 Four-point bending test

The four-point bending test is considered in the ASTM C393 standard, although it is stated that is only for historical continuity and is considered as non-standard (see Fig. 57-d). According to Kelsey, this test is not suitable because only the core between the supports and the loading points is subjected to shear stress.

2.2.3.5 Double-double block test (Double lap test)

This test is not standardized, although it has been used in several works like the method for testing thick honeycomb composites developed by the NASA [74], [75]. According to Kelsey in ref. [66], this test is a better option compared to the double block test, although there can be some problems with its manufacture (see Fig. 57-e).

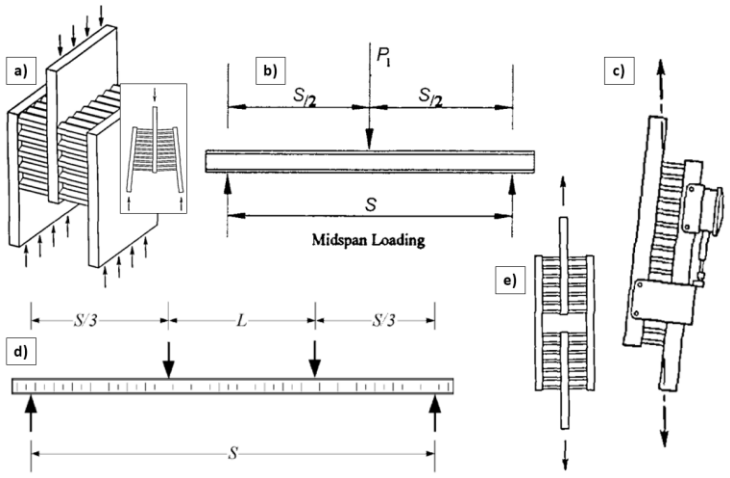

Fig. 57: Different shear testing specimens for honeycomb cores: a) Double block, b) Three-point bending, c) Single block, d) four-point bending tests, e) Double-Double block [66], [67], [69].

2.2.4 On the shear behavior of honeycomb cores.

2.2.4.1 Analytical approaches

There have been only a few works related to the shear behavior of honeycomb cores. One of the first researchers that treated this subject was Kelsey in 1958 in ref. [66]. He proposed an analytical approach to estimate the shear moduli of a honeycomb core, this approach gives an interval of values in which the shear moduli should be found. However, this model was only made to predict the initial linear response:

$$\frac{G_{13}}{G_s} = \frac{\sin^2(\alpha)}{2}\left(\frac{\rho}{\rho_s}\right) \quad 11$$

$$\frac{(1+\cos(\alpha))^2}{4}\left(\frac{\rho}{\rho_s}\right) \leq \frac{G_{23}}{G_s} \leq \frac{1+\cos^2(\alpha)}{2}\left(\frac{\rho}{\rho_s}\right) \quad 12$$

Where ρ and ρ_s are the density of the honeycomb and foil material respectively, G_s the shear moduli of the foil material and α the cell angle.

In 1992, Zhang and Ashby [9] did a study on the honeycomb core, including the shear behavior. They considered that the honeycomb failure occurs when the cells start to buckle. They endorsed this hypothesis with the fact that, for some panels, once the cells start to buckle, the adhesive of the skins/core interface breaks causing debonding of the skins. According to them, the shear stress that causes this buckling of the cells can be estimated by the following formulas, where E_s is the Young moduli of the solid cell wall material.

$$\tau_W = 1.7E_s\left(\frac{\rho}{\rho_s}\right)^3 \quad 13$$

$$\tau_L = 2.6E_s\left(\frac{\rho}{\rho_s}\right)^3 \quad 14$$

However, many researchers noticed that the experimental shear strength of honeycombs, and the predicted by the equations of Zhang and Ashby, were very different.

In 2006, Pan et al. [72] used the elastic buckling theory to predict the shear strength of an aluminum honeycomb core, as an intent to provide a better approximation. However, when they compared the obtained theoretical values against experimental data they found that the predicted strength was only 56% of the experimental value.

In 2008, Bianchi et al. [41] after an analytical analysis on the buckling load of a metallic honeycomb cores, suggested that the shear behavior of the cells operates mostly in the postbuckling regime.

This result explains why the analytical shear failure criteria (including the one of Zhang and Ashby) were inaccurate. Also, this means that to predict the shear strength, an analysis of the postbuckling behavior of honeycomb cores is necessary, which is very complex to do analytically due to the multiple imperfections, multiple buckling modes, etc.

2.2.4.2 F.E. approaches

Recently, a shift on the strategy to predict the shear strength of honeycomb appeared. With the recent development of the computing technology and F.E.A. software, it was possible

to create very refined models that include the imperfections and buckling modes in order to analyze and study the postbuckling behavior of the honeycomb structure.

As it's normally for honeycombs, most of the F.E. models were developed to study the compression properties of the structure. Asprone et al. [76] did a very detailed study of the compression behavior. Their conclusion was that the initial behavior of the honeycomb is linear and then, a bifurcation point is reached, resulting in a stable buckling configuration. Nevertheless, this was only made for the compression case.

Concerning the study of the shear behavior, some models were developed, although the studies are more demonstrative (to show it was possible to be made) than conclusive. In 2009, Heimbs in red. [65] did a study on the virtual testing of honeycomb cores, showing that it was possible to correlate experimental results through F.E. models. Although he focused its research to the compressive behavior, he stated that some simulations were made to correlate the shear behavior but the results were not shown. He stated that parameter having more influence on the results was the mesh size, because coarser meshes are not able to reproduce the cell wall folding. He concluded that the size of the mesh was correct if it was less than 0.2 mm per element. Another important aspect was that the number of simulated cells was important because the specific boundary conditions of the cells can't be reproduced using a symmetry.

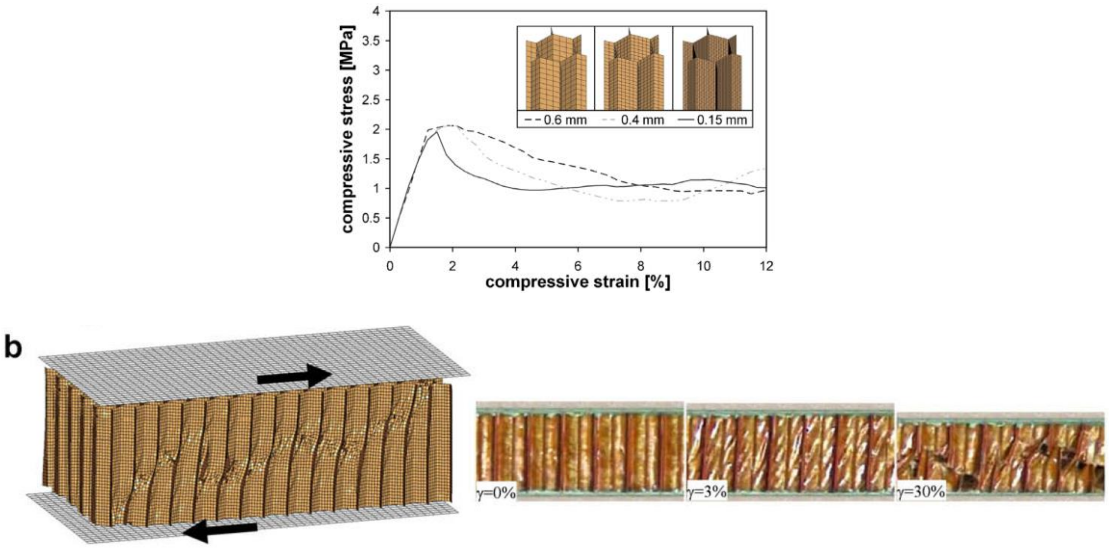

Fig. 58: Shear testing of honeycomb cores; experimental vs numerical scenarios [65].

In 2012, Giglio et al. [77] modeled a three point bending test. As Heimbs, they stated that a mesh with a size less than 0.4 mm captured correctly the folding of the cells. Although they made emphasis that for the zones that were not subjected to extreme folding, a much more coarser mesh can be used and still obtain good results.

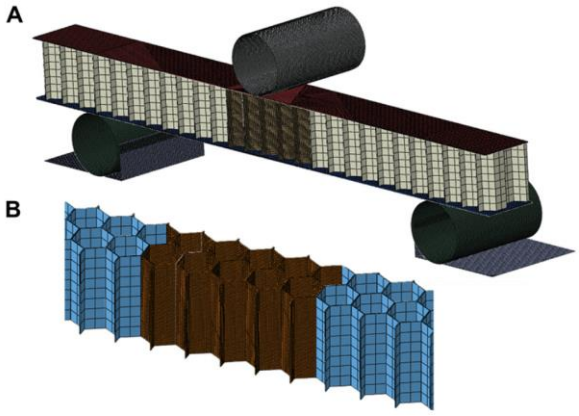

Fig. 59: Modeling of a three point bending [77].

By the last decade (since 2010) it was clear that the F.E. analysis was the preferred tool for the analysis of honeycomb cores, as it allowed to simulate complex tests and to make the analysis easier. In this context, in 2016, Seeman [12] did a very deep and detailed study about the modeling aspects of the virtual testing of honeycomb cores at mesoscale.

Beside of the mesh size, they found that defects had a considerable influence on the results, above all the resin in the corners of the cells, which at the same time can be emulated by considering a cell as if it had a perfect shape.

He proved that it was possible to correlate the experimental results of the shear test with the virtual tests.

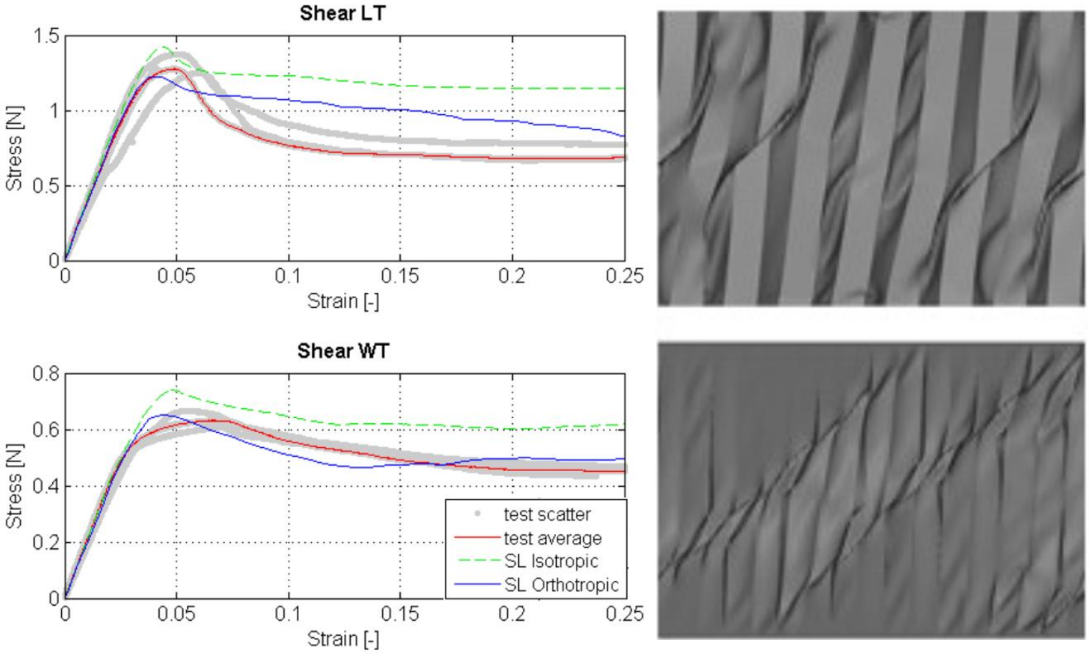

Fig. 60: Virtual shear testing of honeycomb cores [12].

As the modeling of honeycomb cores gained in importance, the number of features that had to be included into these models increased too, requiring a very high expertise and development time. This is normal considering that the aim of the models developed for research purposes is to capture and understand the more precise behavior of the cells, therefore the simulation time becomes a secondary parameter.

2.2.4.3 F.E. reduced models

However, these very detailed models are not suitable for the industry, where very large models are developed and it is not practical to implement such detailed models. For this reason, even if the shear behavior can be simulated through virtual tests, a deeper understanding of the phenomena enables to perform simpler simulations that can be incorporated into bigger scale models. This work has been done only for the compressive behavior of honeycomb.

In 2008, Castanié [78], [79] developed an approach that captures the overall nonlinear behavior of the honeycomb core, and is simple enough to be implemented for larger models. The idea is to consider the honeycomb core as springs that have a nonlinear behavior equivalent to the compression behavior of the honeycomb core. The main advantages of this approach are its simplicity and efficiency, proving that it was possible to obtain very accurate results using minimal computational resources.

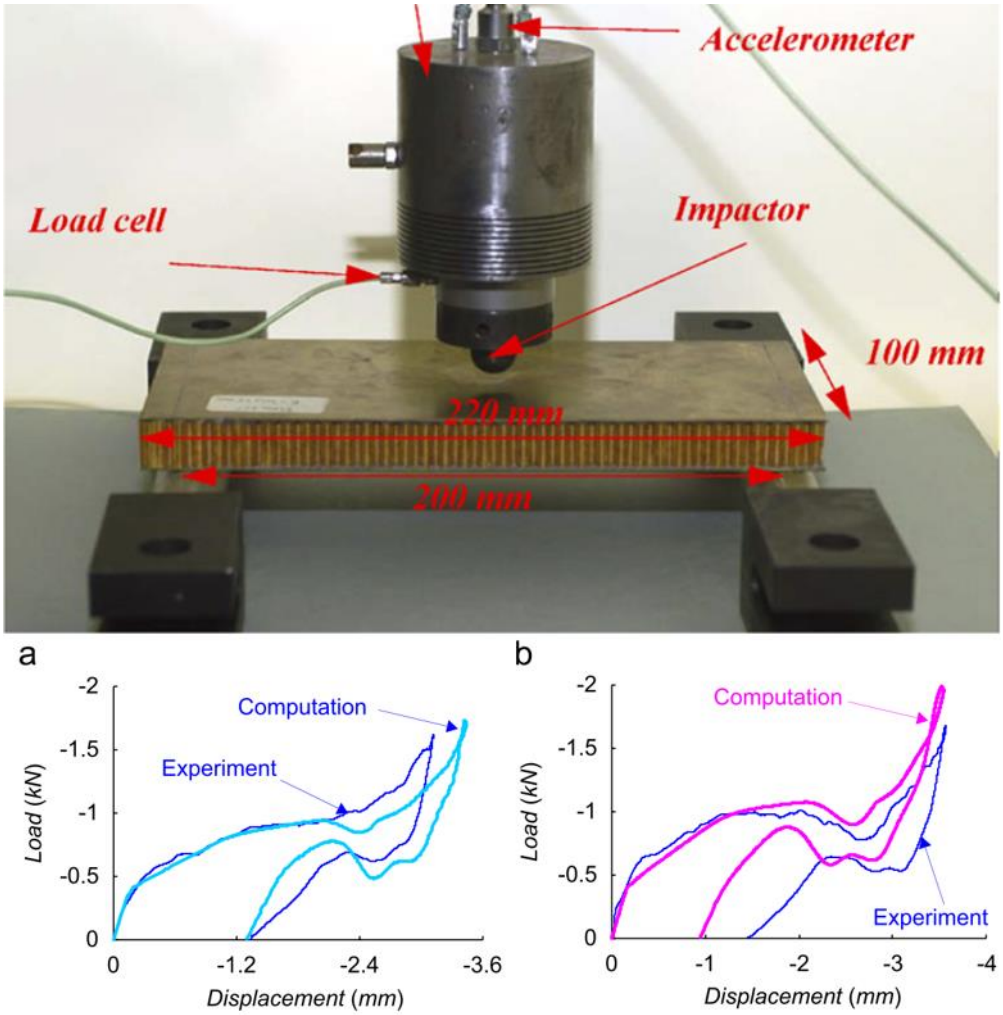

Fig. 61:Impact modeling of a Nomex® honeycomb sandwich panel; numerical vs experimental results [78].

In 2013, Kolopp et al. [80] used a similar approach to reproduce the response of low energy impacts on an aluminum sandwich panel. Their idea was very similar to Castanié, only that instead of using springs they used an User Material to introduce the crushing behavior and used only one element through the thickness of the sandwich panel. This is very arguable, although proved its efficacity when it was compared to experimental results. Also, they represented the postbuckling behavior of the cells by an analytical expression considering the strain rate of the material.

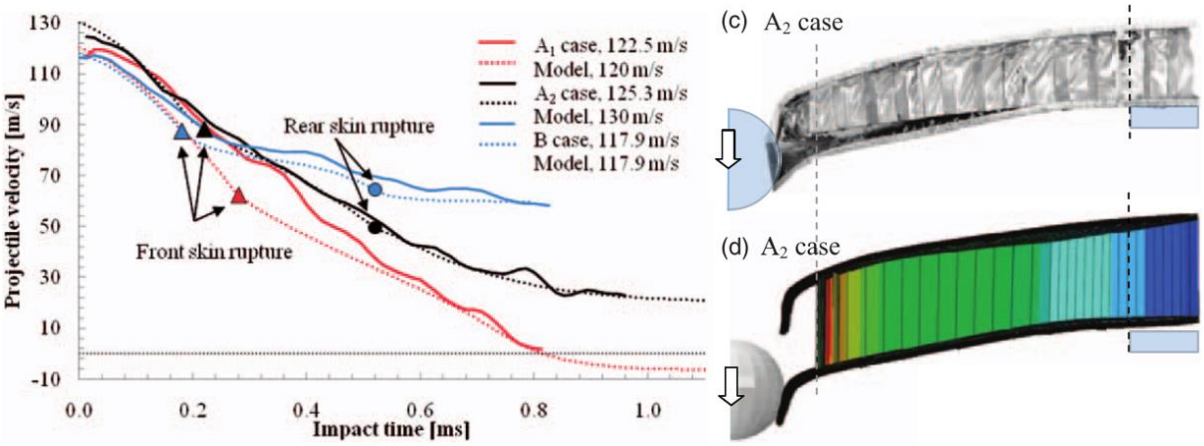

Fig. 62: Modeling of the impact on an aluminum sandwich panel, experimental vs numerical results [80].

Both approaches of Castanié [78] and Kolopp [80] proved that by understanding the structural behavior of the honeycomb it is possible to propose a simplified discrete model that captures the global nonlinear behavior of the honeycomb core under compression with very accurate results and that is suitable for large scale simulations. Although this is only possible through the mastering of the nonlinear behavior, and this has only been done for the compression case and not for the shear case.

2.2.5 Conclusions on the honeycomb's shear buckling

When an insert is pulled-out, the cells surrounding it are subjected to shear stress. The evidence indicates that the insert strength is proportional to the buckling resistance of the core. Therefore, a deeper understanding of the shear buckling of the honeycomb core is necessary.

There are only a few studies concerning the Nomex® paper, however, it can be considered as a very well-known material. The honeycomb structure present many different fabrications defects like waving on the walls, irregular cell geometry, thickness variations, resin accumulation on the borders, pre-buckling among other microdefects.

The shear behavior of honeycomb cores has been studied analytically, more specifically, its shear moduli and its shear strength although the proposed approaches do not include the honeycomb defects nor the postbuckling behavior. And this is relevant because the honeycomb structure starts to buckle at relatively low stresses and works mostly in a postbuckling regime.

Considering the complexity of the problem, virtual testing has been proposed to determine the shear properties of the honeycomb core, although all the related researches have only shown that this was feasible without describing or explaining the honeycomb shear postbuckling and its maximal strength. On the other hand, this approach requires high expertise, and computing resources and is not suitable to be implemented in large scale models.

Other researchers have developed reduced models of honeycomb cores that can reproduce the crushing behavior including the postbuckling and collapse of the cells. They did this by understanding and parametrizing the behavior instead of focusing on the modeling of the structure. This approach has proven to be very accurate and efficient in terms of computational power. Although this has only been done for the crushing and not for the shear of honeycomb cores.

The purpose of the next chapter is to increase the understanding of the shear behavior of the Nomex® honeycomb core, but also to investigate how exactly it's related to the insert failure.

Chapter three: Experimental and numerical analysis of honeycomb cores

In this section the shear behavior of honeycomb cores is investigated. First an experimental study is made, then, a numerical approach to study the buckling of the interior cells. Also, an investigation on the influence of the honeycomb's boundary conditions is made, especially for the insert case. Finally, a CDM (Continuum Damage Mechanics) approach is proposed to model the nonlinear shear behavior of these types of cores.

3.1 INTRODUCTION 69
3.1.1 Objectives and proposed methods 69
3.2 BENCHMARK OF SPECIMENS FOR SHEAR TESTING OF HONEYCOMB CORES 73
3.2.1 Specimens description 73
3.2.2 Verdict and test results 75
3.2.3 Conclusions 79
3.3 SHEAR TESTING OF HONEYCOMB CORES 81
3.3.1 Specimen fabrication 81
3.3.2 Test setup 83
3.3.3 Test results 84
3.3.4 Analysis of the buckling and postbuckling behavior of the cells 86
3.3.5 Conclusions 94
3.4 NUMERICAL STUDY OF SHEAR BUCKLING OF HONEYCOMB CELLS 99
3.4.1 Properties of the T-722 Nomex® paper 99
3.4.2 Study of the shear buckling of the Nomex® honeycomb core 100
3.4.3 Conclusions of the numerical analysis of the shear buckling 107
3.5 EXPERIMENTAL AND NUMERICAL STUDY OF THE CORE BOUNDARY CONDITIONS FOR INSERTS. 111
3.5.1 Numerical study 111
3.5.2 Experimental study 116
3.5.3 Conclusions on the boundary conditions 118
3.6 REDUCED CDM MODELING STRATEGY OF THE NONLINEAR SHEAR BEHAVIOR OF HONEYCOMB CORES 121
3.6.1 Analysis of the nonlinear shear stages of the honeycomb 121
3.6.2 Decoupled CDM approach for the shear behavior of honeycomb cores 124
3.6.3 Validation of the proposed approach 128
3.6.4 Conclusions 134
3.7 CONCLUSIONS 135

3.1 Introduction

According to several authors, the shear failure of the core is what causes the insert failure when is subjected to pull-out. Because of this, the insert failure analytical approaches estimate the insert's strength principally based on the shear moduli and strength of the honeycomb core.

The shear loading limits of these cores can be obtained by following normalized tests standards such as the ASTM C365 or the C273.

The literature review presented in the last chapter showed that, as simple as it may seem, until today there is not a consensus on what is exactly the shear failure of a honeycomb core, because this has not been properly studied yet.

To our knowledge, most of the related researches focus directly on obtaining the shear loading curve and developing a F.E. model of the core for validation. But there is not even one work that is focused on the detailed description of the shear buckling of honeycomb cores and many questions are still without response.

There are just some pieces of puzzle that can be assembled together to have a general overview of this shear behavior, but nothing conclusive concerning the phenomenology or the cell's damage scenario.

3.1.1 Objectives and proposed methods

3.1.1.1 Realize a benchmark study of shear test specimens

The first step of this research is to investigate the different shear testing specimens that will help us to study the desired aspects of the honeycomb, more specifically, the elastic buckling reversibility domain. A very complete review of shear testing specimens was made by Kelsey in 1958 [66] but it was only focused on the overall behavior and aspects like the analysis of the buckling or damage of the cells were not included.

3.1.1.2 Define a failure criteria based on the cells integrity and not on the ultimate stress

Both C273 and C393 ASTM standards, allows to determine the shear strength of a honeycomb core based on the load peak of the loading curve [69], [67]. However, the integrity of the cells is not taken into consideration. If the ultimate shear stress is used as failure criterion the core strength may be overestimated. Also, although many authors identify the shear buckling of honeycomb cells perfectly, no author to date has raised the question of the reversibility of postbuckling.

If we suppose that the cells are loaded just a little below the shear strength limit, according to this criterion the core should remain elastic. However, the reality is that the cells could have been damaged, plasticized or ripped; losing their stability and therefore weakening the sandwich panel.

We think that the shear strength value must assure the integrity of the honeycomb cells too, to keep the integrity of the panel. Therefore, the shear failure of the core must be related directly to the apparition of structural and permanent damage of the cells.

Therefore, a detailed study will be made on the shear properties of the honeycomb. The aim is to define the effective elastic shear stress of the honeycomb. To do this, the honeycomb will be subjected to an incremental cyclic load until the effective shear moduli is damaged (see Fig. 63)

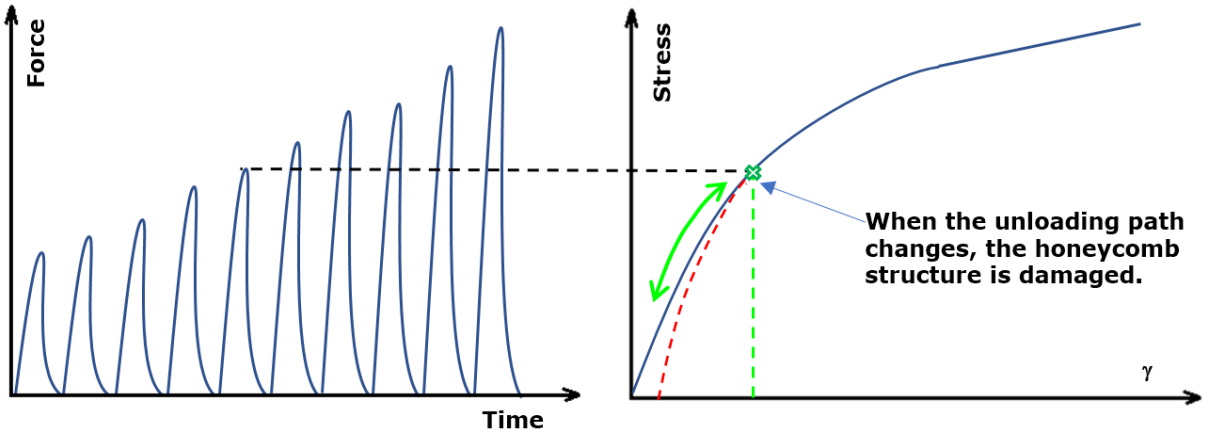

Fig. 63: Identification of the effective damage of the honeycomb core.

3.1.1.3 What's exactly the buckling of a honeycomb cell?

Another aspect that is not clear is the magnitude of the buckling of the cells. The cells present many different fabrication defects like; waving of the walls, irregular thickness, fillet corners, among others. Therefore, due to the waviness of the cells (see Fig. 52-e), what exactly what should we consider as buckling of the cells? And, how do these defects influence the structural stability of the honeycomb

It's well known that the structural buckling of the cells in compression is influenced by the presence of initial defects, but this has not been studied for the shear case for honeycomb cells. Therefore, it will be interesting to describe the influence of these defects in the linear and postbuckling stages of the cells.

Also, when the core is subjected to shear stress, the hexagonal geometry of the cells makes that the walls are not subjected directly to shear stress. It should be more like shear/compression combined to the fact that the vertex of the cells are straight.

A detailed study on the honeycomb shear buckling will be made using 3D digital correlation cameras, paying special attention to the size and scale of the buckles created by shear loading.

3.1.1.4 How do the cells fails near the insert?

Seemann et al. in ref. [12] performed several shear tests on a honeycomb equivalent to the HRH10 of 20 mm thickness. They used the ASTM C273 test standard. When the honeycomb was tested, the cells started to buckle until the classical shear marks of 45 ° appeared as showed in Fig. 64.

Nevertheless, when this scenario is compared to a honeycomb core near to an insert there can be observed that the buckling shape is not the same.

A numerical and experimental study of the honeycomb cells near the insert will be made to investigate the effects.

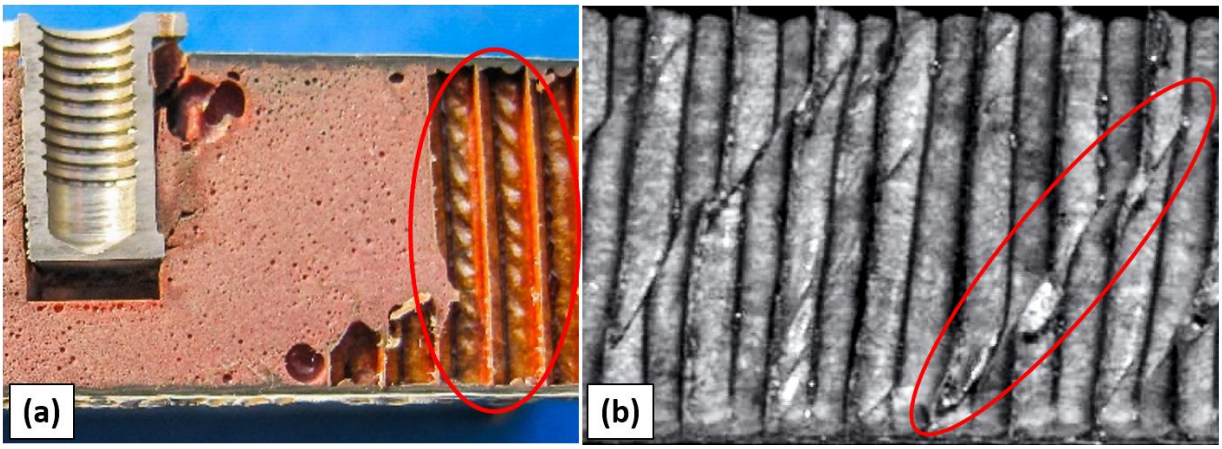

Fig. 64: Comparison of the buckling pattern of two Nomex® honeycomb cores subjected to shear loads: (a) an insert specimen after a pull-out test where the cells have plasticized (extract from [15]), versus (b) a single rail shear test (reproduced from Seemann [12]).

3.1.1.5 Development of a modeling technique for the shear behavior of honeycomb cores

The detailed modeling of honeycomb core is not suitable for large scale simulations or, as is our case, for intensive calculations. Therefore, we also want to define a method to speed up the simulation time for the developing of our insert failure mode map. Then, a CDM modeling will be proposed for the modeling of the shear behavior of the honeycomb core.

3.2 Benchmark of specimens for shear testing of honeycomb cores

The first part of this work consisted of a study of different conceptual designs of specimens to test the shear properties of honeycomb cores. Five different types of specimens were fabricated and tested to observe the advantages offered by each design for a study of the shear properties of a honeycomb core. The aim was to select a design that fits the best to obtain the following characteristics:

- The average shear stress vs gamma curve
- The shear moduli of the core structure
- The maximal average shear stress of the core structure
- Observe the evolution of the nonlinear behavior of the structure
- Observe the evolution of buckles in the structure
- Simple fabrication
- Obtain repetitiveness of the results

Several types of conceptual designs were tested to find a design that allows to obtain the correct and maximal quantity of data from the tests. In the following section this procedure is described. The double rail shear test described in ASTM C273 [69] was excluded from this study because of its inability to make proper cyclic tests after the buckling of the cells.

3.2.1 Specimens description

All the specimens were fabricated using the HRH-78-3/16-3.0 Nomex® honeycomb core of 20 mm thickness. According to the manufacturer, the shear moduli are 24.13 MPa and 31.71 MPa for the W and L directions respectively and the shear strengths are 0.5133 MPa and 0.785 MPa for the W and L directions respectively (using the recommended thickness correction factor). [70]

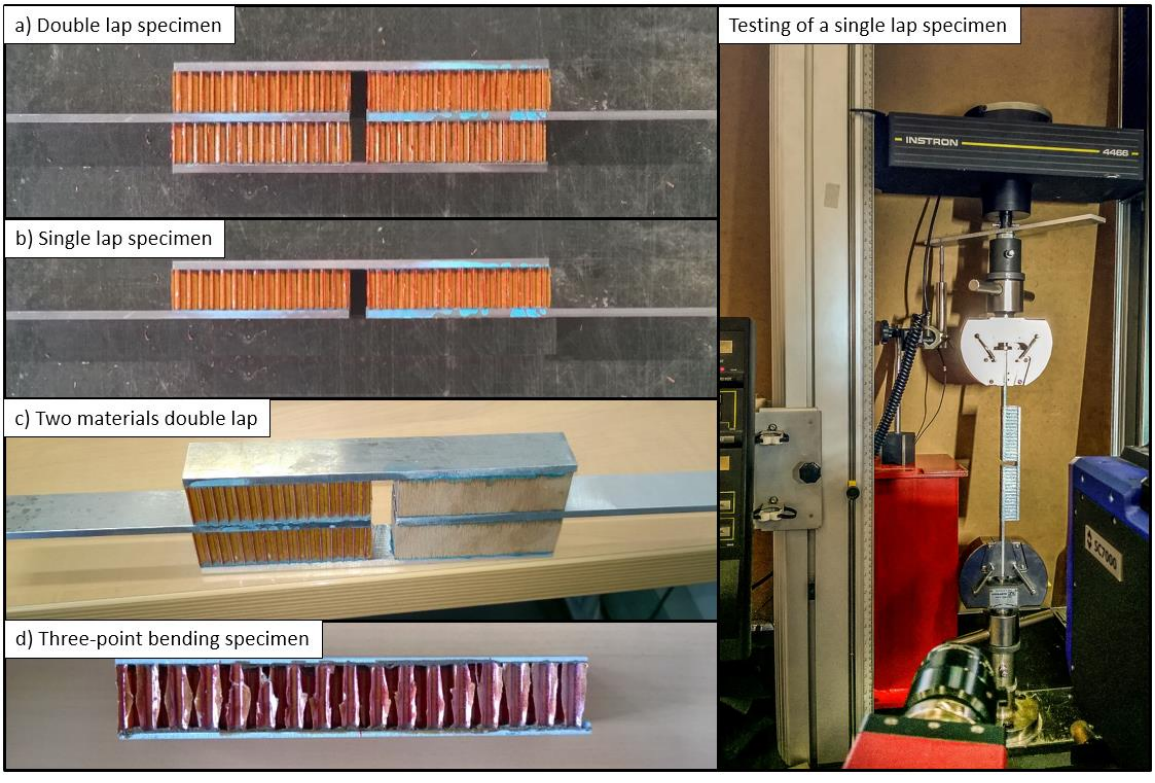

Fig. 65: Specimens fabricated for the benchmark study and testing of a single rail specimen.

3.2.1.1 Three-point bending specimen

This configuration has been largely used for testing the shear properties of honeycomb cores. The dimensions of this specimen were 20 mm wide x 20 mm high x 160 mm long. The core was oriented in the L direction and the skins were made of aluminum that was 2 mm thick. This specimen was identical to those used by Bunyawanichakul in [36]. The distance between the supports was 140 mm (see Fig. 65-d)

From a theoretical point of view, the shear stress should be uniform in the core between the loading points. However, some studies pointed that this was not completely true because of the Saint Venant's effects (the buckling was concentrated in the middle of the specimen and is complex to analyze) [77].

3.2.1.2 Double lap specimen

This specimen was not recommended by Kelsey [66], however, we considered it for our research for the following reasons:

- This specimen configuration avoids the classical specimen rotation of the rail test described by the ASTM C273 [69] which facilitates the measuring of the displacement and the installation of cameras to record the test.
- This design allows the core to behave naturally. The four pieces of Nomex® honeycomb core are distributed symmetrically and the flexural forces on the skins are annihilated.
- The force is distributed in the four Nomex® pieces which creates a homogenization response that reduces the influence of fabrication defects.

Four pieces of honeycomb of 5 by 15 cells were bonded to four aluminum 6061 skins of 5 mm thickness as shown in Fig. 65-a. The honeycomb was oriented in the W direction.

Two specimens were made with two different fabrication procedures. In the first one the adhesive films were putted in different steps separately to avoid the dripping caused by gravity. In the second, all the adhesive films were putted at once and then cured in the oven.

3.2.1.3 Double single lap specimen

This specimen was considered only because the fabrication was simpler in comparison with the double lap test. The core is subjected principally to shear, but also to flexural stress caused by asymmetry of the configuration.

Two pieces of honeycombs of 15 by 5 cells were bonded to three 6061 aluminum skins of 5 mm thickness (see Fig. 65-b). The honeycomb was oriented in the W direction

Two specimens were made using different fabrication procedures, first avoiding the dripping of adhesive, and the other in one shot.

3.2.1.4 Two materials double lap specimen

The idea of this configuration was to use a secondary stiffer material to concentrate the shear forces on the Nomex® honeycomb core. By doing this, it's possible to control where the failure of the specimen is going to take place, which was not possible with the normal double rail test. First a nylon was used as secondary material but the adhesive didn't work. Finally, plywood was used (see Fig. 65-c).

Two pieces of honeycomb of 15 by 5 cells of length, but also two pieces of plywood of an equivalent size were cut and bonded to four 6061 aluminum skins of 5 mm diameter. This was made for the W and L directions.

The fabrication was made with special attention to avoid the dripping of adhesive.

3.2.1.5 Modified double lap specimen

This configuration consists in using the same concept as for the double lap specimen. The difference is that one side of the specimen is slightly smaller than the other. This feature concentrates the shear stress in the smaller side, which allows to predict where failure is going to appear. In contrast to the two materials double lap, only one type of material is used for the specimen (see Fig. 66).

Two specimens of this type were fabricated. For both, the skins were made of 6061 aluminum of 5 mm diameter. Concerning the honeycombs, in one side two Nomex® pieces of 15 by 5 cells were used. For the other side, for one specimen two pieces of 13 by 5 cells and the other one of 14 by 5. This was only made for the W direction.

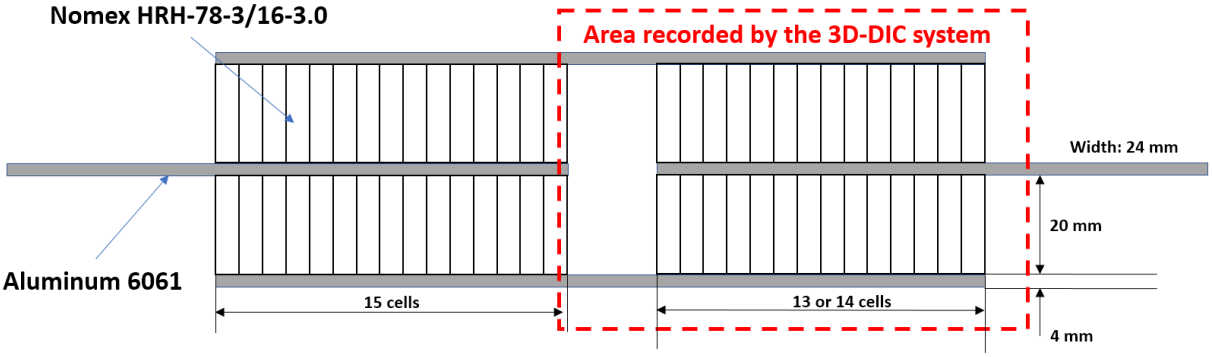

Fig. 66: Characteristics of the modified double lap specimen.

3.2.2 Verdict and test results

All specimens were tested using a 10 kN Instron machine except the double lap which was tested using a 100 kN machine. The force was directly measured from the machine and an external LVDT sensor was installed to measure the imposed displacements.

A 3D-DIC system (VIC-3D) was used to measure the displacement field in and out of the plane of the cells and the skins.

For the beam specimen, the analytical beam theory was used to calculate the shear stress. For the case of the lap specimens the average shear stress τ_{avg} was calculated by dividing the applied force *F* between the area projection A of the specimens; this is:

$$\tau_{avg} = \frac{F}{A}$$

The shear angle gamma (γ) was the relative displacement δ of the two skins divided by the thickness of the core *h*, (based on the 3D-DIC data):

$$\gamma = \frac{\delta}{h}$$

For all the tests a photo was taken every 2 seconds by the VIC-3D system. All the test specimens are compared in Fig. 67.

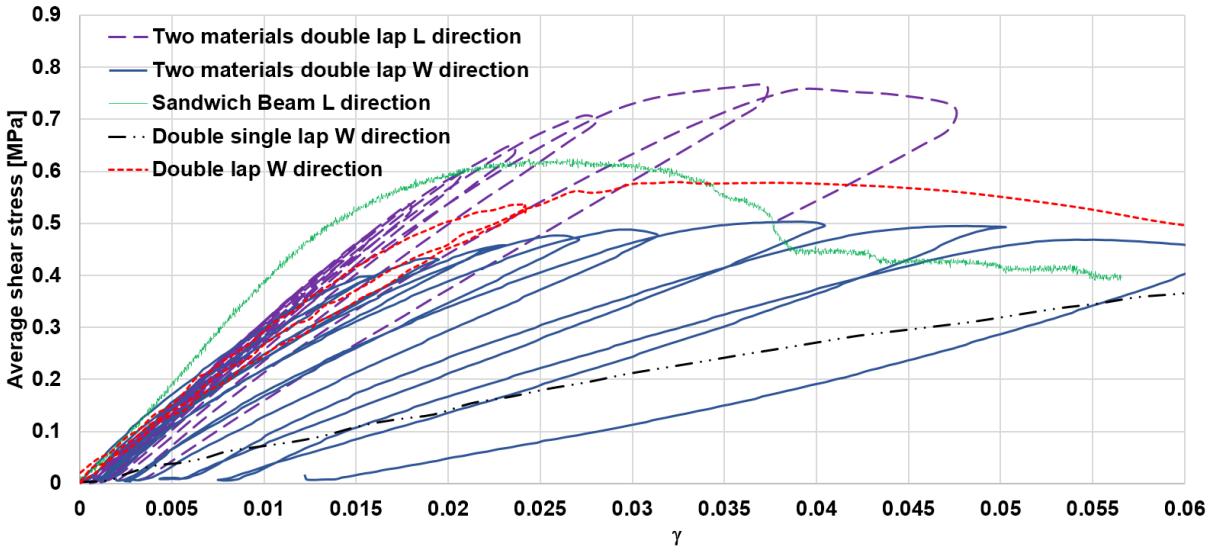

Fig. 67: Representative curves of the average shear stress vs gamma for the different type of specimens.

3.2.2.1 Beam specimen

The buckling of the cells was not uniform. Even if the specimen was symmetrical, the buckling started at the middle with the crushing of the cells near the identation and propagated only to one side.

The measurements using the 3D DIC system were not very useful. The principal problem was that the beam was not correctly aligned with the visualization plane of the 3D correlation cameras and, as result, it was very difficult to measure the small deformations normal to each cell wall. In other words, to measure the out-of-plane displacements, each cell had a different normal direction and needed to be measured using a different scale. This was because of the view perspective of the cameras that was not aligned perfectly with the beam specimen.

However, it was possible to analyze the cells separately by creating an individual region of interest for each cell. Nevertheless, the analyze cell by cell was extremely inefficient and slow.

Also, it is not possible to calculate gamma using the same technique as for the others specimens because the skins displacements are in both vertical and horizontal directions.

Concerning the shear stress in the core, it can only be calculated using analytical approaches, which works well for the linear behavior but might be not accurate for the postbuckling behavior.

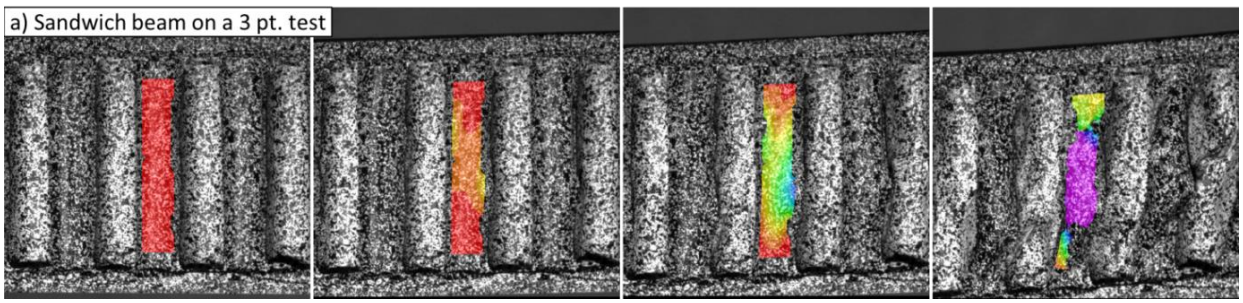

Fig. 68: Displacement field measured in the out-of-plane direction of the sandwich beam.

3.2.2.2 Double lap specimen

The specimen without dripping of the adhesive was tested successfully, while the other one broke at the middle of the test. The buckling was uniform and it was correctly measured using the 3D-DIC system. The buckles appeared randomly all along the specimen.

The displacements of the skins in the thickness direction of the core (like compressing it) were very small and uniform all along the specimen. The experimental results were coherent to the manufacturer data.

The only drawback was that failure may occur randomly on both sections of the test specimen. This is a major problem because if failure appears where the cameras are not recording the testing is useless.

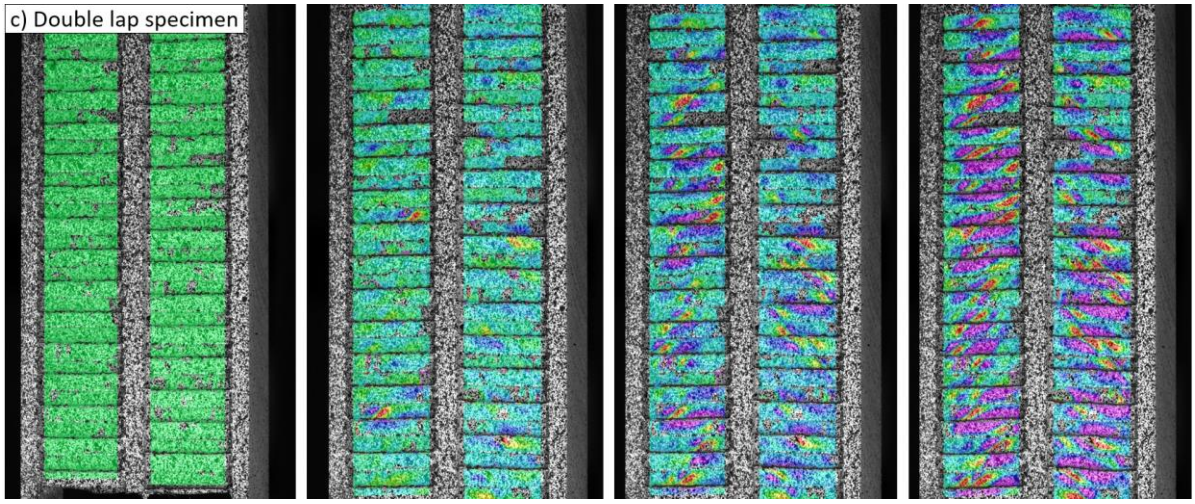

Fig. 69: Displacement field measured in the out-of-plane direction the double lap specimen.

3.2.2.3 Double single lap specimen

The specimen on which the dripping of adhesive was avoided was tested until complete failure, the other one broke at the middle of the test.

The bending of the central skin was evident, it was about 15 mm on its maximal amplitude. Also, the compression of the honeycomb was 10 times bigger than for the double rail specimen, which is very large. This strongly suggested that the effect of the flexural forces is very important and shouldn’t be ignored.

The buckling of the cells was not uniform. They start to appear where the flexural forces are more present, suggesting that the flexural forces compress the honeycomb and in consequence the buckles appear. Thus, the buckles are caused by the flexural forces and not by the shear stress.

Finally, the shear moduli and strength were very different to the reference values of the manufacturer.

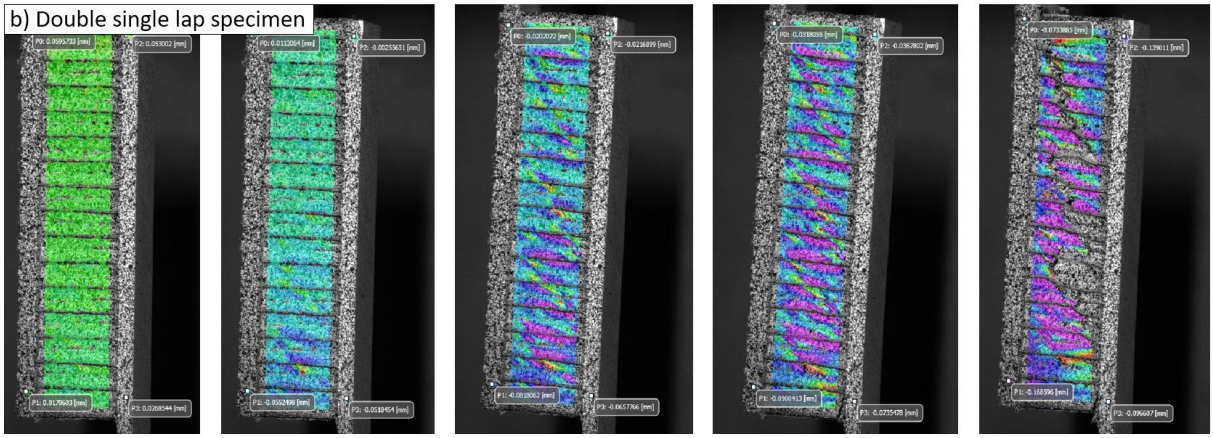

Fig. 70: Displacement field measured in the out-of-plane direction of the double single lap specimen.

3.2.2.4 Two materials double lap specimen

Many increasing charge and discharge cycles were performed for this configuration. For both directions, L and W failure occurred in the honeycomb side, as desired.

Concerning the honeycomb buckling, it was visible and identical to what was obtained by the normal double lap test.

The measured shear modulus was coherent to the manufacturer data. However, the shear strength of the core was significantly lower than expected.

This may have been caused by the difference of shear moduli between the honeycomb and the plywood. The plywood doesn't allow the reduction of height of the honeycomb cells during shear, and therefore, by blocking this degree of freedom the buckling behavior of the cells is not natural.

In other words, because of the different gamma evolution of the two materials, the out-of-plane displacements were different and generated overstresses in the honeycomb.

3.2.2.5 Modified double lap specimen

Two fabricated specimens were tested; the 15 vs 14 cells specimen and the 15 vs 13 cells. Theoretically, for the specimen that had only 13 cells at one side, the average stress was incremented of about 11.3% in the side with less cells. For the other with 14 cells on one side, the increment was of about 7.1%.

For both specimens, the buckles were totally visible and the shear moduli and ultimate shear strength were coherent with the manufacturer data.

Initially both specimens had the same behavior. However, it was seen that when the stress on the smaller side arrives near the point of failure the behavior is slightly different. This should be caused by the difference of stress concentration due to the different areas.

To measure the impact of this effect, both specimens were compared to the normal double lap specimen, which was considered as the reference.

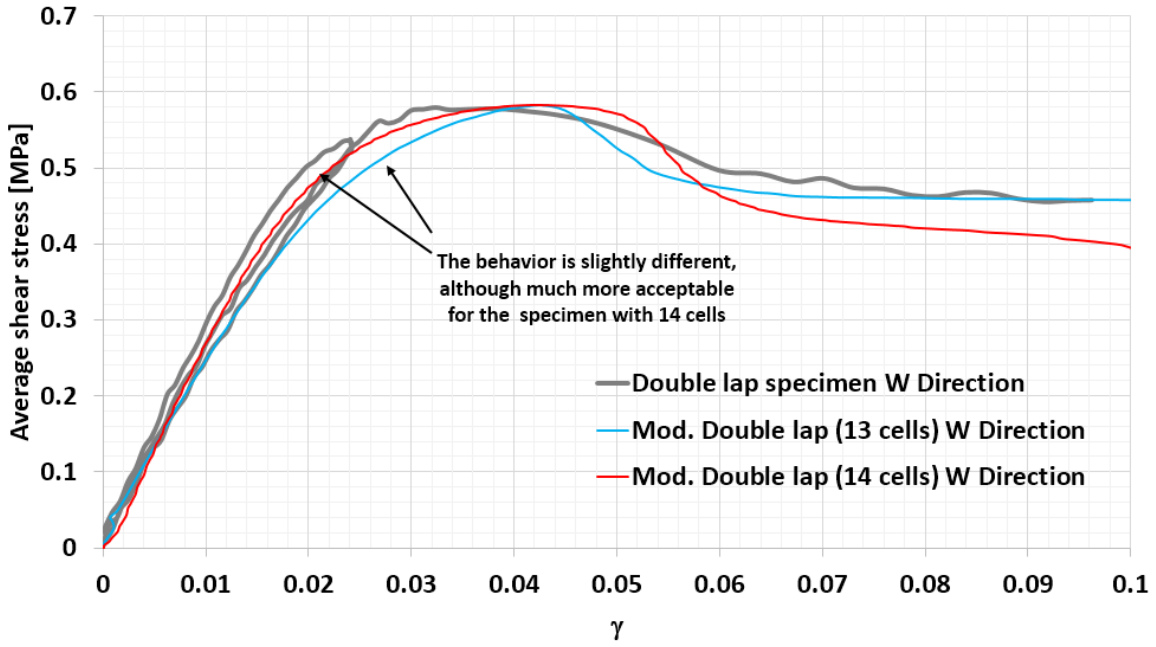

Fig. 71: Comparison of the shear curves of the normal and modified double lap specimens.

For the specimen with 13 cells, this effect was more important, while for the specimen with 14 cells, this effect was not even noticeable, as shown in Fig. 71. This highlights the sensitiveness of the honeycomb core to the boundary conditions.

3.2.3 Conclusions

Concerning the fabrication, the Redux 609 was a good choice as it worked well for the tested specimens. Also, it was seen that the dripping of adhesive reduced considerably the strength of the bonding, therefore it should be avoided.

The main conclusion of this section is that all the specimens could be used to study the elastic shear properties of the core expect for the single rail specimen, because the flexural forces are very important.

However, it is important to emphasize that, although the responses in the linear domain may be identical, the nonlinear part differs significantly from one trial to another, showing the high sensitiveness of the honeycomb structure to the imposed boundary conditions.

The beam specimen is the easiest to make, however, the buckling of the cells was not uniform and the cells in the middle fail due to compression instead of shear. Also, it was impossible to analyze its buckling accurately. Even if this kind of test is recommended by the ASTM C393, it can be said that this kind of testing is not recommended if a correlation system is used.

The double single lap specimens were simple to make but the results were not as expected. The effect of the flexural forces was very strong, generating a large out-of-plane deflection. Thus, it shouldn’t be used for shear testing of honeycomb cores.

The best results were obtained by the double lap specimens. Concerning the two-material specimen, the shear strength is reduced, although it might provide correct results if the skins thickness is increased.

Considering these facts, the most suitable design for our research was the modified double lap specimen, which allows obtaining all the advantages of the double lap specimen and at the same time inducing failure on the desired side.

100 kN and 10 kN Instron machines were used for the tests. Concerning the 100 kN machine the electrical noise at the loading measure was important because of the relative low forces needed to test the specimen until failure which was about 3 kN. Therefore, much better results were obtained with the 10 kN machine.

By performing the test, we realized that the frequency of the photos is related to the number of points of load-displacement curve. If a determined minimal of points is desired for the loading curve, a photo should be taken each determinate time.

To calculate the interval between the photos, the following formula can be easily obtained.

$$T = \frac{60}{v_m}\left(\frac{d_a}{N}\right)$$

Where N is the desired number of points for a distance d_a (in mm) imposed to the specimen. Variable T is the interval of time in seconds between the photos and v_m is the speed of the machine (mm/min).

3.3 Shear testing of honeycomb cores

The second phase of the research consisted in testing three types of honeycombs, the **HRH-78**, **HRH-10** and **ALU 5052 3/8** in both L and W directions. All of them of 20 mm thickness.

Two kinds of test where be performed:

The first one consists with testing until complete failure the honeycombs. This test purpose is to measure the shear moduli and ultimate shear strength, but also recording and analyze the buckles of the honeycomb cells using the 3D cameras.

The second tests consist into submit the core to an incremental cyclic displacement, which will be useful to determine the exact point at which the cells start to be damaged.

The number of tests was: three types of honeycombs, multiplied by the two directions L and W, multiplied by the two type of tests, and performing three test each time to obtain reliable results: 3 x 2 x 2 x 3. This results in a total of 36 test specimens to fulfill the mentioned requirements.

The specimen configuration that will be used is the modified double lap, because the buckle of the cells is very clear, the deformation of the specimen is symmetrical and because there is almost no flexural stress.

3.3.1 Specimen fabrication

144 plates of 2024 aluminum alloy were cut for the specimens. The dimensions are given in Fig. 72 and Table 7.

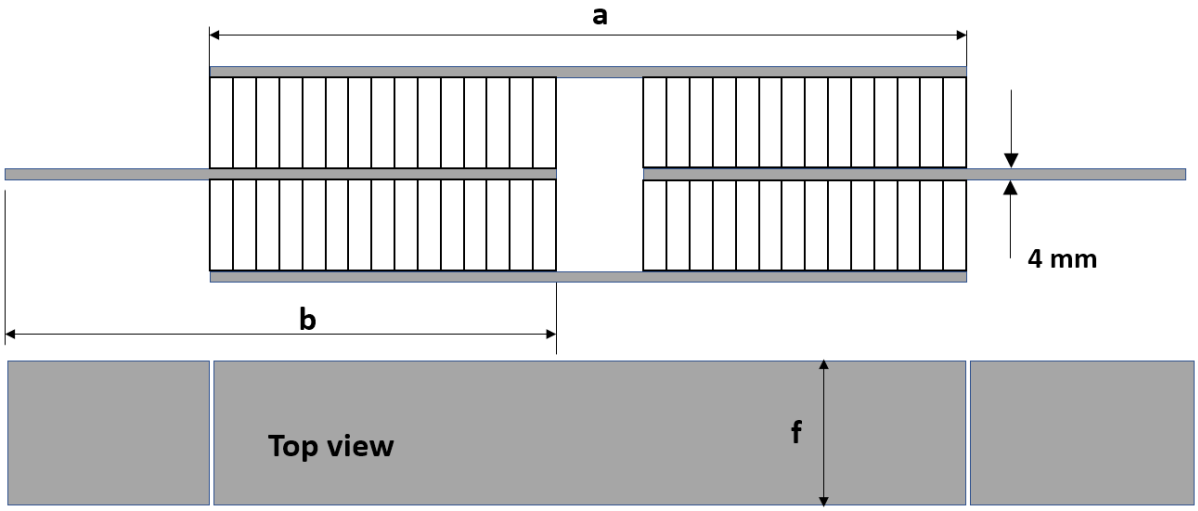

Fig. 72: Specimen description for the shear testing of honeycombs.

144 pieces of Nomex® were cut, 48 pieces of HRH78, 48 of HRH10 and 48 Alu ep 20, 24 pieces for each L and W directions. All the specimens were cut using a cutter, even for the aluminum honeycomb.

For the adhesive, layers of Redux 609 were used, the films where cut according to the size of the honeycomb pieces. Unfortunately, the material was already expired (according to the manufacturer). However, this is a very common issue because all these materials are fabricated for industries and only a few remnants are available to be sold to others institutions. However, we estimate that this inconvenient won't affect the results. The Redux 609 is a resin that is designed to hardly stick to surfaces. This resin is very toxic so the use of safety equipment was mandatory.

Description	Thickness [mm]	Length in L direction [mm]	Length in W direction [mm]	Number of pieces
Exterior skin for the HRH78 & HRH10 shear test L direction	4	a=159.23 (160)	f=29 (30)	12x2=24
Interior skin for the HRH78 & HRH10 shear test L direction	4	b=164.62 (165)	f=29 (30)	12x2=24
Exterior skin for the HRH78 & HRH10 shear test W direction	4	a=182.4 (183)	f=23.372 (24)	12x2=24
Interior skin for the HRH78 & HRH10 shear test W direction	4	b=176.2 (177)	f=23.372 (24)	12x2=24
Exterior skin for the Aluminum honeycomb shear test L direction	4	a=288.46 (289)	f=57.15 (58)	6x2=12
Interior skin for the Aluminum honeycomb shear test L direction	4	b=229.23 (230)	f=57.15 (58)	6x2=12
Exterior skin for the Aluminum honeycomb shear test W direction	4	a=334.8 (335)	f=46.744 (47)	6x2=12
Interior skin for the Aluminum honeycomb shear test W direction	4	b=252.4 (253)	f=46.744 (47)	6x2=12

Table 7: Size of the aluminum skins for the fabrication of the specimens.

The honeycomb pieces were cleaned using pressurized air. For the aluminum skins, they were degreased using acetone two times to assure a proper surface. This was also carefully made for the honeycomb surface facing the aluminum skins. This procedure was done in a controlled room for security reasons.

The protective layers of the adhesive films were removed using a freezer spray and the pieces were assembled together.

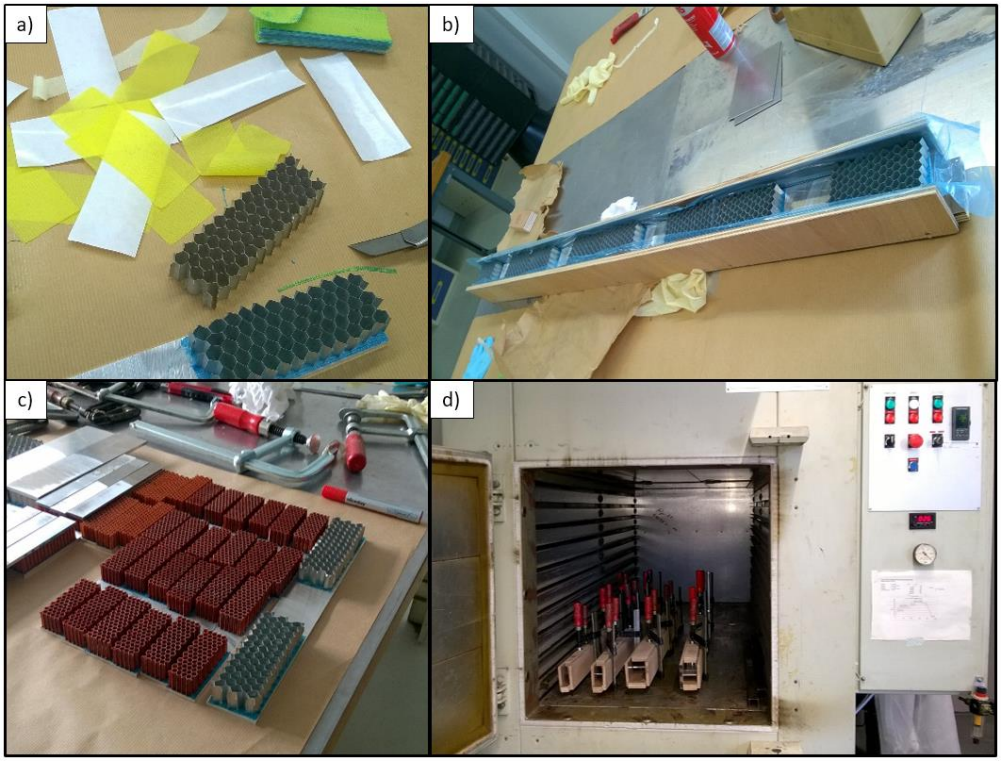

Fig. 73: Assembly of the test specimens, b) specimens in the molds c) specimens ready for the second curing process, d) molds in the oven.

Six molds made of plywood and covered with a Teflon film were fabricated to assure a good contact between the parts. The molds were made according to the size of every specimen (see Fig. 73).

Then the pieces were carefully placed in the molds and tight firmly with clamps to assure good contact between the pieces. Every mold was filled with 3 specimens at each time.

The molds were putted in the oven to start the first curing of the pieces during 2 hours. The fabricant specified 60 min at 120°C, however, this doesn't consider the heat distribution.

To avoid the dripping of adhesive, the pieces were fabricated in three steps. In the first one, both sides are placed separately into the oven to stick the exterior aluminum skin and one side of the Nomex®. In the second step, the interior skin was stick to one side of the already cured parts. The third step consisted in bonding the other side. In all cases a Teflon layer was put when it was needed to avoid undesired adhesion of parts.

Finally, the specimens were only painted in the area to be recorded with the 3D correlation system. The specimens were painted in white color with black speckles using common spray-paint.

3.3.2 Test setup

The specimens were tested with a 10 kN Instron machine, the machine speed was set to 1 mm/s. The force was measured directly from the machine. For the displacement, a LVDT sensor was used. Both signals were sent to a laptop computer, and the values were recorded using the CAT MAN software.

Fig. 74: The 10 kN Instron machine and the 2 VIC 3D cameras.

The 3D DIC system was placed in front of the testing machine to measure the buckles of the honeycomb cells but also to measure the individual displacement of the aluminum skins. An external flash was used to illuminate the surface of the specimen, the light source was installed in a position where the effect of the shadows created by the geometry of the test specimen was minimized.

The resolution of the cameras was 29 MP (mega pixels) each one, the format of the image is 4/3. They had a fixed focal distance. The aperture range of the diaphragm was from f/2.8 to f/20.

The camera configuration was set to f/11 with an exposition time of 15 ms. The same adjustments were used in both cameras.

Once the cameras and the light were adjusted, the software VIC 3D was calibrated using 30 to 50 of a target provided with the system according to the specimen's size. (X=12; Y=9; OX=3; OY=3; NX=7; NY=4 with a step of 3 mm).

The period of the photos was of T=600 ms, which allows to have 50 points for 0.5 mm of displacement.

3.3.3 Test results

3.3.3.1 Tests on the HRH-10 Nomex® core

Two HRH-10 specimens were tested but they both broke at the middle of the tests. The failure mode was the debonding of the Nomex® pieces instead of the desired shear failure. This might be caused by the poor quality of the redux 609 as mentioned before. Also, the cohesive failure occurs at the larger side which could mean that the failure is caused by the bad quality of the redux 609. Consequently, no more specimens were tested.

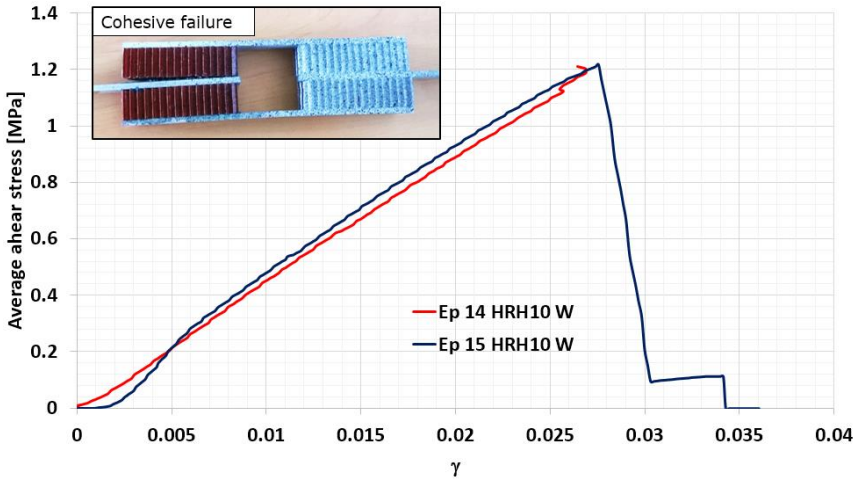

Fig. 75: Test results of the HRH-10 honeycomb core.

3.3.3.2 Alu 5052 3/8 honeycomb core

The same failure of the HRH-10 was found: cohesive debonding of the core-skin interface. Consequently, the rest of the specimens were not tested (see Fig. 76).

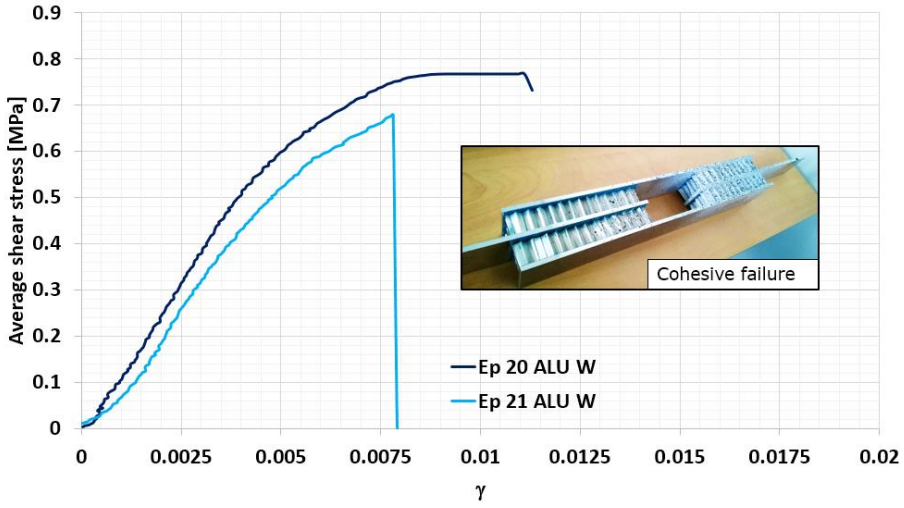

Fig. 76: Test results of the Alu 5052 honeycomb core.

3.3.3.3 Testing of the HRH-78 Nomex® core

After testing the first six specimens, it was found that the average shear moduli of the W and L directions were 25 MPa and 32 MPa, respectively, and the maximum shear stresses were on average 0.58 MPa and 0.76 MPa, respectively. These results are consistent with the data provided by the manufacturer [37]. The failure mode was the same for the 12 specimens. It began with an accentuated deformation of the smaller side, then there was a major collapse of only one piece of honeycomb, followed by collapse of the other one (Fig. 77).

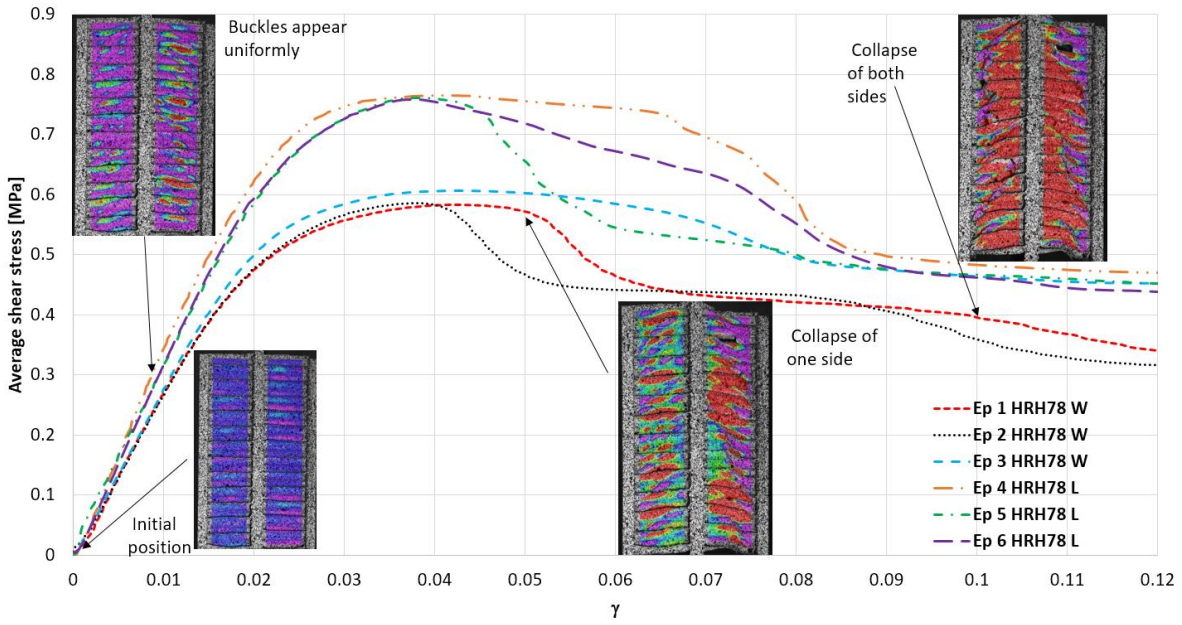

Fig. 77: Average shear stress vs gamma curves of the HRH-78 in W and L direction.

The remaining six specimens were subjected to incremental cyclic displacements. At each cycle, the maximum displacement imposed was increased slightly in order to be able to identify the stress and gamma at which the honeycomb structure started to become damaged (see Fig. 78). Showing the elastic limit in the complete curves was complicated because the cyclic loading makes difficult the appreciation of the data, therefore only the initial part of each curve was analyzed (see Fig. 79).

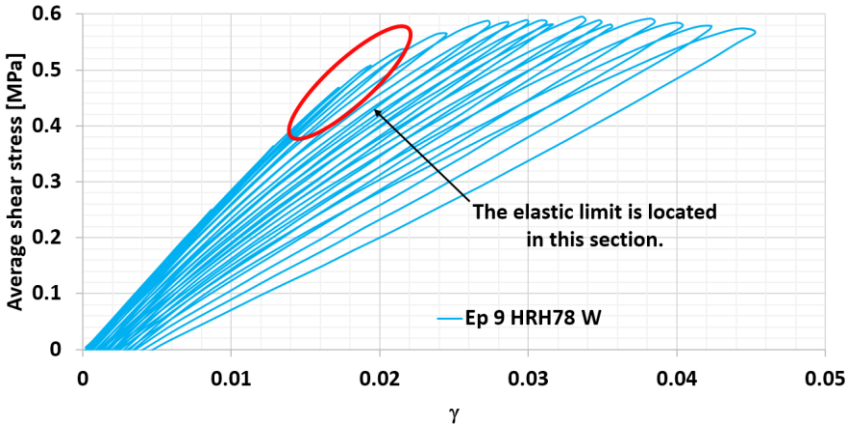

Fig. 78: Incremental cyclic testing of the specimen 9.

As expected, hysteresis was only slight at the beginning. The cyclic tests revealed that there was a significant reduction of the stiffness once γ exceeded 0.0211 (0.52 MPa) in the W direction and γ = 0.022 (0.65 MPa) in the L direction. This could mean that, at this point, the deformations of the cells were severe enough to initiate the damage of the honeycomb structure.

Before this point, shear buckling probably occurred without damaging the phenolic resin at the surface of the cells and so the buckling was reversible.

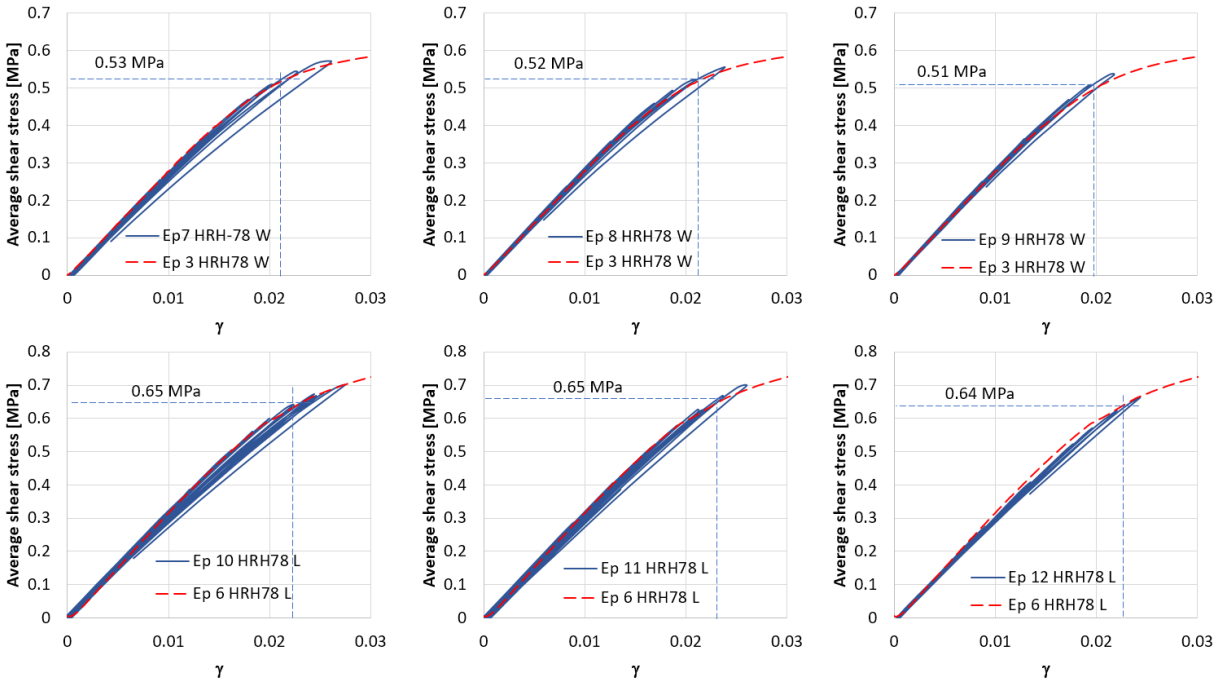

Fig. 79: Incremental cyclic testing of the HRH-78 core: average shear stress vs gamma.

3.3.4 Analysis of the buckling and postbuckling behavior of the cells

Only the HRH-78 specimens could be tested, therefore this analysis is focused on this material. The cells of the honeycomb core were weaker when they were tested in the W direction, because of the orientation and the thicknesses of the walls. For this reason, the refined analysis of the buckling of the cells is presented only for cases with the loading applied in the W direction.

The 3D-DIC system allows to represent the displacement field in the three directions, x, y and z with a color scale, making possible to look more closely at the evolution of buckling of the walls at the exterior surface of the test specimens.

3.3.4.1 Buckle scale

The cell walls were expected to buckle towards ± 30° from the plane of view of the cameras but, considering that the magnitude of the deformations should be very small, we considered that measuring the deformations only in the Z direction with respect to the cameras would be accurate enough.

Determining a scale to measure buckling was complicated because the buckled shape was not necessarily the same in all the cells. Also, the magnitude of the buckling increased with increasing gamma.

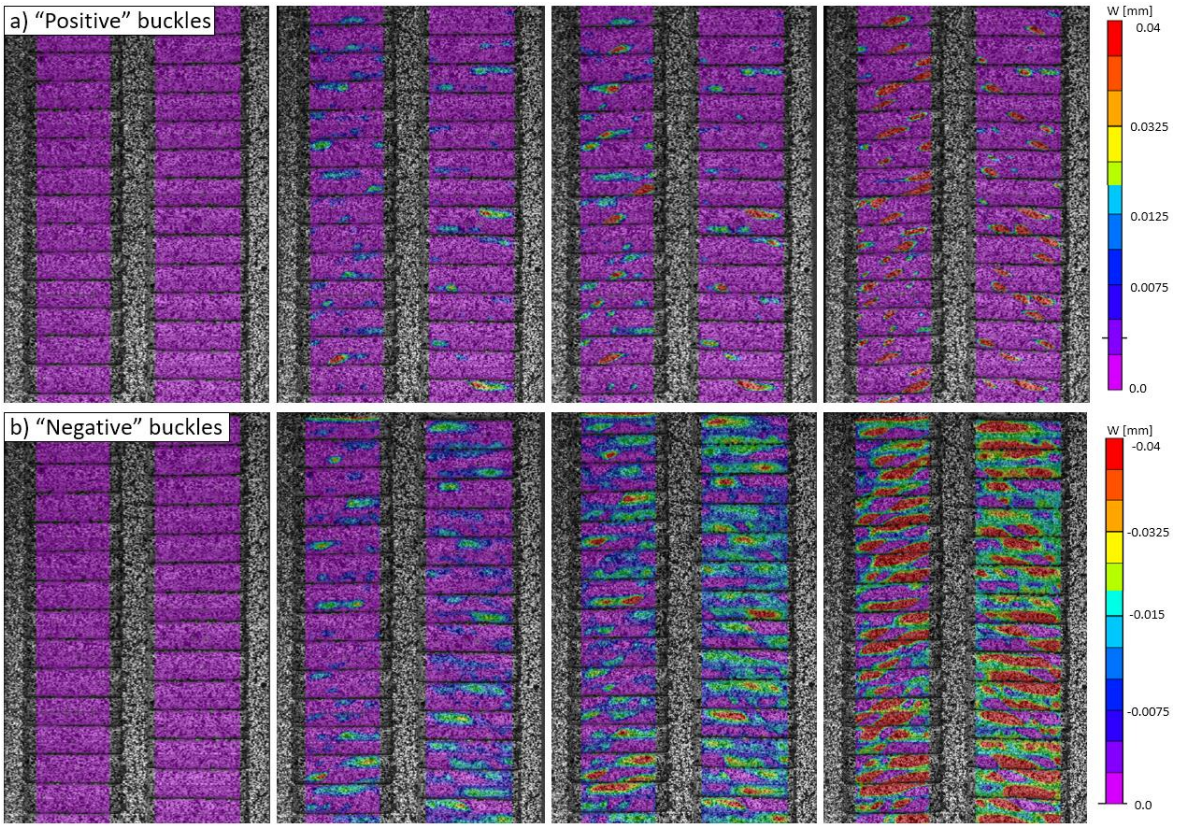

Fig. 80: Evolution of out-of-plane displacements measured from a) 0 mm to 0.04 mm and b) 0 mm to -0.04 mm.

One difficult part of this research was to find the right configuration of the VIC-3D software that allowed detecting the buckles. After several iterations using different configurations the one that gives the best results was using a grid of 35 and a step of 3. Also, a relative displacement scale must be used to detect the buckles (scale W in the software), this allowed measuring only the changes caused by the imposed displacement, and ignoring the initial cells defects. The initial position was frame one.

By inspecting the videos of the tests, we found that changing the analysis scale allowed to study different aspects of the buckles.

If the scale was set to measure the out-of-the plane deformations from 0 mm to 0.04 mm, it was observed that the size of the buckles on the out-of-plane direction grew but the deformations did not visibly propagate to the adjacent cells. Therefore, we assumed that they were not directly related to the collapse of the cells. (Fig. 80-a)

If the scale was set to measure the deformations inside the plane from 0 mm to -0.04 mm i.e. inwards the interior of the honeycomb, the shape of the buckles was observed to grow and propagating buckling to the adjacent cells. And so, we assumed that the negative deformations were related to the collapse of the cells (Fig. 80-b).

The buckling was not symmetric probably because the exterior cells were cut, and therefore were not stabilized by all the surrounding cells.

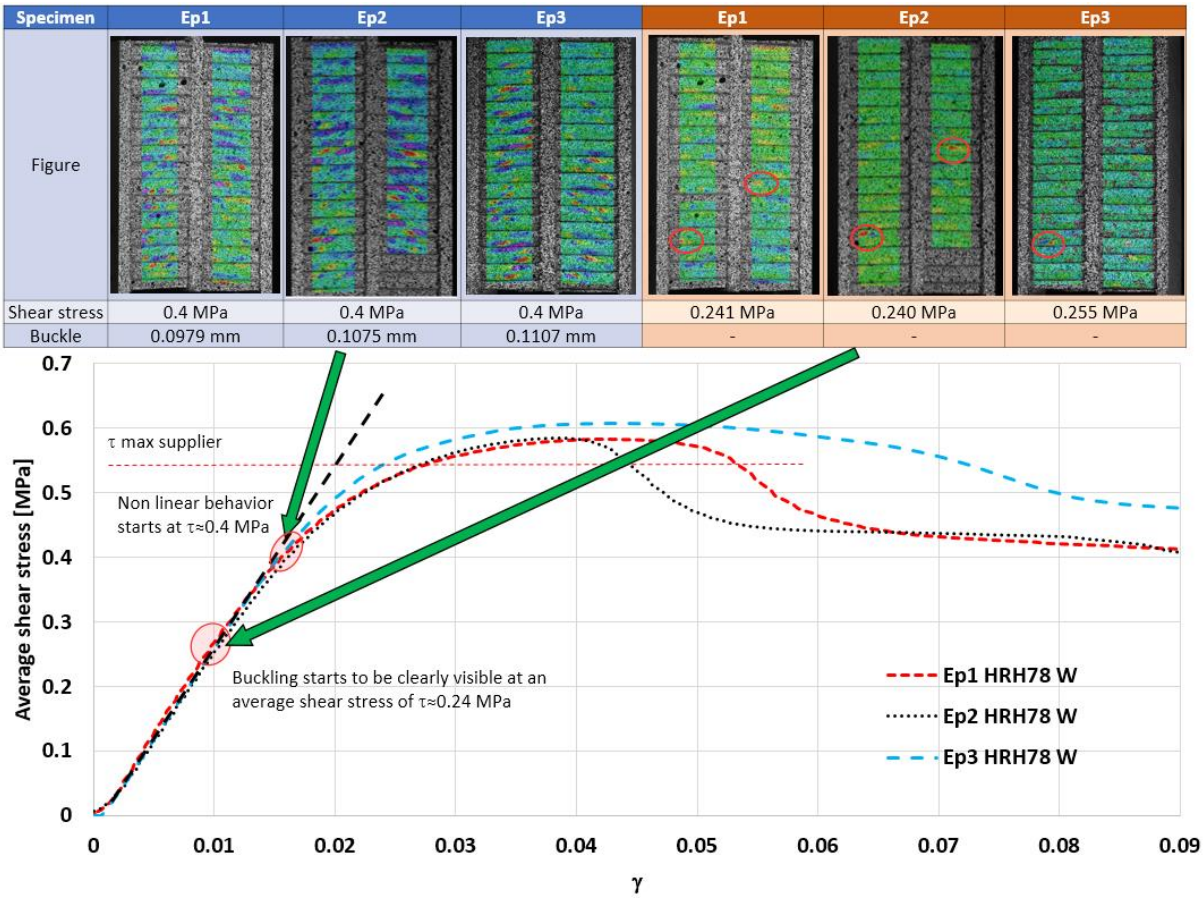

Fig. 81: Buckling of the cells at 0.24 MPa and 0.4 MPa.

Regardless of the scale, some buckles started to be clearly visible at an average shear stress of 0.24 MPa (Fig. 81). Also, the recorded images of the three specimens were inspected when the average shear stress was 0.4 MPa (Fig. 81), which is also where the nonlinear behavior presumably starts. Thus, we hypothesized that, at this point, the buckling occurred at sufficiently numerous places to affect the stability of the honeycomb, but also that the buckling size was large enough to cause the nonlinear behavior, thus changing the loading slope.

The range of the buckles measured by the software varies from one specimen to another, this was attributed to the difference of deepness position of each specimen in the machine jaws. At the time of the tests this undesired effect was not foreseen and not care was not taken for the specimen position and rotation. Therefore, an individual analysis scale had to be defined for every specimen.

The maximum extent of buckling towards the inside-of-the-plane direction was measured automatically by the VIC-3D software at 0.4 MPa. The average size value of the three specimens was -0.1054 mm.

Tests specimen	Zero buckling reference [mm]	Buckling size at 0.4 MPa [mm]	Amplitude [mm]	Average [mm]
EP1	-0.03	-0.1375	-0.1075	-0.1054
EP2	-0.031	-0.089	-0.116	
EP3	0.02	-0.0727	-0.0927	

Table 8: Summary of the amplitude of the buckles of the EP1, EP2 and EP3.

Considering the above information, the scale of the three recorded videos was set to be the same, between 0 mm and -0.1054 mm to measure the buckles. The resulting images can be seen in Fig. 82.

3.3.4.2 Buckling of the cells and nonlinear behavior

In the first frames the cell keep their initial shape and buckles start to appear gradually. The buckles start as very small and isolated deformations. At a certain point, their shape grows and covers a significant area of the cell walls.

When the buckles are big enough the cell loses its regular geometry, and the cell inertia drops drastically, thus its stability too.

Then, the buckles propagate to the adjacent cells, causing the shear collapse of vertex and thus, a collapse of the buckled cell and surrounding cells.

Finally, when the displacement continues the cell continues to be freely deformed. Of course, we also observed that the cells did not collapse all at the same time.

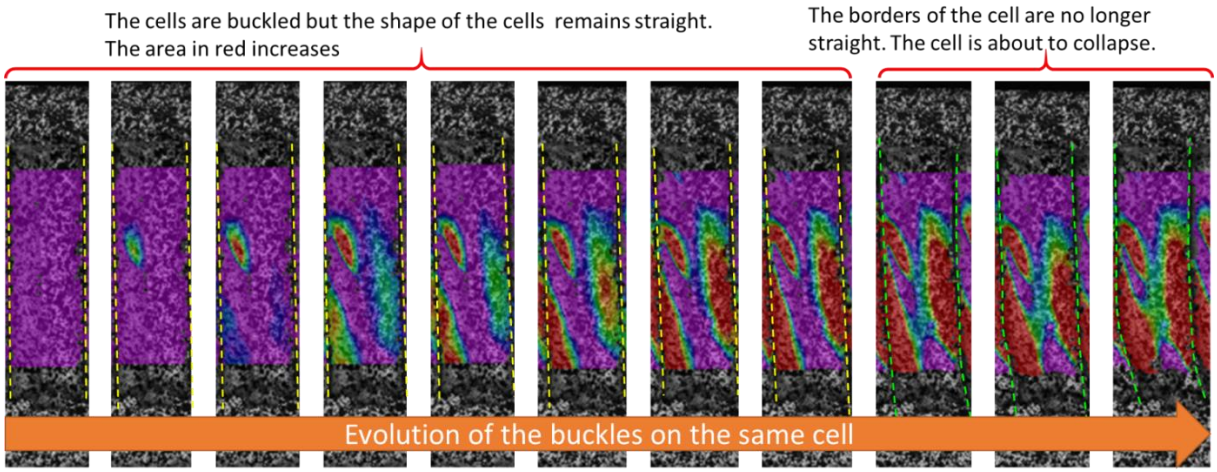

Fig. 82: Buckling evolution of a cell: from initial buckling to collapse.

Counting the buckles

At this part of the research, we assumed that since the buckles appeared while the specimen was being tested, there should be a direct relation between the start of the nonlinear behavior and the number of buckles (later we learned that this assumption was wrong).

To examine more about the influence of buckles on the structural stability of the cells, we counted the number of visible buckles of every specimen for every frame of the videos. This was a tedious task because each specimen has an average of 139 frames, multiplied by the number of specimens and considering that each specimen had two pieces of Nomex® to analyze and every piece between 12 to 15 cells, this gives a total near of 13,334 inspections that had to be visually performed by the author of this thesis. The Photron software was used to review frame by frame.

The buckles were counted when the buckle started to be red, meaning that the magnitude of the buckle was enough to alter the stability of the cell. In many cases, we had to decide if the buckles were well formed or not, this was very subjective.

In Fig. 83 the number of buckles vs the average shear stress and gamma is given. Although there was dispersion, it was clear that buckles can appear between 0.24 and 0.42 MPa, and that the maximum number of buckles per specimen was between 15 to 22 buckles.

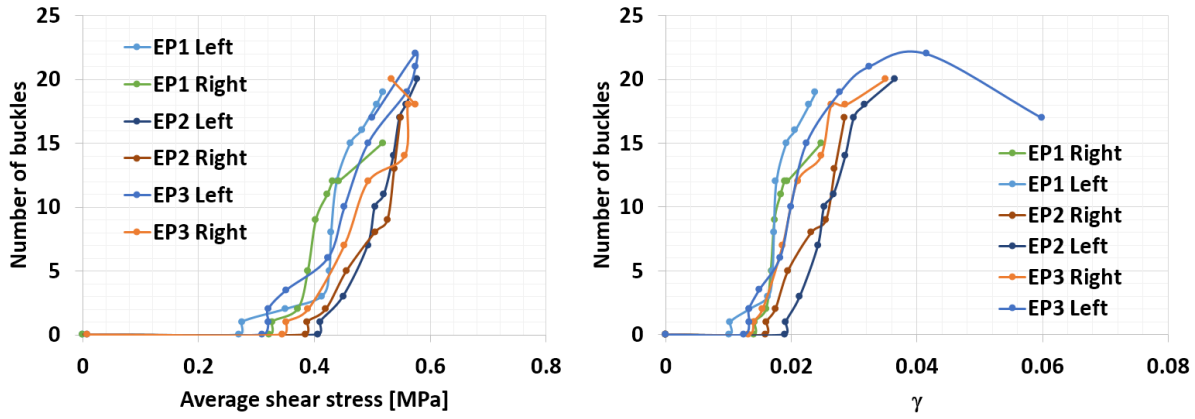

Fig. 83: Number of buckles vs average shear stress and gamma.

Counting the cells about to buckle

The number of buckles that appeared at each specimen and in every cell, was different and arbitrary. In some specimens, there are much more buckles, even if the shear behavior is very similar. This could mean that the number of buckles in the cells may not be directly related to the shear stress of the honeycomb core.

Then, we did another hypothesis. We assumed that the local buckles were not the cause of the nonlinear behavior, but a consequence. And thus, we assumed that what causes the nonlinear behavior was the folding of the cells from the top to the bottom, regardless of shape or number of the local small buckles.

With this idea in mind, instead of counting individually the buckles, we started to study the stability of the cells.

We observed that the small local buckles in the cells were growing when the cells had its vertex completely straight (see Fig. 82). In contrast, when the vertex were no longer straight, the buckles remained of the same size but the cells started to fold.

Another way so see this is thinking of the cells as a spring that stores the deformation energy. The first mechanism of storage is the creation of local buckles; later, when the first storage mechanism is "full", the second mechanism begins, storing (or releasing) the energy by folding the entire cell.

This means that by inspecting the growth of buckles and the vertex of the cells we might find a good correlation to the shear nonlinear behavior, and that we should be focused in to look for only two possible scenarios; folded or not folded.

And so, we proceeded to analyze the videos using the Photron software again, specimen by specimen, frame by frame, cell by cell, looking for folded cells.

Since the number of cells varies from specimen to specimen, in order to compare them, an average of the buckled cells is taken into account, where 0% is for zero buckled cell and 100% when all the cells are buckled. This counting is made visually and includes the subjective judgement of the author. This was made for the EP1, EP2 and EP3 specimens. The counting of folded cells is given in Fig. 84.

It can be observed that, as for the counting of buckles, there was dispersion in the obtained data. However, we did a comparison of the "average shear strain vs γ" and "percentage of buckled cells vs γ" curves, using the same scale.

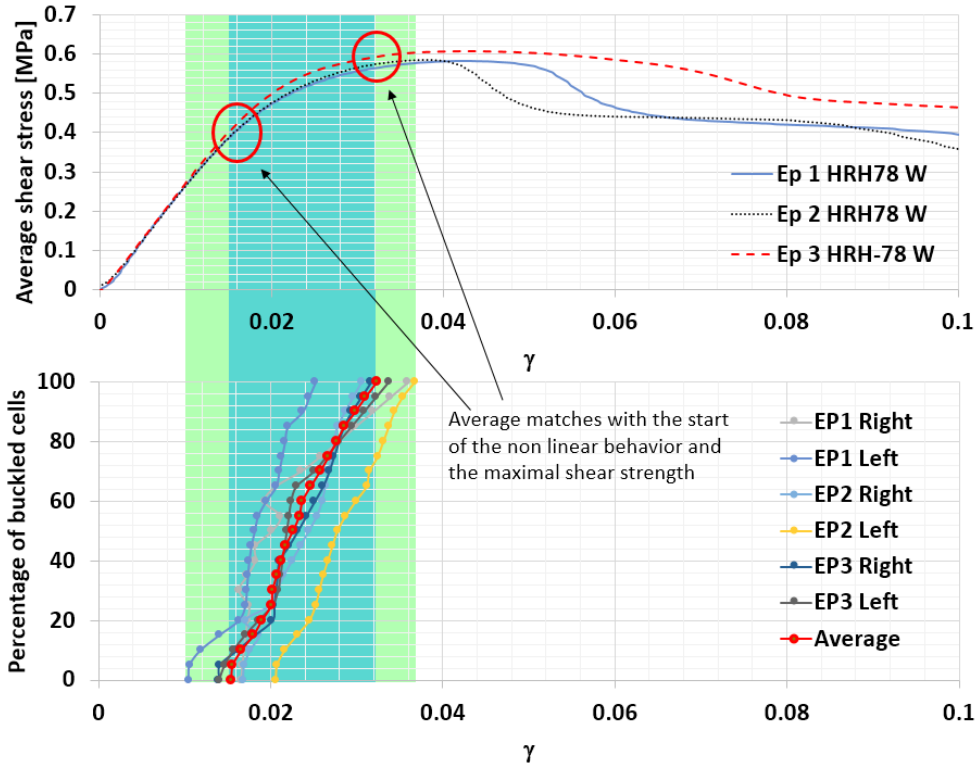

Fig. 84: Buckled cells and average shear stress comparison, analysis made by ourselves.

We observed that there was a relation between the percentage of folded cells and the start of the nonlinear behavior, but also with the maximal load capability of the shear test specimens.

This suggests that start of the nonlinear behavior (at 0.4 MPa) is caused by the start of the folding of the cells instead of the formation of buckles (at 0.24 MPa). But also, that once all the cells are folding the maximal shear strength is reached.

However, this study should not be considered very reliable because it was made under subjective judgment. Therefore, even if the conclusions were interesting, a more trustable procedure should be developed.

Counting the cells about to buckle using an objective method

To confirm the obtained results, a deterministic method should be proposed. However, the identification of the buckled cells was complicated, it depended on several parameters that were very subjective:

- The magnitude or size of the buckle
- The area of the buckle
- The position of the buckle in the cells
- The colors in the buckle
- The inclination of the lateral axis of the cell.

To simplify this task and reduce the variables that influence the buckle counting of the cells, the simplest way is by using a system that learns to identify these characteristics and then use this system to analyze the videos. In other words, using an artificial intelligent system capable to detect the folding of a cell.

An artificial neural network was chosen because it seems to fill perfectly the requirements, also the author was familiarized to its application. This was developed using MATLAB.

An artificial neural network is a computational approach that loosely models the way a biological brain solves problems. They can have several entries for the neuron but only one exit value. There is also an activation function that defines the value of the exit for each connection. These systems are self-learning and should be trained.

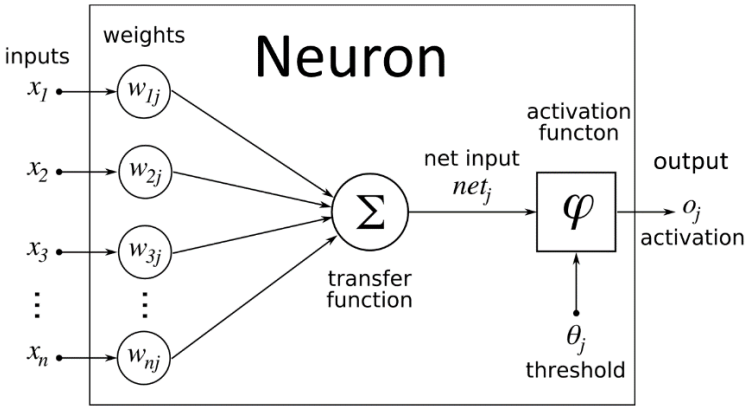

Fig. 85: Description of an artificial neuron.

Normally, neural network consists with multiple layers, but for this case we started with the simplest form, an adaptative lineal network (AdaLiNe). The detection of the folded cells only requires one exit, meaning that only one neuron is required.

The images pixels are the input of the neuron, and the challenge is to make the neuron able to recognize if the cell in the image is folded or not. Therefore, the output is defined as folded (1) or not folded (0).

Since the neuron read only images, it's necessary to make a pretreatment to the test videos, to convert them into an input format that the neuron can read. This pretreatment consisted with:

- Decompose the video into individual frames
- Decompose every frame into individual cells (all images must be of the same size)
- Apply a color segmentation to the cells to facilitate the identification of buckles.

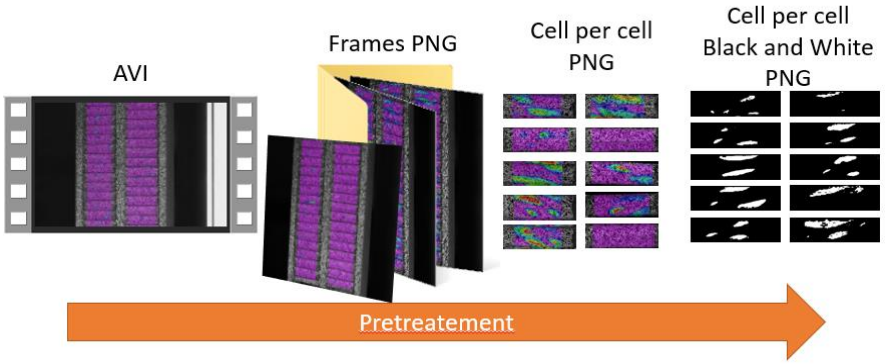

Fig. 86: Description of the pretreatment of the test videos.

First, using Photron, the videos were decomposed in to .png frames. This option is available in the menu save as.

Then, a script was developed to be able to segment the frames; in the script the user had to specify the number of cells and the region of interest where those cells are located. Then, the program automatically cuts the frame to the shape of the cells. The images were cut and resized to have the all same dimension of 200x70 pixels.

Finally, knowing that the buckles of interest are of red color, a segmentation should be made to isolate these buckles. Three tones of red are used by the VIC-3D software, therefore the segmentation must include these three tonalities.

Also, the intensity of red depends on the background, if the buckles are placed where the sparkles are black, the tonality of the red color will be darker, if the background is withe the color will be light red. To take all of this into consideration, a sampling of colors was taken from the images. In the RGB format of 255 bits (by its components [Red Green Blue]) they are:

```
Normal red = [121    19    19];
Light red  = [226   124   124];
Dark red   = [117    15    15];
```

In all the cases the colors are very different, but a useful characteristic is observed. The first valor of the vectors (the red layer) was always much bigger than the others, meaning that, we have only to verify that the first number is much bigger than the others two.

Several tests of this hypothesis were made and the conclusion was that the red color is well detected when the red layer is 75 units higher than the other two. The results were very satisfactory as can be seen in Fig. 87.

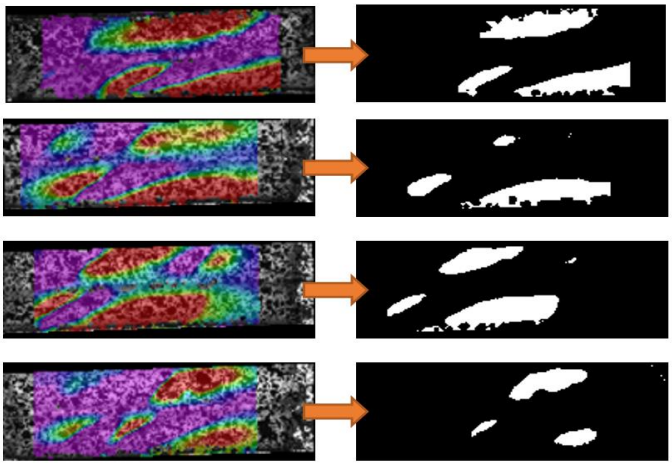

Fig. 87: Image of cells before and after color segmentation.

Once that the images are ready to be read, the next step was to train the neuron.

Several examples of folded and non-folded images were given to the neuron to learn to identify the folding cells. It is important to mention that the characteristics that the neuron uses to identify a folded cell are determined by itself. They are automatically defined by the neuron in the training process. Thus, they are not determined by the user and the decision if a cell is buckled or not relays only on the neuron.

Since the interest of this study is to detect when the cells pass from an initial buckling state to the collapsed state, the buckling profile that is detected by the neuron should be the closest possible to a cell about to collapse, i.e. the transition between the two states. Therefore, the ANN was trained with 29 examples of cells that were about to collapse and 50 examples of non-buckled cells selected by the author. Some examples can be seen in Fig. 88.

After the training, the ANN learned how to detect 29 different buckling patterns. This was very helpful because it enabled the ANN to detect the collapse of the cells almost regardless of the buckling pattern.

This ANN was used to analyze the images from the tests. The results are shown in Fig. 89. Both the left and right sides of the specimens were analyzed. The analysis revealed that the nonlinear behavior started before any cell was detected as being about to collapse. This means that initial nonlinear behavior of the curve is caused by the initial local buckling.

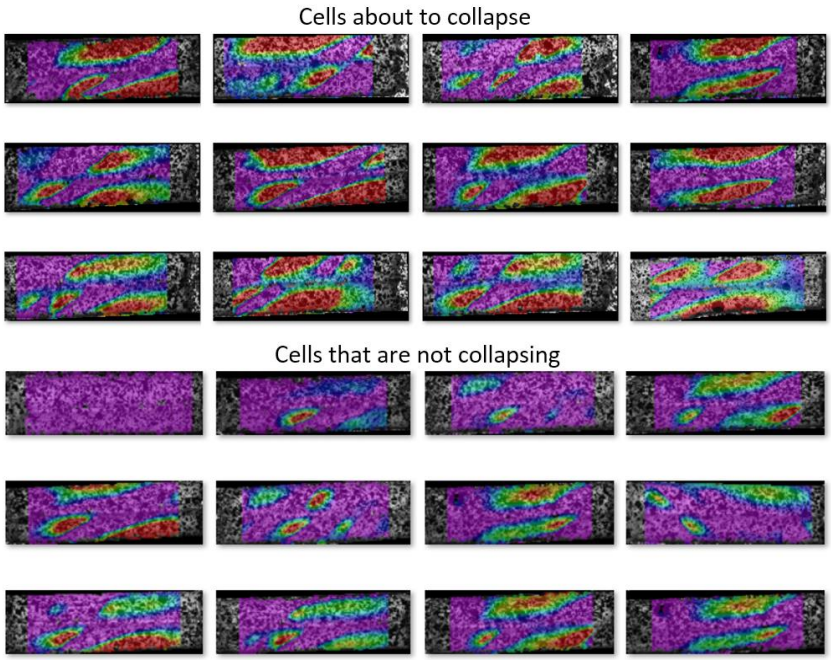

Fig. 88: Examples of collapsing and non-collapsing cells to train the ANN.

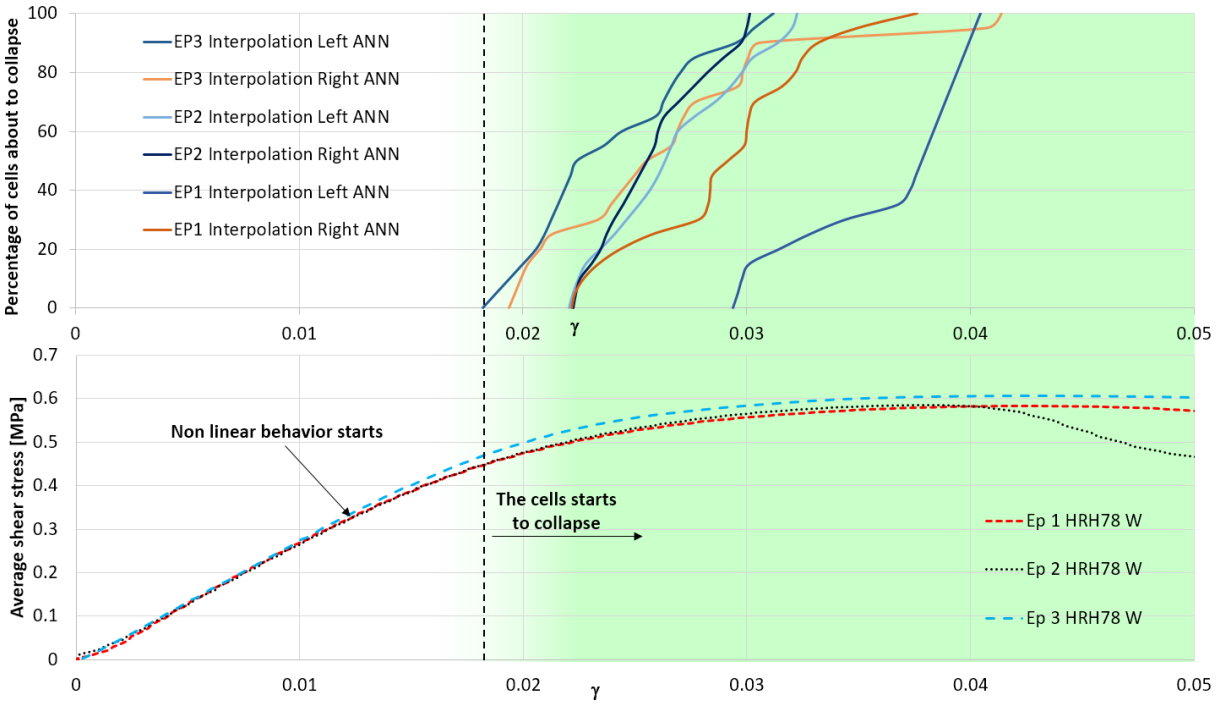

Fig. 89: Collapse of the cells according to the results given by the ANN vs the average shear stress.

3.3.5 Conclusions

This kind of detailed study has never been done in the literature, and so this adds a new insight to the shear buckling of honeycomb cores.

We showed that the buckling of the cells appears at very low shear stress levels, proving that the honeycomb behavior is mostly in the postbuckling domain, as Bianchi et al. suggested in [41]. In general terms, this means that it's wrong to define a shear failure criterion based on the buckling or postbuckling state of the cells. In consequence, we proved that the shear failure criterion proposed by Zhang and Ashby in [9] is inaccurate, because it's based on the start of the shear buckling of the core.

Moreover, it was observed that the buckling of the cells is elastically reversible far beyond the linear limit. Therefore, saying that the elastic limit is when the nonlinear response starts, would be equivalent to underestimate the shear strength of the core, as most of aircraft manufacturers do [52].

Also, it was shown that the initial imperfections of the core are not important for the shear linear response, because, even if the initial imperfections are different for every cell, when they are subjected together to shear, the average shear stress values are very regular.

On the other hand, we observed that the nonlinear response of the core is importantly influenced by the boundary conditions of the cells. Therefore, the failure of the core depends on the boundary conditions too, being possible to be increased or decreased (see Fig. 67). This suggests that it's not possible to define an accurate general shear strength criterion as Pan et al. in [72] did, without considering the effect of different boundary conditions.

Regarding the fabrication, the adhesive film Redux 609 worked well only for the HRH-78 honeycomb core. The maximum average shear stress for this specimen was smaller than the needed for the HRH-10 and the Alu 5052-3/8. This suggests that better results could have been obtained if a stronger adhesive were used.

Three different honeycomb cores were available, however only one provided useful results, the HRH-78, therefore our analysis was only focused on this one.

The double rail specimen was a good choice to study the buckling of the cells. We found very similar shear moduli and shear strength between our tests and the manufacturer data. However, for the nonlinear behavior it was seen that this test specimen provided different curves from one specimen to another. This was in part caused by the configuration of the specimen; one piece of Nomex® core collapses first and then the other one as shown in Fig. 90.

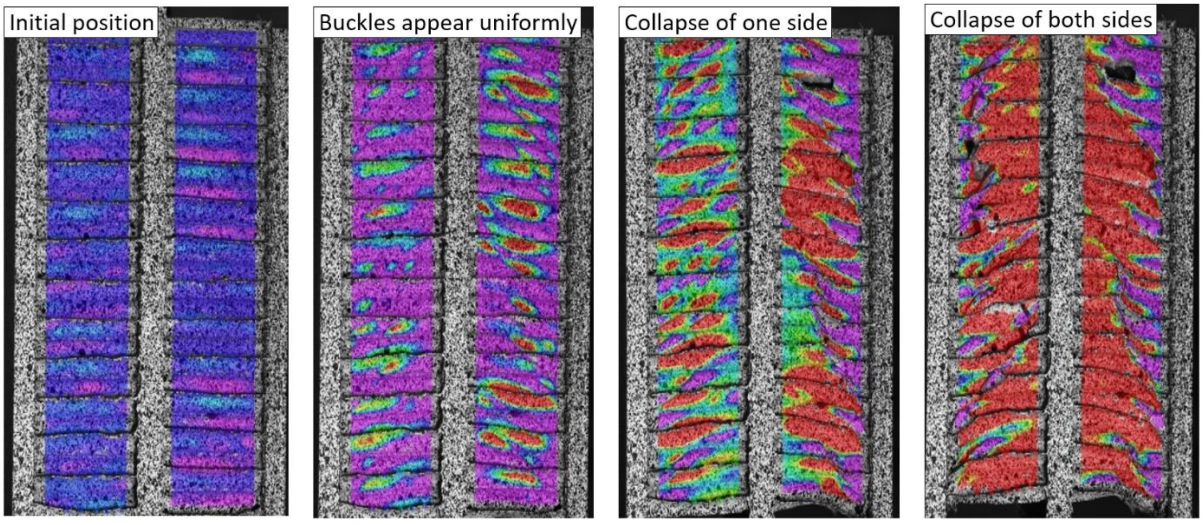

Fig. 90: Failure scenario of the specimens.

The incremental cyclic testing revealed that the core effective response remains nonlinear elastic, even if the honeycomb had already buckled.

Also, we learned that studying the exterior surface of the honeycombs was not probably the best, because the exterior cells don't have the same boundary conditions than the interior cells of the specimen. This was evident when we observed that the buckles propagated more towards the interior of the cells than to the exterior. However, studying the cells at the interior requires the use of other more complex equipment like X rays or ultrasound, which would add complexity to the problem. Also, since we focused the analysis on the vertex of the collapsing cells and growing of the buckles (rather than only the shape of the buckles), we considered this approach was valid for its purpose.

Determining the correct scale for the buckles was very useful because it allowed us to estimate their shape and magnitude independently of the initial defects of the cells. Also, we detected that the buckles start to appear at very low levels of the shear stress. Thus, most of the shear behavior of honeycomb cores is on postbuckling. This is relevant because it proves that the shear failure of the core is not determined by the buckling point of the cell, therefore the analytical approaches that used this hypothesis to estimate the shear strength of honeycombs are very far to be correct.

Concerning the inspection of the cells buckling, we successfully provided a detailed description of the buckling scenario. More important, we detected two mechanisms that the honeycomb structure uses to support the shear deformations. The first one starts with the creation of small buckles that are apparently elastic. Once the cell is saturated of buckles they stop growing and the second mechanism is activated. It consists with the folding of the cell vertex that eventually leads to the collapsing of the cell.

We detected three different stages of the nonlinear shear behavior of the cells:

- The cells deform linearly until small buckles start to appear in the cells.
- Apparently, this buckling configuration is stable and the cell can support bigger loads while the size of the buckles is increasing.
- The buckles stop to grow but the vertex starts to fold. When the extent of buckling is large enough, propagation of the buckled shape to the adjacent cells causing collapse of the cells which leads to global collapse.

As for the number of buckles in the cells, this was not conclusive and we didn't found a direct relation of these with the nonlinear behavior. This might be because the shape and number of buckles was affected by the boundary conditions of the exterior cells.

Moreover, we found a relation between the number of collapsed cells in the specimen and the nonlinear behavior. First, we investigated this by ourselves, and the results suggested that the start of the nonlinear behavior was caused by the start of the folding of the collapsing of the cells. Later, we did the same analysis but using an artificial neural network which should provide more trustable results, which suggested that the nonlinear behavior was caused by the growing of small buckles. Both results were exclusive, and as the second method was more objective from a scientific point of view we choose to believe the second result (later this is confirmed through F.E. analysis).

Finally, we can provide a detailed description, stage by stage, of the nonlinear behavior of the HRH-78 honeycomb core, which may also be compatible for similar honeycomb cores in terms of buckling scenario:

- From $\gamma = 0$ to $\gamma = 0.00845$ (0 MPa to 0.24 MPa), the magnitude of the buckles is very small, almost undetectable. The overall behavior of the honeycomb is linear elastic (see Fig. 81).
- From $\gamma = 0.00845$ to $\gamma = 0.01542$ (0.24 MPa to 0.4 MPa) the buckles start to be clearly visible, affecting the linear behavior of the honeycomb structure very slightly. The cell walls buckle progressively. The honeycomb structure works in a reversible postbuckling regime. The overall behavior of the honeycomb is still elastic (See Fig. 81).
- From $\gamma = 0.01542$ to $\gamma = 0.01822$ (0.4 MPa to 0.46 MPa) the average shear stress vs. gamma curve indicates more visible nonlinear behavior. The incremental cyclic test presumably indicates that the honeycomb structure remains elastic without hysteresis (see Fig. 79). The honeycomb structure still works in a reversible postbuckling regime. The overall behavior of the honeycomb is nonlinear elastic.
- From $\gamma = 0.01822$ to $\gamma = 0.02151$ (0.46 MPa to 0.52 MPa) the buckles have propagated enough to cause instability of some cells, which start to collapse (see Fig. 89). However, the incremental cyclic test indicates that the structure remains elastic (see Fig. 79). This could mean that the buckling of the Nomex® paper was still elastic or that the overall

deformations were very small or not large enough to cause significant damage of the structure.

- From $\gamma = 0.02151$ to $\gamma = 0.03$ (0.52 MPa to 0.59 MPa) the cyclic test indicates that the structure is permanently damaged (see Fig. 79). The first one is the deformation of the cells propagates and they continue to collapse. The maximum average shear stress is presumably reached when the last cell is about to collapse (see Fig. 89). At this point, the Nomex® paper tears in some areas.

Considering the above, it can be said that the nonlinear behavior of the honeycomb in shear is related to two different phenomena. The apparition of local buckles in the cells that cause a slight loss of stiffness. And the second one is the cells collapse, causing a major loss of stiffness of the structure (see Fig. 82). When all the cells have collapsed, it would be logical for the shear stress to decrease. However, the analysis detected that all the cells were already collapsing at approximately γ=0.04 while the measured shear stress was still τ=0.5 MPa, which suggests that the collapse is slow, no dramatic and gradual. Also, once the cells have collapsed, if the displacement of the skins continues to increase, the cells start to break at approximately $\gamma = 0.06$. After this, they are completely sliced and therefore there is almost no contact between the remaining parts of the superior or inferior skins, therefore the cells are are no longer inclined (see Fig. 91) and so this residual strength can be mostly attributed to the breaking and tearing of the paper of the honeycomb cells.

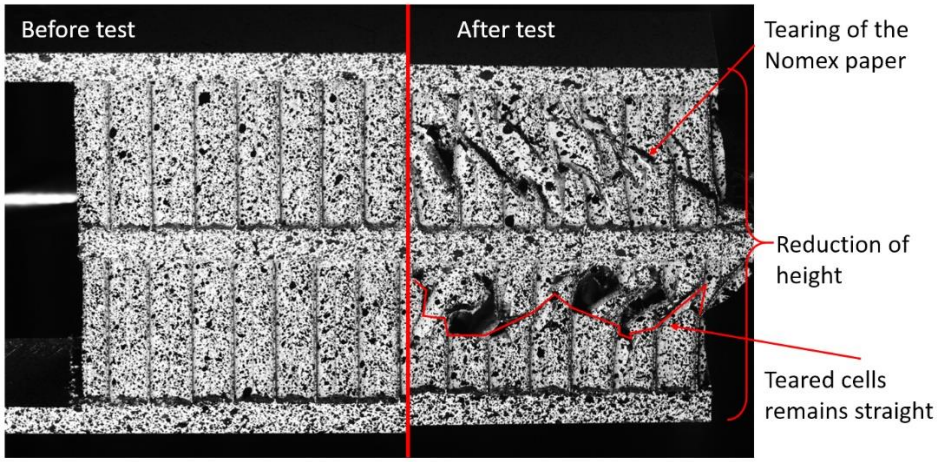

Fig. 91: Comparison of a specimen before and after the test.

These results were considered important to the scientific the community and led to a publication in [13].

3.4 Numerical study of shear buckling of honeycomb cells

The experimental study revealed that the onset of buckling of the cells appeared under relatively low shear stress. When the honeycomb was subjected to shear loading, it initially showed linear behavior that could be described with a shear modulus. If the stress was increased further, the slope of the curve changed. Our research suggests that at least two different phenomena are involved in the nonlinear behavior of the honeycomb in shear. Presumably, local buckling initiates the nonlinear behavior. Then, after a postbuckling stage, the collapse of the cells causes the final degradation of the shear moduli.

However, one of the limitations of the last study was the inability to inspect the interior cells of the specimens, which can be interesting because this is the real buckling shape of the honeycomb cells when they are subjected to shear.

The hypothesis made about the measuring of the buckles only in the out-of-plane direction also should be investigated.

We want also to study the different buckling mechanisms of the honeycomb structure. The previous research showed that the buckles of the cells can be divided in two stages, first the local buckling of the cell walls, and secondly the collapse of the cells, characterized by the growth of the local buckling until the cell shape is lost.

For this reason, the study of the buckling of the cells is complemented with the development of several FE models of the 20 mm thick HRH-78-3/16-3.0 honeycomb that will be compared to the experimental tests. These models allowed other aspects of the buckling of the cells to be inspected.

The models were created using Abaqus implicit because the models were subjected to low velocity displacements. Also, these models helped to analyze the initiation of buckling under shear loading.

Seeman et al. [4], did a very detailed study on the modeling of Nomex® honeycomb cores at the mesoscale and this study will be taken as main reference for this section.

The first step of the modeling of the honeycomb core is to determine the properties of the materials. In the case of the HRH-78, it's made of the Nomex® commercial grade paper T-722.

3.4.1 Properties of the T-722 Nomex® paper

According to the manufacturer, the HRH-78 is not made for aerospace applications [44]. Bitzer explains that this is because the T-22 paper does not satisfy the FAR 25.853 flammability afterglow requirement [45]. Also, it seems that the mechanical properties of the T-722 paper are slightly lower than those of the T-412, which is used for aeronautical applications.

This is useful because there is no data available of the testing of the T-722 paper, but only of the T-410 [56] and T-412[81] [12] . In this study, we assumed these papers were all very similar and had the same mechanical properties.

This hypothesis is endorsed by Roy et al. research in [56]. They found that the phenolic coating on the Nomex® paper strongly modifies the behavior of the paper. Therefore, if the coating layer has the same thickness, the mechanical properties should be very similar too.

The elastic properties of the paper alone are Ex=3000 MPa and Ey=850 MPa, while for the phenolic resin the Young's modulus is E=4800 MPa.

However, if the coated Nomex® paper T-722 is homogenized, it can be considered as isotropic with a Young modulus of 4000 MPa. Also, according to Seeman et al. [12], the elastic limit of the paper should be around 90 MPa.

3.4.2 Study of the shear buckling of the Nomex® honeycomb core

To better understand how the local buckling appears and how should it look like, we proposed to start by analyzing the honeycomb core at different scales by means of creating models that helps to understand the problem.

First, we started by a model of a simple cell wall subjected to very similar to shear conditions, then we did the same but to a single cell, and finally for 8 cells together. These cases are presented as follows:

3.4.2.1 Case 1: Shear buckling of a single cell wall

Endorsed by the study of Seemann et al. and other authors, the thickness of the Nomex® paper and the phenolic coat was considered of 52 μm and 3 μm respectively [12] . The cell wall size corresponds to a single wall of a cell of 4.7625 mm diameter.

The properties in the out-of-plane direction are unknown. However, knowing that the Ez moduli should be smaller because there are not fibers oriented in this direction, we proposed Ez=0.5Ex. Finally, only C3D8 volume elements are used and the properties of the paper were E_x=3000 MPa, E_y=850 MPa, E_z=1700 MPa, $\nu_{xy}=\nu_{xz}$=0.02, ν_{yz}=0.2, G_{xy}=800 MPa, G_{yz}=800 MPa and G_{xz}=800 MPa.

The coating of phenolic resin was considered as a layer of an isotropic material with a Young modulus of 4800 MPa and a Poisson ratio of 0.389.

The boundary conditions of the F.E. model of the wall are shown Fig. 92; the cell wall is not subjected to pure shear but to a very similar kind of loading, which is much simpler to implement. Also, judging by the dimensions of the wall, the fact that the dimension of the cell in the X direction is relatively small in comparison with the other side, added to the fact that the displacement in the X direction is restricted, should give very similar values than a pure shear case. First a buckling analysis was made to obtain the different buckling modes. Then, the first six buckling modes were introduced as initial deformations (scaled by the thickness of the wall divided by ten) to induce the buckling. Finally, an imposed displacement of 0.3 mm was imposed to create the shear.

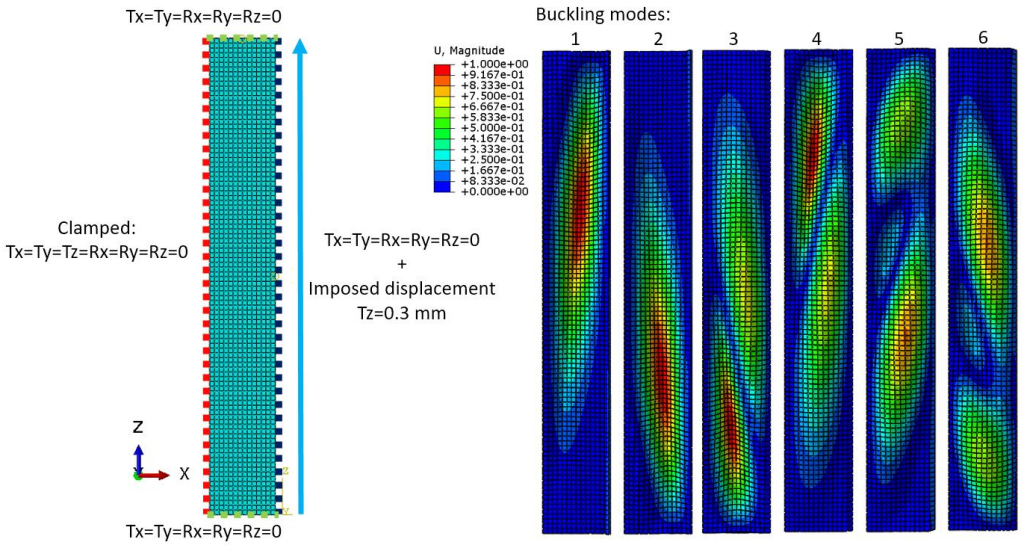

Fig. 92: Cell wall boundary conditions and buckling modes.

The buckling modes of the walls are similar to what is observed in the experimental tests. However, the final buckling shape of the simulation differs to the observed ones in the experimental study. This may be caused by the different boundary conditions.

In the tests, the superior and inferior boundaries of the cells are fixed to the skins through the adhesive. But also, the lateral borders of the cells are fixed to the surrounding cells.

These conditions are very complex to reproduce for only one wall because the skins are not completely rigid but elastic, thus the horizontal boundary is not exactly clamped. Also, for the lateral sides fixe to the surrounding cells, the vertices are rigid but not enough to be considered as full clamped.

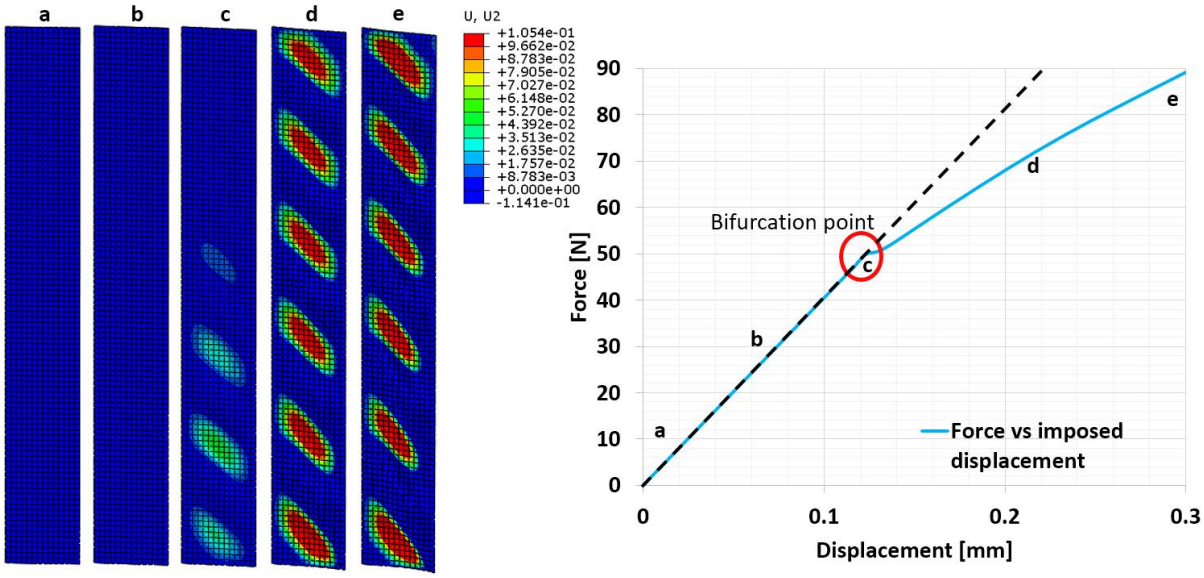

Fig. 93: Buckling of a cell wall (out-of-the-plane displacement) and force vs displacement curve.

What we obtained is the aspect of a honeycomb wall subjected to a purer shear that in the real tests and this is relevant because this suggests that even if the honeycomb structure is subjected to shear, the cell walls are not only subjected to shear loading but to a combination of complex forces.

Also, we detected that once the cell wall starts to buckle, it reaches a bifurcation point and the cell wall shear stiffness of the cell wall is reduced, although it can support higher loads, therefore this is a stable buckling configuration.

Another interesting point is that the required forces to make buckle the cell wall are relatively high.

Finally, we confirmed that the scale determined in the experimental study was accurate, as it allows visual detection of the bifurcation point of the walls is reached (the scale of Fig. 93 and the scale determined experimentally in Table 8 is the same).

3.4.2.2 Case 2: Shear buckling of a single cell

A simulation of the buckling of one honeycomb cell was made to better understand the propagation of buckles in the honeycomb structure.

For this model, the cell was considered as a perfect hexagon with a cell diameter of 4.7625 mm. The single and double walls of 0.06 mm and 0.12 mm thickness were also considered.

The coated Nomex® paper was homogenized and the properties were considered isotropic with an elastic modulus of 4012 MPa and a Poisson ratio of 0.3, although no plasticity or failure was considered for any of these materials.

Only shell elements were used. The geometry and small thickness of the honeycomb allows obtaining accurate results and reducing the simulation time using this feature.

The boundary conditions are similar to the conditions of the real test. The vertical borders were tied together while a displacement is imposed as shown in Fig. 94. No symmetry conditions were used.

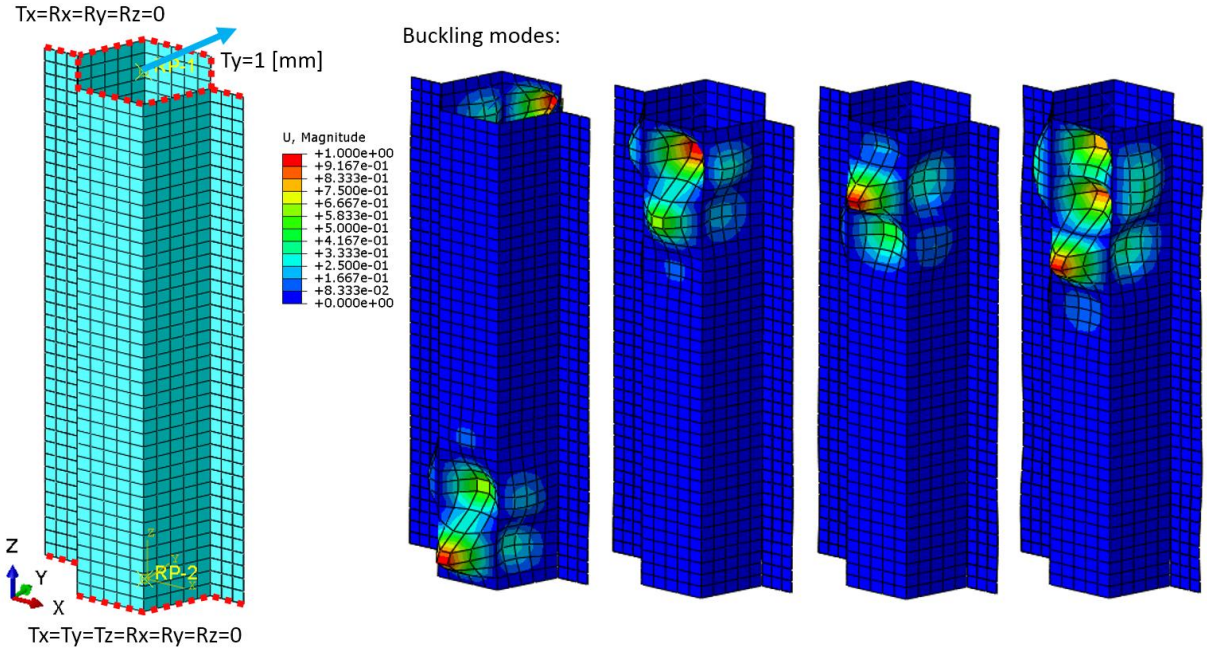

Fig. 94: Single cell boundary conditions and buckling modes.

First, the buckling modes were obtained to use them as initial defects to force the buckling of the cell. After that, a displacement of 1 mm was imposed in the y direction.

To show the results, the same scale of 0 to -0.1054 mm was used, therefore only the buckles that goes towards the interior of the structure (negative buckles) are colored (see Fig. 95).

The first interesting remark is that the shear force required to buckle the cells is much lower in comparison with the cell wall simulation. This suggests that the used boundary conditions don't submit the cell walls directly to shear. It's more like if we were measuring the structure behavior of the honeycomb more than the combined behavior of six cell wall subjected to shear, which is relevant.

Also, the isolation of the cell allowed us to detect that the presence of the surrounding cells is very important for the cell to keep its shape. This becomes clear in Fig. 96. While the displacement was imposed in Y direction, the single wall borders are curved towards the interior and the double walls towards the exterior, which probably would not happen if the surrounding cells were present.

Concerning the behavior of the cell, it's initially linear and after it buckles. There is a change in the stiffness of the cell, which apparently means that it can support higher loads. It seems to be a stable buckling configuration.

Finally, it's interesting to notice that the cell buckles following a "S" shape (white lines in Fig. 95). This pattern can be seen as the folding of the cell from the top to the bottom, plus two diagonals at 45°. This may represent the combination of the two observed buckling scenarios, the buckling of the hexagonal cell plus the buckling of the cell walls.

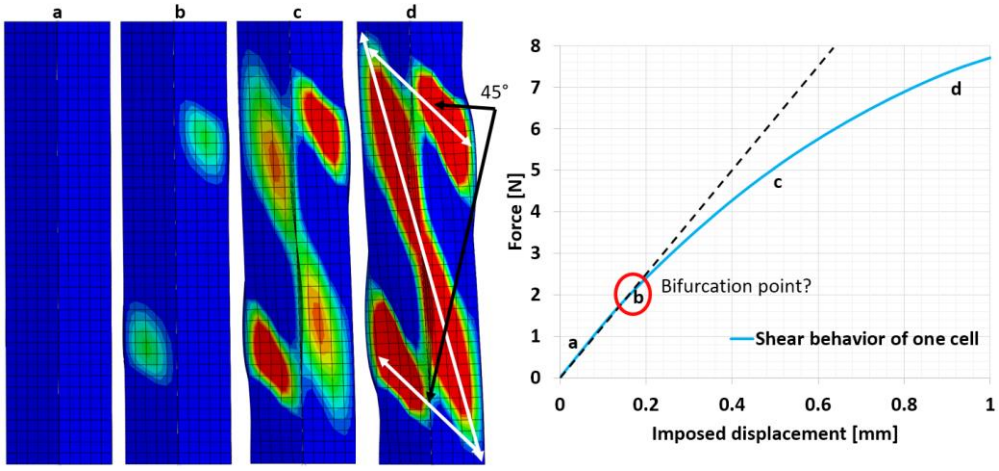

Fig. 95: Buckling of a single cell (scale: 0 to -0.1054 mm) and force vs displacement curve.

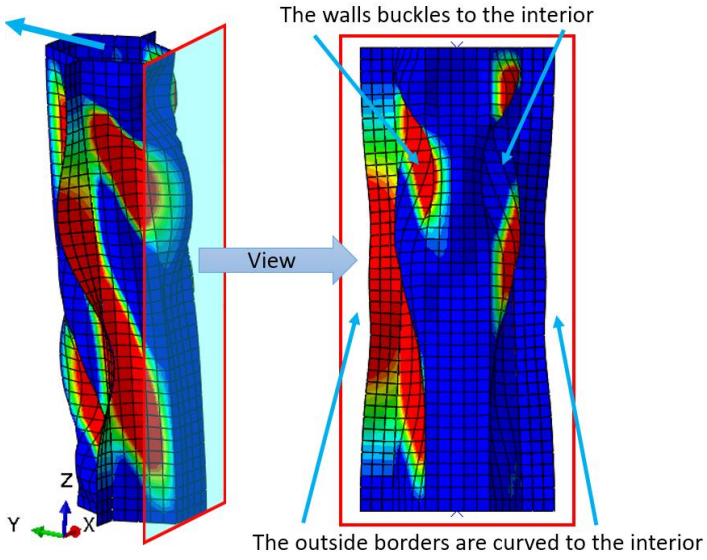

Fig. 96: The buckling shape suggests the importance of the surrounding cells.

3.4.2.3 Case 3: Shear buckling of the honeycomb core

Finally, we did a F.E. model of the honeycomb core to be able to observe the interior of the honeycomb cells.

Model features

The cells were considered as perfect hexagons with a cell diameter of c=4.7625 mm. The variation of thickness of the single and double paper walls was considered; they were 0.06 mm and 0.12 mm thick respectively.

The model consisted of an array of 3 by 3 cells for a total of 8 honeycomb cells and only S4R shell elements were used. The approximate global size of the elements was 0.27 mm.

The bottom of the cells was fixed in displacement and rotation, the top was fixed in a similar way but displacements in the Z and X directions were allowed (see Fig. 97).

The imperfections due to the fabrication process of the hexagonal cells, like waviness or variation on the cell thickness were not considered because it was not very recommended by Seeman et al. Indeed, according to them, including these variations increases the accuracy of the model by around 10 %, but it will also introduce a very high complexity in to the model.

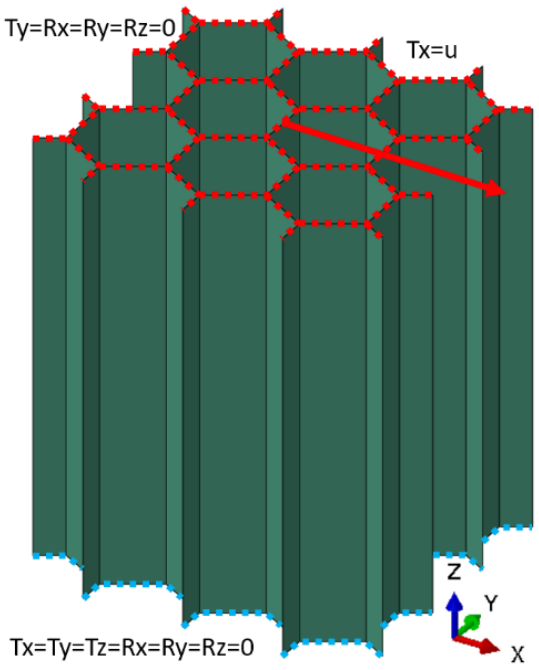

Fig. 97: Boundary conditions of the double lap test model.

No symmetry conditions were imposed on the exterior borders of the cells because this could alter the natural support between the cells and therefore the buckling shape.

First, a buckling analysis was made to determine the buckling modes of the structure. Then, some buckling modes were incorporated into the model as initial imperfections in order to make a postbuckling analysis of the structure.

These buckling shapes were introduced as small deformations with a magnitude of the thickness of the cell wall divided by 10 for the first buckling mode, then, the magnitude was divided by 10^2 for second, and so on.

These imperfections are not of the same type of the fabrication imperfections. The main difference is the scale and the shape.

The coated Nomex® paper was considered to have a perfectly plastic behavior starting at 64 MPa.

Also, to determine if the plasticity of the buckles had any notable influence on the overall shear behavior of the honeycomb structure, two simulations were run considering plastic and non-plastic behavior of the Nomex® paper.

Analysis of the results

No tearing of the Nomex® paper was considered in the model, so the FE model shouldn't be representative of the real test beyond approximately γ =0.055, i.e. when the tearing of the paper is detected in the experimental results.

To compare the buckles in the F.E. model and the real tests, the color scale of the F.E. model was set to the same as the one used in the analysis of the experimental results (0 mm to -0.1024 mm).

The numerical simulations of the shear test showed good correlation with the real tests. The buckling pattern of the cells was very similar, as the shear curves (Fig. 98). This comparison allows developing an experimental/numerical results dialog, on which the aspects that were not clear by one approach can be clarified by the other, which is very useful.

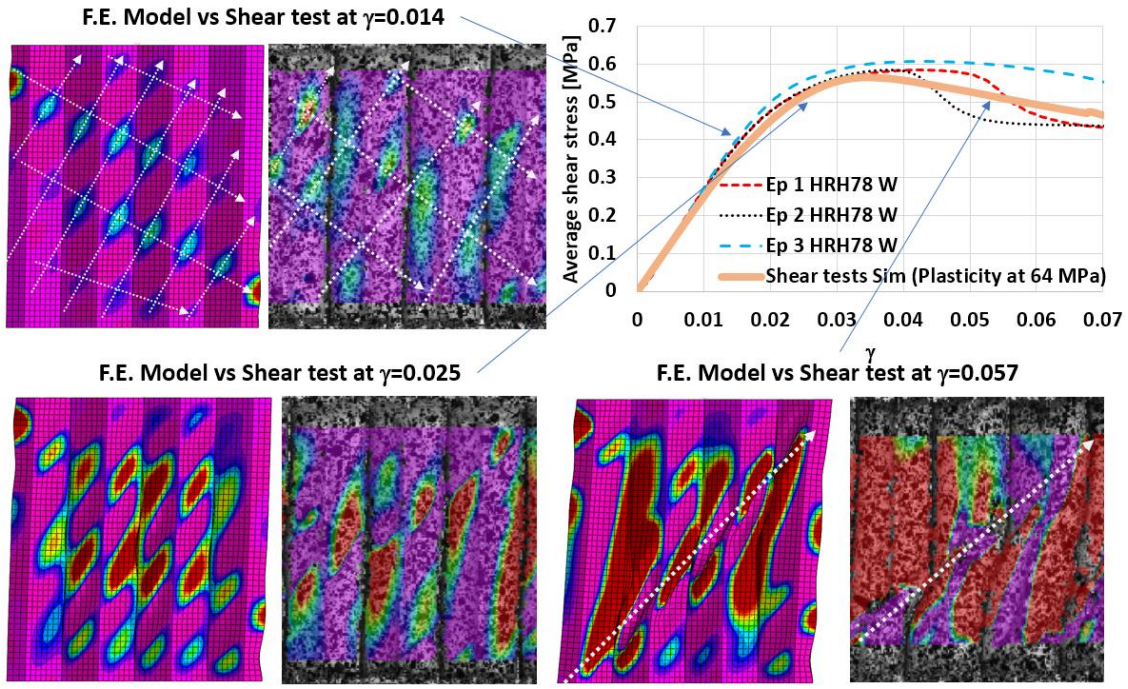

Fig. 98: Real tests vs simulation of HRH-78.

Also, it was possible to make a cut in the F.E. model to compare the buckles in the interior and exterior of the honeycomb core, this is shown in Fig. 99.

The pattern is similar but the exterior cells are slightly more folded toward the inside of the structure. Also, it's interesting to notice that there is a diagonal folding that starts to appear from the corners of the honeycomb structure in both interior and exterior cells.

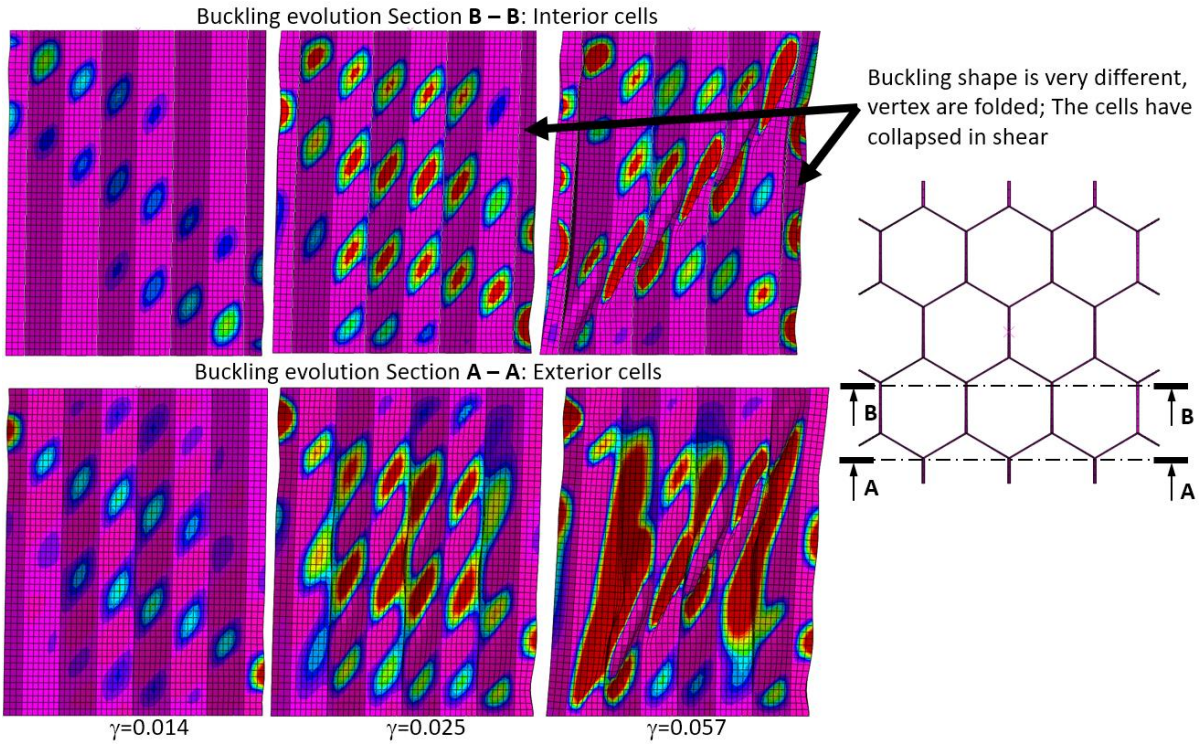

Fig. 99: Cell buckling experienced by the exterior and the interior of the specimen of the double lap test.

To analyze the buckling stability of the cells, it is necessary to find a way to measure the buckles of the cell walls. One way to do this could be to measure the rotations of the nodes

of each wall but this would hardly be practical since buckling of the cells may occur in any direction.

We considered that the best method was to obtain the sum of the rotations of all the nodes in every direction as Roy et al. did in [33]. This would give us a general estimation of the start of buckling in the F.E. model, and any abrupt change in this quantity would mean that the buckling configuration of the cells had changed. Fig. 100 shows the average shear stress vs the total nodal rotation.

A bifurcation point can be detected at 0.31 MPa, corresponding to the onset of buckling. After this, the rotations of the nodes are seen to increase with the shear stress, meaning that this buckling configuration is stable. Finally, the cells collapse at 0.56 MPa.

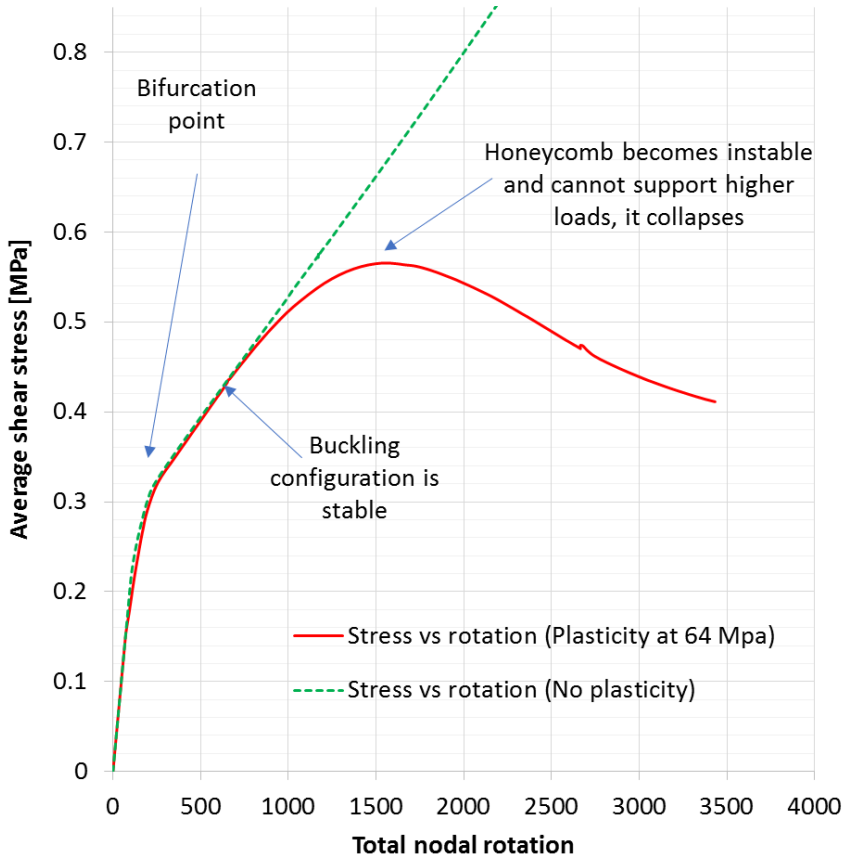

Fig. 100: Average shear stress vs nodal rotation of the double lap F.E. model.

Also, when no plasticity was considered in the F.E. model, the cells did not collapse, meaning that the collapse of the cells was caused by the degradation of the Nomex® paper and, therefore, that the stability of the honeycomb cells may be attributed to the geometry of the cell that buckles into a stable configuration.

In this way, it can be said that two phenomena take place when the honeycomb is crushed. First, the postbuckling of the cells in a stable configuration, and then the collapse of the cells because the material plasticizes and the edges fail.

Also, by comparing the curves as shown in Fig. 101, we noticed on the F.E. model that even though the buckled areas started to plasticize at $\gamma = 0.018$ (0.42 MPa) the two curves were similar until $\gamma = 0.024$ (0.48 MPa).

By inspecting the simulations, it is observed that the paper starts to plasticize at $\gamma = 0.018$, but the cyclic tests indicate that the global behavior of the structure is not affected until $\gamma = 0.021$, which indicates that the buckled areas may plasticize without affecting the

global behavior of the structure (although this hypothesis relies on the hypothesis made for the plastic behavior of the Nomex® material).

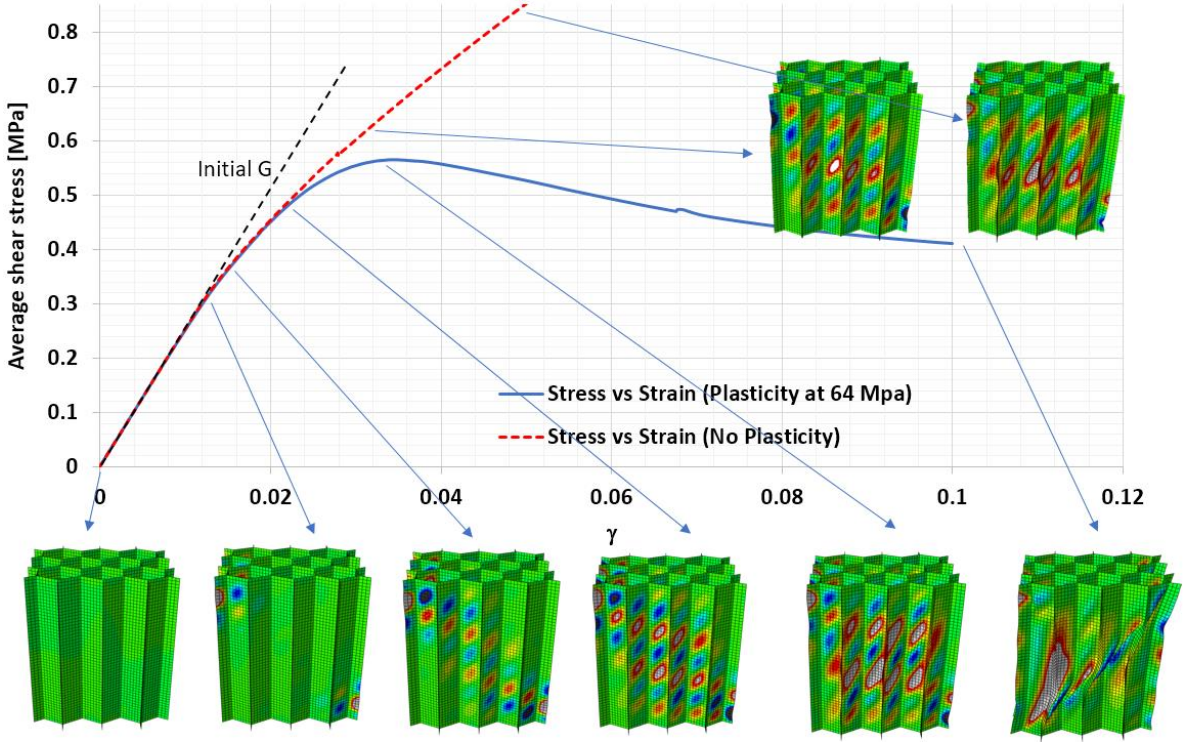

Fig. 101: Average shear stress vs gamma of the double lap F.E. model: when the Nomex® paper was considered to be totally elastic the cells doesn't collapse.

3.4.3 Conclusions of the numerical analysis of the shear buckling

The F.E.A. tools allowed us to study in detail the buckling of the inside cells of the Nomex® honeycomb core.

The study of the three cases (cell wall, single cell, honeycomb structure) allows comparing the different shapes of the buckles.

The buckling shape of the single wall and the single cell were very different. This suggests that in both cases the walls are experiencing different structural loads. On the other hand, the buckling shape of the honeycomb structure presents a similar buckling to those of the cell wall.

Judging only by the appearances, this indicates that the presence of the surrounding cells is very important, explaining why for the single cell the buckles are different. Apparently, the presence of the surrounding cells restricts the vertical and horizontal displacements of the cell's vertex which induces a very similar effect to the fixing conditions assumed for the modeling of the cell wall.

Concerning the F.E. model of the honeycomb and the tests, despite its relative simplicity and some discrepancies between experiment and numerical analysis, a very good correlation of the force vs displacement was obtained. This indicates that the buckling shape of the honeycomb cells' model should be very similar to the buckles of the real test and therefore, we can say that this F.E. model is a legitimate virtual representation of the real test.

Regarding the exterior and interior buckling shapes, they are similar for low stresses and then start to be different as the shear stress increases. In consequence, the exterior cells experiment a weaker resistance to the shear buckling.

Also, we observed that the coated paper can plasticize at the buckles without altering the elastic behavior of the honeycomb structure, which means that the material of the honeycomb can support certain degradation without affecting the effective structural behavior of the honeycomb.

By comparison of the shear buckling of a single cell wall and a single cell, it can be deducted that the walls are not subjected to pure shear and that the failure is not caused by the individual buckling of the cell walls.

So far, the shear behavior of the honeycomb core was investigated experimentally and numerically, the analysis of the nonlinear behavior of the honeycomb cells under shear stress is summed up in Fig. 102.

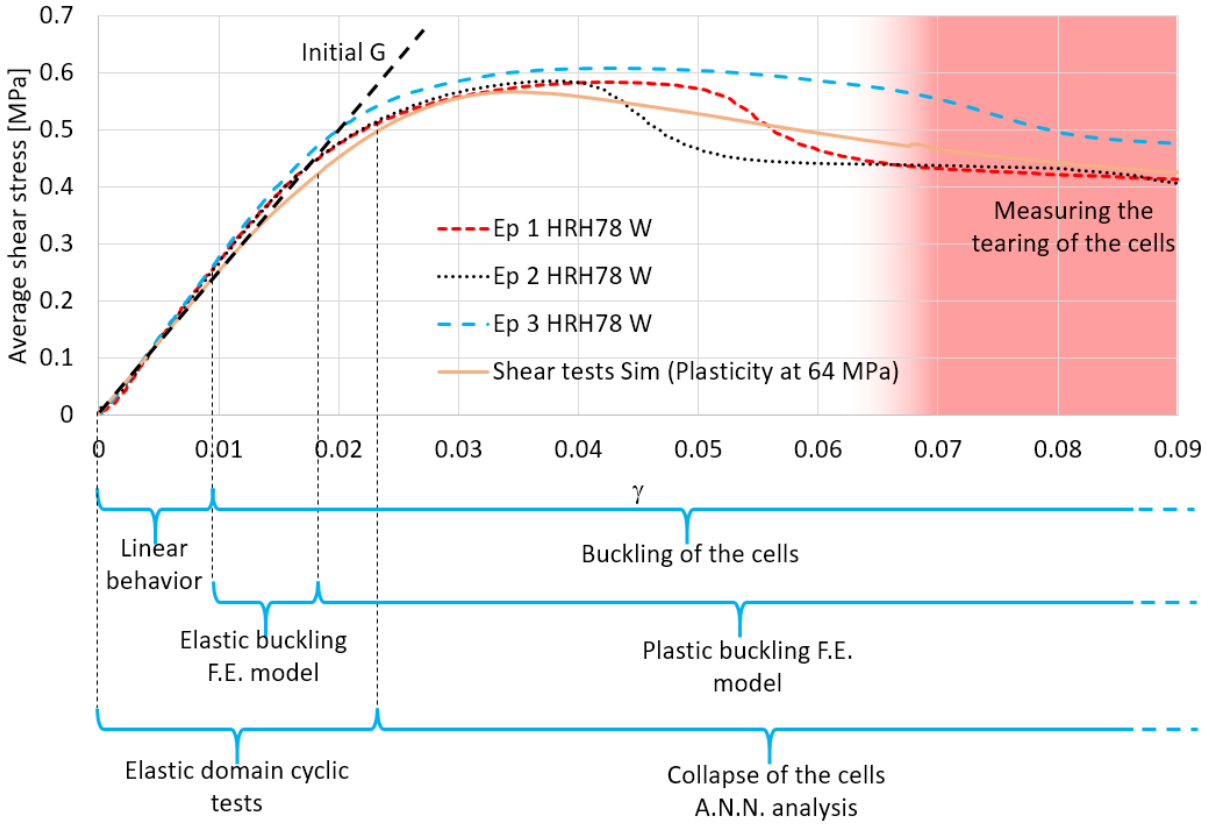

Fig. 102: Description of the nonlinear behavior of the Nomex® honeycomb core HRH-78.

Both numerical analysis and experiments have highlighted and confirmed the different nonlinear behavior of honeycomb under shear when different boundary conditions are used. Although it should be obvious, it is nevertheless worth recalling here that honeycomb is firstly a complex structure, so the boundary conditions have strong effects, especially for buckling and postbuckling.

The results show that the buckling of Nomex® honeycomb core presents nonlinear elastic behavior beyond the buckling point. This is due to reversible postbuckling as in aerospace structures. This could be useful for inserts or corners (see ref. [35]), where their strength is commonly based in the linear shear limit of the honeycomb core. In this sense, switching the linear limit criterion for the actual elastic limit (which includes the elastic buckling of the cells could reduce the oversizing.

Answering the question of section 3.1.1.3, at this point we identified the different buckling stages of the Nomex® honeycomb core at different scales, for a cell wall, for a single cell and for a group of cells. We can say that the shear buckling of the honeycomb is a very complex phenomenon related to several factors like; the size of the cell, the boundary conditions, the surrounding cells, the initial defects, the cell wall material, among others.

For the same reason, the nonlinear response of the honeycomb should be analyzed under similar boundary conditions as in the real case, and this must be important for inserts. In the next chapter this subject is studied by imposing on the honeycomb core similar boundary conditions to those present in an insert.

3.5 Experimental and numerical study of the core boundary conditions for inserts.

To answer the question of section 3.1.1.4 we should study the buckling of the cells that are near the insert. As explained previously, the comparison of two different cases of shear for honeycomb cores, shows that the buckling shapes that occur during a rail shear test and in proximity to inserts are very different, although the core is subjected to shear in both cases. This suggests that the two honeycomb cores may experience different structural behavior under shear loading, and this is relevant because this has never been formerly studied yet.

The present study reports a detailed experimental and numerical investigation of Nomex® honeycomb core buckling and postbuckling under different boundary conditions through different types of tests. This part of the investigation consisted in to a numerical study of the buckling shapes of the honeycomb and an experimental test to validate the numerical results.

3.5.1 Numerical study

To better understand the conditions that cause the different buckling shapes in the rail test and in the insert pull-out, we studied and compared three cases of F.E. models under different boundary conditions. As shown in the last section, this method allows to establish a very useful dialog between the experimental tests and the numerical simulations, which together allow to better understand the studied phenomenon. This analysis was only made for the W direction since it's weaker than the L direction.

3.5.1.1 Case 1: Double lap test

The previous study allowed us to observe the buckling of the honeycomb cells of a rail test (see Fig. 103. This is just a reminder of the results obtained in the previous section.

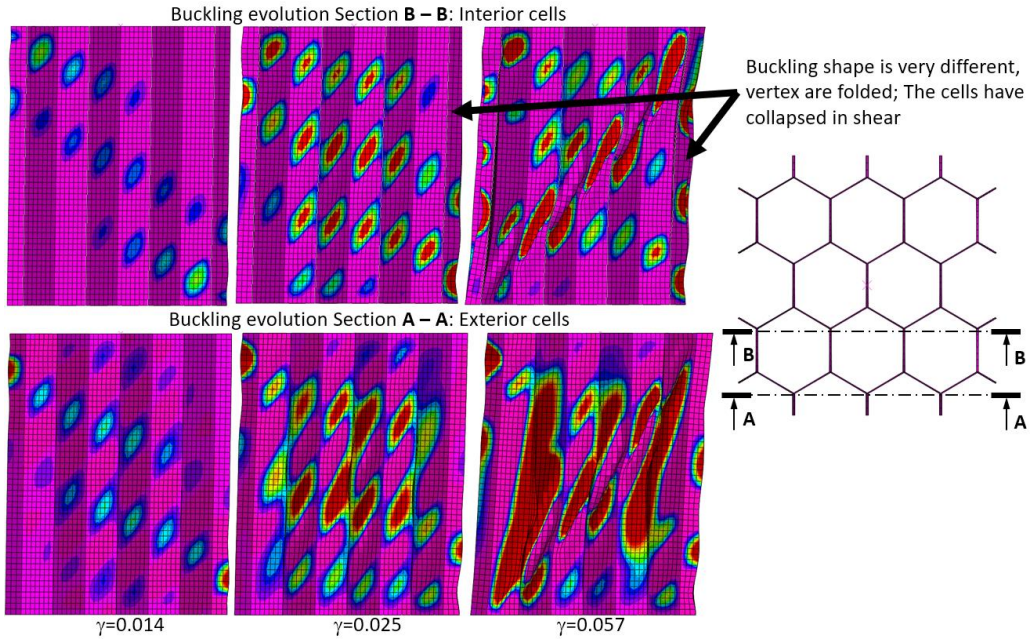

Fig. 103: Cell buckling experienced by the exterior and the interior of the specimen of the double lap test.

3.5.1.2 Case 2: Sandwich beam with potting resin at the borders in a three-point bending test.

Regarding the boundary conditions of the insert pull-out test, an inward force normal to the sandwich panel surface was applied, then the skins allowed the panel to be deformed in this direction.

Also, the potting blocked the displacement and rotation of the adjacent cells to it. In this sense, a three-point sandwich beam test could be similar to the insert pull-out test as it allowed deformation of the skins in the displacement direction.

To include the clamping effect of the potting in the beam specimen, the cells of the middle and the extremities of the sandwich beam were filled with potting resin. It was assumed that putting the potting at the extremities and in the middle of the sandwich beam would create similar conditions in all the cells between them.

A F.E. model of the sandwich beam with potting was created using Abaqus implicit (see Fig. 104). Because of symmetry, only the half of the specimen was modeled.

The mechanical properties of the Nomex® paper were the same as for the double lap tests. The number of cells was 3x3 (as for the model of the double lap test).

The mechanical properties of the skins were similar to those of the G939 woven plies: $E_x = E_y = 51169$ MPa, $E_z = 5000$ MPa, $\nu_{xy} = 0.09$, $\nu_{zx} = \nu_{yz} = 0.29$, $G_{xy} = 32400$ MPa, $G_{xz} = 3500$ MPa, $G_{yz} = 3500$ MPa.

The potting was considered as an isotropic material with $E_x = E_y = E_z = 1300$ MPa; this value is extracted from [5].

The honeycomb cells and the skins were bonded using shell to solid coupling. The rest of the coupled instances were bonded using tie constraints. Symmetry conditions were set at the middle of the beam to simplify the calculations.

A displacement of 2 mm in the Z direction was imposed in the middle of the beam, the displacement of the lower border of the sandwich was blocked in the Z direction to simulate a simple support as shown in Fig. 104.

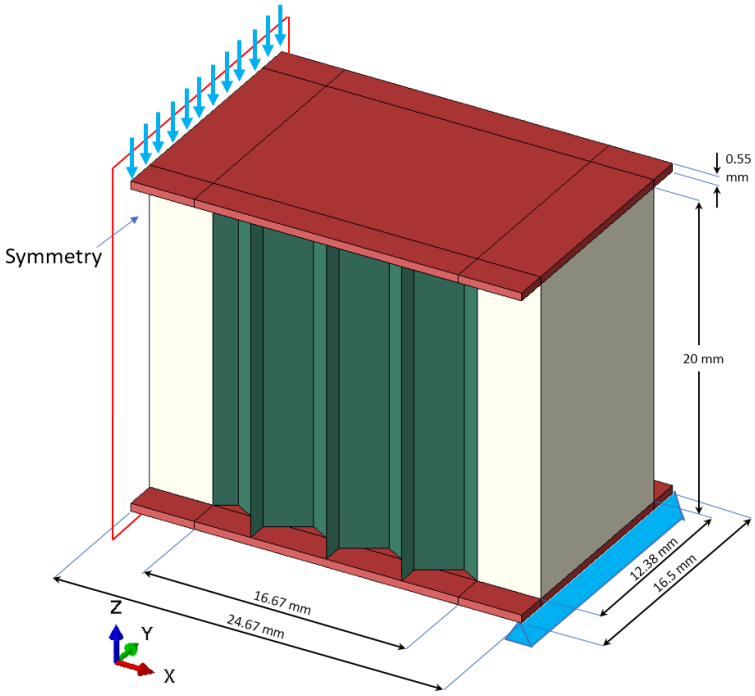

Fig. 104: Characteristics of the sandwich beam model with potting resin at the borders.

First, a buckling analysis was performed to determine the buckling modes of the structure, which were then incorporated into the model as initial imperfections for the analysis of the post buckling behavior of the structure.

The buckling of the cells outside and inside the specimen were very different (see Fig. 105). The exterior cells buckled towards the interior of the structure and collapsed similarly to their behavior in the rail test while, in the interior, the buckling pattern kept a stabilized shape even when the displacement was large. This may have been due to the free borders of the exterior cells while the interior cells were stabilized by the surrounding cells. For the section, B-B (Fig. 105), the buckling of the cells was mostly uniform, appearing three to four buckles in each cell wall.

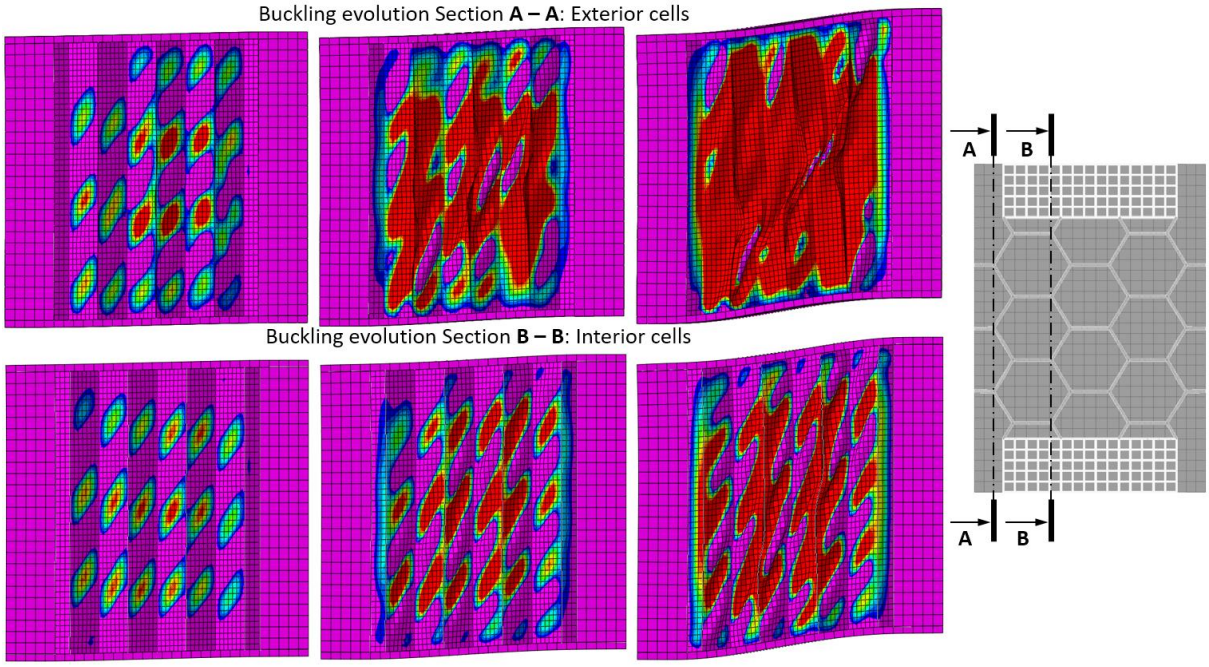

Fig. 105: Buckling of the exterior and interior cells of the sandwich beam with potting resin at the borders.

Also, it's interesting to see that the shape of the buckles is very similar to the shear buckling of the single wall cell. This suggest that the cell walls of the honeycomb near the potting are subjected to a purer shear state like in the rail test.

The average gamma deformation of the honeycomb core is not easy to evaluate because the deformations of the skins are not uniform near the potting (see Fig. 105). However, an approximation was obtained by neglecting the curvature of the skins. The average shear stress was obtained by dividing the applied force by the projected surface of the cells in the potting. The resulting curve is shown in Fig. 106.

The comparison of the results shows that the average shear moduli of the core on the FE model is slightly smaller than in the experimental test. This is, possibly, because for these boundary conditions, the skins are also subjected to flexural forces, and in consequence, part of the force imposed in the displacement is supported by the skins.

The potting simply created a more rigid boundary condition, allowing the honeycomb structure to take higher loads. It was also noticeable that the global response of the honeycomb with such a boundary condition was similar to the nonlinear law used by Bunyawanichakul [15] for the modeling of inserts, which is relevant. Although both F.E. models shown in Fig. 106 shows a different behavior, the fact that no failure criterion is implemented for the Nomex® paper, limits the conclusions that can be made about these differences, thus experimental tests are necessary.

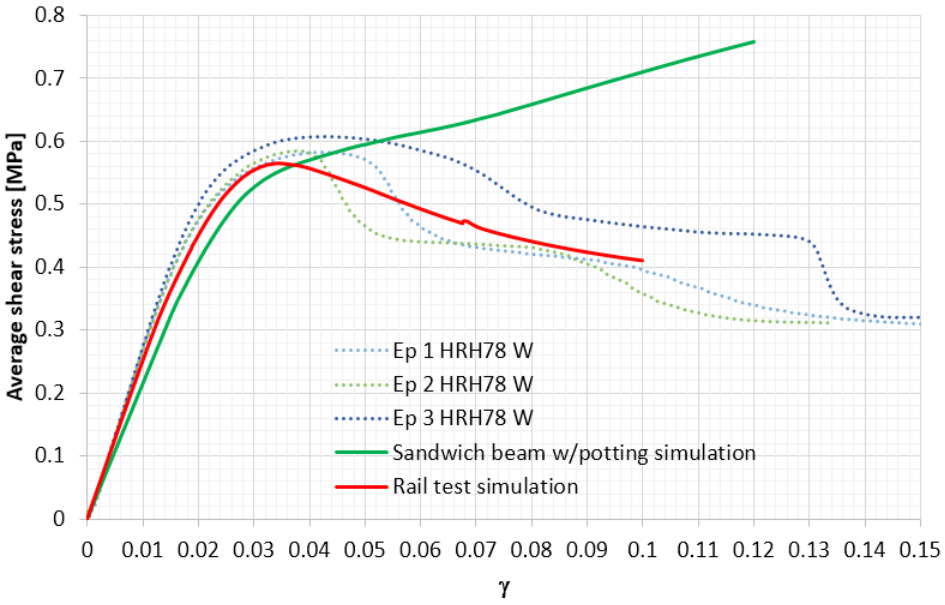

Fig. 106: Average shear stress vs gamma: Double lap tests and sandwich beam with potting at the borders.

An analysis of the rotation of the nodes of the honeycomb showed that the buckling configuration of the cells was more stable than in the rail tests, as the bifurcation point was slightly higher (Fig. 107).

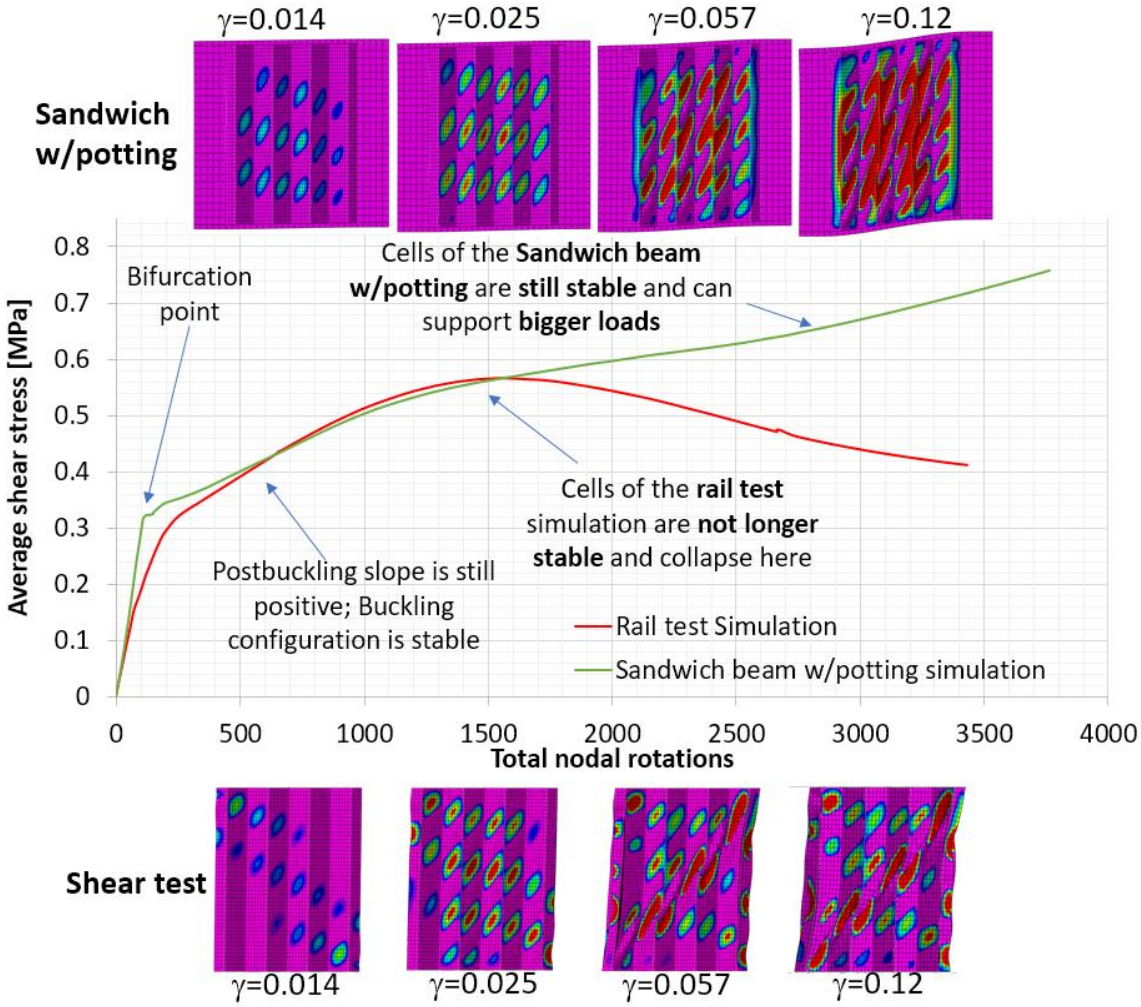

Fig. 107: Average shear stress vs total nodal rotation of the elements: Double lap tests vs sandwich beam with resin at the borders.

Also, the sandwich configuration with the potting apparently avoided the collapse of the cells by collapsing the vertical edges. In Fig. 105, the vertical edges remain almost straight, which is also consistent with the pattern obtained after a pull-out test on an insert (see Fig. 64). However, since only the plasticity and not the tearing of the Nomex® paper were considered in the model, the results are yet to be validated and compared to a real test.

3.5.1.3 Case 3: Honeycomb with potting and without skins

To study the importance of the sandwich skins of the sandwich for the buckling of the cells, the skins were removed from the model of the case two.

Instead of a simple support, the potting resin was clamped; no rotation or displacement was allowed. As for the previous model, symmetry was used to simplify the calculations. Also, a displacement of 2 mm was imposed on the upper surface of the middle potting. The same method of postbuckling analysis was followed as for the other models (see Fig. 108). The simulation showed that the core without skins buckled in a totally different way in comparison with the previous models.

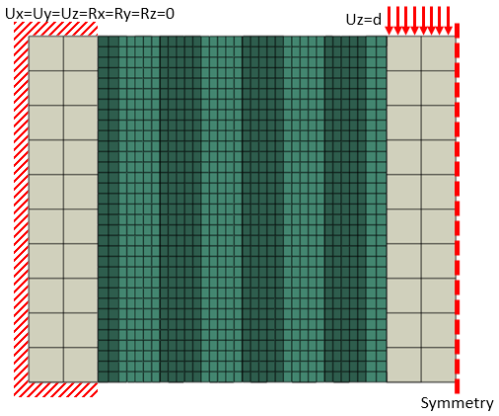

Fig. 108: Characteristics of the model of the honeycomb core without skins.

There was no local buckling of the honeycomb walls. Instead, the whole honeycomb structure buckled rather like an accordion. The average shear stress vs gamma curve was extracted using the same procedure as for the case two. The measured average shear moduli and core strength were very small in comparison to the manufacturer's data as can be seen in Fig. 109. This is logical because the shear stress implies the apparition of forces on the four sides and since the skins are not there, the force is fully provided by the honeycomb structure alone.

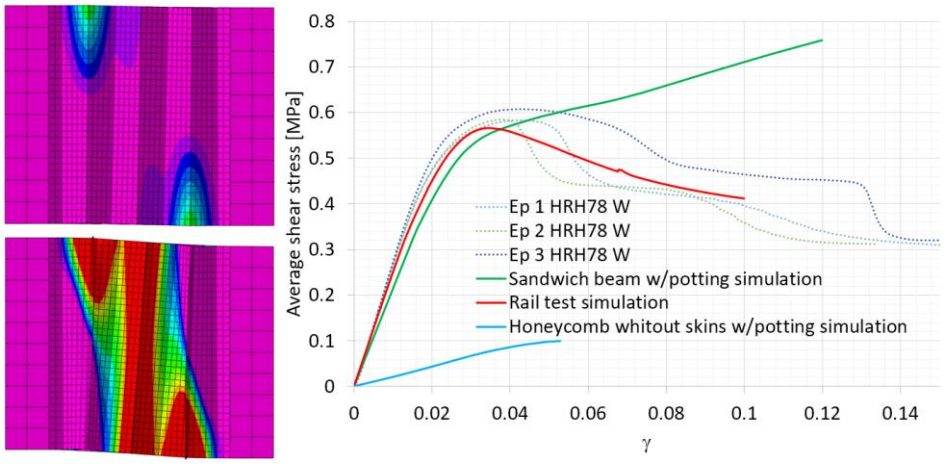

Fig. 109: Buckling of the cells and the average shear stress vs gamma: three cases.

3.5.2 Experimental study

The numerical study pointed out that the presence of a lateral stabilization such as an insert, combined with the stabilization provided by the skins, increases the shear strength of the honeycomb core as the cells were more stable.

Also, it was shown that the buckling of the interior and exterior cells were different, as the interior cells were also stabilized by the adjacent cells.

This effect was particularly accentuated when the lateral stabilization was present. Nevertheless, these conclusions were obtained by a F.E. analysis where the failure of the Nomex® paper was not considered, with several other assumptions as usual.

To validate such conclusions, the tests of the real structure under the considered boundary conditions are reported below.

Six text specimens (three in the W and three in the L direction) that were similar to those of the case two were fabricated and tested. Knowing that the lateral stabilization had more influence on the interior cells, the specimen was 7 cells thick; all dimensions are shown in Fig. 110.

The skins were made of G939 prepreg of 0.275 thickness. Two layers were used for the skins (oriented at 0°), so the total thickness was 0.55 mm.

The HRH-78 Nomex® honeycomb core used here was the same as in the previous tests. The potting is manufactured with araldite resin AV121 B mixed with 10 % of phenolic micro-spheres as indicated in [15].

The skins were bonded using Redux 609 epoxy adhesive film, two steps being used to avoid dripping of the glue.

The supports of the beam were 150 mm apart.

To measure the displacement of the skins, four small squares of glue were formed in the skins as shown in Fig. 111, then the specimens were painted with a speckle pattern on one side to measure the displacements of the skins.

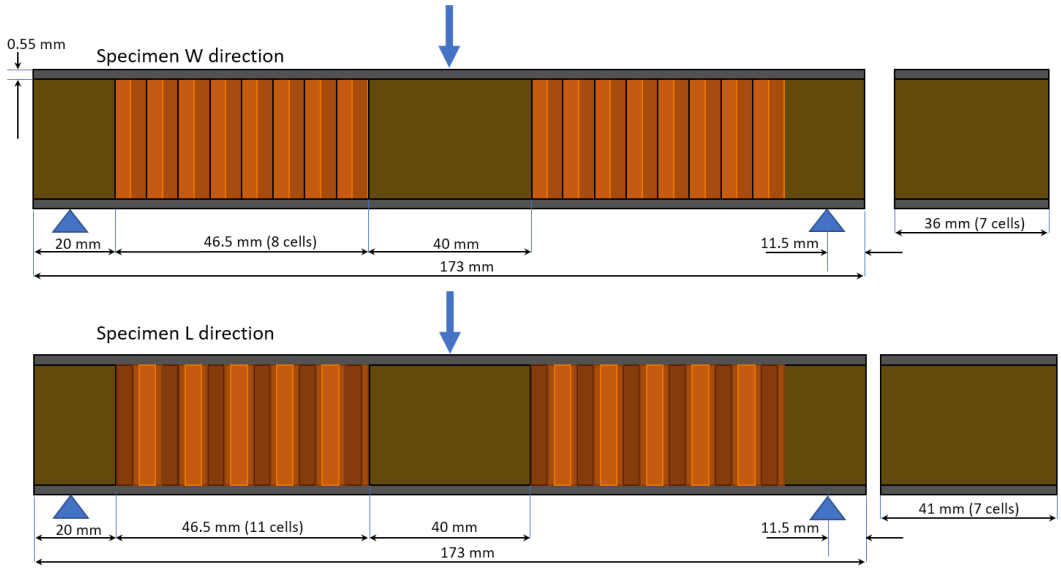

Fig. 110: Characteristics of sandwich beam specimens with potting at the borders.

The imposed displacement was measured with a 3D DIC system and an LVDT sensor. One photograph was taken every 600 ms.

The buckling of the exterior cells was not analyzed because the main concern of the study was to determine whether the honeycomb core could tolerate higher loads if it was stabilized by the potting.

An Instron 10 kN machine was used to test the specimens; a displacement of 1 mm/min was imposed and the force was measured directly by the machine.

The average shear stress and gamma were measured as in the study of the case two; the flexural deformation of the skins being neglected.

The beams failed at only one side (Fig. 111), so it was difficult to measure the average post failure behavior of the honeycomb core as only one side of the specimen was filmed.

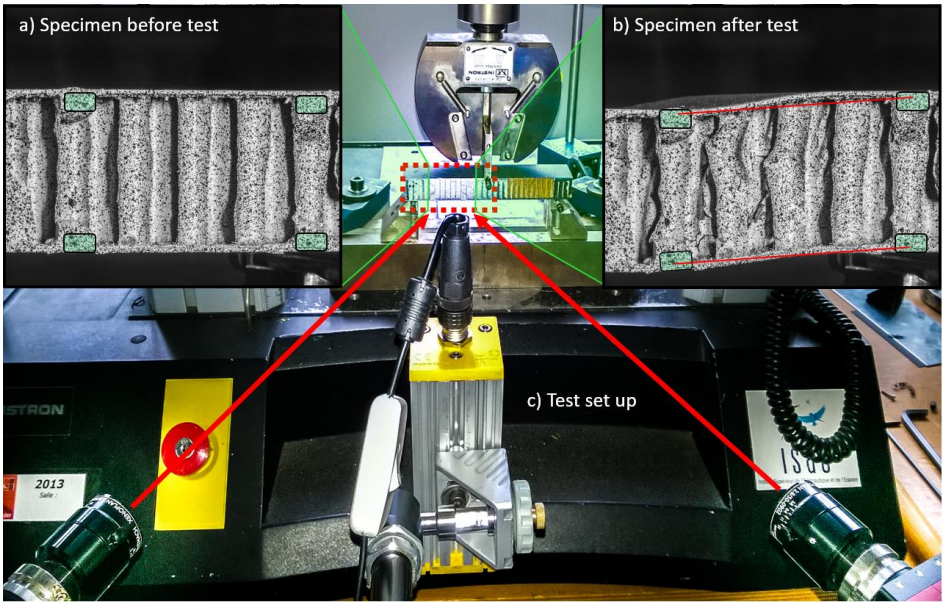

Fig. 111: Testing of the sandwich beam specimens with resin at the borders, before and after the tests.

The maximum shear stress for the W specimens was 0.63, 0.64 and 0.62 MPa for EP13, EP14 and EP15 respectively. The average value was 0.63 MPa

The maximum shear stresses for the L specimens were 1.0607, 0.9830 and 1 MPa for EP16, EP17 and EP18 respectively. The average value was 1.0145 MPa.

According to the manufacturer, the shear strength was 0.55 and 0.855 MPa for the W and L directions, respectively. The tests revealed that the shear strength increased by 15% compared to the values given by the manufacturer and 8% compared to the values of the rail tests for the W direction (see Fig. 112).

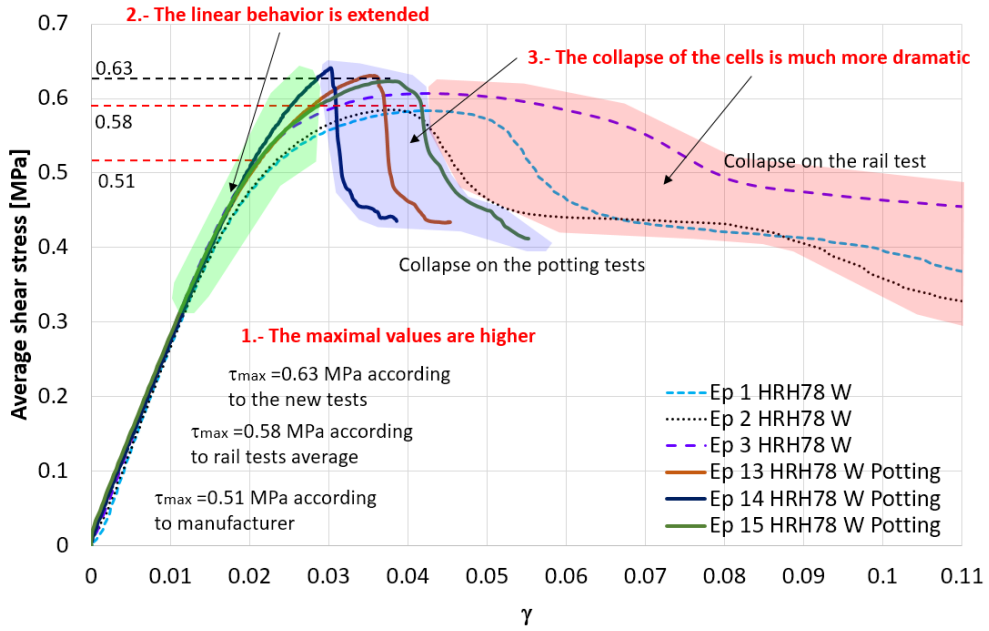

Fig. 112: Curves of the double lap tests vs the sandwich beam test with potting at the borders (W-Direction).

For the L direction, there was an increment of 18.6 % compared to the manufacturer's values and 35% compared to the rail tests presented previously (see Fig. 113).

Thus, the tests confirmed that the honeycomb core could support more shear stress when the insert and the skin are present.

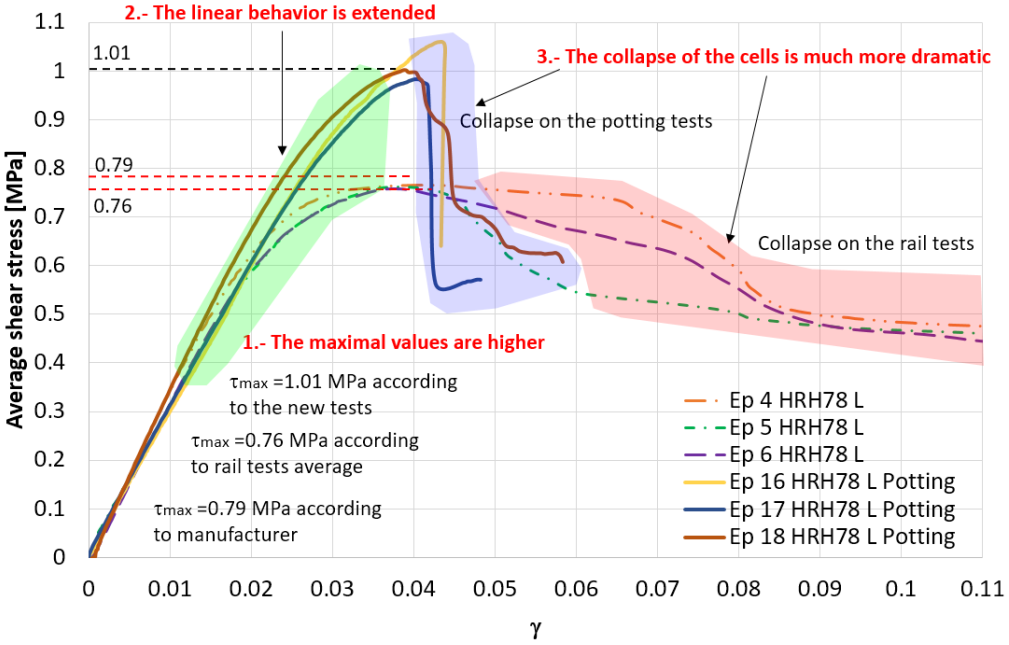

Fig. 113: Curves of the double lap tests vs the sandwich beam test with potting at the borders (L-Direction).

3.5.3 Conclusions on the boundary conditions

Depending on the load direction and the boundaries of the honeycomb, the failure scenarios may differ. The analysis presented in this section shows the strong influence of boundary conditions on the buckling loads and mode of the cells.

In classical tests, such as double rail shear tests or double lap shear tests, the main loading direction is orthogonal to the cell edges at the vertex of the hexagonal shape. Thus, after a postbuckling regime, the honeycomb fails by collapse of these edges in shear.

Since the boundary conditions of the core for the double lap shear or double rail shear tests (known as classical tests) are very different to the those of the cells near an insert, the strength allowables for both cases should be different.

The specimens with potting (see Fig. 110) mimic the inserts in sandwich panels quite well, the loading direction is parallel to these cell edges and the structure tolerates the shear buckling more easily, thus generating a gain in the allowable of up to 35 % in the L direction.

Also, endorsed by the present work, it can be said that, the shear strength values obtained by a rail test should not be directly used for the insert sizing analytical formulas since the strength of the insert is judged directly proportional to the shear strength of the core.

In other words, the strength of the insert should be proportional to the shear strength of the core when it is laterally stabilized by the potting, in any other way the allowable of the insert is underestimated.

There are several publications about insert design. Mostly, the dimensioning of inserts is obtained by analytical approaches that rely on the elastic shear properties of the honeycomb core [82] [29]. A general method is also provided by the Insert design book of ESA in [1] where the effective strength of the core is proportional to 1.36 times the shear strength of the core in the W direction, this is according to them, to consider the effect of the number of foils of W and L directions.

Although this factor is not very clear, it endorses the fact that the strength of inserts should be higher than the calculated one by considering only the W direction shear strength (obtained mostly by a rail test).

In contrast, this research may indicate that this effective shear strength factor should be of about 1.16 times the shear strength in the W direction (see Fig. 112) and it's not because of the foils on both W and L directions but because of the lateral stabilization provided by the potting over the honeycomb cells.

Heimbs [35], did several pull-out test on inserts and found that using the analytical approach of the ESA without considering the effective shear strength correction factor, the strength of the inserts is underestimated by 23 %. If the correction factor of the ESA of 1.36 is used, the strength of the insert is overestimated by 18.8 %. In contrast, if the correction factor issue of this research is used (1.16 instead 1.36), the shear strength is overestimated by 0.45 %. This same comparison procedure was applied to the inserts tested in the works of Kumsantia [48], Roy et al [33], Bunyawanichakul et al [8], and Song [40], the overestimation errors using the correction factor of the ESA (1.36) were 23.29%, 21.12 %, 32.63 % and 18.91% respectively. When the correction factor issue of this research was used (1.16) the errors where 4.25%, 2.42%, 12.15 %, and 0.55% respectively, which is much smaller and may indicate that this research could be very useful to explain and understand the errors of insert sizing methods.

Also, the ESA recommends testing the inserts in all cases, as the best method to determine their strength as Song et al did in [40]. However, this is not an approach that allows the properties of the insert to be predicted properly. Other methods based on F.E. modeling have been developed to reduce the oversizing of inserts. In [36] and [8] Bunyawanichakul developed an insert model based on the nonlinear behavior of the materials of the insert and the model was more able to capture the failure scenario. For insert design, the parameters that the designer should modify are only the radius and the potting material, while the thicknesses of the skins and the core material are selected by the main application of the sandwich panel.

In this sense, if designers tested their honeycomb materials with similar boundary conditions to those of inserts as explained before, they might find that their designs are oversized, which could lead to a reduction of the weight of the sandwich panel.

3.6 Reduced CDM modeling strategy of the nonlinear shear behavior of honeycomb cores

With the recent development of the computing technology and FEA software's, it is possible to create very refined models to analyze the mechanical behavior of the honeycomb structure as we did in the precedent sections. This has been done by several other researchers too.

Implicit and explicit codes were used to study several complex aspects such as the effect of borders and imperfections on the cell walls, the crushing and post impact behavior [76], [79], [83], the inserts [11], [33], [35], [36], the buckling of the cells on a three point test [68], [77], the debonding of the cell walls [84], among many others phenomena's.

In the recent literature, it's clear that, as the modeling of honeycomb cores gains in importance, the number of features that must be included increases too. Therefore, more and more high level of expertise and long development times are needed.

This is normal considering that the aim of the models developed for research purposes is to capture the more precise behavior of the cells, without paying too much attention to the simulation time, which becomes a secondary parameter.

However, these detailed approaches are not suitable for industry, where very large models are run and it is not practical to implement such detailed models.

Instead, the honeycomb cores are modelled as isotropic or orthotropic continuum materials with strength kept within the linear limit to avoid dealing with the structural nonlinear effects. This simplification is very arguable, also the shear strength of the honeycomb core is underestimated leading to oversizing.

Other researchers have developed very efficient approaches that capture the overall nonlinear behavior of the honeycomb core and could be simpler enough to be implemented for the industry.

They have proven that by understanding the structural behavior of the hexagonal cell it is possible to propose a simplified discrete model that captures the global nonlinear behavior of the honeycomb core under compression with very accurate results [78]–[80], [83].

However, in the literature, this strategy has not been explored to model the shear behavior of the honeycomb structure. In this section, this approach is developed using the results discussed on the previous parts of this chapter.

3.6.1 Analysis of the nonlinear shear stages of the honeycomb

The previous sections showed that when the honeycomb structure is subjected to shear, the overall nonlinear response of the structure can be explained by two different phenomenological stages; formation of local small buckles and then, the collapse. This is very similar for the W and L directions.

The first observation is that once the cells have buckled or collapsed, the structure shear stiffness is reduced permanently because of the plasticity and tearing of the Nomex® paper, as in Fig. 114; this is similar for the L direction too.

3.6.1.1 Effective stiffness after the buckling of the cells

The first stage consists with the formation of local small buckles which reduce the overall stiffness of the honeycomb structure but the structure remains elastically reversible, i.e. there is no structural damage. At this point the cells are buckled on a stable configuration and the behavior of the honeycomb structure is nonlinear but remains elastic.

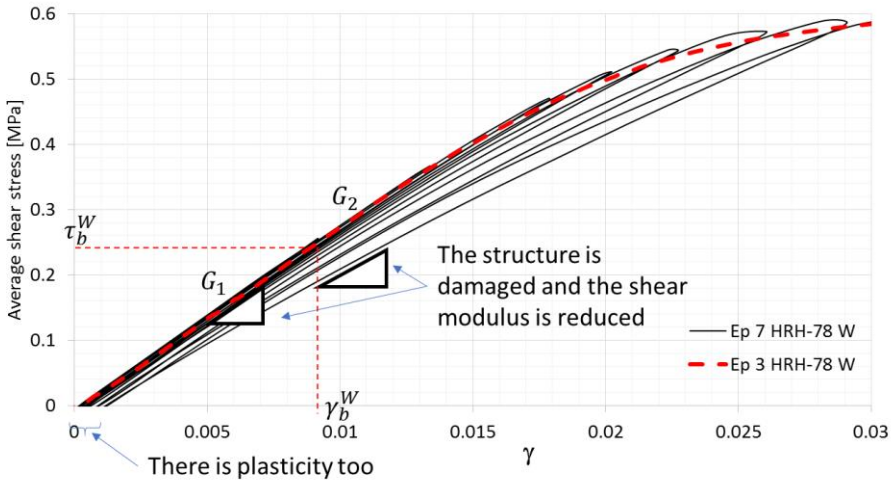

Fig. 114: Incremental cyclic testing of the HTH-78 core: damaged shear behavior of the honeycomb structure.

To isolate the effect of the buckling from the collapse, a numerical simulation was made considering the wall material was totally elastic (considering the hypothesis that the collapse of the cells was caused by the plasticity and breaking of the Nomex® paper).

Under these conditions, the postbuckling response of the structure could be considered linear (Fig. 115 line blue). The fillet effect between the initial and postbuckling state could be explained by the fact that the cells don't necessarily buckle all in the same way. It was detected that the cells start to buckle at τ_b^W=0.25 MPa (γ_b^W=0.0096).

If we consider the postbuckling response to be linear, it's possible to estimate the reduction of the shear stiffness of the structure once the cells are buckled. For very large deformations the final shear stiffness of the structure is equal to the postbuckling slope of curve. According to this, we obtain G_2=0.458G_1.

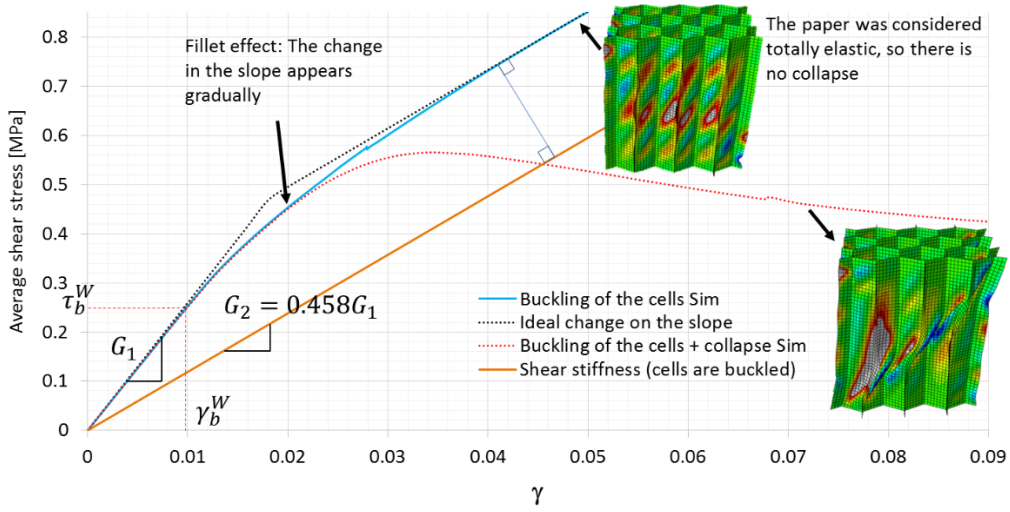

Fig. 115: Change on the shear stiffness of the structure: "Elastic buckling" of the cells vs "buckling & collapse" of the cells in the W direction.

The F.E. model of Fig. 115 is used to perform the same analysis for the cells oriented in the L direction. The reduction of the shear stiffness is evaluated at G_2=0.584G_1, also it was possible to determine that the buckling of the cells started at τ_b^L0.47 MPa (γ_b^L=0.014).

3.6.1.2 Statistical analysis of the collapse of the cells

The second stage is the collapse of the cells, which is characterized by the loss of capability of the cells to support higher loads. At this point the vertical vertex of the cells are no longer straights and folds, leaving a residual strength apparently caused by tearing of the paper.

In this stage, some cells collapse earlier and some other later because they are weaker or stronger respectively. This was determined previously (see chapter 2 section 3.3.4.2) using an Artificial Neural Network (ANN). The start of the buckling and collapse are shown in Fig. 116. Also, the average collapse of the cells is evaluated.

This collapse takes place after the cells have buckled. This study was only performed for the W direction but a similar scenario should describe the collapse for the cells oriented in the L direction.

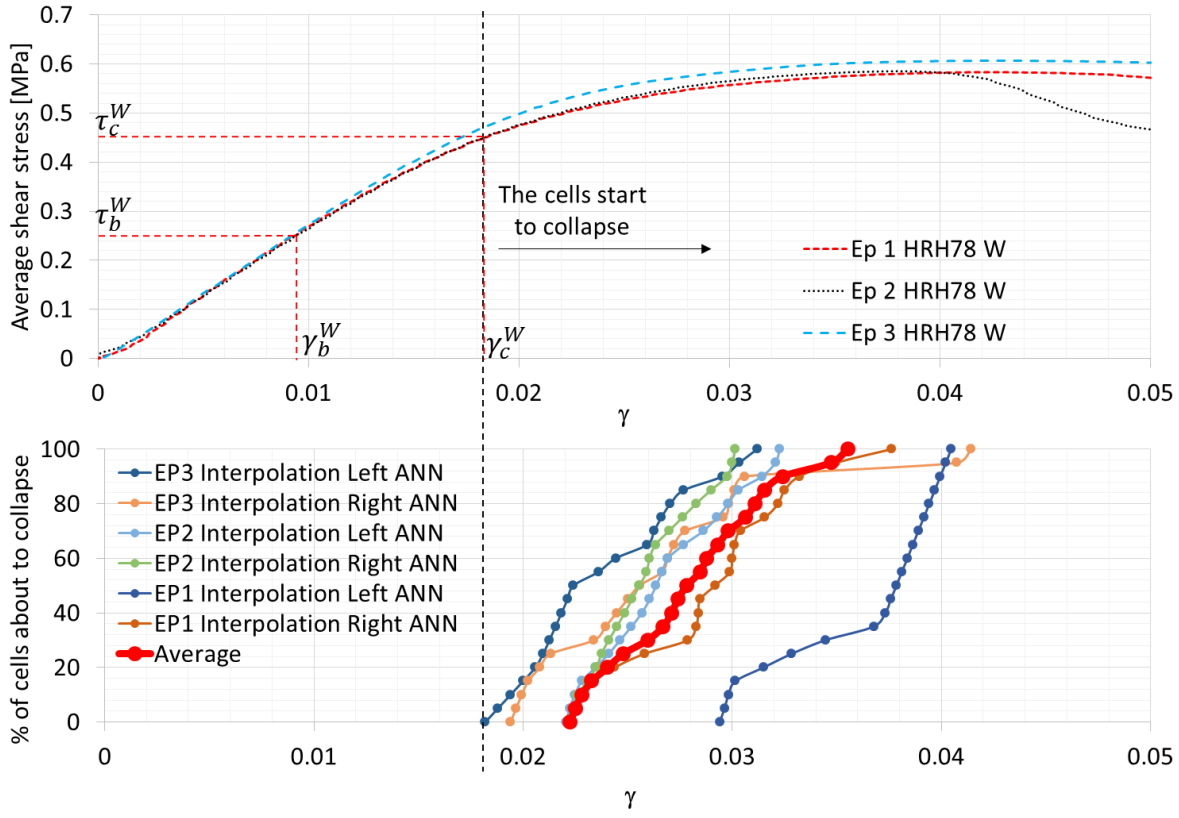

Fig. 116: Detection of the collapse of the cells in the W direction through an ANN (Reminder).

The fact that the cells collapse gradually can be described by a statistical distribution where the weaker cells collapse first and the stronger ones later. In Fig. 117 a Weibull probability distribution function is used to fit the experimental average result of the collapsing cells with a good correlation. The probability density (which is similar to the classical normal distribution of defects) is shown in blue.

Both observations indicate that it is possible to use a statistical approach to describe the buckling and collapse stages. Moreover, that a Continuum damage approach could be suitable to describe the behavior of Fig. 117, making an analogy with the modeling of CRFP where

statistical approaches are used to describe the breaking of fibers with different strengths, for instance [85].

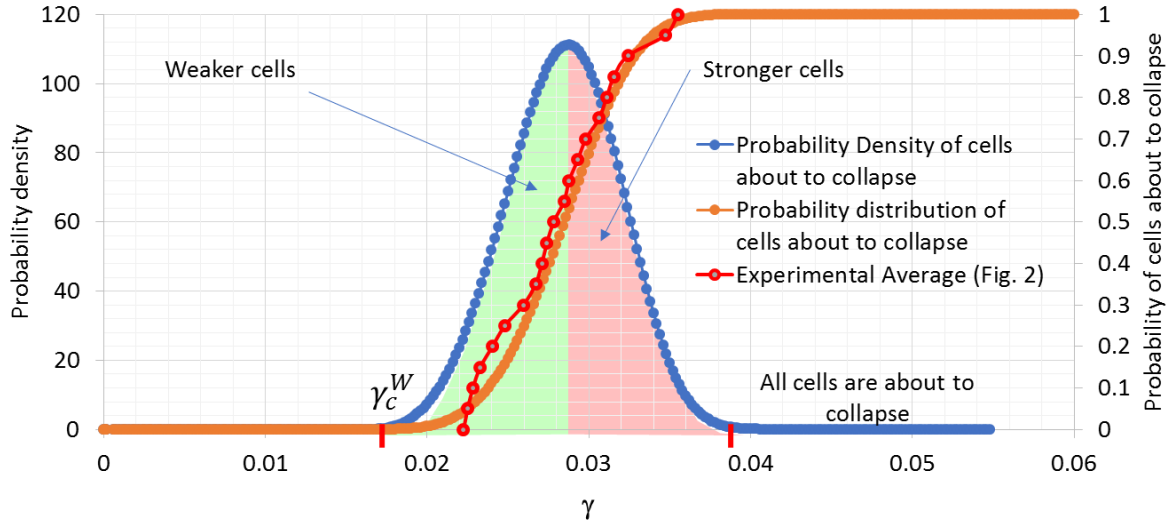

Fig. 117: Fitting of the curve of percentage of cells about to buckle with a probability distribution function; the probability density is shown in blue.

3.6.2 Decoupled CDM approach for the shear behavior of honeycomb cores

All the presented evidence suggests that one way to reproduce the nonlinear shear behavior of the Nomex® honeycomb core might be through a Continuum damage approach. We have proved that the effective stiffness of the core is reduced after the bucking of the cells. Also, after a certain point, the structure is damaged and the effective stiffness is reduced permanently. And of course, all of this happens gradually.

Thus, the next logical step is to represent all of this in an equation that can be used to describe the damage evolution of a homogenized volume, that represents the honeycomb.

Since the buckling and collapse of the cells has been described as two different stages, we will describe the shear behavior by superposing both. This is for both W and L directions.

3.6.2.1 Initial buckling

As explained before, as γ increases the final stiffness is reduced to 45.8% and 58.4 % of the initial shear moduli for the W and L directions respectively. Also, it's known that the cells start to buckle at γ_b^W= 0.0096 (τ_b^W =0.25 MPa) and γ_b^L =0.014 (τ_b^L =0.47 MPa) for the W and L directions respectively. Using the previous information, the equation 15 is proposed to describe the damage of the honeycomb structure.

$$D_b = A_b\left(1 - e^{-\langle\frac{\gamma-\gamma_b}{\lambda_b}\rangle^{k_b}}\right) \qquad 15$$

Where A_b represents the final stiffness reduction of the bucked honeycomb, γ_b is the shear strain that causes the buckling of the cells, thus the starting of the nonlinear behavior. The parameters A_b^W, A_b^L and γ_b^W, γ_b^L have been already determined, while λ_b^W, λ_b^L and K_b^W, K_b^L are chosen to fit the honeycomb response with totally elastic walls (see Table 9 and Fig. 114).

3.6.2.2 Collapse of the cells

Modeling the collapse of the cells may not be very simple because the nonlinear response of the honeycomb core is strongly influenced by the boundary conditions of the cells.

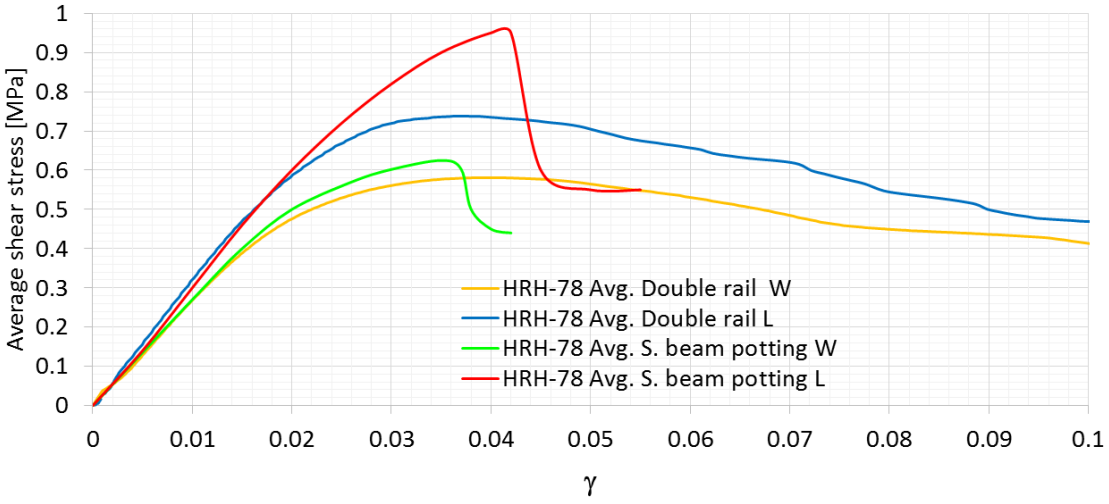

Fig. 118: Average curves of the "double rail tests" vs the "sandwich beam with potting at the borders".

Previously, we proved that the response of the rail test and the three-point sandwich beam with potting at the borders were not the same for the nonlinear response. For the sandwich beam specimens the loss of loading capability of the cells was caused by an apparently dramatic collapse of the cells (at $\gamma = 0.045$). While for the rail tests, the reduction of the loading capability was caused by a mix of tearing of the Nomex® paper and collapse of the cells (see Fig. 118).

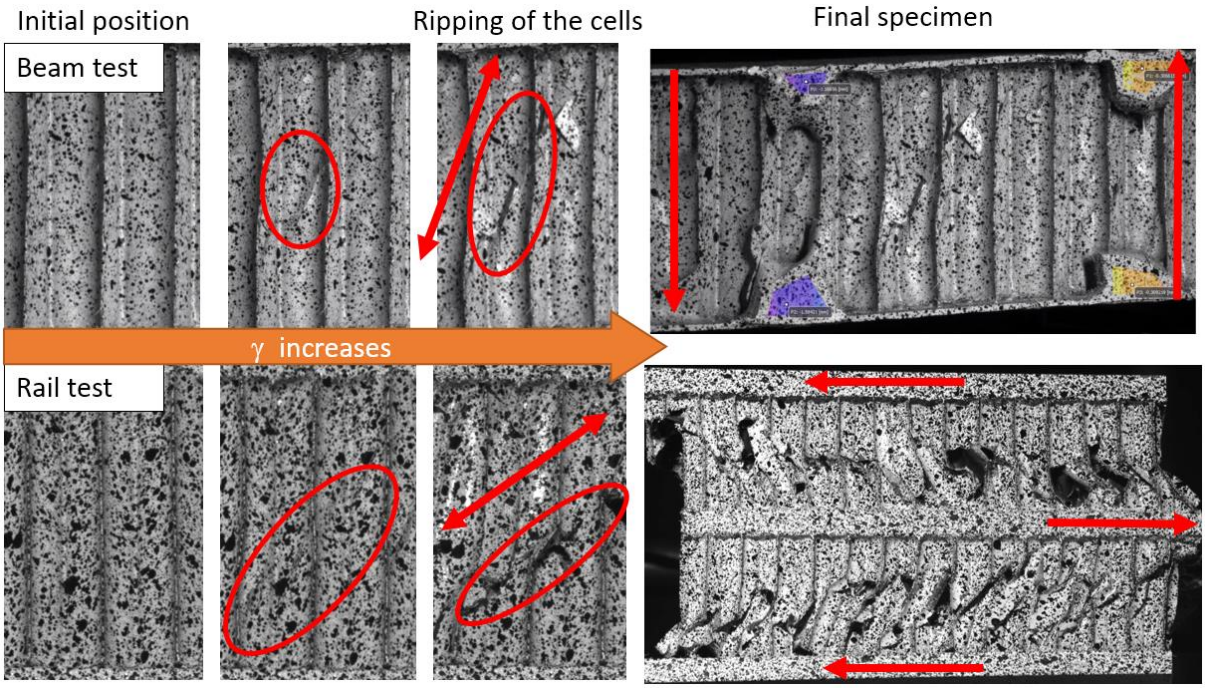

Fig. 119: Comparison of the cells ripping in a 3-point bending test with potting resin at the borders and a double rail test.

This can be explained as follows: Initially, the loading is distributed uniformly between all the cells. Then, when the cells are about to collapse, their stability decreases and their height is reduced, which has a similar effect as the necking for traction tests. Then, the fragile stability

of the cells combined with the necking effect and the fact that the skins are thin, allows the cells to collapse individually or by zone. Therefore, the shear deformation is concentrated where the first cells collapsed (see Fig. 128). Also, the collapsing and ripping of the paper occurs very quickly, leading to a sudden failure and a residual shear stiffness (see Fig. 119).

In the other hand, for the rail tests, the skins are stiffer and the displacement is imposed directly on them. Therefore, all the cells clamped to the skins are subjected to the same imposed displacement. Consequently, all the cells are subjected to shear at the same time, which remains the same even after postbuckling.

For this reason, the modeling of the collapse stage with different boundary conditions presents different behaviors, and therefore they should be done separately.

Here, a general approach to model the collapse phase is presented. It is assumed that the cells collapse gradually due to the fabrication defects and this is represented by a Weibull distribution function. Also, we suppose that the loss of capability to support loads after the collapse of the cells can be represented with a coefficient A_c. If A_c= 0 there is no collapse but if A_c=1 then the cells capability to support any load is totally lost. So, the residual stiffness can be represented by 1- A_c. This approach should describe the shear nonlinear behavior of the honeycomb under the rail and the three-point testing boundary conditions (equation 16).

$$D_c = A_c\left(1 - e^{-\langle \frac{\gamma-\gamma_c}{\lambda_c} \rangle^{k_c}}\right) \qquad 16$$

The γ_c value is determined experimentally (Fig. 116); the W oriented cells start to collapse at about γ_c^W = 0.018, unfortunately there is not enough data available for the L direction. The rest of the other values are chosen to fit the experimental curves (see Table 9).

		W direction	L direction
Initial buckling stage	A_b	0.458	0.584
	λ_b	0.029	0.04
	γ_b	0.0096	0.014
	k_b	1	1
Collapse stage	A_c	0.85	0.85
	λ_c	0.044	0.046
	γ_c	0.018	0.018
	k_c	1.9	1.45

Table 9: Values used to fit the experimental curves of the HRH-78 tests.

3.6.2.3 Superposition of both stages

Now that both initial buckling and collapse stages have been represented with a damage variable, it is possible to describe the overall response of the structure, this is made through equation 17.

$$\tau = G\gamma(1 - D_b)(1 - D_c) \qquad 17$$

The values of Table 9 allow to reproduce the overall nonlinear behavior of the honeycomb structure under shear stress with a good correlation (Fig. 120).

The decoupling of the buckling and collapse stages, on the shear response of the honeycomb, allows identifying the two phenomena separately. This is very practical because it enables to filter the behavior of the cells in very clear stages, elastically buckled, buckled with damage or even collapsed, all of this in a very simple manner.

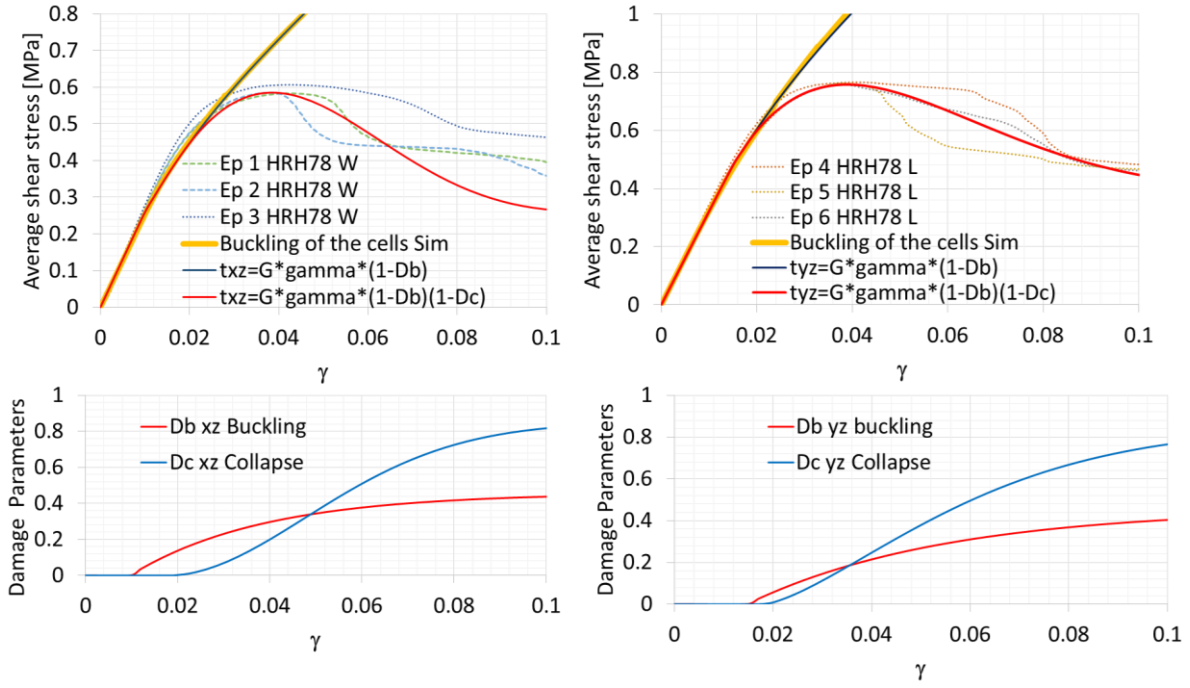

Fig. 120: Fitting of the experimental rail shear testing curves of the HRH-78 in the W and L directions using the CDM proposed approach.

Both buckling and collapse stages are represented by probability distributions even if the values that are chosen to fit the experimental results may not be the only possible combination.

However, the parameters with physical meaning such as the starting of the buckling or collapse, or even the shear stiffness reduction are determined experimentally or through a numerical analysis, thus, they should be consistent. The rest of parameters that are selected to fit the experimental curves (λ_b and k_b) have a statistical meaning that can be interpreted by looking at the shape of its density distribution function (equations 18 and 19), for the buckling and the collapse stage respectively.

$$Density\ of\ D_b = \frac{k_b}{\lambda_b}\left(\frac{\gamma-\gamma_b}{\lambda_b}\right)^{k_b-1} e^{-\left(\frac{\gamma-\gamma_b}{\lambda_b}\right)^{k_b}} \quad 18$$

$$Density\ of\ D_c = \frac{k_c}{\lambda_c}\left(\frac{\gamma-\gamma_c}{\lambda_c}\right)^{k_c-1} e^{-\left(\frac{\gamma-\gamma_c}{\lambda_c}\right)^{k_c}} \quad 19$$

The shape of the probability density that represents the initial buckling (k_b=1) suggests that the cells buckle at γ_b^W= 0.0096 all sudden but then buckling rate is almost constant (Fig. 121). This indicates that the buckling of the cell walls may not be very sensitive to the initial defects. In other words, most of the cells buckle at a similar shear stress, or γ, regardless of the initial defects. Thus, the initial buckling of the cells should be more sensitive to the structural shape.

Regarding the distribution of the collapse of the cells, the shape of the density function (k_c^W=1.9 or k_c^L=1.45) suggests that some of the cells collapse earlier and some later (as expected). This could mean that this stage is more sensitive to the initial defects (Fig. 121), especially when the cells are loaded in the W direction.

This could be useful to understand how imperfections affect the honeycomb structure. For example, in perforated aluminum honeycomb cores used for aerospace applications, on

which a very tiny hole is drilled in the middle of the cells. Since the initial buckling stage is not sensitive to initial defects, the shear moduli should remain unaffected. However, since the collapse stage is sensitive to imperfections, this tiny hole should reduce the shear strength. Although these are only assumptions that are still to be confirmed.

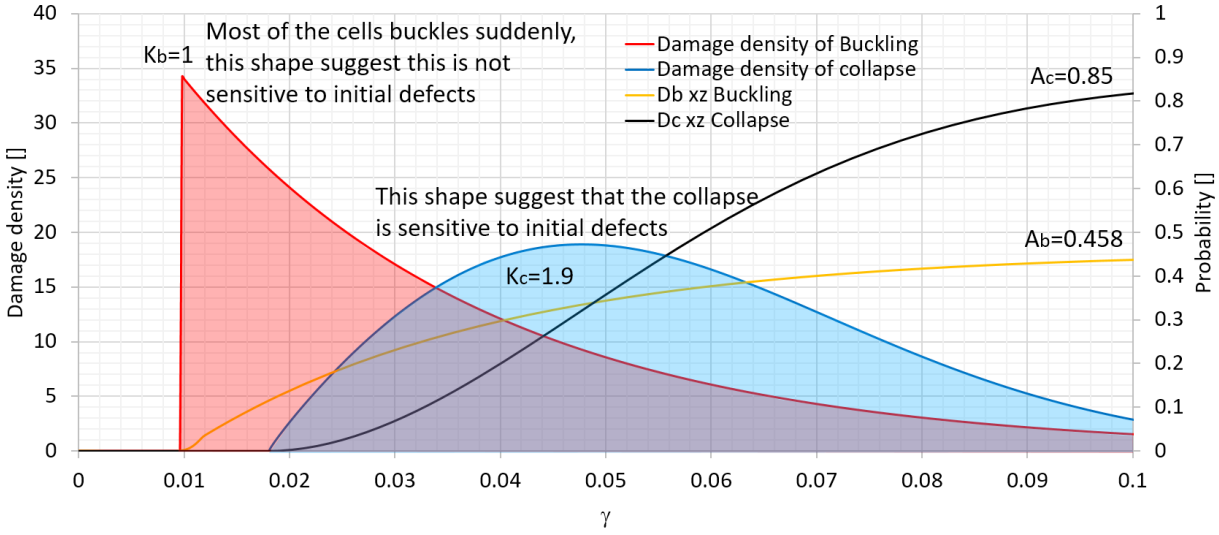

Fig. 121: Density distribution curves representing the buckling and collapse stages of the cells.

3.6.3 Validation of the proposed approach

The next step was to validate the proposed CDM approach into a F.E. model. For this, the honeycomb is represented only with volume elements, as if it were an orthotropic material.

However, since the honeycomb core presents a softening behavior after the collapse of the cells, there can be an undesired damage localization depending on the size of the mesh. To avoid this effect, the core is represented with only one element through the thickness (C3D8) and the length and width size of the elements are adjusted to the radius of the honeycomb alveolus.

The proposed damage laws were implemented into an UMAT subroutine. To take into consideration the nonlinear elastic behavior of the honeycomb core, the damage activation function records the damage only after the nonlinear elastic limit is reached. As the nonlinear behavior of the double rail and potting beam specimens are different for the collapse stage, both models are presented separately.

3.6.3.1 Double rail test specimen

For this specimen (Fig. 122), the skins were made of aluminum (E=75000 MPa) of 5 mm of thickness. Also, the core was glued to the skins using a Redux 609 epoxy film and therefore in the simulations the pieces are bonded using a tie constraint.

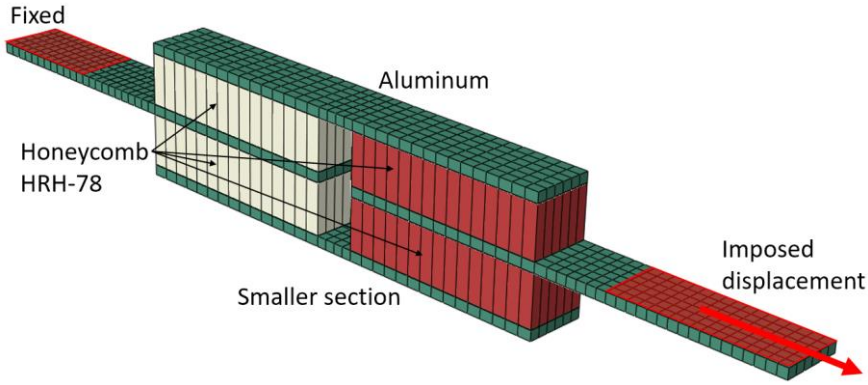

Fig. 122: Mesh of the double rail test model.

The core was oriented in the W direction. To model the HRH-78 Nomex® honeycomb core, the data from [70] and the orthotropic mechanical properties given by the manufacturer are used; $E_z = 125\ MPa$, $v_W = 0.02$, $v_L = 0.02$, $G_W = 24\ MPa$ and $G_L = 32\ MPa$. Also, it is considered that the honeycomb remains undamaged until $\gamma_W = 0.024$ and $\gamma_L = 0.023$ for the W and L directions respectively. The values of Table 9 are used to include the buckling and collapse of the cells for the shear stiffness reduction. Finally, a cyclic displacement was imposed to the test specimen, this consists of increments of 0.25 mm each until 2.5 mm is reached. The comparison of the numerical and experimental results is shown in Fig. 123 (the variations of the nonlinear are caused by the flexural deformation of the specimen too).

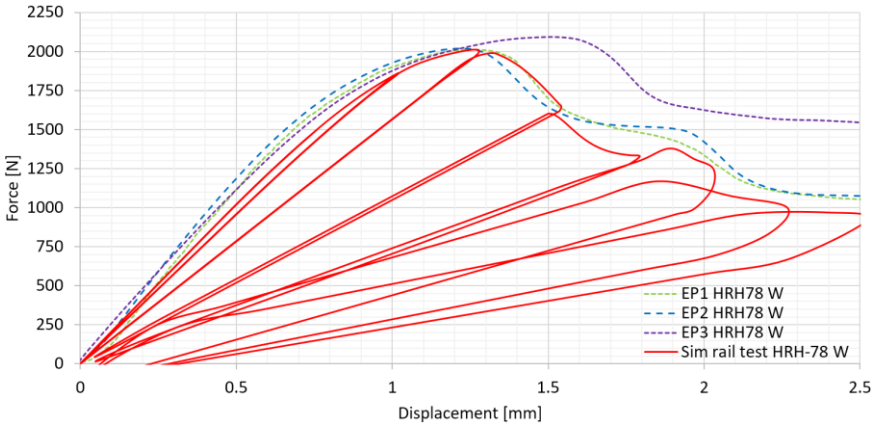

Fig. 123: Force vs displacement curves of the double rail tests: Experimental vs numerical results for the W direction.

The time step is of 1, the maximum increment is 0.001 and the required number of increments is 1031. The simulation runs under 8 CPU's during 12 min 34 s. There were some convergence issues when the negative slope of the core material started to appear. Nevertheless, the results show a good agreement with the experiments.

3.6.3.2 Three-point test with lateral stabilization specimen

For the laterally stabilized sandwich beam test (Fig. 124), the skins were made of two plies of the G9389 (carbon woven/epoxy) with a total thickness of 0.55 mm, the core and the skins were glued using the same adhesive as the rail tests. The potting was made of Araldite AV-121 N mixed with 10% of ponderal weigh phenolic micro-spheres (E=1312 MPa). The core was oriented in the L direction.

The same orthotropic stiffness values for the core as for the rail tests were used. Since the boundary conditions were different, the general nonlinear response should be different too.

Unfortunately, there is no experimental reference for the nonlinear elastic limit. So, it was supposed to be the same as for the previous case. This is arguable, however, it's important to highlight that the main difference is not in the elastic regime, but in the collapse stage.

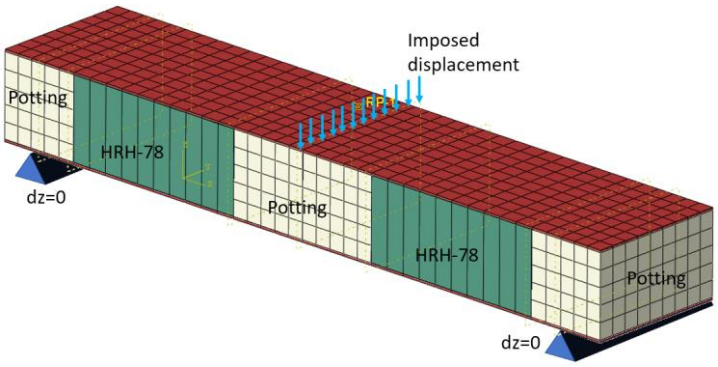

Fig. 124: Mesh of the sandwich beam with potting at the borders.

The lateral stabilization provided by the potting on the HRH-78 causes several differences that should be taken into consideration.

The linear limit of the honeycomb is increased (see Fig. 118). Moreover, the collapse happens later than in the rail tests but also in a quicker way.

By using the proposed CDM approach it's possible to modify only the collapse parameters to fit the experimental results. The collapse initiation is set to appear later than for the rail tests, at γ_c^L=0.039 (γ_c^L=0.018 for the rail tests). The effect of the sudden collapse is included by selecting a small-scale parameter λ_c^L=0.005 (λ_c^L=0.046 for the rail tests). The resulting behavior law is shown in Fig. 125 under the label of law 1.

Unfortunately, the proposed law causes convergence problems when the simulation is run. This is because of the very pronounced negative slope at the collapse of the cells, a common problem when an implicit solver is used.

To avoid this, another technique is used to reproduce the desired curve. First, the initial behavior of the cells (only the initial buckling stage) is fitted using equation 15. Then, instead of using equation 16 to fit the collapse of the cells, equation 20 is used, which reduces the shear stiffness of the core immediately to simulate the sudden collapse of the cells.

$$A_c = \begin{cases} 0.0 & if \quad \gamma \leq \gamma_c \\ 0.9 & if \quad \gamma > \gamma_c \end{cases} \qquad 20$$

This last approach is equivalent to pick a small-scale λ_c^L and to consider A_c=0.9 in equation 16. This technique is widely used as it represents the loss of stiffness and maintains a positive slope on the behavior of the material, avoiding the problems of convergence created by negative slopes. The values used for this approach (see Fig. 126) are shown in Table 11.

		W direction	L direction
Law 2 (lateral stabilized core, Fig. 126)	A_c	0.9	0.9
	λ_b	0.045	0.073
	γ_{b0}	0.018	0.017
	k_b	1.05	1
	γ_c	0.038	0.044

Table 10:Values used to fit the experimental curves of the HRH-78 three point tests with lateral stabilization.

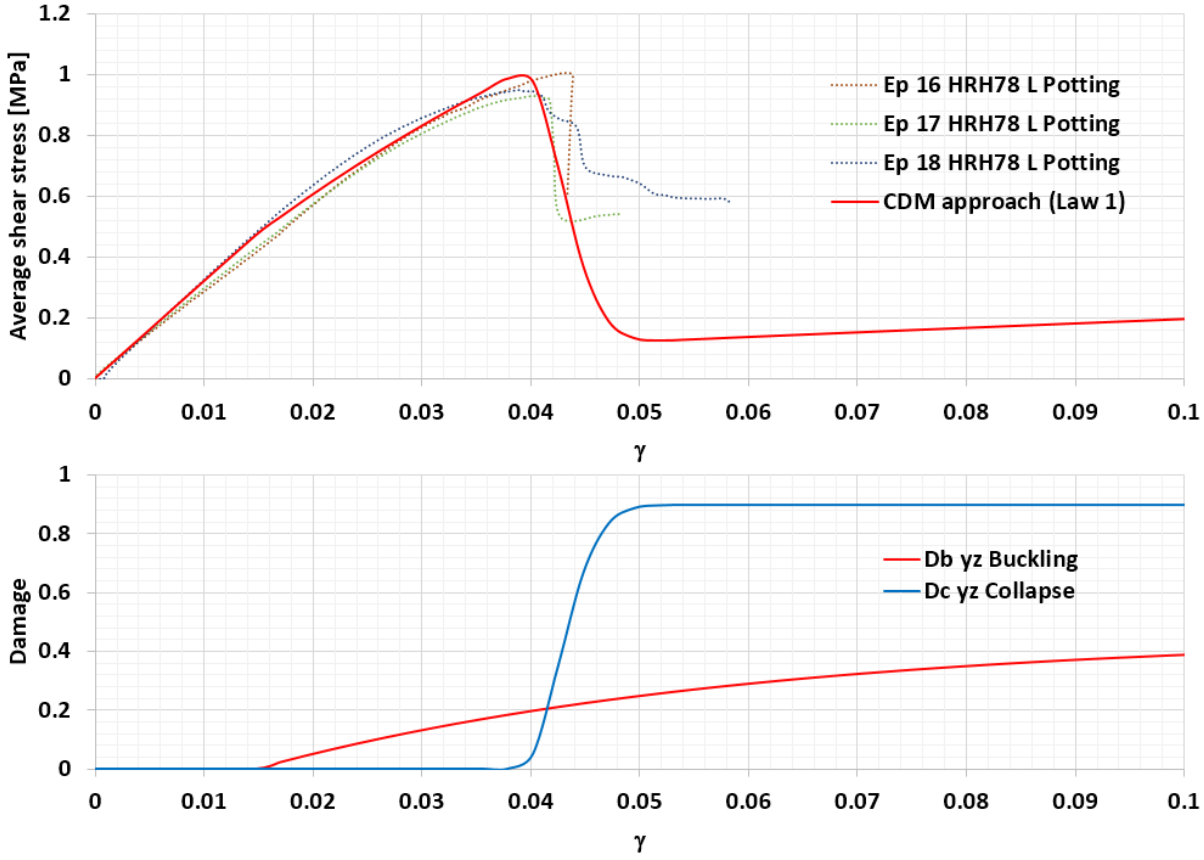

Fig. 125: Fitting of the experimental sandwich beam with potting at the border in the L direction using the CDM proposed approach that creates convergence issues.

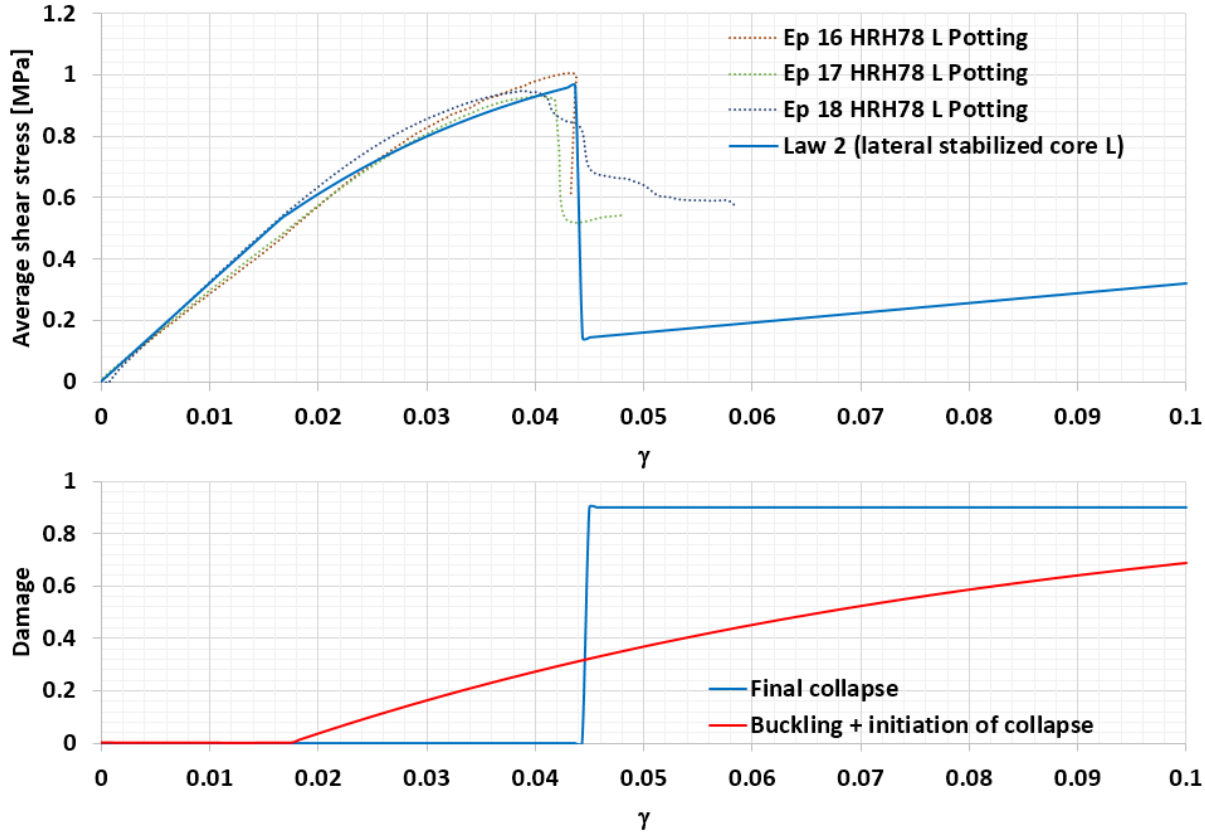

Fig. 126: Fitting of the experimental sandwich beam with potting at the border in the L direction; law 2 avoids convergence issues (see Table 10).

A comparison of the experimental and numerical results of the testing of the sandwich beam specimens can be made. In Fig. 127 the force vs displacement curves are compared showing a good correlation even for the nonlinear behavior, also the failure scenario between the numerical and experimental results are very similar (see Fig. 128) proving that this technique gives good results.

The time step is of 1, the maximum increment is 0.01 and the required number of increments is 105. The simulation run under 8 CPU's during 2 min 25 s. In general, the results show a good correlation with the experiments.

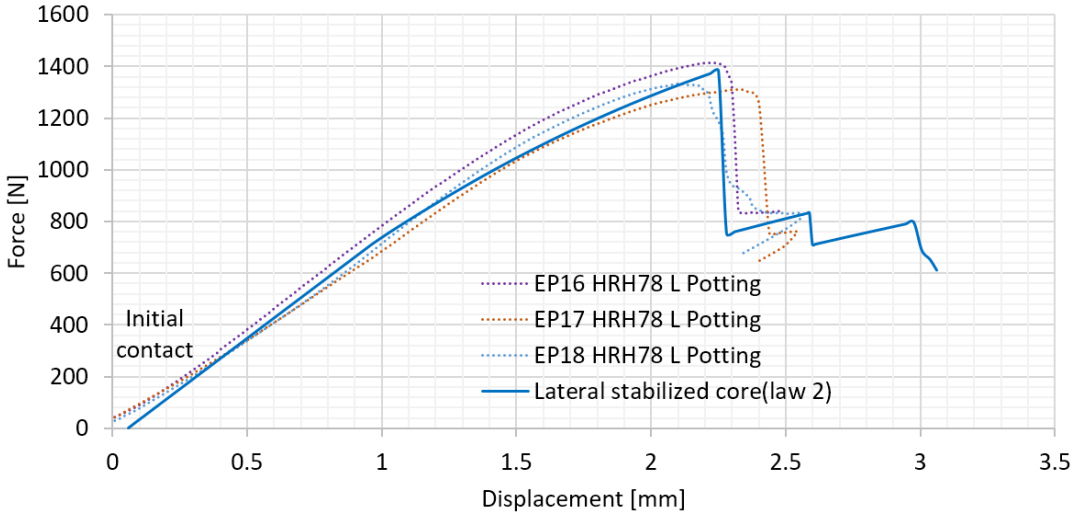

Fig. 127: Force vs displacement curves of the sandwich beam tests: Experimental vs numerical results.

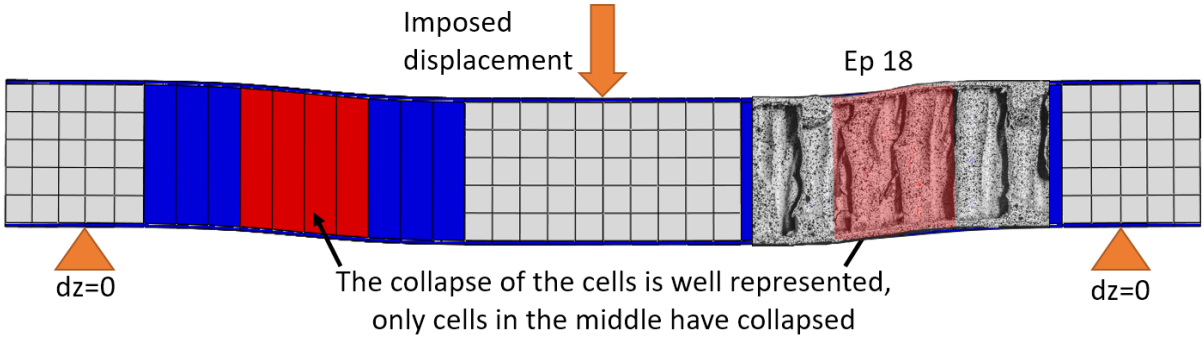

Fig. 128: Comparison of the failure scenario of the numerical model vs real tests, the results are consistent.

3.6.3.3 Discussion about the modeling strategy of both specimens.

The behavior laws that were used to represent the shear behavior or the HRH-78 honeycomb core for the double rail tests and the sandwich beam with potting were very different. Initially, the behavior in both cases was identical but the collapse stage was very different. It seems that the lateral stabilized cells follow the case when the cells are totally elastic, until they collapse at γ_c^L=0.039 (Fig. 129).

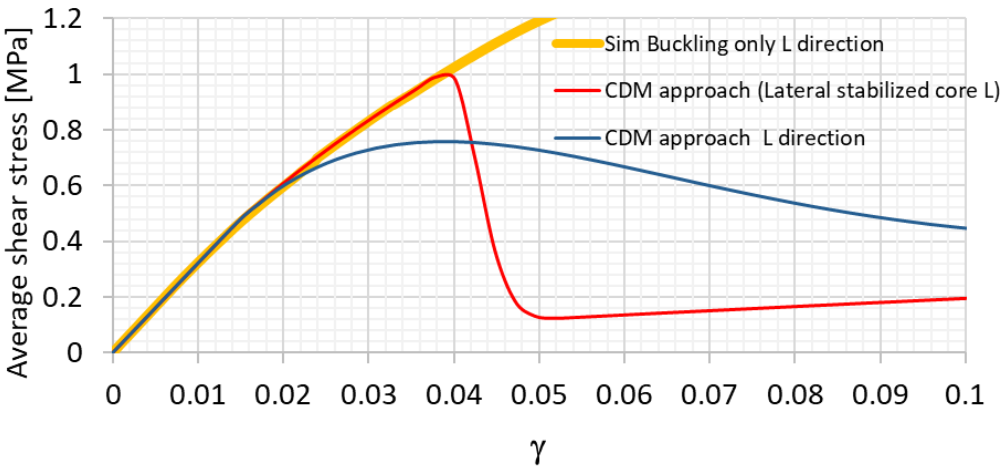

Fig. 129: Force vs displacement curves of the sandwich beam tests: Experimental vs numerical results.

This makes clearer that the boundary conditions are very important for the honeycomb core. For both studied cases, this is relevant because when the cells are laterally stabilized, their shear strength is increased but also the collapse arrives later and appears suddenly. If these two effects are not considered within the design phase, the sandwich structure may be oversized, and the ruin modes will not be predicted accurately.

To show this, the model of the sandwich beam with lateral stabilization is retaken. The obtained results (see Fig. 127) using the damage law proposed in Fig. 126 and Table 10 will be compared to the results using another damage law.

For this new damage law, the increase of the shear strength is taken away. However, the cells still collapse earlier. The used values are shown in Table 11 and the comparison of both laws is shown in Fig. 130-a.

		W direction	L direction
Law 3 (see Fig. 130)	A_c	0.9	0.9
	λ_b	0.04	0.044
	γ_{b0}	0.017	0.017
	k_b	1	1
	γ_c	0.038	0.045

Table 11:Values used to fit the experimental curves of the HRH-78 three point tests with lateral stabilization with no increment in the shear strength.

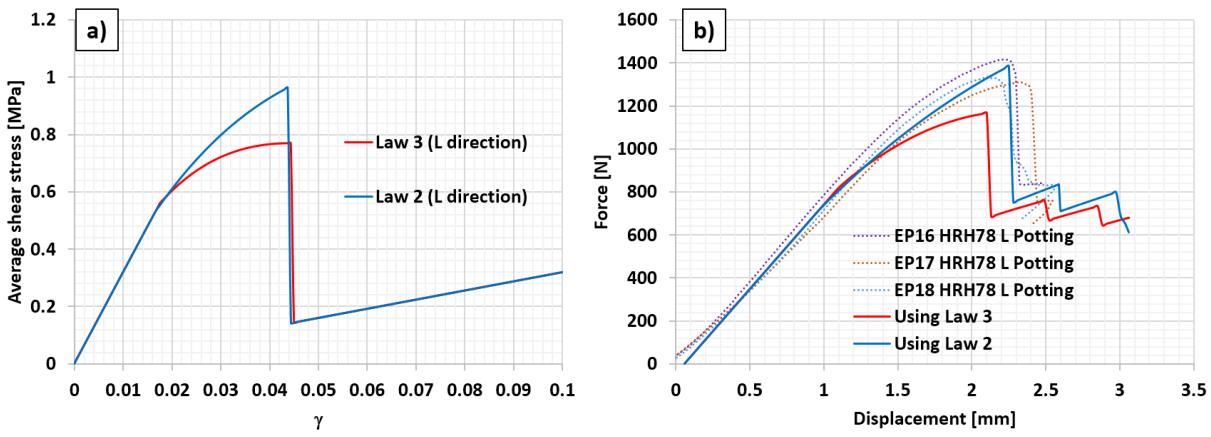

Fig. 130: Two different laws are used to model the shear behavior of the HRH-78 cells, with and without the effect of the lateral stabilization of the cells.

When the effect of the increase of the shear strength is not considered, the numerical results do not show a good agreement with the experimental curves. The maximal force is smaller and the breaking of the specimen arrives earlier than it should (see Fig. 130-b).

Finally, it is important to mention that the simulation time required for these models is very low in comparison with the refined models. The detailed model consisted of only 8 alveoli, the required simulation time of an imposed displacement of 1 mm in the L direction was of 3.28 hrs. (197 min.). In comparison, for the double rail model 300 alveoli were represented using the proposed approach and a total displacement of 27.5 mm was imposed to the specimen, the required simulation time was only 12.5 min.

3.6.4 Conclusions

This strategy enables a set of different physical effects related to the buckling and collapse stages of the cells to be represented in a very simple and practical way.

The behavior of the honeycomb structure presents a nonlinear elastic behavior beyond the buckling point of the cells and the shear strength can be increased by stabilizing the cells laterally. This is explained by reversible postbuckling as in aerospace structures.

The inclusion of this feature in sandwich panel design should be interesting as it reduces the weight. Also, it can be of interest for inserts, as they are designed using analytical formulas that are based on the shear strength of the honeycomb core.

One of the advantages of the modelling strategy presented is allowing to consider the nonlinear effects of the honeycomb structure, such as the buckling and collapse of the cells. Therefore, providing an effective and useful method for the detection of collapsed cells, to avoid it. Moreover, all of this for a very low computational cost.

This is very advantageous in comparison with the very detailed models that can be found in the related literature (see for example [11], [12], [32], [76]), where the computational cost for very small models is huge but also because every cell should be inspected to determine whether it is damaged or collapsed, which generally takes a lot of time.

Another advantage is it require less expertise, and so the costs of the embodiment design stage are decreased, as the computational and development times can be reduced dramatically.

The proposed approach is supported by several observations made after a very detailed analysis of the shear behavior of the honeycomb core. It is interesting to mention that the inclusion of probability functions allows the average general behavior of this type of cellular structure to be well described.

The assumption of using only one element through the thickness helped to reduce the simulation time and to include the post buckling softening behavior of the honeycomb structure, avoiding the damage localization problem. This feature is very debatable. The main drawback is it excludes the possibility of studying the buckling of the cell walls or collapse of the cells in detail, as the honeycomb structure is replaced by an orthotropic virtual material. However, from a practical point of view, obtaining a detailed description of the buckling or the collapse shape of the cells is not the main preoccupation in most cases, e.g. when large structures are being simulated.

However, it is indeed important to include the nonlinear behavior of the honeycomb structure, as well as to be able to know whether cells have collapsed or not. Thus, this approach can be considered as a shortcut to include the nonlinear behavior of the honeycomb structure without having to invest considerable computing and development time to observe features that, at the end of the day, are irrelevant for the analysis (such as the exact shape of the cells during buckle or collapse).

3.7 Conclusions

In this part, the most important aspects found in this chapter are discussed.

The first part, that consisted of experimental tests of the honeycomb core in two different ways, complete testing and incremental cyclic testing, allows to say the following:

The buckling of the cells appears at very low shear stress levels, indicating that the honeycomb shear behavior occurs mostly in the postbuckling domain (see Fig. 81).

Also, the initial imperfections of the core are not important for the linear shear response, because, even if the initial imperfections are different for every cell, when they are subjected together to shear, the average shear stress values are very regular (see Fig. 77).

Moreover, it was observed that the buckling of the cells is elastically reversible, far beyond the linear limit (see Fig. 79).

We identified two "mechanisms" in which, the honeycomb cells store the deformation energy; the first one, consist of a very light shear buckling of the honeycomb walls, characterized by the formation of small local buckles. And the second one, consisting of the buckling of the entire honeycomb cell structure (see Fig. 82, Fig. 93, Fig. 95 and Fig. 98).

Likewise, when a cell is surrounded by other cells, the walls of the surrounded cell are vertically and horizontally more restricted compared to a single cell alone. This explains that the cells surrounded by other ones are stronger, i.e. the interior cells are stronger that the exterior cells.

Also, by inspecting the cell buckling, we separated the cell shear buckling in different stages. The first one, consists of the linear shear deformation of the cells. The second one, called initial buckling, is characterized by the growing of local small buckles that are apparently elastic. And finally, when the local small buckles have grown larger enough that the cells vertex can't be non-longer straight, and the collapse begins. Also, we observed that the coated paper can plasticize in the buckles without altering the elastic behavior of the honeycomb structure. This means the material of the honeycomb can support certain degradation without affecting the effective structural behavior of the honeycomb (see Fig. 101 and Fig. 102).

Another important aspect is that, the shear strength of the honeycomb core is importantly influenced by the boundary conditions of the cells, being possible to be increased or decreased (see Fig. 67, Fig. 112 and Fig. 113). Although this characteristic could seem obvious (by thinking on the honeycomb core as a structure) it has never been reported, studied or analyzed in any publication at the knowledge of the author.

It has been shown that for inserts, the honeycomb core shear strength should be from 1.16 to 1.32 larger than the value given by the manufacturer. Although this was only been made for the HRH-78 Nomex® honeycomb core.

Finally, a reduced CDM approach was performed (see section 3.6) to represent all the mentioned aspects in a very simple and practical way. This is very convenient for big scale simulations, on which accuracy is desired but the implementation of a detailed modeling is not viable. This model will be implemented for the insert virtual model, where its efficiency will be tested.

All in all, this research helps clarifying many aspects of the core shear failure that were ambiguous in the literature review.

Chapter four: Study of synthetic polymer foams for inserts

In this chapter, the mechanical properties of a Syntactic Polymer Foam (SPF) used as potting for inserts in [15] *are investigated. First, an experimental campaign was made including traction, compression and a special pull-out test in the SPF while a DIC system was used. Finally, a numerical approach is used to model the complex behavior of the potting.*

4.1 INTRODUCTION 139
4.1.1 Potting failure of inserts 139
4.1.2 Syntactic polymer foams as insert's potting material 140
4.1.3 Objectives and proposed methods 143
4.2 MECHANICAL CHARACTERIZATION OF SPF FOR THE INSERT'S POTTING 145
4.2.1 Study of the potting under uniaxial tension and compression 145
4.2.2 Study of the potting failure in inserts 151
4.2.3 Conclusions of the experimental study 159
4.3 NUMERICAL STUDY 161
4.3.1 Modeling of the potting behavior 161
4.3.2 Modeling of the potting pull-out tests 165
4.3.3 Results and discussion 166
4.4 CONCLUSIONS 169

4.1 Introduction

4.1.1 Potting failure of inserts

Several researchers have found evidence suggesting that, besides the core shear buckling of the cells, the insert's failure scenario include the potting's failure too. To show this, two examples are given by Yong-Bin Park et al (see ref [39] and Fig. 131-a) and Heimbs and Pein (see ref [35] and Fig. 131-b). They have found that when an insert is subjected to pull-out loads, the potting might fail simultaneously or even before the core. After having performed several insert's pull-out tests, they cut the "post mortem" specimens in half and found the following failure pictures:

In Fig. 131-a the core was shear buckled, but not teared, and the fastener was already detached from the insert. Also, in Fig. 131-b the potting and core were teared following the same path, this may suggest that the potting failed first and the fracture propagated to the core.

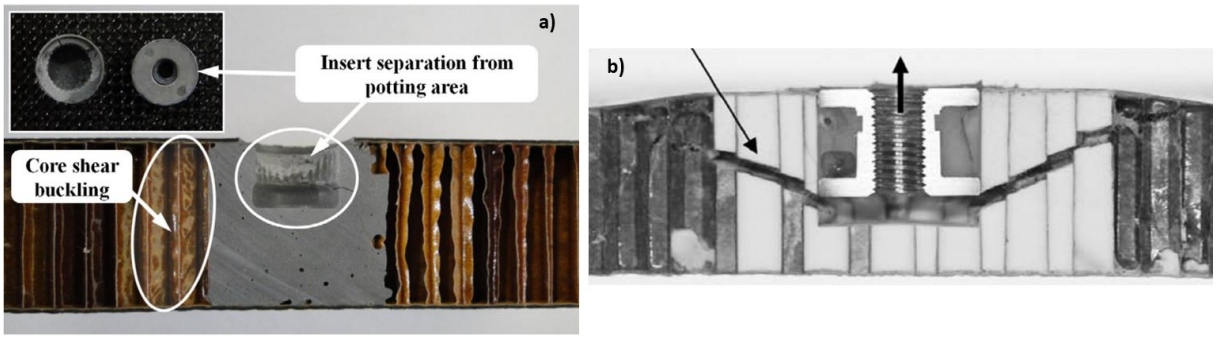

Fig. 131: Failure scenario after a pull-out test performed by Yong and Heimbs [39], [35].

Furthermore, it's possible to see this kind of failure scenario in the inserts tested by Bunyawanichakul in ref. [15] where the potting compound was made of the Araldite AV121-N mixed with phenolic micro-spheres. Also, the inserts were tested under pull-out loading and then cut in half to inspect the different failure modes (see Fig. 132).

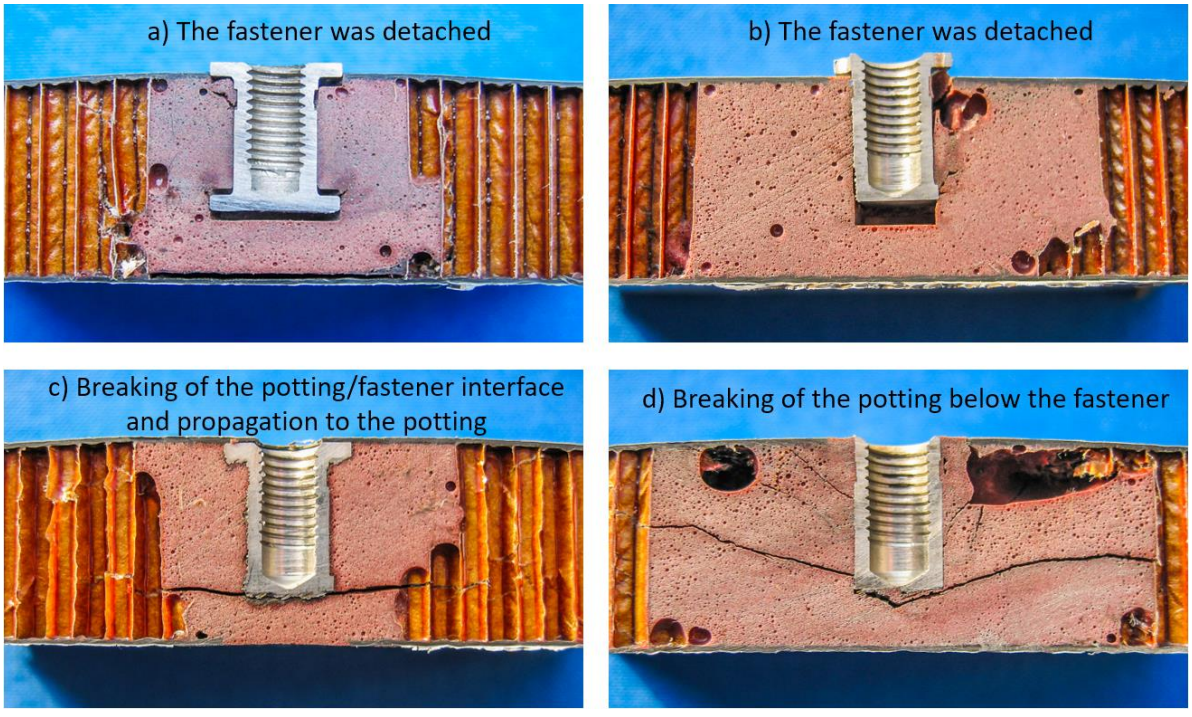

Fig. 132: Failure scenario after a pull-out test performed to different type of inserts. [15]

It's noticeable to observe the discrepancy in the shape of the potting and the presence of air bubbles due to the handmade manufacture method.

As shown in Fig. 132-c,d, the potting and core were found to be broken apparently in tension, which occurs when the stress concentration in the interface fastener/potting overpasses the allowable strength.

For the other cases (Fig. 132-a,b) the fastener was found to be detached from the potting, causing the potting to plasticize locally in compression. This last failure mode might have been caused firstly by a breaking of the potting/fastener interface, that after been broken, allowed the fastener to be displaced, compressing the potting and obtaining the presented scenario.

In light of the presented examples, it's not surprising that the insert design handbook of the ESA includes a method to calculate the pull-out strength based on the failure of the potting as first insert's failure mode. Although, the ESA reference only includes the failure due to traction, which might be useful for the failure cases of Fig. 132-c,d and Fig. 131-b, but not for the rest of the cases where the failure was not caused directly by traction but by the debonding of the insert and plasticity of the potting.

To inquire more in this subject, an analysis of the material properties of the potting compound is necessary, and this chapter is focused into investigate this.

4.1.2 Syntactic polymer foams as insert's potting material

The potting material used in the inserts of Bunyawanichakul in ref. [15] was a mix of adhesive and micro-spheres, which in the literature is commonly referred as a Syntactic Polymer Foam (SPF).

Structural adhesives are widely used for aircraft construction. Indeed, their use is advantageous as it allows to bond very thin parts such as honeycomb cores, or to reduce the structural weight by replacing bolted junctions [86].

For sandwich construction, these adhesives are also used to imbibe metallic fasteners into the panels to be able to install bolted junctions, also called inserts. When these adhesives are used for inserts, they are also called potting, and this compound fulfills some service functions:

- Dissipates stress concentrations due to the loading
- Protects the core and the core/skins interface of the environment
- Bonds the fastener to the sandwich panel.

The potting is the key component of the insert technology, as it provides most of the desired protection functions. Concerning the insert's potting material itself, it must be also selected to be resistant to moisture and to isolate or protect the core from the exterior environment, to be strong enough to support the fatigue in the desired load range, but also to be lightweight.

SPF possesses low density and high resistance to humidity, which makes them ideal as potting material for inserts. These foams have been studied since the 50's and in the last decade (2010) there have been significant advances on the understanding of their mechanical properties. One of the most important aspects is the fact of adding micro-spheres as reinforcements alters their behavior.

For most of the cases, polymers are supposed to be isotropic which is a good estimation of the real properties of these materials. Their mechanical properties might be determined by test standards such as the ASTM D638 [87], the ASTM D695 [88] or the ASTM D732 [89] for traction, compression and shear behavior respectively.

However, for SPF, the behavior is strongly influenced by the micro-spheres volume fraction, the size and the wall thickness of the micro-spheres, the fabrication procedure, among

others as explained in [90]. Also, the behavior under traction, compression and shear are different.

These materials are a mixture of adhesive and rigid hollow micro-spheres that, when mixed, present superior specific mechanical properties than the adhesive alone, which fills perfectly the requirements of the potting for inserts.

The used micro-spheres are hollow particles that reinforce the polymer and reduces the weight at the same time. They are called micro-spheres because their size fits in the micro scale. Their shape is regular although the diameter can vary. The materials used for their fabrication are relatively strong and resistant to moisture and other chemicals products to ensure chemical stability. Some common micro-spheres materials are glass, polymers, carbon, ceramic and metals.

4.1.2.1 Effect of the micro-spheres volume ratio

The mechanical properties of syntactic foams are directly related to the properties of the matrix and the spherical reinforcements. However, adding micro-spheres as reinforcement changes completely the foam behavior compared to the matrix alone.

According to several researchers, the traction behavior of syntactic foams is related to the debonding properties of the interface between micro-spheres and the matrix, but also to the formation of microcracks in the matrix (see Fig. 133) [91].

Several authors used F.E. analysis tools to study the effect of these micro-spheres on the effective elastic moduli. They found that the failure of micro-spheres had an important influence on the average behavior of the foam. Other researchers observed that also the densification of the crushed spheres and the voids due to the fabrication were important and that some spheres crush under very low compressive forces, thus the effective moduli are difficult to predict (see ref. [92]–[94]).

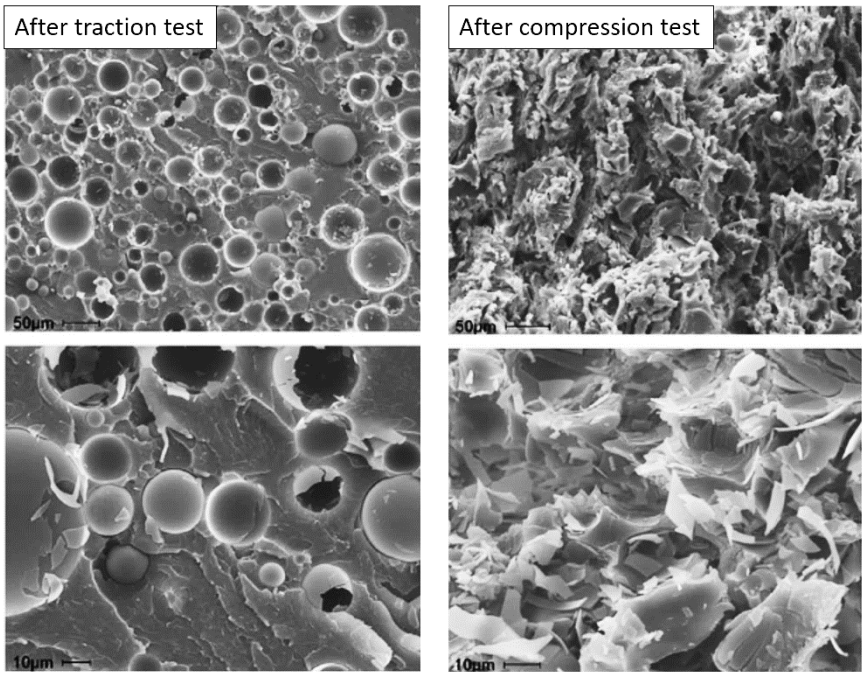

Fig. 133: Difference between the failure in traction and compression of syntactic foams. [91]

The behavior of these syntactic polymer foams is so complex that classical analytical approaches like the rule of mixtures do not provide reliable estimations of the mechanical properties, especially when the micro-balloons volume fraction is high. In 2008, Porfiri et al. [90] proposed an analytical method to calculate the elastic moduli of syntactic polymer foams.

It consists of 14 coefficients that should be calculated to describe the properties of the material. This approach has been validated with experimental references, although, when the foam contained more than 60% of micro-spheres the experimental values were lower than the predicted analytically. This was attributed to the voids in the foam that increase considerably as the micro-balloon volume fraction does.

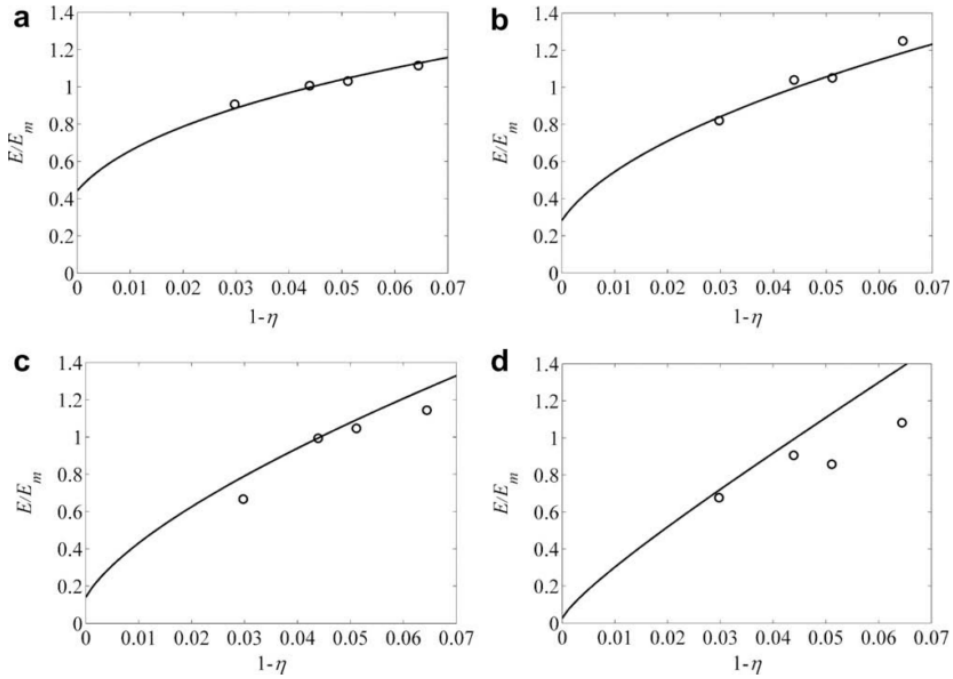

Fig. 134: Comparison of the analytical estimation vs the experimental results by [91]

In 2009, Gupta et al. [91] did an experimental study of the compression and traction properties of this kind of material. Classical curves of the compression and traction behavior can be seen in Fig. 135. Some general remarks that should been considered are:

- Higher compression moduli are obtained through lower micro-spheres volume fractions and thicker walls.
- Higher traction moduli are only obtained through decreasing the microballoon volume fraction.
- Even if the resulting foams have an inferior Young's modulus, the specific Young's modulus (moduli divided by the mass) is superior to the matrix alone.
- The failure of the material in traction is fragile, while the failure in compression is plastic.
- The higher the microballoon fraction, the fragile the material becomes, even in compression [95]

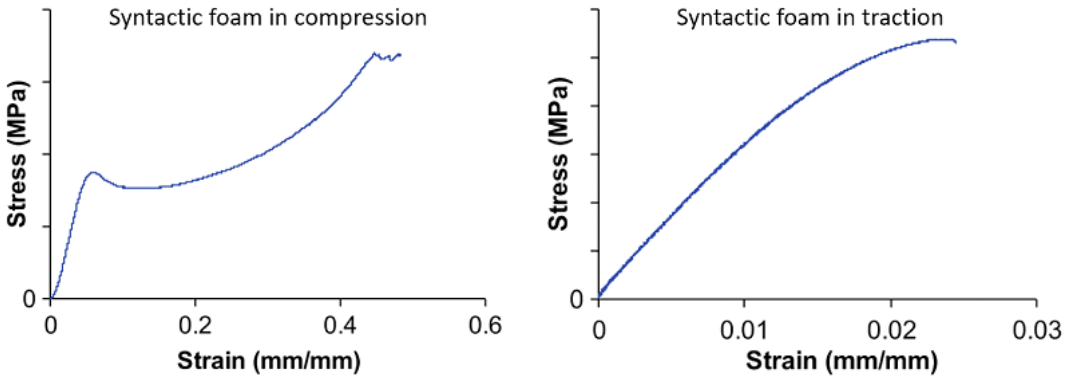

Fig. 135: Classical behavior of syntactic foams in compression and traction by [91]

4.1.2.2 Fabrication defects

Also, when SPF are fabricated, the micro-spheres are added gradually to the adhesive forming a colloid with very high viscosity. In consequence, the micro-spheres cannot spread in the matrix and their concentration is highly non-uniform.

To show this, a post mortem specimen of the inserts tests made by Bunyawanichakul was examined under the microscope (see Fig. 136). Indeed, the potting micro-spheres were not uniform in size nor concentration, for example there are more micro-spheres in the areas showed in Fig. 136-b-1 than in Fig. 136-b-2. This might be especially relevant for inserts since they concentrate loads in a small section of the potting surface. To understand this, suppose that the micro-spheres concentration is higher at the potting/fastener interface, then the foam at the contact zone will be brittle and could lead to a premature failure.

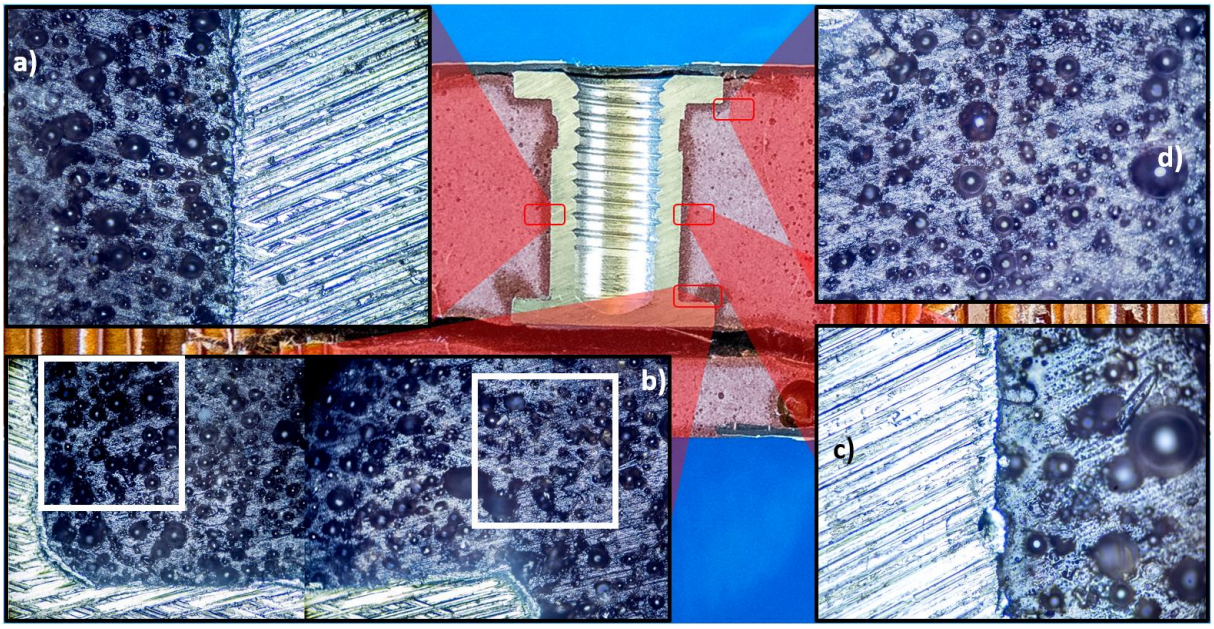

Fig. 136: Potting under the microscope

4.1.3 Objectives and proposed methods

Our brief bibliographical study about SPF's indicates that, even if syntactic polymer foams have been widely used for sandwich construction [96], these foams started to be better understood only recently (mostly through F.E. modeling). Also, it is noticeable that we didn't find any published reference focused on the study of SPF for inserts. Therefore, this chapter is focused in to the study of SPF as potting for inserts, including the SPF behavior but also a study of the potting failure modes.

For this study the potting used by Bunyawanichakul in ref. [15] is taken as reference. Also, this research has three main objectives.

4.1.3.1 Analyze the effect of volume fraction of micro-spheres on the SPF used by Bunyawanichakul

The elastic moduli of syntactic foams cannot be well estimated when the micro-spheres volume ratio is high [90], as it's the case for this potting material. Therefore, testing is the best way to determine its mechanical properties. However, this material was only tested in compression. Thus, more tests are still to be made.

Also, the effects of the non-homogenous distribution of the micro-spheres are still to be investigated. Especially because micro-spheres fraction has a big influence on the effective potting elastic moduli and plasticity.

We propose to make an experimental study of the effect of the micro-spheres volume fraction variation on the effective mechanical properties of the foam. For this, different micro-spheres ratio will be used in the fabrication of specimen to test them.

4.1.3.2 Analyze the SPF insert failure scenarios through original technological tests

In the literature, there wasn't a recommended procedure to study the potting failure of inserts. For this reason, we proposed an original approach based on a technological type of test that will be useful to observe the formation of the failure scenario.

In the insert pullout tests, the evolution of the failure scenario of the potting is impossible to observe, because the fastener is imbibed at the interior of the insert.

Our original approach consisted into reproducing the insert pull-out tests passing from the cylindrical and closed approach to an orthogonal open shape. In this way, the symmetry of the test is kept, but most importantly, the evolution of the failure scenario is now observable and can be recorded by the cameras.

4.1.3.3 Develop a SPF nonlinear law to be implemented in to an UMAT

Finally, a modeling strategy that allows including the potting behavior into the insert F.E. model was developed. This behavior includes the effect of variation of the micro-spheres concentration and the failure of the potting under traction and compression.

4.2 Mechanical characterization of SPF for the insert's potting

4.2.1 Study of the potting under uniaxial tension and compression

The first step concerning the potting's study consisted of performing a test campaign to observe the failure of the material under traction and compression.

Since the microballoon volume fraction of the potting changes drastically the effective mechanical properties of the adhesive, this aspect has been included in the investigation.

The potting used in the studies of Bunyawanichakul in ref [15] is taken as reference. The Araldite AV-121 B (which can be purchased in black N or withe color B) epoxy adhesive was mixed with 15% of its ponderal weight with the HY 991 hardener. According to the fabrication description, this adhesive was then mixed with 10 % of phenolic micro-spheres which had an average diameter of 90 μm. The resulting SPF was then used as potting for inserts. The compressive modulus of this material was of 1312 MPa under compression and its density between 900 and 1000 kg/m^3. Also, a compression test of the adhesive alone was made (potting without micro-spheres). The tests consisted in testing the adhesive with and without porosities (not microspheres), both test curves are shown in Fig. 137. The material presents some plasticity and then it broke. No more data is provided.

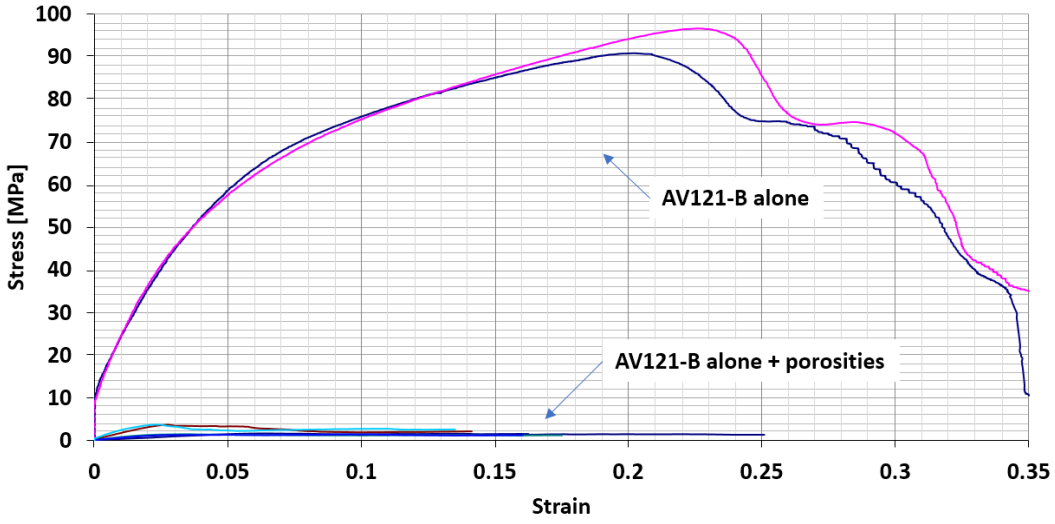

Fig. 137: Compression tests made by Bunyawanichakul on the adhesive AV121-B alone with and without porosities.

Also, Bunyawanichakul stated that the potting fabrication was handmade and therefore the micro-spheres distribution in the adhesive matrix was not homogenous.

As proof of this, we measured the density of a sample of this same potting (a tube of 11.9 mm of diameter per 55 of high) and we measured a density of only 670.2 Kg/m^3 which is 41% lower than the expected value, indicating that the micro-spheres concentration was higher. This density variation on the potting material could have been caused by several reasons:

- Human error: The potting was hand made.
- The low density of the micro spheres: An error of 1 g represents a considerable amount of volume.
- Precision of the weighing machine: The tolerance of some classical weighing devices is 1 g, considering the low density of the micro-spheres, this is equivalent to add much more micro-spheres volume than desired.

- The amount of potting: the less amount of potting is fabricated, more the error is relevant.
- The accumulated errors: Since all the components are weighed separately, once all the substances are mixed together the error is accumulated.
- To the nature of the material itself: The distribution of the micro-spheres in foams is mostly random, therefore, the foam density varies in all directions.

Considering all these factors, we made the hypothesis that unintentional variations on the syntactic polymer foam density will always be present and therefore it's a variable that needs to be considered for the potting behavior analysis.

Also, at microscale, the non-homogenous micro-spheres distribution of the potting makes that for small sections the effective Young moduli varies too. (see Fig. 136)

For this reason, since Bunyawanichakul claimed to have mixed the adhesive with phenolic micro-spheres at 10% of the ponderal weight, we decided to study the behavior of the potting with 7, 10 and 13 % of its ponderal weight of micro-spheres which is equivalent to a micro-spheres volume fraction of 42.2 %, 60.3 % and 78.5 %. We considered this interval reasonable to consider the influence of the error on the fabrication procedure and the non-homogenous micro-spheres distribution.

The number of tests is: three different micro-spheres concentrations, tested in compression and tension, tested three times to obtain reliable results: 3 x 2 x 3 =18 tested specimens.

4.2.1.1 Fabrication of the specimens

For each different micro-spheres concentration (7,10 and 13 %), all the specimens were fabricated using the same mixture and two type of specimens were used for tension and compression.

Rod shaped specimens for compression testing

These specimens had the shape of a cylindrical rod and their height was the double of its diameter as recommended by the ASTM D695. All the specimens were fabricated using a syringe which was filled with potting carefully to avoid the creation of air bubbles. Then, the potting was left to polymerize at room temperature for 6 days. After that, the material was extracted from the syringe with compressed air and cut to the desired size in a lathe. Special care was taken in this last step to obtain uniform faces. Finally, the specimen's dimensions were 6.11 mm of radius by 24.9 mm of height (see Fig. 138).

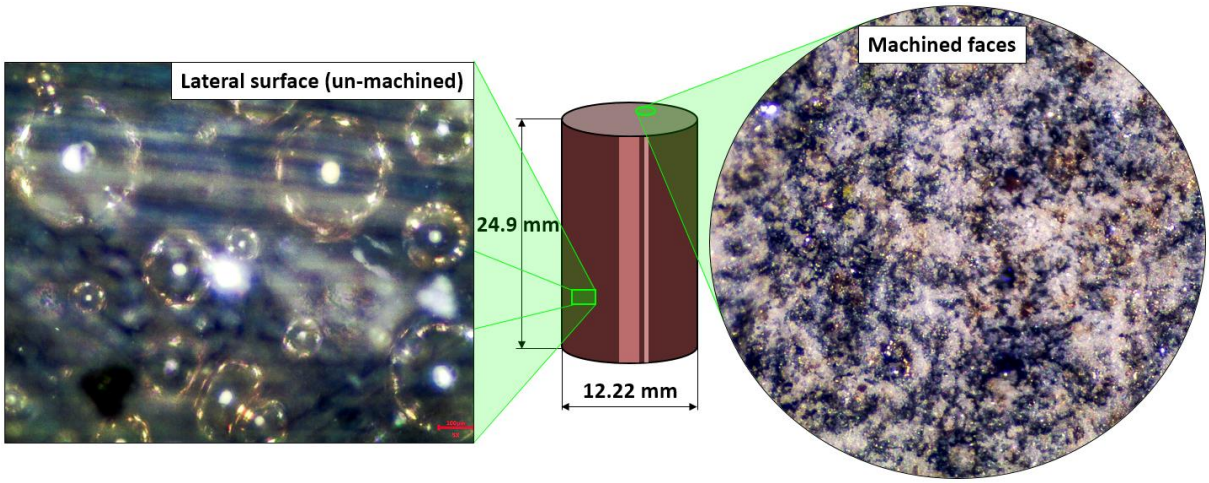

Fig. 138: Size of the compression specimens and view of the surfaces under the microscope.

Since the fabrication required dispersing all the micro-spheres in the adhesive, the paste was stirred intensively several times, although no special care was taken to leave intact the micro-spheres. Therefore, to verify that they were not damaged, we inspected the exterior surfaces of the polymerized specimen under a microscope.

In the superior surface, we found that there was no trace of the micro-spheres, all were broken by the lathe, which was normal. For the lateral surfaces, we could observe the micro-spheres inside the polymer that were in good state (see Fig. 138).

"Dog Bone" shaped specimens for tensile testing

For the tensile tests the recommendations of the ASTM D638 were followed. A specific shape for the traction specimens was used, commonly called dog bone. The dimensions of the specimen are shown in Fig. 139. This shape allows minimizing the effect of stress concentrations.

The specimens were fabricated using a mold made of wood. For all the specimens, the potting was left to polymerize for 6 days at room temperature.

Initially, the thickness of the specimen was of 10 mm, but unfortunately due to the maximal opening of the testing machine clamps, this thickness had to be reduced through milling to 7 mm.

Finally, the specimens were painted with speckles to be analyzed with a 3D digital image correlation system.

For the tensile tests four specimens of each type were fabricated although only 3 were tested. This was just in case one specimen breaks in the demolding process.

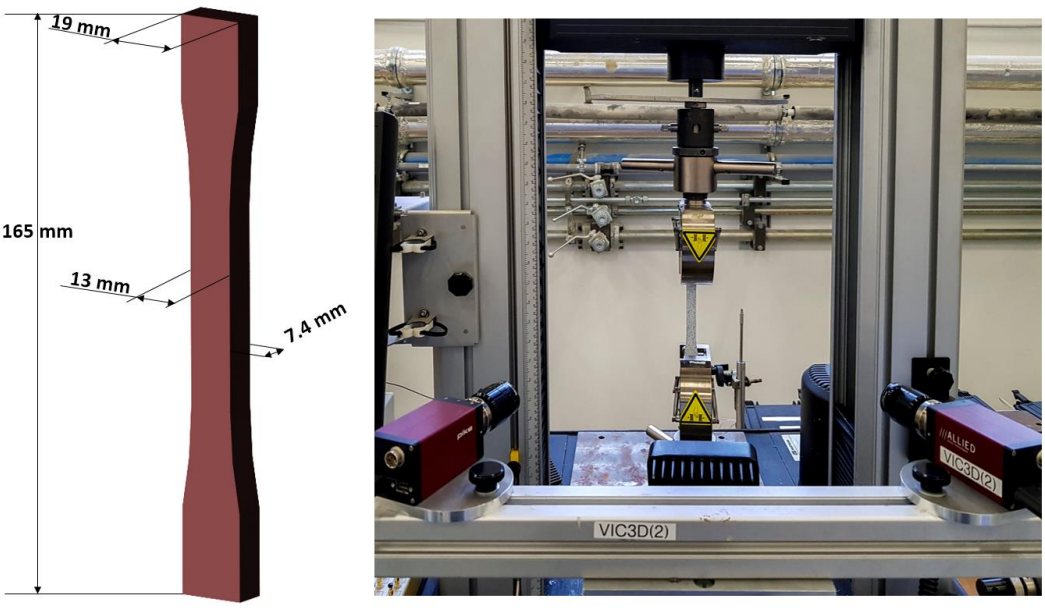

Fig. 139: Shape and set up of the traction tests specimens.

4.2.1.2 Test setup

All the specimens were tested using an Instron 10 kN machine. For the compression test, two rectified metal blocks were used between the machine and the specimen to ensure the contact and parallelism. An external LVDT sensor was used to measure the displacement of the machine.

For the tensile specimens, a 3D DIC system was installed to measure the deformation field in the plane of the specimen. One image was taken every two seconds.

For all the tests, the force was measured directly from the machine. For both cases the machine speed was set to 0.5 mm/min.

4.2.1.3 Test results and discussion

The test results are shown in Fig. 140 and Fig. 141 for tension and compression respectively. The specimens with different percentage of micro-spheres are speared by color; blue for 7%, yellow for 10 % and green for 13%.

In tension, the average elastic moduli were 2190, 1851 and 1670 MPa for 7, 10 and 13% of micro-spheres weight respectively. In the same order, the loss of linearity started at 10, 9.5 and 9 MPa and the tensile failure occurred at 17.4, 15 and 13.8 MPa (see Fig. 140 and Table 12).

Micro-spheres ponderal weight	0%	7%	10%	13%
Micro-spheres volume fraction f	0	42.2	60.3	78.5
E_t [MPa]	4000	2190.2	1851.3	1670
Loss of linearity traction [MPa]	unknown	10	9.5	9
$\sigma_{t\,max}$ [MPa]	19	17.4	15	13.8

Table 12: Summary of the tests results for the traction tests of the potting.

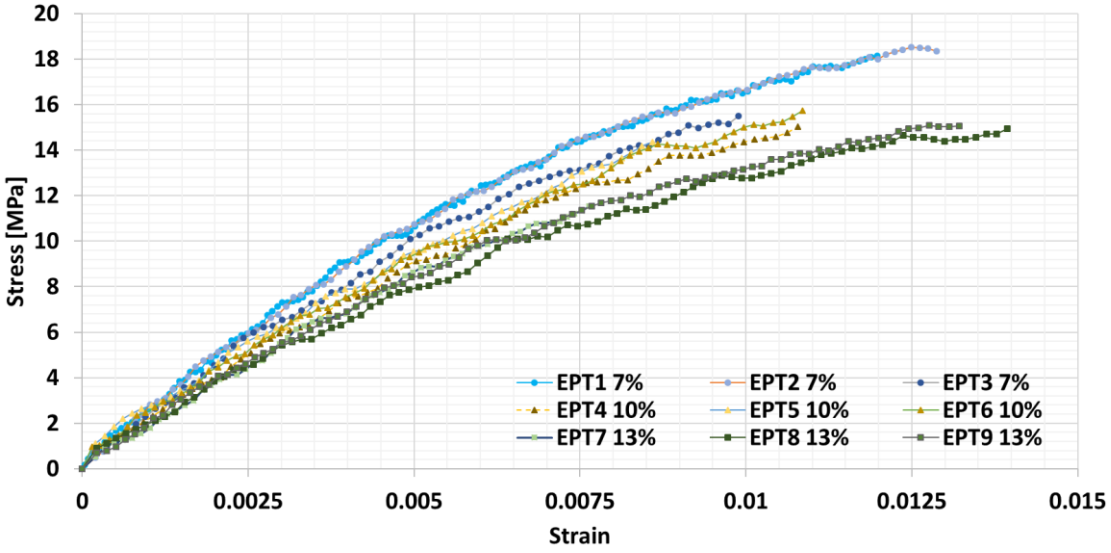

Fig. 140: Experimental curves of the tensile tests of the potting.

The averages in compression were 1290, 1233 and 1226 MPa for 7, 10 and 13% of the micro-spheres weight respectively, also, in the same order, the loss of linearity started at 20, 19 and 17 and the specimens presented a perfectly plastic behavior at 34, 31.5 and 30 MPa respectively (see Fig. 141 and Table 13).

Micro-spheres ponderal weight	0%	7%	10%	13%
Micro-spheres volume fraction f	0	42.2	60.3	78.5
E_c [MPa]	4000	1290.6	1233	1226.3
Loss of linearity compression [MPa]	unknown	20	19	17
$\sigma_{t\,max}$ [MPa]	unknown	34	31.5	30

Table 13: Summary of the tests results for the compression tests of the potting.

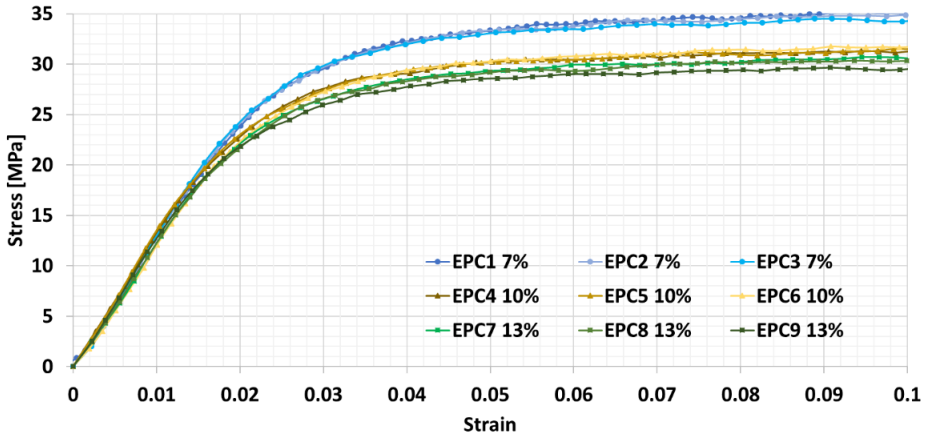

Fig. 141: Test results of the compression tests of the potting

The elastic moduli in compression and tension were different which is characteristic of these foams. Also, the percentage of micro-spheres used in the potting fabrication clearly influenced the elastic modulus. The foam became stiffer when the micro-spheres volume fraction is smaller, and vice versa.

Another aspect that is worth mentioning, is that the behavior of these SPF might vary if it were to be subjected to biaxial or triaxial stress, due to the nature of the material itself. However, in this study only uniaxial tests were performed due to the reduced time of the investigation.

4.2.1.4 Effect of the percentage of micro-spheres on the potting

The density of the potting should depend on the density of the components that are used to create the compound, which are the Araldite AV-121-N1, the hardener HY-991 and the micro-spheres, therefore, the final density of the mixing compound ρ_f should be given by the rule of mixtures:

$$\rho_f = \frac{m_{av} + m_h + m_b}{V_{av} + V_h + V_b}$$

Where *m* is used for mass, *v* for volume, *av* for the araldite adhesive, *h* for hardener and *b* for micro-spheres.

We measured the density of the samples with different percentage of micro spheres. The calculated and experimental values were very similar (see Fig. 142). However, the density of the samples of the Bunyawanichakul's potting had a density of 667 kg/m^3. By comparing it to our chart of densities, we believe that the quantity of micro spheres used to fabricate those specimens was far superior to 10 %.

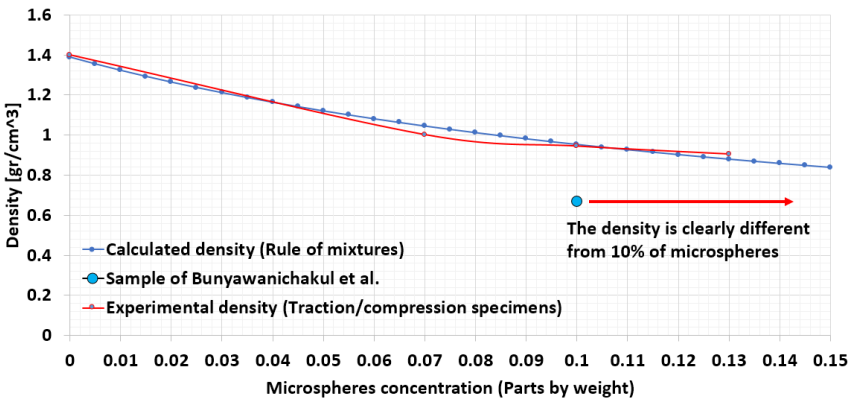

Fig. 142: Density of the SPF as function of the micro-spheres concentration.

Concerning the elastic moduli, without micro-spheres, the compressive elastic moduli of the adhesive provided by the manufacturer, which is 4000 MPa (the traction moduli is not provided; therefore, it's assumed it's both have similar values). Also, using the obtained values after the tests, we can estimate the elastic moduli as function of the micro-spheres concentration (see Fig. 143).

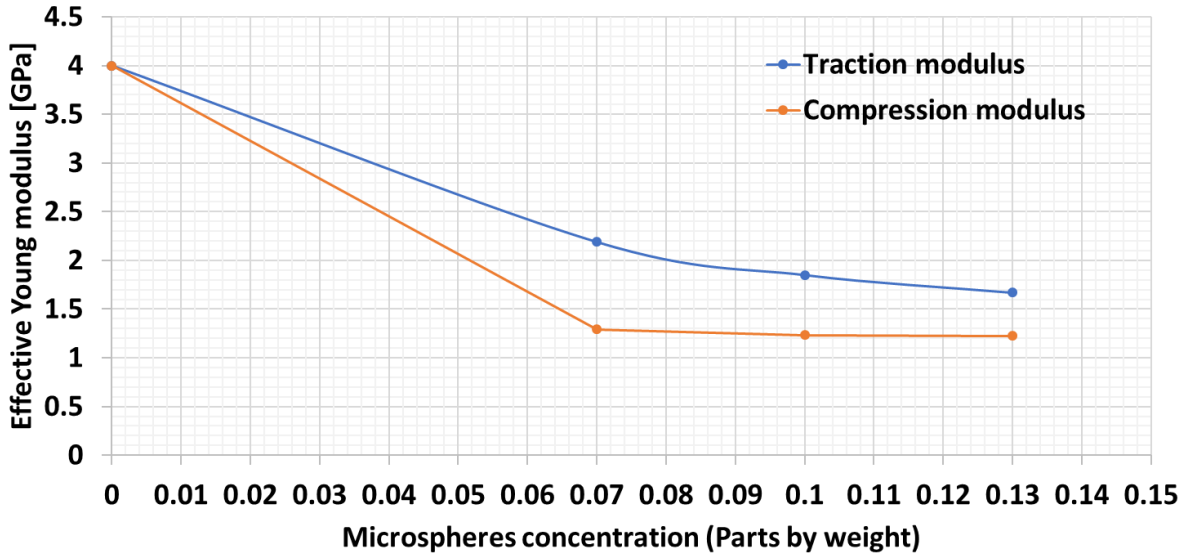

Fig. 143: Experimental effective Young moduli in traction and compression as function of the micro-spheres concentration.

Finally, the resistance of the material under tension and compression varies depending on the micro-spheres concentration as shown in Fig. 144. The value of the adhesive without micro-spheres taken from the manufacturer specifications and of the compression tests made by Bunyawanichakul (see Fig. 137).

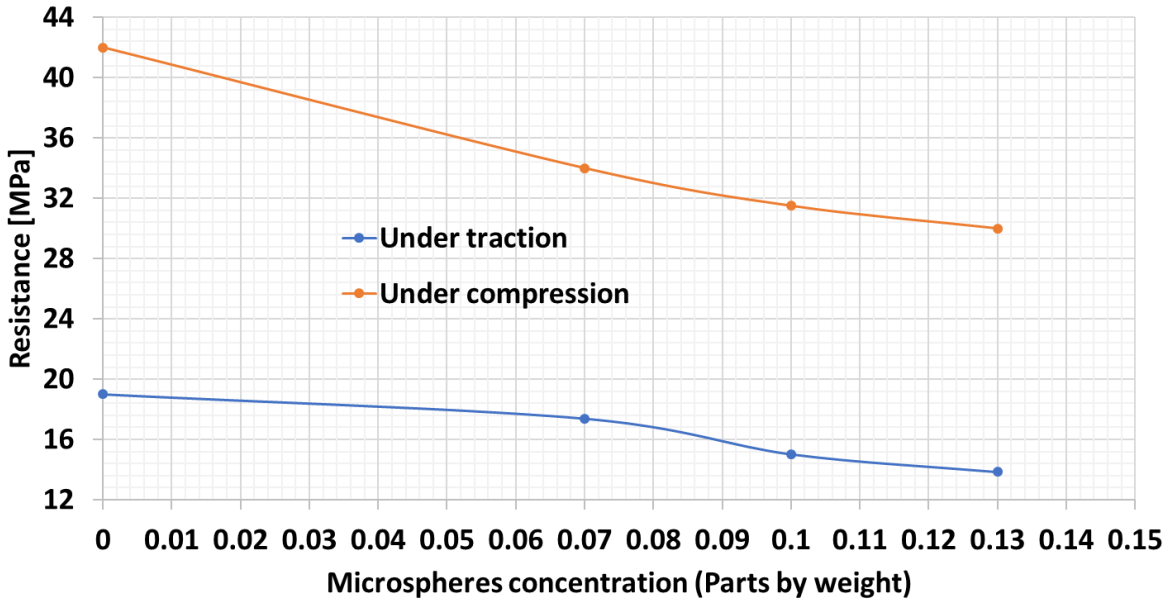

Fig. 144: Resistance to failure under traction and compression as function of the micro-spheres concentration.

4.2.2 Study of the potting failure in inserts

When the fastener is pulled out, the potting is subjected to a complex state of stresses until it breaks. However, due to the cylindrical geometry of the fastener and insert, it is not possible to observe at the interior of the insert to see the potting's failure.

4.2.2.1 Technological tests description

To overcome this problem, we made the hypothesis that the failure scenario of the insert was very similar at every angle of the periphery of the insert. The idea was to submit the potting to similar boundary conditions of those in the insert while it is possible to see the breaking of the potting/fastener interface.

Therefore, we proposed a similar test. It consisted in to using a rectangular shape instead of the cylinder shape of the insert. In this way, the cylindrical symmetry of the insert is replaced by an orthogonal symmetry, making possible to design a test on which the potting failure can be observed easily.

For this purpose, we proposed four types of tests that could reproduce similar failure modes to those of Fig. 132 found by Bunyawanichakul (see Fig. 145).

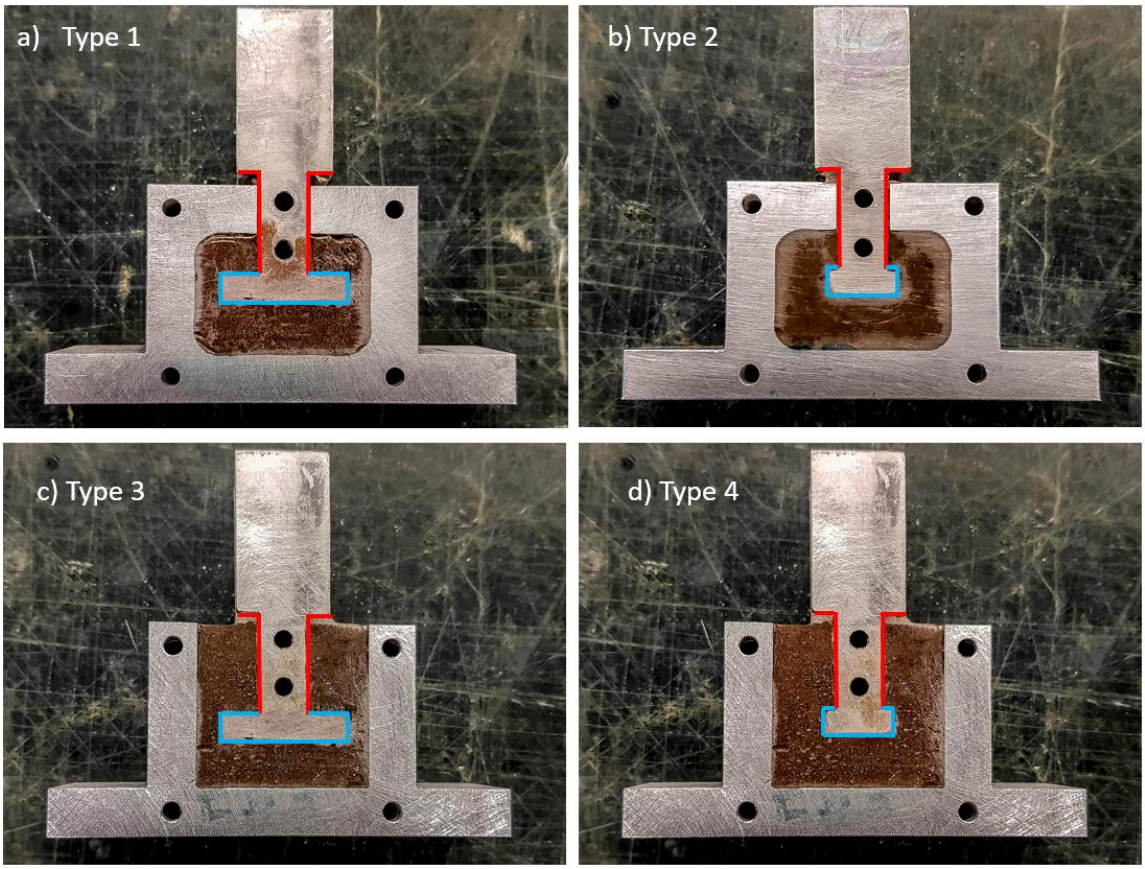

Fig. 145: Test specimens subjected to pull-out.

This test campaign consisted in performing four different type of tests, on which a metal rod that was surrounded by the potting material was pulled out as on the insert tests. Our idea was to test the potting in a similar way of the insert pull-out tests but privileging some aspects that might activate different failures, one at each time. This will facilitate to define the conditions that propitiate each failure mode.

- In the specimen type 1 the metal rod/potting interface was very large, therefore we expected to see a failure of the potting, due to compression or traction.

- On the specimen type 2 the surface of the interface metal rod/potting was smaller and we expected to see this interface break.
- On the specimen type 3 the conditions were like the type 1 test, but the potting container box was open, so the potting was subjected pronominally to traction.
- Finally, on the type 4 the interface metal rod/potting was subjected to traction and shear, but the box was open.

Also, since the influence of the micro-spheres ratio for the potting failure is unknown, it's included in this study. For this reason, different percentage of micro-spheres were used to fabricate the 16 specimens, it goes from 10% to 15%.

It is worth mentioning that the free faces of the metal rods, on which it is possible to see the potting failure may reduce the desired orthogonal failure symmetry. For this reason, the specimens were thick enough to reduce the influence of this border effect.

4.2.2.2 Fabrication of the test specimens

To complete the four types of tests we manufactured only two different metal rods, and two different type of boxes to contain the potting; all the pieces had a thickness of 25 mm (see Fig. 146).

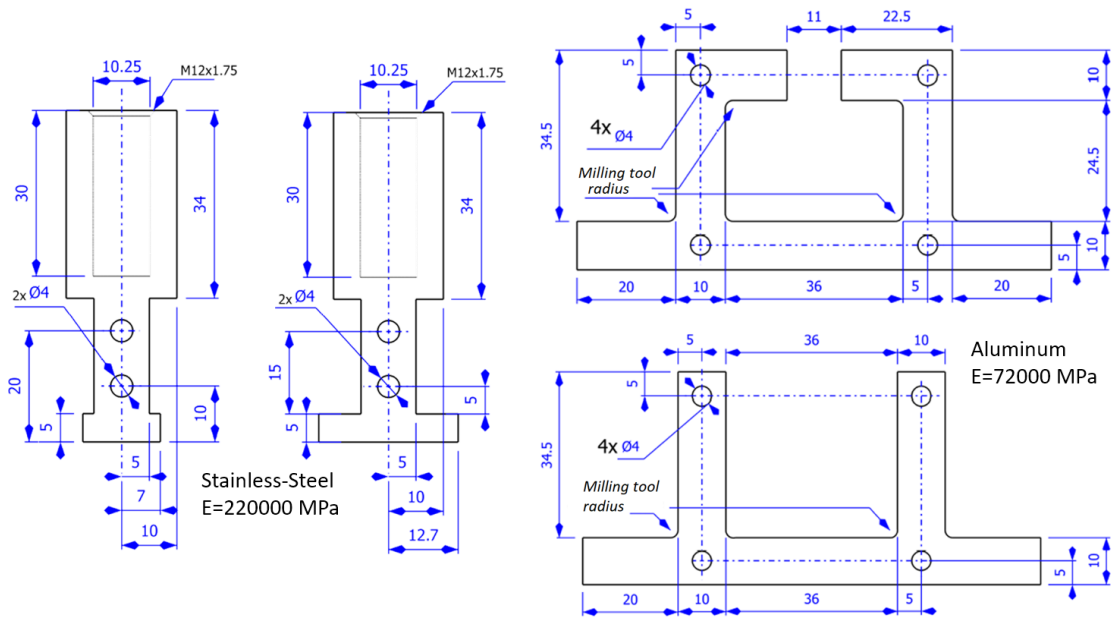

Fig. 146: Geometry of the rods and potting containers.

The metal rods were made of stainless steel to represent the fastener. The boxes that contained the potting were made of aluminum and provided a similar fixation as when the potting is imbibed in the sandwich panel.

Therefore, the percentage of every component used for the potting was different for every specimen, which can be seen in Table 14. Also, for some specimens, the stainless-steel rod was not degreased to see how this affected the results of the tests.

Moreover, as for the previous tests, the potting was made by mixing the adhesive araldite AV-121-N with the HY 991 hardener. However, for some cases a surplus of hardener was used on purpose to observe the variation of the mechanical properties of the resulting compound. This variation may be attributed to the human error handmade manufacturing.

The borders showed in red in Fig. 145 were covered with a Teflon tape to avoid the adhesion of those surfaces. This made easier to analyze the results of the tests because the deformation of the potting was caused only by the end of the metal rod.

Once all the metal pieces were manufactured, they were assembled and then filled with potting. The combination of the four different geometries resulted in a combination of four different type of specimens as can be seen in Fig. 145. Then the specimens were polymerized at 100°C, except for specimens EP13 to EP16 which were left at 40° for 1 hour and specimens EP17 to EP20, which were left to polymerize at room temperature.

Also, since the number of metallic pieces was reduced, the tests were made gradually. First, only one specimen was tested to see if the results were as expected, then the potting fabrication was adapted at each time to try to obtain the desired failure scenarios. All this process, combined with the fact that many tests provided very different evidences, resulted in a very random number of specimens of different characteristics.

The characteristics of each specimen are listed in Table 14. The specimens are sorted by specimen type, from 1 to 4 (column two). The first column shows the name of the specimen, and the associated color is to identify the specimens that were made the same day.

Specimen	Type	% of micro spheres	Observations
EP3	1	11	Left at 100°C 1 hr.
EP4	1	13	Left at 100°C 1 hr.
EP6	1	15	Not degreased, left ta 100°C 1 hr.
EP10	1	15	Left at 100°C 1 hr.
EP13	1	12	Left at 40°C 1 hr.
EP20	1	11	Left at room temp.
EP2	2	11	Left at 100°C 1 hr.
EP7	2	15	Not degreased, left at 100°C 1 hr.
EP12	2	15	Left at 100°C 1 hr.
EP16	2	12	Left at 40°C 1 hr.
EP17	2	11	Left at room temp.
EP1	3	10	left at 100°C 1 hr.
EP9	3	15	20% more of hardener, left at 100°C 1 hr.
EP14	3	12	Left at 40°C 1 hr.
EP19	3	11	Left at room temp.
EP5	4	13	Left at 100°C 1 hr.
EP8	4	15	Not degreased, left at 100°C 1 hr.
EP11	4	15	20% more of hardener, left at 100°C 1 hr.
EP15	4	12	Left at 40°C 1 hr.
EP18	4	11	Left at room temp.

Table 14: Characteristics of the tests specimens for the potting pull-out tests.

4.2.2.3 Test setup

Once the specimens were fabricated, they were painted with black speckles. A 100 kN Instron machine was used to test the specimens. The force and displacement were measured directly from the machine. The specimens were fixed to the machine using clamps as shown in Fig. 147.

Then the displacement was imposed from the inferior part of the machine. The superior part of the Instron machine was fixed. A DIC 3D system was used to measure the displacement field of the test specimen. The images were taken with a frequency of 2 Hz.

The force signal was measured directly from the machine. The measurement of the displacement was calculated using the vertical displacement measured at points P1, P2, P3, and P4 using the following equation.

$$d_{ins} = \frac{P_{y0} + P_{y1} + P_{y2}}{3} - P_{y4}$$

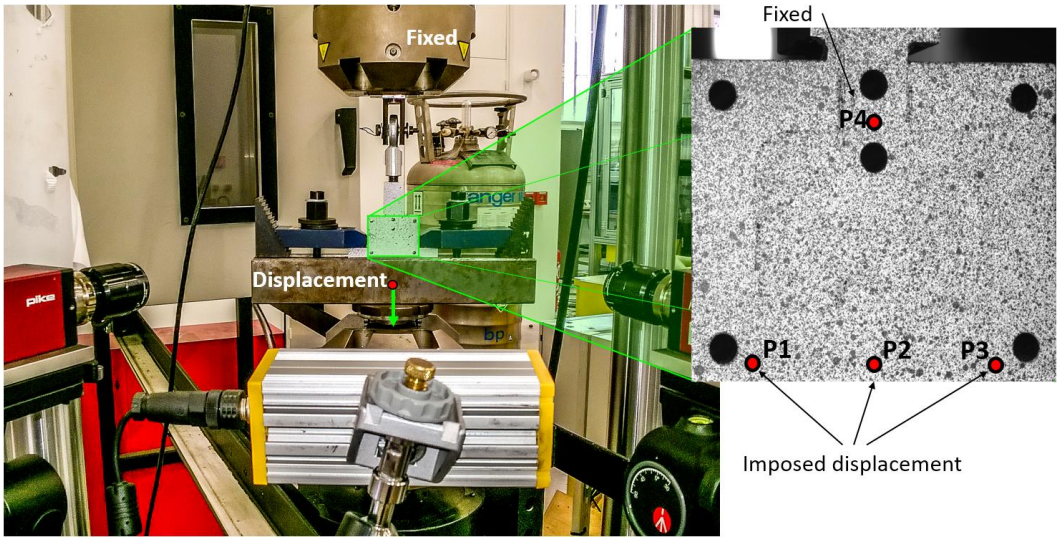

Fig. 147: Test set up and measuring of the pull-out displacement of the rod

4.2.2.4 Tests results and discussion

Once the tests were made, the obtained data was analyzed and compared. The results were divided by specimens' types.

Specimens type 1

On the tests of specimens EP3, EP4 and EP20 the activated failure mode was the breaking of the potting below the metal rod. On the EP10 specimen it was the breaking of the metal rod/potting interface and propagation of the fracture. For the specimens EP6 and EP13, the metal rod was not bonded to the potting, this was like a fabrication defect. (see Fig. 148)

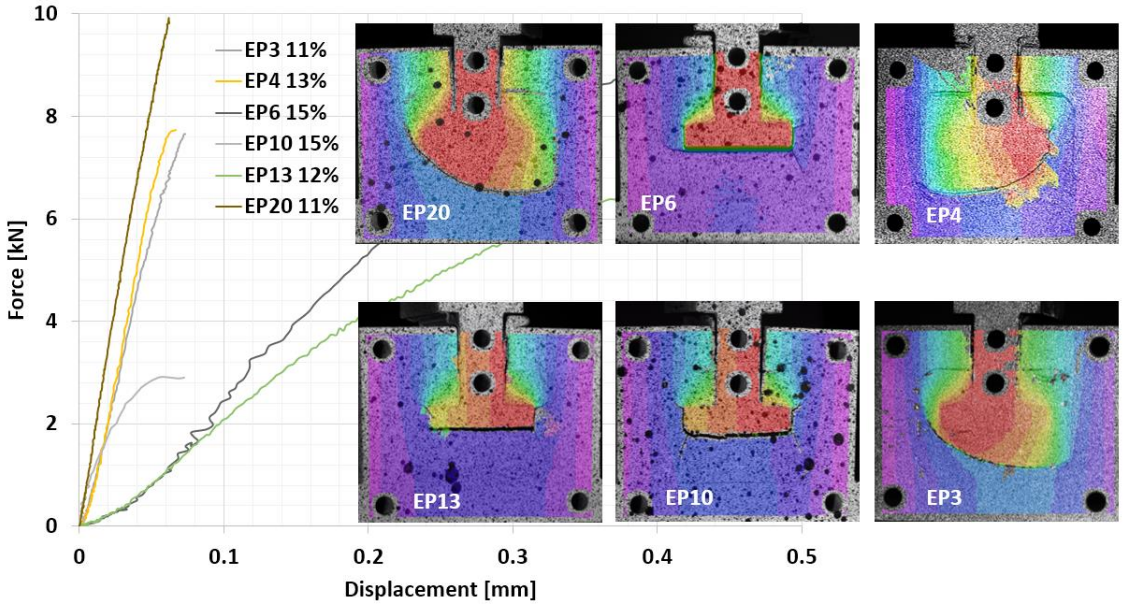

Fig. 148: Experimental results of the test specimens type 1.

Specimens type 2

The EP2 and EP17 specimens presented a failure of the potting below the metal rod. For the specimens EP7, EP12 and EP16 the steel rod was not bonded to the potting. (see Fig. 149)

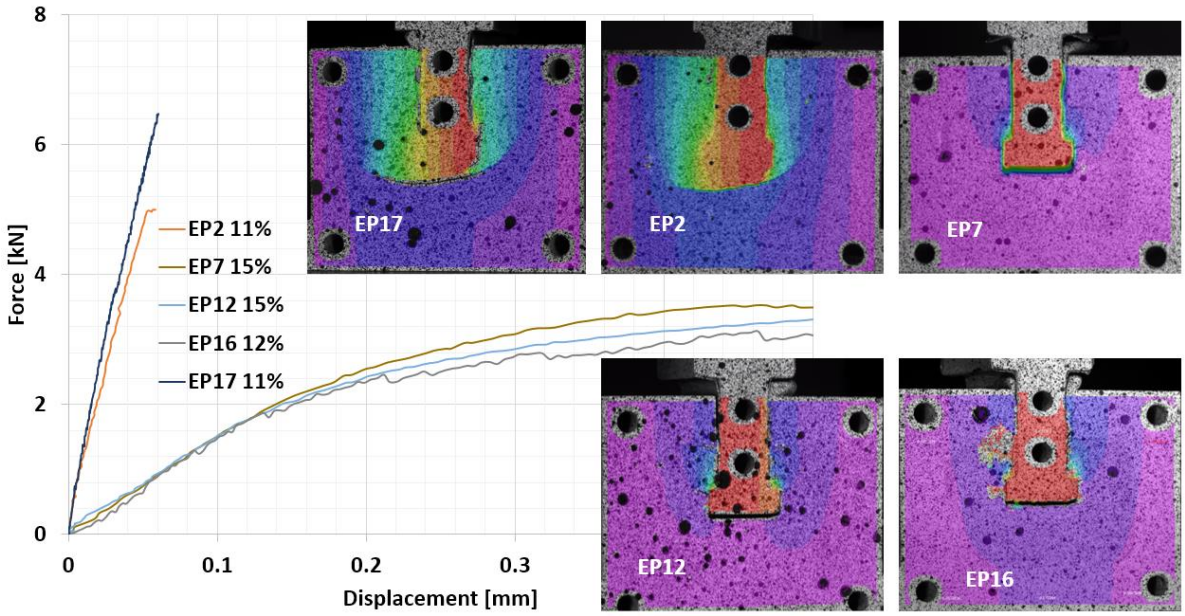

Fig. 149: Experimental results of the test specimens type 2.

Specimens type 3

For the specimens EP1, EP14 and EP19 the failure was caused by the breaking of the potting below the metal rod. For the specimen EP9 the failure was the breaking of the interface between the steel and the potting. (see Fig. 150)

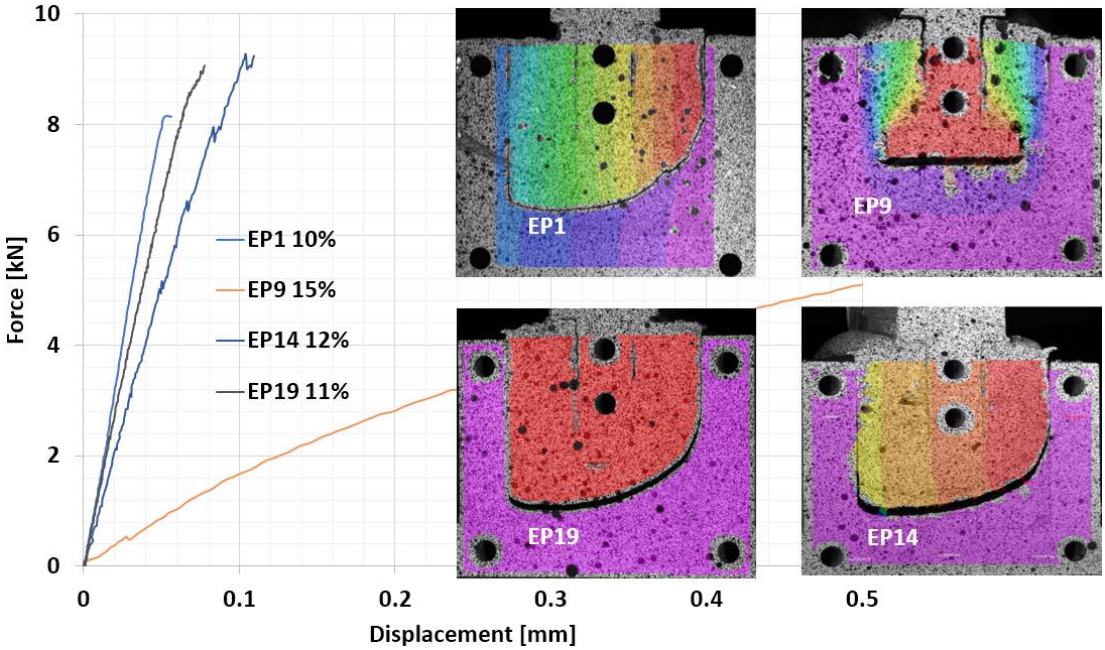

Fig. 150: Experimental results of the test specimens type 3.

Specimens type 4

The specimens EP5 and EP18 presented the breaking of the metal rod/potting interface with propagation of the fracture into the potting. The failure of specimens EP8 and EP15 was a combination of the breaking of the potting and the breaking of the interface between the rod and the potting; finally, EP11 failed due to the breaking of the potting rod interface. (see Fig. 151)

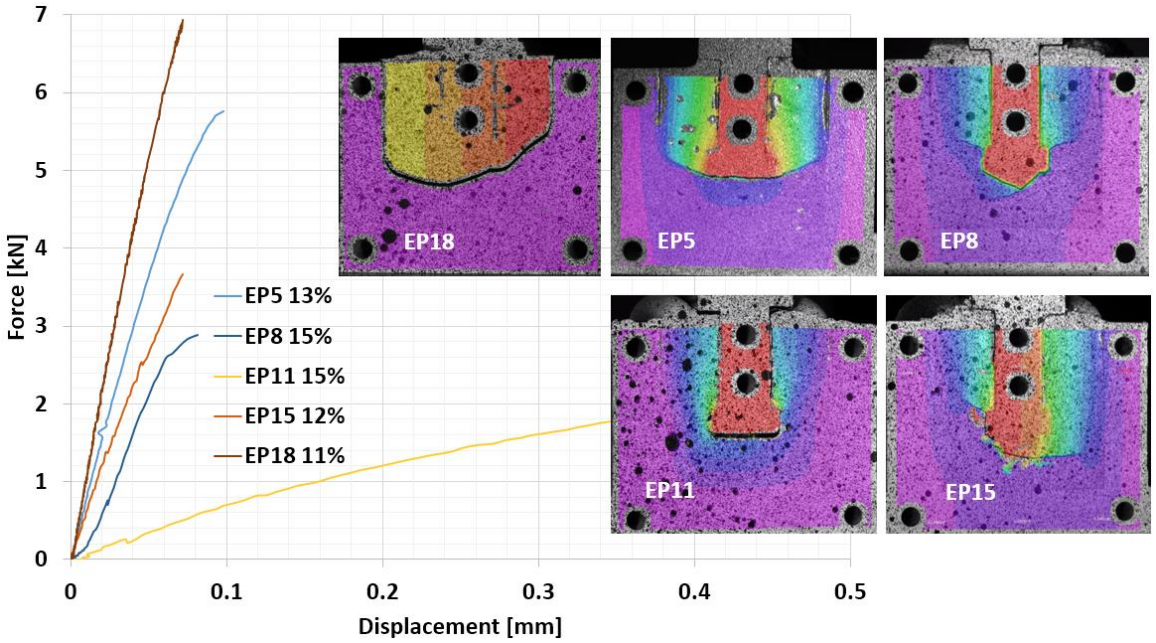

Fig. 151: Experimental results of the test specimens type 4.

All the specimens, their characteristics and failure modes are summarized in Table 15, also, their failure modes are abbreviated as follows:

- A: Breaking of the potting below the rod (color blue of the failure mode column)
- B: Breaking of the interface potting/rod (color green of the failure mode column)
- C: Not bonded (color yellow of the failure mode column)

Specimen	Type	% of micro-spheres	Observations	Max load [kN]	Failure mode
EP3	1	11	Left a 100°C 1 hr.	7.658	A
EP4	1	13	Left a 100°C 1 hr.	7.732	A
EP6	1	15	Not degreased, left a 100°C 1 hr.	-	C
EP10	1	15	Left a 100°C 1 hr.	2.908	B
EP13	1	12	Left a 40°C 1 hr.	-	C
EP20	1	11	Left at room temp.	10.0	A
EP2	2	11	Left a 100°C 1 hr.	5.005	A
EP7	2	15	Not degreased, left a 100°C 1 hr.	-	C
EP12	2	15	Left a 100°C 1 hr.	-	C
EP16	2	12	Left a 40°C 1 hr.	-	C
EP17	2	11	Left at room temp.	6.25	A
EP1	3	10	left a 100°C 1 hr.	8.15	A
EP9	3	15	20% more of hardener, left a 100°C 1 hr.	6.108	B
EP14	3	12	Left a 40°C 1 hr.	8.9	A
EP19	3	11	Left at room temp.	8.675	A
EP5	4	13	Left a 100°C 1 hr.	5.765	B
EP8	4	15	Not degreased, left a 100°C 1 hr.	2.886	B
EP11	4	15	20% more of hardener, left a 100°C 1 hr.	2.956	B
EP15	4	12	Left a 40°C 1 hr.	3.6683	B
EP18	4	11	Left at room temp.	6.9	A

Table 15: Summary of the potting pull-out test campaign.

All the failure modes observed in the insert tests of Bunyawanichakul were also present in our tests. Nine specimens (EP4, EP3, EP2, EP1, EP14, EP17, EP18, EP19 and EP20) failed due to the breaking of the potting below the metal rod. In five other specimens (EP6, EP13, EP7, EP12 and EP16) the metal rod was not bonded to the insert. The other six specimens

(EP10, EP9, EP5, EP8, EP11 and EP15) failed due to the breaking of the potting/metal rod interface and in some cases combined to the fracture of the potting.

Concerning the breaking of the potting in the specimens, it's possible that is occurs due to traction or shear, but it's not easy to choose one.

On one hand, the fracture of the tested specimens occurs most of the time at ± 45°. Also, when the metal rod is being pulled-out, it clearly submits the potting to shear forces because of its geometry (withe borders of EP1 and EP5 in Fig. 152). On the other hand, there are some specimens on which the fracture of the potting happens at 0°. Moreover, during the tests, the failure of the potting was like a brittle material.

However, it was seen that this material has a brittle failure in traction and a ductile failure under compression, which suggests that the shear failure should be a combination of both, although the resistance in traction is lower than in compression. Therefore, even if the potting is subjected to shear, the traction component will activate the failure before the compression, therefore the failure under tension should be privileged.

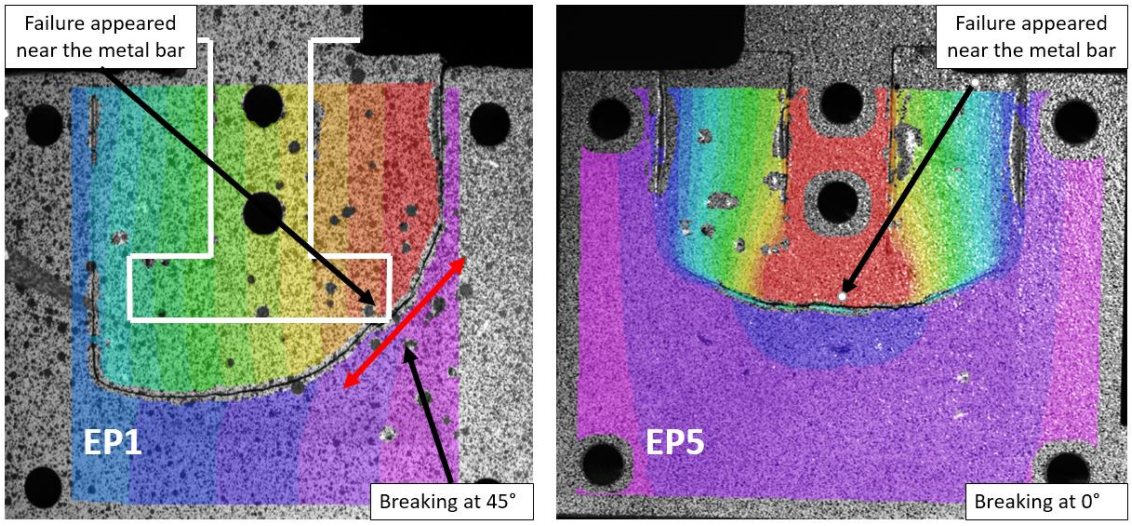

Fig. 152: Supposed potting failure due to traction of specimens EP1 and EP5.

For the specimens that were not degreased (EP6, EP7 and EP8) the pieces were not correctly bonded, as expected. However, for the specimens EP13, EP12 and EP16 this was unexpected because these defects were not intentional.

By looking at the displacement fields of the tested specimens we found that we could attribute the debonding of the metal rod to three main causes (see Fig. 153). The first one was that all the surfaces were not bonded since fabrication. The second one was that only the lateral surfaces were not bonded, therefore, when the inferior surface of the rod detaches; the breaking doesn't propagate to the potting. Finally, for EP9 and EP11 we observed that when the quantity of hardener was higher than the recommended one, the potting became a very soft and ductile material; therefore, the fracture doesn't propagate.

Our hypothesis is that the surfaces were not bonded because of the gradient of temperature in the fabrication process, which causes different dilatation on both materials. The thermal conductivity of the steel rod is much bigger in comparison with the potting. Also, these adhesives are commonly designed to be applied as thin layers to stick the parts together, not to be used as matrix for SPF and used to create a massive block to imbibe (surround) a fastener.

The combination of these conditions could have caused the formation of small fractures when the interface was forming at the interface between the two materials, and therefore the bond between the parts was very weak or non-existent. Although these hypotheses might be too simple for such a complex phenomenon.

The breaking of the metal rod/potting interface appeared only on the specimens of type 4 (EP5, EP8, EP11 and EP15 denoted by letter B in Table 15), on which the size was similar to the fastener of the insert tests. This may suggest that because of the rod size, the stress at the interface increases, causing the breaking.

Also, it's interesting to see that when 15% of micro-spheres were used (90.5 % of volume fraction) the potting was weakly bonded or not bonded at all to the metal rod (white color for the % of micro-spheres column of Table 15). This may suggest that for micro-spheres concentrations, near to or beyond 15% of the ponderal weight, the potting losses its adhesive properties, although more tests are necessary to confirm this.

Also, it's interesting that when the fastener is not bonded the potting near the metal rod breaks locally and small cracks are formed at the sides (see Fig. 153). Presumably, these cracks are what the shear failure of the SPF could look like.

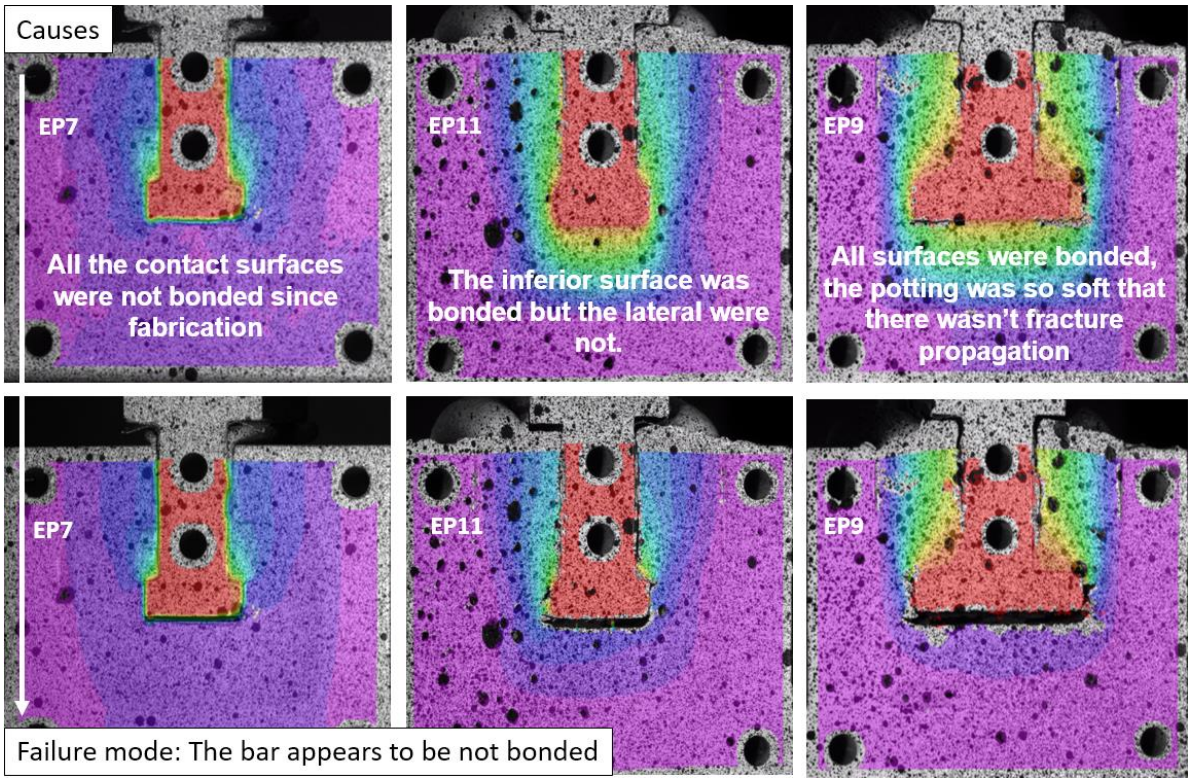

Fig. 153: Causes of the detaching of the metallic rod.

These small shear cracks can be also seen in the postmortem insert specimens of Bunyawanichakul. To show this, a specimen was analyzed under the microscope (see Fig. 154). The evidence shows that the micro-spheres are crushed (which indicates failure due to compression) but also that the potting is broken (which indicates failure under traction).

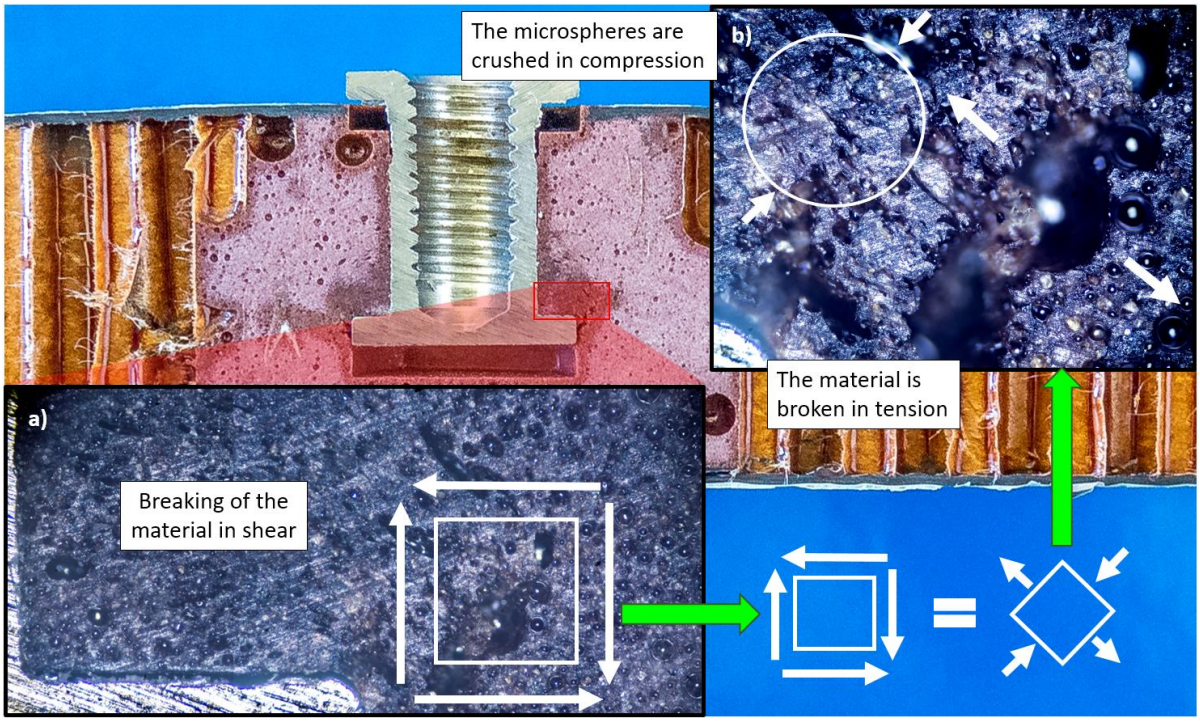

Fig. 154: Failure of the potting in shear

However, this compression/fracture shear scenario is different from the previously studied cases because here the breaking of the potting is localized and doesn't propagate. Also, the fact that this material has a different failure behavior in compression and tension should influence the shear failure.

Moreover, since in the insert tests made by Bunyawanichakul, most of inserts presented this failure scenario, this shear failure of the material might also be important and should be included in the insert F.E. model. Unfortunately, this feature was not considered when this test campaign was planned.

4.2.3 Conclusions of the experimental study

The experimental study allowed to obtain very similar failure modes to those that can be found in inserts as shown in Fig. 155 and Fig. 156.

We detected that two main failure scenarios are possible for the potting failure. The first one occurs when the fastener is firmly bonded to the potting of the insert (see Fig. 155). In this scenario, the potting breaks at the inferior fastener/potting interface or below this level.

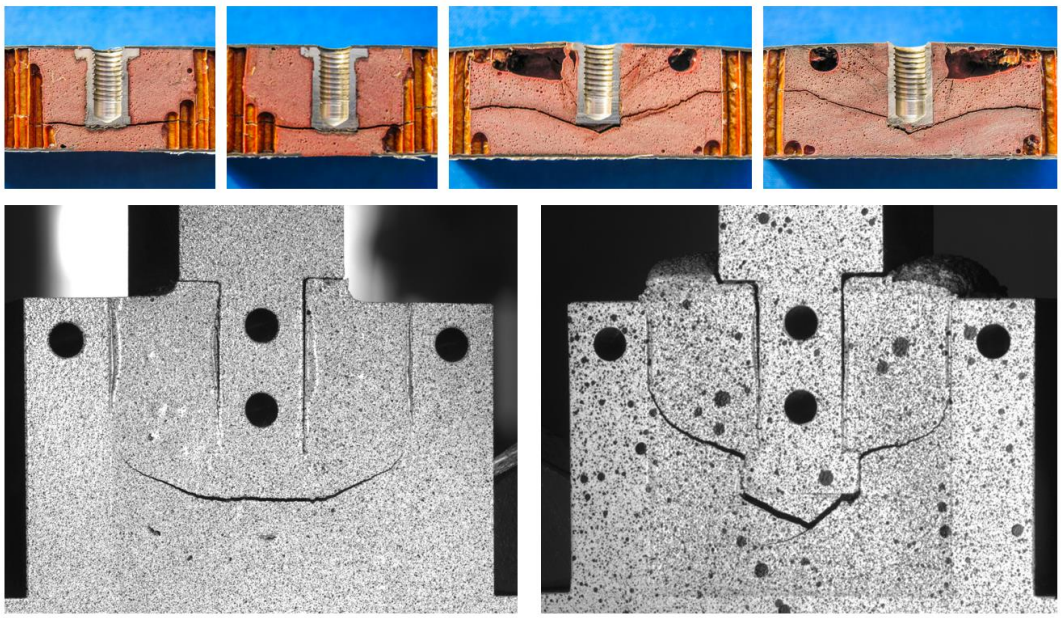

Fig. 155: Comparison of the failures of inserts and the potting test; the fastener was firmly bonded.

The second scenario is when the fastener is defectively or not bonded to the potting (see Fig. 156). This defect can be caused by several factors:

- The insert was partially/not bonded: this defect may can be caused by the temperature gradient at the fastener/potting interface, which is caused by the different thermal conductivity of both materials. Also, because the fastener was not correctly degreased before installation.
- The potting fabrication is defective: The quantity of hardener or excessive micro-spheres may result in very soft potting that will break very easily.

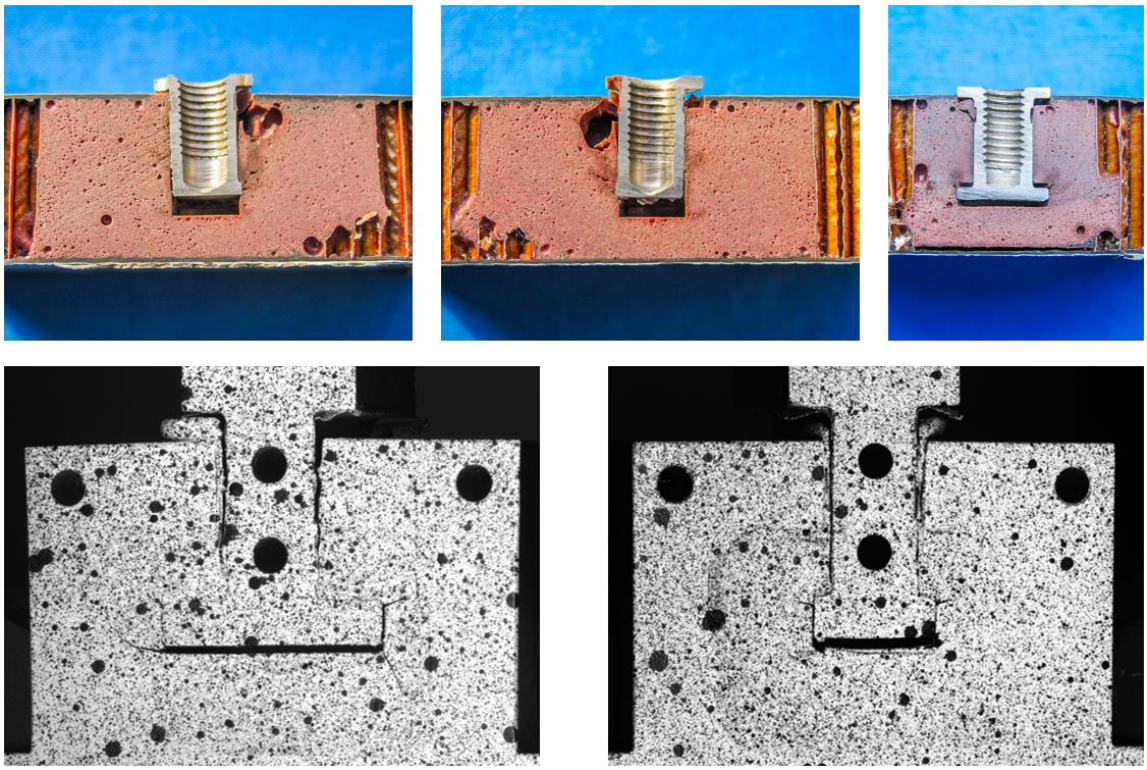

Fig. 156: Comparison of the failures of inserts and the potting test; the fastener was not bonded.

4.3 Numerical study

The uniaxial experimental study showed that varying the micro-spheres concentration for the potting resulted in a variation of the behavior in tension and compression.

Moreover, when the potting failed under tension, it broke as if it was a brittle material, while in compression it plasticized. This nonlinear behavior needs to be implemented in Abaqus to be used for the insert virtual model, as explained in the introduction of this thesis.

Also, when an insert is subjected to pull-out, the fastener shape makes that some sections of the potting are subjected to tension and a few others to compression, and to date, there are no studies that shows how this influences the insert's potting failure.

For inserts, the amount of material subjected to compression or tension depends on the shape of the fastener. For this reason, the tests presented in the previous section on which a metal rod of different geometries is pulled-out are retaken. It might be useful to observe the stress distribution in the potting, which will allow detecting the points of interest where the potting might fail, which can be made numerically.

Unfortunately, this behavior is not easy to implement under the Abaqus environment using the provided behaviors in the software. In 2000 Rizzi et al. (see ref. [97]) achieved to implement a similar behavior for a different type of SPF with accurate results, however, they did it by means of a user subroutine.

In this part of the research, the potting's test presented in previous section tests are numerically modeled. This is made to be able to develop a user material subroutine that allows including the potting nonlinear behavior in to the F.E. code. The aim is to calibrate the material law by comparison of the numerical and experimental results.

4.3.1 Modeling of the potting behavior

The experimental behavior of Fig. 140 and Fig. 141 was intended to be implemented into an Abaqus UMAT. Both compression and traction stresses induce different elastic responses for the same material. Also, the nonlinear response of the material under compression is very similar to a perfectly plastic behavior, while the failure in traction was a complete fracture of the material. The summary of the tests for the different percentage of micro-spheres is given in Table 12 and Table 13.

To represent the material behavior under compression, an isotropic perfect or ideal plasticity model is used, which implies that the yield surface is constant after failure (no hardening).

As for the fracture of the material under traction, several methods were tested to try reproducing a similar behavior. At the end, a CDM (Continuum Damage Mechanics) approach is selected to represent this breaking because of the reduced calculation time. When the Von Mises stress reaches the maximal traction stress the element's stiffness is reduced by 99.9%.

For the shear behavior, there were no experimental references available. However, since the shear behavior is a combination of traction and compression, an estimation of the shear moduli is obtained through the following equation:

$$G = \frac{1}{(1+\mu)} \frac{1}{\left(\frac{1}{E_t} + \frac{1}{E_c}\right)}$$

These features were included in to the UMAT code but we still found two principal problems:

- When different points of the same element had a different nonlinear behavior, there were convergence problems.
- When the software does several iterations and the nodes passes from traction to compression in the same time step, the software use the traction moduli for the recalculations when the material is in compression, and vice versa.

To overcome these problems, the algorithm shown in Fig. 157 was implemented.

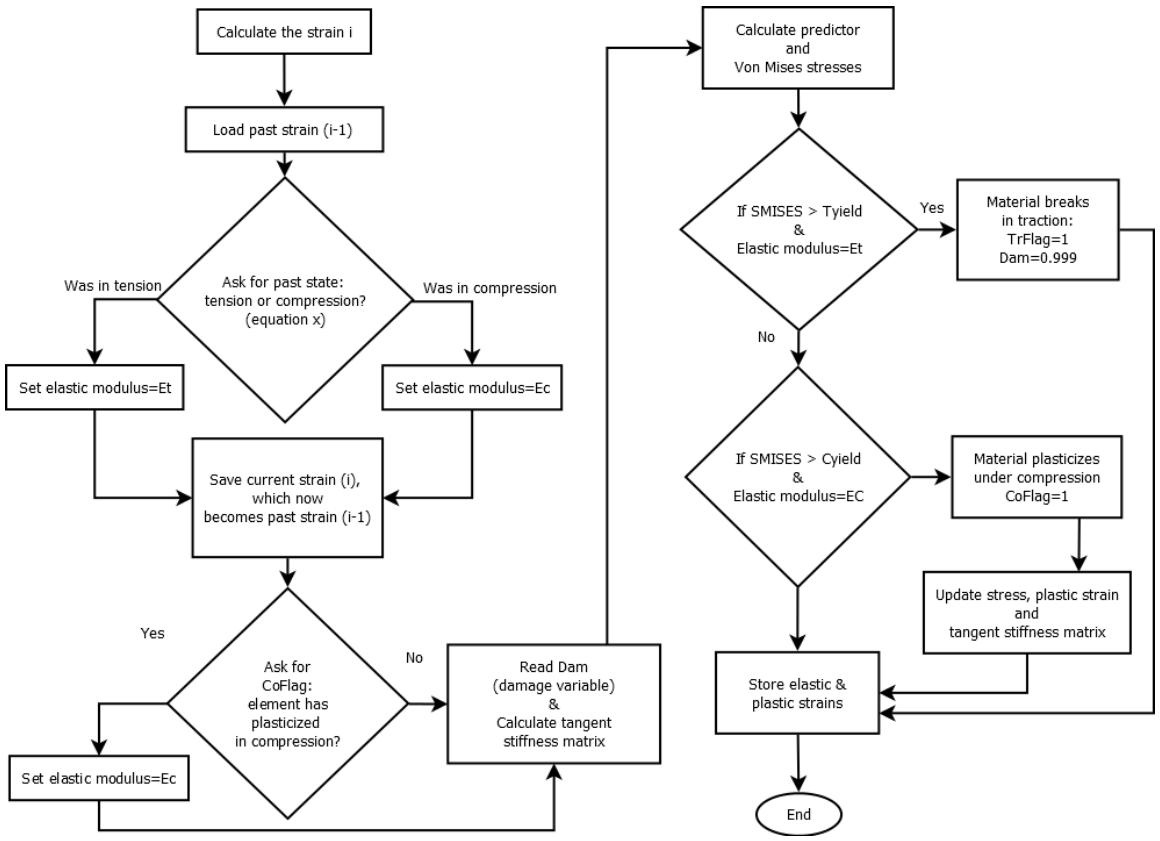

Fig. 157: Algorithm implemented in to an UMAT to represent the potting material behavior.

First, to avoid the problem of having different nonlinear behaviors in the same element, a hypothesis is made. When an element is subjected predominantly to compression, the compression moduli is used for the entire element and it can only fail due to plasticity, while when the predominant loading is traction, the traction moduli is used for the entire element and it can only fail in traction due to a brittle fracture.

This hypothesis means that each element can fail only in traction or compression, but not in both. However, this approach should work fine for this problem because the applied loads are static, which implies that elements rarely fail due to traction and then to compression (or vice versa).

Also, this hypothesis implies that the shear failure is not included in this modeling (which should be a combination of a brittle fracture plus the plasticity effect). Even so, considering that we don't have any experimental value of the shear moduli, strength or nonlinear behavior of this SPF, we consider this modeling to be accurate enough for our proposes.

To determine when an element is subjected predominantly to traction or compression, the trace of the deformation matrix is used. The sign of the trace allows determining when the element is subjected predominantly in traction or compression regardless of the loading direction. This is:

$$if \quad \varepsilon_{xx} + \varepsilon_{yy} + \varepsilon_{zz} > 0 \quad \rightarrow \quad traction\ \ behavior$$

$$if \quad \varepsilon_{xx} + \varepsilon_{yy} + \varepsilon_{zz} < 0 \quad \rightarrow \quad compression\ \ behavior$$

Also, to avoid the problem of the change of moduli between iterations for the same time step, the choice of the elastic moduli is made based on the previous state of the element, traction or compression. In this way, even if the elastic moduli changes, the previous modulus is used for the calculation and no convergence issues are generated. This method might be not very recommended for simulations that involve intensively charging and discharging of elements, however for static loadings, the transitory effects can be neglected.

Then, the elastic moduli (in traction and compression), the yield in compression and fracture stresses in tension were determined after several attempts to correlate the experimental results. The values are shown in Table 16 and the materials laws implemented in to the UMAT are shown in Fig. 158, Fig. 159, Fig. 160 and Table 16.

	%7	10%	13%
E_t [MPa]	2190	1851	1670
E_c [MPa]	1290	1233	1226
Poisson ratio	0.3	0.3	0.3
$\sigma_{t\ fracture}$ [MPa]	17.5	16.25	14.5
$\sigma_{c\ yield}$ [MPa]	31.5	28.5	27

Table 16: Failure stresses used in the UMAT

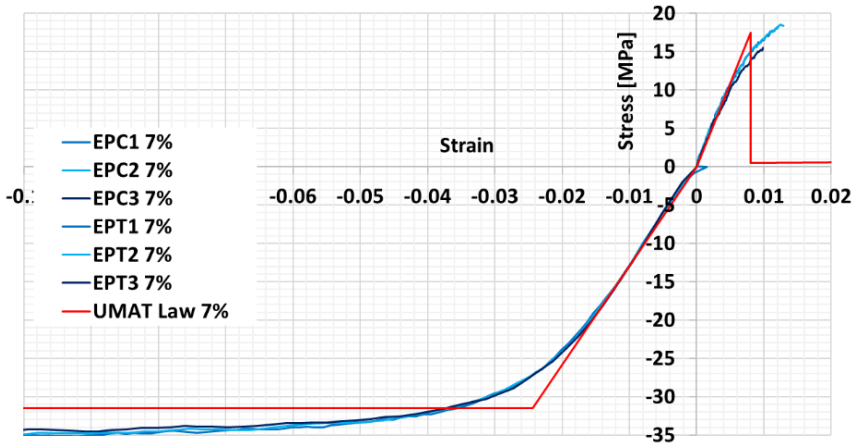

Fig. 158: Comparison of the experimental and numerical laws for the potting with 7% of micro-spheres

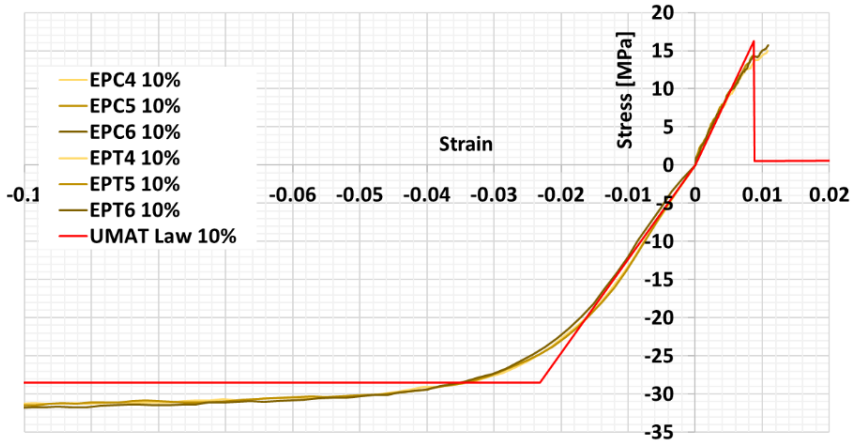

Fig. 159: Comparison of the experimental and numerical laws for the potting with 10% of micro-spheres

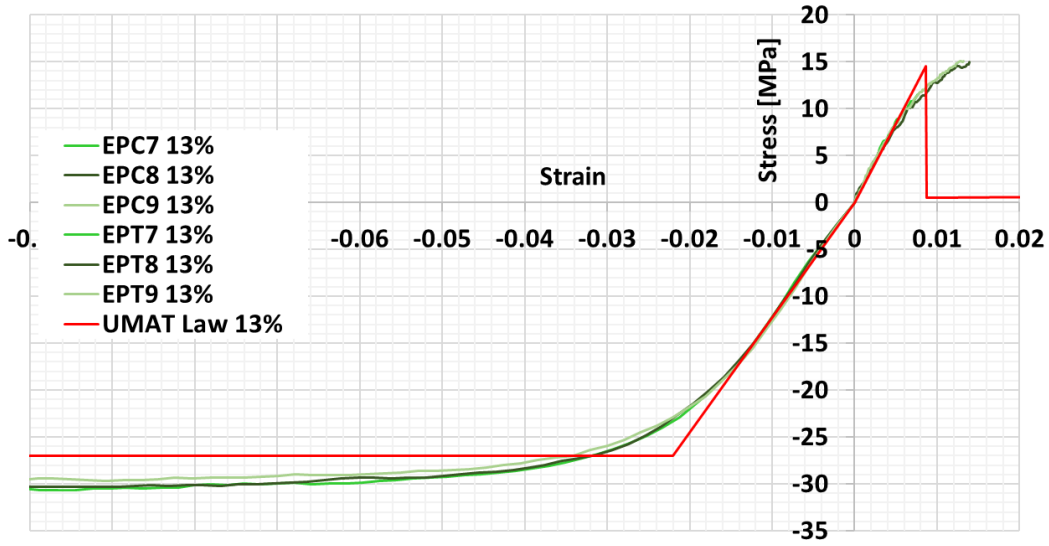

Fig. 160: Comparison of the experimental and numerical laws for the potting with 13% of micro-spheres

4.3.1.1 Validation of the material law

The traction and compression tests presented in the previous section were reproduced in Abaqus to implement the proposed behavior laws. Similar boundary conditions were used as in the real tests and only brick volume elements were used.

The results of the simulations are shown in Fig. 161 and Fig. 162. The comparison of both experimental and numerical results showed good agreement in a very low calculation time.

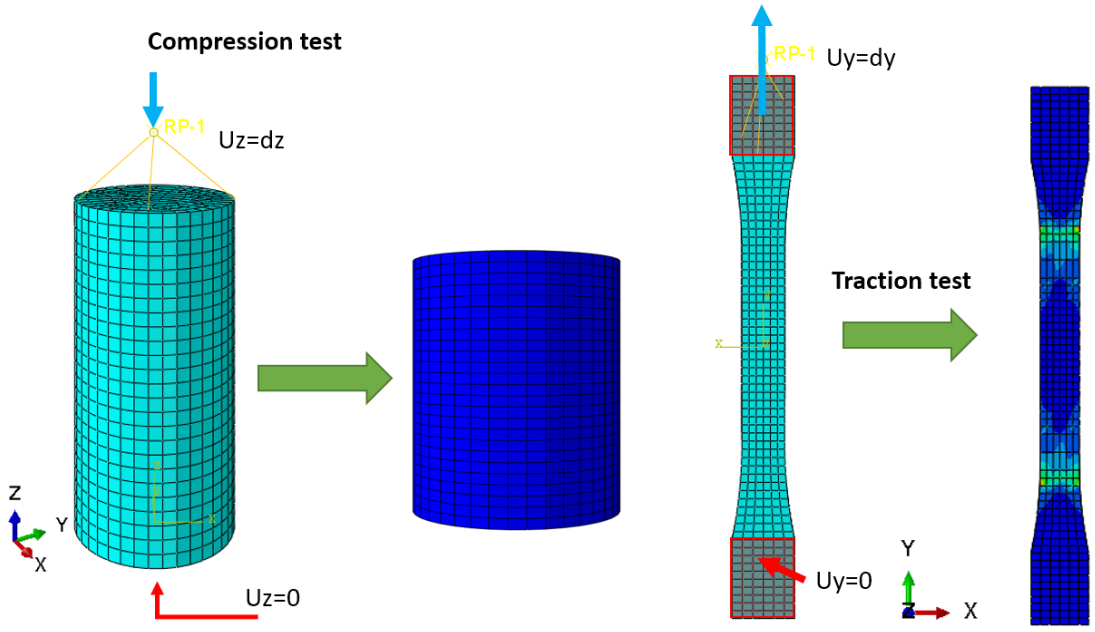

Fig. 161: Modeling of the traction and compression tests.

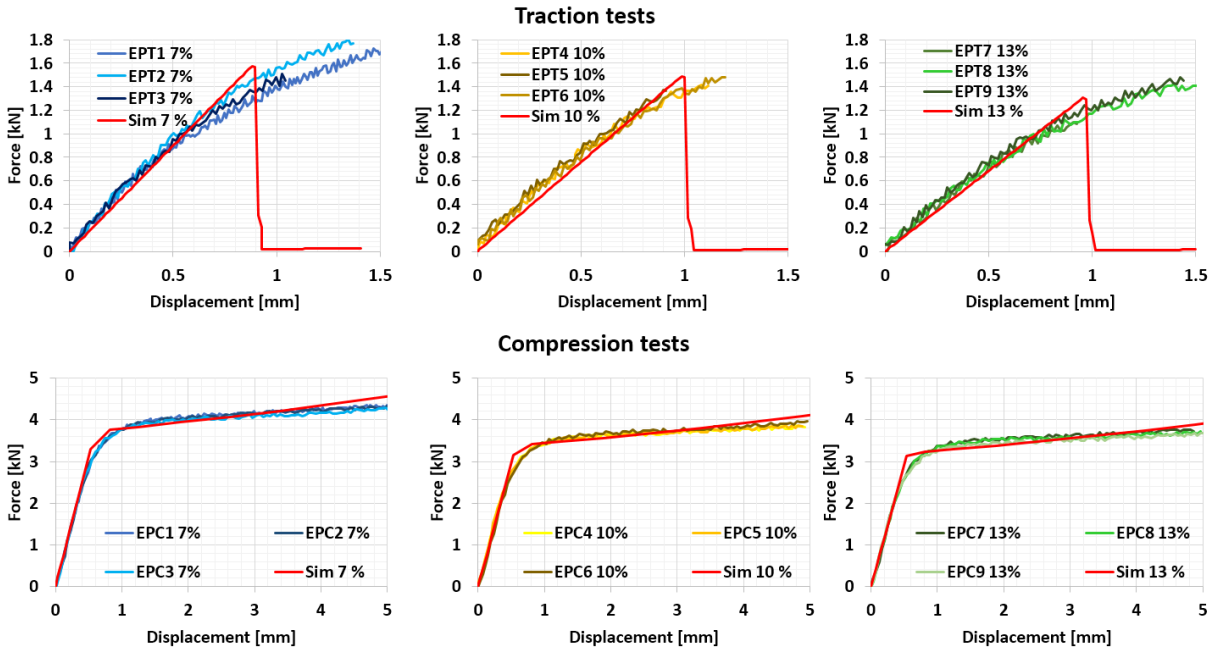

Fig. 162: Experimental vs numerical results; traction and compression tests.

4.3.2 Modeling of the potting pull-out tests

The four types of specimens used to study the inserts' potting failure were modeled using Abaqus standard. Since the specimens were symmetrical, only half of the model was simulated to reduce the computational cost. The elastic moduli of the materials are 220 000 MPa and 75000 MPa for the stainless steel and aluminum respectively.

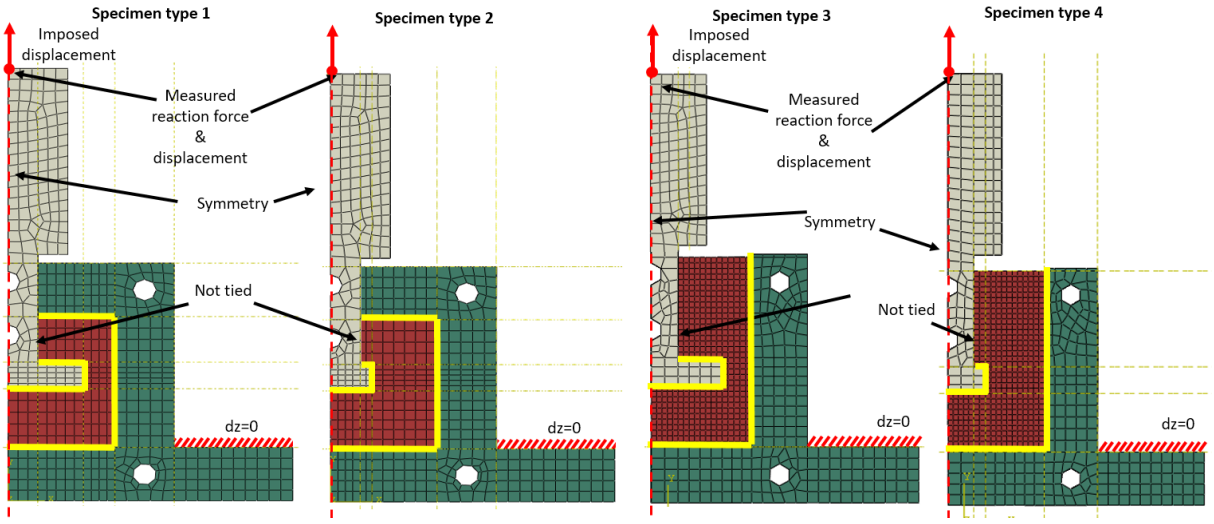

Fig. 163: Modeling of the potting pull-out tests.

The assembly was partitioned to be meshed in a simpler way, also only C3D8 elements were used. All the parts were bonded using the tie constraint (yellow line) as showed in Fig. 163. The displacement was imposed at the superior face of the rod and the clamping of the specimens was put at the inferior border of the box where the Z displacement was fixed. All these characteristics are shown in Fig. 163.

For the potting material, the UMAT presented previously was used to reproduce the desired behavior.

For the 7%, 10 % and 13% of micro-spheres concentration the mechanical properties of the potting of Table 16 are used. For the rest of different micro-spheres concentration, the curve shown in Fig. 143 was used as start point.

Only the specimens on which the metal rod was bonded were simulated, the specimens are indicated with letters A and B in Table 15 (EP3, EP4, EP20, EP2, EP17, EP1, EP14, EP19, EP18, EP10, EP9, EP5, EP8 and EP15, EP11 and EP15).

4.3.3 Results and discussion

The experimental and numerical results are compared. Concerning the vertical displacement fields of the specimens and the virtual model, they are very similar, therefore it can be said that these F.E. models are representative enough for our purpose (see Fig. 164).

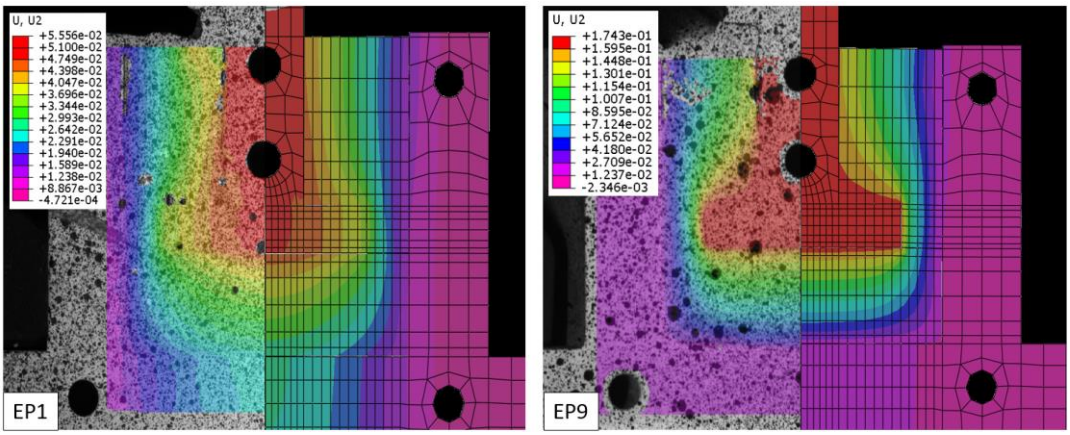

Fig. 164: Comparison of the vertical displacement field between the experimental and numerical results for EP1 and EP9 specimens.

Concerning the slope of the loading curves, there is a noticeable difference between experimental and numerical results (for type 1 and 2 see Fig. 165 and for type 2 and 3 see Fig. 166). This can be explained because of the fabrication defects such as the partial bonding between the rod and the potting, the presence of air bubbles, and the small variation of the fixation conditions. For the failure of the specimen it's well represented for specimens EP4 and EP3, however for the rest the failure load is higher. This can be caused by the difference of the failure of the virtual potting material and the actual real material, which is brittle and breaks suddenly, while the virtual material breaks element by element, one at the time. However, this can be caused by a partial weak bonding between the parts, in which case, it can be concluded that the actual potting failure can occur at the failure force obtained by the F.E. simulation or lower due to a defective bonding.

It's possible that a better correlation can be obtained if the shear failure is included into the material behavior, which also means to perform more tests. Yet, this is only a first approach and the obtained are considered accurate enough for the purpose of the model.

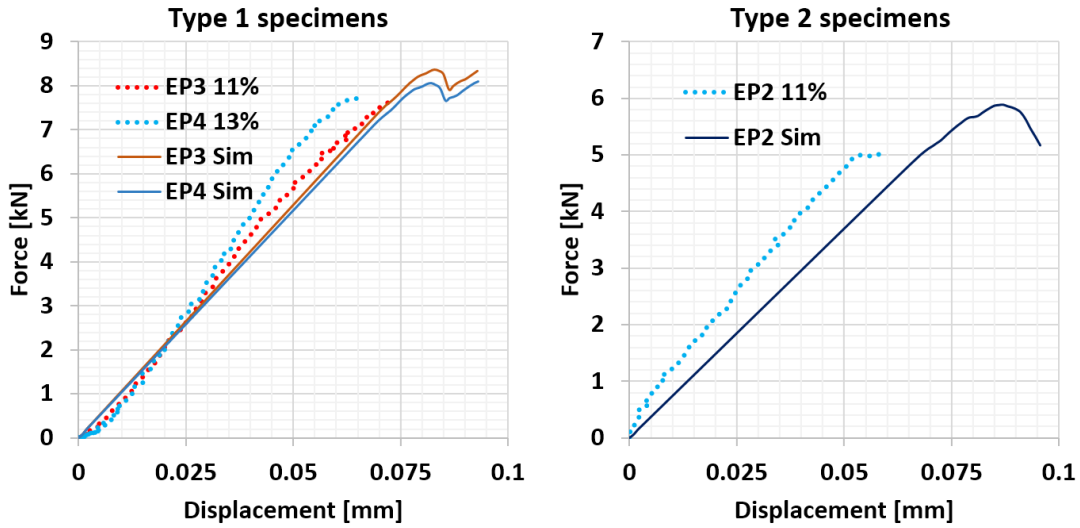

Fig. 165: Experimental vs numerical results: loading curves of the specimens' type 1 and 2.

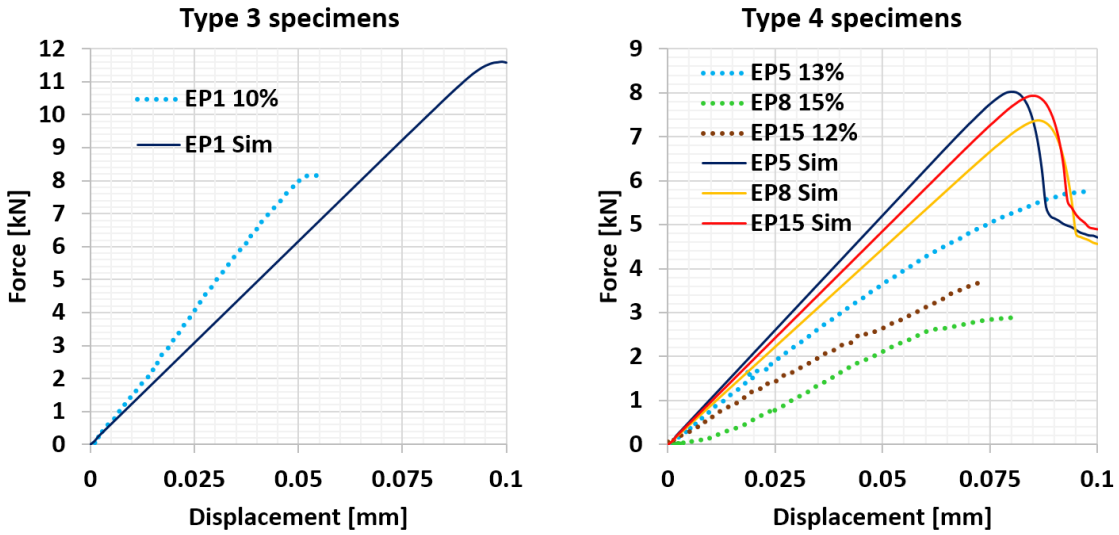

Fig. 166: Experimental vs numerical results: loading curves of the specimens' type 3 and 4.

Also, the modeling of these specimens allowed us to validate the curves proposed in Fig. 142, Fig. 143 and Fig. 144, for the density, the elastic moduli and the resistance to traction and compression as function of the percentage of micro-spheres.

Theoretically, the rule of mixtures could also be used to estimate the elastic properties of the compound:

$$E_{pot} = \left(\frac{1}{1 + \frac{\rho_m}{\rho_{\mu b}} P_{\mu b}} \right) E_m + \left(1 - \frac{1}{1 + \frac{\rho_m}{\rho_{\mu b}} P_{\mu b}} \right) E_{\mu b}$$

Nevertheless, when the experimental data and the predicted values by the rule mixtures are compared, the error is very significant (see Fig. 167).

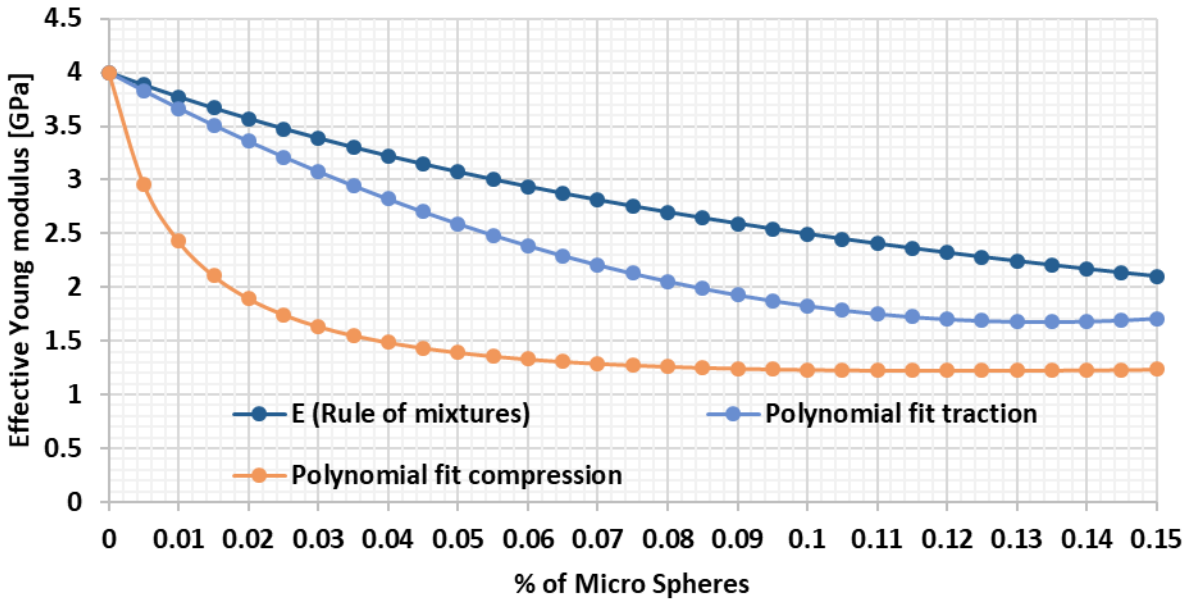

Fig. 167: Effective young moduli: obtained values vs the prediction of the rule of mixtures.

4.4 Conclusions

Only the mechanical aspects of SPF were evaluated in this research.

The experimental study shown in this chapter suggest that the different potting's failure scenarios found by Bunyawanichakul in its PhD thesis might have different causes.

When the fastener is not bonded, the failure scenario of Fig. 154 appears. The reasons of this defect can be the absence or bad degreasing of the fastener before installation, a curing of the insert that involves relatively high temperatures, an excessive amount of hardener in the adhesive, the weakening of the potting due to in service high temperatures or the oversaturation of the adhesive with micro-spheres (15% or more, of the ponderal weight).

When the insert is strongly bonded, the failure scenario of Fig. 156 appears. The potting failure is caused by the breaking of the potting beneath the fastener or the breaking of the potting/fastener interface, depending on which of both is weaker.

Concerning the micro-spheres concentration on the potting compound, different mixtures were tested and the obtained values allowed tracing the effective Young moduli in traction and compression as function of the micro-spheres concentration. This is useful because it allows including the variation of the mechanical properties of the potting in the insert analysis.

Also, it was shown that the micro-spheres concentration reduces the potting effective mechanical properties, but increases the specific mechanical properties. This aspect is interesting because it allows reducing the potting weight in function of the desired failure load, although this aspect needs to be investigated together with the core and skins strengths.

Finally, the numerical study proved that it's possible to create a virtual representation of the potting material that allows including the different failure modes. This will be used in the next chapter of this thesis.

Chapter five: Virtual testing of inserts and failure mode maps

In this final chapter, the full development of failure mode maps based on the virtual testing of inserts is presented. First, the F.E. modeling of three different types of inserts is made by using the results of the previous chapter. The numerical and experimental results show good agreement. Afterwards, a description and a study of the influence of the defects for inserts is introduced. Then, a parametric insert model is developed considering the defects influence. Finally, the failure mode maps are drawn.

5.1 INTRODUCTION 173
5.1.1 Insert sizing through the analytical methods 173
5.1.2 Insert sizing through F.E. modeling 175
5.1.3 Proposed methods 176
5.2 STUDY OF DEFECTS IN INSERTS 179
5.2.1 Analysis of the different defects of inserts 180
5.2.2 Evaluation of the criticality of defects in inserts 184
5.2.3 Analysis of variations of the potting radius 187
5.2.4 Conclusions about the defects in inserts 193
5.3 DEVELOPMENT OF THE INSERT F.E. MODEL 195
5.3.1 Description of the insert's experimental reference 195
5.3.2 Insert F.E. model features 206
5.3.3 Implementation of the behavior laws 208
5.3.4 Parametrization of the F.E. with Abaqus scripting 221
5.3.5 Conclusion about the F.E. modeling of inserts 223
5.4 DEVELOPMENT OF THE FAILURE MODE MAPS 225
5.4.1 Exploration of the influence of the principal design variables 225
5.4.2 Sweep of the real potting radius: from 9.5 to 23.5 mm 228
5.4.3 Swept of the potting properties 228
5.4.4 Sweep of the skin thickness 229
5.4.5 Failure mode maps 230
5.4.6 Insert mass optimization 235
5.4.7 Loss of linearity criteria (LLC) vs first failure criterion (FFC) 237
5.5 CONCLUSIONS 239

5.1 Introduction

5.1.1 Insert sizing through the analytical methods

The literature references about inserts for sandwich structures were presented in chapter 2, where the Insert design handbook of the ESA [1] stands out. In this reference the approach developed by Ericksen (see ref. [3]) is proposed to estimate the shear stress in the core, and thus, to calculate the insert strength. It's not surprising that this method is the most used in the industry.

In the light of this, one might ask, does this method really work? Is it accurate?

Recently, Wolff et al. (see ref. [4]) published a research about inserts in sandwiches with aluminum honeycomb core. They evaluated the accuracy of the estimated failure load of the ESA method by comparison to a few experimental results. They used the 2% linear regression criterion to identify the insert failure. According to them, the ESA method underestimates the insert failure load by -18 to -21%.

For this thesis, we did the same kind of study using the ESA method and the experimental data of the inserts tested by Block et al. in reference [53]. The inserts were installed in a sandwich panel with aluminum honeycomb core. First, we calculated the failure load using the method of the ESA, and then the obtained values were compared to the experimental values. It is worth to mention that every insert was tested 8 times and the insert failure criterion was the first failure or when plastic deformation occurs. The calculated load showed a good agreement with the experimental results. The error varied from -4% to +68 % with an average overestimation of 25%.

Both studies show different results. According to Wolf et al. the insert strength was underestimated by -18%, while our study indicated that the load is overestimated by 25%. Yet, this range of (-18% < error < 25%) is not too far from the experimental strengths. The discrepancy of both studies could be attributed to the fact that different failure criteria were used to detect the insert failure. Also, it's possible that defects such as an incomplete filling of the cells or the correct bonding of the parts played an important role too.

This last aspect is important because most of inserts are installed manually, often introducing defects into the insert. Indeed, the ESA method includes the influence of the irregular shape of the potting by proposing an effective potting radius that is given by equations that considers the typical and minimal effective radius.

However, other imperfections such as the incomplete filling of the cells (or air bubbles), the weak bonding of the parts (studied in chapter 4), or the variations of the material properties are not considered in the method.

As example of this last aspect is the shear strength of the Nomex® honeycomb, which can be increased by 16% or 32% in the W and L directions respectively if the cells are laterally stabilized by the insert. Also, the concentration of micro-spheres for the potting may cause small variations on the mechanical properties of the material.

Including all these variations or defects into the ESA analytical method introduces more variables into model. In consequence, there will be more than one possible path to calculate the insert strength (see Fig. 168).

The inclusion of the defects or variations in to the analytical model will allow to better estimate the failure load of an insert. On the other hand, there will be more than one path to calculate the insert strength. In other words, it gives the possibility to obtain an accurate result by increasing the error interval.

This error could be attributed to the hypothesis and simplifications that were made, which also reduces the physical meaning of the model. For example, the ESA method relates the failure of the core to the damage of both W and L directions because they are coupled, therefore an equivalent shear strength is calculated by multiplying the shear strength of the W direction by a factor of 1.36. In contrast, the research presented in chapter two suggests that the boundary conditions influence the stability of the cells increasing its shear strength which could explain this factor of 1.36 too.

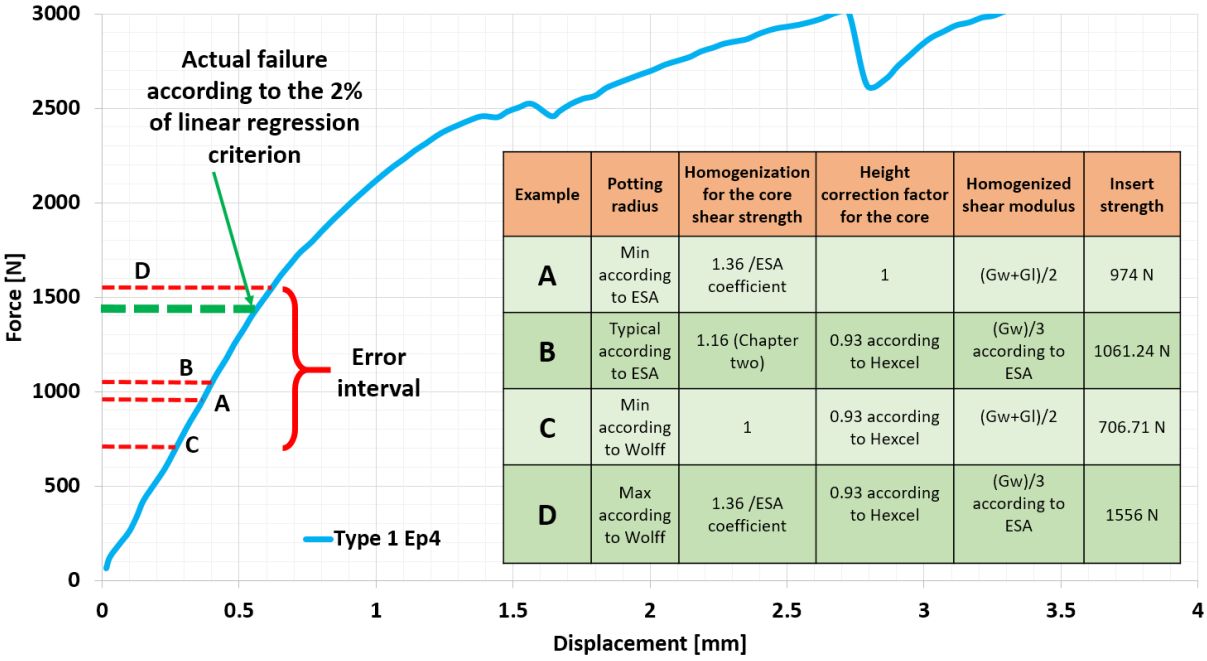

Example	Potting radius	Homogenization for the core shear strength	Height correction factor for the core	Homogenized shear modulus	Insert strength
A	Min according to ESA	1.36 /ESA coefficient	1	(Gw+Gl)/2	974 N
B	Typical according to ESA	1.16 (Chapter two)	0.93 according to Hexcel	(Gw)/3 according to ESA	1061.24 N
C	Min according to Wolff	1	0.93 according to Hexcel	(Gw+Gl)/2	706.71 N
D	Max according to Wolff	1.36 /ESA coefficient	0.93 according to Hexcel	(Gw)/3 according to ESA	1556 N

Fig. 168: Example of the application of the ESA method to the insert type 1 (see next section) using different hypothesis for the materials and geometries.

To sum up, the accuracy of the analytical methods relies on the correct selection of parameters. If they are chosen correctly, the result of the method should be accurate. And so, the drawback of the analytical predictions can be generalized in two main problems:

- There are plenty of very different propositions to assign a value to each parameter for the insert strength calculation.
- Inserts are mostly handmade, and thus, many defects should occur.

The first problem has been treated by Wolff et al. in ref. [4]. In their research, they managed to take in to account all kind of propositions to improve the accuracy of the ESA method in a very skilled way. They had to choose from 2 mathematical formulations for the insert strength, 6 different proposed coefficients to determine the shear strength of the core, 4 homogenization methods for the shear moduli of the core, and finally 4 different models to consider the variations of the potting radius. The complexity of the analysis is remarkable.

The second problem related to defects involves two things; inserts are full of defects that can't be avoided, and secondly, the defect types might be different for each insert or installation. Also, defects can't be completely seen until the specimens are fabricated, tested and then cut to be analyzed.

And thus, the problem is that the analytical approaches don't include the influence of defects in anyhow, Nevertheless, their influence on the failure load might be important and can't just be simply neglected.

All in all, the insert analysis is very complex. The analytical predictions are based in assigning values to different parameters, and these values might differ according the research, which is ambiguous. Finally, the experimental insert strength might be very different to the

estimated by the analytical calculations due to the influence of defects or manufacturing discrepancies.

5.1.2 Insert sizing through F.E. modeling

Another approach has been proposed to analyze inserts. F.E. methods seems like a good alternative for the insert design, which may provide more accurate predictions than the analytical approaches [5], [34].

This method may offer several serious advantages, since it makes possible to understand how inserts fails, in which order do the parts starts to break and which ones are the most critical failures, but also, allowing to include and evaluating the influence of some defects.

On the other hand, there are also disadvantages. Even if this method is supposed to be more accurate, the correct modeling of core and insert geometry demands a very good expertise and time investment, due to the numerous features that should be included.

In 2015, this approach was used by Seemann et al. for the virtual testing of inserts (see ref. [34], [98] for example). First, they focused on the modeling of honeycomb cores for a considerable period of time (maybe two years) [12], [99]. Later, with the acquired knowledge, they developed a detailed model of an insert pull-out test. At the end, the results showed a very good agreement with the experimental results. They could reproduce the insert pull-out post-failure behavior, which is quite a good achievement considering the complexity of the problem.

Nevertheless, the invested time for the development of a detailed insert virtual model makes impossible to perform this kind of analysis every time an insert needs to be designed.

Also, considering the honeycomb cells geometry, and all the possible potting shapes, it might be necessary to perform one simulation for each possible potting configuration, which is not practical.

This chapter is framed by the lack of accuracy of analytical methods, but also, the very high complexity of the detailed F.E. modeling of inserts.

Summarizing, the main limitation of the insert sizing through F.E. modeling is related to the three mains problems:

- The level of detail, mostly related to the honeycomb modeling.
- The required number of simulations to consider all scenarios, which is related to all the possible potting geometries.
- The development time, which is related to the efficacy of the implementation of this method.

To contribute to the solution of the first problem, we developed a rapid CDM (Continuum Damage Mechanics) modeling approach that allows to simulate the shear nonlinear response of honeycomb cores in a very quick and accurate way in terms of computational cost (see chapter 3 and ref. [14]).

As for second problem, our first thought is taking the approach of the ESA, in which they propose the use of an equivalent potting radius that considers all the possible potting geometry variations. Also, the study presented in chapter four helped us to identify the most important characteristics that should be implemented into its modeling. A formal discussion of this second problem is presented in the following sections of this chapter.

Now, if the first two problems are partially solved, the calculation time of the model should be relatively short.

Finally, as for the third problem, even if the model is very simple and has a low computational cost, a package of specialized software is required (Abaqus and Fortran for example) to perform the simulations.

Moreover, the obtained results should require an interpretation based in the wide background and hypothesis that were made for all the complex phenomena discussed within this PhD thesis.

We think that the best (or only) way to implement this approach, is by stablishing a method, like a recipe, that shows how to implement it in an efficient way.

Since the calculation time is short, we propose to parametrize the insert F.E. model to perform several numerical tests inserts (as Zenkert [5] proposed and Seeman [34] did) for the drawing of failure mode maps (as the ESA and the military handbook 23A proposed in [2], [37]),

The idea is very simple, instead of modeling an insert every time a calculation is needed, it's better to have a chart on which the insert failure load can be easily read. In this sense, all the simulations could be performed by a specialist, and then, the failure maps can be easily shared, providing an accurate and rapid insert sizing tool for engineers.

Our solution to the problems presented previously is presented in the next section.

5.1.3 Proposed methods

5.1.3.1 Perform a study of the defect in inserts

The only way to include these defects into the insert strength calculation, is by predicting their appearance and by evaluating their influence on the insert integrity. However, this kind of study is not available in the related literature. Therefore, a statistical study using all the available data in the literature review is performed. This must include the frequency of the defects, analyze if they can be avoided or not, but most of all, their effect on the insert strength.

The results of this research could provide different suggestions for the inclusion of defects into the insert design.

5.1.3.2 Modeling of three different type of inserts

In the literature, there are several F.E. models that were created to analyze the failure of inserts in sandwich structures. These models had different purposes but in general they were descriptive models. That is to say, those models were created to reproduce numerically the test results. Enabling to do an experimental-numerical dialogue, which results very useful to understand the causes and the failure scenario of inserts.

In this chapter, three descriptive models of inserts are developed. The models will be compared to experimental test results to establish a dialogue that allows to understand the effect of each of the insert characteristics.

Our method consists of including different failure modes intrinsic to each material, and then, see how this influences the insert model loading curve. We will suppose that, the more the experimental and numerical curves are similar, the more accurate are our hypotheses about the failure modes and their order of appearance. This method will be useful to determine the "how and why" of the failure scenario described by Bunyawanichakul in its PhD thesis (see ref. [15]).

5.1.3.3 Develop a failure mode map for inserts

Instead of modeling the inserts each time a calculation is needed, it's better to have a chart on which the insert failure load can be easily read.

Therefore, the best way we found to use this model is through the sweep of the design parameters inside a pertinent range, which allows obtaining different charts of the estimated failure load as function of the design parameters.

For this, the insert F.E. model is parametrized. This is accomplished using Abaqus scripting and Python.

The variation of the principal insert design variables such as the potting properties and size radius are presented first, but also the sweeping of the core density and thickness of the skins.

Then, the obtained data is used to draw the failure mode maps as function of the design variables. This is practical because all calculations are made only once, and then, the created charts can be easily shared.

5.2 Study of defects in inserts

Composites are potentially subjected to many different type of defects, thus, it is well known that the consideration of imperfections is very important for the design of composite materials parts (see for example ref. [100]).

However, in the literature review, only Raghu et al. in ref. [28] performed a similar study, but their results only include a small range of variations. Beside this, there is not a quantitative analysis of the influence of defects, nor how these affect the insert strength, or how they should be considered for design purposes. So, this section is dedicated to clarify this aspect.

Since our specimen database is relatively small, we decided to include the evidence shown by the other researchers too. All the works cited in the literature review (Table 2, Table 3, and Table 4) and that contain visual evidence of inserts are considered for this section.

And so, we could identify seven types of defects that are commonly present in inserts:

- The potting shape of the insert (see Fig. 169).
- A weak bonding of the fastener (see Fig. 170).
- Presence of air bubbles in the potting (see Fig. 171).
- Irregular borders of the potting (see Fig. 172).
- Incomplete filling of the cells (see Fig. 173).
- Variations of the micro-spheres concentration (see Fig. 174-a).
- Potting radius smaller than the insert radius (see Fig. 174-b).

Each defect influences the integrity of the insert in a different way. For this reason, their criticality should be analyzed individually.

To show this, let's consider the bonding problem studied in chapter four. When the fastener was not bonded to the potting as result of a poor bonding between the potting adhesive and the surface of the fastener. This defect makes the entire pull-out force concentrated into the small inferior contact section between the potting and the fastener, which makes breaking and plasticize the potting very easy, thus reducing drastically the insert strength.

While other defects such as the trapped air inside the potting, presumably has almost no influence on the insert strength, since the potting is much stiffer than the core.

Considering this, the seven type of defects are analyzed in terms of:

- Frequency: if a defect is always present, it can be considered as a part of the insert itself, if the defect is not very common, it might not be interesting to consider it for the design.
- Size: certainly, it's not the same to have small imperceptible micro defects rather than defects of the size of the insert.
- Avoidability: it's important to determine if defects are caused by a bad design, human error or even if it can be avoided or not, so their origin is important
- Influence on the insert strength: Some defects have more influence than others.

A discussion about the main aspects of each one of these seven defects is presented in the next section. Then, the criticality of the different defects is determined as a function of this analysis.

5.2.1 Analysis of the different defects of inserts

5.2.1.1 Variations of the potting shape

This defect should be present in all inserts due to the characteristic honeycomb geometry. The size of the defect should be considered at mesoscale because, if the skins are removed, it could have been observed with the naked eye.

The potting shape is given by the cell size and the position of the perforation regarding the honeycomb cells. If the perforation is made slightly different the shape of the potting zone may totally change, since inserts are handmade. This means that the potting shape can't be controlled or predicted, therefore this defect can't be avoided.

Also, depending on the number of cell walls that are opened by the drilling tool, the potting area might be bigger or smaller for the same perforation diameter as explained by the ESA. Therefore, the insert strength might be increased or decreased significantly depending of the number of cells that are filled with potting (see Fig. 169).

Moreover, depending of the potting shape, the honeycomb cells might be subjected to shear in only one direction, or two at the same time, depending of the insert geometry. Therefore, the cells strength might be increased as seen in chapter two (see Fig. 169).

Also, predicting the shape of the radius is very complex, and a discussion about this topic is introduced in later sections.

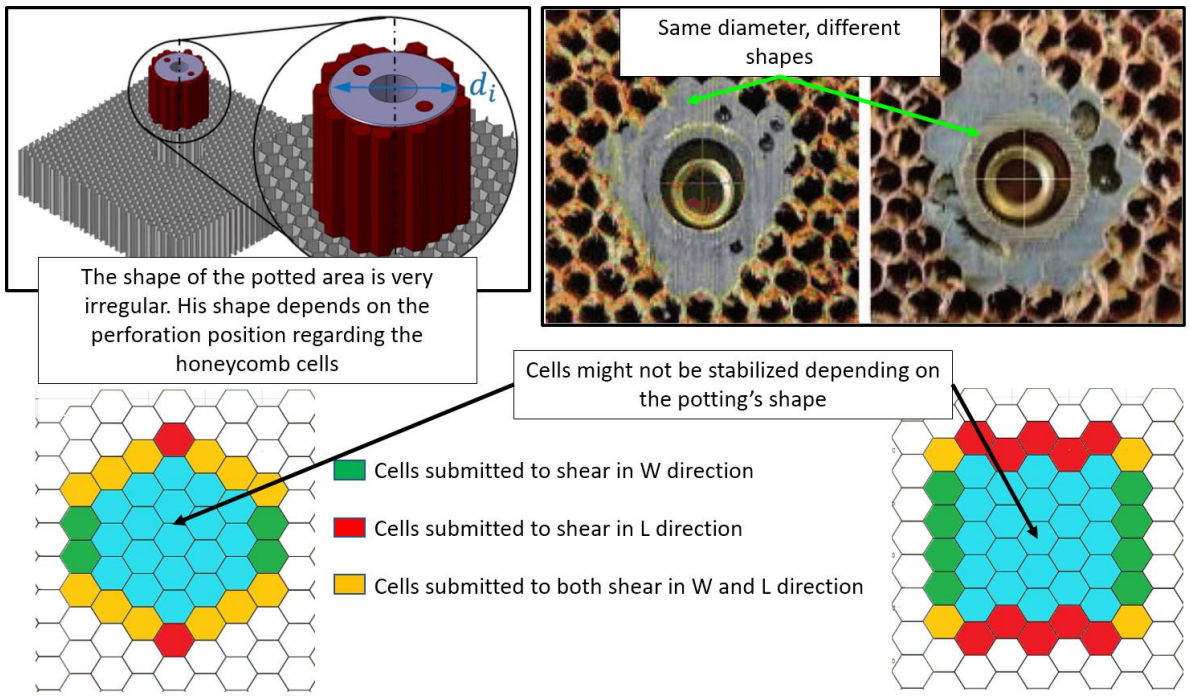

Fig. 169: Examples of variations of the potting shape for inserts [4], [28].

5.2.1.2 Weak bonding of the fastener

This kind of defect was very present in the tested specimens in the PhD thesis of Bunyawanichakul (see ref. [15]) where a SPF was used as potting. Besides this, this defect was only observed when inserts where tested under high temperatures beyond 260° C (see ref. [39]). Therefore, it can be said that this defect is not very common.

This defect is observable only after the insert pull-out test are performed, the fastener goes out as shown in Fig. 170, thus it occurs at mesoscale.

The causes of this defect were analyzed in chapter four. However, they were just hypothesis because the way adhesive works is still not very clear among scientists. However, this defect was not observed in the work of all the other authors, therefore it can be said that this defect should be taken as part of a bad design, thus avoidable.

Also, it has a big influence on the insert strength, most of all because if the fastener is not well bonded, the load is transmitted directly between the contact point of the fastener and the potting. And since the contact area is relatively small, the potting plasticizes at very low pull-out loads.

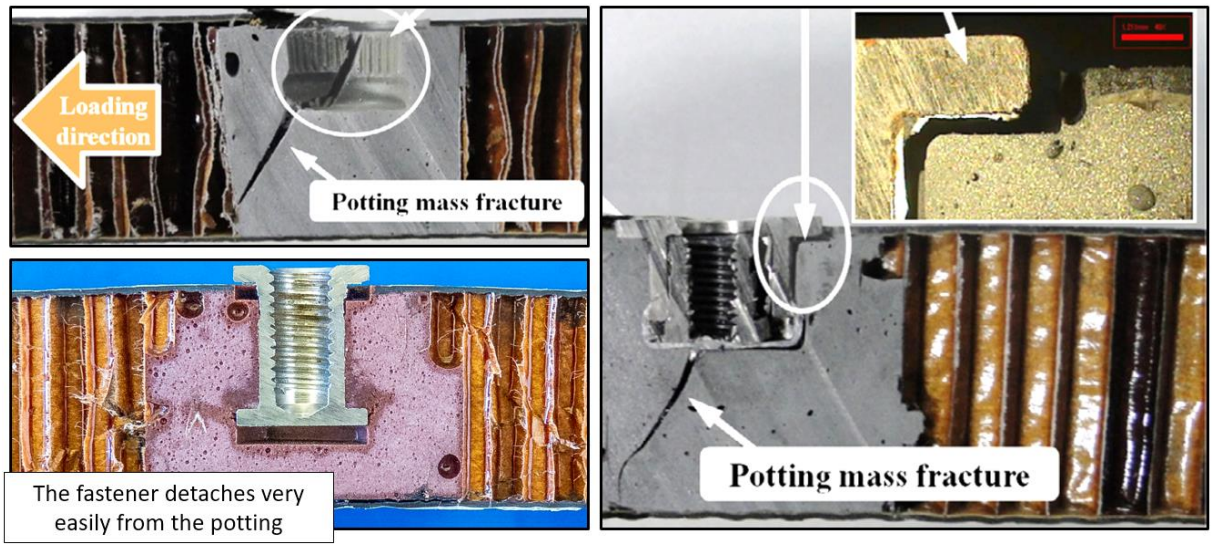

Fig. 170: Example of detaching of the fastener [15], [39].

5.2.1.3 Presence of Air bubbles

This defect is very common, it was present in almost all for the visual evidences (see Fig. 171). The size of the trapped air bubbles is visible once the specimen is cut by the half, thus it should be considered at mesoscale.

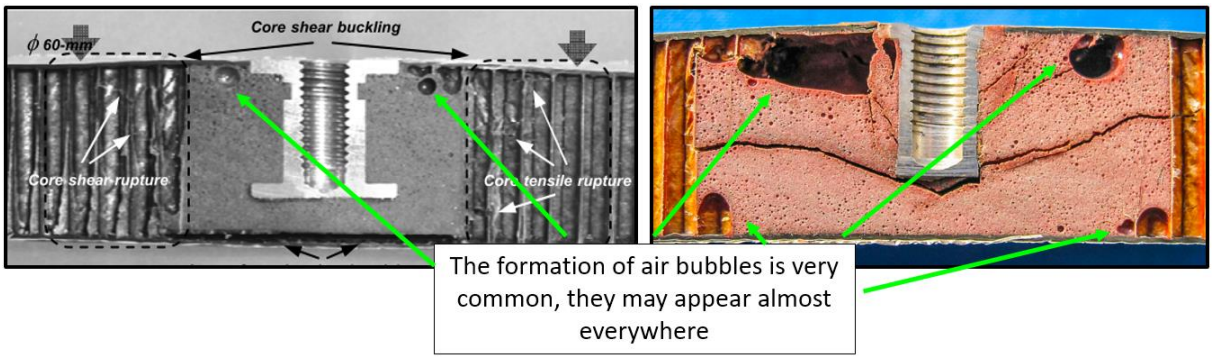

Fig. 171: Examples of the formation of air bubbles in inserts [15], [48].

The causes might be the high viscosity of the potting compound or even because the injection was made too quickly, therefore it can be considered as part of a defective installation, thus avoidable.

Concerning its influence, considering that this defect was always present in specimens and that in general the curves don’t show a significant dispersion, it can be said that the influence of this defect should be considered as low.

5.2.1.4 Irregular borders of the potting

This defect was present in a considerable number of the insert specimens in the literature. The irregular shape of the potting is visible once the specimen is cut in half, thus a mesoscale defect (see Fig. 172).

It is caused by the partial removal of the honeycomb walls when the panel is perforated. Therefore, it might depend on the position of the perforation regarding the honeycomb cells but also of the perpendicularity of the drilling tool regarding the panel. Also, in some cases the panel is undercut to make bigger the potting area to increase the insert strength. This technique may also induce this defect on inserts. This defect is caused due to a bad installation, thus avoidable.

The influence of this defect on the insert strength is that if the borders are irregular, hotspots are introduced into the cells surrounding the insert.

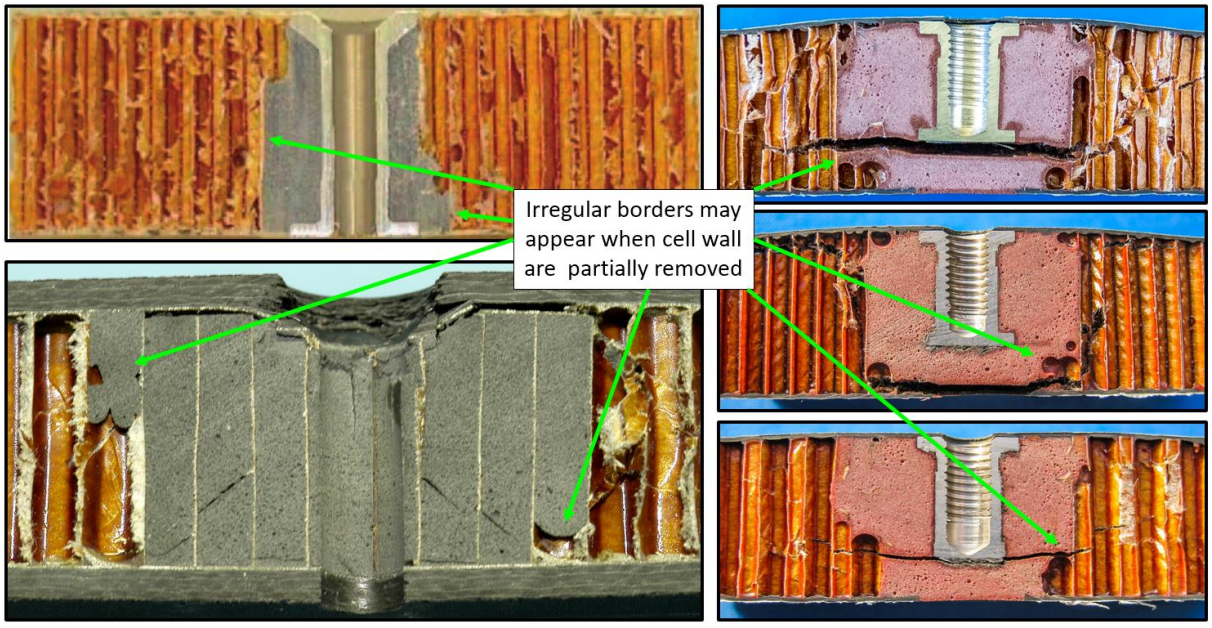

Fig. 172: Examples of the irregular borders formed in inserts due to partial removal of the honeycomb cell walls [15], [28], [36].

This is particularly important because in chapter two we detected that the shear strength of the honeycomb can be increased if the cells are stabilized by the potting. However, only by observing the vertical potting shapes it's hard to imagine that the cells could be stabilized because they are very irregular.

Instead, the irregular potting shape should introduce some irregularities or hard points on the honeycomb cells, which might weaken the cells, and therefore, they could fold easily, which is the contrary of what was observed in chapter two.

Another aspect that was not studied in chapter two is the behavior of the honeycomb cells when they are subjected to combined shear stresses. This should be relevant for inserts since the shape is mostly irregular, thus cells are rarely subjected to shear in only one direction (see Fig. 169).

In this way, with the available evidence, we can say that the potting could increase or reduce the shear strength of the cells depending if its borders are regular or irregular. In this sense, the effect of the potting in to the surrounding cells is something similar to what is commonly called a two-edged sword. If the insert is installed properly, the cells may be stronger, if not, the cells are actually weaker.

5.2.1.5 Incomplete filling of the insert underneath the insert

According to our brief research, this defect was present in a small number of inserts. This defect is visible once the specimen is cut in the half, thus a mesoscale defect Fig. 173.

This defect appears when the potting viscosity is too high according to the ECSS [1]. Thus, it can be caused due to a bad design or a bad installation, thus avoidable.

Its effect should be very similar to the trapped air bubbles; therefore, its effect must be considered low.

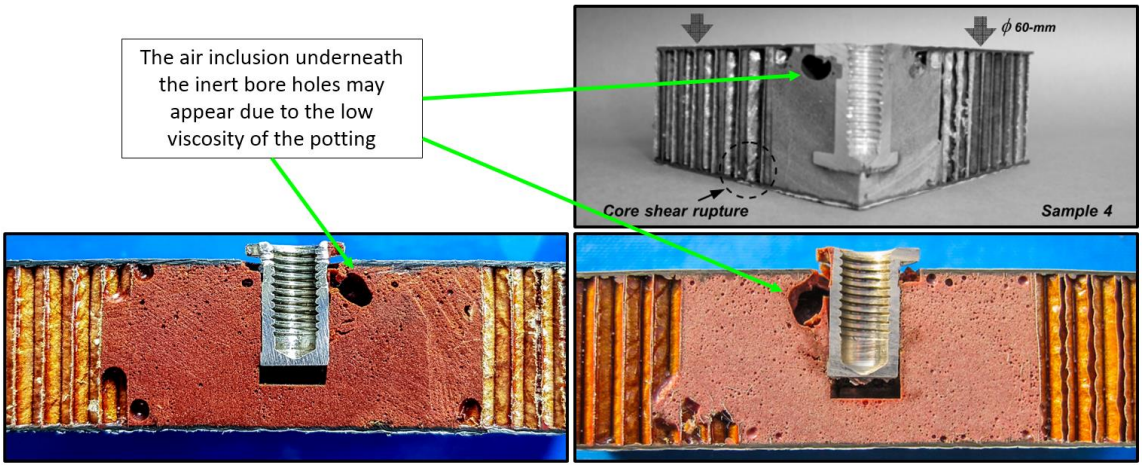

Fig. 173: Examples of incomplete filling underneath the fastener boreholes [15], [48].

5.2.1.6 Variation of porosities or micro-spheres concentration

If only the studies performed by Bunyawanichakul, Kumsantia and Bianchi, on which the inclusion of micro-spheres and porosities was considered for the potting, 100% of the cases will present this defect. Naturally, for all the other research about inserts on which only the adhesive alone is used, this defect is never present (see Fig. 174).

The size of this defect depends on the average size of the porosities and filler particles., thus it can be classified as a micro or mesoscale defect.

The density of porosities or micro-spheres can't be controlled, it's a part of the foam nature itself. Thus, this defect can't be avoided.

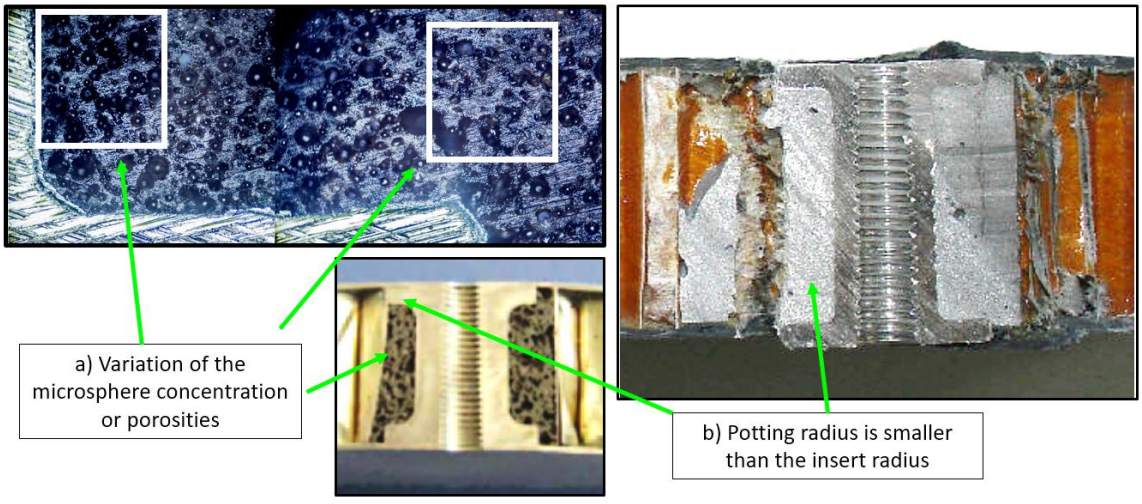

Fig. 174: Examples of a) variation of the micro-spheres concentration or porosities, b) example of an insert on which the insert is smaller than the insert radius [40], [41].

SPF are used in inserts because they increase the specific properties of the potting compound while increasing the resistance against moisture. Something similar was done by Bianchi in [41], who included porosities in the potting, probably to reduce the insert weight.

However, the effect of changing the effective elastic modulus of the potting compound should be almost imperceptible for inserts, since their shear modulus is much higher than the core. Nevertheless, if this defect is combined with the weak bonding defects, the influence might be very important.

The reason is because when the insert is well bonded, the potting is mostly subjected to tension, while if it is weakly bonded, the potting will be subjected mostly to compression. And this is relevant because porosities and micro-spheres might turn the potting into an easily crushable foam. Thus, this defect should be taken into consideration only if SPF or potting with porosities are used for the insert.

5.2.1.7 Potting is smaller than the insert radius

This defect was present only a few of the considered cases. It is visible when the insert is cut in half, thus a mesoscale defect (see Fig. 174).

This defect is caused when the perforation to install the insert is too small, or when the cells are only partially removed. Therefore, this defect can be avoided by the potting radius is increased or if the installation is performed correctly, thus it's avoidable.

The main problem is that the insert strength is reduced because the fastener is not well bonded to the honeycomb panel. However, the effect of this defect on the insert strength was not studied in this thesis because none of the specimens presented this defect.

5.2.2 Evaluation of the criticality of defects in inserts

Considering the information of the precedent section, these defects were evaluated using the available visual evidence in the literature.

Not all the works show visual evidence of all the defects, nor about all their tested inserts Therefore, the evaluation was made according to the available data as follows:

To measure if the defect was present in the inserts of each research, a coefficient between 1 and 0 is assigned. Following this, 1 is for present in all the results of the research, 0 is for never present, and fractional number means present only in part of the results.

Of course, this evaluation is subjective since it was performed by the author of this manuscript. This also means that if this analysis is performed by another person the results could be different.

The results of the evaluation are presented in Table 17.

This study was useful to observe the frequency of the apparition of the defects. The most important one was the variation of the potting shape was the most frequent with 100% of presence. Secondly, the presence of trapped air in the potting appeared in 41.7 % of cases. Then, the irregular borders of the potting were present at 38.7 % of times.

Then, the next step was to evaluate if the defects should be considered for the insert design. To do this, an analysis of the cause of the defects is done to determine if the defect can be avoided, for example if the installation/design is modified.

Finally, an assignment of the influence of the defects was also made according to the evidence of the literature review and chapter three and four of this thesis. The complete result of this study is given in Table 18.

Research with visual evidence	Real potting radius variation of the insert	Weak bonding of the fastener	Variation of the micro-spheres concentration	Air bubbles in the potting	Irregular borders of the potting	Incomplete filling of the cells	Potting radius smaller than insert radius
Blind full potting insert (Kumsantia 2010) [48]	1	0	1	1	0.5	0.25	0
Through-thickness insert (Song 2008) P01 [40]	1	0	0	0	0.33	0	0.33
Through-thickness insert (Song 2008) P02 [40]	1	0	0	0	0.33	0	0.33
Through-thickness insert (Song 2008) P03 [40]	1	0	0	0	0.33	0	0.33
Through-thickness insert (Song 2008) P04 [40]	1	0	0	0	0.33	0	0.33
Through-thickness insert (Song 2008) P05 [40]	1	0	0	0	0.33	0	0.33
Through-thickness insert (Song 2008) P06 [40]	1	0	0	0	0.33	0	0.33
Through-thickness insert (Song 2008) P07 [40]	1	0	0	0	0.33	0	0.33
Through-thickness insert (Song 2008) P08	1	0	0	0	0.33	0	0.33
Through-thickness insert (Roy 2013) [33]	1	0	0	1	1	0	0
Through-thickness insert (Roy 2013) [33]	1	0	0	1	1	0	0
Through the thickness insert (Raghu 2009) [28]	1	0	0	0.67	0.33	0.33	0
Blind full potting insert (Raghu 2009) [28]	1	0	0	0.67	0.33	0.33	0
Blind partial potting (Raghu 2009) [28]	1	0	0	0.67	0.33	0.33	0
Blind full potting (Yong-Bin Park 2014) [39]	1	0.67	0	0.67	0.67	0.5	0
Blind full potting type 1 (Bunyawanichakul 2005) [15]	1	0.75	1	1	1	0	0
Blind full potting type 2 (Bunyawanichakul 2005) [15]	1	0.75	1	1	1	0.75	0
Full potting type 3 (Bunyawanichakul 2005) [15]	1	0	1	1	1	0	0
Through-thickness insert (Trap door Airplane) (Bunyawanichakul 2005) [36]	1	0	0	0	1	0	0
Metallic Insert full potting (Heimbs and Pein 2009) [35]	1	0	0	0	0	0	0
Blind full potting insert (Seeman et. al. 2016) case 1 [34]	1	0	0	1	0	0	0
Blind full potting insert (Seeman et. al. 2016) case 2 [34]	1	0	0	1	0	0	0
Blind full potting insert (Seeman et. al. 2016) case 3 [34]	1	0	0	1	0	0	0
Through the thickness insert (Bianchi 2010) [41]	1	0	0	0	0	0	0
Blind full potting insert(Bianchi 2010) [41]	1	0	1	0	0	0	0
Through the thickness insert (Wolff 2018) AL-01 [4]	1	0	0	0	0	0	0
Through the thickness insert (Wolff 2018) AL-02 [4]	1	0	0	0	0	0	0
Partial potting insert (Seemann 2018) [11]	1	0	0	0	0	0	0
Frequency of apparition	100.00%	7.74%	17.86%	41.67%	38.69%	8.93%	9.52%

Table 17: Statistical study of the frequency of the appearance of defects for inserts.

The result of this rough evaluation determined that only two defects must be included in to the insert design.

The first one is the variation of the shape of the potting. This is because it's always present, it can't be avoided and has an important effect on the insert strength. Predicting the shape of the potting may be very complex, for this reason a discussion is presented separately in a later section.

The second defect that should be included is the irregular borders of the potting because it was present almost 40% of the times, it can't be avoided because it depends on the cells tears when they are removed, but most important of all, its effect on the surrounding cells is important, able to make them stronger or weaker:

- There are two main characteristics that inserts must have for the honeycomb to be stabilized or stronger. First, the hole needs to be drilled carefully and in the exact normal direction to the panel, in this way, there won't be any partially open cells, thus neither irregular borders. Secondly, the shape of the potting must be almost square for the cells to be subjected to shear in only one direction (see Fig. 169).
- However, if the hole is made quickly and the perpendicularity of the drilling tool regarding the sandwich panel can't be ensured, it's almost sure that the insert possesses irregular borders, thus the cells that surround the inserts fold easier.

This is endorsed by the fact that the potting shape is always irregular, and that the irregular borders of the cells are present almost 40% of the time. The increase of the shear strength of the honeycomb core should be neglected. Instead, the cells should be considered to collapse easier and earlier, i.e. weaker.

The defects that should not be considered for the insert design are:

- The weak bonding of the fastener, because this defect appears under very specific conditions i.e. when SPF is used or when inserts are tested under high temperatures. The same goes for the variation of micro-spheres or porosities.
- The presence of air trapped as well as the incomplete filling of the cells in the cells should be neglected because their effect is supposed to be almost imperceptible.
- Finally, the defect of the smaller potting radius regarding the fastener should be neglected because it is attributed to a bad insert design/installation, thus, it could be easily avoided.

Defect	Frequency	Size	Cause	Can be avoided	Effect	Considered for the design
Real potting radius variation of the insert	100.00%	Mesoscale	Honeycomb shape	NO	Increases-Decreases the insert strength	YES
Weak bonding of the fastener	7.74%	Mesoscale	High temperature/micro-spheres oversaturation/Insufficient cleaning of the fastener	YES	Damages the potting at very low loads	NO
Variation of the micro-spheres concentration	17.86%	Microscale	handmade stirring	NO	Almost imperceptible	NO
Air bubbles in the potting	41.67%	Mesoscale	bad installation	YES	Not very well studied	NO
Irregular borders of the potting	38.69%	Mesoscale	Cell removal, Undercut	NO	Makes the surrounding cells to collapse earlier	YES
Incomplete filling of the cells	8.93%	Mesoscale	bad installation/Too low viscosity of potting pass	YES	Not very well studied	NO
Potting radius smaller than insert radius	9.52%	Mesoscale	Bad design	YES	Not very well studied	NO

Table 18: Analysis of the criticality of defects in inserts for sandwich structures.

Now that the defects that should be considered for the insert design are detected, the next step is to define how these defects should be considered. The most difficult one to consider

is the variation of the potting radius. A discussion about this subject is presented in the next section.

5.2.3 Analysis of variations of the potting radius

When an insert is installed into a sandwich panel with a honeycomb core, the insert potting's shape is always very irregular. This is intrinsic of inserts and is caused by the honeycomb structure and the space inside their cells.

When a hole is drilled into a sandwich panel, all the honeycomb walls inside the hole's area are removed. Then, the fastener is placed in the panel and the potting resin is injected. Since the potting is not polymerized yet, it behaves like a high viscosity fluid that spreads and fills the space of the cells that were opened by the hole, this is how it obtains its final shape. Thus, the potting shape depends on which and how many walls are removed.

Which cell walls are removed depends mostly on the size of the drilling tool, but also on the position where the hole is made, because if the position changes, different cell walls are removed.

Also, the cell geometry of the honeycomb core is mostly irregular due to the geometrical imperfections of the cells (see Fig. 52 for example). Thus, it's impossible to determine the exact position of the cells inside the panel.

Moreover, the position of inserts is chosen according to the assembly needs, and not according to the honeycomb cells.

All of this makes the potting's exact shape very hard to determine, and this is especially important because the insert strength depends of the potting's size. For this reason, the ESA in ref. [37] proposed a statistical approach to estimate the average and minimal potting size as a function of the hole diameter b_i and the size of the cells *Sc*.

The first approach is based on the hypothesis that the double walled cells are much stronger than the single walled cells. Therefore, when an insert is pulled-out and the core breaks, only the single walls fails. This means that the geometry that should be considered to calculate the pull-out load is not the geometry that is surrounding the potting shape, but the geometry that surrounds the potting shape and the double cell walls as shown in Fig. 175 with dotted red lines.

Then, the average of the distances between the hole's center and the nearest single walls that should break is obtained. Finally, this average distance is named Effective Potting Radius (from now on EPR) and is used as an equivalent of the perimeter that is subjected to shear as it the potting were a perfect cylinder.

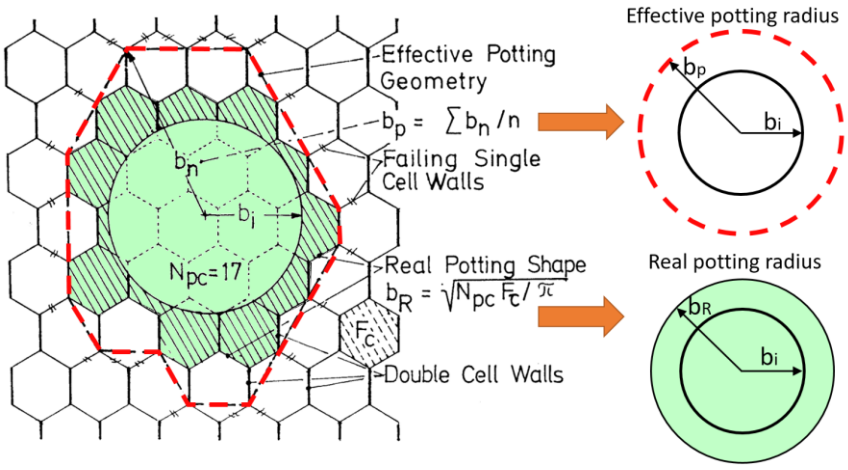

Fig. 175: Definition of the effective potting radius (EPR) and the real potting radius (RPR) according to the ESA [1].

The second approach is based on the area of the filled cells. The irregular polygon formed by the filled cells is transformed into a circle that contains the same area. Then, the radius of this circle b_R is called the Real Potting Radius (RPR from now on) and is highlighted in green in Fig. 175.

5.2.3.1 Effective Potting Radius vs Real Potting Radius

Both quantities are defined by the ESA in the Insert design handbook (see ref. [1]), a brief description is provided here.

Concerning the EFP, since the potting real shape varies very easily (as explained before), the ESA did a statistical study about the variations of the potting effective radius. Finally, they give four analytical expressions (see equations 4, 5, 6 and 7) that can be used to estimate the minimal and average EPR of an insert. The provided equations have the following form:

$$b_p = d_i a_1 + a_2 S_c + a_3 \qquad 21$$

Where the constants a_1, a_2, and a_3 change to consider an average or minimal values, but also when the honeycomb core is perforated, for example for sandwich panels for the spatial applications.

Recently, Wolff et al. in ref. [4] did the same study, they considered that the results given by the ESA were not accurate because the coefficients are the same for all the typical cell sizes. The coefficients of the ESA and Wolff are given in Table 19.

Visibly, the coefficients found by Wolff et. al. (which are supposed to be more accurate) suggest that the coefficients provided by the ESA are underestimating the size of the potting

Coefficients	ECSS (for all Sc) min	ECSS (for all Sc) avg	ECSS (for all Sc) max	ECSS (for all Sc) perforated core min	ECSS (for all Sc) perforated core avg	ECSS (for all Sc) perforated core max	Wolff et. al. (Sc=1/8'') min	Wolff et. al. (Sc=1/8'') avg	Wolff et. al. (Sc=1/8'') max	Wolff et. al. (Sc=3/16'') min	Wolff et. al. (Sc=3/16'') avg	Wolff et. al. (Sc=3/16'') max	Wolff et. al. (Sc=1/4'') min	Wolff et. al. (Sc=1/4'') avg	Wolff et. al. (Sc=1/4'') max	Wolff et. al. (Sc=3/8'') min	Wolff et. al. (Sc=3/8'') avg	Wolff et. al. (Sc=3/8'') max
a1	0.9	1	-	0.93	1.00	-	1.059	1.05	1.038	1.07	1.05	1.04	1.07	1.06	1.05	1.09	1.06	1.04
a2	0.7	0.8	-	0.87	0.94	-	0.86	1.05	1.23	0.84	1.03	1.20	0.84	1.03	1.19	0.80	1.01	1.19
a3	0	0	-	-0.66	-0.71	-	0	0	0	0	0	0	0	0	0	0	0	0

Table 19: Coefficients for the equation 21 for the calculation of the effective potting radius (EPR) by the ESA and Wolff [1], [4].

On the other hand, the RPR of the ESA should be simpler to estimate since it only depends of the number of cells that are filled with potting. Since the area of the surface covered with potting is converted to a circle, the radius of the circle can be calculated using the following equation:

$$b_r = \sqrt{\frac{N_{PC} F_C}{\pi}}$$

Where N_{pc} is the number of filled cells with potting and F_c is the surface of a honeycomb cell, which depends of the cell size.

As for the EPR, the ESA gives an analytical expression to estimate the average and minimal real potting radius under the following form:

$$b_r = a_1 b_i + a_2 S_c \qquad 22$$

And the values that are given to estimate the average and minimal values are $a_1=1$ and $a_2=0.35$ for the minimal potting real radius, and $a_1=1$ and $a_2=0.5$ for the average potting real radius.

Both EPR and RPR could be used to calculate the insert strength, however, the hypothesis of the single and double walls of the EPR seems to be closer to reality than the RPR. Nevertheless, there are some arguments and evidence which might suggest that considering the EPR for calculations might not be very accurate:

- Even if the double walls are much stronger than the single walls, the potting being much more stiff than the Nomex® paper should induce a stress concentration effect in both single and double walls that could make fail both indifferently.
- The shear failure of the core never appears in only one cell wall, but in many cells at the same time, following a 45°shear line as shown in Fig. 176. Therefore, the surface that is subjected to shear stress is not just the insert's perimeter.
- The honeycomb cells walls buckle elastically before they break. This buckling reduces the stiffness of the cell walls, and may allow a uniform distribution of the shear loads between the cell walls instead of concentrating it only in the double or single walls.

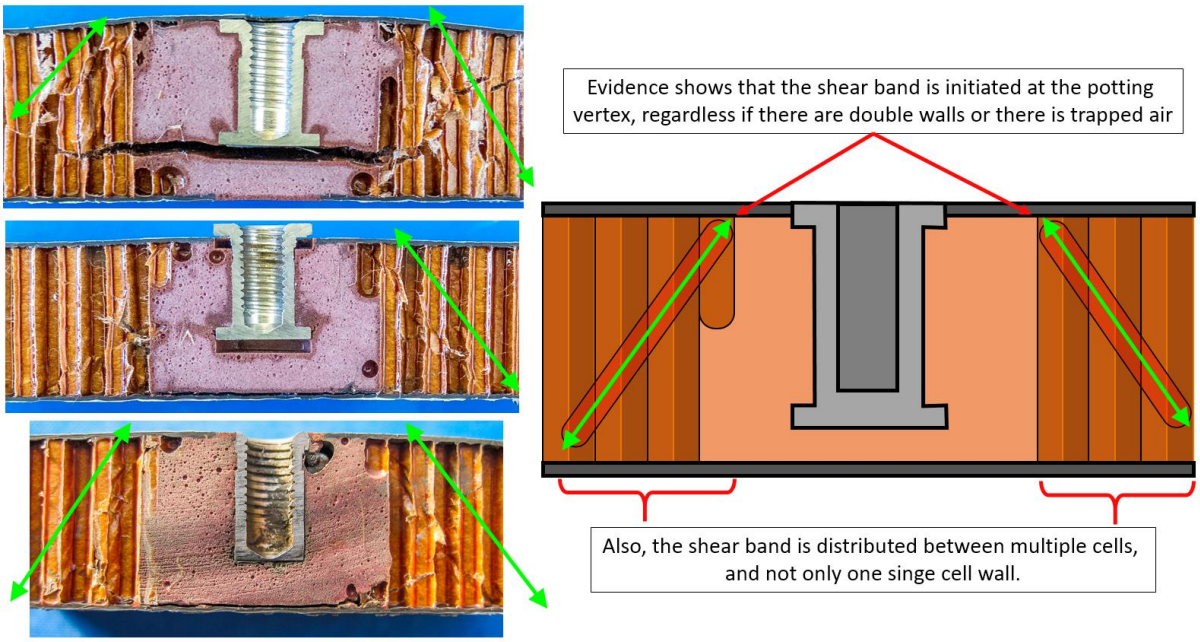

Fig. 176: Evidence shows that the failure appears from the potting real shape instead of from the double cell walls.

Endorsed by this evidence and arguments, we believe that it might be more accurate to consider the RPR for the calculation rather than the EPR.

However, as Wolff et. al. suggested in ref. [4], there is no information about how the coefficients of the ESA were determined but also they might lack of accuracy because they all address to all the typical cell size at once. For this reason, a study of this RPR is presented in this section.

5.2.3.2 Number of filled cells vs tool diameter

The first step of is to determine which cells are opened when the sandwich panel is perforated. For this it's important to consider all the possible locations for the hole's center regarding the honeycomb. Then, the cells that were opened by the drilling tool should be filled with potting when the insert is installed. Finally, the filled cells can be counted. All of this is developed into a MATLAB script.

The honeycomb core cells are represented by polygons created using the *polyshape* function of MATLAB. The size of the polygons is given by the Sc parameter, which represents the diameter cell as in honeycomb cores. The thicknesses of the double and single cells are neglected because their thicknesses might be considered too small compared to the cell geometry imperfections (which can't be controlled).

Using polygons is very useful because it allows the use of another function called *overlaps*, which detects if two or more polygons intercept each other.

Once the honeycomb core is drawn using polygons, the drilling tool is represented by a circle (as a polygon of many sides). Then the *overlaps* function is used between the honeycomb polygons and the circle to determine if the cells are opened by the drilling tool. If yes, it's supposed that the cell will be filled with potting. This is represented by coloring the opened cells in red (see Fig. 177).

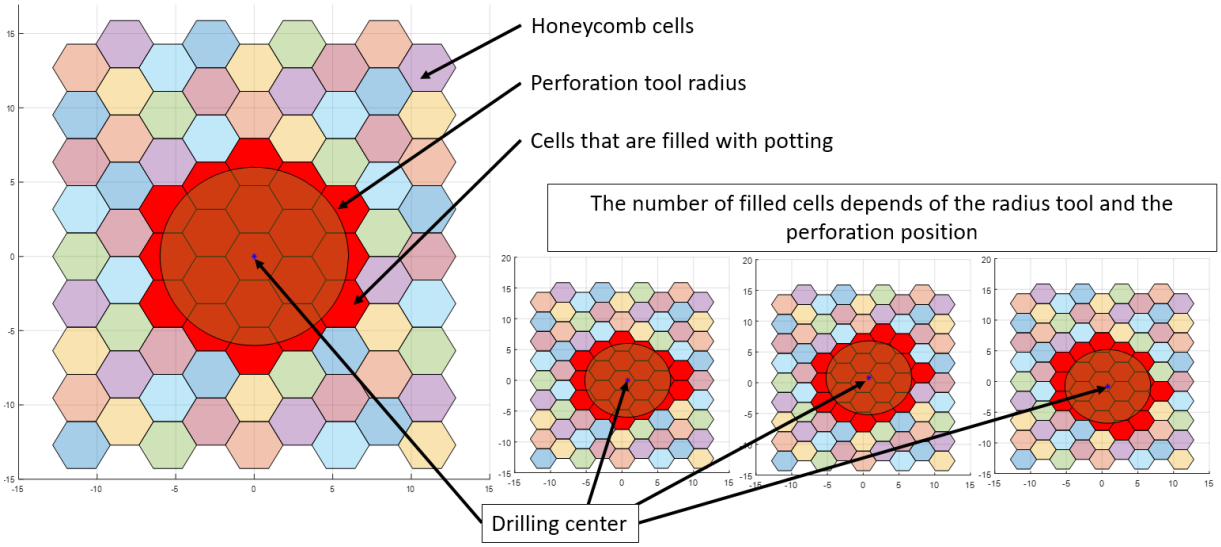

Fig. 177: Results of the script developed in MATLAB: The cells that are filled changes with the position of the perforation

Finally, since the numbers of positions where the hole can be made inside a honeycomb cell are infinite, we considered that it's a good estimation to define a grid of points inside a cell. Then, each point represents the coordinates where the hole could be made (see Fig. 177). The grid contained a total of 85 different center that are tested.

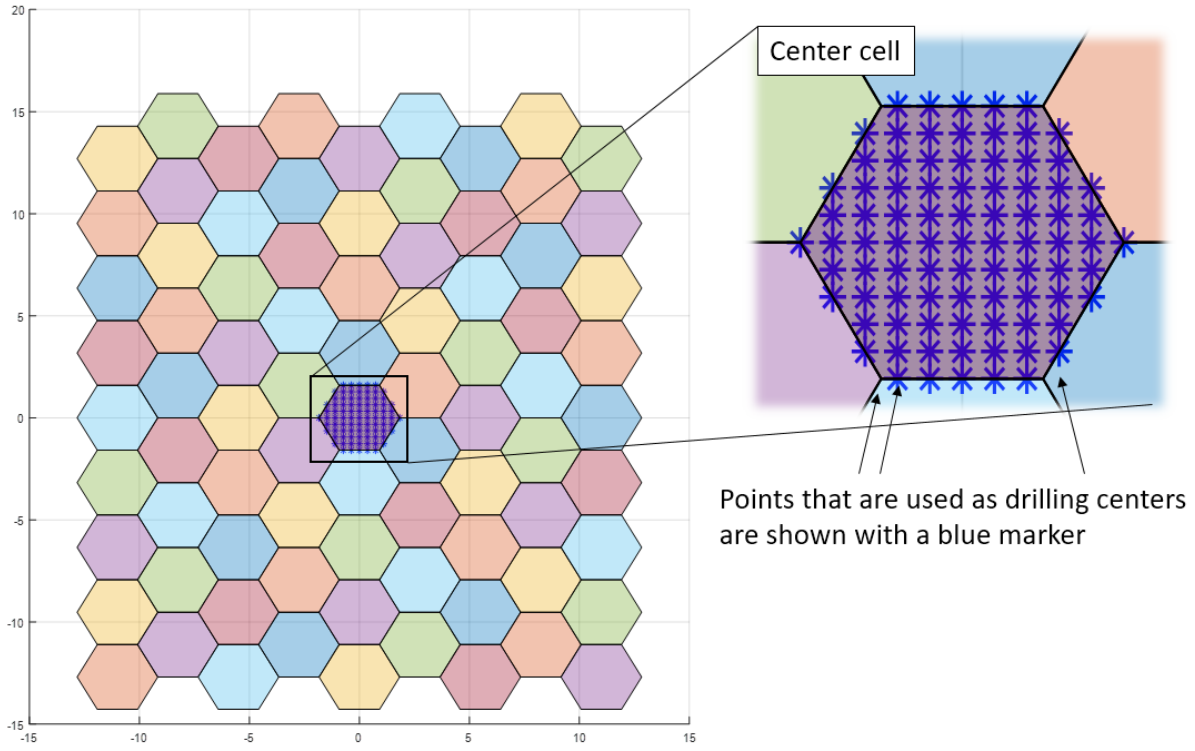

Fig. 178: The perforation was tested from different centers shown in blue.

The procedure explained previously was made for the most typical cell sizes; 1/8 inch, 3/16 inch, 1/4 inch and 3/8 inch.

The results suggest that that there is an almost square relation between the diameter of the drilling tool and the number of filled cells (see Fig. 179). However, the exact number of filled cells is varying over a small range of randomness. Therefore, the results are presented in terms of the maximum, minimal and the average filled cells as function of the tool diameter.

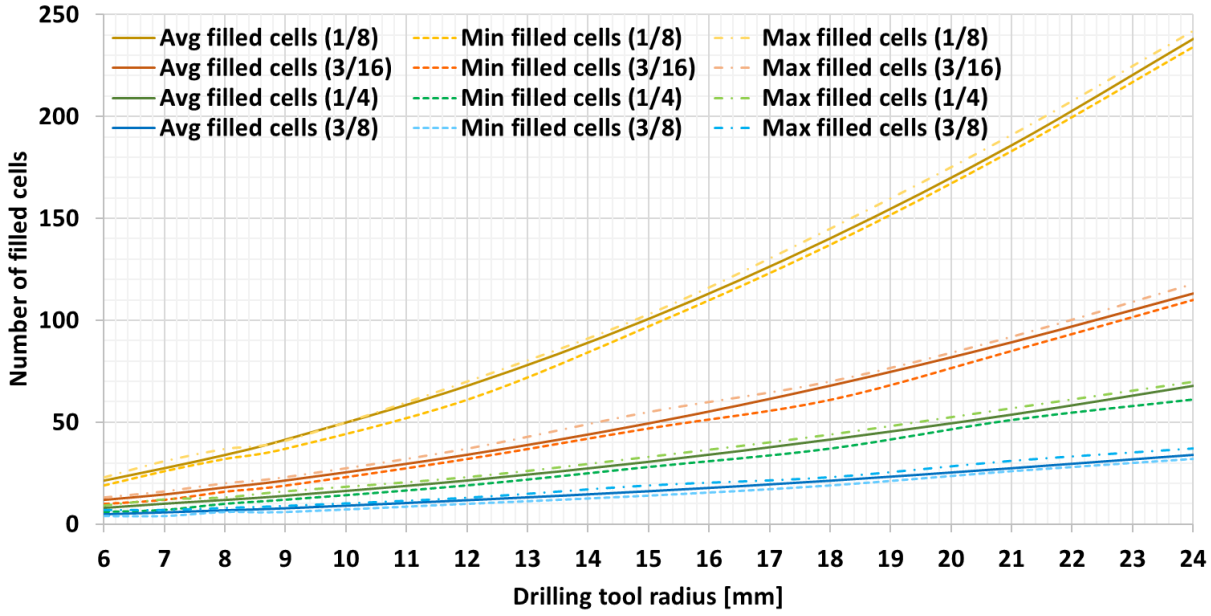

Fig. 179: Average, minimal, and maximal number of filled cells for different cell sizes (Sc=1/8”, 3/16”, 1/4” and 3/8”).

Moreover, the relation between the tool diameter and the potting real radius is shown in Fig. 180. It can be clearly seen that the relation for all the studied cell sizes is almost linear with some small variations.

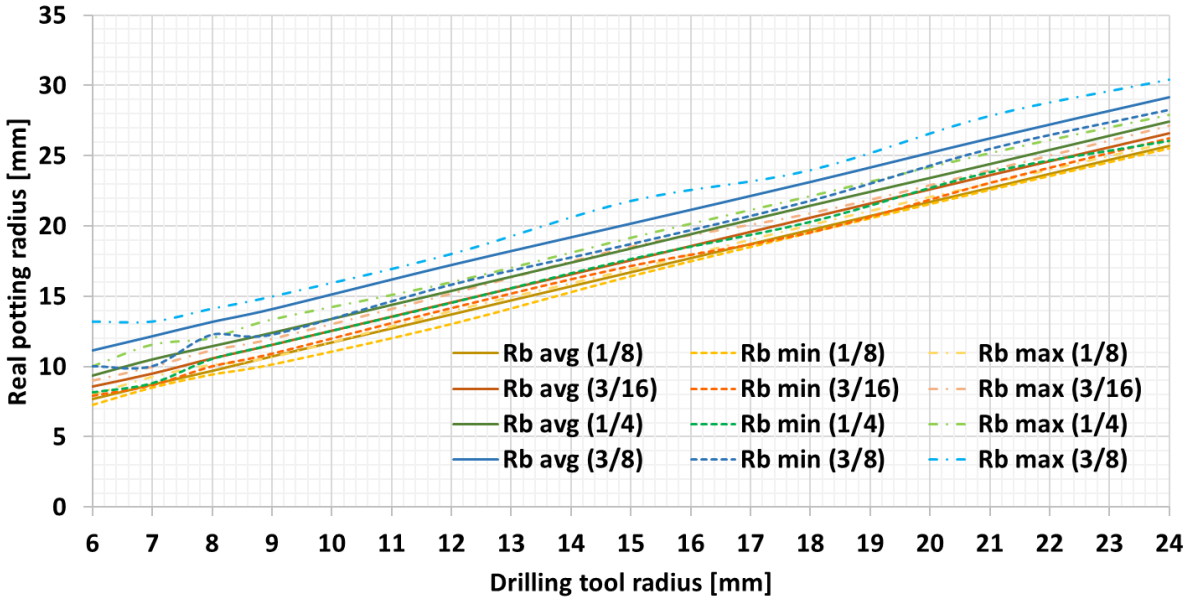

Fig. 180: Average, minimal, and maximal real potting radius (RPR) for different cell sizes (Sc=1/8", 3/16", 1/4" and 3/8").

The next step was to evaluate the accuracy of the equations provided by the ESA (see equation 22) by comparing their estimation against the obtained results through the MATLAB. This is shown separately for all the studied cells sizes in Fig. 181. The average estimation of the ESA is shown in red and the minimal estimation is shown in black. Visually there is a very good correlation and thus, these equations can be considered very accurate.

Also, we observed that using $a_1=1$ and $a_2=0.63$ allowed to fit the maximal real potting radius values. This is useful since the ESA does not provide any coefficients for the evaluation of the maximal real potting radius. Then the coefficients that are useful to estimate the real potting radius and that should be used for the equation 22 are given in Table 20.

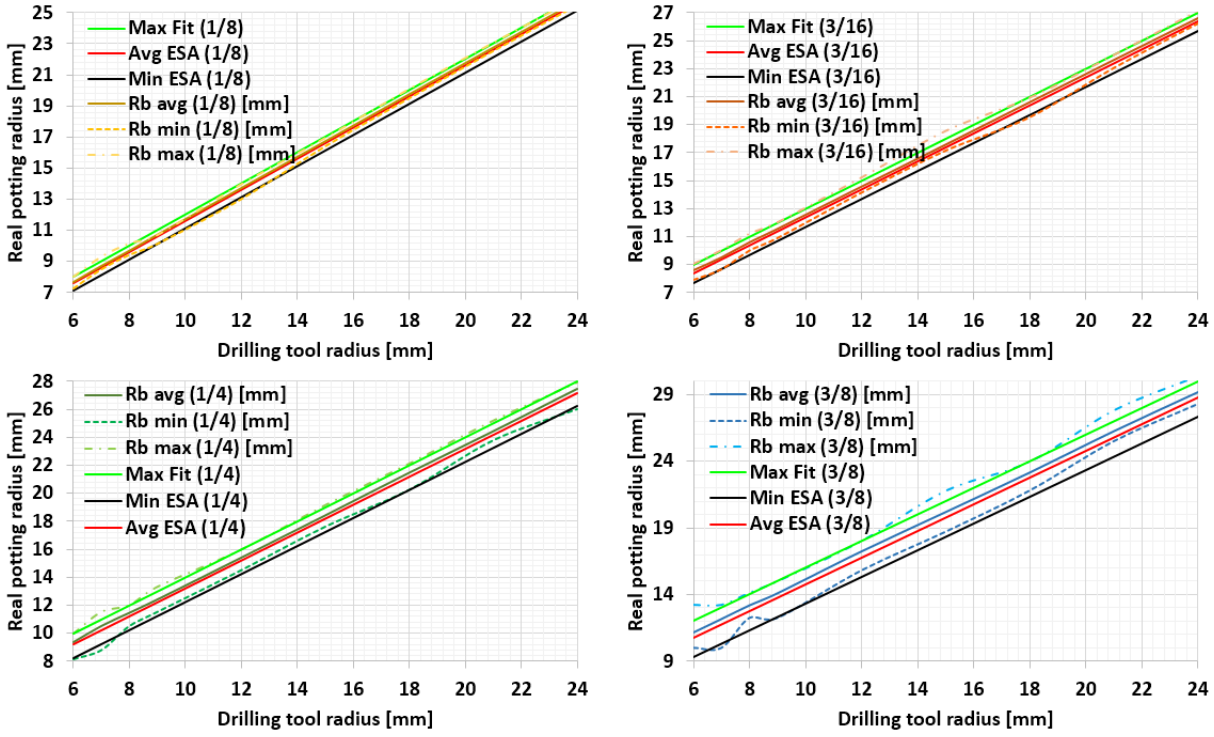

Fig. 181: Real potting radius (RPR) for different cell sizes: estimation of the ESA vs the obtained results.

Also, since the area of the real shape of the potting and the real potting radius are supposed to be the same, this real potting radius should be useful to estimate accurately the mass of the insert.

	ECSS for all Sc (min)	ECSS for all Sc (avg)	Rodriguez (max)
a1	1.00	1.00	1.00
a2	0.35	0.50	0.63

Table 20: Coefficients for the equation 22 for the calculation of the real potting radius (RPR) by the ESA and our results [1], [4].

Finally, since the data of this research and the MATLAB code might be of interest for other researchers, they are given in the Annex A.

5.2.4 Conclusions about the defects in inserts

The study presented in this section determined that only two defects should be considered for the insert design: the irregular borders of the insert and the variation of the potting shape, which are the most frequent and has the stronger effects.

Also, two recommendations are given to include these defects into the design calculation:

The effect of the irregular borders of the potting is weakening the cells surrounding the insert. Therefore, to include this defect for the design, the strength of the cells that are surrounding the insert are likely to collapse early and their shear strength is equal or slightly lower than the specified by the manufacturer.

As for the variation of the shape of the potting, the evidence (see Fig. 176) shows that a good estimation of an average size value is obtained by considering the real potting radius, which is also defined by the ESA and the coefficients issue of our research (see Table 20).

Also, it's important to highlight that the potting effective radius proposed by the ESA exaggerates the equivalent size of the insert, since it considers the double walls of cells as part of it. The evidence shows that even the double cell walls start to buckle in the superior vertex formed by the core, the potting and the skins (see Fig. 176).

Moreover, the surface that is subjected to shear is not only the contour of the potting effective radius, but it looks more like if the surface subjected to shear were the one formed by a cut at 45° of the core (see Fig. 176).

The study of the variation of the potting size presented here, proves that the equations provided by the ESA are accurate to estimate the real potting radius, except for its maximal value since the coefficients are not provided, but an estimation is given in Table 20.

5.3 Development of the insert F.E. model

The metallic inserts tested by Bunyawanichakul in its PhD thesis (see ref. [15]) are taken as reference for the development of the insert model. The tests were done for Eurocopter under industrial constraints and some experimental measurements done 15 years before were found to be not consistent. Moreover, it was not possible to make a new test campaign during the time allowed to the PhD. Thus, some extrapolations were made in this chapter. The first step of this section is describing completely these inserts, including the materials, the geometry and the testing conditions. The second step consists into modeling these inserts using the techniques developed in chapter three and four.

5.3.1 Description of the insert's experimental reference

Three types of metallic inserts were tested and studied by Bunyawanichakul. All the specimens were manufactured using the same materials, only the geometry was different. They are classified as type1, 2 and 3. They are showed in Fig. 182.

5.3.1.1 Inserts description

The differences between them are the potting radius and the installation procedure. For the type 1 and type 3 the nominal insert diameter is 18 mm while for the type 2 it is 36 mm. Concerning the installation procedure, for the type 1 and 2 it was the same, while for the type 3 the insert was installed from the bottom. Therefore, for the insert type 3, the sandwich panel is perforated in both sides and the fastener is placed under the superior skin. It's important to remark that the specimens were handmade and that all the inserts were left to polymerize at room temperature. Also, according to witnesses, the fabrication of these specimens was handmade but also very quickly, which could explain the presence of defects.

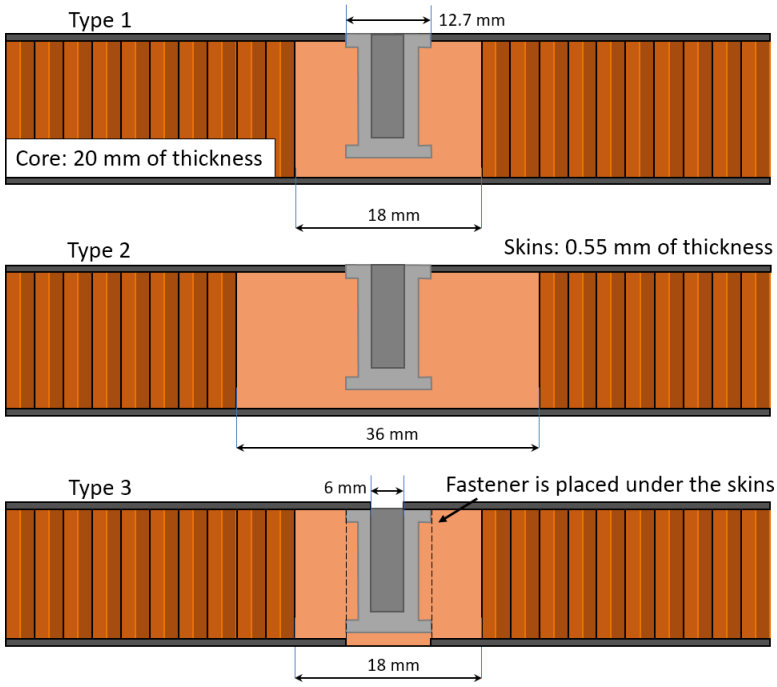

Fig. 182: General description of the inserts type 1, 2 and 3.

The core was a Nomex® Honeycomb of 48 kg/m^3 (3.0 lb/ft^3) and 20 mm of thickness with a cell diameter of 3.175 mm, although the exact nomenclature of the honeycomb is unknown (possibly the HRH-10-1/8-3.0). The core shear moduli in the L and W directions were

determined experimentally (3 tests by direction) in a short three-point bending test, which were not performed until complete failure of the specimens, but a little before that point. These experimental curves are shown in Fig. 183-a.

It's worth mentioning that, even if the three point bending test is recommended by the ASTM C393 [67], this method is only accurate to determine the shear moduli and shear strength of the core, but it doesn't provide reliable values for the nonlinear behavior, especially for the collapsing stage of the cells. This is because, in a three-point test, the cells beneath the loading bar always collapse first (the cells in the middle of the specimen). Therefore, while the linear behavior must be accurate, once the cells started to buckle the curve only reflects the buckling of the middle cells as shown by Giglio in [13] and [77].

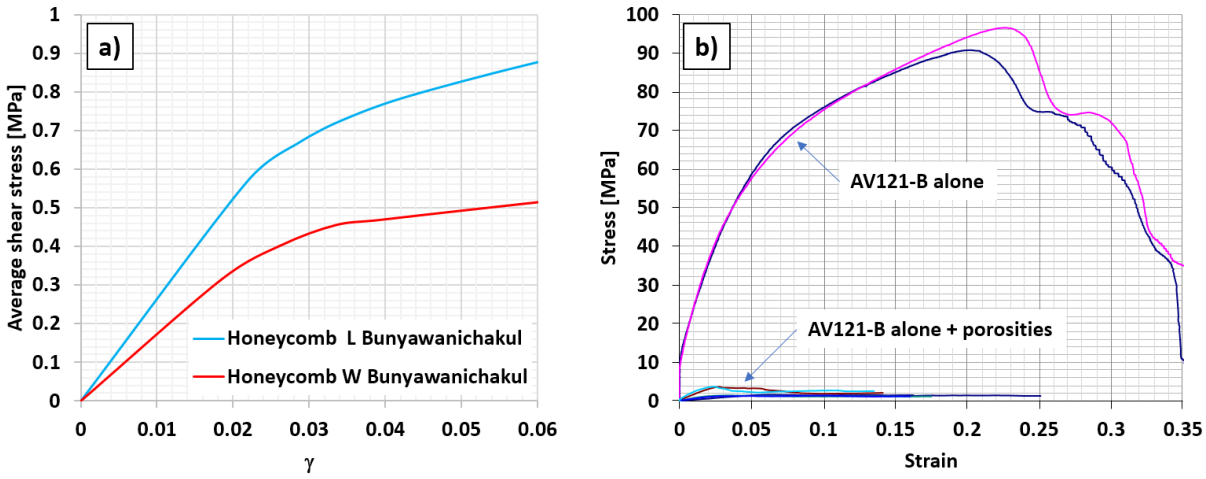

Fig. 183: Experimental curves of a) the shear testing of the honeycomb core, b) the adhesive used to fabricate the potting.

Concerning the potting, it was made of the adhesive Araldite AV-121-B (and the hardener HY-991) mixed with 10% of its ponderal weight with micro-spheres. Bunyawanichakul performed several compression tests to determine the properties of the adhesive alone. She found that there was a considerable difference in the behavior when there were porosities (not micro-spheres). The test results are shown in Fig. 183-b.

The skins were made each of two layers of the G939/145.8 [0,90] carbon fiber woven with a total thickness of 0.55 mm, also, the fibers are distributed equally in the l and t directions, 50% each. There were not tests made on this material, but the data from the manufacturer are shown in Table 21.

Material	Thickness [mm]	E_1 [MPa]	E_2 [MPa]	E_3 [MPa]	υ_{12}	υ_{21}	υ_{21}	G_{12} [MPa]	G_{13} [MPa]	G_{23} [MPa]	σ_1 [MPa]	σ_2 [MPa]	σ_3 [MPa]	τ_{12} [MPa]	τ_{13} [MPa]	τ_{13} [MPa]
Skins G939/145.8	0.275	50500	50500	5000	0.02	0.29	0.29	32000	3500	3500	634	634	-	100	80	80
Honeycomb core 48 kg/m³	20	1	1	94	0.29	0.02	0.02	1	17	26	???	???	7.5	-	0.3	0.48
Potting 10% of phenolic micro-spheres	-	1312	1312	1312	0.3	0.3	0.3	504	504	504	35	35	35	-	-	-

Table 21: Properties of the materials used for the sandwich panel and the insert.

The specimens were supported with a plate that had a hole of 60 mm of diameter, as shown in Fig. 184-b. This plate authorized the bending of the specimen while the insert is pulled out.

The metal fastener was the same type for all the specimens. It was made of stainless steel (isotropic material with E=220 GPa) and the nomenclature is DIN 65307-0615D. The dimensions of this fastener are shown in Fig. 184-a.

Then, the inserts were subjected to pull-out using a 100 kN Instron machine with a loading speed of 0.5 mm/min. The imposed displacement was measured using a dial bore gauge comparator, and the force was measured directly from the machine. Four specimens of each type were tested.

It's worth mentioning that, according to Bunyawanichakul, the displacement measurements for specimens 1 and 2 were not correct because the dial bore gauge was placed in the wrong place. The loading curves are separated by type and are shown in Fig. 185, Fig. 187 and Fig. 189.

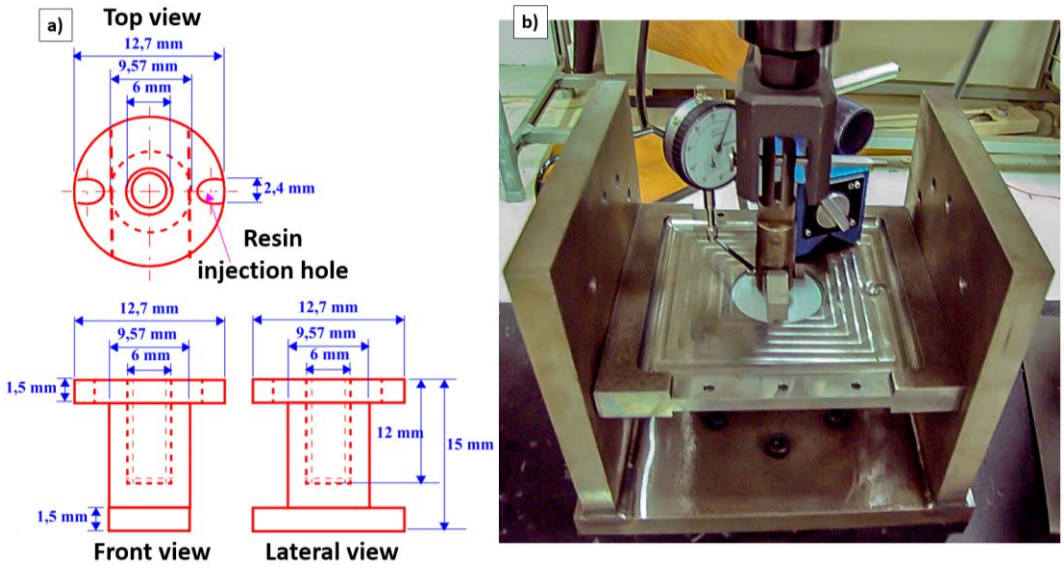

Fig. 184: a) Size of the fastener, b) set-up for the performed pull-out tests [15].

Also, many other tests were performed, where the inserts were pulled-out in different directions and not only perpendicularly to the sandwich panel. However, these tests are not described here.

5.3.1.2 Tests results: Insert type 1

According to Bunyawanichakul, the average stiffness of specimens from specimens Ep3 and Ep4 is 6296 N/mm. The failure loads are identified based on the 1% of linear regression criterion, the average of the failure loads was 1465 N.

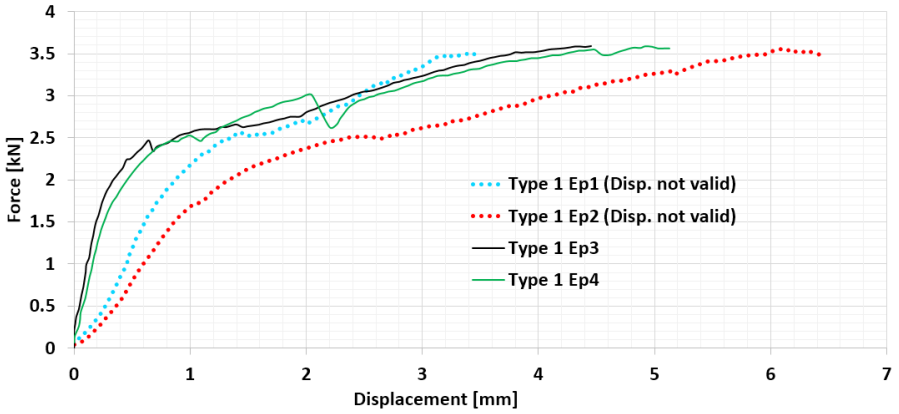

Fig. 185: Experimental curves of the pull-out test of the inserts type 1 [15].

Also, she stated that after the pull-out tests, 3 of the 4 specimens had the fastener visibly detached from the panel and that it was possible to see a pushing deformation in the inferior skins (probably caused by the shear buckling of the core). Finally, the "postmortem" specimens Ep1 and Ep4 were cut by the half, in addition, we cut the specimen Ep3 too (see Fig. 186). Several remarks were made:

- The potting diameter was supposed to be of 18 mm, but in the specimens, it varied from 23.5 mm to 30 mm.
- There was a large number of air bubbles.
- The honeycomb was folded until the diameter of the support of 60 mm.
- The failure modes were: Shear buckling of the cells, breaking of the inferior skin/potting interface, (that only in the case of insert 1 propagated to the core), irreversible compression of the potting, detaching of the fastener from the potting (for specimens 2-4) and breaking of the inferior potting/skin interface.

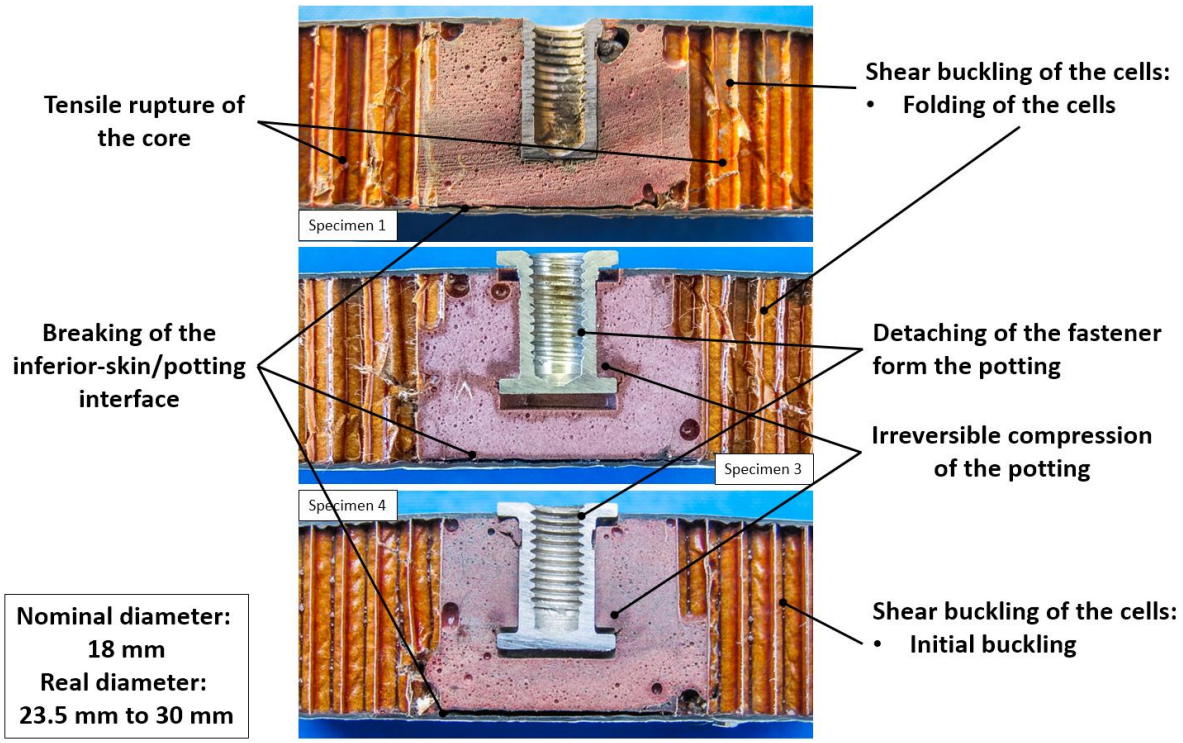

Fig. 186: Damage scenario of the inserts type 1 [15].

5.3.1.3 Tests results: Insert type 2

The stiffness of the different specimens presented a considerable variation, therefore the average is considered meaningless and is not provided. The limit loads are identified based on the 1% of linear regression criterion, the maximal load is 2543 N and the minimal is 2128 N with an average of 2260 N. The fasteners were detached from 3 of the four tested specimens. After the tests, only the specimen 5 presented a breaking of the superior skin, apparently, a traction failure. The "postmortem" specimens 5 and 8 were cut by the half to see the defects (see Fig. 188), some remarks are made:

- The potting diameter was supposed to be 36 mm but varied from 40.16 mm to 46.3 mm.
- There was a very large bubble air defect on specimen 5.
- The failure modes were similar of those of insert type 1, except that for these specimens there were no breaking of the inferior skin/potting interface.

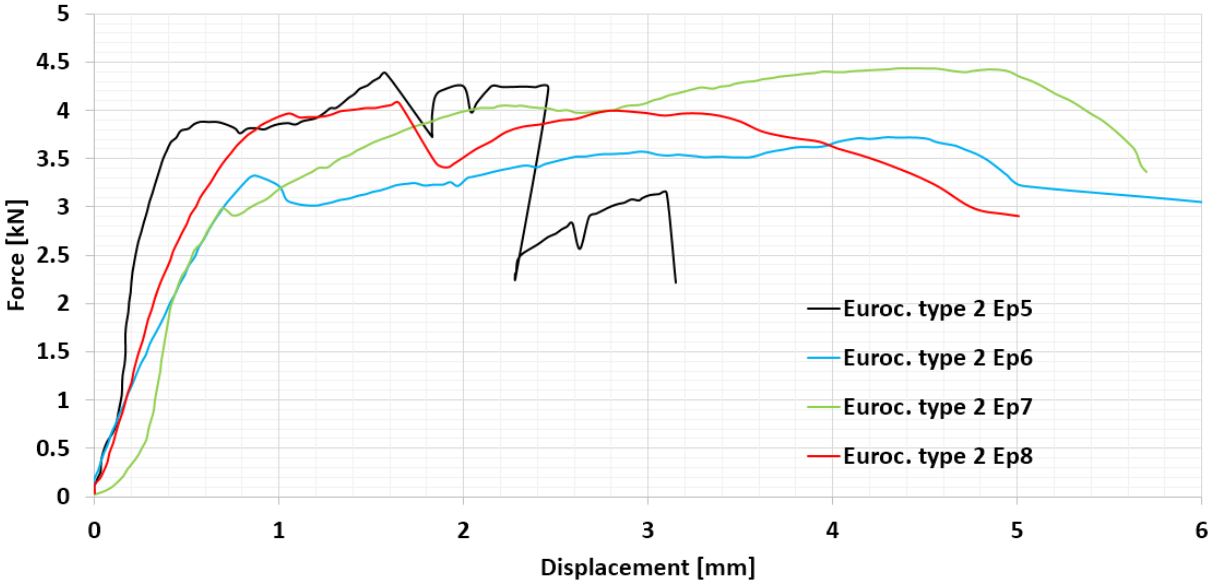

Fig. 187: Experimental curves of the pull-out test of the inserts type 2 [15].

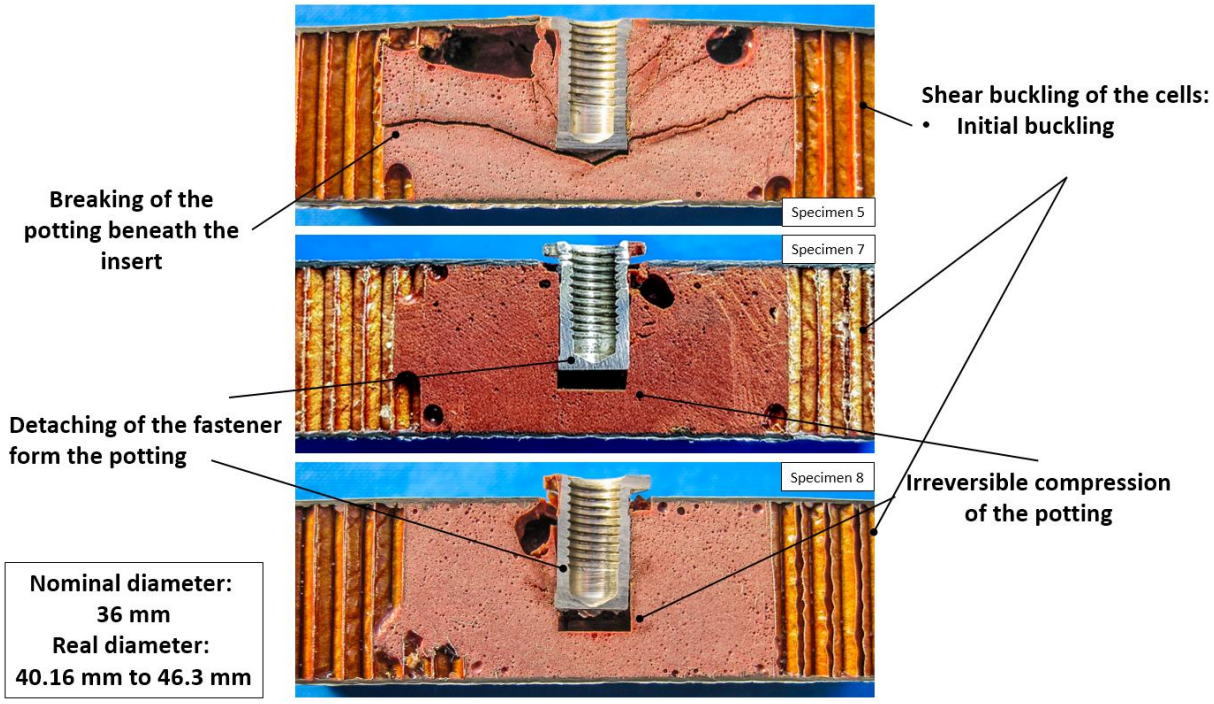

Fig. 188: Damage scenario of the inserts type 2 [15].

5.3.1.4 Tests results: Insert type 3

For this insert type, the variation of stiffness was of about 1%, the average value was of 3566 N/mm. The failure load was detected using the same criterion as for the other inserts, the maximal value was 1189 N and the minimal was 1121 N with an average of 1150 N. After the tests, the specimen presented the breaking of the superior skins due to traction. All the specimens were tested until complete failure (around 7 mm) except for the specimen 12, which was tested only until the first drop of the loading curve. The specimens 11 and 12 were cut in half and were analyzed (see Fig. 190), the remarks are:

- The potting diameter was supposed to be of 18 mm but varied from 20.47 mm to 31.5 mm.
- There were a lot of air bubbles.

- The failure modes were: Breaking of the honeycomb core in traction, breaking of the inferior-skin/potting interface, breaking of the potting beneath the fastener.

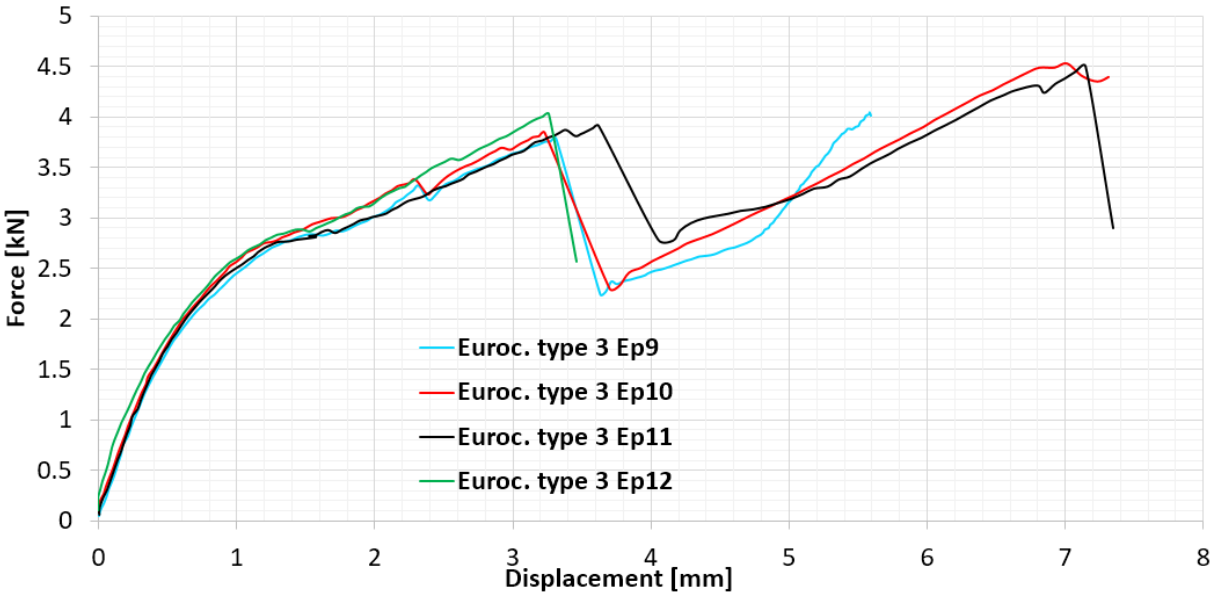

Fig. 189: Experimental curves of the pull-out test of the inserts type 3 [15].

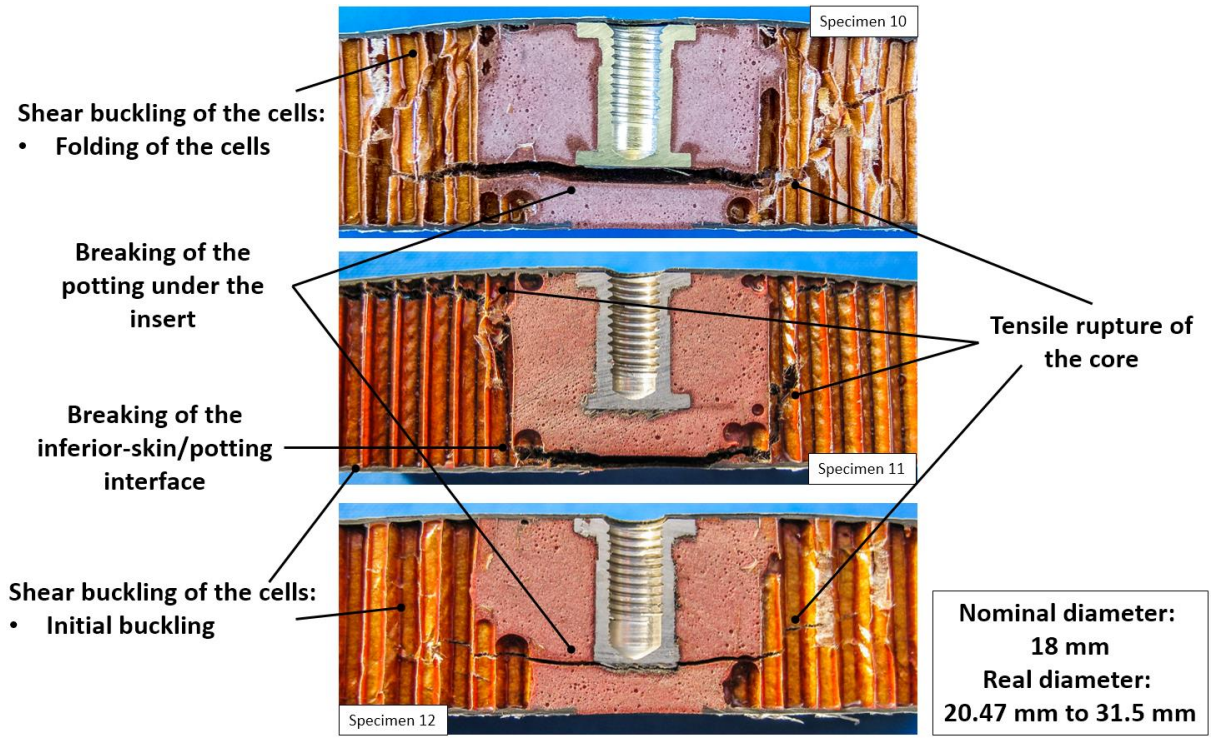

Fig. 190: Damage scenario of the inserts type 3 [15].

5.3.1.5 Defects inspection

Here, the defects that can be visually identified in the postmortem specimens are presented.

To begin with, the most visibly defect are the irregular borders of the potting (see Fig. 186, Fig. 188 and Fig. 190), which might have been caused due to the partial removing of the cell walls. Presumably, this happened because of a bad alignment of the drilling tool, which was not perpendicular to the sandwich panel.

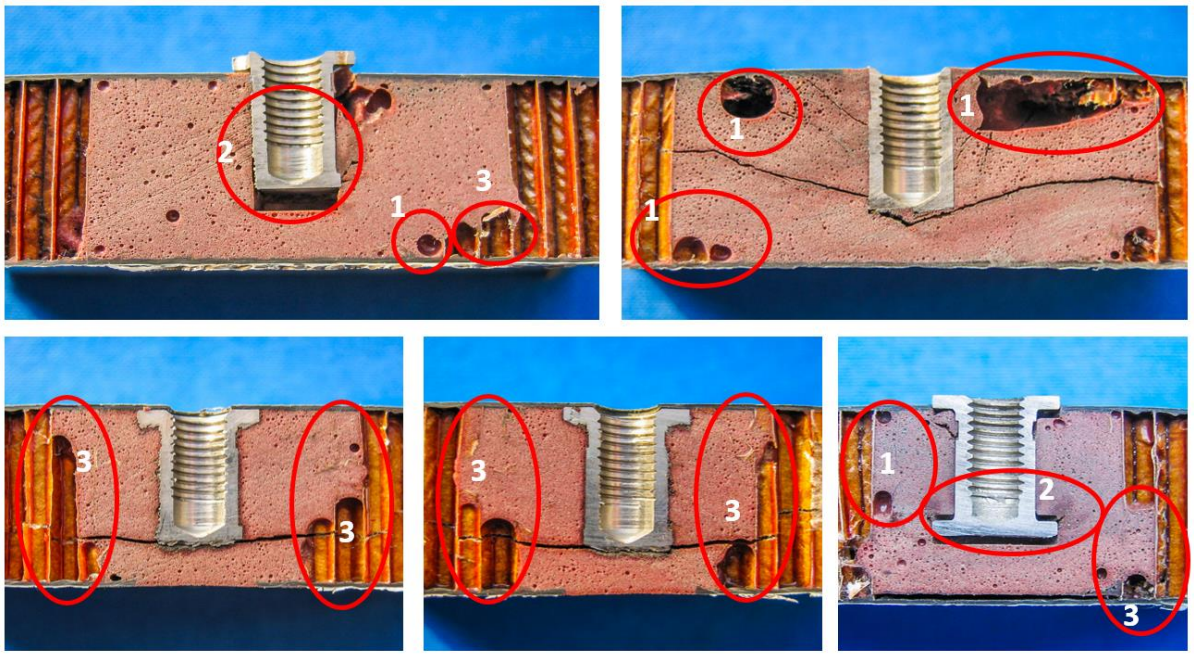

Fig. 191: 1. Trapped air in the cells, 2. Insert was not bonded 3. The insert is irregular

Another aspect that should be important is the presence of air bubbles in to the potting of the specimens. This is a very common defect and some examples are presented in Fig. 191 identified under the number 1 for capsuled air bubbles and 3 when they were placed at the borders of the potting.

Another defect that was commonly detected in the inserts tested by Bunyawanichakul is that the fastener seemed to be weakly bonded or not bonded at all to the potting. This happened in 6 of 8 testes specimens (see Fig. 186, Fig. 188 and Fig. 190, see Fig. 191 number 2 and ref. [15]).

Finally, another important defect when a S.P.F is used is the micro-spheres concentration. Most of the time the potting mixture is handmade, therefore the mixing rations are not always respected at 100%. This is particularly important when micro-spheres are added to the adhesive in order to reduce the density (see chapter four, Fig. 136).

All these defects and their corresponding effects should be included in to the modeling.

5.3.1.6 Discussion about the dispersion of the test curves

Another aspect that draws the attention of the tested specimens of Bunyawanichakul is that for most of the cases, the testing curves of the same type of inserts show very different stiffness (see Fig. 185, Fig. 187 and Fig. 189), given that they are supposed to behave similarly since they have the same properties.

One of the main reasons could have been that the dial bore gauge was not initially positioned in the pull-out axis as shown in Fig. 192, this is specifically for Ep1 and Ep2. As for the other specimens, according to witnesses, the tool used to pull out the tests authorized rotations and thus there were small rotations that could have caused the shifts in the curves.

For this reason, only the linear parts of the curves should be considered. However, their stiffness seems to be very different. In this section, a linear correction of the displacement measured by Bunyawanichakul is proposed.

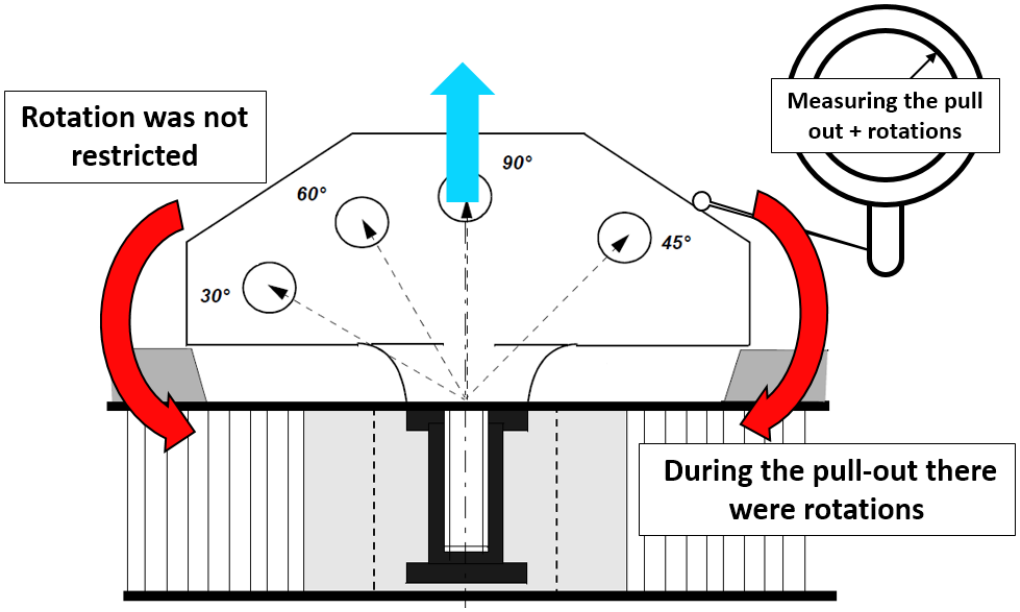

Fig. 192: The dial bore gauge could have been poorly positioned, also the tool used to pull-out the inserts authorized small rotations.

To analyze the causes of this dispersion it could be useful to make an analysis of the stiffness reference value of the inserts.

For this purpose, all the materials are considered to behave linearly. In consequence, the insert stiffness can be approximated by the insert geometry and the materials stiffness.

Since the shear moduli of the core is about 20 times smaller than the potting (21.5 MPa vs 500 MPa respectively), and 4000 times smaller compared to the stainless steel of the fastener (21.5 MPa vs 84600 MPa respectively), the core is clearly the softest part. For this reason, when a pull-out displacement is imposed to an insert, the deformations of all the other parts can be neglected compared to the honeycomb core deformation. Therefore, the insert stiffness might be accurately calculated in function of the shear deformation of the core and the imposed displacement (see Fig. 193).

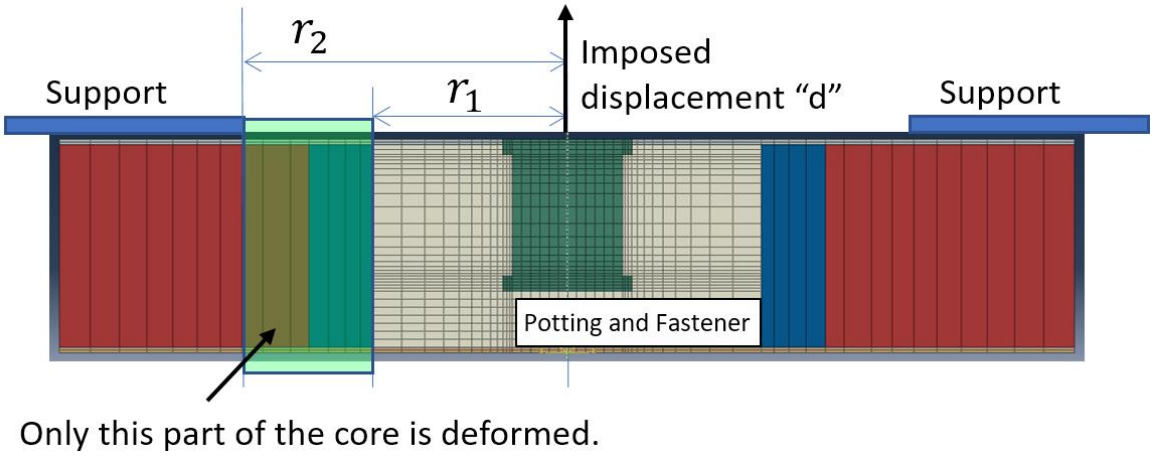

Fig. 193: The insert stiffness should be given mostly by the core shear deformation.

This reasoning is useful because it allows estimating the insert stiffness as function of the insert and supporting radius. Then, the imposed displacement should be equal to the sum of the shear deformations from the support radius r_2 to the potting radius r_1. Therefore, the insert stiffness should be given by the following equation.

$$k = \frac{F}{d} = \frac{2\pi hG}{ln(\frac{r_2}{r_1})} \quad (23)$$

This assumes that the potting shape is a perfect cylinder that represents the equivalent radius of the irregular potting shape, which is the same concept of the real potting radius proposed by the ESA in the insert design handbook.

Also, this equation assumes that the shear forces are uniformly distributed in the section highlighted in green in figure Fig. 193, and neglects the contribution of the bending deformation of the sandwich panel. These assumptions are not true, however, for small deformations it shouldn't be far from reality, allowing to estimate the linear behavior of the insert.

Moreover, it's important to understand that the core is always subjected to the same shear stress without being affected by the support radius, as in the three or four point bending tests. Indeed, analogically, the stiffness value given by the honeycomb area between points r_1 and r_2 that is subjected to shear stress, which according to Ericksen's model, has the same distribution shape regardless of the support's radius.

Summing up, this means that the failure load remains the same even if the support radius changes.

By using the equation 23, the real potting radius formula proposed by the ESA of equation 22, and the values of Table 20, it's possible to estimate a range of stiffness for the loading slope of the inserts type 1, 2 and 3.

Case: Insert type 1

According to Bunyawanichakul, the radius of the perforation was 9 mm. However, when the postmortem specimens were cut in half, the measured radius was about 11.75 to 15 mm. This is normal because the potting smeared in the cells as explained in previous sections. For this reason, the measured radius of the postmortem specimens shouldn't be considered, and the use of equation 22 and Table 20 is recommended to estimate the minimal and maximal real potting radius.

Finally, the minimal, and maximal values are 10.14 mm and 11.06 mm respectively. Using these values and equation 23 the analytical range of stiffness is obtained for this insert (see Fig. 194).

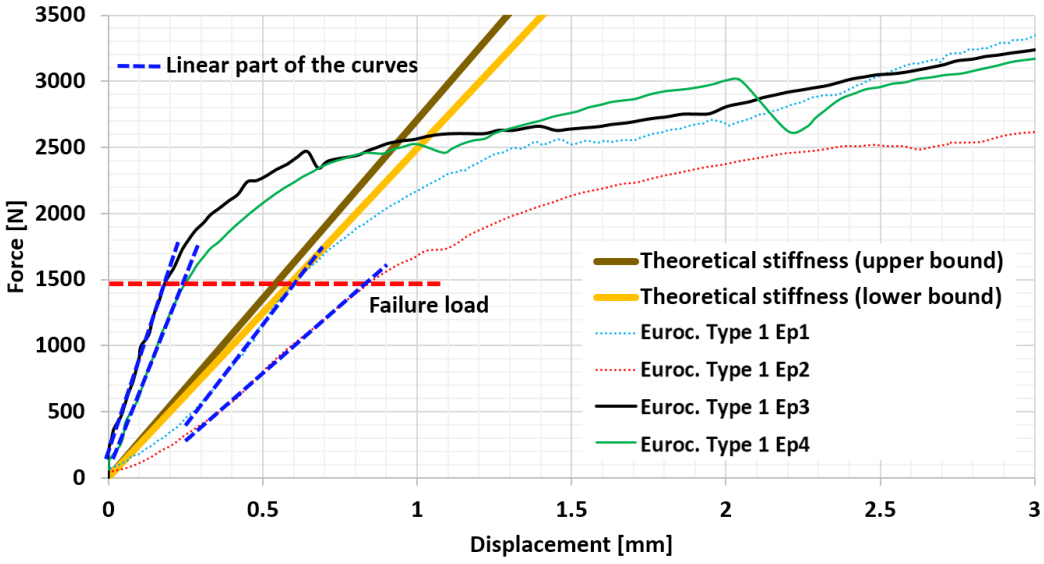

Fig. 194: Range of minimal and maximal stiffness according to the ESA real potting radius formulations.

However, when these bounds are compared to the experimental results they are very different. Considering the big difference of the initial slope of the curves, we privilege the hypothesis that these differences were caused by a bad positioning of the dial bore gage.

This is justified because the loss of force linearity is very similar between the four specimens, which indicates that the core shear failure arrived at similar forces for all the specimens. In consequence, this strongly suggests that the real insert radius was very similar for all the specimens. If the radius were different, insert strength would have been different too.

Also, according to the given experimental curves, the insert stiffness of specimens Ep3 and Ep4 are about 6000 N/mm which is approximately 2 times the analytical estimated stiffness.

For this reason, we assume that the measured force signal was correct, but the displacements were not (as Bunyawanichakul indicated in its PhD thesis in ref. [15]). Then, the displacements are modified to adjust the linear part of each of the curves (blue lines in Fig. 194) to the range of the estimated stiffness. The displacements are multiplied by a constant to modify their scale (except for Ep1), and for Ep3 and Ep4, additionally the curves are displaced to the right by adding an offset.

The only objective of this modification is to gather them into the range of correct stiffness. The fixed curves are shown in figure Fig. 195.

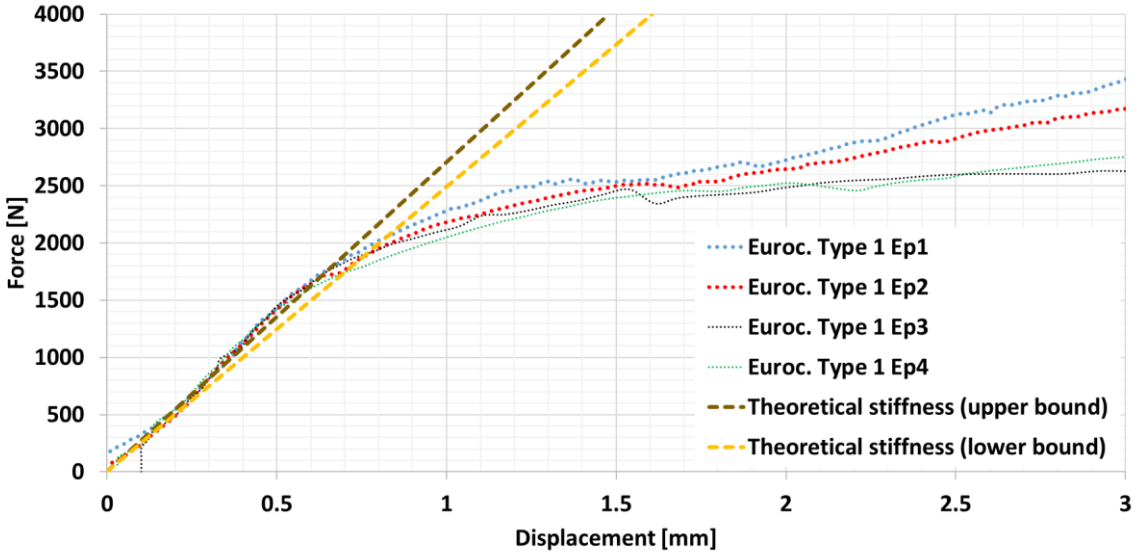

Fig. 195: Experimental curves of Bunyawanichakul with the fixed displacement, now the values are set to be in an accurate stiffness range.

Case: Insert type 2

The insert radius of the postmortem specimens varies from 20.8 to 23.15 mm. However, the minimal and maximal RPR are 19.51 mm and 20.07 respectively. The bounds are calculated analytically using the previous values. The linear part of the curves is shown with a blue line in Fig. 196. Visibly, the slopes present a significant dispersion, except for Ep8.

So, the same procedure used for the insert type 1 is applied here. The displacement of the curves is modified and an offset is applied to gather them in the range of correct stiffness. The modified curves are shown in Fig. 197.

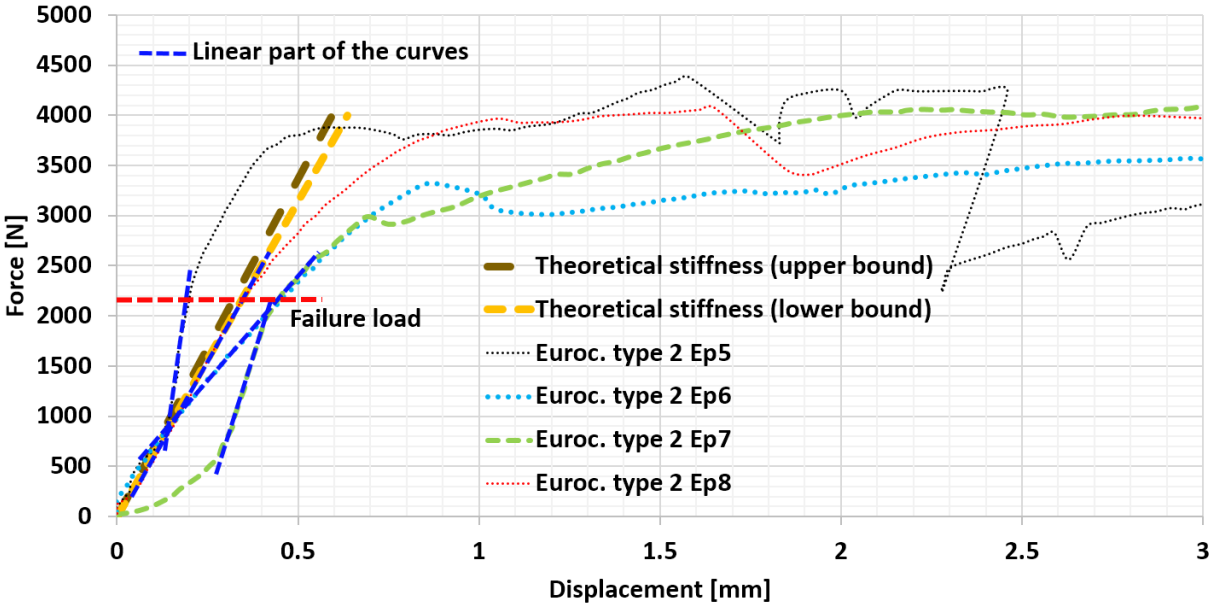

Fig. 196: Comparison of the experimental, analytical and numerical stiffness of the inserts type 2.

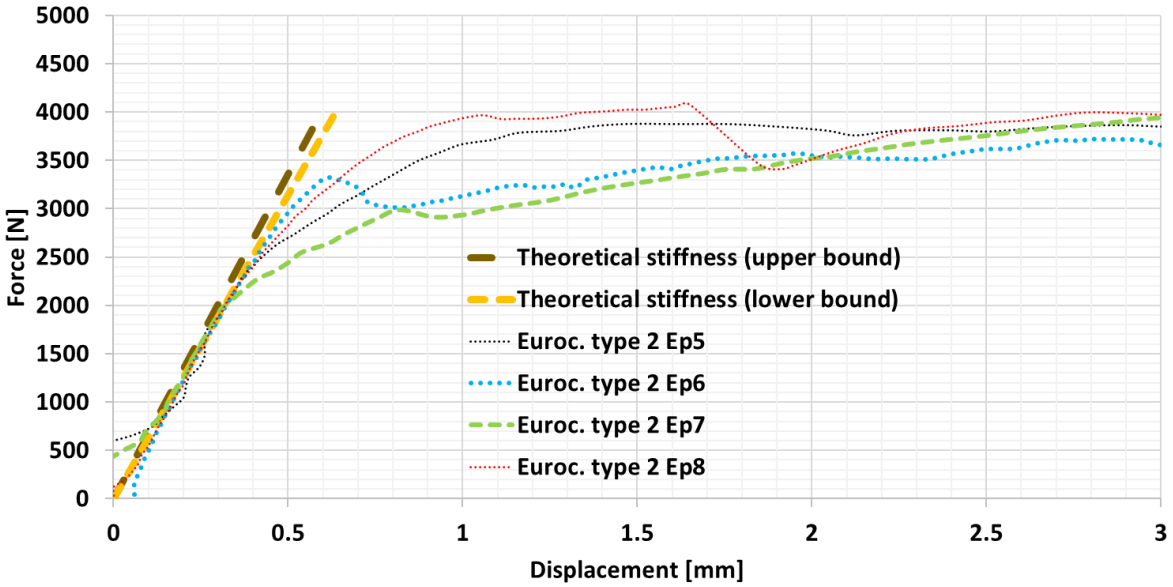

Fig. 197: Comparison of the experimental, analytical and numerical stiffness of the inserts type 2.

Case: Insert type 3

The insert real radius was the same as for the inserts of type 1 and presented very similar radius variations. The same procedure of used for the previous inserts is applied. The minimal and maximal values are of the RPR are 10.14 mm and 11.06 mm respectively.

The experimental tests presented a different stiffness compared to the analytical bounds and the F.E. simulation. Nevertheless, there is no too much dispersion in the tests results, this might be because since the fastener were supported by the skins, they restricted the rotations that caused the variation for the past insert tests.

Finally, the displacements were adjusted and the fixed curves are shown in Fig. 199.

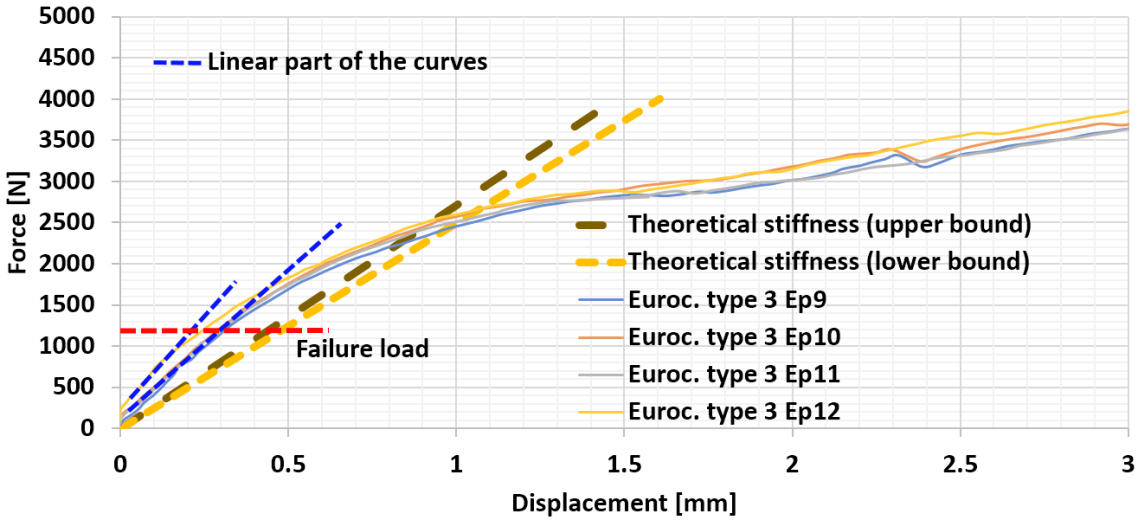

Fig. 198: Comparison of the experimental and analytical stiffness of inserts type 3.

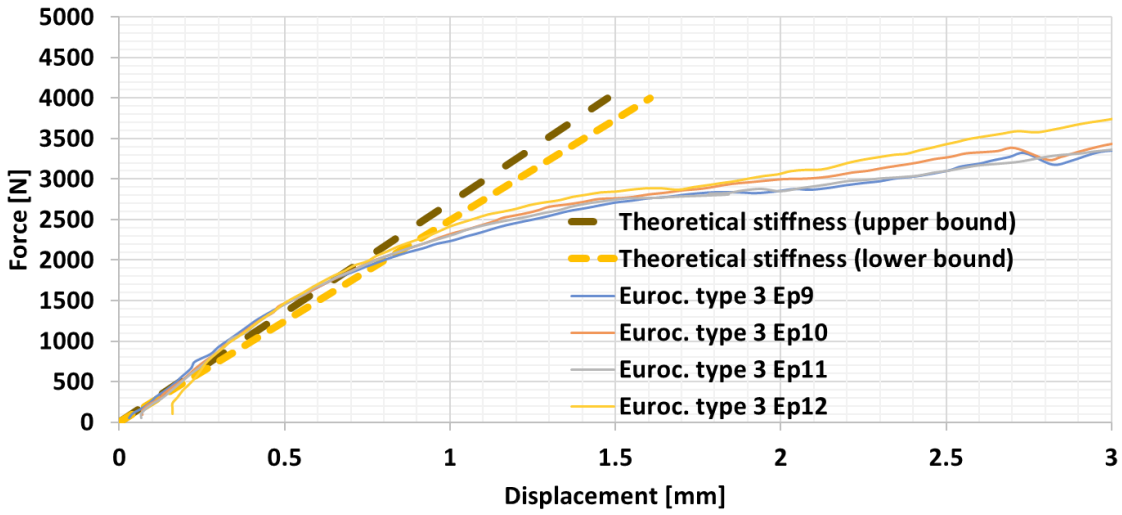

Fig. 199: Loading curves of inserts type 3 with the modified displacement.

5.3.2 Insert F.E. model features

The insert specimens presented previously are modeled using Abaqus. Since the testing speed of the insets was of 0.5 mm/min, they are static tests and are modeled using the implicit solver.

In contrast to the very detailed models of Seemann [34], [98], Roy [33], Smith [31], Slimane [32] among others, the models developed here will be as simple as possible, nevertheless, they include the most relevant aspects in order to be as accurate as possible.

As seen in chapter two, the honeycomb cells that are surrounding the insert experience a different shear behavior. This is because the insert creates a stabilization effect that increases the shear strength. For this reason, the core is divided in two sections. The first one which is near the insert (Fig. 201-a in blue) with radius of two to four cells after the potting, and the second one, the rest of the honeycomb, which is far from the insert in red color.

In order to reduce the calculation time and simplify the meshing of the parts, the fastener geometry was simplified. However, the original contact surface area was kept in the simplified fastener by using an equivalent surface (see Fig. 200-b). This simplification was made for the inserts type 1 and 2 but for the type 3 the fastener shape remains as the original.

Concerning the fastener, most of the time it is not bonded and the potting is compressed until it plasticizes (see Fig. 186 and Fig. 188). Therefore, we assumed that the most important parameter was the contact area highlighted in red in Fig. 200-b.

Concerning the potting geometry, it is a perfect cylinder with a determined radius. Their radius (typicall RPR by the ESA) are 10.32 mm, 19.74 mm and 10.32 mm for the insert type 1,2 and 3 respectively.

For the elements type, only brick elements are used to represent the materials, including the skins, the honeycomb core, the potting and the fastener. For the core, this choice allowed to implement the CDM approach presented in chapter two. For the skins, this feature allows to take into consideration the transversal shear moduli of the skins which is relevant and will be presented in the following sections.

As for the meshing, the skins had two elements of thickness, the core only one element as explained in [14] and chapter two, and for the rest of the parts the size varied according to the desired accuracy of stress field.

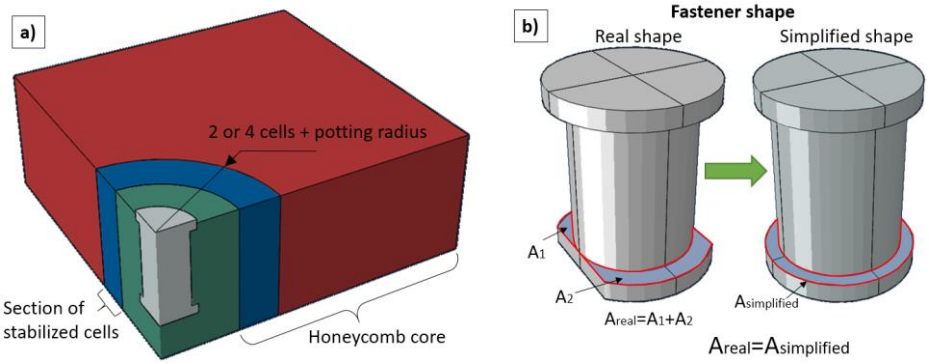

Fig. 200: a) The core near to the insert is divided into a different section because its behavior is different, b) the fastener geometry is simplified.

Concerning the boundary conditions, the Z displacement of the uper skin nodes at a radius of 15 mm is fixed to simulate the support of Fig. 184-b. Also, the displacement is imposed at the center of the fastener as shown in Fig. 201. Due of the characteristics of the test, it is possible to use symmetry to simplify the model and simulate only one quarter of the specimen. This feature will reduce the simulation load by 4.

For the materials behavior, the linear properties given by Bunyawanichakul are used as a start point (see Table 21). However, different behavior laws are implemented through an UMAT subroutine. In the next section the implemented laws and the influence on the insert behavior are explained and analyzed.

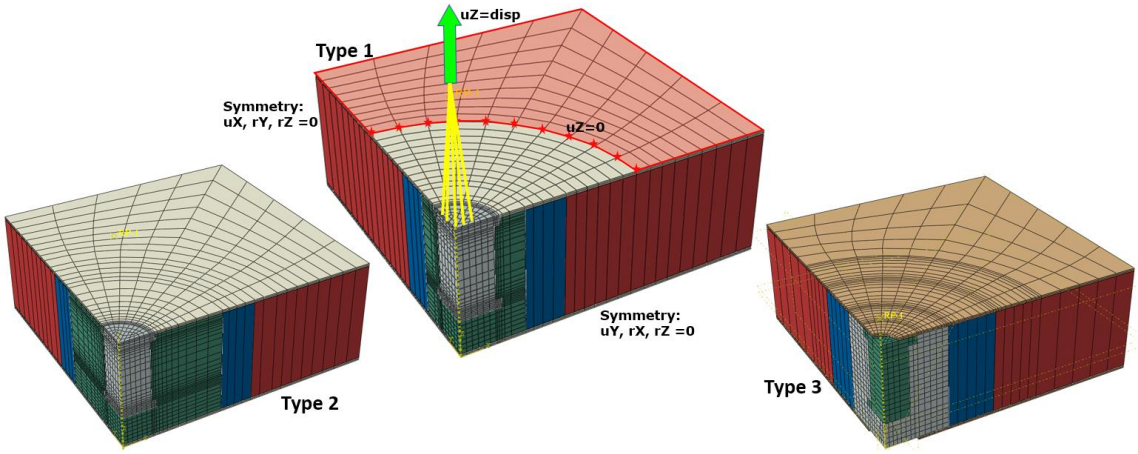

Fig. 201: Reduced F.E. models of inserts type 1,2 and 3.

5.3.3 Implementation of the behavior laws

Now, the behavior laws are included in the insert F.E. model. Each one is implemented individually to observe and discuss about the influence that they have on the insert behavior.

First, the materials were considered to behave linearly for the three types of inserts, then, the three models were simulated. The comparison of the experimental and numerical results is shown in Fig. 202.

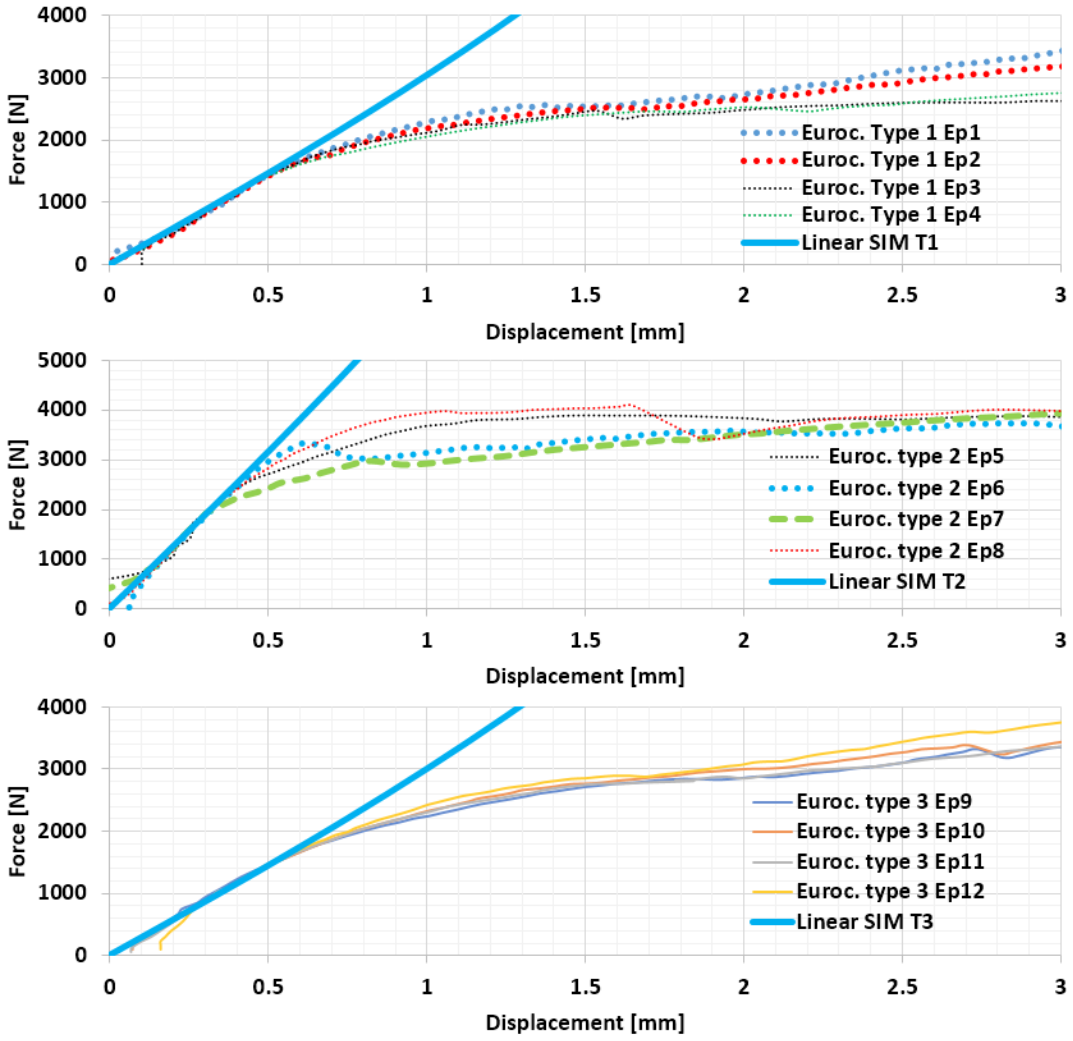

Fig. 202: Comparison of the experimental, analytical and numerical stiffness of the inserts type 1.

The numerical and experimental results show a good correlation because the curves were corrected to fit the analytical stiffness, which only indicates that the analytical stiffness proposed by equation 23 was accurate. The only reference to compare the experimental and numerical results shall be the failure load, and in consequence, the start of the nonlinear behavior. This is made in subsequent sections.

Also, it could be confusing and long to show the implementation of the laws for the three insert types. Therefore, for the sake of brevity, this is only shown for the insert type 1.

5.3.3.1 Implementing the core shear failure law

Several authors [15], [33], [37] claimed that the first failure that appears when an insert is pulled out is the core shear buckling. In chapter two it was seen that the core shear failure is a complex phenomenon that is composed of different phenomenological stages and can be altered by the boundary conditions.

The first stage is the initial buckling, during which vertex cells remain straight and therefore the buckles created by the shear loads are small and local; and even if the Nomex® material may plasticize in these small buckles, the effective shear moduli of the honeycomb core structure remains the same.

The second stage is the collapse of the cells, on which the cell vertex starts to fold and the cell stability is lost. In consequence, the buckles grow and propagate to the adjacent cells and the Nomex® paper starts to be torn. The effective shear moduli of the honeycomb structure is gradually reduced as the shear deformation is increased.

During the study of chapter two, it was seen that the boundary conditions of the cells play an important role for the shear strength of the honeycomb core. When the cells are laterally stabilized (for example with an insert), the experimental results suggested that the shear strength can be increased up to 16% and 32% for the W and L directions respectively. But also, the collapse of the cells arrives earlier in a more dramatical way compared to shear tests on the honeycomb without insert.

However, the defects study presented previously suggests that the only effect that should be included in the behavior of the cells that are near the inserts is an early collapse of the cells (see section 5.2.4 of this chapter).

For the development of the shear behavior law of the honeycomb core, the experimental tests on the honeycomb core made by Bunyawanichakul in ref. [15] are taken as reference. Unfortunately, these tests were performed using a three-point bending specimen, which gives only the initial part of the shear testing curve (see Fig. 183-a).

Therefore, in order to estimate the natural complete shear behavior of this honeycomb core, the curve is completed by comparison to other shear testing curves of honeycomb cores (ref. [12] and [13] for instance). Finally, the proposed shear behavior laws for the W and L directions are shown in Fig. 203.

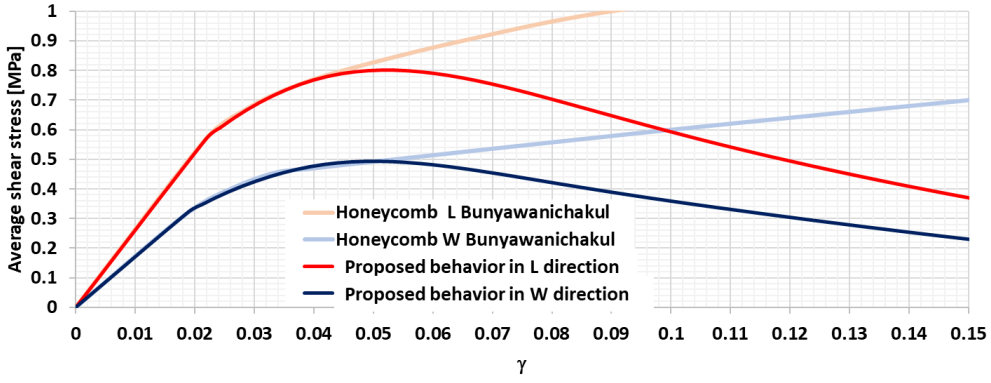

Fig. 203: The shear behavior measured by Bunyawanichakul is valid until the cells starts to fold, therefore semi-experimental curves were proposed to mimic the actual behavior.

Presentation of the different shear behavior laws for the model

The implementation of different behavior laws into the materials for the insert F.E. model allows to analyze the effect that such laws have on the insert behavior.

The different behavior laws are developed using the same approach, which was explained and developed in chapter 3 and ref. [14]. Four different behavior laws of the shear nonlinear behavior of the honeycomb core are implemented into the insert F.E. model, they are:

- A behavior law that only considers the initial buckling of the cells
- A behavior law that considers both initial buckling and collapse of the cells
- A behavior law that considers the early collapse of the cells
- A behavior law that considered the cells laterally stabilized (see chapter 2)

The first behavior law (see Fig. 204) allows isolating the influence of the initial buckling of the honeycomb cells into the insert loading curve. The part that represents the collapse is set to zero to consider only the effect of the initial buckling of the cells.

The second behavior law (see Fig. 205), should allow understanding how the collapse stage of the cells affects the insert loading curve.

The third behavior law (see. Fig. 206) allows incorporating the influence of the irregular borders of the potting that were found in Fig. 191. Which according to the discussion about defects presented in this chapter, should make the cells to collapse early.

Finally, the fourth behavior law (see Fig. 207) should allow understanding how the behavior of the insert would have been without defects. The evidence of chapter two suggested that the increase should be around 16% and 32 % for the W and L directions respectively. This is because the honeycomb cells that are closer to the insert are much more stable due to the presence of the potting, and therefore, have a different shear behavior.

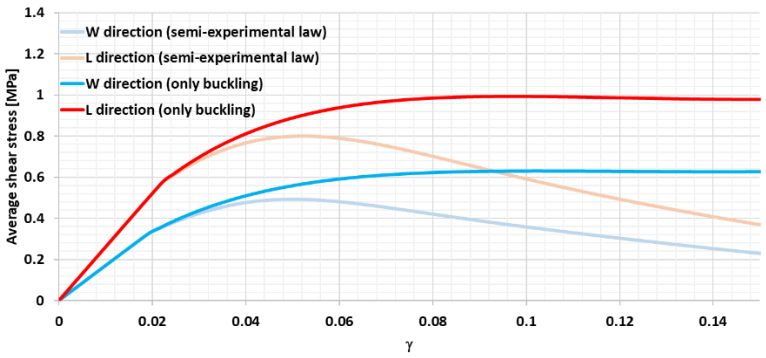

		W direction	L direction
Initial buckling stage	A_b	0.85	0.85
	λ_b	0.06	0.06
	γ_{b0}	0.019	0.022
	k_b	1	1
Collapse stage	A_c	0	0
	λ_c	0	0
	γ_{c0}	0	0
	k_c	0	0

Fig. 204: Behavior law implemented to consider only the initial buckling of the cells.

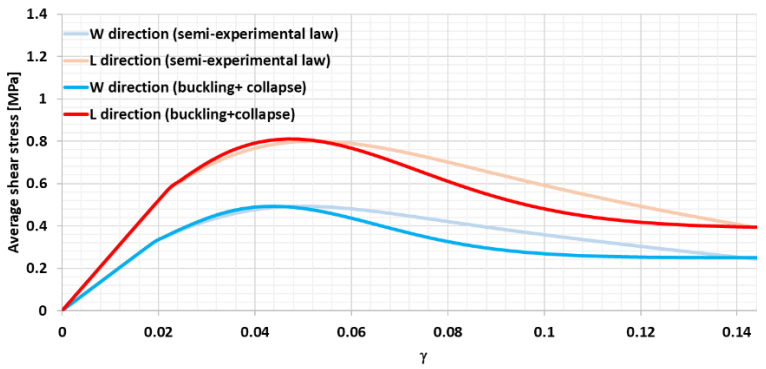

		W direction	L direction
Initial buckling stage	A_b	0.85	0.85
	λ_b	0.06	0.06
	γ_{b0}	0.0188	0.022
	k_b	1	1
Collapse stage	A_c	0.6	0.6
	λ_c	0.04	0.05
	γ_{c0}	0.03	0.03
	k_c	2	2

Fig. 205: Behavior law implemented to consider the initial buckling of the cells and the collapse.

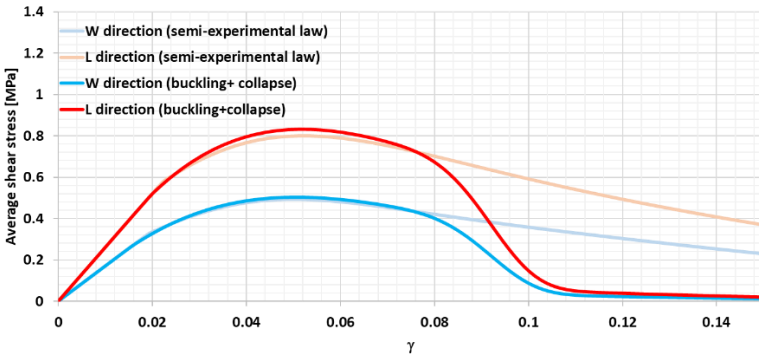

		W direction	L direction
Initial buckling stage	A_b	1	1
	λ_b	0.057	0.57
	γ_{b0}	0.015	0.019
	k_b	1.3	1.3
Collapse stage	A_c	0.9	0.9
	λ_c	0.03	0.03
	γ_{c0}	0.066	0.066
	k_c	4	4

Fig. 206: Shear behavior of the honeycomb when the potting borders are irregular, causing a premature collapse of the cells with no increase in the shear strength.

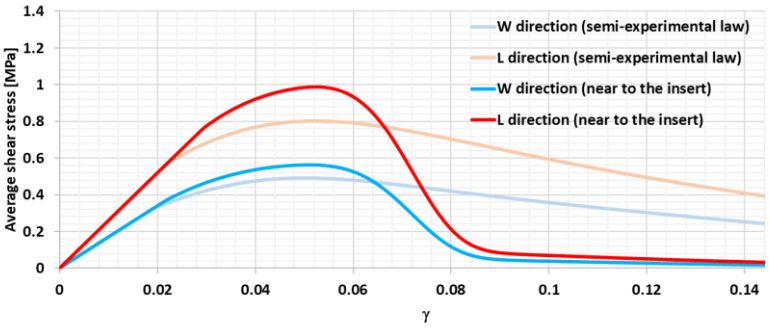

		W direction	L direction
Initial buckling stage	A_b	1	1
	λ_b	0.057	0.057
	γ_{b0}	0.021	0.028
	k_b	1.3	1.3
Collapse stage	A_c	0.9	0.9
	λ_c	0.03	0.03
	γ_{c0}	0.045	0.045
	k_c	4	4

Fig. 207: Shear behavior of the honeycomb when the potting borders are irregular, causing a premature collapse of the cells with increase in the shear strength.

Effect of the initial buckling of the cells

The behavior law that represents only the buckling of the cells (see Fig. 204) is implemented into the 3D F.E. model and the resulting loading curve is compared to the experimental results in Fig. 208.

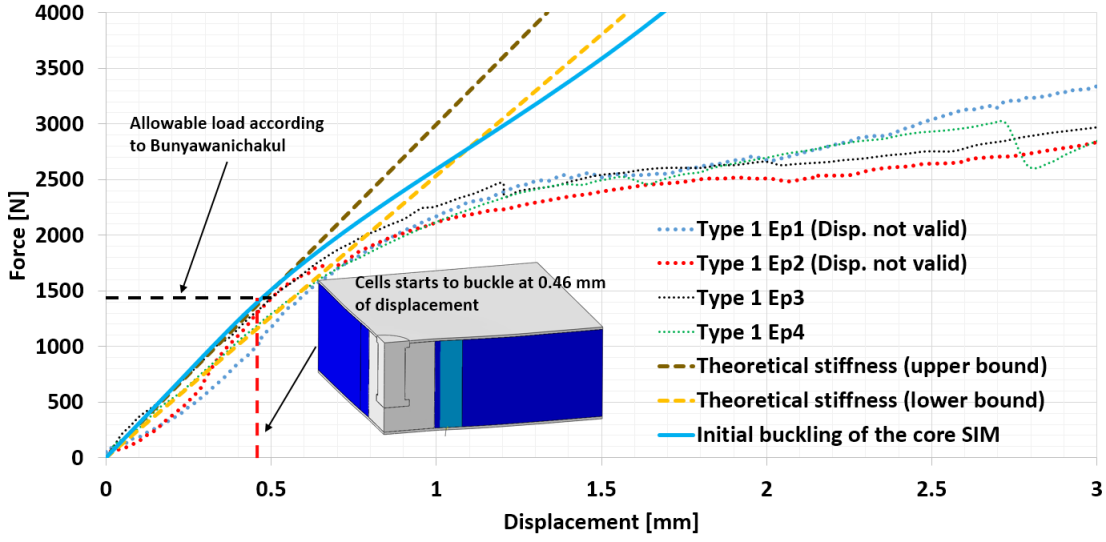

Fig. 208: Comparison of the experimental and numerical results, the buckling of the cells is coincident with the allowable load according to Bunyawanichakul in ref. [15].

According to Bunyawanichakul, the allowable load for this type of insert was around 1465 N (using the 1% of linear regression criterion), while in the numerical simulation, the initial buckling of the cells arrives around 1400 N or 0.46 mm of imposed displacement. Visibly, both failure loads are very similar.

This also confirms the conclusions of the research of Seemann et al. in ref. [11], where they suggested that reduced insert models are useful to detect the first failure of the insert.

Moreover, this fits perfectly to the conclusions of Roy et al. in ref. [33] where they stated that a good estimation of the allowable load for inserts can be obtained by measuring buckling of the cells walls.

They developed a very detailed insert F.E. model for their investigation, while for our research, we obtained similar results using a simplified F.E. model which is easier to feed with experimental data and to be implemented.

Moreover, it's interesting to mention that the criteria based on a certain percentage of the linear regression of the loading curve of the inserts, detects the bifurcation point of the buckling of the cells. However, in chapter two it was seen that postbuckling of the honeycomb cells is in a stable configuration, but also that the postbuckling was elastic until a certain limit.

This suggests that the insert behaves elastically beyond the linear limit, therefore, the linear regression criteria might underestimate the insert's strength.

Effect of the core shear failure (initial buckling plus cells collapse)

In chapter two it was seen that the Nomex® honeycomb structure had an elastic postbuckling behavior until a certain point. This means that the insert strength should be calculated using the nonlinear elastic limit of the honeycomb core, instead of the linear limit.

It was also seen that the nonlinear elastic limit of the honeycomb core was actually, the start of the collapse of the cells. That is to say, the elastic limit of the insert should be the start of the collapse of the cells, instead of the buckling point. For this reason, the effect of the complete shear failure (initial buckling plus collapse of the cells) of the insert will be now investigated.

Unfortunately, the study made in chapter two concerned only one specific type of honeycomb (HRH-78). Thus, since there is not an experimental data about when the cells start to collapse for this specific honeycomb core, factice values had to be proposed (see Fig. 205).

The elastic limit (or the collapse stages) is supposed to start at γ=0.03, which is considered a good estimation. The results of the simulation can be seen in Fig. 209.

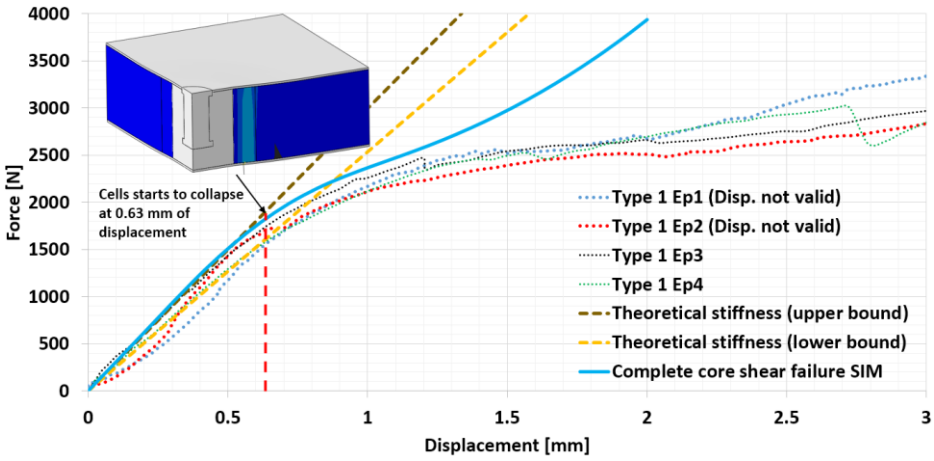

Fig. 209: Comparison of the experimental and numerical results; the point where the cells start to collapse should be the elastic limit the insert. [15].

The F.E. model detected the start of the collapse of the cells at 0.63 mm of displacement or around 1600 N. In this way, this criterion based on the detection of the collapse of the cells gives an allowable load that is around 10 % higher compared to the detection of the buckling of the cells.

Effect of the irregular borders of the potting on the shear failure of the core

The study of defects presented previously in this chapter suggests that the cells that surround the inserts collapses easier if there were irregular borders of the potting.

Supposing that only the cells that are near the insert collapses easier, the cells that are far from it have a natural behavior. Therefore, the behavior law of Fig. 206 is implemented in the section that is surrounding the insert, and the law of Fig. 205 is used for the section of the honeycomb core that is far from the insert.

The results of the simulation are shown in Fig. 210. Compared to the results shown in Fig. 209, the simulation curve is slightly smaller, which could be attributed to the early collapse of the cells.

Visibly, there is a good correlation with the experimental results until 1.25 mm. Maybe, this discrepancy is caused given that the potting failure or the skins failure has not been implemented yet.

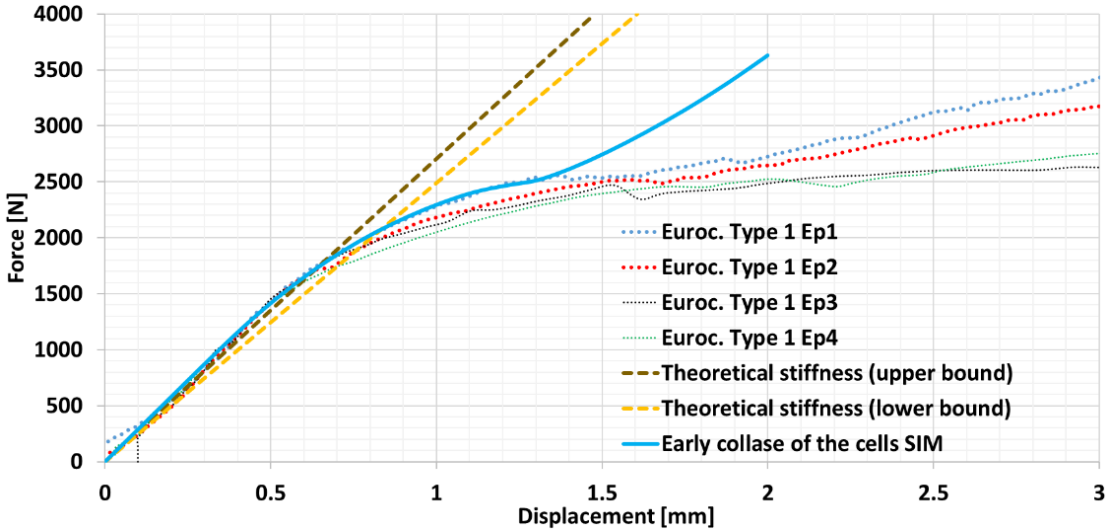

Fig. 210: Considering the effect of the irregular borders in the honeycomb core.

Behavior of the insert without potting defects

Now, the behavior law shown in Fig. 207 is implemented into the F.E. model. This law assumes that there are no defects in the potting, and therefore the cells near it are laterally stabilized. For this reason, it's only used for the section that is surrounding the insert, while the rest of the core has the behavior presented in Fig. 205.

Also, to investigate the influence of the radius of the section representing the cells near the insert, first its radius is set to 4 and then to 2 cells. The simulation results can be seen in Fig. 211.

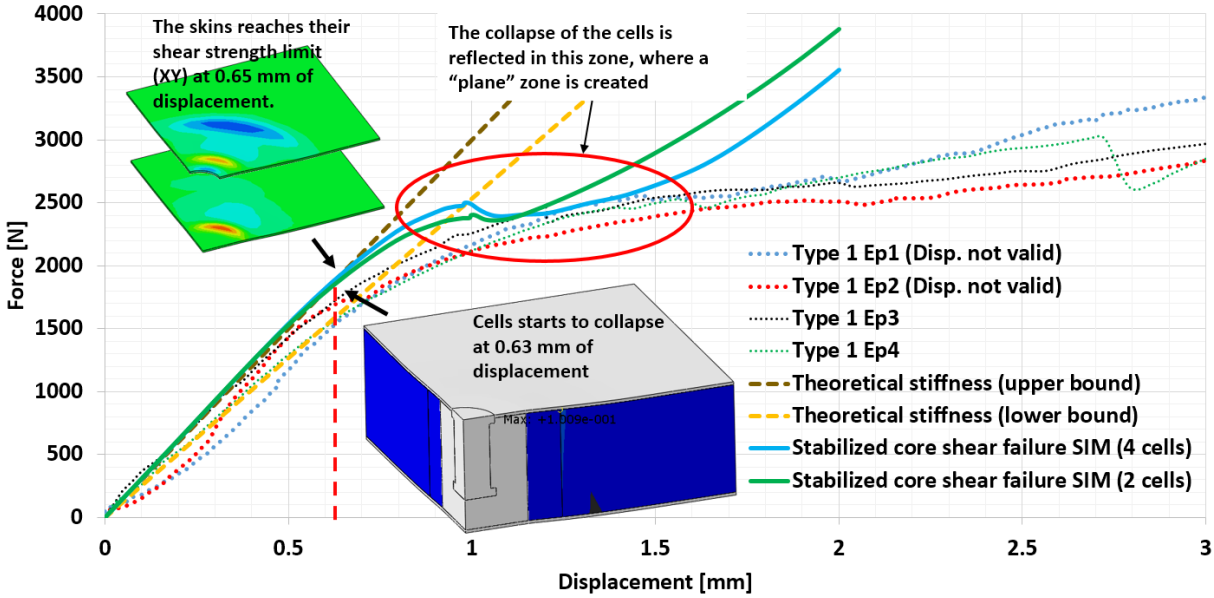

Fig. 211: Comparison of the experimental and numerical results considering the lateral stabilization effect on the cells surrounding the insert.

Concerning the collapse of the cells, the imposed displacement that causes its collapse in this and the previous cases are very similar. Both arrive at 0.63 mm of displacement. However, the allowable load for this case is around 1900 N which is 30% higher compared to the allowable load calculated by the detection of the buckling of the cells.

Also, it's interesting to observe that there is a plane zone created by the collapse of the cells. This effect was more visible when the number of stabilized cells was set to 4, also the maximal force the plane zone is slightly reduced. It seems that including the stabilized collapse of the cells increases the agreement between the experimental and numerical results. Nevertheless, from 0.5 mm to 1.2 mm of displacement there is a slight difference that can be attributed to the increment of the core shear strength due to the stabilization effect of the potting.

Moreover, by inspecting the numerical simulation it was seen that the in-plane stress and transversal shear stress in the skins were higher than the allowable values of the manufacturer. At 0.65 mm, the in-plane shear strength of the skins (100 MPa) is reached, at 0.8 mm the transversal shear strength (80 MPa) is reached, and at 1.81 mm the strength in the principal directions (634 MPa) is reached. This suggests that a better agreement could be obtained if a failure criterion for the skins is implemented.

5.3.3.2 Effect of the skin damage

In the previous section, it was seen that the skins failed when the insert was pulled out. The detected failure modes were the transversal shear damage of the skins, the in-plane shear damage of the skins and finally, the damage in the principal directions of the skins.

To improve the accuracy of the F.E. model the skin damage is included. Unfortunately, due to the relatively short time of this thesis, it was not possible to perform any tests on the G939/145.8 [0,90] skins used to fabricate the insert specimen. Therefore, there is no experimental reference of the behavior this material. The only available data are the manufacturer references.

Also, it's worth mentioning that the damage of woven stratifies is complex to model and requires high expertise (see for example Pascal and Navarro works in [101], [102]).

For this reason, the skins are homogenized in order to simplify the representation of damage of the material. The approach proposed by Bunyawanichakul to model the out-of-the plane shear matrix failure for thick skins is retaken here. This technique consists into reduce the shear elastic moduli once the elastic limits are reached. For our specific case, the values of Table 22 are used as strength values and the stiffness is reduced to 15% of the original value. This was implemented for the three shear directions; the damages laws are not coupled. The resulting curves are shown in Fig. 212.

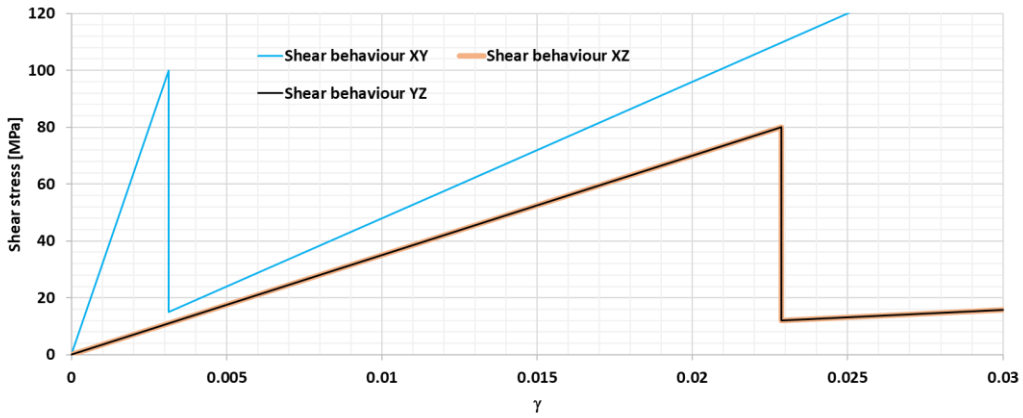

Fig. 212: Skin's shear behavior laws.

For the principal directions, no damage laws are implemented, however, since the allowable stresses are known, it's possible to evaluate if the skins are damaged. The material laws were implemented and the numerical and experimental results can be seen in Fig. 213.

Material	$+\sigma_1$[MPa]	$-\sigma_1$[MPa]	$+\sigma_2$ [MPa]	$-\sigma_2$ [MPa]	τ_{12} [MPa]	$\tau_{13\text{-}23}$ [MPa]
Skins G939/145.8	634	500	634	500	100	80

Table 22: Strength values of the G939 5-satin carbon fiber reinforced prepreg.

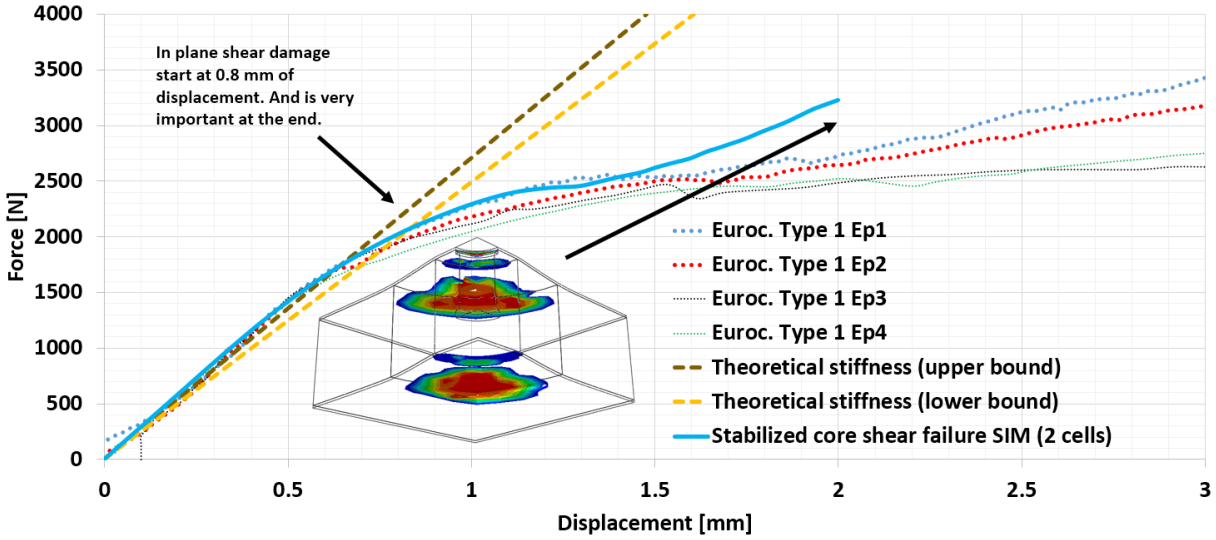

Fig. 213: The inclusion of the skin damage allows a better agreement with the experimental results.

The experimental and the numerical results show a very good agreement for a displacement from 0 mm to 1.5 mm. After this, the experimental and numerical curves differ probably because the damage in the principal direction of the skins is not implemented.

The skin in-plane damage for these inserts was not investigated in the PhD thesis of Bunyawanichakul. Here, the evidence points that the skins presented a matrix failure due to the in-plane and transversal shear stresses. However, since the proposed damage laws for the skins are factice, the numerical simulations cannot be considered conclusive.

Also, the proposed damage evolution laws were not modified or improved because we don't have experimental references. The agreement between the experimental and numerical curves was good enough for the purpose of the model.

Nevertheless, the potting failure has not yet been included in to the F.E. model. This aspect is analyzed in the following section.

5.3.3.3 Effect of the potting failure

In chapter four it was seen that the potting had different elastic moduli when it was subjected to tension or compression. Also, it was seen that depending on the micro-spheres concentration the mechanical properties of the potting varied. However, the most important aspect was that there were two principal failure scenarios for the potting material (see section 4.2.3 chapter 4).

The first one occurred when the fastener was firmly bonded to the potting. For this case the failure mode of the potting is the fracture of the material beneath the fastener.

The second one happened when the fastener was not really bonded to the potting. This happened to most of the tested specimens of Bunyawanichakul and it was unintentional, more like a defect. For this case, the potting starts to be compressed until it fails due to compression and shear stress.

Both failure modes will be now implemented in the insert F.E. model.

For the first failure case, the fastener is tied to the potting. The only difference is that the UMAT developed in chapter four will be used to include the bi-moduli behavior and the failure in traction or compression of the potting material.

For the second failure case, the fastener is not tied to the potting, instead a normal and tangential contact is set between the two pieces.

Moreover, to analyze the sensitivity of the micro-spheres concentration in the potting, a variation of +- 3% of the micro-spheres concentration is considered. In this sense three different potting material are used for the numerical model; soft, and hard with 7% and 13% of micro-spheres concentrations respectively (see Fig. 214 and Table 16 of chapter four).

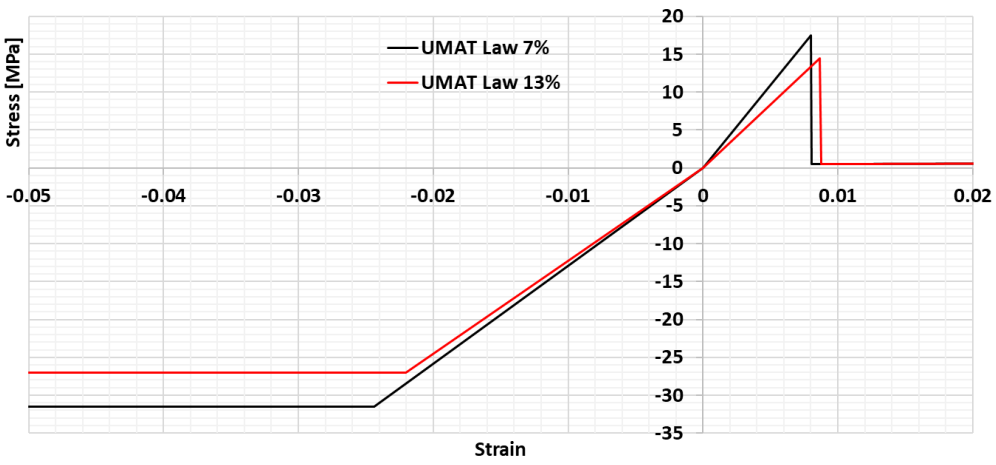

Fig. 214: Behavior laws that describes the potting behavior under tension and compression.

First, two simulations were made, with hard and soft potting. The fastener was well bonded in both cases, the results can be seen in Fig. 215.

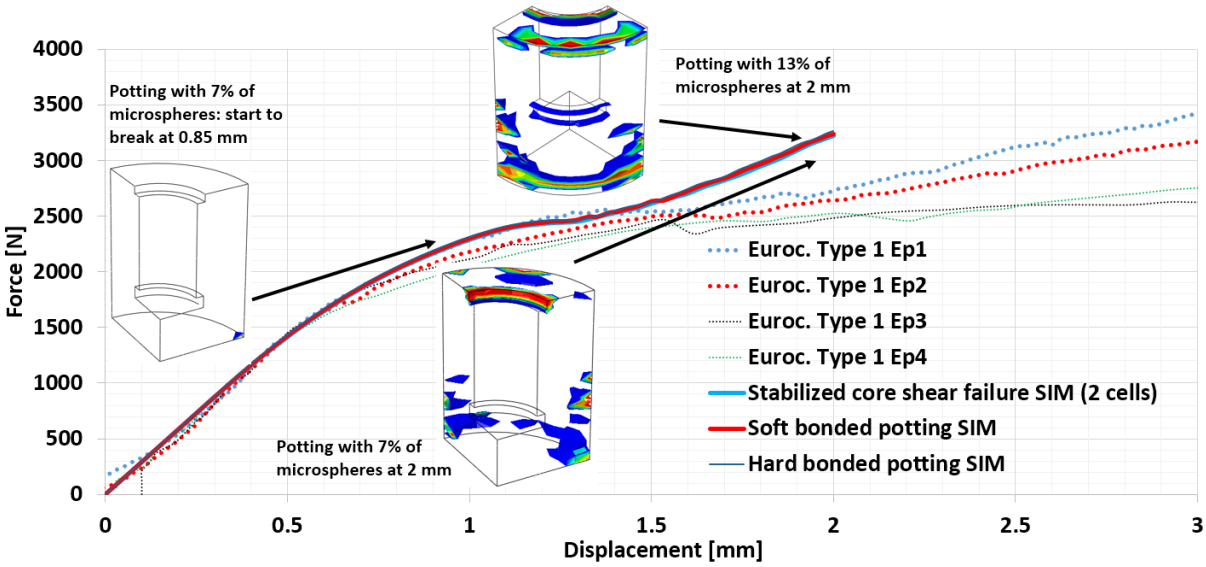

Fig. 215: Comparison of the experimental and numerical results considering the potting failure when is firmly bonded: traction damage of the potting.

By comparing the numerical loading curves, it was seen that the incorporation of this feature had no influence since the curves are very similar. However, concerning the damage scenario, it was seen that the potting starts to fail in compression at the inferior skin/potting interface around 0.85 mm of displacement, in concordance with the experimental evidence (see Fig. 186). This aspect was more visible for the soft potting.

After this, two other simulations were made considering that the fastener was not bonded. The results are shown in Fig. 216.

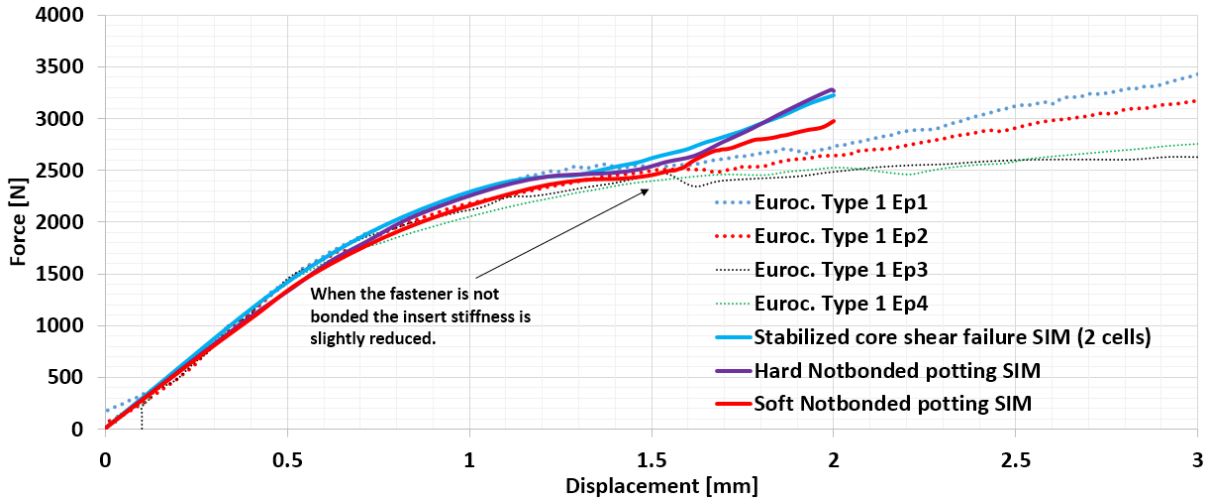

Fig. 216: Comparison of the numerical loading curves when the fastener is not bonded.

5.3.3.4 Comparison of the best and worst cases

Based on the previous study and the discussion about defects, it was concluded that they were important for the insert design. In order to evaluate the effect of defects in inserts, two simulations cases are presented here, the best and worst cases.

For the best case, the insert is considered to be designed and installed in a proper way. Therefore, there are no defects; the potting shape makes that the real potting radius (RPR by the ESA) is the biggest possible for the drilling tool of 9 mm, the cells surrounding the insert are stabilized as seen in chapter two, also, this stabilization effect is propagated until 4 cells after the potting, the fastener is well bonded to the potting, and finally, the potting is harder than it should be.

In contrast, for the worst case, the insert is considered to be installed and designed careless by. Therefore, it is full of defects; the potting shape means that the real potting radius RPR is the smallest possible for the drilling tool of 9 mm, the cells surrounding the insert collapse easily, and this effect is propagated only until 2 cells after the potting, the fastener is not well bonded, and finally, the potting is oversaturated of micro-spheres and is softer than it should be.

All these characteristics are summed up in table X for the insert type 1.

Insert description	Sim IT1 worst case	Sim IT1 best case
Potting radius [mm]	10.14	10.67
Potting	13% of Micro-spheres	7% of Micro-spheres
Bonded insert	No	Yes
Stabilized core	Cells collapses early but there is no strength increase (see Fig. 206)	Yes
Number of stabilized cells	2	4

Table 23: Characteristics of the worst and best cases for the insert type 1.

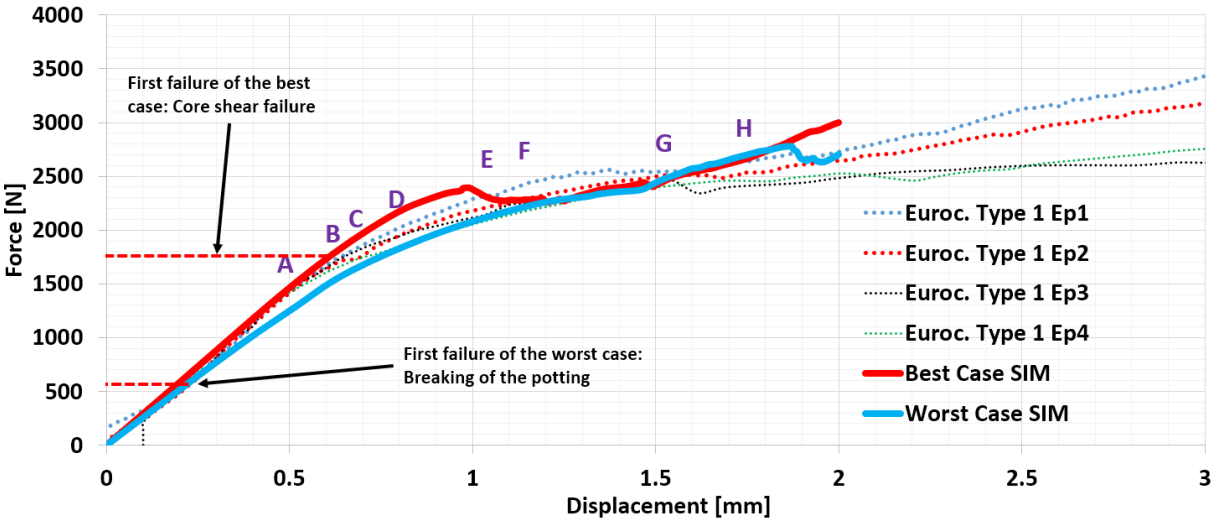

Fig. 217: Comparison of numerical best and worst cases and the experimental results (type 1), see also Fig. 219.

It can be seen that the experimental results match almost perfectly the worst-case simulation, which is not surprising because the real specimens were indeed full of defects, because they were quickly handmade. This is congruent to the testimony of the persons that were present at the day the inserts were fabricated.

The deformation of the potting is well represented, the shear deformation of the core too. Indeed, the failure scenarios are very similar (Fig. 218). The only failure mode that is not well represented is the breaking of the inferior potting/skin interface.

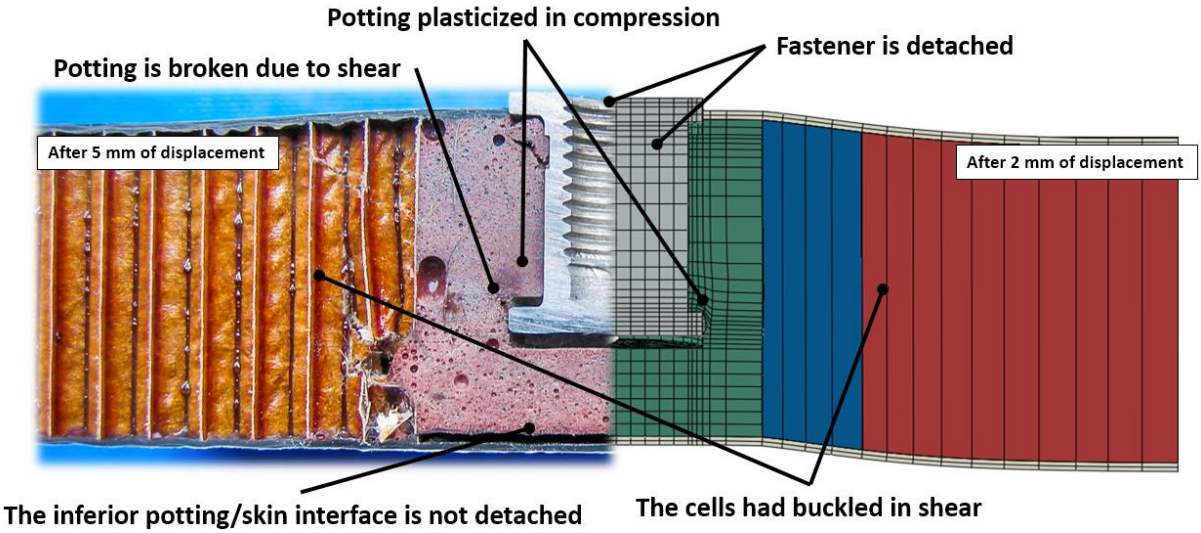

Fig. 218: The comparison of the experimental and numerical failure scenario shows a good agreement.

Moreover, this approach allows to detecting several failure modes at each step of the simulation. They are shown in Fig. 218 and Fig. 219.

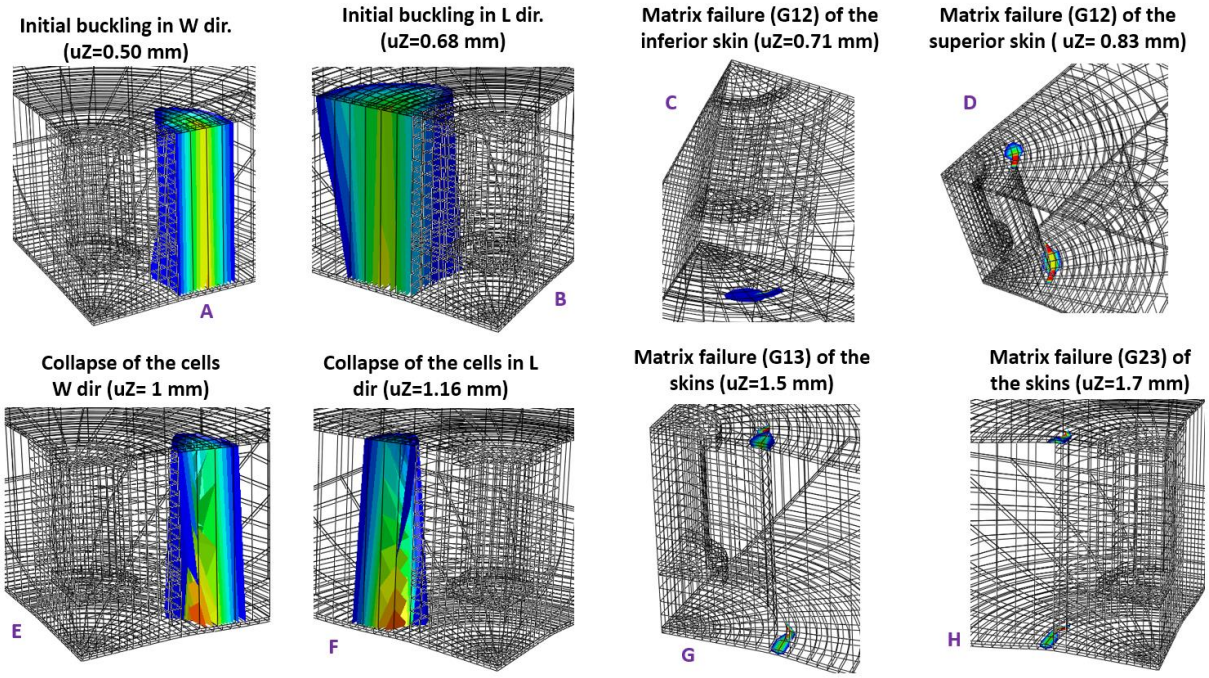

Fig. 219: Different failures in the simulation of the best case of the insert type 1.

This same procedure was made for the inserts type 2. The best and worst cases characteristics are shown in Table 24 and the loading curves are shown in Fig. 220.

Insert description	Sim IT2 worst case	Sim IT2 best case
Potting radius [mm]	19.51	20.07
Potting	13% of Micro-spheres	7% of Micro-spheres
Bonded insert	No	Yes
Stabilized core	Cells collapses early but there is no strength increase (see Fig. 206)	Yes
Number of stabilized cells	2	4

Table 24: Characteristics of the worst and best cases for the insert type 2.

For the simulation of the worst case, the simulation crashed after a displacement of 0.86 mm. This is explained because, since the fastener is not bonded, it punches the potting, submitting it to compression in the contact surface, but also slicing the potting by shear at the perimeter of the contact surface. And since the shear post failure behavior of the potting was not implemented into the UMAT, the simulation can't converge.

Nevertheless, the experimental results are inside the envelope formed by the worst and best cases. For this type of inserts it's especially interesting to see that the envelope is bigger compared to the envelope of the insert type 1. This can be explained because the number of cells subjected to shear stress is bigger than for the insert type 1, therefore the shear stress is distributed in a larger number of cells, while the contact area between the fastener and the potting remains the same. In other words, the potting becomes the softest part of the insert and the loading slope when it is bonded is much stiffer than when it's not.

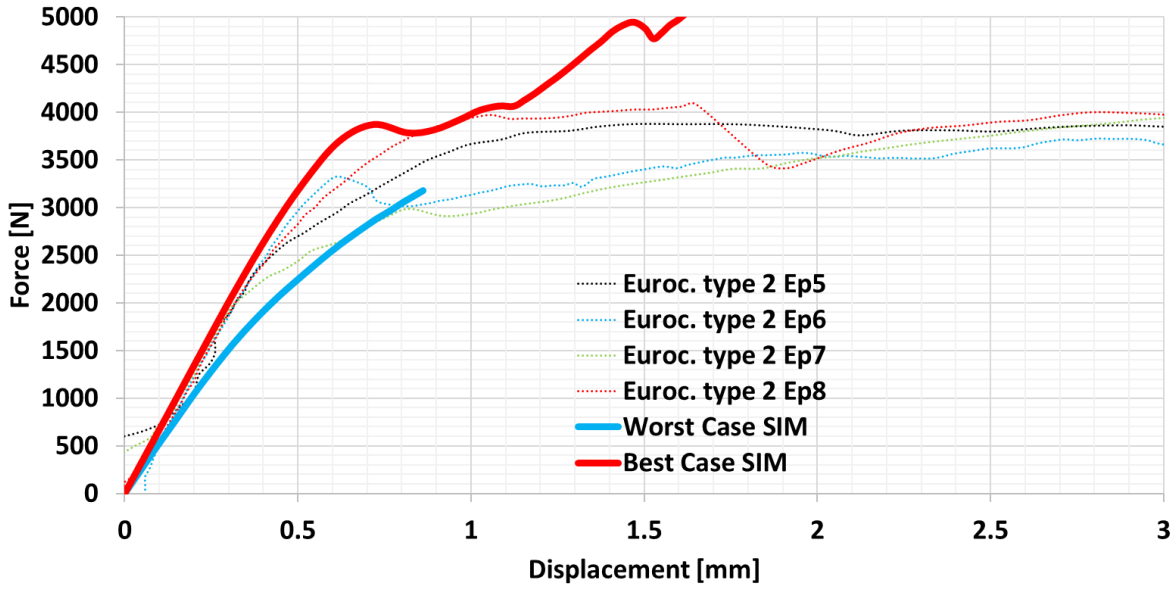

Fig. 220: Comparison of numerical best and worst cases and the experimental results (type 2).

Finally, for the insert type 3, since the fastener was placed under the skins and its geometry was not simplified (see Fig. 200) only an average case is simulated. The selection of parameters was made by looking at the postmortems specimens of Fig. 190.

Insert description	**Sim IT3 average case**
Potting radius [mm]	10.74
Potting	10% of Micro-spheres
Bonded insert	No
Stabilized core	Cells collapses early but there is no strength increase (see Fig. 206)
Number of stabilized cells	2

Table 25: Characteristics of the average case for the insert type 3.

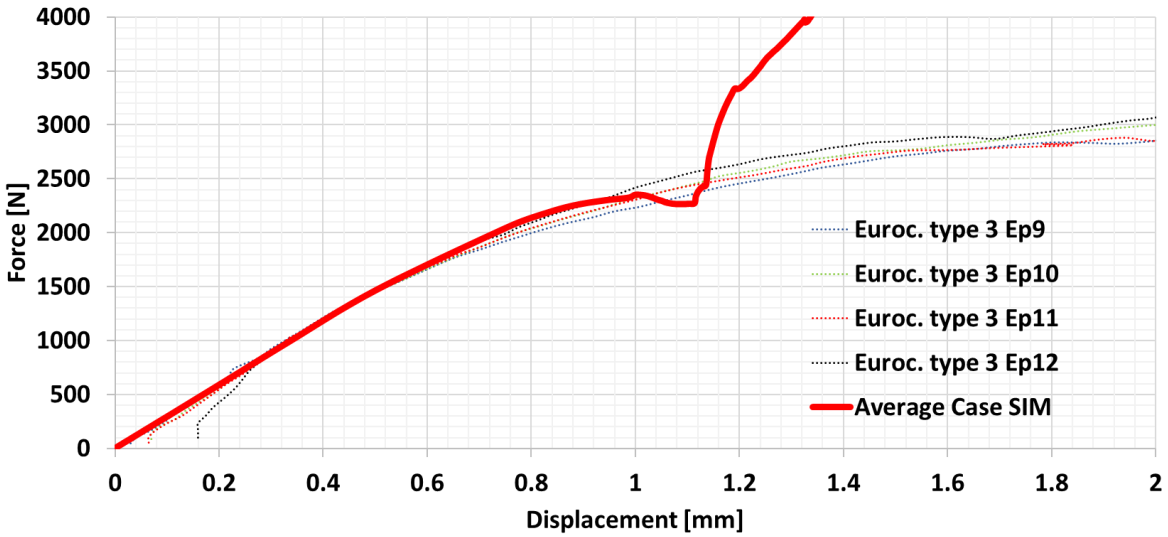

Fig. 221: Comparison of numerical average case and the experimental results (type 3).

It can be seen that the simulation and the experimental results show a good agreement until a displacement of 1 mm. After this point, the stiffness of the model increased dramatically presumably because the fiber failure of the skins is not properly included in the insert model.

Now that the efficiency of the F.E. modeling of the insert has been proved, the next step is to use this model to explore the variation of its principal design parameters, such as the different sizes and material properties. For this, the model should be easily modifiable. To include this feature into this study, the F.E. model is translated to Abaqus scripting.

5.3.4 Parametrization of the F.E. with Abaqus scripting

To do this, each step made on the CAE was recorded using the macro editor. In this way, Abaqus writes the necessary scripting code by itself and then it can be modified by the user according to the needs. Also, this is practical because is not necessary to have a solid background of Abaqus scripting commands.

The script was developed in a similar same order as if the model was developed insert Abaqus CAE (Fig. 222). Only the more relevant aspects are discussed here.

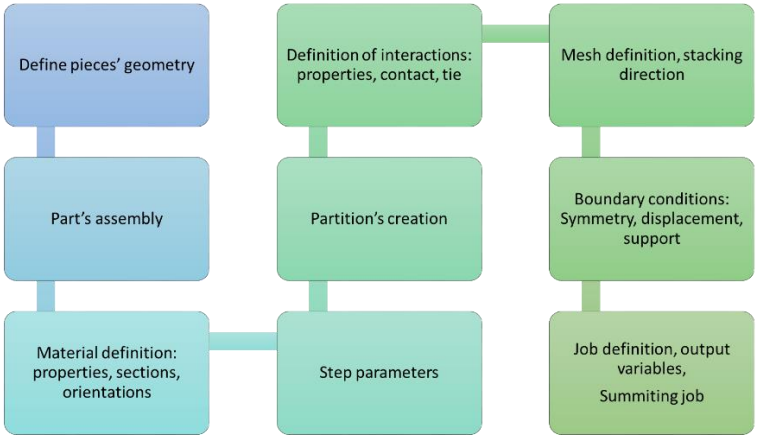

Fig. 222: Description of the sections contained in the python script of the insert.

It is important to mention that this model is only useful to model fully potted inserts. The model's geometry is parametrized according to the description given in Fig. 223.

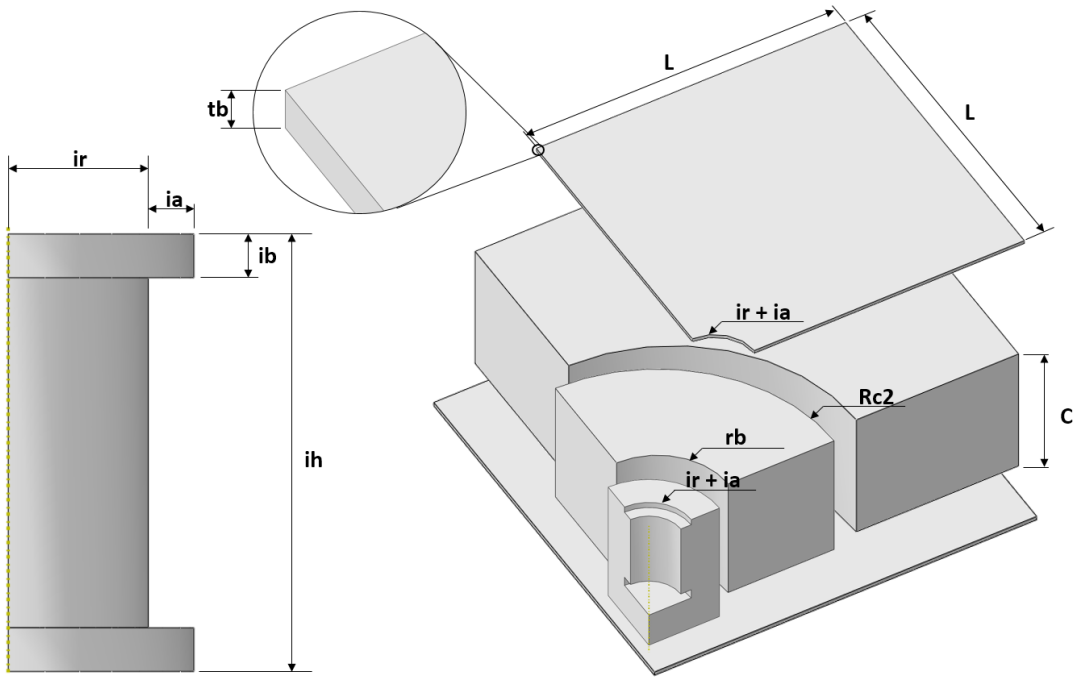

Fig. 223: Description of the model geometry and parameters.

Concerning the support radius, we realized that its diameter has an important influence on the transversal shear stress generated in the core.

If the distance between the potting and the support is too small, the border effects will be too strong on transversal core shear stress (see Fig. 32 of chapter one). Therefore, the simulation will not be representative of a real case, when the supports are located very far from the insert.

The bibliographic review showed that there is not consent about the size of support (see support radius in Table 2, Table 3 and Table 4 of chapter two). Therefore, we considered that the support radius should be 15 mm bigger that the potting radius to avoid this problem (see Fig. 224-a).

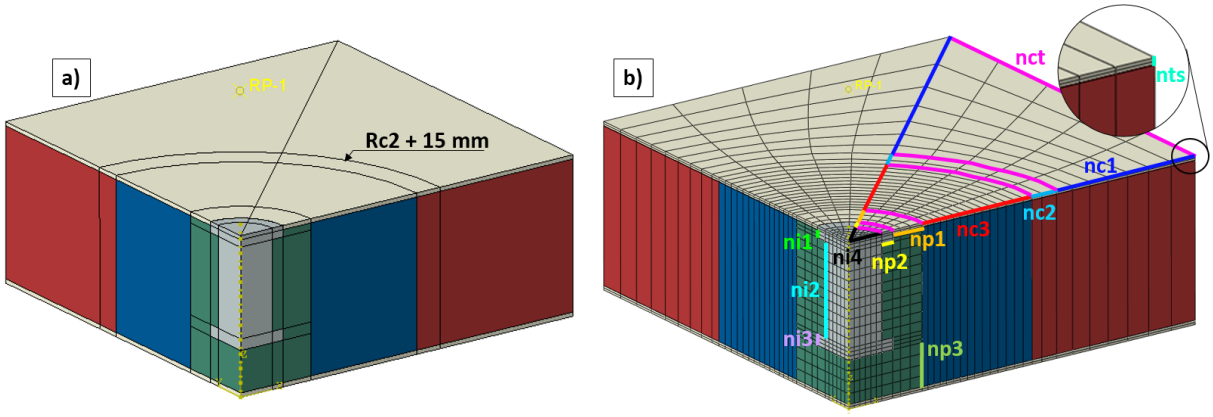

Fig. 224: Description of the support, Description of the meshing parameters used for the model.

Another important aspect was the meshing of the model, all the parameters that determined this meshing are identified in Fig. 224-b. Each color represents the line that is attached to the mesh variable shown in the same color and the number of elements was set according to the geometrical dimensions.

Finally, to make easy the tracking of the simulations, the script was modified to perform and arrange the simulations in different directories. In this way, the simulations are numbered, stored and described automatically.

5.3.5 Conclusion about the F.E. modeling of inserts

As for the modeling of the inserts, the proposed approach in chapter two and [14] was very useful to include the nonlinear behavior of the honeycomb core for the insert model. Also, it allows to have an important reduction of the calculation time (about 12 min per simulation), which is crucial when a parametrical study is foreseen.

Also, the different hypotheses made to develop the presented behavior laws (see Fig. 204, Fig. 205, Fig. 206 and Fig. 207) seem to be useful to understand how the core shear failure influences the nonlinear behavior of the insert.

When the pullout load is applied, the core is subjected to shear stress. Then, the first slope's change of the insert behavior is caused by the buckling of the honeycomb core, which reach a bifurcation point. This hypothesis was confirmed by implementing the behavior law shown in Fig. 204.

Moreover, by inspecting the 3D model, it was possible to detect that the skins matrix failed due to shear.

Concerning the potting, it was seen that the variation of the elastic moduli had a very low influence on the insert nonlinear behavior, as should be expected.

Moreover, it is interesting to notice that when the fastener is not well bonded, the potting failure in compression appears at relatively low pull-out loads, which means that the insert strength is significantly lower than it should be (see Fig. 217).

The inclusion of the nonlinear aspects and behavior laws of the materials, introduced one by one, was useful to understand how the different aspects affect the insert failure. Thus, the order of appearance of the different failure modes was detected (see Fig. 219). Nevertheless, these results are based on a series of hypotheses and simplifications, thus, they shouldn't be considered to as conclusive.

Naturally, the only way to validate this model, is by performing more tests of inserts with different radius, but due to the time limitations, this was not performed, using good quality specimens.

The consideration of the worst and best cases resulted useful to describe the range where the insert loading curves should be found.

Finally, the model was parametrized using Abaqus python, which will be useful to develop the failure mode maps of the following section.

5.4 Development of the failure mode maps

The mass optimization of aeronautic structures is about finding the best balance between the structural weight and its resistance. However, in most cases, when structures are subjected to complex loads, the ruin of the structure can be caused by the activation of different failure modes such as buckling, breaking, wrinkling, plasticization, etc.

In general terms, it's possible to describe the failure mode of a structure in terms of its intrinsic properties like dimensions, materials, boundary conditions, etc.

An example of this was presented in 1987, by Triantafillou et al. in ref. [103] in which they represent the different failures of the sandwich structure using a map. They did a compilation of the formulas that are used to calculate the different failure modes of sandwich panels under determined conditions, like face yielding, face wrinkling, core shear failure, among others. Then, all these expressions were evaluated to determine which failure mode is activated first. At the end, they obtained a chart on which according to the properties of the sandwich the different failure modes are activated (see Fig. 225).

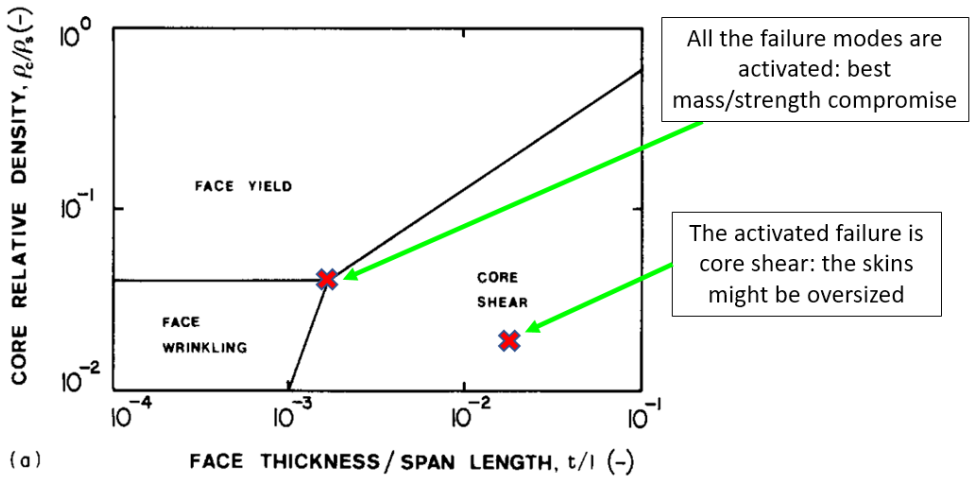

Fig. 225: Example of a failure mode map for sandwich structures [103].

This kind of approach allows to detect the transition zones between the different failure modes, which is useful to avoid oversizing (see Fig. 225).

The creation of failure mode maps allows detecting the failure transition limit, which is of special interest for mass reduction problems because it allows to detect the properties of the structure on which the best compromise strength/mass is obtained.

This same approach has been proposed by other authors, like Petras et. al. in ref. [104] for the analysis of sandwich panels with honeycomb cores, Vitale et al. in ref. [105] for the description of the failure of natural and synthetic fiber reinforced composite sandwich panes, Andrews et al. in ref. [106] to represent the failure modes of composite sandwich panels subjected to air blast loading, among others.

In this section, this same approach is developed for inserts in sandwich structures. This will allow detecting the transition between the failure modes of inserts to avoid oversizing.

5.4.1 Exploration of the influence of the principal design variables

Many different types of sandwich panels are used in the industrial sector. The materials and thicknesses of the skins and core are chosen according to the needs. For inserts, selection of the fastener, the potting material and the insert size should be chosen in the same way.

For this reason, it's almost impossible to make a general failure mode map of inserts since their strength depends on the materials and geometries that are used.

In this sense, we will only show here the procedure that must be followed to draw the failure mode maps using the materials that have been studied in the past chapters.

Since in our bibliographical research (see Table 2, Table 3 and Table 4) there are only a few works using SPF (by adding micro-spheres to the adhesive), for this study the potting is considered to be made of nothing more than adhesive. However, to represent the use of different adhesives with different properties, the mechanical properties of the Araldite AV-121 B are taken as a starting point, and then the values are swept until its mechanical properties are divided by 4.

The real potting radius (see equation 22) is swept from 9.5 mm to 24 mm, since most of the inserts size of the literature review are inside this range.

Concerning the sandwich panel, the same honeycomb core used for the inserts of Bunyawanichakul is considered, with a cell size of 1/8 inch. a 20 mm thickness and a density of 48 kg/m^3.

As for the skins, the same G0939/145.8 CFRP woven is used. The number of layers is swept from 1 to 4, which is equivalent to sweeping from 0.225 mm to 0.9 mm. Each layer is stacked following a [0,90] orientation regarding the precedent one.

As for the fastener, the same geometry is used.

Since the interest of this study is to determine the linear elastic limit and the start of the insert damage, a displacement of only 1 mm is imposed for the virtual tests.

The starting point for the model has the characteristics shown in Table 26.

Skins							
Reference	e [mm]	E [MPa]	v	S1 max [MPa]	S2 max [MPa]	t12 max [MPa]	t13,23 max [MPa]
G0939/145.8 [0/90]	0.55	52000	0.09	634	634	100	80
Core							
Reference	C [mm]	G_W [MPa]	G_L [MPa]	t_adm W [MPa]	t_adm L [MPa]	Cell size [mm]	Density [pcf]
Nomex® phenolic	20	17	26	0.32	0.55	3.175	3
Insert							
Reference	Real potting radius [mm]	E [MPa]	v	St max [MPa]	Sc max [MPa]	v	Support radius [mm]
Araldite AV-121B	9.58125	4000	0.3	19	42	0.3	24.58125

Table 26: Parameter used as starting point of the parametrical study of inserts.

5.4.1.1 About the insert's failure criteria

In practice, when an insert is tested under pull-out loading, it's said that it fails when the loading slope is no longer linear. This is often done by performing a linear regression analysis on the experimental pull-out test loading curves, where the insert's failure load is found when a determined variation percentage is reached. Most of the time, this variation is in the range of 1% to 5%.

This criterion is an extension from the structural failure criterion for aeronautic structures, which identifies the structural failure by three aspects:

- The behavior of the structure is non-longer linear
- The behavior of the structure present bumps.
- The structure has plasticized.

Specifically, for inserts, using this criterion is equivalent to saying that the loss of linearity is caused by the breaking or damage of the insert's materials, which is not entirely true. Even so, this criterion has been largely used for inserts testing as it is practical and estimates the failure load with a certain security (see for example, ref. [53]).

Endorsed by the analysis of several authors (see ref. [36], [41] for example), the start of the nonlinear behavior of inserts is directly related to the shear buckling of the honeycomb cells. Also, endorsed by the results of the chapter two, this buckling is elastic until a certain limit.

Both results suggest that, since the buckling of the cells is elastic, the loss of linearity might not be an accurate criterion for the insert's failure.

For this reason, we believe that the insert's failure should be when the insert integrity starts to be really compromised, i.e. when any of the components actually start to be damaged.

The main problem with this idea is its application, because it's difficult to detect the damage or plasticization of the components inside the sandwich structure, since its interior is not visible to the naked eye. However, there are some techniques that might allow observation of what is happening at the interior of the insert.

One way to do it is by performing the test while a tomography of the specimen is taken which might not be very practical. Also, due to the geometry of the honeycomb core, the obtained images might not be very clear or confusing.

Another technique can be by incremental cyclic loadings as it was done for the honeycomb core in chapter two (see Fig. 78 and Fig. 63). The failure of the insert should appear when the loading path changes, meaning that the skins, the potting, or the honeycomb core have plasticized or are starting to be damaged.

Finally, although arguable, another method is through simulation. In this chapter the development of the reduced model is described in detail. The experimental and numerical results are compared showing a good agreement. Therefore, this model is considered accurate enough to estimate the insert's failure load.

In this sense, the reduced model is used as a "black box" that, when fed with the insert characteristics, it gives the state of the insert's integrity for each increment of load. Then, failure load can be detected when any of the model's elements fails.

Concerning the skins, they are considered to fail when the strength values of Table 22 are reached. Due to the layer orientation and woven nature of the skins, any shear failure in the three directions is related to the matrix, and any failure in the principal directions is directly related to the fibers. However, the skins are considered to have failed when there is matrix or fiber failure without distinction.

As for the potting, it's considered to have failed when the strength in compression or tension is reached in any part of it. This choice is made due to the brittle failure of this kind of material, because any failure can propagate causing the fracture of the material.

Finally, for the honeycomb core, since the cells can buckle elastically, it's considered to have failed when the cells start to collapse rather than to buckle. This is similar to the hypothesis made by Smith et al. in ref. [31], when they observed that the buckling of the cells appeared at relatively low loads, and since they considered this buckling as the core shear failure (now, in chapter two we know that this buckling is elastic), they concluded that the insert's failure can't be detected only by the buckling of the cells.

All these failure criteria are implemented in the following sections to determine the insert load capability when different design variables are swept over a range of values.

5.4.2 Sweep of the real potting radius: from 9.5 to 23.5 mm

All the design variables shown in Table 26 are fixed, except for the real potting radius. A total of 23 simulations were performed and at each one the real potting radius was varied in the range of 9.5 mm to 23.5 mm. Then, the loads at which the failure of each of parts appears are recorded. It's important to highlight that for the skins, the matrix failure always appeared before the fiber failure, which was never reached in the 1 mm of pull-out displacement applied to the insert. The results are shown in Fig. 226.

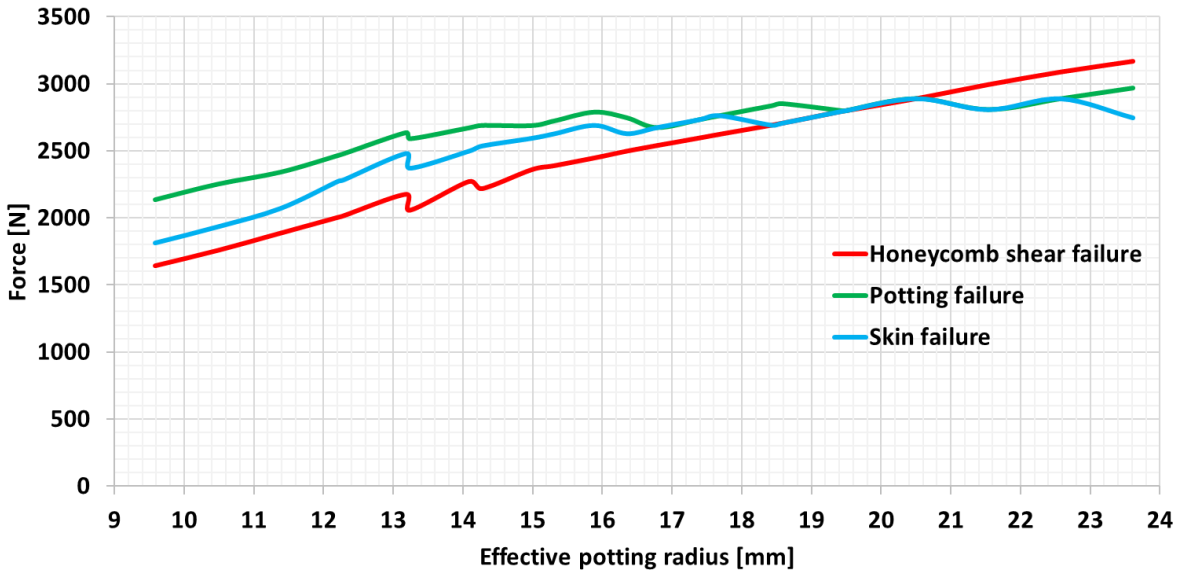

Fig. 226: Failure of the skins, potting and honeycomb core; insert failure load vs the real potting radius.

The first remark is the presence of small variations (like noise) in the curves. These could have been caused by the different time increments of the simulations, because they were set automatically by the software. However, the general tendency of the curves is still very clear.

Also, it's interesting to notice that between a real potting radius of 9.5 mm to 18.5 mm it is the shear core that arrives first. This is coincident with the observations of the ESA [1] and most of researchers [31], [36] that have performed pull-out tests with inserts in this range of real potting radius.

Then, for the interval of 18.5 mm to 20.5 mm the three parts fails almost simultaneously, wile for a real potting radius bigger than 20.5 mm to 22.5 mm, the potting and skins fails before the core and finally, when the radius is bigger than 22.5 mm the skins fails before all the other parts. This shows that for a relatively big real potting radius the scenario the triple failure it's possible, and since the skin matrix failure could only be detected by looking the specimen skins under the microscope, it might escape from the sight of researchers because the potting failure is much more visible.

Moreover, it can be appreciated that the insert's strength is influenced by the real potting radius. The relation between these two parameters is almost linear; as the radius decreases, the insert's strength decreases too.

5.4.3 Swept of the potting properties

The same procedure is applied to sweep different potting materials. The properties of Table 26 are fixed, except for properties of the potting material.

Since the traction/compression strength values of adhesives in the web are generally incomplete, the properties of the Araldite AV-121 B that are well known were considered as the start point. Then these properties are changed until the same properties but divided by four.

This is made for the density, the elastic moduli, the tensile strength and the compressive strength, the values are shown in Table 27.

	Original properties	Sweep values											Properties /4
Traction Strength [MPa]	19	17.81	16.6	15.4	14.3	13.1	11.9	10.7	9.5	8.3	7.1	6.0	4.8
Compression Strength [MPa]	42.5	39.8	37.2	34.5	31.9	29.2	26.6	23.9	21.3	18.6	16.0	13.3	10.6
Elastic Moduli [MPa]	4000	3750	3500	3250	3000	2750	2500	2250	2000	1750	1500	1250	1000
Density [kg/m³]	1400	1312.5	1225	1137.5	1050	962.5	875	787.5	700	612.5	525	437.5	350

Table 27: Sweeping values for the adhesive based on the Araldite AV-121B.

A total of 13 simulations were performed, the results are shown in Fig. 227.

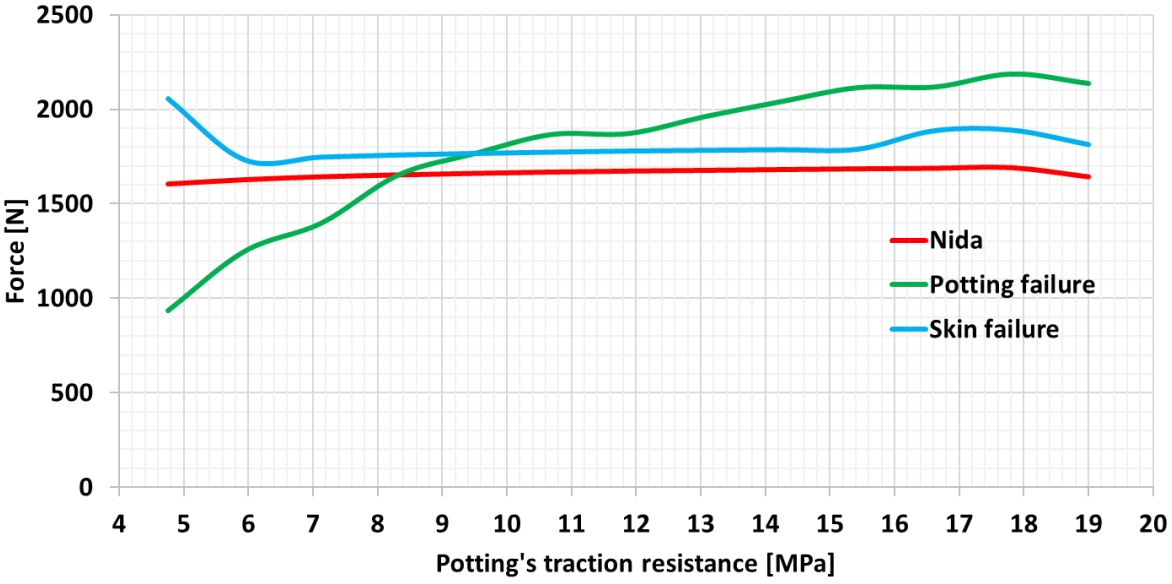

Fig. 227: Failure of the skins, potting and honeycomb core; insert failure load vs potting traction's resistance.

It's important to notice that the potting sweep is represented only by the potting traction strength because it is the parameter that influenced more the insert's failure.

In chapter five it was seen that the elastic moduli of the potting doesn't influence the insert's pull-out strength. This might be caused because the shear moduli of the honeycomb core is much smaller compared to the potting's.

According to the Fig. 227, the insert first failure arrives mostly at the core. Therefore, the insert strength remains constants until the potting's resistance to traction reaches 8.5 MPa. Then, the potting fails in traction and becomes the first type of failure.

5.4.4 Sweep of the skin thickness

The same procedure as for the other two variables is applied to sweep different values of the skin thickness. As in the previous cases, the properties of Table 26 are fixed, except for the thickness of the skins.

Since the skins are formed by pre-preg layers, each one of 0.225 mm thickness, the total thickness of the skin is discretized as function of this initial value. The swept was only performed between the thicknesses of 1 to 4 layers because if more layers were to be included, the script would have to be completely modified.

Also, it's important to remark that skins had the same number of elements as layers in the thickness, except for only one layer, where two elements are considered.

The same mechanical properties of the prepreg are used for all the thicknesses. This might be arguable because in general when prepreg is stratified, its general mechanical properties are slightly reduced because of porosities, voids among other defects are introduced. However, these effects were neglected to simplify the study of this variable.

The number of layers varied from 1 to 4 (0.275 mm, 0.55 mm, 0.825 mm, and 1.1 mm), but also a thickness of 0.6875 mm was considered, so 5 simulations were performed. The results are shown in Fig. 228.

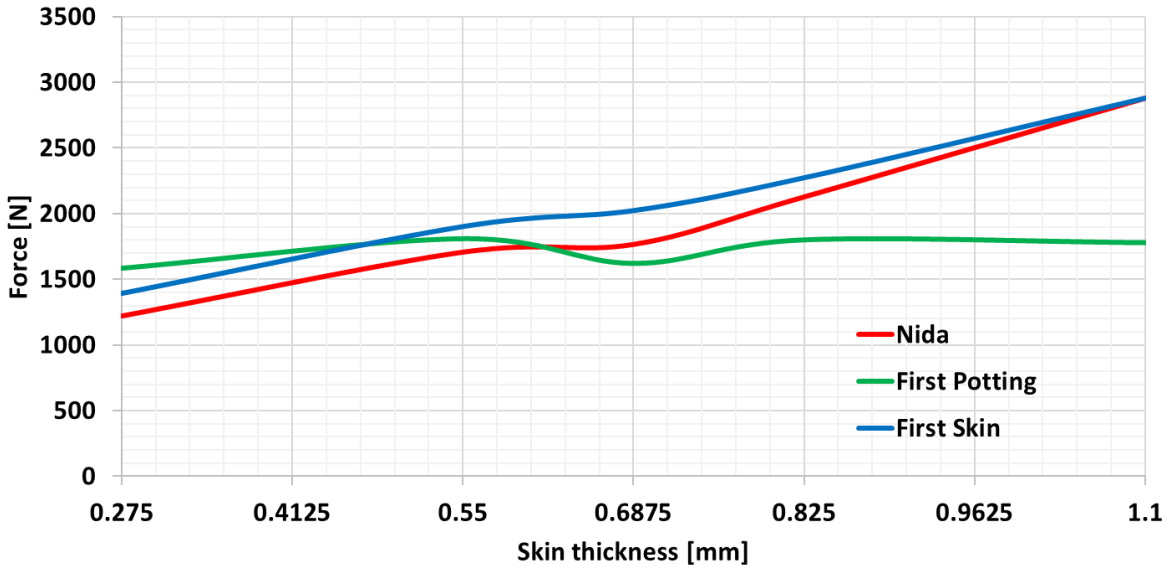

Fig. 228: Different insert failure modes vs the thickness of the skins.

The results show that there is a failure transition when 2 and 3 layers are used for the skins. When the skins are thin, the first failure is the core shear failure, while when the skins are thick, the predominant failure is the potting failure.

This is not surprising because when the skins are thin, the core can be easily deformed in shear, while for thick skins, the shear forces are absorbed by the skins too.

5.4.5 Failure mode maps

Finally, the failure mode maps of inserts can be obtained by sweeping the design parameters at the same time. Since many combinations are possible, the results are presented separately.

5.4.5.1 Real potting radius vs potting traction strength

Each simulation took around 5 min to be completed, and a total of 60 simulations were made, i.e. each surface is composed of only 60 points of reference. Although more points could have been obtained, this was considered enough to study the tendency of the failure modes. This is shown in Fig. 229.

Each surface represents the failure of each component. Therefore, the fact that the surfaces intersects between them means that the insert strength (obtained using the first failure criteria) should be given by the failure of the three principal components, the skins, the potting and the honeycomb core.

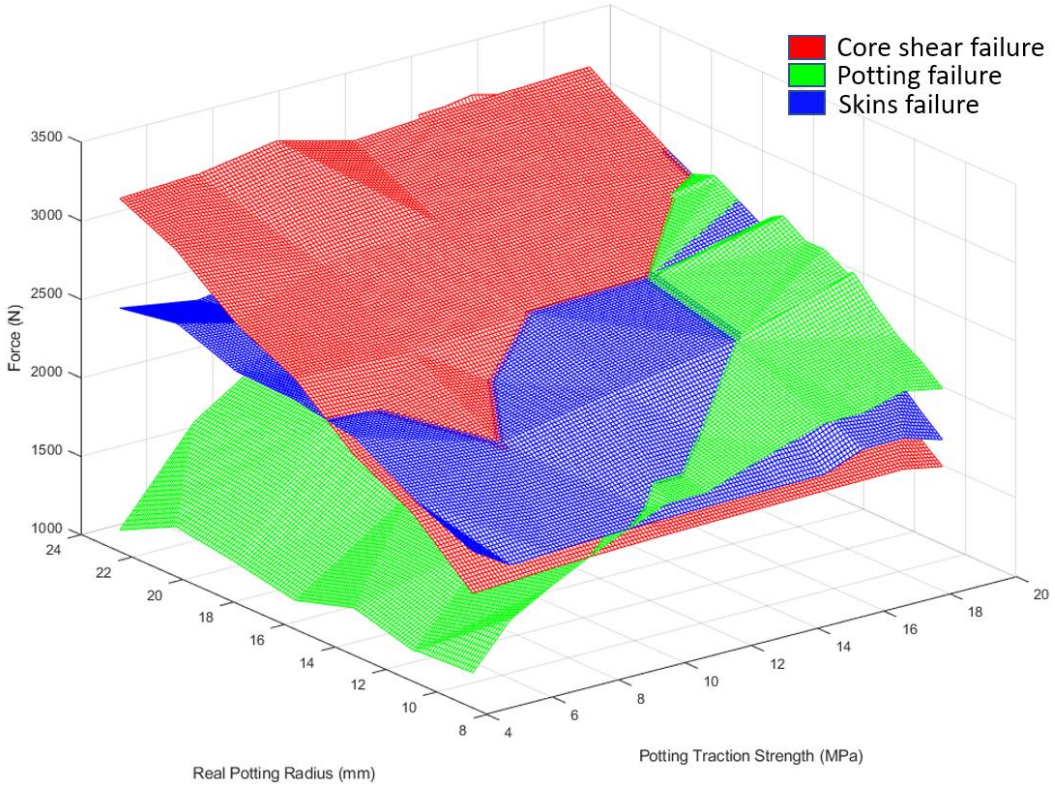

Fig. 229: Failure surfaces of the core, the potting and the skins: RPR vs Potting traction strength.

The first failure should be the lower point at which the failure arrives for the different configurations, this is equivalent to observe the surfaces from a bottom view. This is shown in Fig. 230. Most of the time, it is the core or the potting that fails, and only a small area is composed by the skin failure (only matrix failure).

As for the results of the failure mode map:

When the insert radius is increased, the potting failure is predominant. This is logical since the contact area between the potting and the fastener remains the same while the area of the honeycomb core subjected to shear is increased. Thus, the stress at the fastener/potting increases as the inserts strength does, until the potting reaches the elastic limit and breaks.

Also, as the potting traction's resistance increases, the core shear failure is predominant. This occurs because the potting becomes stronger, and it can support higher loads, while the honeycomb core has the same resistance.

When both variables are increased at the same time, there is a transition between the potting failure and the core shear failure, until the insert strength is high enough to start to damage the skins, which is logical too.

Also, in order to show the insert strength at the same time that the failure modes, colors are used to represent a range of the insert strength in the map. This is shown in Fig. 231.

It's clear that the insert strength is increased as the design parameters are increased too (see Fig. 231). The color range shows that there are different insert configurations which authorize similar strengths. Therefore, the one with the lower mas should be used.

A discussion about this mass optimization is presented later in this chapter.

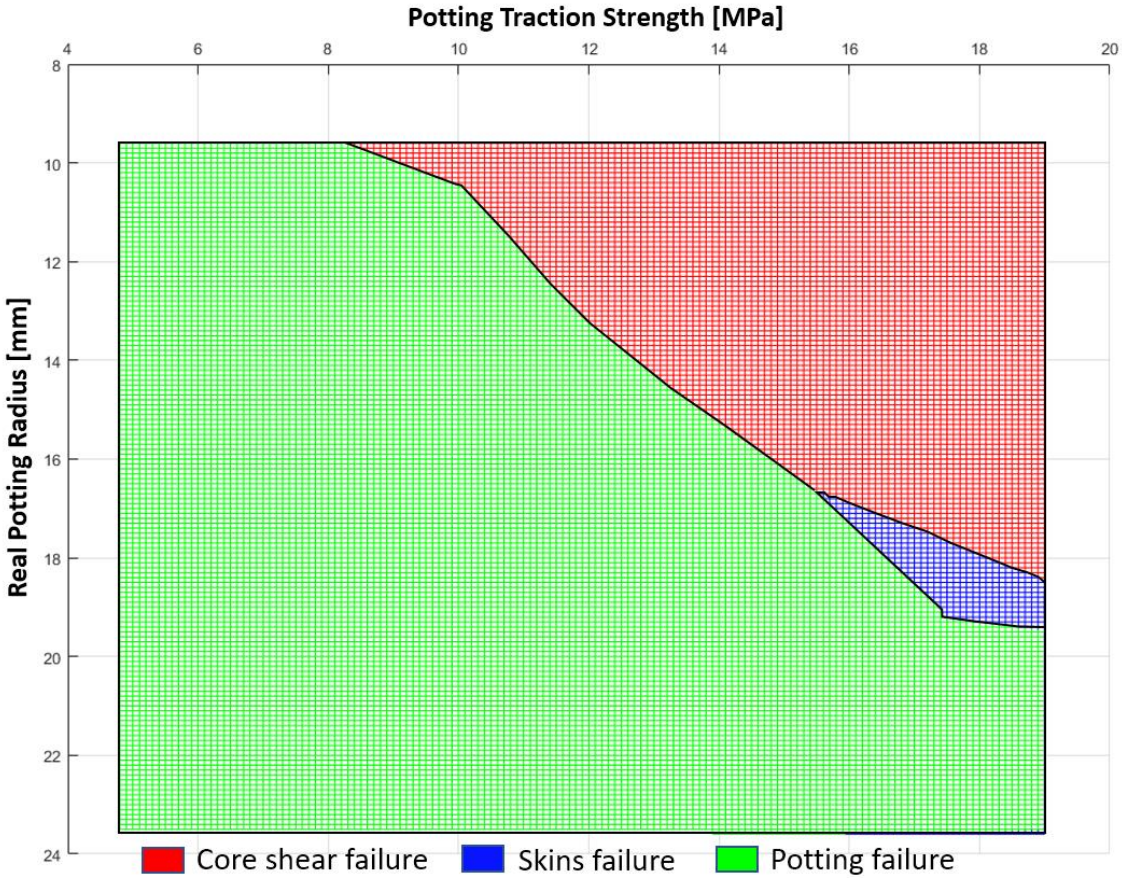

Fig. 230: Bottom view of the surfaces: failure mode map of inserts

This type of tool should be very useful for design purposes since it allows compacting a huge quantity of information into a single 2D chart that can be easily shared between designers.

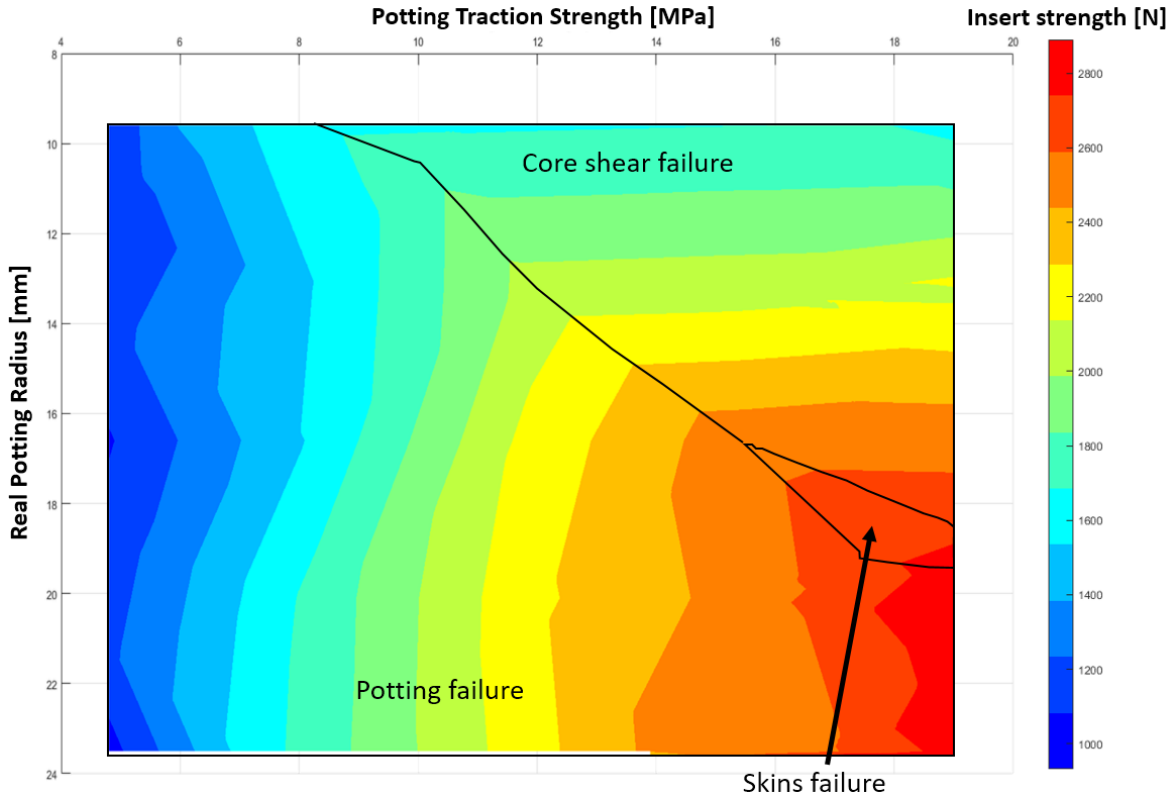

Fig. 231: Failure mode map of inserts and failure load.

5.4.5.2 Real potting radius vs skin thickness

A total of 40 simulations were made, i.e. each surface is composed of 40 points of reference. This is shown in Fig. 232.

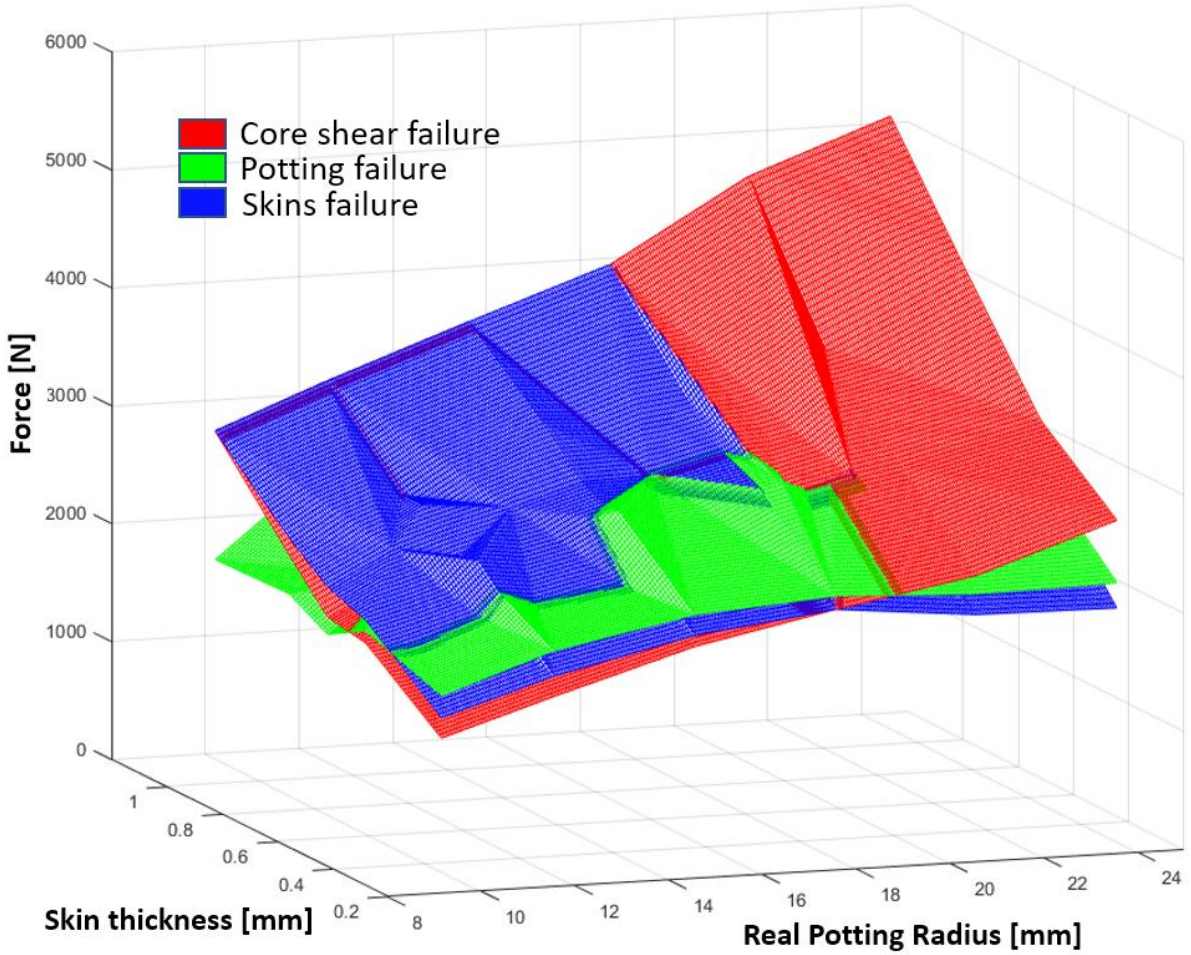

Fig. 232: Failure surfaces of the core, the potting and the skins: Skin thickness vs RPR.

The bottom view, which represents the first failure of the insert, is shown in Fig. 233. Most of the time, it is the core and the potting that fails. However, a considerable section is formed by the skin failure.

As for the results of this failure mode map:

When the skins are thin, the failure of the insert is governed by the failure of the core, while as the skins increase, the insert strength is determined by the potting failure. The explanation for this might be that, as the skins thickness increases, they absorb more and more of the shear forces, therefore the honeycomb core is subjected to lower shear stresses as the thickness of the skins increases.

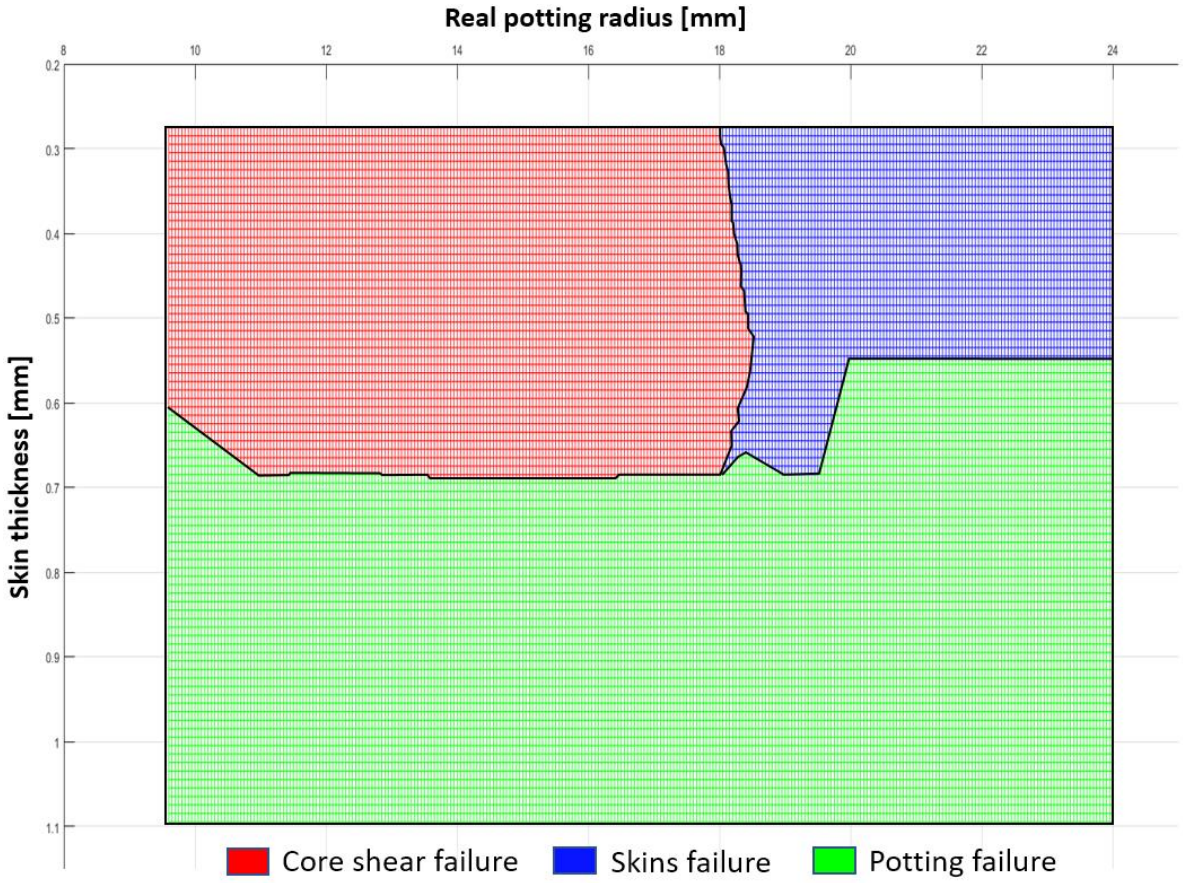

Fig. 233: Failure mode map, skin thickness vs RPR.

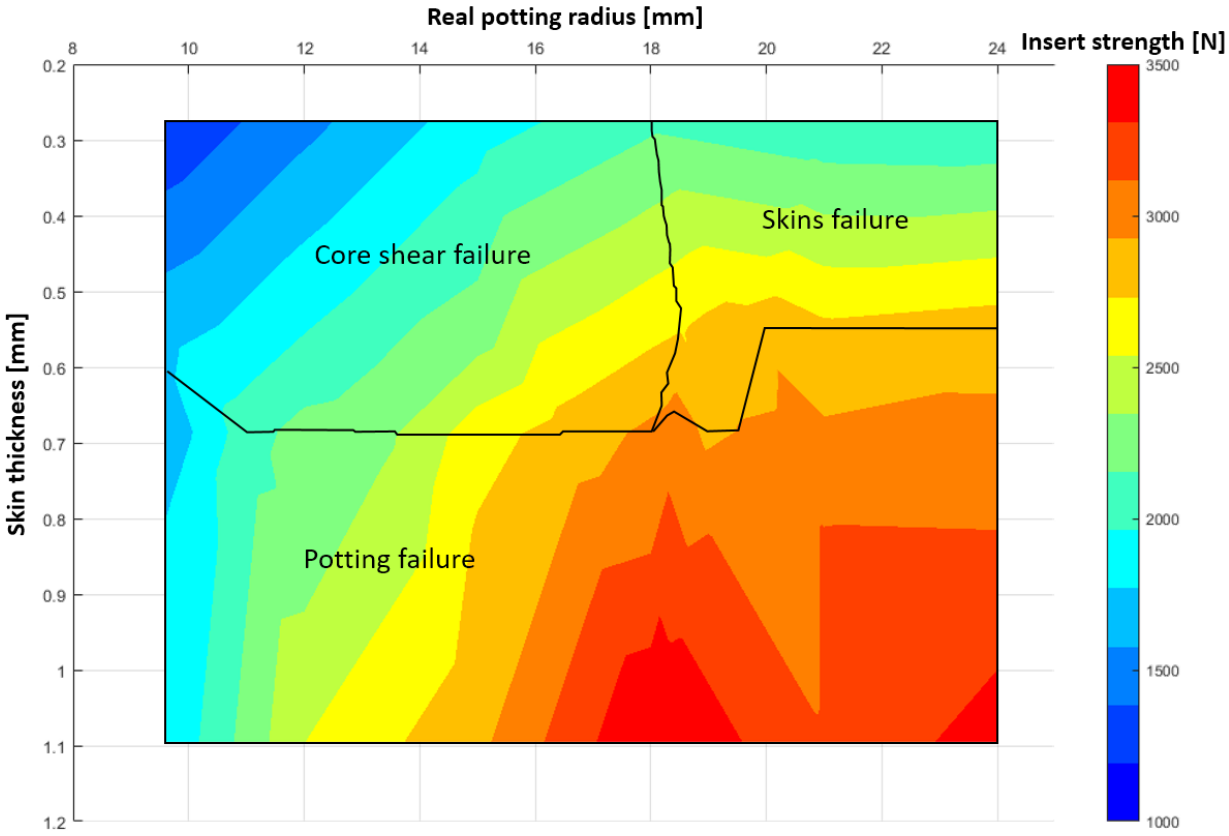

Fig. 234: Failure mode map, skin thickness vs RPR and strength in color scale.

If the skin thickness is increased simultaneously with the radius of the potting, the predominant failure is the potting failure, however, for values lower than 2 layers, the skins

failure appears first. This might be explained because the thin skins supports less shear stress than the honeycomb core.

As for the previous case, to show the insert strength simultaneously with the failure modes, a color is used to represent the strength ranges. This is shown in Fig. 234.

The tendency is very similar to the previous case. As the variables are increased, the insert strength increases too, and the same remarks can be made: there are several insert configurations that authorize similar pull-out strengths, therefore the one with the lower mass should be chosen.

5.4.6 Insert mass optimization

It might be interesting to investigate the mass of inserts at the light of the failure mode maps. This is possible if an optimization function is defined.

For inserts, two principal quantities are important, the first is the mass, and the second its strength. The optimization that is desired for inserts is the reduction of the mass, without compromising its resistance. Therefore, a function must be defined that allows to measure both quantities.

Indeed, these variables are related because if the mass is increased, typically, the insert strength is raised and vice versa.

The function that is proposed is the strength to mass ratio, which is simply expressed by diving the strength by the mass.

$$S.M.R. = \frac{F_{max}}{W_i}$$

Where the mass is calculated as function of the RPR of the ESA and the density of the adhesive.

As the mass is reduced, the strength to mass ratio (SMR) increases, also as the insert strength is increased, the *SMR* increases. In the other hand, when the mass is increased, *SMR* is reduced and when the insert strength is reduced, *SMR* is reduced too. Therefore, this simple function is useful for our purpose.

Using the results of Fig. 226, it's possible to evaluate the weight to strength ratio of inserts. The mass of inserts can be estimated if the real potting radius and its density are known. For this particular case the density of the potting is of 1400 kg/m^3 and the weight of the potting is given by the number of filled cells that was obtained in Fig. 179. Also, the fastener weight is about 5 gr.

Using these values, the insert strength to mass ratio can be calculated (see Fig. 235).

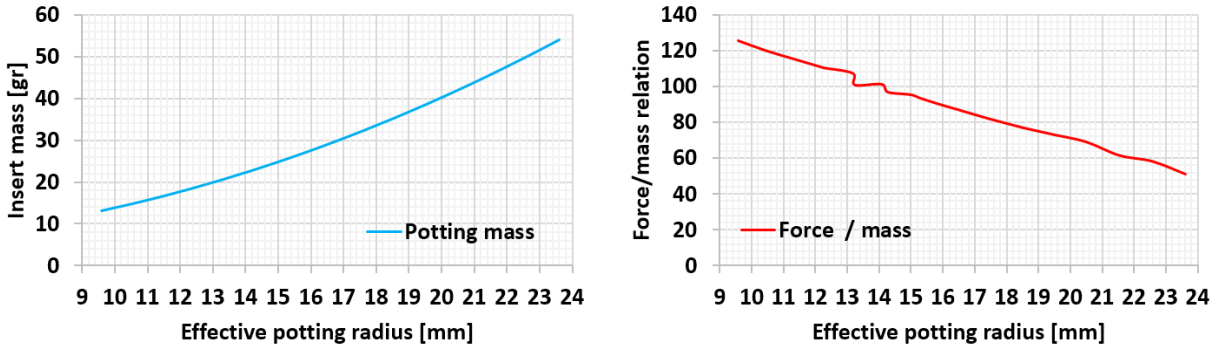

Fig. 235: Potting mas and strength to mass ratio vs real potting radius

Keeping in mind that the bigger the force to mass ratio is, the better the mass efficiency for the insert, the tendency is clear. The smaller the insert is, the better performance it has. This confirms what would seem to be logical, designers should always propose the smaller insert size for the required load.

Also, using the variation of the potting density, the strength to mass ratio can be calculated too. The results are shown in Fig. 236.

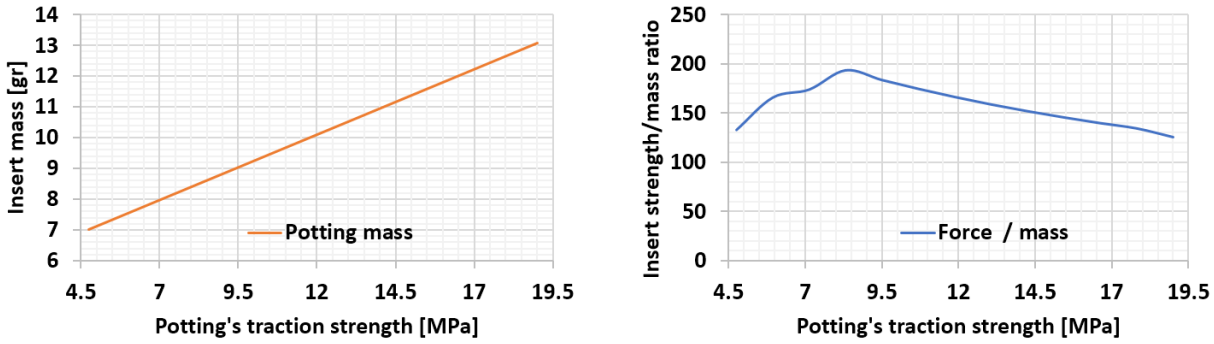

Fig. 236: Potting mass and insert strength to mass ratio vs potting traction strength.

The graphic shows that the best performance is obtained when the potting properties makes that the potting fails simultaneously with the honeycomb core (see Fig. 227 for a potting strength of 8.5 MPa). For this particular case this happens at 8.5 MPa. This confirms another aspect that should be logical for inserts, the potting material should be chosen according to the desired insert strength.

Again, the insert strength to mass ratio is calculated using the result of the failure mode maps shown in Fig. 231. The result is plotted in Fig. 237. The tendency confirms that the best insert design is the one on which the radius is the smallest possible and the potting material is selected according to the insert strength requirement.

It’s important to highlight that this optimization takes only into consideration the principal variables that are related to the insert design, which are the inserts weight and its strength.

The rest of variables that are involved in the insert design, such as the core thickness or density, the skin thickness and strength, etc. are not taken into account because they are not directly related to the insert design. Instead, these variables should be chosen according to the sandwich panel application.

Therefore, the sandwich weight, formed by the skins, and core, are not considered for this optimization.

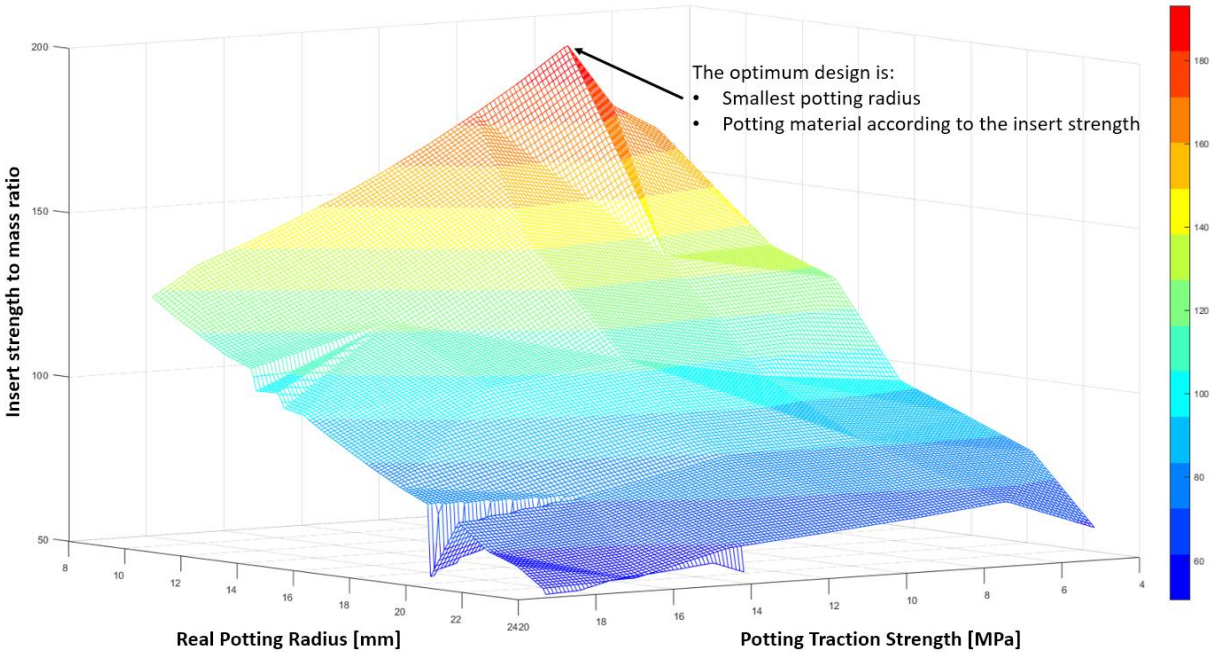

Fig. 237: Optimization chart for the insert mass.

5.4.7 Loss of linearity criteria (LLC) vs first failure criterion (FFC)

It could be interesting to see the difference between the LLC and the FFC. To do this, the loss of linearity of the loading curves of all the simulations of the virtual tests is analyzed.

It's worth mentioning that the number of increments for each simulation determines how many points there are in the virtual testing loading curves. If there are only a few points, the detection of the loss of linearity might not be accurate. On the other hand, even if the ideal is to have as many points as possible, the simulation time will be huge and it's not convenient.

For this reason, it's preferred a reduced number of points and making an interpolation between them. For this, the maximal increment was fixed to t_{max}=0.05. In this way, we can have all the points that are needed for this analysis without increasing the simulation time.

To detect the load at which the loss of linearity occurs, a linear regression analysis is made using the virtual testing curves. Since the simulations represent the ideal case where the contact is perfect between the parts and the roughness of the pieces is neglected, the classical irregularities of loading curves will not appear.

The algorithm shown in Fig. 238 is used to detect the start of the nonlinear behavior.

It consists of determining a line that allows describing the series of points with an allowable error.

First, only the first two points are considered to define a linear regression model, then the coefficient error R is determined. If this coefficient is greater than R=0.999 the nonlinear limit is detected, if not, another point is added to the analysis and the linear regression model is updated using the old points and the new point. This process is repeated until R> 0.999, that is the point when the linear limit is reached.

The R coefficient is calculated by the equation shown in Fig. 238 where y_i is the vertical component of the i point of the curve, f_i is the value of vertical given by the regression model, and $\bar{y}$ is the mean of all the vertical components of all the points considered for the analysis.

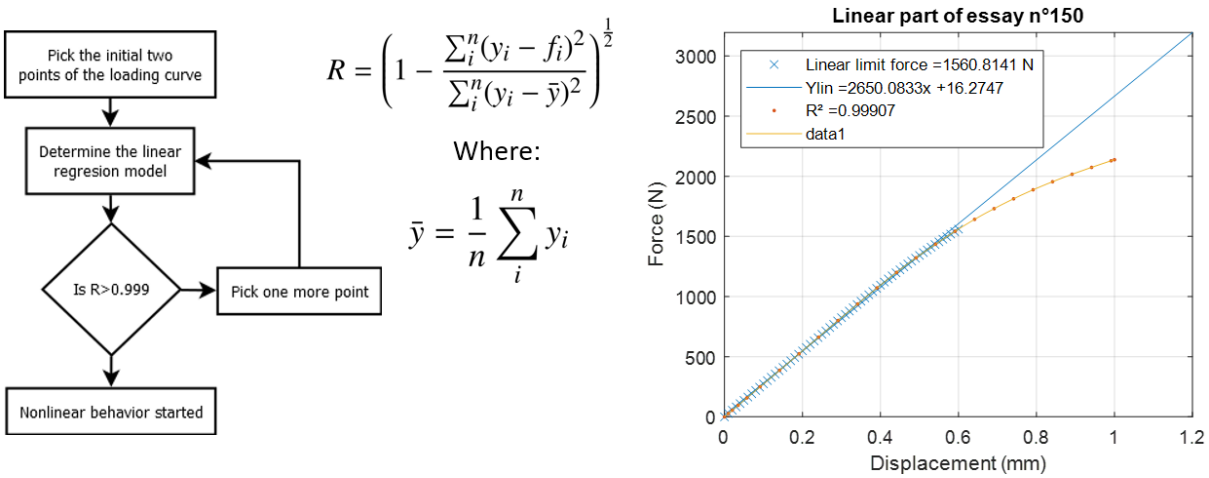

Fig. 238: Calculation of the linear limit of the virtual testing loading curves: algorithm and example

Then, using the data from the simulation, the Fig. 239 can be obtained.

In general, the difference of the failure loads between both criterions is about only 7% and the linear criterion is generally activated first. However, since most of the time the breaking of the potting occurred at the superior part of the insert, it doesn't affect the linear behavior of the insert. This is the reason why the first failure criterion is reached before the LLC when the potting traction strength is reducing.

However, the fact that the FFC is activated first suggest that this criterion should be more accurate than the typical linear regression criterions of 1,2 or 5%. This is not surprising since the failure detection was made using a F.E. model that allowed seeing at the interior of the insert, while this is not possible with the criteria.

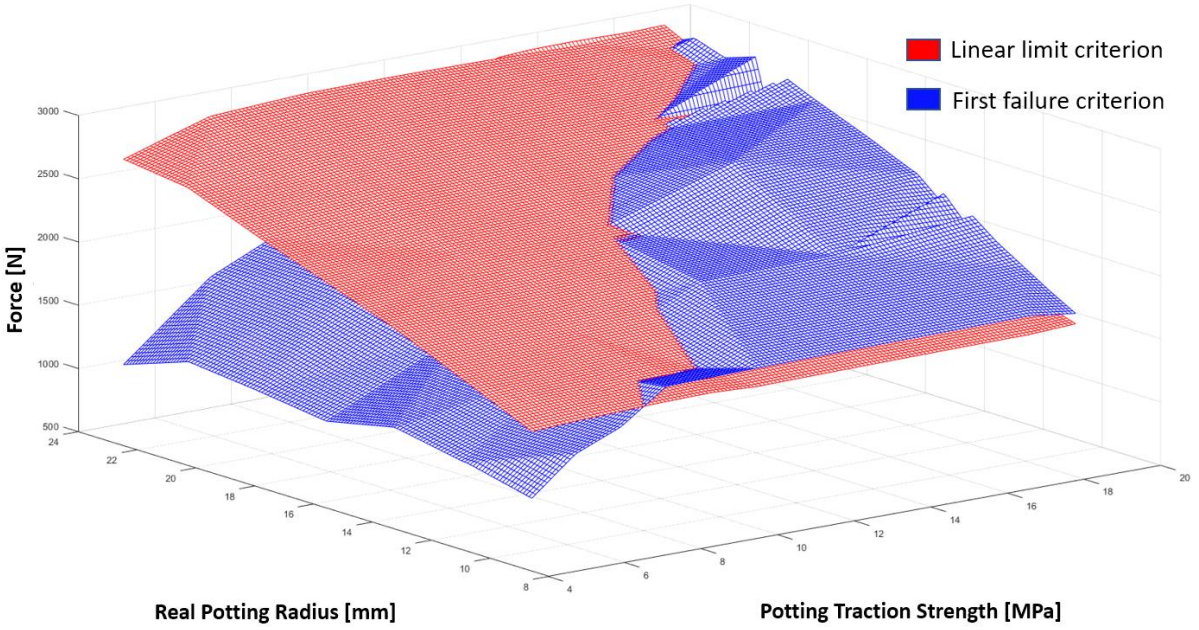

Fig. 239: Linear limit vs first failure criteria.

5.5 Conclusions

The study of defects for inserts in sandwich structures was important because it shows which defects are important and should be considered for the insert design. This kind of study was not found in the related literature.

Also, the evaluation about the effective potting radius (EPR) and the real potting radius (RPR) approaches (both proposed by the ESA), determined that the RPR should be considered since the evidence shows that is closer to the reality (see Fig. 176). Also, the coefficients for the maximal RPR which are not provided by the ESA were found issue of this investigation.

Moreover, the proposed method allows simulating the behavior of inserts at a very low computational cost and obtaining very accurate results. Also, in contrast to the detailed modeling of inserts, this method is easier to implement.

Another interesting aspect is that, the consideration of the best and worst cases seems a good method to determine the strength range of inserts. Compared to the analytical approach of the ESA, the error interval is greatly reduced.

Moreover, it was shown that for practical terms, the start of the nonlinear behavior of the insert can be easily detected using a homogenized approach instead of a detailed modeling, which is much more easy to implement.

Also, it was shown that the influence of small variations of the parameters of the materials, or defects, plays a very important role in the insert behavior. These conclusions were previously made by Raghu et al. in ref. [28]. However, the influence of the defects has never been studied qualitatively as it is presented in this chapter.

The potting radius played a very important role since the stiffness and strength of the insert is determined by this parameter. However, it's nearly impossible to control the exact radius of the inserts due to the honeycomb geometry of the core. Therefore, a good way to consider this variation is the real potting radius (RPR) approach proposed by the ESA.

Also, in this chapter is detected that stabilizing the cells with the potting is more complicated than expected. Most of the time, the potting irregular borders mean that the cells fold easily and probably collapse earlier. Therefore, this lateral stabilization could be only possible if the insert borders are regular.

Another defect that appeared in most of the tested inserts was the weak bonding of the fastener to the potting. This defect should be considered as part of a bad design and must be avoided. Because the fastener is not bonded, the contact surface is reduced and the potting starts to plasticize at relatively small pull-out loads.

Moreover, another defect was the micro-spheres concentration in the potting. This defect is much more relevant when the potting is not bonded. Also, if the adhesive is saturated of micro-spheres the bonding of the fastener may be very weak.

Concerning the interval of worst and best cases, the range of the obtained results seems to describe the range of maximal strength of all the experimental tests which is relevant. Also, there is a general good agreement between the failure scenario of the numerical and experimental results. Visually (see Fig. 218), the failure modes of the real test specimens seem well represented; the shear buckling and collapse of the cells, the plasticity of the potting and the deformation in the skins.

Finally, the proposed method allows to detect the order of appearance of the different failures for the materials. The proposed approach in [14] allows to discern the elastic buckling from the permanent damage of the cells. The same for the in-plane and transversal shear failures of the skins.

Nevertheless, this F.E. model was only compared to three type of inserts with tests curves that had significant discrepancies. Therefore, more tests are necessary to validate the model.

As for the failure mode maps, they allow to observe in a very easy way the strength of an insert as a function of the principal design variables, which are the size of the potting and the potting material.

This tool should be very useful for engineers since it compresses the very accurate results based in F.E. simulations, in a simple 2D chart.

Also, it was show that the insert size should be designed by choosing the lowest weight possible. This is easy to see in Fig. 237. The best insert design is the one with the lower radius and with a potting material selected to resist the required pull-out strength.

General conclusions and perspectives

The general aspects of jointing through inserts were presented in the bibliographical study of chapter one and two.

First, some general remarks about inserts were presented, where two mains disadvantages of this technique were found.

The first one is related to the lack of understanding of the insert pull-out failure scenario (failure modes and order of appearance), being the main subject of this PhD thesis.

The second was the microcracking formation of inserts due to fatigue, which is not investigated here.

Then, a review of the most common insert sizing analytical methods was presented, where two main references stood out; the insert design handbook of the ESA, and the military handbook 23-A, in which the Ericksen insert pull-out formulation, developed in 1953, is used to estimate the insert pull-out failure load.

In this approach, the core's shear stress distribution is calculated as a function of the sandwich properties and the insert's geometry, and then the insert failure pull-out load should be determined by the core shear strength.

Indeed, most of the presented experimental evidence indicates that, when an insert is pulled out, the first failure mode is the core shear buckling, which, according to several authors, happens because the insert's surrounding cells are subjected to shear stress and after a certain limit they buckles.

Nevertheless, the accuracy of this analytical approach is arguable because of the simplifications that were made. Also, it is reported that the pull-out strength is affected by the defect's influence, although there are no conclusive results in terms of providing a better approach to include these on the insert design.

Even so, given the importance of the core shear buckling for the analytical approaches, a specific bibliographical research was made about this topic.

We detected that most research about honeycomb buckling is about the compressive behavior (for energy absorption applications for example), and there is an important lack of general knowledge concerning its shear behavior.

Zhang and Ashby give an analytical formulation to estimate the honeycomb core shear strength by assuming that the start of the buckling is the elastic limit of the structure. Then, several authors, suggested this was incorrect by pointing that the elastic shear behavior of honeycomb structure was mostly in the postbuckling regime.

Given the complexity of the problem, some researchers propose the virtual testing approach to determine the shear properties of the honeycomb core. Nevertheless, this requires high expertise, and is expensive in terms of computing resources.

On the other hand, a simplified approach was proposed that allow including the nonlinear behavior of the honeycomb core, without performing a detailed modeling of the cellular structure. Nonetheless, this was only made for the honeycomb compressive behavior.

Summing up, we detected that there was not an appropriate study about the shear failure of honeycomb cores for understanding the insert pull-out failure. And since the core shear

buckling is considered the first failure of inserts, we dedicated the entire chapter three to the study and modeling of the shear behavior of honeycomb cores.

To begin with, we did a benchmark study of different type of specimens that could be used for the shear testing of honeycomb cores. The result was that all specimens (expect for the non-articulated single rail specimen) showed very similar responses for the linear behavior, but not for the nonlinear response, which apparently, was very sensitive to the imposed boundary conditions. Finally, the specimen that fitted the best for our research was a modified double lap specimen because it was easy to fabricate, easy to test, and allowed to observe the buckling of the exterior cells.

Then, we proceeded with a shear testing campaign using three different types of honeycomb cores. Unfortunately, for the HRH-10 and the aluminum honeycomb core shear specimens, the failure occurred due to skin's debonding instead of shear buckling. Thus, the results were not useful. On the other hand, the test performed using the HRH-78 Nomex® honeycomb core provided valuable information about the shear behavior of this structure.

After having performed several shear tests until failure, but also incremental cyclic tests, we provided a detailed description of the cell buckling scenario. First, we observed that the honeycomb shear behavior is mostly in the postbuckling domain, and that this buckling is elastically reversible far beyond the linear limit. Therefore, it's not appropriate to define a shear failure criterion based on the buckling of the cells.

Also, we observed experimentally that the shear strength of the core is importantly influenced by the cell's boundary conditions, being possible to be increased or decreased (up to 35% and 16% in the L and W directions respectively). To understand this effect, we developed a detailed honeycomb F.E. model allowing us to study in detail the buckling of the inside cells under different boundary conditions. Finally, we observed that the buckling shape of the cells changes according to the imposed boundaries, which could explain the previous effect.

Finally, we developed a CDM technique that allows to consider all these nonlinear aspects of the honeycomb core at a very low computational cost.

This study on the shear buckling of the honeycomb added a new insight to the shear buckling of honeycomb cores, and as result, two original articles were published. Nevertheless, this study was only made for the HRH-78.

Once the general aspects governing the core shear failure for inserts were studied, we proceeded with another topic, which was, the study of the potting failure for inserts.

The bibliographical research suggested that the insert's potting failure could be predominant under certain specific conditions, and definitively, should be considered as part of the insert failure scenario. Initially, the evidence suggested that this failure happens because of the breaking of the potting material, or by the fastener's debonding.

Nevertheless, in the insert literature these failure modes are almost not covered. Moreover, since the insert's specimens of Bunyawanichakul were made with the Araldite AV-112N and phenolic microspheres, thus, a Syntactic Polymer Foam (SPF), we decided to carry our research using these materials. So, a specific study was necessary and we dedicated the entire chapter four to this matter.

The experimental study shown in this chapter, suggest that the different potting's failure scenarios found by Bunyawanichakul in its PhD thesis might have different causes.

First, a short review about the main aspects of SPF is presented. Then, an experimental campaign was made to study the mechanical properties of this foam. Traction and compression specimens were fabricated using three different ponderal weights of micro-spheres; 7 %, 10 % and 13 %.

It was found that, under compression, the foam fails due to the crushing of the phenolic micro-spheres, and the testing curves presented an almost perfectly plastic behavior. While for the traction tests, the Young modulus was higher but the material presents a brittle failure.

Also, by comparing the behavior of the different specimens fabricated with different percentage of micro-spheres, it was seen that the higher the concentration was, the weaker the material became, and thus, the effective potting mechanical properties were reduced. On the other hand, since the weight is reduced, the specific mechanical properties are increased. This aspect could be interesting for inserts because it allows to regulate the potting weight in function of the desired failure load.

After this, a series of technological specimens with different geometries (which were similar to an insert pull-out test) were tested. This experimental campaign allowed to observe how the different potting failure modes appear.

Our results showed that the failure of the potting occurs in two principal ways.

The first one occurs when the fastener is well bonded to the potting, and then, failure occurs when the potting material or the potting/fastener interface reach the maximal strength in traction or shear. This scenario appeared mostly when the potting was left to polymerize at room temperature for 6 days, the correct quantity of hardener-adhesive was used, the parts were well cleaned and degreased, but also the microsphere concentration was below 12% of the ponderal weight.

The second scenario occurs when the fastener is weakly or not bonded to the potting. Then, the fastener/potting interface breaks under very low pull-out forces, and the fastener starts to compress and cut the potting. This scenario appears mostly when the specimens were left to polymerize at the oven, the parts were not correctly degreased, an excessive amount of hardener was used for the compound and when the micro-sphere concentration was superior to 12% of the ponderal weight.

The study suggested that the microsphere concentration plays an important role for this SPF when is used for inserts. Apparently, when the micro-sphere concentration was superior to 12%, the adhesive properties of the material are greatly reduced, maybe caused by an oversaturation. Nevertheless, this is only a hypothesis and many more different tests are necessary to confirm it. Also, it's important to remark that the working principle of adhesives remains mostly unknown for the scientific community, thus, our tests only reflect the combination of factors that could cause the different failure scenarios, without giving a definitive explanation.

Finally, the different behavior in traction and compression of this SPF were implemented into a UMAT subroutine to perform a 3D modeling of the tested specimens. This made possible to create a virtual representation of the potting material that allowed to include the different failure modes, which is an important step because it opens the door to include these features an insert F.E. model.

Recapitulating, the use of SPF for inserts was not documented and an original research was performed. Traction and compression test were carried and it was found that this material presented a different behavior. Then, technological tests were carried on and the same insert's potting failure scenarios of Bunyawanichakul were found. Finally, the material behavior was programed into an UMAT subroutine to make a 3D reproduction of the performed tests.

Once that the core shear and potting failures were studied, the next step should have consisted of studying the skin's failure. Nonetheless, this wasn't done because it wasn't affordable in terms of time. Therefore, we skip directly to the problem of the lack of accuracy of the analytical approaches for the insert pull-out load.

The bibliographical research pointed that the analytical approaches to predict the pull-out load for inserts were not very accurate. This is not surprising considering all the

simplifications that had to be made, but also because of insert imperfections since they are mostly handmade.

For this reason, our efforts were concentrated into developing a sizing approach based on the F.E. method with the objective of obtaining accurate results without being too complicated for its implementation. This consisted of the development of failure mode maps created after several 3D simulations of insert pull-out tests. And considering the high complexity of all the involved tasks, we dedicated the entire chapter five to this subject.

The study begun with an identification and analysis of the most common insert's defects. As result, we identified that only two unavoidable defects were important enough to be considered for the insert design, which were the irregular borders of the insert and the variation of the potting shape.

Then, two recommendations were provided to include these defects in the pull-out load calculation:

For the potting's irregular borders, the cells surrounding the insert are weakened. Therefore, their shear strength should be equal or slightly lower than the value specified by the manufacturer. It's important to remark that this may seem contradictory to what was observed in chapter two, but the difference is the potting borders, which were very regular for the specimens of chapter two.

As for the variation of the potting shape, the evidence shows that a good estimation of an average size value is obtained by considering the Real Potting Radius (RPR), which is defined by the ESA and the coefficients issue of our research. Moreover, our evidence suggests that the Effective Potting Radius (RPR), proposed by the ESA too, exaggerates the insert equivalent size, thus, using it leads to errors.

Then, the modeling of three different types of inserts was made using Abaqus standard. For the potting, the study and modeling developed in the chapter four, and the RPR approach of the ESA were considered. As for the honeycomb core, the modeling was made using the proposed approach of chapter two and ref. [14]. Finally, for the skins, the strength values for the in-plane and transversal failures provided by the manufacturer were used, and the damage evolution approach proposed by Bunyawanichakul (in its PhD thesis) was used to model the matrix failure. It's important to remark that a specific investigation on this topic is necessary and should be performed as a perspective for this research.

These simplifications allowed to perform accurate nonlinear simulations and reducing the calculation time to 12 min.

Then, the loading curves of the simulations of an insert without defects (the best case), but also full of defects (worst case) were compared against the experimental curves. The results were that the experimental curves were inscribed within the area formed by the best and worst cases. Also, the failure modes were very similar.

Naturally, the correlation of the numerical and experimental results was obtained after several hypotheses. The only way to fully validate this F.E. model, is by performing more tests of inserts with different radius and materials.

Finally, the F.E. model was parametrized using Abaqus Python, this allowed to change the properties and geometry in a very easy way. Of course, this was useful to develop the failure mode maps.

Then, a total of 100 simulations were performed, and for each one, the principal failure modes: core shear failure, potting failure and skin's failure were detected. After this, the failure modes were used to trace 3D surfaces as function of the potting radius, the potting traction's resistance, and the skin thicknesses. The bottom view of these surfaces were the failure mode maps that we were looking for since the beginning.

These charts were specific for the materials that we used for our simulations. Nevertheless, the same method could be used to obtain failure mode maps with other materials or geometries. These charts could be very useful for engineers since they compress the accurate results based in F.E. simulations, into a simple 2D chart.

Also, it was shown that, in terms of mass optimization, the insert size and potting material should be chosen to resist the required pull-out strength.

Further work can be performed using this research as staring point. Some of these perspectives are listed as follows:

- Even if it's apparently one of the main causes for the water entry into sandwich panels, the microcracking formation of inserts under fatigue is not well studied since there are almost no publications about this. Given its importance, a proper study should be performed.

- After some discussions with international researchers, we detected that, the development of a reduced modeling technique for honeycomb cores, including simultaneously both compression and shear nonlinear behaviors, could be very interesting for industry because it will allow reducing the complexity and simulation time of sandwich panels. The most difficult aspect should be the coupling of the nonlinear behaviors, which probably requires experimentation and modeling.

- The study of the SPF was only made experimentally for the traction and compression cases, but not for the shear behavior. This last aspect could be interesting to be studied since it combines both traction and compression simultaneously and in our brief bibliographical research we didn't find any reference about this. Thus, it could be interesting for the scientific community.

- The skin's damage evolution used for the insert specimens needs to be studied in detail. Especially for the in-plane shear damage, which apparently is predominant when an insert pull out tests is performed.

- The insert F.E. model used to develop the failure mode maps was compared against the experimental results of only three different insert types. Therefore, a full validation is still necessary by comparing it to more tests using different size of inserts and materials.

References

[1] European Space Agency, “ECSS-E-HB-32-22A: Insert Design Handbook,” no. March. p. 488, 2011.

[2] Departement of defense USA, “MIL-HDBK-23A.pdf.” 1974.

[3] W. S.; F. P. L. Ericksen, “The Bending of a Circular Sandwich Plate Under Normal Load,” 1953.

[4] J. Wolff, M. Brysch, and C. Hühne, “Validity check of an analytical dimensioning approach for potted insert load introductions in honeycomb sandwich panels,” *Compos. Struct.*, vol. 202, no. May, pp. 1195–1215, May 2018.

[5] D.Zenkert, *The handbook of sandwich construction*. London: Emas, 1997.

[6] S. Abrate, B. Castanié, and Y. D. S. Rajapakse, *Dynamic Failure of Composite and Sandwich Structures*, vol. 192. Springer Netherlands, 2013.

[7] J. E. Shafizadeh, J. C. Seferis, E. F. Chesmar, and R. Geyer, “Evaluation of the in-service performance behavior of honeycomb composite sandwich structures,” *J. Mater. Eng. Perform.*, vol. 8, no. 6, pp. 661–668, 1999.

[8] P. Bunyawanichakul, B. Castanie, and J. J. Barrau, “Experimental and numerical analysis of inserts in sandwich structures,” *Appl. Compos. Mater.*, vol. 12, no. 3–4, pp. 177–191, 2005.

[9] J. Zhang, M. F. Ashby, C. Ei, G. G12, G. Gs, and L. Peril, “THE OUT-OF-PLANE PROPERTIES OF HONEYCOMBS,” *Int. J. Mech. Sci*, vol. 34, no. 6, pp. 475–189, 1992.

[10] L. J. Gibson and M. F. Ashby, *Cellular solids: Structure and properties, second edition*, vol. 28. Cambridge: Cambridge University Press, 2014.

[11] R. Seemann and D. Krause, “Numerical modelling of partially potted inserts in honeycomb sandwich panels under pull-out loading,” *Compos. Struct.*, vol. 203, no. June, pp. 101–109, 2018.

[12] R. Seemann and D. Krause, “Numerical modelling of Nomex honeycomb sandwich cores at meso-scale level,” *Compos. Struct.*, vol. 159, pp. 702–718, 2017.

[13] J. de D. Rodriguez-Ramirez, B. Castanie, and C. Bouvet, “Experimental and numerical analysis of the shear nonlinear behaviour of Nomex honeycomb core: Application to insert sizing,” *Compos. Struct.*, vol. 193, no. March, pp. 121–139, 2018.

[14] J. de D. Rodríguez-Ramírez, B. Castanié, and C. Bouvet, “Damage Mechanics Modelling of the shear nonlinear behavior of Nomex honeycomb core. Application to sandwich beams,” *Mech. Adv. Mater. Struct.*, vol. 6494, pp. 1–10, 2018.

[15] Phacharaporn BUNYAWANICHAKUL, “Contribution à l’étude du comportement des inserts dans les structures sandwichs composites,” École Nationale Supérieure de l’Aéronautique et de l’Éspace, 2005.

[16] Boeing, “Boeing: 787 Low Fuel Consumption,” *2015*. [Online]. Available: http://www.boeing.com/commercial/787/#/design-highlights/exceptional-value/lower-fuel-consumption/. [Accessed: 07-Apr-2015].

[17] Boeing, “The Boeing 787 Dreamliner: More than an Airplane.” pp. 1–29, 2005.

[18] S. Abrate, “Localized Impact on Sandwich Structures With Laminated Facings,” *Appl.*

Mech. Rev., vol. 50, no. 2, p. 69, 1997.

[19] T. Bitzer, *Honeycomb Technology: Materials, Design, Manufacturing, Applications And Testing*. London: Chapman & Hall, 1997.

[20] Boeing, "Boeing: Boeing's Satellite Family," *2015*. [Online]. Available: http://www.boeing.com/space/boeing-satellite-family/. [Accessed: 12-May-2015].

[21] Boeing, "Boeing: Space Launch System," *2015*. [Online]. Available: http://www.boeing.com/space/space-launch-system/. [Accessed: 12-May-2015].

[22] C. BINÉTRUY, "Structures sandwiches," *Tech. l'ingénieur Matériaux Compos. présentation renforts*, no. ref. article : am5141, 2008.

[23] D. Gay, *Composite Materials: Design and Applications, Third Edition*. CRC Press, 2014.

[24] B. Solitario, "AEM / S Stepping Stone To Stealth," 2003. [Online]. Available: https://calhoun.nps.edu/bitstream/handle/10945/53709/AEMS_Stepping_Stone_to_Stealth.pdf?sequence=1&isAllowed=y. [Accessed: 08-Dec-2018].

[25] G. BLACHERE, R. LAMBERTI, and J. M. BERTHIER, "A survey of composite structure technology at the aerospatiale helicopter division," *Aerosp. Helicopter Div. Marignane, Fr.*, pp. 1–12.

[26] J. Wolff, "Application of analytical formulation for strength prediction of orthogonal loaded, cold bonded insert load introductions in sandwich elements," in *ICCS 20*, 2017.

[27] J. W. Lim and D. G. Lee, "Development of the hybrid insert for composite sandwich satellite structures," *Compos. Part A Appl. Sci. Manuf.*, vol. 42, no. 8, pp. 1040–1048, 2011.

[28] N. Raghu, M. Battley, and T. Southward, "Strength Variability of Inserts in Sandwich Panels," *J. Sandw. Struct. Mater.*, vol. 11, no. 6, pp. 501–517, 2009.

[29] O. T. Thomsen, "Sandwich plates with 'through-the-thickness' and 'fully potted' inserts: evaluation of differences in structural performance," *Compos. Struct.*, vol. 40, no. 2, pp. 159–174, 1997.

[30] O. T. Thomsen and W. Rits, "Analysis and design of sandwich plates with inserts—a high-order sandwich plate theory approach," *Compos. Part B Eng.*, vol. 29, no. 6, pp. 795–807, Nov. 1998.

[31] B. Smith and B. Banerjee, "Reliability of inserts in sandwich composite panels," *Compos. Struct.*, vol. 94, no. 3, pp. 820–829, 2012.

[32] S. Slimane, S. Kebdani, A. Boudjemai, and A. Slimane, "Effect of position of tension-loaded inserts on honeycomb panels used for space applications," *Int. J. Interact. Des. Manuf.*, pp. 1–16, 2017.

[33] R. Roy, K. H. Nguyen, Y. B. Park, J. H. Kweon, and J. H. Choi, "Testing and modeling of Nomex^{TM} honeycomb sandwich Panels with bolt insert," *Compos. Part B Eng.*, vol. 56, pp. 762–769, 2014.

[34] R. Seemann and D. Krause, "Virtual Testing of Nomex Honeycomb Sandwich Panel Inserts," in *20th International Conference on Composite Materials*, 2015, no. July, pp. 19–24.

[35] S. Heimbs and M. Pein, "Failure behaviour of honeycomb sandwich corner joints and inserts," *Compos. Struct.*, vol. 89, no. 4, pp. 575–588, 2009.

[36] P. Bunyawanichakul, B. Castanié, and J.-J. J. Barrau, "Non-linear finite element analysis of inserts in composite sandwich structures," *Compos. Part B Eng.*, vol. 39, no. 7–8, pp. 1077–1092, Oct. 2008.

[37] ESA PSS-03-1202 Issue 1, European Space Agency PSS-03-1202 Issue1, and ESA PSS-

03-1202 Issue 1, *Insert design handbook*, no. March. 1987.

[38] J. Wolff, F. Trimpe, R. Zerlik, A. Systems, and V. Materials, "Evaluation of an Analytical Approach Predicting the Transversal Failure Load of Insert Connections in Sandwich Structures," no. July, pp. 19–24, 2015.

[39] Y. Bin Park, J. H. Kweon, and J. H. Choi, "Failure characteristics of carbon/BMI-Nomex sandwich joints in various hygrothermal conditions," *Compos. Part B Eng.*, vol. 60, pp. 213–221, 2014.

[40] K.-I. Song, J.-Y. Choi, J.-H. Kweon, J.-H. Choi, and K.-S. Kim, "An experimental study of the insert joint strength of composite sandwich structures," *Compos. Struct.*, vol. 86, no. 1–3, pp. 107–113, 2008.

[41] G. Bianchi, G. S. Aglietti, and G. Richardson, "Static performance of hot bonded and cold bonded inserts in honeycomb panels," *J. Sandw. Struct. Mater.*, vol. 13, no. 1, pp. 59–82, 2011.

[42] SHUR-LOK company, "Shur-Lok." [Online]. Available: http://www.shur-lok.com/. [Accessed: 20-May-2015].

[43] SHUR-LOK company, "Fasteners for Sandwich Structure Catalog." 1999.

[44] B. J. Kim and D. G. Lee, "Characteristics of joining inserts for composite sandwich panels," *Compos. Struct.*, vol. 86, no. 1–3, pp. 55–60, 2008.

[45] SHUR-LOK company, "Advanced Composites Catalog." 1999.

[46] SHUR-LOK company, "Design Manual Fasteners for Sandwich Structure." 1999.

[47] Hexcel, "HRH-78 Nomex Comercial grade honeycomb Product data." Hexcel, pp. 6–9, 1998.

[48] P. Kumsantia, B. Castanié, and P. Bunyawanichakul, "An investigation of failure scenario of the metallic insert in sandwich structures," in *The First TSME International Conference on Mechanical Engineering*, 2010.

[49] L. Mezeix, S. Dols, C. Bouvet, B. Castanié, J.-P. Giavarini, and N. Hongkarnjanakul, "Experimental analysis of impact and post-impact behaviour of inserts in Carbon sandwich structures," *J. Sandw. Struct. Mater.*, p. 109963621668758, 2017.

[50] H. M. Montrey, "Bending of a Circular Sandwich Plate by Load Applied Through an Insert." U.S. DEPARTMENT OF AGRICULTURE, p. 31, 1973.

[51] O. T. Thomsen, "Theoretical and experimental investigation of local bending effects in sandwich plates," *Compos. Struct.*, vol. 30, no. 1, pp. 85–101, 1995.

[52] ANDRE. S., "Synthèse du programme d'évaluation d'inserts fortes épaisseurs pour application RTM," *La recherche aérospatiale*. 1996.

[53] J. Block and M. Lambert, "Study on Carbon Fibre Tube Insert summary Report," 2004.

[54] DuPont, "Nomex Brand ® | DuPont™ | DuPont USA." [Online]. Available: http://www.dupont.com/products-and-services/personal-protective-equipment/thermal-protective/brands/nomex.html. [Accessed: 28-Mar-2018].

[55] DuPont, "DuPont™ Nomex® 410." 2016.

[56] R. Roy, S. J. Park, J. H. Kweon, and J. H. Choi, "Characterization of Nomex honeycomb core constituent material mechanical properties," *Compos. Struct.*, vol. 117, no. 1, pp. 255–266, 2014.

[57] T. Wierzbicki, "Crushing analysis of metal honeycombs," *Int. J. Impact Eng.*, vol. 1, no. 2, pp. 157–174, 1983.

[58] R. K. MC FARLAND, "Hexagonal Cell Structures Under Post-Buckling Axial Load,"

AIAA J., vol. 1, no. 6, pp. 1380–1385, 1963.

[59] F. Nazzi, "The hexagonal shape of the honeycomb cells depends on the construction behavior of bees," *Sci. Rep.*, vol. 6, 2016.

[60] F. H. C. Fischer and A. Hauffe and K. Wolf, "Influence of Imperfections on the Structural Behaviour of Honeycomb Cores," *ECCM17 - 17th Eur. Conf. Compos. Mater. Munich, Ger. 26-30th June 2016* , no. June, pp. 26–30, 2016.

[61] J. P. Menachem Lewin, *Handbook of Fiber Science and Technology Volume 2: High Technology Fibers*. 1993.

[62] C. Chiang Foo, G. Boay Chai, and L. Keey Seah, "Mechanical properties of Nomex material and Nomex honeycomb structure," *Compos. Struct.*, 2007.

[63] S. Fischer, K. Drechsler, S. Kilchert, and A. Johnson, "Mechanical tests for foldcore base material properties," *Compos. Part A Appl. Sci. Manuf.*, vol. 40, no. 12, pp. 1941–1952, Dec. 2009.

[64] J. D. Fuller and M. R. Wisnom, "Pseudo-ductility and damage suppression in thin ply CFRP angle-ply laminates," *Compos. Part A Appl. Sci. Manuf.*, vol. 69, pp. 64–71, 2015.

[65] S. Heimbs, "Virtual testing of sandwich core structures using dynamic finite element simulations," *Comput. Mater. Sci.*, vol. 45, no. 2, pp. 205–216, Apr. 2009.

[66] S. Kelsey, R. A. Gellatly, and B. W. Clark, "The Shear Modulus of Foil Honeycomb Cores," *Aircr. Eng. Aerosp. Technol.*, vol. 30, no. 10, pp. 294–302, 1958.

[67] ASTM International, *ASTM C393/C 393 M - 06 Standard Test Method for Core Shear Properties of Sandwich Constructions by Beam Flexure*, vol. i. 2009, pp. 1–8.

[68] M. Giglio, A. Manes, and A. Gilioli, "Investigations on sandwich core properties through an experimental–numerical approach," *Compos. Part B Eng.*, vol. 43, no. 2, pp. 361–374, Mar. 2012.

[69] ASTM International, "C273 (2000) Standard test method for shear properties of sandwich core materials," *ASTM, West Conshohocken*, vol. 15, pp. 1–4, 2000.

[70] HexWeb, "HexWeb Honeycomb Attributes and Properties." 1999.

[71] G. Bianchi, G. S. Aglietti, G. Richardson, G. Bianchi, G. S. Aglietti, and G. Richardson, "Static and Fatigue Behaviour of Hexagonal Honeycomb Cores under In-plane Shear Loads," *Appl Compos Mater*, vol. 19, pp. 97–115, 2012.

[72] S. D. Pan, L. Z. Wu, Y. G. Sun, Z. G. Zhou, and J. L. Qu, "Longitudinal shear strength and failure process of honeycomb cores," *Compos. Struct.*, vol. 72, no. 1, pp. 42–46, 2006.

[73] ASTM International, "ASTM C273 Shear Fixture for Sandwich Cores | GC273-193," *Annu. B. ASTM Stand.*

[74] A. J. Hodge and A. T. Nettles, "A novel method of testing the shear strength of thick honeycomb composites," *NASA Technical Paper 3108*. 1991.

[75] L. Gornet, S. Marguet, and G. Marckmann, "Modeling of nomex honeycomb cores, linear and nonlinear behaviors," *Mech. Adv. Mater. Struct.*, vol. 14, no. 8, pp. 589–601, 2007.

[76] D. Asprone, F. Auricchio, C. Menna, S. Morganti, A. Prota, and A. Reali, "Statistical finite element analysis of the buckling behavior of honeycomb structures," *Compos. Struct.*, vol. 105, pp. 240–255, 2013.

[77] M. Giglio, A. Gilioli, and A. Manes, "Numerical investigation of a three point bending test on sandwich panels with aluminum skins and Nomex™ honeycomb core," *Comput. Mater. Sci.*, vol. 56, pp. 69–78, 2012.

[78] B. Castanié, C. Bouvet, Y. Aminanda, J. J. Barrau, and P. Thevenet, “Modelling of low-energy/low-velocity impact on Nomex honeycomb sandwich structures with metallic skins,” *Int. J. Impact Eng.*, vol. 35, no. 7, pp. 620–634, 2008.

[79] Y. Aminanda, B. Castanié, J.-J. Barrau, and P. Thevenet, “Experimental Analysis and Modeling of the Crushing of Honeycomb Cores,” *Appl. Compos. Mater.*, vol. 12, pp. 213–227, 2005.

[80] A. Kolopp, R. a. Alvarado, S. Rivallant, and C. Bouvet, “Modeling impact on aluminium sandwich including velocity effects in honeycomb core,” *J. Sandw. Struct. Mater.*, vol. 15, no. 6, pp. 733–757, 2013.

[81] Y. Tsujii, K. Tanaka, and Y. Nishida, “Analysis of Mechanical Properties of Aramid Honeycomb Core,” *Trans. Jap. Soc. Mech. Eng.*, vol. 61, no. 587, pp. 1608–1614, 1995.

[82] E. Bozhevolnaya, A. Lyckegaard, O. . T. Thomsen, and V. Skvortsov, “Local effects in the vicinity of inserts in sandwich panels,” *Compos. Part B Eng.*, vol. 35, no. 6–8, pp. 619–627, Sep. 2004.

[83] B. Castanié, Y. Aminanda, C. Bouvet, and J. J. Barrau, “Core crush criterion to determine the strength of sandwich composite structures subjected to compression after impact,” *Compos. Struct.*, vol. 86, no. 1–3, pp. 243–250, 2008.

[84] L. Liu, P. Meng, H. Wang, and Z. Guan, “The flatwise compressive properties of Nomex honeycomb core with debonding imperfections in the double cell wall,” *Compos. Part B Eng.*, vol. 76, pp. 122–132, 2015.

[85] E. J. Barbero, *Finite Element Analysis of Composite Materials using AbaqusTM*. 2013.

[86] E. M. Petrie, *Handbook of adhesived and sealants*. 2007.

[87] ASTM D638, “Standard test method for tensile properties of plastics,” *ASTM Int.*, vol. 08, pp. 46–58, 2015.

[88] ASTM International, “Standard Test Method for Compressive Properties of Rigid Plastics,” *Annu. B. ASTM Stand.*, pp. 1–8, 2008.

[89] ASTM International, “ASTM D 732 -02 Standard Test Method for Shear Strength of Plastics by Punch Tool,” pp. 1–4, 2010.

[90] M. Porfiri and N. Gupta, “Effect of volume fraction and wall thickness on the elastic properties of hollow particle filled composites,” *Compos. Part B*, vol. 40, pp. 166–173, 2008.

[91] N. Gupta, R. Ye, and M. Porfiri, “Comparison of tensile and compressive characteristics of vinyl ester/glass microballoon syntactic foams,” *Compos. Part B*, vol. 41, pp. 236–245, 2009.

[92] L. Bardella, F. Malanca, P. Ponzo, A. Panteghini, and M. Porfiri, “A micromechanical model for quasi-brittle compressive failure of glass-microballoons/thermoset-matrix syntactic foams,” *J. Eur. Ceram. Soc.*, vol. 34, no. 11, pp. 2605–2616, 2014.

[93] R. Huang and P. Li, “Elastic behaviour and failure mechanism in epoxy syntactic foams: The effect of glass microballoon volume fractions,” *Compos. Part B Eng.*, vol. 78, pp. 401–408, 2015.

[94] G. Nian, Y. Shan, Q. Xu, S. Qu, and Q. Yang, “Failure analysis of syntactic foams: A computational model with cohesive law and XFEM,” *Compos. Part B*, 2016.

[95] F. V Antunes, J. A. M. Ferreira, and C. Capela, “Numerical modelling of the Young’s modulus of syntactic foams,” *Finite Elem. Anal. Des.*, vol. 47, pp. 78–84, 2010.

[96] N. J. Mills, *Polymer Foams Handbook: Engineering and Biomechanics Applications and Design Guide*, no. April. 2007.

[97] E. Rizzi, E. Papa, and A. Corigliano, “Mechanical behavior of a syntactic foam: Experiments and modeling,” *Int. J. Solids Struct.*, vol. 37, no. 40, pp. 5773–5794, 2000.

[98] R. Seemann, “Virtual Testing of Composite Sandwich Structures in Aircraft Interior – an Industrial Case Study,” in *ECCM18 - 18th European Conference on Composite Materials*, 2018, no. June, pp. 24–28.

[99] R. Seemann and D. Krause, “Numerical modelling of nomex honeycomb cores for detailed analysis of sandwich panel joints,” *11th World Congr. Comput. Mech. (WCCM XI), fifth Eur. Conf. Comput. Mech. (ECCM V), sixth Eur. Conf. Comput. fluid Dyn. (ECFD VI)*, no. July, pp. 1–12, 2014.

[100] R. Heslehurst, *Defects and Damage in Composite Materials and Structures*. CRC Press, 2014.

[101] F. Pascal, P. Navarro, S. Marguet, and J. F. Ferrero, “On the modelling of low to medium velocity impact onto woven composite materials with a 2D semi-continuous approach,” *Compos. Struct.*, vol. 134, pp. 302–310, 2015.

[102] P. Navarro, J. Aubry, S. Marguet, J. F. Ferrero, S. Lemaire, and P. Rauch, “Semi-continuous approach for the modeling of thin woven composite panels applied to oblique impacts on helicopter blades,” *Compos. Part A Appl. Sci. Manuf.*, vol. 43, no. 6, pp. 871–879, 2012.

[103] T. C. Triantafillou and L. J. Gibson, “Failure mode maps for foam core sandwich beams,” *Mater. Sci. Eng.*, vol. 95, no. C, pp. 37–53, 1987.

[104] A. Petras and M. P. F. F. Sutcliffe, “Failure mode maps for honeycomb sandwich panels,” *Compos. Struct.*, vol. 44, no. 4, pp. 237–252, 1999.

[105] J. P. Vitale, G. Francucci, J. Xiong, and A. Stocchi, “Failure mode maps of natural and synthetic fiber reinforced composite sandwich panels,” *Compos. Part A*, vol. 94, pp. 217–225, 2017.

[106] E. W. Andrews and N. A. Moussa, “Failure mode maps for composite sandwich panels subjected to air blast loading,” *Int. J. Impact Eng.*, vol. 36, no. 3, pp. 418–425, 2009.

Annex A: Tables of the real potting radius for inserts

Tool radius [mm]	Avg eff. Radius [mm]	Avg filled cells (1/8)	Rb avg (1/8) [mm]	Min filled cells (1/8)	Rb min (1/8) [mm]	Max filled cells (1/8)	Rb max (1/8) [mm]
6.00	8.54	21.38	7.71	19.00	7.27	23.00	7.99
7.00	9.54	27.49	8.74	26.00	8.50	31.00	9.28
8.00	10.54	33.97	9.72	32.00	9.43	37.00	10.14
9.00	11.54	41.49	10.74	37.00	10.14	44.00	11.06
12.00	14.54	67.84	13.73	61.00	13.02	70.00	13.95
15.00	17.54	100.72	16.73	97.00	16.42	103.00	16.92
18.00	20.54	140.20	19.74	137.00	19.51	145.00	20.07
21.00	23.54	185.91	22.73	183.00	22.55	191.00	23.04
24.00	26.54	238.05	25.72	234.00	25.50	242.00	25.93

Table 28: Values of real potting radius b_r for Sc=1/8 inch cells size.

Tool radius [mm]	Avg eff. Radius [mm]	Avg filled cells (3/16)	Rb avg (3/16) [mm]	Min filled cells (3/16)	Rb min (3/16) [mm]	Max filled cells (3/16)	Rb max (3/16) [mm]
6.00	8.54	11.85	8.61	10.00	7.91	13.00	9.02
7.00	9.54	14.51	9.52	12.00	8.66	16.00	10.00
8.00	10.54	17.97	10.60	16.00	10.00	20.00	11.18
9.00	11.54	21.38	11.56	19.00	10.90	23.00	11.99
12.00	14.54	33.98	14.58	32.00	14.14	37.00	15.21
15.00	17.54	49.36	17.57	47.00	17.14	55.00	18.54
18.00	20.54	67.85	20.60	61.00	19.53	70.00	20.92
21.00	23.54	89.13	23.61	85.00	23.05	92.00	23.98
24.00	26.54	113.05	26.59	110.00	26.23	118.00	27.16

Table 29: Values of real potting radius b_r for Sc=3/16 inch cells size.

Tool radius	Avg eff. Radius [mm]	Avg filled cells (1/4)	Rb avg (1/4) [mm]	Min filled cells (1/4)	Rb min (1/4) [mm]	Max filled cells (1/4)	Rb max (1/4) [mm]
6.00	8.54	7.92	9.38	6.00	8.17	9.00	10.00
7.00	9.54	9.99	10.54	7.00	8.82	12.00	11.55
8.00	10.54	11.85	11.48	10.00	10.54	13.00	12.02
9.00	11.54	13.89	12.43	12.00	11.55	16.00	13.34
12.00	14.54	21.38	15.41	19.00	14.53	23.00	15.99
15.00	17.54	30.55	18.43	28.00	17.64	33.00	19.15
18.00	20.54	41.49	21.48	37.00	20.28	44.00	22.12
21.00	23.54	53.72	24.44	51.00	23.81	57.00	25.17
24.00	26.54	67.85	27.46	61.00	26.04	70.00	27.89

Table 30: Values of real potting radius b_r for Sc=1/4 inch cells size.

Tool radius	Avg eff. Radius [mm]	Avg filled cells (3/8)	Rb avg (3/8) [mm]	Min filled cells (3/8)	Rb min (3/8) [mm]	Max filled cells (3/8)	Rb max (3/8) [mm]
6.00	8.54	4.95	11.13	4.00	10.00	7.00	13.23
7.00	9.54	5.89	12.14	4.00	10.00	7.00	13.23
8.00	10.54	6.93	13.16	6.00	12.25	8.00	14.14
9.00	11.54	7.92	14.07	6.00	12.25	9.00	15.00
12.00	14.54	11.85	17.21	10.00	15.81	13.00	18.03
15.00	17.54	16.25	20.16	14.00	18.71	19.00	21.80
18.00	20.54	21.38	23.12	19.00	21.80	23.00	23.98
21.00	23.54	27.49	26.22	26.00	25.50	31.00	27.84
24.00	26.54	33.98	29.15	32.00	28.29	37.00	30.42

Table 31: Values of real potting radius b_r for Sc=3/8 inch cells size.

ScriptCells.m

This program used the function FillTests2.m to determine the number of filled cells using different hole's centers. It gives the average, minimal and maximal number of filled cells.

```
clc;
clear all;
close all;

Sc=3/8*25.4;            %Sice of cells
a=Sc/(3^0.5);           %Apothem of honeycomb cell
n=21;                   %Size n x n of the honeycomb sample
r=24;                    %Perforation tool radius


% % % Create honeycomb polygon
t = (0:1/6:1-1/6)'*2*pi;    %Angle steps for the hegagonal cells
x = a*cos(t);                    %Obtain x points for poligon centered in X0 and Y0
y = a*sin(t);                    %Obtain y points for poligon centered in X0 and Y0
polyhex= polyshape(x,y);%Create each polygon

%Create a grid

step=0.1;
px=[-0.5:step:0.5]*2*a;
py=[-0.5:step:0.5]*Sc;
[z,m]=size(px);
k=1;
for i=1:m
    for j=1:m
        Pin = isinterior(polyhex,px(i),py(j));
        if Pin == 1
            gp(k,:)= [px(i) py(j)];
            k=k+1;
        end
    end
end

plot(polyhex)
hold on
plot(gp(:,1),gp(:,2),'*b')
grid on
axis square

xp=gp(:,1);
yp=gp(:,2);
[z,m]=size(xp);

for i=1:z
% % %     figure
    [a(i)] = FillTest2(Sc,n,r,xp(i),yp(i));
end
```

```
[ts poly] = FillTest2(Sc,n,r,xp(1),yp(1));
% % % Plot circle
cstep=0.1;
t = [0:cstep:2*pi];
xc = r*cos(t);
yc = r*sin(t);
[ma,na]=size(xc);
an=na-1;
polyc= polyshape(xc(1:an),yc(1:an));

avg=sum(a,2)/z
min=min(a)
max=max(a)
plot(poly)
hold on
% plot(xp,yp,'*b')
% plot(polyc)
axis square
```

FillTest2.m

This program defines the function FillTests2.m to determine which cells are filled with potting when a hole is drilled into a honeycomb core.

```
function [nfc, poly] = FillTest2(Sc,n,r,X,Y)
% clc;
% clear all;
% close all;

% n=9;                    %Size n x n of the honeycomb sample in terms of cells
% Sc=1/8*25.4;            %Sice of cells
a=Sc/(3^0.5);           %Apothem of honeycomb cell
% r=9;                    %Perforation tool radius

% X=0;                    %X Placement of the tool (regarding the centroid of the honeycomb
sample)
% Y=0;                    %Y Placement of the tool (regarding the centroid of the honeycomb
sample)

an=1;                   %Initiate number of polygons

t = (0:1/6:1)'*2*pi;    %Angle steps for the hegagonal cells
for i=1:n
    for j=1:n
        b = mod(i,2);   %Decide if the cell is even or not
        if b>0          %Decide if the cell is even or not
            ne=0;
        else
            ne=1;
        end
        X0=1.5*a*(i-1)-0.5*(1.5*a*(n-1));   %Asign X0 for hexagon
        Y0=Sc*(j-1)+Sc/2*ne-Sc*(n-1)/2;     %Asign Y0 for hexagon
        x = a*cos(t)+X0;                    %Obtain x points for poligon centered in X0 and Y0
        y = a*sin(t)+Y0;                    %Obtain y points for poligon centered in X0 and Y0
        poly(an) = polyshape(x(1:6),y(1:6));%Create each polygon
        an=an+1;
% % %         hold on
    end
end
% % % plot(poly)
% % % hold on
% % % grid on
% % % axis square

cstep=0.1;
t = [0:cstep:2*pi];
xc = r*cos(t)+X;
yc = r*sin(t)+Y;
[ma,na]=size(xc);
an=na-1;
polyc= polyshape(xc(1:an),yc(1:an));
TF = overlaps(poly,polyc);
nfc=sum(TF,2);
```

```
[z,m]=size(TF);
t = (0:1/6:1)'*2*pi;    %Angle steps for the hegagonal cells
k=0;
for i=1:n
    for j=1:n
        k=k+1;
        if TF(k)==1
            b = mod(i,2);
            if b>0
                ne=0;
            else
                ne=1;
            end
            X0=1.5*a*(i-1)-0.5*(1.5*a*(n-1));
            Y0=Sc*(j-1)+Sc/2*ne-Sc*(n-1)/2;
            x = a*cos(t)+X0;
            y = a*sin(t)+Y0;
% % %             fill(x,y,'r');
            nfc(i,j)=1;
        end
    end
end
% % % plot(polyc)
nfc=sum(TF,2);
% % % plot(X,Y,'*b')
end
```

Résumé

Analyse du comportement non-linéaire d'inserts de structures sandwichs : application à une méthode de dimensionnement innovante.

Le dimensionnement des inserts pour les structures sandwich se fait usuellement par les méthodes proposées par le « Insert design handbook » de l'ESA, ou le « Military handbook 23A ». Ces méthodes analytiques basées sur la formulation développée par Ericksen en 1953 mènent à des erreurs de la charge admissible à l'arrachement d'environ ±20 % pour certains cas.

Dans cette thèse, les principaux modes de rupture d'inserts sont étudiés ; l'endommagement du nid d'abeille Nomex® en cisaillement et la rupture du potting.

Une analyse fine du postflambement en cisaillement du nid d'abeille Nomex® est effectuée qui permet de proposer un modèle d'endommagement à 2 paramètres.

Puis, les résultats obtenus sont utilisés pour développer un modèle virtuel d'insert qui est validé par comparaison à des essais d'arrachement puis utilisé pour tracer des cartographies des modes de rupture. En utilisant cette méthode, la charge admissible à l'arrachement peut être estimée plus précisément.

Cette méthode peut être une alternative face aux modèles analytiques pour le dimensionnement des inserts. Les graphiques obtenus peuvent être fournis aux ingénieurs pour le dimensionnement des inserts comme un outil qui peut réduire le temps de conception-validation.

Mots-clés : Structures Sandwich, Inserts, Nid d'abeille Nomex, E.F. non-linéaire

Abstract

Analysis of the nonlinear behavior of inserts in sandwich structures: application to an innovative sizing method.

The insert sizing for sandwich structures is usually made using the methods proposed in the "Insert design handbook" of the ESA and the "Military handbook 23A". These analytical methods based in the in the research carried by Ericksen in 1953 could lead to errors of the pull-out allowable load prediction in the range of ±20 % for some cases.

In this thesis, the principal failure modes of inserts are investigated; the core shear damage of the Nomex honeycomb core, and the potting failure.

A detailed analysis of the shear postbuckling of the Nomex honeycomb core is made, allowing to propose a two variables damage model.

Then, the obtained results are used to develop an insert virtual model that is validated through comparison with pull-out tests, and then used to draw failure mode maps of inserts. Using this method, the admissible pull-out load of inserts can be estimated more precisely.

This method could be an alternative to using the analytical methods for the insert sizing. The resulting charts could be given to engineers as a tool for the insert sizing which could reduce the insert's design-validation time.

Keywords: Sandwich Structures, Inserts, Nomex Honeycomb, nonlinear F.E.